

---

IRON LOSSES IN NON-ORIENTED STEEL  
SUBJECTED TO MATRIX AND DC-LINK  
CONVERTER SUPPLY.  
AN EXPERIMENTAL AND ANALYTICAL STUDY  
ON VARIABLE SPEED DRIVES.

---

BY JUAN SAGARDUY OCHOA DE ERIBE

THESIS FOR THE DEGREE  
OF DOCTOR OF PHILOSOPHY (PhD)

WOLFSON CENTRE FOR MAGNETICS  
CARDIFF SCHOOL OF ENGINEERING  
CARDIFF UNIVERSITY

OCTOBER 2009

UMI Number: U585313

All rights reserved

INFORMATION TO ALL USERS

The quality of this reproduction is dependent upon the quality of the copy submitted.

In the unlikely event that the author did not send a complete manuscript and there are missing pages, these will be noted. Also, if material had to be removed, a note will indicate the deletion.



UMI U585313

Published by ProQuest LLC 2013. Copyright in the Dissertation held by the Author.  
Microform Edition © ProQuest LLC.

All rights reserved. This work is protected against  
unauthorized copying under Title 17, United States Code.



ProQuest LLC  
789 East Eisenhower Parkway  
P.O. Box 1346  
Ann Arbor, MI 48106-1346

## ACKNOWLEDGEMENTS

---

I am indebted to Prof Anthony J Moses for his guidance during the PhD study. His advice and experience during my stay in Wales have been greatly appreciated.

I would like to thank Dr Fatih J. Anayi for his support and encouragement as second supervisor.

I would like to show my gratitude to Prof Jon Clare and Dr. Patrick W. Wheeler for giving me the chance to gather useful knowledge on matrix converter topology at the PEMC group at the University of Nottingham.

Sincere thanks go to Prof David Jiles for his drive and enthusiasm as Director of the Wolfson Centre for Magnetics.

My time at Cardiff could not have been successful without stimulating discussion with all Wolfson members, especially fellow PhD students. Thank you all!

The work carried out during this PhD study has been challenging. The company and joy brought by my wife Jinjiu, my daughter Maitane Tianrui and my son Daniel Wanming have made it a wonderful experience. My heart is always with you.

I would like to thank my parents Heliodoro and Mercedes, my brother Guillermo and sister Susana for the love and trust enjoyed during many years in my hometown Bilbao. Your constant support still remains essential to me.

A system approach to variable speed drives consisting of two low voltage induction motors (Y and  $\Delta$  connection) fed by matrix and two-level DC-link converters is developed (chapter 7). The ratio of iron to copper winding losses is studied based on the induction motor equivalent circuit and constant V/f converter control. Electrical efficiency increased by up to 10% (partial load and low speed) in Y-connected motors fed by the matrix converter. While similar values of efficiency were observed in  $\Delta$ -configured motors, up to 8% higher output power is extracted from the machines under two-level DC-link converter supply.

---

# INDEX

---

## ACKNOWLEDGEMENTS

## INDEX

## ABSTRACT

## CHAPTER 1. INTRODUCTION

1.1. PhD thesis contribution.....	1
1.2. Energy landscape .....	2
1.3. AC drives.....	3
1.3.1. Definition.....	3
1.3.2. Market.....	4
1.3.3. Potential energy savings.....	5
1.3.4. Efficiency in variable speed drives.....	6
1.4. Non-oriented electrical steel.....	7

## CHAPTER 2. NON-ORIENTED STEEL UNDER DIRECT/INDIRECT AC-AC CONVERTER EXCITATION

2.1. Introduction.....	12
2.2. Non-oriented steel.....	12
2.2.1. Applied electromagnetics theory.....	13
2.2.1a. Maxwell's equations.....	13
2.2.1b. Constitutive equations of the material.....	15
2.2.1c. Poynting vector.....	15
2.2.2. Magnetic losses.....	16
2.2.2a. Static hysteresis loss.....	16
2.2.2b. Classical eddy-current losses.....	17
2.2.2c. Excess losses.....	17
2.3. Matrix converters: direct AC-AC conversion topology.....	18
2.3.1. Description.....	18
2.3.2. Historical review.....	19
2.3.3. Bidirectional switch.....	20
2.3.3a. Hardware implementation.....	20
2.3.3b. Commutation scheme.....	21
2.3.4. Auxiliary equipment.....	21
2.3.5. Applications.....	22
2.4. Back-to-back converter.....	23
2.4.1. Description.....	23
2.4.2. Pulse-Width-Modulation [PWM].....	25
2.4.2a. PWM schemes.....	26
2.4.2b. Impact of PWM scheme on harmonic distortion.....	29
2.5. Mathematical formulae.....	35
2.5.1. Total harmonic distortion [THD].....	35
2.5.2. Frequency-weighted THD.....	35
2.5.3. Form factor.....	36
2.6. Summary.....	36

## CHAPTER 3. IRON LOSSES IN SOFT MAGNETIC MATERIALS: A SURVEY

3.1. Introduction.....	42
3.2. Fundamentals of losses in ferromagnetic materials.....	42
3.2.1. Weiss domains.....	42
3.2.2. Crystalline structure.....	43
3.2.3. Physics of magnetisation.....	43
3.2.4. Domain wall motion.....	44
3.3. Modelling losses in soft magnetic materials.....	46
3.3.1. Dynamic component.....	46
3.3.2. Pry and Bean model: rigid domain walls.....	46
3.3.3. Anomalous losses.....	47
3.3.4. Domain wall bowing.....	49
3.3.5. Statistical approach by Bertotti.....	51
3.3.5a. Concept.....	51
3.3.5b. Experimental validation.....	52
3.3.6. Linear frequency dependence.....	53
3.3.7. Domain wall interaction.....	54
3.3.8. Dynamic hysteresis model.....	54
3.4. Distorted magnetising conditions.....	56
3.4.1. Minor loops.....	57
3.4.2. Effect of PWM supply on iron losses.....	58
3.4.2a. Modulation index.....	58
3.4.2b. Switching frequency.....	59
3.4.2c. Analysis of losses.....	60
3.4.2d. Impact of full/half bridge inverter topologies.....	61
3.4.3. Magnetisation under square wave voltage.....	62
3.4.4. High frequency flux harmonics.....	63
3.4.5. Stator/rotor core of induction machines.....	63
3.4.5a. Loss increase under PWM supply.....	63
3.4.5b. Loss distribution in teeth and yoke.....	64
3.4.5c. Introduction of finite-element analysis.....	65
3.5. Rotational magnetisation.....	66
3.6. Iron loss calculation.....	67
3.6.1. Classical Steinmetz equation.....	67
3.6.2. Engineering approach.....	68
3.7. Efficiency in a PWM inverter-fed motor: an overview.....	70
3.8. Summary.....	72

## CHAPTER 4: EXPERIMENTAL PROCEDURE

4.1. Electrical steel characterisation.....	80
4.1.1. Laminations.....	80
4.1.2. 25cm Epstein frame.....	81
4.1.3. Single strip tester.....	82
4.2. Power converters and auxiliary equipment.....	83
4.2.1. Frequency converters.....	83
4.2.1a. Matrix converter.....	83
4.2.1b. Dc-link converter.....	84
4.2.2. Auxiliary equipment.....	85
4.2.2a. Power analyser.....	85
4.2.2b. Signal generator.....	86
4.2.2c. Digital oscilloscope.....	86

4.2.2d. Power amplifier.....	87
4.2.2e. Multi-meters.....	87
4.2.2f. Variable transformers.....	88
4.3. Losses under pulsating excitation (Epstein frame).....	88
4.3.1. Line-neutral matrix converter signals.....	88
4.3.2. Line-line DC-link converter signals.....	90
4.4. Modelling of direct and indirect AC-AC converters.....	93
4.4.1. Matrix converter.....	94
4.4.2. Two-level DC-link converter.....	97
4.5. Losses under pulsating excitation (Single Strip Tester).....	99
4.6. Analysis of experimental inaccuracy.....	100

## CHAPTER 5: MAGNETISATION OF NON-ORIENTED STEEL UNDER MATRIX CONVERTER EXCITATION: RESULTS AND DISCUSSION

5.1. Energy Flux: Poynting vector.....	107
5.1.1. Poynting vector and eddy-current losses.....	109
5.1.2. Linearity between magnetic field and induction.....	110
5.1.3. Non-linearity between magnetic field and induction.....	113
5.2. Analytical modelling of iron losses.....	117
5.2.1. Eddy-current loss.....	117
5.2.1a. Classical approach.....	117
5.2.1b. Eddy-current shielding effect.....	118
5.2.2. Iron loss model (non-linearity and shielding effect – NL+SE).....	124
5.2.2a. Coefficient determination (NL+SE).....	124
5.2.2b. Coefficient determination (Bertotti).....	126
5.3. Line-neutral supply (matrix converter).....	128
5.3.1. Total power losses.....	128
5.3.2. Eddy-current losses.....	132
5.3.3. Experimental benchmarking of (NL+SE) model.....	140
5.3.4. Sideband harmonic pattern in high clusters.....	148
5.3.4a. Matrix converter.....	148
5.3.4b. DC-link converter.....	153
5.4. Line-line supply (matrix converter).....	161
5.4.1. Total power losses.....	161
5.4.2. Harmonic distortion and form factor.....	165
5.5. Space-vector modulation [sampling frequency].....	169
5.5.1. Total power losses.....	169
5.5.2. Flux density and induced voltage.....	171
5.5.3. Eddy-current losses.....	177
5.6. Conclusions.....	180

## CHAPTER 6: POWER CONSUMPTION IN DC-LINK CONVERTER-FED INDUCTION MOTORS: AN EXPERIMENTAL STUDY

6.1. Description of goal and methodology.....	182
6.1.1. Motivation.....	182
6.1.2. Methodology.....	183
6.1.2a. Electrical parameter identification of induction motors.....	183
6.1.2b. Harmonic characterization of line-line voltage.....	185
6.1.2c. No-load measurements in the induction motors.....	185
6.1.2d. Loss segregation.....	186
6.1.2e. Calculation of stator core mass.....	187
6.1.2f. Determination of specific apparent power in stator core.....	189

6.2. Experimental procedure.....	191
6.2.1. Test bench.....	191
6.2.2. Induction motors.....	192
6.2.3. DC-link converters.....	194
6.2.3a. Toshiba Tosvert VF-A3.....	194
6.2.3b. ABB ACS140 standard 400V series.....	194
6.2.4. Power consumption (Toshiba converter supply).....	196
6.2.4a. Motor A.....	196
6.2.4b. Motor B.....	198
6.2.5. Power consumption (ABB converter supply).....	200
6.2.5a. Motor A.....	200
6.2.5b. Motor B.....	201
6.3. Peak flux density vs PWM modulation index.....	203
6.4. Conclusions.....	207
CHAPTER 7. DIRECT AC-AC CONVERSION TOPOLOGY: AN ANALYTICAL VIEW ON VARIABLE SPEED DRIVES	
7.1. Analytical procedure.....	209
7.1.1. Voltages typical of matrix / DC-link converters.....	209
7.1.2. Squirrel-cage induction motors.....	210
7.2. Efficiency.....	217
7.2.1. Line-neutral voltage (Y-configuration).....	217
7.2.2. Line-line voltage ( $\Delta$ -configuration).....	218
7.3. Ratio of iron to Joule losses.....	221
7.3.1. Line-neutral voltage (Y-configuration).....	221
7.3.2. Line-line voltage ( $\Delta$ -configuration).....	221
7.4. Conclusions.....	223
CONCLUSION AND FUTURE WORK.....	225
APPENDIX	
A1. Publications.....	
A1.1. J. Sagarduy, A.J. Moses, F.J. Anayi, "Eddy-Current Losses in Electrical Steels Subjected to Matrix and Classical PWM Excitation Waveforms", <i>IEEE Transactions on Magnetics</i> , Vol 42, No 10, pp 2818-2820.....	I
A1.2. J. Sagarduy, A.J. Moses, "Impact of Sideband Harmonic Pattern on Losses in Laminated Non-Oriented Steels", <i>Journal of Magnetism and Magnetic Materials</i> , in Press, April 2008.....	II
A1.3. J. Sagarduy, A.J. Moses, "Copper Winding Losses in Matrix Converter-Fed induction Motors: a Study Based on Skin Effect and Conductor Heating, 39 <sup>th</sup> IEEE Power Electronics Specialists Conference, Rhodes (Greece), pp 3192 -3198, 16-20 June 2008.....	III
A1.4. J. Sagarduy, A.J. Moses, F.J. Anayi, J. Clare, P.W. Wheeler, "Iron Losses under Voltage Excitation by Novel and Classical Frequency Converters", 12 <sup>th</sup> International Conference on Power Electronics and Motion Control EPE-PEMC, Portoroz (Slovenia), pp 131-136, Aug 2006.....	IV

A1.5. J. Sagarduy, A.J. Moses, F.J. Anayi, J. Clare, P.W. Wheeler, “Matrix vs Pulse-Width-Modulation Frequency Converters. Iron Losses under Pulsating Forms of Voltage Excitation”, *37<sup>th</sup> IEEE Power Electronics Specialists Conference*, Jeju island (South Korea), 16-20 June 2006.....V

A.1.6. J. Sagarduy, A.J. Moses, F.J. Anayi, “Effect of AC-AC Conversion Topology on Separation of Losses in Si-Fe Steel”, *10<sup>th</sup> Joint Magnetism and Magnetic Materials / InterMag Conference*, Baltimore (US), 7-11 Jan 2007.....VI

A.1.7. A.J. Moses, J. Sagrduy, “Impact of PWM and matrix converters on performance of Electrical Steel”, *UK Magnetics Society Seminar on Developments in Magnetic Materials*, QinetiQ Farnborough (UK), 25 April 2006.....VII

A.1.8. J. Sagarduy, A.J. Moses, F.J. Anayi, J. Clare, P. Wheeler, “Computational Technique for Modelling of Frequency Converters and Analysis of Generated Waveforms”, *6<sup>th</sup> International Conference on Computational Electromagnetics*, Aachen (Germany), 4-6 April 2006.....VIII

A.1.9. A.J. Moses, F. Anayi, J. Sagarduy, S. Zurek, “Additional Losses in Inverter-Driven Electrical Machines”, *2<sup>nd</sup> International Workshop on Magnetism and Metallurgy*, Freiberg (Germany), 21-23 June 2006.....IX

A.1.10. X. G. Yao, A. J. Moses, J. Sagarduy, F. J. Anayi, “Influence of Switching Frequency on Eddy-Current Losses in a Three-Phase, Three-Limb Transformer Core Subjected to PWM Voltage Excitation”, *Power Engineering Conference (POWERENG)*, Setubal (Portugal), pp 324-329, 12-14 April 2007.....X

A2. Modelica code for space-vector PWM simulation (Dymola).....XI

A3. Eupec IGBT modules for a matrix converter.....XII

A4. Specifications on the PM3000 power analyser.....XIII

A5. Specifications on the TTi TGA1230 signal generator.....XIV

A6. Specifications for the BK Electronics MXF900 power amplifier.....XV

A7. S-function code for space-vector-modulation of matrix converters.....XVI

A8. Technical data on 15kW and 3kW ABB induction motors.....XVII

## LIST OF FIGURES

Fig 1.1. Total and industrial electricity consumption [million GWh] in 006.....	3
Fig. 1.2. Segmentation of total motor energy consumption in the EU by industry applications.....	4
Fig. 1.3. British and European AC drives markets (2005).....	5
Fig. 1.4. Potential energy savings achievable by VSD in industry.....	5
Fig. 1.5. Potential energy savings achievable by VSD in the tertiary sector.....	6
Fig. 1.6. Potential energy savings in industry by type of load in VSD.....	6
Fig. 1.7. Potential energy savings in the tertiary sector by type of load in VSD.....	6
Fig. 1.8. Segmentation of world production of soft magnetic materials in terms of volume and value.....	8
Fig. 1.9. Segmentation of world steel export products between 2001 and 2005.....	9
Fig. 2.1. Simplified B-H curve of a material reaching saturation under sinusoidal magnetisation.....	16
Fig. 2.2. Simplified representation of a three-phase matrix converter .....	18
Fig. 2.3. Input and target output voltages without considering common-mode voltages.....	19
Fig. 2.4. Input and target output voltages (null output states of the converter).....	19
Fig. 2.5. Representation of a complete matrix converter.....	22
Fig. 2.6. Back-to-back converter based on diode-bridge rectifier circuit.....	23
Fig. 2.7. Back-to-back converter with active front-end rectifier .....	24
Fig 2.8. (a) symmetrical – (b) asymmetrical regular-sampled PWM .....	26
Fig 2.9. Line-neutral voltage (natural-sampling PWM) .....	29
Fig 2.10. Line-neutral voltage (asymmetrical regular sampled PWM).....	30
Fig 2.11. Line-neutral voltage (symmetrical regular sampled PWM).....	30
Fig 2.12. Line-neutral voltage (space-vector PWM).....	31
Fig 2.13. Load current in motor (15kW) - (natural-sampling PWM).....	32
Fig 2.14. Load current in motor (15kW) - (asymmetrical regular sampled PWM).....	33
Fig 2.15. Load current in motor (15kW) - (symmetrical regular sampled PWM).....	33
Fig 2.16. Load current in motor (15kW) - (space-vector PWM).....	34
Fig. 3.1. Simplified B-H curve with $B_s$ (induction at saturation), $H_s$ (magnetic field at saturation) and $B_r$ (retentivity), $H_c$ (coercive field).....	44
Fig. 3.2. Transition layer between two $180^\circ$ anti-parallel domains .....	45
Fig. 3.3. Variation of predicted and measured frequency-dependent losses with magnetising frequency in 3% grain-oriented steel.....	49
Fig. 3.4. Segmented domain wall subjected to bowing .....	49
Fig. 3.5. Variation of eddy-current losses with fundamental frequency in a triangular magnetising waveform .....	50
Fig. 3.6. B-H loop (minor loops caused by flux reversals in the induction wave-shape).....	57
Fig. 3.7. Dynamic B-H loops under voltage by (a) full (b) half-bridge inverter.....	62
Fig 3.8. Efficiency [%] for 4-pole induction motors of different rated power .....	71
Fig 3.9. Fraction of resistive (stator + rotor), iron, windage, friction and stray load losses in fully-loaded 4-pole induction motors of different rated power .....	72

Fig. 4.1. 25 cm Epstein frame .....	81
Fig. 4.2. Single strip tester [SST].....	82
Fig. 4.3. Matrix converter prototype [PEMC – University of Nottingham].....	84
Fig. 4.4. DC-link indirect converter [TOSHIBA –TOSVERT VF-A3].....	85
Fig 4.5. Universal power analyser (VOLTECH PM3000A).....	85
Fig. 4.6. TTi TGA 1230 signal generator.....	85
Fig. 4.7. Digital oscilloscope (YOKOGAWA DL716) .....	86
Fig. 4.8. BK Electronics MXF 900 power amplifier.....	86
Fig. 4.9. Multimeters CLARKE, TENMA and HEWLETT PACKARD.....	87
Fig. 4.10. Three-phase variable transformers A and B.....	88
Fig. 4.11. Experimental set-up for iron loss measurement in Epstein frame.....	89
Fig. 4.12. Preliminary set-up (matrix converter).....	89
Fig. 4.13. Variation of $THD$ [%] with modulation index $m_i$ in PC-generated line-line two-level PWM converter signals (50Hz).....	91
Fig. 4.14. Variation of form factor $FF$ with modulation index in PC-generated line-line two-level PWM converter signals (50Hz).....	91
Fig. 4.15. Correlation between $OV$ [%] and $m_i$ (50 Hz).....	92
Fig. 4.16. Equivalence between $OV$ [%] and $m_i$ (100 Hz).....	92
Fig. 4.17. Equivalence between $OV$ [%] and $m_i$ (200Hz).....	93
Fig. 4.18. Line-line output voltages in a three phase matrix converter (50 Hz).....	95
Fig. 4.19. Matlab-Simulink model used to generate matrix converter voltages.....	96
Fig 4.20. Line-line output voltages in a two-level DC-link PWM converter (50Hz).....	97
Fig. 4.21. Matlab-Simulink model used to generate voltages produced by a two-level PWM converter .....	98
Fig. 4.22. Variation of random signal and its rectified mean value over one minute.....	102
Fig. 4.23. Measurement accuracy [%] in M470-50A laminations (Epstein tester).....	103
Fig. 4.24. Measurement accuracy [%] in M530-50A laminations (Epstein tester).....	103
Fig. 4.25. Measurement accuracy [%] in M700-65A laminations (Epstein tester).....	104
Fig. 4.26. Measurement accuracy [%] in M470-50A laminations (SST).....	104
Fig. 4.27. Measurement accuracy [%] in M530-50A laminations (SST).....	105
Fig. 4.28. Measurement accuracy [%] in M700-65A laminations (SST).....	105
Fig. 5.1. System of coordinates and dimensions in a lamination of steel.....	108
Fig 5.2. Variation of the coefficient $\Gamma_{lin}$ with peak flux density (linear assumption) in steel laminations for three constant values of relative permeability.....	112
Fig 5.3. Variation of the coefficient $\Gamma_{non,lin}$ with peak flux density in steel laminations .....	114
Fig 5.4. Variation of $R$ [%] values with peak flux density in cases A, B and C.....	116
Fig. 5.5 $\alpha(y/d)$ in M470-50A, M530.50A and M700-65A laminations at $B_s = 1.0T$ (a) $f_n = 50$ Hz – (b) $f_n = 7.5$ kHz – (c) $f_n = 15$ kHz .....	120
Fig. 5.6. $\alpha(y/d)$ in M470-50A, M530-50A and M700-65A laminations at $B_s = 1.25T$ (a) $f_n = 50$ Hz – (b) $f_n = 7.5$ kHz – (c) $f_n = 15$ kHz .....	121
Fig. 5.7. $\alpha(y/d)$ in M470-50A, M530.50A and M700-65A laminations at $B_s = 1.5T$ (a) $f_n = 50$ Hz – (b) $f_n = 7.5$ kHz – (c) $f_n = 15$ kHz .....	122
Fig 5.8. Variation of $k$ with harmonic frequency $f_n$ at 1.0 T, 1.25 T and 1.5 T in (a) M470-50A – (b) M530-50A – (c) M700-65A laminations.....	123
Fig 5.9. Specific power losses $P$ [W/kg] in M470-50A subjected to matrix and two-level PWM excitation at (a) 50 Hz – (b) 100 Hz – (c) 200 Hz.....	129

Fig 5.10. Specific power losses $P$ [W/kg] in M530-50A subjected to matrix and two-level PWM excitation at (a) 50 Hz – (b) 100 Hz – (c) 200 Hz.....	130
Fig 5.11. Specific power losses $P$ [W/kg] in M700-65A subjected to matrix and two-level PWM excitation at (a) 50 Hz – (b) 100 Hz – (c) 200 Hz.....	131
Fig 5.12. Specific eddy-current losses $P_{ec}$ [W/kg] in M470-50A laminations at 50, 100 and 200 Hz and (a) $B_p = 1.0$ T – (b) $B_p = 1.25$ T – (c) $B_p = 1.5$ T.....	134
Fig 5.13. Specific eddy-current losses $P_{ec}$ [W/kg] in M530-50A laminations at 50, 100 and 200 Hz and (a) $B_p = 1.0$ T – (b) $B_p = 1.25$ T – (c) $B_p = 1.5$ T.....	135
Fig 5.14. Specific eddy-current losses $P_{ec}$ [W/kg] in M700-65A laminations at 50, 100 and 200 Hz and (a) $B_p = 1.0$ T – (b) $B_p = 1.25$ T – (c) $B_p = 1.5$ T.....	136
Fig 5.15. Eddy-current component [%] at $B_p = 1.5$ T and 50, 100 and 200 Hz in M470-50A – (b) M530-50A – (c) M700-65A laminations .....	139
Fig 5.16 Measured and estimated losses according to Bertotti’s approach and NLSE method in M470-50A under matrix converter magnetizing conditions .....	141
Fig 5.17 Measured and estimated losses according to Bertotti’s approach and the NLSE method in M470-50A under PWM (1.0) magnetizing conditions .....	141
Fig 5.18. Measured and estimated losses according to Bertotti’s approach and NLSE method in M470-50A under PWM (0.8) magnetizing conditions .....	142
Fig 5.19. Measured and estimated losses according to Bertotti’s approach and NLSE method in M470-50A under PWM (0.5) magnetizing conditions.....	142
Fig 5.20 Measured and estimated losses according to Bertotti’s approach and NLSE method in M530-50A under matrix converter magnetizing conditions.....	143
Fig 5.21. Measured and estimated losses according to Bertotti’s approach and NLSE in M530-50A laminations under PWM (1.0) magnetizing conditions.....	143
Fig 5.22. Measured and estimated losses according to Bertotti’s approach and NLSE method in M530-50A under PWM (0.8) magnetizing conditions.....	144
Fig 5.23. Measured and estimated losses according to Bertotti’s approach and NLSE method in M530-50A under PWM (0.5) magnetizing conditions.....	144
Fig 5.24. Measured and estimated losses according to Bertotti’s approach and NLSE method in M700-65A under matrix converter magnetizing conditions.....	145
Fig 5.25. Measured and estimated losses according to Bertotti’s approach and NLSE method in M700-65A under PWM (1.0) magnetizing conditions.....	146
Fig 5.26. Measured and estimated losses according to Bertotti’s approach and NLSE method in M700-65A under PWM (0.8) magnetizing conditions.....	146
Fig 5.27 Measured and estimated losses according to Bertotti’s approach and NLSE method in M700-65A laminations under PWM (0.5) magnetizing conditions.....	147
Fig 5.28. Line-neutral voltage from matrix converter at 50 Hz, 100 Hz and 200 Hz.....	148
Fig 5.29. Harmonic spectra of induced voltages and associated $THD$ [%] under line-neutral matrix converter excitation (50 Hz, 100 Hz, 200 Hz).....	150
Fig. 5.30. Harmonic spectra of induction and associated $THD$ [%] under line-neutral matrix converter excitation (50 Hz, 100 Hz, 200 Hz).....	152
Fig 5.31. Line-line voltages produced by DC-link converter under PWM indices 0.5, 0.8 and 1.0.....	154
Fig. 5.32. Harmonic spectra of induced voltages under DC-link converter excitation for modulation indices 0.5, 0.8 and 1.0 ( $f = 50$ Hz).....	155
Fig. 5.33. Harmonic spectra of induced voltages under two-level PWM converter excitation for modulation indices 0.5, 0.8 and 1.0 ( $f = 100$ Hz) .....	156
Fig. 5.34. Harmonic spectra of induced voltages under two-level PWM converter excitation for modulation indices 0.5, 0.8 and 1.0 ( $f = 200$ Hz) .....	157
Fig. 5.35. One cycle of magnetic induction under PWM line-line converter excitation for modulation indices 0.5 and 1.0 ( $f = 50$ Hz).....	158

Fig. 5.36. One cycle of magnetic induction under PWM line-line converter excitation for modulation indices 0.5 and 1.0 ( $f = 100$  Hz).....159

Fig. 5.37. One cycle of magnetic induction under PWM line-line converter excitation for modulation indices 0.5 and 1.0 ( $f = 200$  Hz).....159

Fig. 5.38. Specific power losses at 1.5T peak flux density and 50Hz, 100 Hz and 200 Hz in laminations subjected to line-line matrix converter and two-level PWM excitation.....162

Fig. 5.39. Incremental losses  $R$  [%] under line-line matrix and two-level PWM converter supply with respect to sinusoidal conditions (1.5 T peak flux density) .....164

Fig 5.40. Line-line voltage of a three-phase matrix converter at 5 kHz SVM sampling frequency (a) 50 Hz – (b) 100 Hz – (c) 200 Hz.....167

Fig 5.41. Line-line voltages produced by DC-link converter under PWM indices 0.5, 0.8 and 1.0.....168

Fig. 5.42. Variation of specific power losses  $P$  [W/kg] with SVM sampling frequency in laminations subjected to line-line matrix converter supply (1.5T) .....170

Fig 5.43. Harmonic spectra of induced voltages produced by the matrix converter and  $THD$  [%] at 50 Hz, 100 Hz and 200 Hz and 2.5 kHz sampling frequency in M700 – 65A laminations (1.5 T peak flux density).....172

Fig 5.44. Harmonic spectra of induced voltages produced by the matrix converter and  $THD$  [%] at 50 Hz, 100 Hz and 200 Hz and 5 kHz sampling frequency in M700 – 65A laminations (1.5T).....173

Fig 5.45. Harmonic spectra of induced voltages produced by the matrix converter and  $THD$  [%] at 50 Hz, 100 Hz and 200 Hz and 10 kHz sampling frequency in M700 – 65A laminations (1.5T).....174

Fig 5.46. One cycle of induction in M700-65A subjected to line-line matrix converter excitation Magnetising frequency: 50 Hz, 100 Hz and 200 Hz || SVM sampling frequency: 2.5 kHz, 5 kHz and 10 kHz.....176

Fig. 5.47. Variation of specific eddy-current losses  $P_{ec}$  [W/kg] in laminations subjected to line-line matrix converter excitation (1.5T).....178

Fig. 5.48. Proportion  $R_{ec}$  [%] of eddy-current losses in laminations subjected to line-line matrix converter excitation (1.5T) and magnetising frequencies 50, 100 and 200 Hz.....179

Fig 6.1 Graphic description of motor characterization.....184

Fig 6.2 Graphic description of no-load measurement in the induction motor.....186

Fig 6.3 Calculation of the mass of steel in the stator core.....188

Fig 6.4. Variation of normalised mass ratio ( $m^*_{fe}$ ) with base teeth diameter ( $d_x$ ).....189

Fig 6.5. Variation of specific apparent power  $s_{Fe}$  [VA/kg] with peak flux density (a) M400-50A (b) M680-50A.....190

Fig. 6.6. Experimental set-up with TOSHIBA VF-A3 inverter.....191

Fig. 6.7. Experimental set-up with ABB ACS 140 inverter.....192

Fig. 6.8. Induction motor A.....192

Fig. 6.9. Induction motor B.....193

Fig 6.10. ABB ACS 140.....195

Fig. 6.11. Frequency variation of modulation index .....195

Fig. 6.12. Variation of RMS current with line-line voltage in motor A supplied by TOSHIBA inverter.....196

Fig. 6.13. Variation of apparent/active power consumed with line-line voltage in motor A under supply by TOSHIBA inverter at (a) 50 Hz – (b) 75 Hz .....197

Fig. 6.13. Variation of apparent and active power consumed with RMS voltage in motor A under supply by TOSHIBA inverter at (c) 100 Hz – (d) 150 Hz .....198

Fig. 6.14. RMS current in motor B under supply by TOSHIBA inverter.....199

---

Fig. 6.15. Apparent and active power consumed by motor B under supply by TOSHIBA inverter at (a) 50 Hz – (b) 75 Hz.....	199
Fig. 6.16. Apparent and active power consumed by motor B under supply by TOSHIBA inverter at 100 Hz.....	200
Fig 6.17. (a) Active power P [W] and apparent power S [VA] - (b) RMS current in motor A supplied by the ABB ACS 140 converter.....	201
Fig 6.18. Frequency variation of (a) active (b) apparent power consumed by motor B with frequency under supply by the ABB ACS 140 converter .....	202
Fig 6.19. Frequency variation of (a) RMS current in motor B under supply by the ABB ACS 140 converter.....	203
Fig 6.20. Relation between average peak flux density and modulation index in motor A under supply by Toshiba inverter.....	205
Fig 6.21. Relation between average peak flux density and modulation index in motor B under supply by Toshiba inverter.....	206
Fig 6.22. Relation between average peak flux density and modulation index in motors A and B under supply by ABB ACS 140 converter.....	207
Fig 7.1. Difference in <i>THD</i> [%] between DC-link and matrix converter (a) line-line - (b) line-neutral voltages.....	211
Fig 7.2. Per-phase equivalent circuit of the induction motor.....	214
Fig 7.3. $\Delta$ and Y configurations for simulating platform.....	216
Fig 7.4. Efficiency in star-connected (line-neutral supply) motors I and II.....	219
Fig. 7.5. Efficiency in delta-connected (line-line supply) motors I and II.....	220
Fig 7.6. Ratio of iron to copper winding losses in motors I and II under delta and star configurations.....	222

## LIST OF TABLES

Table 1.1. Growth in AC drives markets (2002 - 2005) .....	4
Table 4.1. Dimensions & properties of M470-50A/M530-50A/M700-65A laminations.....	81
Table 4.2. Resistance and inductance in Epstein frame windings.....	81
Table 4.3. Resistance of primary / secondary windings of variable transf A and B .....	88
Table 4.4. Accuracy in active power measurements as % of the reading.....	90
Table 4.5. Accuracy in current measurements as a % of the reading.....	90
Table 5.1. Relative permeability at $B_{s,lin} = 1.05T - 1.15T - 1.25T$ (linear assumption).....	111
Table 5.2. Relative permeability for M470-50A, M530-50A and M700-65A for peak surface induction within 0.1 T and 1.6 T (50 Hz) .....	113
Table 5.3. Relative permeability at 1.0 T, 1.25 T and 1.5 T in three materials .....	119
Table 5.4 Eddy-current coefficient $k_e^*$ in M470-50A laminations.....	125
Table 5.5 Eddy-current coefficient $k_e^*$ in M530-50A laminations.....	126
Table 5.6. Eddy-current coefficient $k_e^*$ in M700-65A laminations.....	126
Table 5.7. Hysteresis coefficient $k_h^*$ in the three materials.....	126
Table 5.8. Hysteresis, classical eddy-current and anomalous losses associated to the three materials (Bertotti's statistical approach).....	127
Table 5.9. Values of $\lambda$ [%] in M470-50A laminations at 50, 100 and 200 Hz.....	132
Table 5.10. Values of $\lambda$ [%] in M530-50A laminations at 50, 100 and 200 Hz.....	132
Table 5.11. Values of $\lambda$ [%] in M700-65A laminations at 50, 100 and 200 Hz.....	132
Table 5.12. Values of $\bar{\lambda}$ [%] in laminations at 50, 100 and 200Hz.....	132
Table 5.13. Values of $\lambda_{ec}$ [%] in M470-50A laminations at 50, 100 and 200Hz.....	133
Table 5.14. Values of $\lambda_{ec}$ [%] in M530-50A laminations at 50, 100 and 200Hz.....	137
Table 5.15. Values of $\lambda_{ec}$ [%] in M700-65A laminations at 50, 100 and 200Hz.....	137
Table 5.16. $fwTHD$ [%] values of flux density in laminations at 1.5T .....	151
Table 5.17. Form factor values of flux density in laminations at 1.5T.....	153
Table 5.18. $THD$ [%] values in M700-65A laminations under PWM supply (1.5T).....	160
Table 5.19. $THD$ [%] values in M700-65A laminations under PWM supply (1.5T).....	160
Table 5.20. $THD$ [%] and form factor values in M470-50A laminations (1.5T).....	165
Table 5.21. $THD$ [%] and form factor values in M530-50A laminations (1.5T).....	165
Table 5.22. $THD$ [%] and form factor values in M700-65A laminations (1.5T).....	165
Table 5.23. $THD$ [%] and $fwTHD$ [%] of induction (1.5T peak flux density).....	166
Table 5.24. $THD$ [%] in M700-65A laminations at 2.5, 5 and 10 kHz SVM sampling frequency (1.5T peak flux density).....	175
Table 5.25. Values of $\nu_{ec}$ [%] in laminations at 50, 100 and 200Hz (1.5T).....	177
Table 5.26. Values of $\nu_{ec}$ [%] in laminations at 50, 100 and 200 Hz (1.5T).....	177
Table 6.1. Characteristics of motor A.....	192
Table 6.2. Characteristics of motor B.....	193
Table 6.3. Experimental measured voltages and currents in the locked rotor test .....	193
Table 6.4. Equivalent circuit parameters for the motors A and B .....	193
Table 6.5. Correlation between $OV$ [%] and $U_{RMS}$ [V] (TOSHIBA – motor A).....	194
Table 6.6. Correlation between $OV$ [%] and $U_{RMS}$ [V] (TOSHIBA – motor B).....	194
Table 6.7. Characteristics of ABB ACS 140.....	195

---

Table 6.8. Geometry parameters of induction motors a and B.....	203
Table 6.9. Deep groove single row bearings used in motors A and B.....	203
Table 6.10. Power losses in motors A/B caused by mechanical friction in bearings.....	204
Table 6.11. Specific apparent power $s_{fe}$ [VA/kg] in motors A/B (Toshiba inverter).....	204
Table 6.12. Specific apparent power $s_{fe}$ [VA/kg] in motors A/B (Toshiba inverter).....	204
Table 6.13. Specific apparent power $s_{fe}$ [VA/kg] in motors A/B (ABB inverter).....	206
Table 7.1. Specifications of the induction motors I and II.....	212
Table 7.2. Parameters of the equivalent circuit in motors I and II.....	214
Table 7.3. Difference in efficiency in motors I and II caused by line-neutral supply from matrix or DC-link converters .....	217
Table 7.4. Difference in efficiency in motors I and II caused by line-line supply from matrix or DC-link converters .....	218

## INTRODUCTION

---

### ***1.1 PhD thesis contribution***

The first goal of this PhD thesis is to measure iron losses in non-oriented electrical steel subjected to magnetisation by line-neutral and line-line voltages characteristic of matrix converters. Apart from the novelty of the task, experimental results are analysed by the means of a new modelling approach of iron losses in laminated steel. Shielding effect due to peripheral eddy-currents as well as non-linearity between magnetic field and induction are taken into account explicitly in the calculation of eddy current losses in the material. For that purpose, an equation with only two components (static hysteresis and eddy-current losses) is formulated.

The second goal of this PhD thesis is contextualise iron losses (previously analysed from an experimental and theoretical perspective) in a variable speed drive consisting a two-level PWM converter and an induction motor. A procedure aiming at establishing the analytical relation between motor control (pulse-width modulation index) and average peak flux density in the stator core is proposed. While real physical phenomena are accounted for by experimental loss measurements, the pragmatism of the approach (use of reliable technical information available, analysis based on well-known motor theory) is not compromised. The method, which targets engineers working in industry as well as academics with interest on power electronics and electrical steels, is consistent with an increasing demand on more energy efficient industrial processes.

The third goal of the PhD thesis is to build up a simulation platform to evaluate matrix converters as potential AC-AC links versus conventional two-level indirect frequency converters. The study, which puts emphasis on efficiency and on the proportion of copper and iron losses in the induction motors under wide range of speed and torque operating conditions, also takes into consideration the output power delivered by the machine under Y or  $\Delta$  connections.

## **1.2 Energy landscape**

Energy demand is expected to increase significantly in the next 25 years. In Europe and North America, this growth will remain moderate but vital to ensure prosperity and welfare in well-established economies. In countries like China, India, Brazil or Mexico, the rise in energy consumption owing to developing industrial and tertiary sectors will become a major drive in the fast-changing energy market. As a result of geopolitical instability of main suppliers of fossil-fuel energy (oil, gas) and environmental concerns (CO<sub>2</sub> emissions), energy of renewable sources (solar, wind, tidal) is bound to play an important role due to environmental friendliness and no-limitation of supply. Despite cost-effectiveness, nuclear power is not widely accepted by public opinion and brings out the problem of waste management.

The location of wind farms is defined by orography and meteorological conditions. Tidal stations are in the proximity of the seashore while photovoltaic panels benefit from longer exposure to sunshine. As technological advances in the renewable energy sector are achieved, micro-grids where sources are close to loads (households, factories, hospitals, etc) will be created in the context of distributed generation [1.1]-[1.2]. In order to take advantage of renewable energy, a complex frequency conversion strategy is implemented to generate a three-phase, AC supply at 50 Hz. Additional costs derived from power equipment and engineering expertise are therefore incurred. In order to ensure continuous supply and avoid dips, sags or swells, energy storage stations capable of releasing or absorbing peak power have to be incorporated [1.3] - [1.4]. Changes in the origin of energy and its generation and distribution are meant to be gradual but are seen as unavoidable. Strategic investment to promote, develop and integrate renewable energy is already taking place worldwide [1.5] - [1.7]. Nevertheless, a hypothetical rise in electricity costs may be shared by consumers (households, industries...) based on consumption rate and/or by governments through taxation. The quality of supply in micro-grids is affected by non-linear converters [1.8] and reactive loads such as computers, lighting equipment and electrical machinery. A tighter legislation will be enforced and include financial penalties to entities injecting line current harmonics to the network. Industry and tertiary sector need to tackle harmonic cleanliness and efficiency in applications with the highest consumption rates and/or with the largest potential for energy savings. While complying with the legislation may yield tax reductions

and enhance public image, lower electricity costs will certainly improve profitability in the medium-long term.

### 1.3 AC Drives

#### 1.3.1 Definition

Total and industrial electrical energy consumed by en of the most powerful economies in 2006 is introduced in fig 1.1. China leads the proportion of total electricity consumed by the industrial sector with a staggering 68%. In India and Germany, between 40% and 45% of the total electricity was absorbed by industrial activity. Countries like Japan, France and the United Kingdom registered lower ratios in the vicinity of 35%. In the world largest economy (United States), the residential sector accounts for the highest electricity consumption (36%) compared to a moderate 25% by the industrial sector.

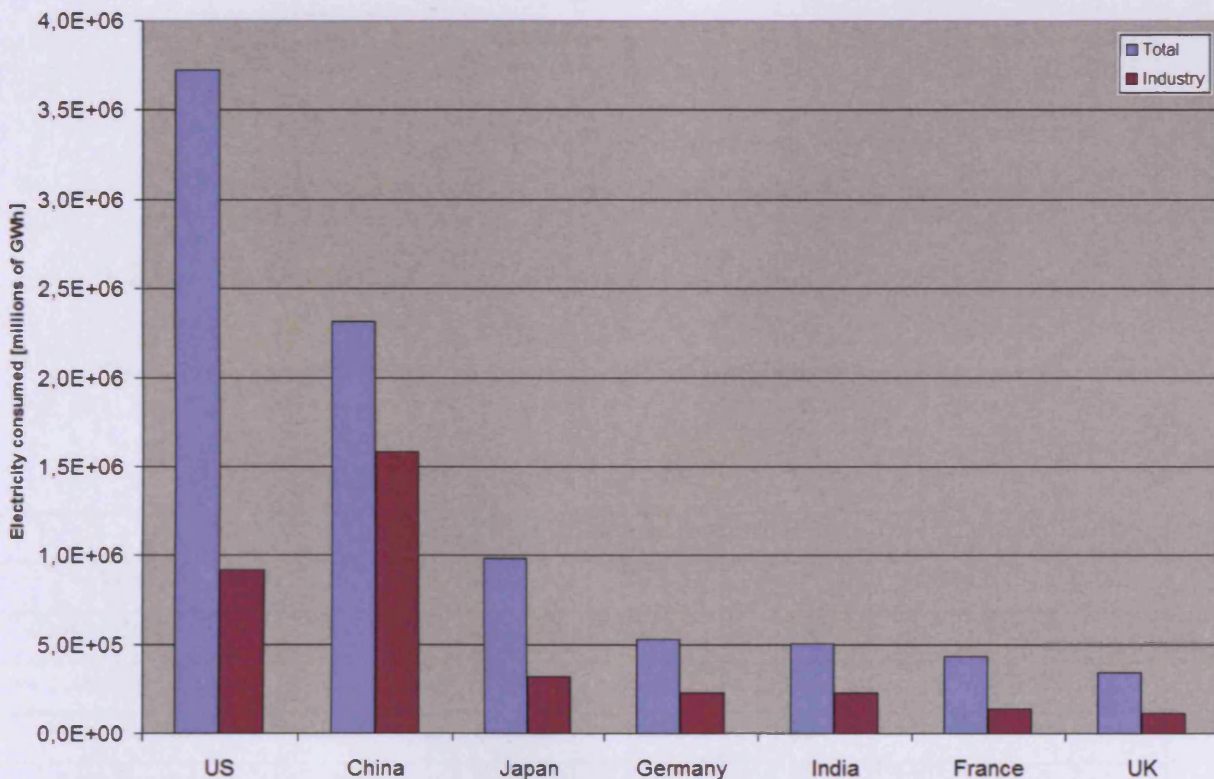


Fig 1.1. Total and industrial electricity consumption [million GWh] in 2006 [1.9]

Fig. 1.2 illustrates the important role that fan and pump applications play on energy consumption. Commonly used squirrel-cage induction motors with laminated stator cores of electrical steel are known to be largely inefficient [1.10]. Their performance is affected by load and external conditions such as under/over-voltage, transients and quality of power supply [1.11] - [1.12]. When the asynchronous machine is fed by a frequency converter, the system is called Variable Speed Drive [VSD]. It is not uncommon to find the term AC drive.

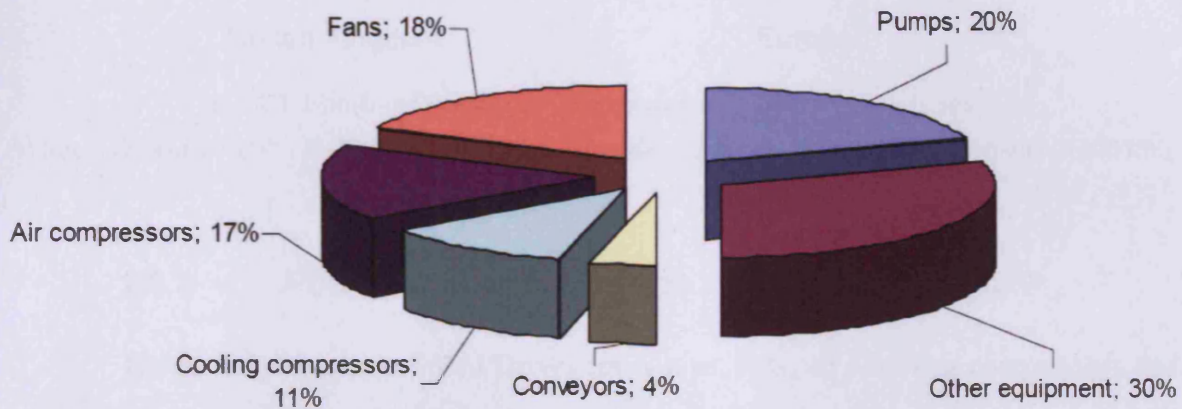


Fig. 1.2. Segmentation of total motor energy consumption in the European Union by industry applications [1.10]

### 1.3.2 Market

The market for AC drives has shown sustained growth worldwide (table 1.1).

Table 1.1. Growth in AC drives markets (2002 - 2005) [1.13 - 1.16]

Year	Growth [%] in AC Drives Market				Total Market Value (million €) in 2005
	2002	2003	2004	2005	
United Kingdom	2.00	2.20	3.00	3.10	155.7
Europe	3.10	3.50	3.40	3.30	1659.1
United States	1.00	1.30	3.90	4.70	910.6
Asia-Pacific	2.10	2.60	4.50	4.20	2001.7

The AC drives market can be analysed in terms of power range categories: (a) Micro-drives (up to 4 kW) - (b) Low-end (5 to 40 kW) - (c) Mid-range (41 to 200 kW) and (d) High-end (more than 200 kW) [1.13] Its segmentation in the United Kingdom and Europe (2005) is shown in fig. 1.3 [1.13] - [1.16]. AC drives in the low power range (< 40 kW) accounted for 70.2% and 70.5% of British and European markets in 2005, respectively.

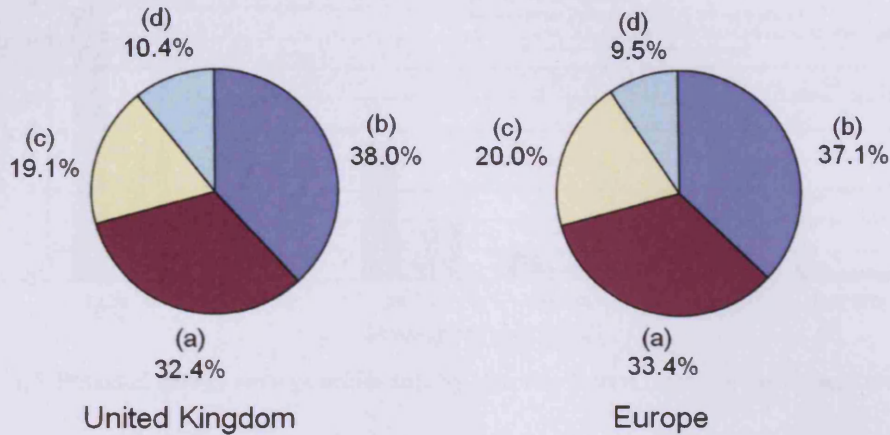


Fig. 1.3. British and European AC drives markets (2005) [1.13] – [1.16]

(a) Micro-drives (< 4 kW) - (b) Low-end (5 - 40 kW) - (c) Mid-range (41 - 200 kW) - (d) High-end (> 200 kW)

### 1.3.3 Potential Energy Savings

The use of Adjustable Speed Drives for pumps, fans, air / cooling compressors and conveyors has already been highlighted as key to reducing electricity consumption [1.17]. Apart from substantial energy savings, better process control, less wear in mechanical equipment and lower acoustic noise can be achieved. Fig. 1.4 and fig. 1.5 illustrate technical and economical potential energy savings, achievable by 2015 within the European Union in industry and the tertiary sector, respectively [1.18]. Constant and increased price (by 5%) of VSDs are the two hypotheses considered.

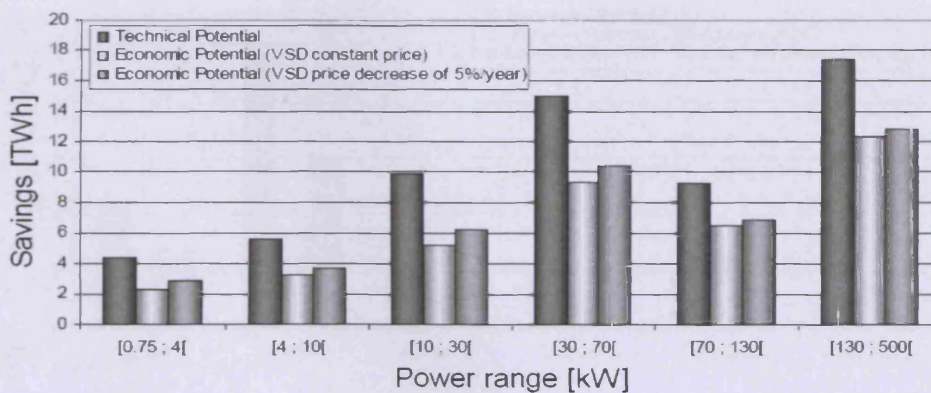


Fig. 1.4. Potential energy savings achievable by Variable Speed Drives in industry

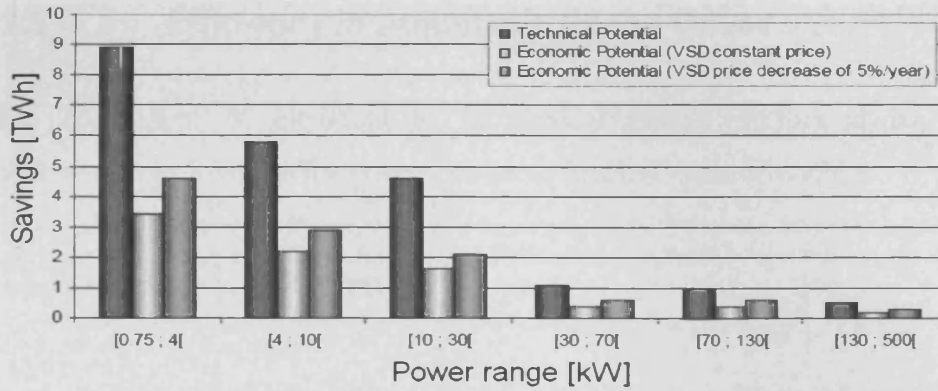


Fig. 1.5. Potential energy savings achievable by Variable Speed Drives in the tertiary sector

Fig. 1.6 and fig. 1.7 introduce potential energy savings achievable by VSDs for different types of load in industry and tertiary sector, respectively.

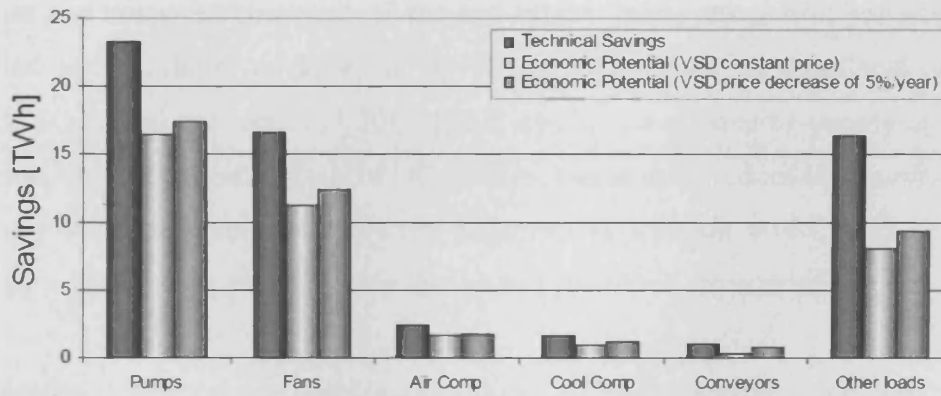


Fig. 1.6. Potential energy savings in industry by type of load in Variable Speed Drives

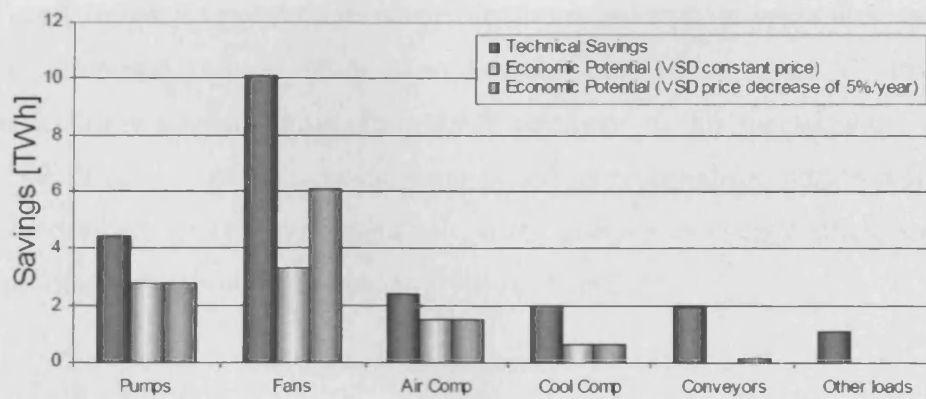


Fig. 1.7. Potential energy savings in the tertiary sector by type of load in Variable Speed Drives

### 1.3.4 Efficiency in Adjustable Speed Drives

The conversion of electrical to mechanical energy performed by VSDs is accompanied by energy losses in the power converter and the rotating machine.

#### 1.3.4a - Frequency Converter

In applications of nominal power below 500 kW, Pulse-Width-Modulated [PWM] Voltage-Source Inverters [VSI] are commonly used. As a mature and cost-efficient technology, they are the first choice for VSDs in the low power range. In traction and industrial applications of nominal power above 500 kW, forced-commutated Current Source Inverters [CSI] are supported by their robust performance at low speeds and insensitivity to short-circuit and noisy environments. In the last fifteen years, research in power electronics has resulted in significant advances in novel topologies such as multilevel and matrix converters. Multilevel converters [1.19] - [1.20] synthesize alternating supply at a selected output frequency from several levels of DC voltage. Based upon reduced harmonic distortion in multi-step voltage waveforms, they are an attractive solution as AC grid interfaces to photovoltaic and fuel cells or energy storage devices (batteries, capacitors).

Matrix converters are based upon a direct AC-AC conversion topology where the three input phases are connected to the three output phases by the means of nine bidirectional switches. Thanks to the absence of a DC-link, they are gaining industrial interest for VSDs in aerospace and military applications where operation at high temperatures and reduced volume are paramount. As a result of its well-established position in the AC drives market, PWM VSI topology appears as an unavoidable reference in this investigation. Due to the novelty of the direct AC-AC conversion concept and its potential for industrial applications, matrix converters are given a prominent role in the analysis of energy efficiency in VSDs. Detailed information on both topologies is given in chapter 2.

#### 1.3.4b - Induction motor

Voltages, produced by fast-switching converters in the kilo Hertz range and applied to stator windings, contain harmonics that affect the overall performance of the machine and represent a major cause for inefficiency. At full load, resistive losses in stator windings and aluminium rotor bars are predominant. When the load decreases, iron losses in laminated

cores of non-oriented electrical steel become proportionally larger. As a result of their prominent role in system efficiency, both components of loss are given special attention in this investigation. Because distorted voltages cause undesired flux harmonics in the high frequency range, iron losses in the silicon-iron alloy are strongly affected by the output voltage produced by the frequency converter. Its impact on magnetic and resistive losses in induction motors is therefore analysed.

### 1.4 Non-Oriented Electrical Steel

A full study of iron losses can not be carried out without underlining the economic importance of non-oriented silicon-iron alloys in the world industrial market. Non-oriented electrical steels are soft magnetic materials widely used in laminated stator and rotor cores of induction machines. Due to low intrinsic coercivity, these silicon-iron alloys can be easily magnetised and demagnetised. As opposed to anisotropic grain-oriented steel used in transformers subjected to unidirectional flux, isotropy makes non-oriented steel suitable for rotating machinery with revolving flux. Non-oriented steels represent around 80 % of the world production of soft magnetic materials (fig. 1.8). Owing to a more straightforward manufacturing process, their cost is lower than that of grain-oriented steels. Nevertheless, their value accounted for 53.0 % of the total market [1.21].

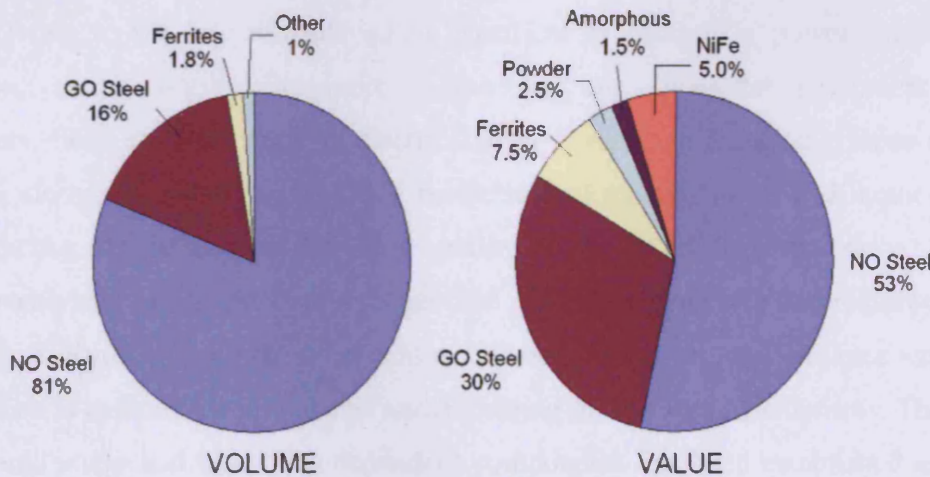


Fig. 1.8. Segmentation of world production of soft magnetic materials in terms of volume and value [1.21]

A segmentation of world steel exports between 2001 and 2005 is introduced in fig. 1.9 [1.22] to provide a global view on the current role played by electrical steel. The values given

are in millions of metric tons (MMt). A broad definition of steel related products, and the exports of 37 countries that represent 90 % of the world trade, were considered for building up the table (fig.1.8). In 2005, Japan was the highest net exporter of steel (26.8 MMt) while the United States ranked first in the net importer list (30.2 MMt).

	2001	2002	2003	2004	2005
Ingots and semi-finished material	47.3	50.5	51.0	58.9	59.5
Railway track material	2.5	2.5	2.7	2.4	2.4
Angles, shapes and sections	17.8	17.1	17.7	19.4	18.5
Concrete re-inforcing bars	13.2	13.0	14.8	15.9	17.9
Bars and rods, hot-rolled	9.3	8.5	9.1	9.9	10.2
Wire rod	16.3	17.6	17.9	20.6	19.8
Drawn wire	4.2	4.5	4.9	5.5	5.4
Other bars and rods	3.8	3.6	3.9	4.8	4.9
Hot-rolled strip	3.4	3.4	3.2	3.2	3.3
Cold-rolled strip	3.2	3.4	3.6	4.5	4.5
Hot-rolled sheets and coils	43.7	49.0	50.0	54.9	53.3
Plates	17.7	18.2	20.6	24.1	26.2
Cold-rolled sheets and coils	26.9	28.4	29.8	31.2	29.9
Electrical sheet and strip	2.6	2.7	3.4	3.7	3.7
Tinmill products	6.0	6.2	6.4	6.5	6.0
Galvanised sheet	20.5	23.1	24.3	26.8	25.6
Other coated sheet	6.1	6.7	6.8	7.4	7.3
Steel tubes and fittings	23.8	24.5	23.8	28.2	31.0
Wheels (forged and rolled) and axles	0.3	0.3	0.3	0.4	0.4
Castings	0.5	0.5	0.6	0.9	0.9
Forgings	0.8	0.8	0.8	1.1	1.0
Other	0.0	0.0	0.0	0.0	0.0
<b>Total</b>	<b>270.0</b>	<b>284.5</b>	<b>295.7</b>	<b>330.0</b>	<b>331.9</b>

Fig. 1.8. Segmentation of world steel export products between 2001 and 2005 [1.22].

Owing to the key role played by electrical machinery in power generation and distribution, automatisation, transport engineering and industrial equipment [pumps, compressors, fans, etc], the study of electrical steel is relevant. Increasing focus on energy efficiency, along with strong competition between steel manufacturers and motor suppliers, emphasises the industrial need for high quality steels at an attractive price. Providing electrical steels that can be efficiently magnetised is a challenging task that requires excellent knowledge of manufacturing processes and metallurgy. Moreover, acquaintance with physics of magnetism is essential to a thorough understanding of iron loss mechanisms. The analysis of losses into static and frequency-dependent components has been established as a useful concept to explain and quantify the effect of pulsating, distorted excitation on the performance of electrical steel.

- [1.4] D. Reicher, C. Curtis and J. McNamara, "Risk and Cost in Small-Scale DG Plants", *Energy User News*, pp 12-13, August 2003.
- [1.5] The Economist Intelligence Unit Ltd, "Industry Forecast December 2005. Australasia", pp 28-35, 2006.
- [1.6] The Economist Intelligence Unit Ltd, "Energy and Electricity Forecast December 2006. Denmark", pp 109-116, 2006.
- [1.7] National Petroleum News, "Report: Government should increase investment in renewable energy", pp 13, November 2006.
- [1.8] R. Yacamini, "Power System Sources. Part 1: Harmonic Sources", *Power Engineering Journal*, pp 193-196, August 2004.
- [1.9] International Energy Agency, "Electricity Consumption by Country in 2005", <http://www.iea.org/Textbase/country/index.asp>
- [1.10] J. Bickel, "Monitor Induction Motors to Drive Power Quality", *Plant Engineering*, pp 47-49, June 2006.
- [1.11] J. Reinert, P. Karlsson, "Improving Performance and Energy Consumption in Industrial Processes by Using Variable Speed Drives", *European Centre for Energy Efficiency Electronics Seminar. Towards Energy Gain and Savings – Emerging Drive Technologies*, Warsaw (Poland), 15 – 16 April 2008.
- [1.12] W. Stebbins, "Basics of Motors and Drives". *Energy User News*, pp 32-34, August 2000.
- [1.13] Datamonitor Plc., "AC Drives in the United Kingdom. Industry Profile", *Ref 0001-0669*, pp 1-18, July 2006.
- [1.14] Datamonitor Plc., "AC Drives in Europe. Industry Profile", *Ref 0201-0669*, pp 1-18, July 2006.
- [1.15] Datamonitor Plc., "AC Drives in the United States. Industry Profile", *Ref 0001-0070*, pp 1-17, July 2006.
- [1.16] Datamonitor Plc., "AC Drives in Asia-Pacific. Industry Profile", *Ref 0200-0070*, pp 1-15, July 2006.

- [1.17] H. De Keulenaer, R. Belmans, E. Blaustein, D. Chapman, A De Almeida, B. De Wachter, P. Radgen, “Energy Efficient Motor Driven Systems. Motor Challenge Programme”, *European Copper Institute (Belgium)*, pp 1-23, April 2004.
- [1.18] A. De Almeida, F. J. T. E. Ferreira, P. Fonseca, B. Chretien, H. Falkner, J. C. C. Reichert, M. West, S. B. Nielsen, D. Both, “Variable Speed Drives for Electric Motor Systems”, *Save II Programme 2000*, pp 1-105, 2000.
- [1.19] N. P. Schibli, T. Nguyen, A. Rufer, “A Three-Phase Multilevel Converter for High-Power Applications”, *IEEE Transactions on Power Electronics*, Vol 13, Issue 5, pp 978-986, September 1998.
- [1.20] J. Rodriguez, J. S. Lai, F. Z. Peng, “Multilevel Inverters: a Survey of Topologies, Controls and Applications”, *IEEE Transactions on Industrial Electronics*, Vol 49, issue 4, pp 724-738, August 2002.
- [1.21] O. Fischer, J. Schneider, “Influence of Deformation Process on the Improvement of Non-oriented Electrical Steel”, *Journal of Magnetism and Magnetic Materials*, Vol 254-255, pp 302-306, 2003.
- [1.22] International Iron and Steel Institute, “World Steel in figures. 2007.”, Wb/PDF Version, July 2007.

## NON-ORIENTED STEEL SUBJECTED TO DIRECT/INDIRECT AC-AC CONVERTER EXCITATION

---

### **2.1 Introduction**

The study of the performance of non-oriented steel subjected to frequency converter excitation is an exciting but challenging task. Apart from a solid command of magnetism and electrical steels, a good understanding of AC-AC conversion topologies that produce unique pulsating, magnetising excitation is essential. This chapter covers relevant aspects treated in this investigation. First, an overview on non-oriented steels, which includes applied electromagnetism theory and iron losses, is presented. Due to the novelty of the topology, a review on matrix converters is introduced. Historical developments, hardware implementation and Space-Vector-Modulation [SVM] are the points treated. A description on back-to-back two-level converters and a survey on Pulse-Width-Modulated [PWM] schemes are presented. Mathematical formulae, relevant to the analysis of harmonically distorted waveforms, are included in the final subsection.

### **2.2 Non-Oriented Steel**

Non-oriented steels belong to the family of soft magnetic materials, of which the main characteristic is low intrinsic coercivity (less than  $1000 \text{ A.m}^{-1}$ ). Several categories of soft magnetic materials are described in [2.1]. Special attention is devoted to electrical steels. Amorphous alloys are metallic materials with disordered atomic scale structure that consist of nickel, iron and/or cobalt combined to one or more of the following elements: boron, phosphorous, silicon and carbon. In addition to better resistance to wear and corrosion due to the absence of grain boundaries, their extremely low coercivity and high electrical resistance result in a substantial reduction in eddy current losses. They are ideal for low current applications and small devices, such as sensors, where they compete with Ni-Fe alloys. Silicon-iron alloys, also known as electrical steels, are used in electrical machinery (transformers, generators, motors). Depending on their micro-structure, which defines their magnetic properties, they are classified as grain-oriented and non-oriented steels. The latter

are divided into finally annealed (fully processed), not finally annealed and semi-processed. Electrical steel grades are defined by European Standard EN 10027-1 [2.2]. The designation of the steel begins with the letter *M* [electrical steel]. The initial number corresponds to one hundred times the value of specific power losses [W/kg] in the material subjected to sinusoidal magnetisation at 50 Hz and 1.5T peak flux density. The second number is one hundred times the nominal thickness [mm] of the lamination. The final letter is used to characterise the steel within one of the following categories:

- Non-oriented steel in the fully processed state (A)
- Electrical unalloyed steel in the semi-processed state (D)
- Electrical alloyed steel in the semi-processed state (E)
- Grain-oriented steel with normal loss (N)
- Grain-oriented steel with reduced loss (R)
- Grain-oriented steel with high permeability (P)

### *M 600 – 50A*

Designation of non-oriented fully-processed steel of nominal thickness 0.50 mm and maximum specific power loss 6.00 W/kg (50 Hz, fundamental peak flux density 1.5T)

## **2.2.1 Applied Electro-Magnetics Theory**

In rotating machines, laminated electrical steels are subjected to cyclic magnetisation and demagnetisation. A good understanding of electromagnetism is therefore necessary to analyse its performance under different magnetising conditions.

### **2.2.1a - Maxwell's Equations**

Basic laws of electricity and magnetism were successfully combined in 1865 by the Scottish mathematician and physicist James Clerk Maxwell to describe how oscillating electromagnetic waves interact with matter. In 1884, Heaviside and Gibbs reformulated the initial system formulated by Maxwell, which consisted of twenty variables, to a simpler set of four equations based upon vector calculus. The first of Maxwell's Equations (2.1) derives from applying Gauss's Law to an electric field. It gives the relation between the electric charge enclosed in a surface and the electric flux flowing out of the surface.

$$\vec{\nabla} \cdot \vec{D} = \rho \quad (2.1)$$

$\rho$  [ $\Omega \cdot m$ ] is the resistivity of the material and  $\vec{D}$  is the electric displacement field. Its magnitude is expressed in  $C \cdot m^{-1}$ . The electric displacement field is related to permittivity of free space  $\epsilon_0$  [ $F \cdot m^{-1}$ ], electric field  $\vec{E}$  [ $V \cdot m^{-1}$ ] and polarization density of the material  $\vec{P}$  [ $C \cdot m^{-2}$ ] as given in (2.2).

$$\vec{D} = \epsilon_0 \vec{E} + \vec{P} \quad (2.2)$$

The second of Maxwell's Equations (2.3) results from applying Gauss's Law to magnetism. Absence of magnetic monopoles within the enclosed volume of material is assumed.  $\vec{B}$  is the vector expression of magnetic flux density expressed in Tesla.

$$\vec{\nabla} \cdot \vec{B} = 0 \quad (2.3)$$

According to Faraday's Law of Induction (1831), a time-varying magnetic flux  $\vec{B}$  flowing through a surface  $S$  [ $m^2$ ] confined by a closed, conducting loop induces an electromotive force of opposite sign in the loop. This introduces the third of Maxwell's equations (2.4).

$$\vec{\nabla} \times \vec{E} = -\frac{\partial \vec{B}}{\partial t} \quad (2.4)$$

Ampere's Law states that a circulating time-varying magnetic field  $\vec{H}$  [ $A \cdot m^{-1}$ ] in a closed loop induces an electric current, characterised by its density  $|\vec{J}|$  in  $A \cdot m^{-2}$ , through the area  $S$  confined by the loop. This law, also known as the magnetic equivalent of Faraday's Law of Induction, was generalised by Maxwell, who noticed an inconsistency in its application to a charging or discharging capacitor and introduced the time-derivative of electric displacement field  $\vec{D}$ . The fourth of Maxwell's Equations is given in (2.5).

$$\vec{\nabla} \times \vec{H} = \vec{J} + \frac{\partial \vec{D}}{\partial t} \quad (2.5)$$

### 2.2.1b - Descriptive – Constitutive Equations of the Material

When the current created by the magnetic field flows through a conducting loop of area  $S$ , a magnetic dipole moment  $\vec{m}$  equal to  $S^2 \vec{J}$  [A.m<sup>2</sup>] is associated with the electric circuit. The magnetisation  $\vec{M}$  of a volume  $V$  of material can be defined as the magnetic moment per unit volume (2.6).

$$\vec{M} = \frac{\vec{m}}{V} \quad (2.6)$$

Magnetic field strength  $\vec{H}$  and flux density  $\vec{B}$  in the material are related to absolute permeability  $\mu$  as given in (2.7). The permeability of free space  $\mu_0$ , equal to  $[4\pi \times 10^{-7} \text{ Wb.A}^{-1}.\text{m}^{-1}]$ , and the relative permeability of the material  $\mu_r$  are commonly used.

$$\vec{B} = \mu \vec{H} = \mu_0 \mu_r \vec{H} \quad (2.7)$$

The induction or flux density  $\vec{B}$  results from contributions by the magnetic field  $\vec{H}$  and magnetisation  $\vec{M}$ . This is given in (2.8).

$$\vec{B} = \mu_0 (\vec{H} + \vec{M}) \quad (2.8)$$

The susceptibility  $\chi$  of the material can therefore be written in terms of the relative permeability  $\mu_r$  (2.9).

$$\chi = \mu_r - 1 \quad (2.9)$$

### 2.2.1c - Poynting's Vector

The energy flux, created by an electromagnetic field in a material of relative permeability  $\mu_r$ , was calculated by John Henry Poynting in 1884 by the means of the vector  $\vec{S}$ . Its direction is coincident with the direction of energy flow and its magnitude expressed in power per unit area [W.m<sup>-2</sup>] (2.10).

$$\vec{S} = \vec{E} \times \vec{H} = \frac{1}{\mu_0 \mu_r} \vec{E} \times \vec{B} \quad (2.10)$$

## 2.2.2 Magnetic Losses

During each cycle of magnetisation, the applied magnetic field  $H$  [ $\text{A}\cdot\text{m}^{-1}$ ] created by alternating currents across primary windings, increases until the steel is magnetised at maximum peak flux density  $B_p$  [T]. The demagnetising process then takes place. Energy losses  $W_s$  [J], often known as iron losses, occur while the magnetising state of the material is changed cyclically. Their value, which is associated to the area of the B-H curve, can be calculated as in (2.11).

$$W_s = \int_{-B_p}^{B_p} B dH \quad (2.11)$$

A simplified B-H curve of a material reaching saturation is shown in fig. 2.3 for sinusoidal flux density.

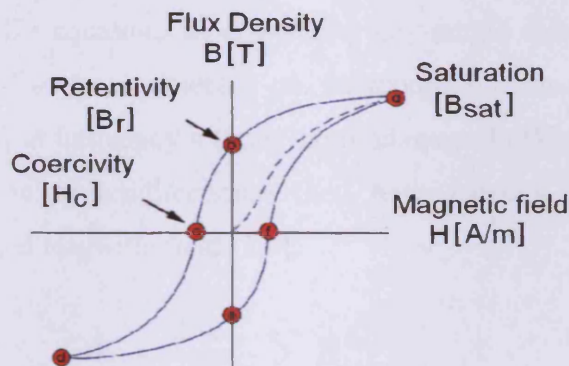


Fig. 2.1. Simplified B-H curve of a material reaching saturation under sinusoidal magnetisation.

The composition of core losses is important to steel manufacturers and machine designers to raise efficiency in electrical machines. The most common analysis of iron losses is founded on their breakdown into three components: static hysteresis  $W_h$  [J], classical eddy-current losses  $W_e$  [J] and excess eddy current (formally called anomalous losses and quantified based upon the statistical approach [2.6]).

### 2.2.2a - Static Hysteresis Loss

The first term, which is assumed to be independent of the magnetising frequency  $f$  [Hz], is affected by peak flux density  $B_p$  and characteristics of the material such as purity, internal stress and grain size, which are incorporated by the constant  $K_h$ . Static hysteresis

losses  $W_h$  [J] are given in (2.12), where the value of Steinmetz's constant  $x$  lies between 1.6 and 2.0.

$$W_h = K_h B_p^x \quad (2.12)$$

### 2.2.2b - Classical Eddy-Current Losses

The second term, of resistive nature, is caused by macro eddy-currents which create a counter-flux in the magnetic material. It is dependent on characteristics of the voltage applied to stator windings, such as frequency and wave-shape. In order to reduce their effect, thin laminations of material of higher resistivity  $\rho$  [ $\Omega \cdot m$ ] are used in cores of induction machines. Although the addition of silicon to the steel proves beneficial to reduce eddy-currents due to low conductivity, the permeability of the material is decreased.. The term  $W_e$  [J] can be derived from Maxwell's equations by calculating Poynting's vector [2.7]. Its value in a lamination of thickness  $d$  [m] subjected to harmonic-rich magnetisation [flux components of amplitude  $B_n$  [T] at frequency  $n$  times the fundamental  $f$  [Hz] ] is determined in (2.13) under the assumption of unidirectional flux, homogeneous permeability and linearity between flux density and magnetic field [2.6].

$$W_e = \frac{\pi^2 d^2}{6\rho} \sum_{n=1}^{\infty} B_n^2 f_n \quad (2.13)$$

### 2.2.2c - Excess Losses

When static hysteresis and classical eddy-current losses are added, the result is always somewhat smaller than the total losses, which lead to the definition of the anomalous losses  $W_a$  [J]. The statistical theory of losses confirmed that this component is caused by micro eddy-currents induced by magnetic domain wall motion within the material at a micro-structural level. Its value is given in (2.14), where  $\sigma$  [ $S \cdot m^{-1}$ ] is the conductivity of the material,  $G$  is a dimensionless coefficient,  $S$  [ $m^2$ ] the cross-sectional area of the sample and  $V_o$  [ $A \cdot m^{-1}$ ] is a physical parameter of the material related to the strength and distribution of internal coercive fields [2.8].

$$W_a = 8\sqrt{\sigma G S V_o} \sum_{n=1}^{\infty} B_n^{3/2} f_n^{1/2} \quad (2.14)$$

## 2.3 Matrix Converters: Direct AC-AC Conversion Topology

### 2.3.1 Description

Matrix converters are forced commutated, frequency converters [2.9]. The three-phase voltage source [A, B, C] is connected to the load [a, b, c], usually a motor, by the means of nine bidirectional switches [ $S_{Aa}$   $S_{Ba}$  ...  $S_{Bc}$   $S_{Cc}$ ] as shown in fig. 2.4.

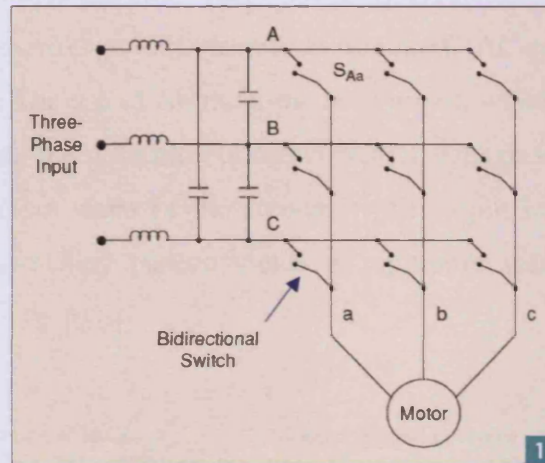


Fig. 2.2. Simplified representation of a three-phase matrix converter [2.9]

The absence of intermediate energy storage elements, reduction in volume when compared to back-to-back DC-link converters, which is estimated to a factor of three, makes them suitable for aerospace and military applications. Functionality without electrolytic capacitors (that require proper cooling in conventional indirect converters) ensures robust operation at high temperatures and longer lifespan, while allowing integration of converter and motor. Matrix converters enable bidirectional flow between source and load. Braking energy, which is generally dissipated in large resistors in common diode-bridge rectifier-based topology, can be injected back to the grid. Control of input power factor and regenerative capability are among the strongest features of matrix converters [2.10].

Prior to hardware and practical aspects of the topology, which include semiconductor switches, input filter and ride-through capability, a brief historical look on matrix converters is presented. The latter is followed by a detailed analysis of the modulation strategy and commutation scheme applied to guarantee high performance, reliability and safe operation. A final look at industrial applications for matrix converters is given.

### 2.3.2 Historical Review

Following advances in power transistor technology (essential to the implementation of bidirectional switches), the development of matrix converters started in 1980 [2.11]. After the “direct transfer function” approach was postulated as the first modulation method, the “indirect transfer function” concept was introduced in 1983 [2.12] and its mathematical analysis completed in 1985 [2.13]. Pulse-Width-Modulation [PWM] technique, of common use in standard Voltage-Source Inverters [VSIs], was selected to define the switching pattern of a converter with “fictitious DC-link” [2.9]. Initial work on adapted modulation strategies highlighted that the output voltage transfer ratio in direct AC-AC converters was limited to a maximum value of 50%. The use of common-mode voltages, which allows full utilisation of input voltage envelopes in the definition of target output voltage signals, was implemented. Redistribution of null output states of the converter (all output lines connected to a single input line) within the switching pattern yields an optimum value of the output voltage transfer ratio, equal to  $\sqrt{3}/2$  [2.9].

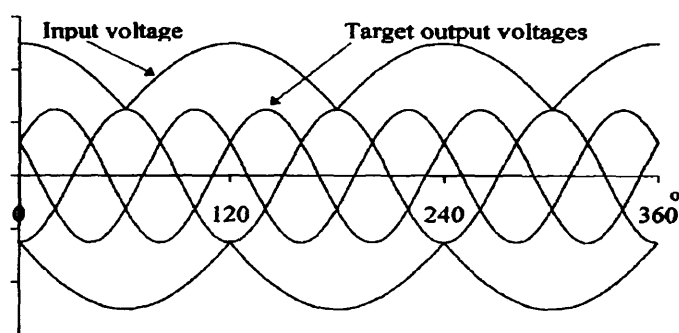


Fig. 2.3. Input and target output voltages without considering common-mode voltages [2.9]

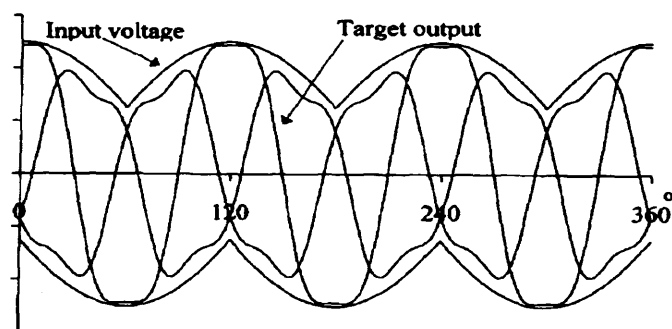


Fig. 2.4. Input and target output voltages by considering null output states of the converter [2.8]

Space Vector Modulation [SVM] was first considered in the control of matrix converters [2.13]-[2.14] in 1983 - 1985. Further work [2.15] consolidated SVM as an

attractive solution to modulation in 1989. Improved theoretical understanding of SVM enhanced its suitability for three-phase AC-AC converters and led to practical implementation of input power factor correction in 1995 [2.16]. Analytical work on modulation techniques was supported by significant advances in Digital Signal Processing [DSP] technology [2.17], which remains essential in the control of power converters [2.18].

An extensive theoretical description of SVM technique applied to three-phase matrix converters confirmed that a suitable use of zero configurations within optimised switching patterns yields a maximum voltage transfer ratio [2.19]. The influence of various modulation schemes, based upon SVM approach, on critical magnitudes to the design and performance of matrix converters, such as input/output current ripple, harmonic quality of output voltages and semiconductor losses, has been recently investigated [2.20]. The modified SVM method uses minimum line-line voltages, in contrast to conventional SVM that uses two maximum voltages. For low transfer ratios (below 0.5), harmonic distortion of output voltages and switching losses are reduced, but harmonic current spectrum is modified.

### **2.3.3 Bidirectional Switch**

#### 2.3.3a. Hardware implementation

Bidirectional switches are core elements in direct AC-AC converters. Control of their hardware configuration is accomplished by a commutation algorithm that takes into account the characteristics of semi-conducting devices in order to ensure safe operation. Despite needing only one gate driver, semiconductor losses caused by current, of uncontrolled direction and flowing through three devices, are important limitations of a single-phase diode bridge [2.9]. Common-collector switch cell configuration consists of two IGBTs and two diodes connected antiparallel. The advantage of using only six isolated power supplies to generate gate driver signals is often mitigated by the constraint of minimum stray inductance. The common-emitter configuration is preferred in matrix converter topology, since independent control of current direction and reduced conduction losses are accomplished [2.9]. This configuration, which requires an isolated power supply for gate drives and relies upon diodes to ensure reverse blocking capability, is suitable for sophisticated commutation methods, as implemented in matrix converters.

#### 2.3.3b - Commutation Scheme

Modulation in conventional converters is straightforward due to the existence of natural freewheeling paths. In matrix converters, advanced commutation methods are unavoidable to ensure safe operation. Firstly, because short-circuit of two input phases leads to over-currents that would destroy the converter, no bidirectional switches can be active at the same time. Moreover, the simultaneous switching off of two bidirectional switches in an open-circuit event results in damaging over-voltages. The non-ideal nature of semiconductor devices (finite switching-on and switching-off times) and propagation delays in control circuitry makes implementation of a suitable commutation scheme a challenging task [2.9]. Elementary strategies such as overlap current and dead-time commutation, which relied upon extra-line inductances to minimise over-currents, proved to be unsuccessful. The use of clamp or snubber circuits had the draw-back of complex design of auxiliary circuits along with additional device losses [2.9]. Reliable commutation, which prevents short or open circuit between input phases, was finally achieved by current-direction-based methodology in common-collector or common-emitter switch configurations. This scheme, which allows full control of current flow direction in the cell, is performed following a four-step sequence. Accurate information on the output line current direction is needed to identify conducting and non-conducting IGBTs within each bidirectional switch. In switching converters in the kilo-Hertz range, current measurement by sensors is not a trivial task, due to experimental uncertainty. Analysis of the voltage across the bidirectional switch was proposed as an alternative solution [2.9].

### **2.3.4 Auxiliary equipment**

In pulsating converters in the kilo-Hertz range, an input filter is essential to reduce high frequency harmonics in input line currents. Since they account for a substantial increase in the weight and volume of the system, elementary LC filters, which reduce the global output voltage transfer ratio, have to be minimised. Damping resistors are connected in parallel to input reactors during transient operation to mitigate possible over-voltages [2.23]. Over-voltages, caused by line disturbances or over-current faults in the motor, can damage the converter and must be avoided. A clamp circuit, where one capacitor is connected to input and output sides of the converter by two six fast-recovery diode bridges, is incorporated [2.24]. In advanced drives, ride-through capability during power supply disturbances ensures efficient use of energy [2.25]. Zero-voltage switching configurations are then applied to the matrix converter. Once motor leakage inductances have stored sufficient energy, the clamp circuit in conducting state can feed control circuitry via a switch-mode power supply [2.26]. A complete matrix converter with auxiliary equipment is shown in fig. 2.5.

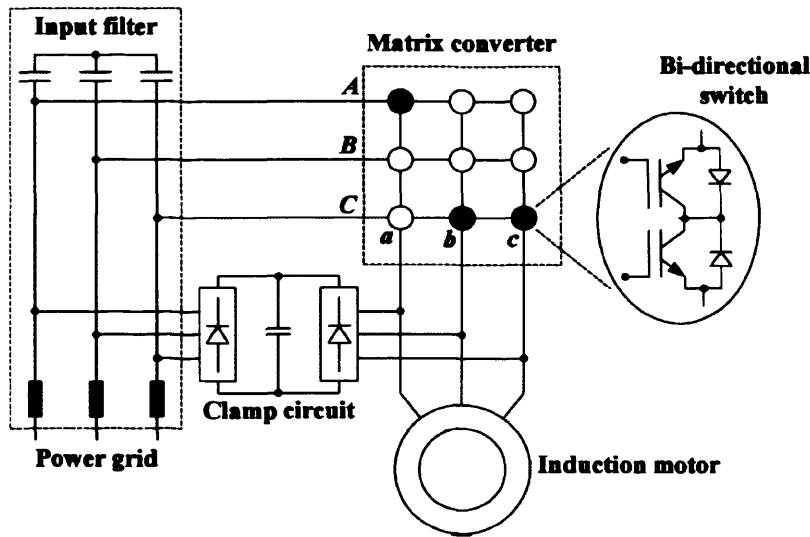


Fig. 2.5. Representation of a complete matrix converter [2.26].

### 2.3.5 Applications

In order to successfully introduce matrix converters to the market, more than two decades of research work on semiconductor technology, hardware implementation and control have been invested to achieve safety and reliability [2.9]. Yaskawa Corporation has recently released the first commercial matrix converter [2.28]. High prices, due to higher number of semiconductors in bidirectional switch cells and the engineering expertise intrinsic to direct AC-AC conversion, are yet to be overcome. Nevertheless, as semiconductor costs go down and the requirement for maximum functionality increases, matrix converters will gain popularity as power electronics solution in more efficient speed drives [2.29] - [2.30]. Reduction in volume and weight, along with robust performance at high temperatures, already supports matrix converters in aerospace [2.31] - [2.32] and marine propulsion [2.33] applications. As a result of their characteristics, they have been identified as an excellent solution in military vehicles [2.34]-[2.35]. The increasing demand of electrical vehicles to reduce energy consumption, noise and pollution in modern-day cities [2.36] opens a new path to matrix converters because of their regenerative capability [2.37]. In wind turbines rotating at random speed, AC-AC converters are needed to produce an alternating signal at a constant frequency (50 Hz). The potential of matrix converter in this particular application has already been highlighted [2.38]. Matrix converter-fed induction machines have been given attention due to their applicability in a wide range of industrial applications [2.39] - [2.40] as integrated AC drives. In order to ensure an optimum performance, research on various control methods has been successfully carried out [2.41]-[2.42].

## 2.4 Back-to-back Converter

### 2.4.1 Description

A back-to-back converter is an indirect frequency converter that consists of a three-phase rectifier connected to a three-phase inverter by the means of a reactive DC load as shown in fig. 2.6.

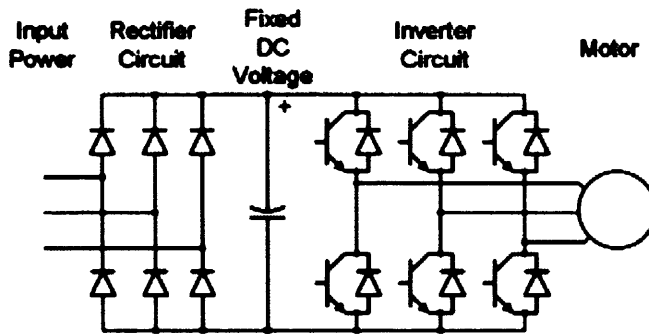


Fig. 2.6. Back-to-back converter based on diode-bridge rectifier circuit.

A diode-bridge circuit is commonly used as rectifier. Low order odd harmonics in line currents, which have to be limited by reactors to prevent mains pollution [2.43], are produced. This passive configuration has been preferred for variable speed drives in industry owing to its low cost and simplicity (no control is needed). Nevertheless, the absence of power factor correction and no bidirectional flow capability remain important limitations. An electrolytic capacitor is used as an energy buffer and maintains a nearly constant DC voltage to supply the inverter. A choke is often incorporated to reduce ripple in the DC current that may cause damage to the capacitive element [2.44]. Moreover, this essential DC-link component is sensitive to high temperature so a cooling system is required to ensure safe operation.

The three-phase full-bridge configuration is the most commonly used inverter topology. Six controlled semi-conducting devices are individually coupled to an antiparallel diode [2.45] in as many switching cells. Each one of the three legs of the inverter consists of an upper and a lower cell. When the upper cell is in a conducting state, the lower one is in a non-conducting mode, and vice versa. Control signals for each of the six switches are commonly generated by Pulse-Width-Modulation [PWM] technique. A more detailed explanation is given in §2.4.2. In low to medium power converters, Metal Oxide Semiconductor Field Effect Transistors [MOSFETs] or IGBTs can be used. Voltage-

controlled MOSFETs are ideal for high switching frequency operation due to short commutation times. Current-controlled IGBTs are often used, because they combine several advantages of power MOSFETs with higher voltage and current capability. While turn-on times are similar in both devices, turn-off times are longer in IGBTs [2.46]. This is an important factor to be taken into account in the modulation technique.

When a three-phase full-bridge configuration is selected as rectifier circuit, the topology is known as an active front-end converter. Regenerative capability, power factor correction and lower line current harmonics are achieved. Since the power drawn from the grid can be adjusted, the size of the DC-link capacitor can be reduced to allow the use of film capacitors [2.47]. Despite lower energy density, their better behaviour at high temperatures extends the lifespan of the speed drive. PWM strategy, which is implemented in the kilo-Hertz range, is accountable for controlling the active rectifier. The ripple of line, pulsating currents must be reduced in accordance with electromagnetic compatibility regulations [2.48]. Although their performance makes them ideal in terms of functionality and energy efficiency, higher cost, along with complexity of design and control, have limited their use in common variable speed drives. Fig. 2.7 shows a back-to-back converter with an active front-end rectifier.

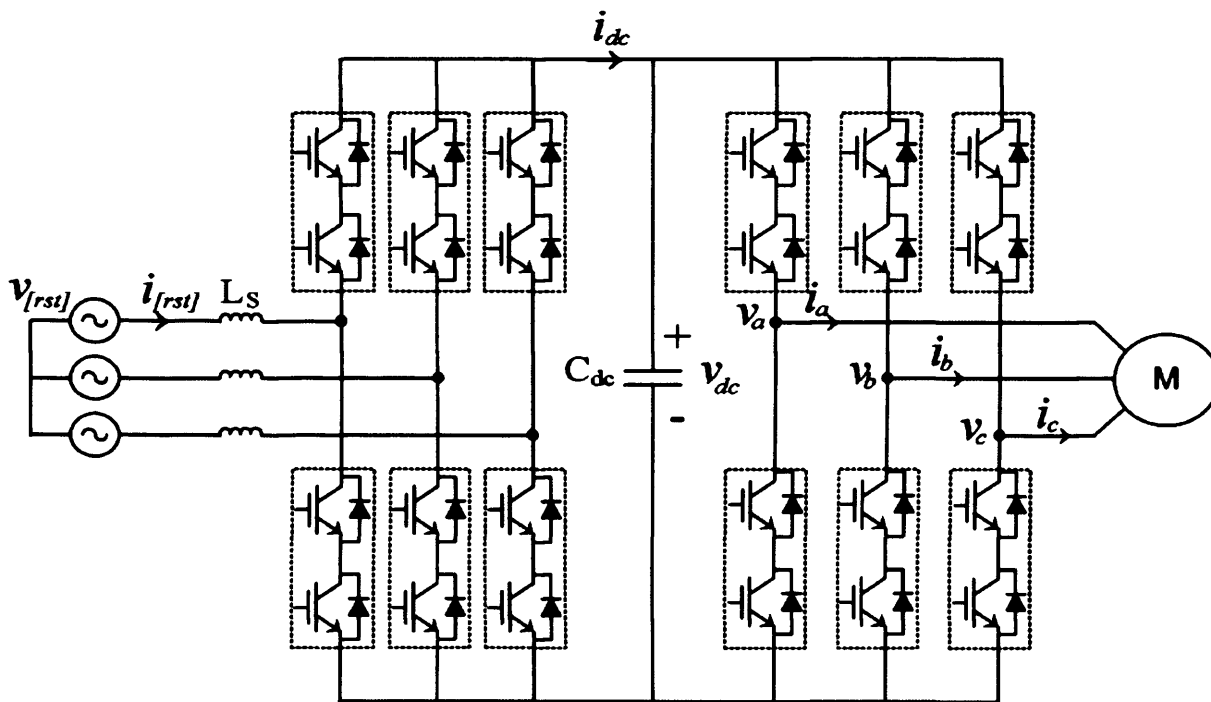


Fig. 2.7. Back-to-back converter with active front-end rectifier [2.49].

## 2.4.2 Pulse-Width-Modulation [PWM]

The control algorithm, generally open-loop constant Volts/Hertz [V/f], generates a three-phase sinusoidal reference consisting of three signals, of relative phase angle  $120^\circ$  and variable amplitude  $A_{ref}$ , at the desired output frequency  $f$  [Hz]. In carrier-based PWM based on the sub-oscillation method, the reference is compared to a triangular signal  $x_c$  of constant amplitude  $A_c$  and switching frequency  $f_w$  to generate logic signals to control the six switches in active rectifier and inverter. Key parameters in PWM are modulation index  $m_i$  and frequency ratio  $m_f$  defined as

$$m_i = \frac{A_{ref}}{A_c} \quad (2.15)$$

$$m_f = \frac{f_w}{f} \quad (2.16)$$

If the upper/lower IGBT is switched on before the lower/upper device is completely turned off, a fatal short-circuit of the electrolytic capacitor occurs. A dead-time, which takes into account characteristic turn-off and turn-on times of semi-conducting devices, is introduced to prevent two IGBTs in the same leg of the converter from being simultaneously active. Many converters in industrial applications are controlled by a DSP, which often incorporates a pre-defined PWM algorithm. Different modulation indices and switching frequencies can be selected by the user within a specified range that ensures safe operation. Some specific applications require more accurate control of the power supplied to the induction machine. Open-loop  $V/f$  speed control is the simplest and most popular method [2.43]. By maintaining a constant ratio of applied voltage to stator windings to frequency of supplied currents, the air gap flux in the machine at steady-state operation is approximately constant. The modulation index is then increased with rotational speed command of the induction motor. In closed-loop  $V/f$  method, a tachometer is incorporated to avoid speed fluctuations inherent to open-loop control. In applications where the dynamic performance of the machine is critical to prevent reaching breakdown torque, slip regulation is implemented under constant  $V/f$  control.

### 2.4.2a. PWM schemes

The basic principle in pulse-width modulation was directly implemented in electronic systems. In the original method, also known as natural sampling PWM, the reference sinusoidal curve is compared to a triangular carrier signal to generate the logic

signals for commutation of semiconductors in three-phase. Owing to continuous sampling of the reference signal, excessive Read-Only Memory [ROM] was required for execution.

As digital signal processing [DSP] reached maturity in the seventies, regular-sampled PWM schemes were developed for motor control. In asymmetric regular sampled PWM, the logic signals are obtained by comparing a sampled reference signal to the carrier signal (fig. 2.8) whenever the latter reaches a positive or negative peak (twice every switching cycle).

The same principle is applied to symmetric regular sampled PWM. However, the reference signal is sampled only when the carrier signal reaches its maximum value (once every switching cycle) [2.49].

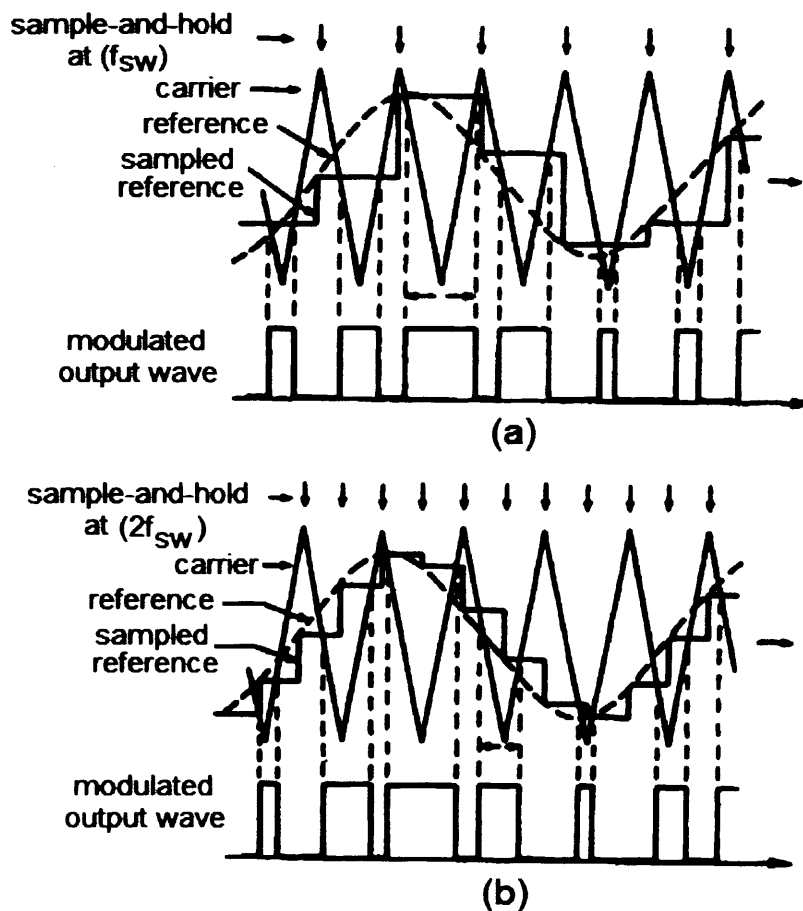


Fig 2.8. (a) symmetrical – (b) asymmetrical regular-sampled PWM [2.49]

Further developments in control theory established space-vector techniques as suitable for motor control. When this concept is applied for pulse-width modulation [SPWM], a reference voltage vector with the required amplitude rotates at the desired pulsation

associated to the target electrical frequency. The plane is divided into six sectors. Depending on its position on the plane, the vector (which is sampled at the rate defined by the switching frequency) is synthesized by a combination of two active and two passive vectors. The switching pattern is then defined by calculating the duty cycle linked to each one of the vectors organized in a pre-defined sequence.

The relation between space-vector modulation and regular-sampled PWM was analysed by Bowes et al in [2.50]. Apart from illustrating the theoretical connection between the two modulation techniques, the authors investigated the introduction of equal null pulse times (periods where all three switches in either upper or lower leg are on or off) in regular-sampled PWM technique. This was derived from the addition of a zero-sequence component to the reference modulating signal. Although extension of linear modulation range and simplification in digital signal processing were claimed as benefits, the authors under-lined that no current harmonic minimization was achieved by the “equal-null” pulse time approach [2.50]. On the contrary, Bowes et al. concluded that the injection of a third harmonic component to the modulating wave lead to reduction of triplen harmonics in voltage and current spectrum and thus *THD* minimization. As the main conclusion of their work, the authors highlighted that space-vector modulation can be defined as a form of asymmetrical regular-sampled PWM.

The potential for harmonic optimization in two-level and multi-level inverters subjected to carrier-based PWM techniques was introduced by Holmes et al in [2.51]. Four different power converter topologies were considered: two-level phase leg, single phase Voltage Source Inverter [VSI], three phase VSI and cascaded multi-level three-phase VSI. The three modulation concepts examined were natural and regular sampled (asymmetrical and symmetrical). The harmonic analysis of line-neutral voltages carried out yielded mathematical expressions as a function of modulation index, DC-link voltage and electric ( $\omega_o$ ) and switching ( $\omega_c$ ) pulsation. While the fundamental frequency was set to 50Hz, PWM switching frequency was 1 kHz and modulation index 0.8. The research undertaken revealed that natural and asymmetric regular sampled PWM schemes suppress half of the sideband harmonic components in cluster at multiples of the PWM switching frequency. Moreover, the authors concluded that the importance of selecting an integer ratio of carrier to fundamental frequency to prevent the presence of supplementary sideband harmonics. This conclusion was pointed as particularly relevant when ( $f_{sw}/f$ ) is lower than nine.

A survey on regular-sampled PWM techniques was accomplished by Bowes et al. in [2.52]. In the study introduced, up to seven different regular-sampled modulation schemes were analysed: asymmetric / symmetric regular sampled PWM, harmonic elimination PWM, harmonic minimization PWM, space-vector PWM, high frequency and hysteresis band. Optimal regular-sampled PWM consists in the addition of a third harmonic component (25% amplitude referred to the fundamental) that guarantees a linear relation between modulation index and fundamental frequency in a broad range of frequency ratios ( $f_{sw}/f$ ). Triplen harmonics are cancelled out voltage harmonic spectra. Should high voltage be considered in a given application, non-linear sampling of the modulating wave must be executed to fulfil identical goal [2.52]. The authors showed that THD reduction thanks to optimal modulation increase with increasing modulation index and decreasing frequency ratio (up to 2% in THD decrease at  $f_{sw}/f = 9$  and  $m_i = 1.2$ ). Bowes et al continue their analysis by identifying sampling of two phase-shifted modulating waves as an effective way of eliminating the 5<sup>th</sup>, 7<sup>th</sup>, 11<sup>th</sup> and 13<sup>th</sup> harmonic voltage components. Nonetheless, it was confirmed by the authors that a odd component (17<sup>th</sup>) with an amplitude of nearly 20% is present in the spectrum. High frequency regular-sampled PWM which consists in raising the carrier frequency in order to move the associated harmonic clusters (sideband components) further from the fundamental frequency. The main drawback for the application of this approach is the need for fast and expensive micro-processing. Bowes et al propose a concept allowing the use of low-cost DSP due to reduction in calculation time. Finally, a hysteresis band based PWM scheme is briefly described as suitable for high-power applications with required low switching frequency to a very simple calculation procedure.

#### 2.4.2b. Impact of PWM scheme on voltage and current harmonic distortion

The impact of four different PWM schemes [natural sampling, asymmetric / symmetric regular sampled, space-vector (§A.2) ] on current THD in the induction motor I (§ 7.1) analysed in chapter 7 is evaluated. The object of the study introduced in this sub-section is to complement the work in chapter 7 in which only natural sampled PWM was considered for control of the two-level DC-link converter.

For this purpose, line-neutral voltages (fig 2.9 to fig 2.12).were then fed to the equivalent circuit describing motors I (§ 7.1). The value of slip was set to the nominal value  $s_{nom}$  [%] in the two cases. When the motor operates at full load, the impedance of the equivalent circuit is lower. As a result, load currents are not filtered by the magnetizing

reactance in the iron loss branch. The effect of modified sideband harmonic pattern of applied voltages on load currents is more clearly visualized than under partial load conditions. The impact of PWM modulation schemes on voltage harmonic spectra is more apparent the lower the frequency ratio of switching ( $f_{sw}$ ) to electrical frequency ( $f$ ) is. In these conditions, the ratio of reference to carrier periods in PWM implementation is closer to unity and any change in the PWM switching pattern is more influential on voltage and current harmonic characteristics. This is why the selected frequency was 200 Hz. In the constant V/Hz control featured in chapter 7, the modulation index  $m_i$  associated to 200 Hz is unity. The PWM switching frequency was 2.5 kHz. The system was simulated in the Dymola environment. The FFT analysis of line-neutral voltages and load currents was performed by Day Post Processor (Ansoft Simplorer).

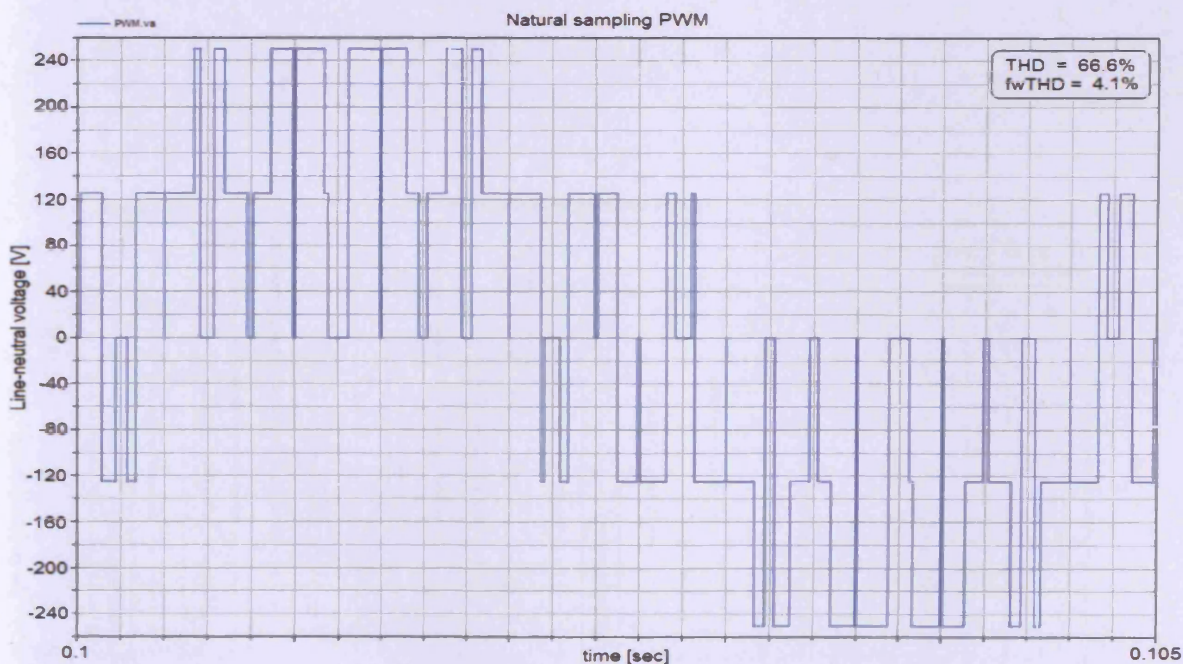


Fig 2.9. Line-neutral voltage (natural-sampling PWM)

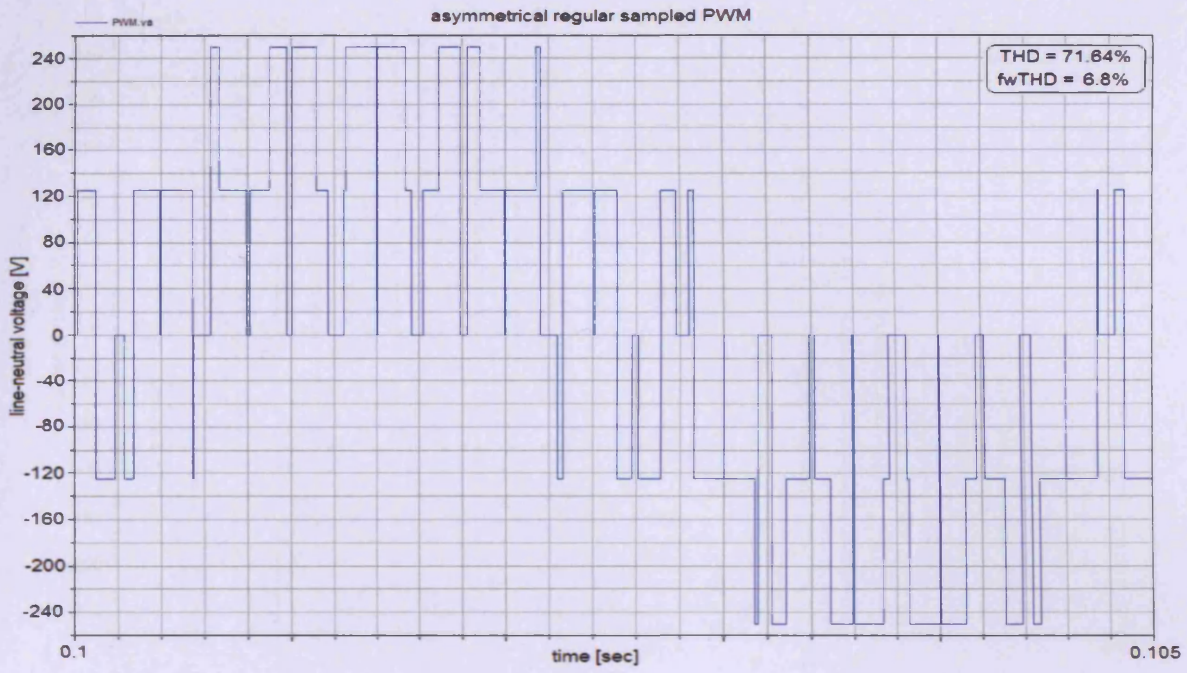


Fig 2.10. Line-neutral voltage (asymmetrical regular sampled PWM)

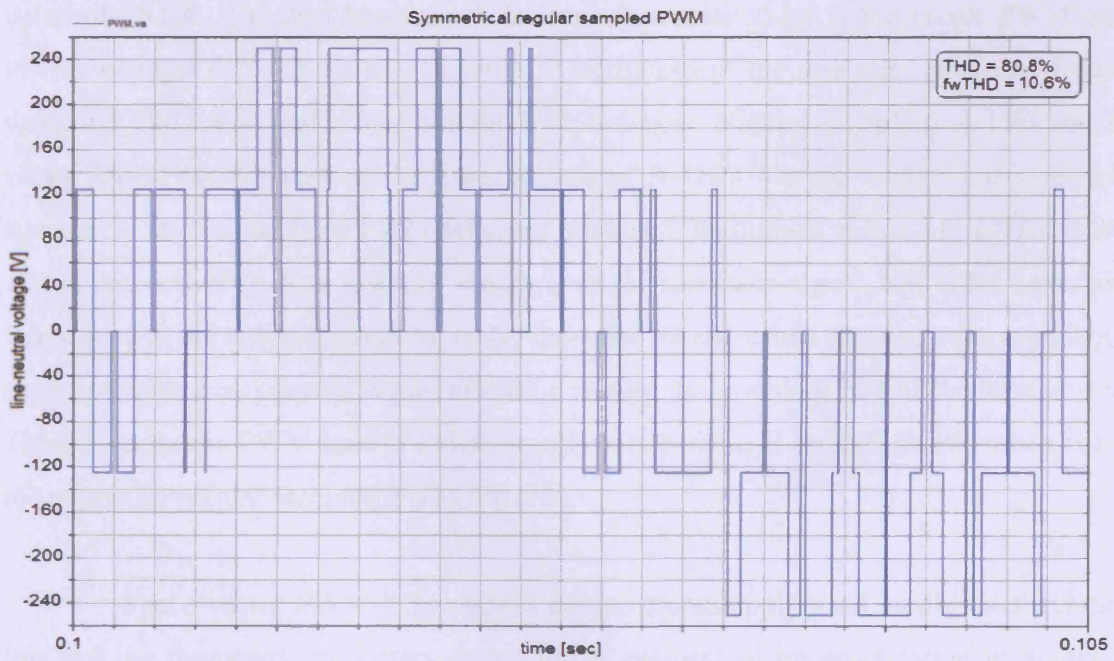


Fig 2.11. Line-neutral voltage (symmetrical regular sampled PWM)

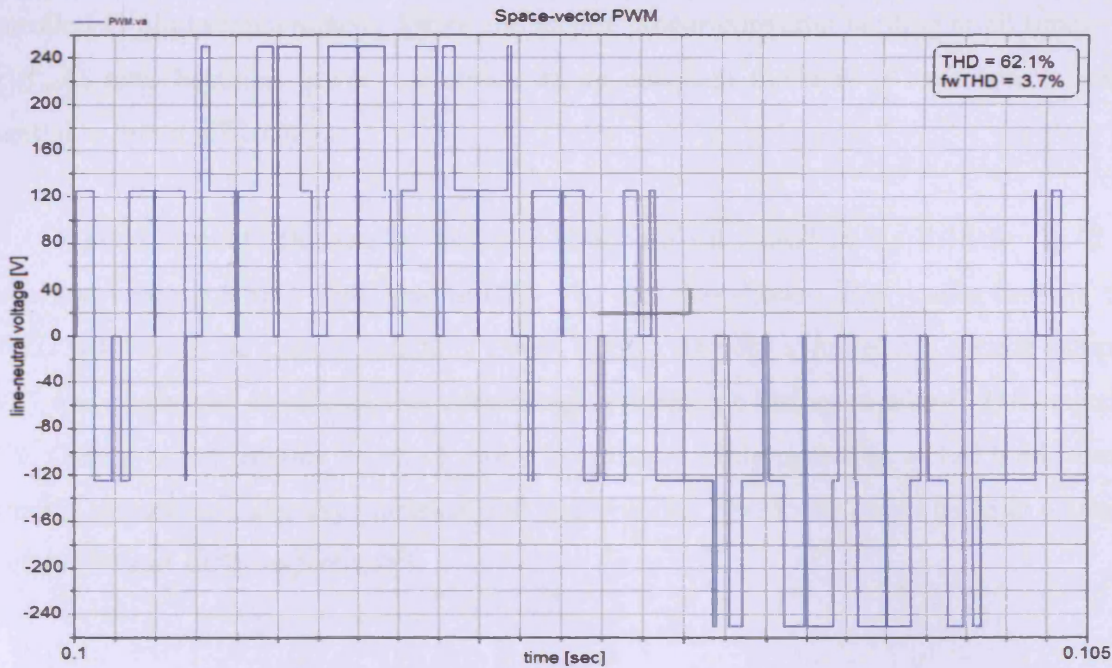


Fig 2.12. Line-neutral voltage (space-vector PWM)

The highest value of THD (80.8%) was found in symmetrical regular sampled PWM. While asymmetric PWM yielded a  $THD$  value of 71.6%, natural sampling PWM lead to a value of 66.6%. The best harmonic behaviour was ensured by space-vector PWM with the lowest voltage  $THD$  of 62.1%. In order to complement the analysis, values of frequency-weighted  $THD$  were calculated for the four voltages. Natural sampling (4.1%) and space-vector PWM (3.7%) yielded the lower values of  $fwTHD$ . On the contrary, asymmetric and symmetric regular sampled PWM schemes produced the highest values of  $fwTHD$  (6.8% and 10.6% respectively). As a result of sampling of the reference signal, low order harmonics are introduced in the voltage wave-shape. By the same token, results show that the introduction of such harmonic components is minimized by raising the sampling rate of the reference signal. Thus, asymmetric PWM lead to a significantly lower value of  $fwTHD$  (6.8%) when compared to symmetric regular sampled PWM (10.6%).

Space-vector PWM is nowadays the most commonly used modulation technique in low voltage frequency converters owing to the easiness of implementation in digital signal processors. Apart from this, the space-vector technique allows the use of zero vectors in the switching pattern which gives more flexibility for harmonic compensation in motor control. The selection of an adequate PWM scheme is particularly important when motor power ratings increase. Then, frequency converter of higher ratings must be used to supply the rotating machine. As a result, PWM switching frequency must be lowered and closely

controlled to limit semiconductor losses and ensure proper converter cooling at all times. As the  $(f_{sw}/f)$  ratio becomes lower, the choice of an adequate modulation technique becomes essential to motor efficiency.

Load currents flowing to motor (15kW) are illustrated in fig 2.13 to fig. 2.16. Numerical values of  $THD$  [%] and  $fwTHD$  [%] are also shown. The results confirm that  $fwTHD$  was lowest for natural sampling PWM (0.5%) whereas symmetrical regular sampled PWM was confirmed as scheme that caused higher harmonic distortion with  $fwTHD$  equal to 1.2%. Owing to the filtering effect of motor impedance while operating at full load, current harmonic distortion under asymmetrical and space-vector PWM was found to be in a similar range (0.9% and 1.0% respectively).

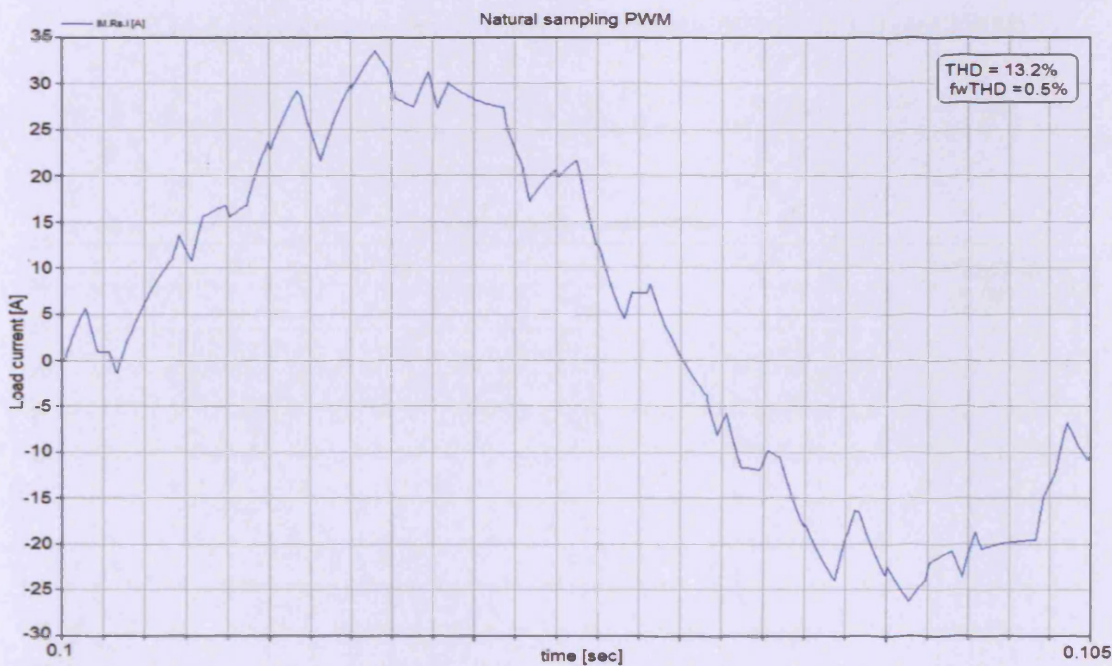


Fig 2.13. Load current in motor (15kW) - (natural-sampling PWM)

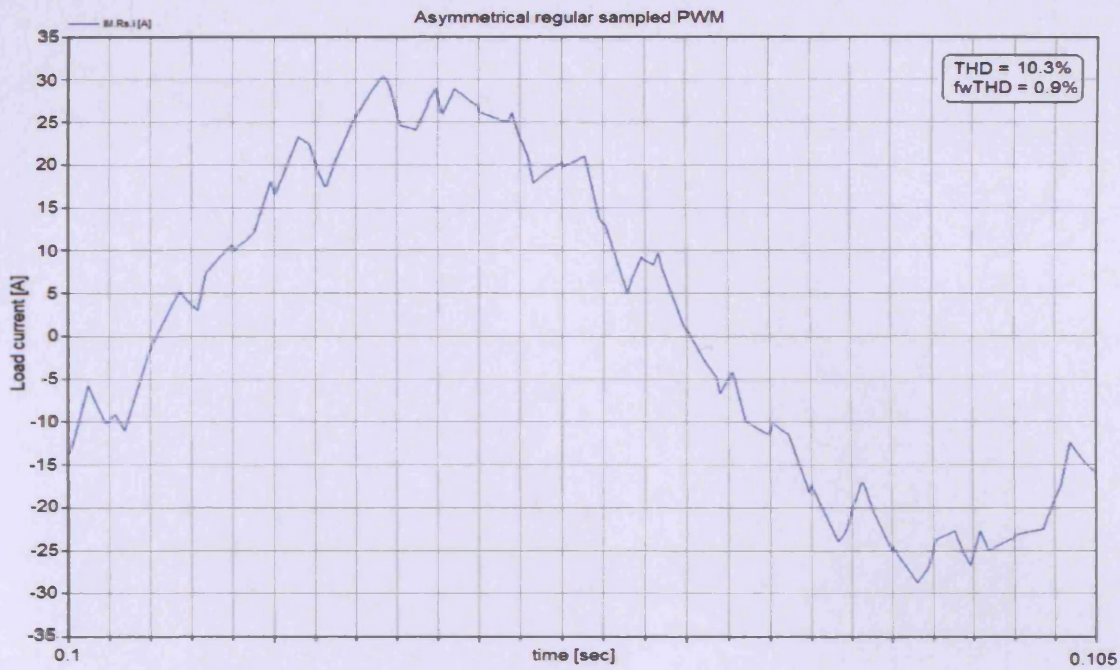


Fig 2.14. Load current in motor (15kW) - (asymmetrical regular sampled PWM)

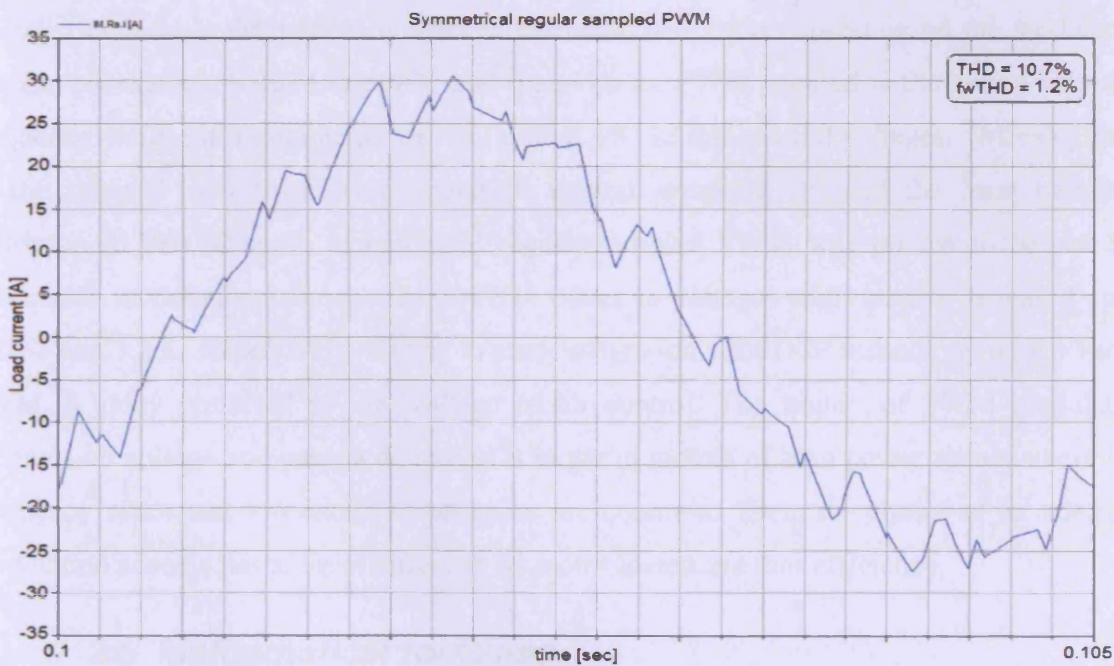


Fig 2.15. Load current in motor (15kW) - (symmetrical regular sampled PWM)

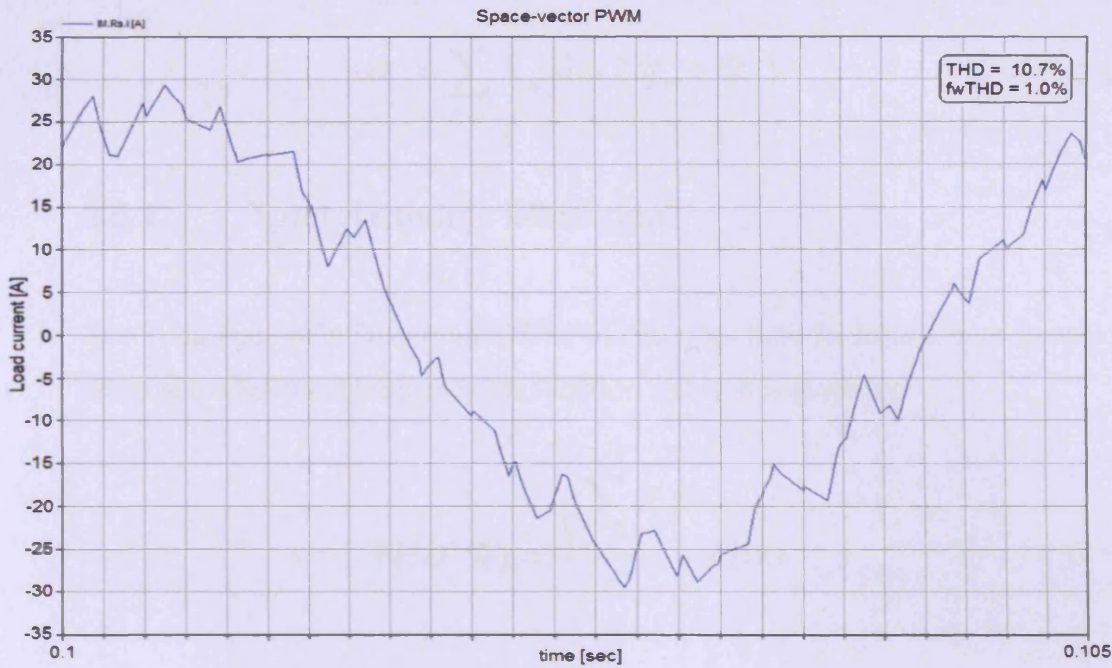


Fig 2.16. Load current in motor (15kW) - (space-vector PWM)

Four different modulation strategies (natural sampling PWM, asymmetrical and symmetrical regular-sampled PWM; space-vector PWM) have been analysed. The study revealed noticeable differences in voltage harmonic distortion depending on the modulation scheme considered. Natural sampling and space-vector PWM resulted in the lowest values of frequency-weighted harmonic distortion (around 4%) in line-neutral voltages. When currents in the referred conditions were analysed, natural sampling ensured the least harmonic distortion (0.5%). Overall, symmetrical regular-sampled PWM was proven to be the less favourable modulation scheme. The  $fwTHD$  values in voltages and currents increased up to 10.6% and 1.2%, respectively. Owing to easy integration with DSP technology, space-vector PWM is today preferred in low voltage motor control. The impact of PWM modulation schemes on voltage and current distortion is larger in motors of high power rating, where low frequency ratios and low motor impedances are common. Then, the choice of an adequate modulation scheme has a direct influence on motor losses and thus efficiency.

## 2.5 Mathematical formulae

A periodical function  $x(t)$ , of fundamental frequency  $f$  [Hz] and null DC value, is analysed as a sum of harmonic sinusoidal signals  $x_n(t)$  of amplitude  $X_n$ , frequency  $f_n$  [Hz] equal to  $nf$  and phase angle  $\Phi_n$  [rad] as given as

$$x(t) = \sum_{n=1}^{\infty} X_n \sin(2\pi f_n t + \Phi_n) \quad (2.17)$$

### 2.5.1 Total Harmonic Distortion

The Total Harmonic Distortion *THD* [%] describes how far from a pure sinusoidal wave of identical fundamental frequency the function  $x(t)$  is. It is given by

$$THD[\%] = \frac{\sqrt{\sum_{n=2}^{\infty} X_n^2}}{X_1} \times 100 \quad (2.18)$$

### 2.5.2 Frequency-weighted Total Harmonic Distortion

In some instances, it is important to consider the position of the harmonic component of order  $n$  in the frequency spectrum, given by its frequency  $f_n$ , along with its amplitude  $X_n$ . The frequency-weighted Harmonic Distortion *fwTHD* [%] is given by

$$fwTHD[\%] = \frac{\sqrt{\sum_{n=2}^{\infty} \frac{X_n}{f_n}}}{\frac{X_1}{f}} \times 100 = \frac{\sqrt{\sum_{n=2}^{\infty} \frac{X_n}{n}}}{X_1} \times 100 \quad (2.19)$$

### 2.5.3 Form Factor

The form factor is often used to describe the harmonic quality of an alternating signal  $x(t)$ . It is obtained by dividing the Root Mean Square [RMS] or quadratic mean value  $X_{RMS}$  of the waveform by its rectified mean value  $X_{rect\_mean}$ . It is given by

$$FF = \frac{X_{RMS}}{X_{rect\_mean}} = \frac{\sqrt{\sum_{n=1}^{\infty} X_n^2}}{\sum_{n=1}^{\infty} |X_n|} \quad (2.20)$$

The ratio  $\Delta$  [%] of rectified mean value  $X_{rect\_mean}$  to the amplitude of the fundamental component  $X_1$  of frequency  $f$  [Hz] takes into account total harmonic distortion and form factor. It is given by

$$\Delta[\%] = \frac{X_{rect\_mean}}{X_1} \times 100 = \frac{100}{FF \sqrt{1 + \left(\frac{THD}{100}\right)^2}} \quad (2.21)$$

## 2.6 Summary

The investigation of the influence of pulsating excitation on non-oriented steel is founded on electromagnetism principles applied to commercial soft magnetic materials of well-defined physical properties. Prior to the measurement of losses, representative voltage waveforms of direct/indirect AC-AC power conversion topologies have to be selected as magnetising signals. This can not be accomplished without a basic understanding of modulation techniques [SVM, PWM] and control strategies, which regulate the energy flow to the rotating machine. In order to explain the performance of steel under distorted magnetising conditions, an in-depth analysis of the harmonic quality of non-sinusoidal alternating quantities is paramount. The characteristics of the induction motor are incorporated in the equivalent circuit, which allows the study of machine performance at various load and speed. Voltage and current harmonic distortion in a 15kW induction motor have been calculated for four different PWM schemes. Asymmetrical regular-sampled and space-vector PWM combine the benefits of natural sampling PWM with a straightforward integration with digital signal processing currently used in drive control.

## References

- [2.1] UK Steel: a division of EEF, "Steel. Material to the Economy > How Steel Is Made", [www.uksteel.org.uk/](http://www.uksteel.org.uk/).
- [2.2] European Committee for Standardisation, "European Standard EN 10027-1. Designation Systems for Steels – Part 1", August 2005.
- [2.3] J. Leicht, "Magnetic Properties of Electrical Steels under Controlled Magnetisation Conditions", *PhD Thesis - Wolfson Centre for Magnetics. Cardiff University*. August 2003.
- [2.4] United States Steel, "The Making, Shaping and Treating of Steel", *Herbick & Held*, 9<sup>th</sup> Edition, 1971.
- [2.5] G. Bertotti, "General Properties of Power Losses in Soft Ferromagnetic Materials", *IEEE Transactions on Magnetics*, Vol 24, No 1, pp 621-630, January 1988.
- [2.6] A. Krawczyk, J. A. Tegopoulos, "Numerical Modelling of Eddy-Currents", *Monographs in Electrical Engineering (N° 32), Oxford Publications*, 1993.
- [2.7] F. Brailsford, "Physical Principles of Magnetism", *Van Nostrand*, London 1966.
- [2.8] G. Bertotti, "General Properties of Power Losses in Soft Ferromagnetic Materials", *IEEE Transactions on Magnetics*, Vol 24, No 1, January 1988.
- [2.9] P. W. Wheeler, J. Rodriguez, J. C. Clare, L. Empringham, "Matrix Converters: A Technology Review". *IEEE Transactions on Industrial Electronics*, Vol 49, No. 2, pp 276-288, April 2002.
- [2.10] Drives & Controls, "The matrix arrives", *Advanced Technology*, pp 18-20, November/December 2005.
- [2.11] M Venturini, "A New Sine Wave In, Sine Wave Out Conversion Technique Which Eliminates Reactive Elements", *Proc POWERCON 7*, pp E3\_1/E3\_5, 1980.
- [2.12] M. Braun, K. Hasse, "A direct frequency changer with control of input reactive elements", in *Proceedings IFAC Control in Power Electronics and Electrical Drives*, Lausanne (Switzerland), pp 187-194, 1983.
- [2.13] G. Kastner, J. Rodriguez, "A forced commutated cycloconverter with control of the source and load currents", in *Proceedings European Power Electronics Conference*, pp 1141-1146, 1985.
- [2.14] L. Huber, D. Borojevich, "Space vector modulator for forced commutated cycloconverters", in *Proceedings of IEEE Industry Applications Society Annual Meeting*, pp 871-876, 1989.

- [2.15] L. Huber, D. Borojevich, N. Burany, "Analysis, design and implementation of the space-vector modulator for forced-commutated cycloconvertors", in *IEE Proceedings*, pp Vol 139, No 2, pp 103-113, March 1992.
- [2.16] L. Huber, D. Borojevich, "Space vector modulated three phase to three phase matrix converter with input power factor correction", *IEEE Transactions on Industrial Applications*, Vol 31, pp 1234-1246, November/December 1995.
- [2.17] V. Vlatkovic, D. Borojevich, "Digital Signal Processor based control of three-phase space vector modulated converters", *IEEE Transactions on Industrial Electronics*, Vol 41, No 3, pp 326-332, June 1994.
- [2.18] G. Vrana, "Motor Control: the Variable Speed Revolution". *Global Report on Industrial automation and Control*, pp 44-50, July 2005.
- [2.19] D. Casadei, G. Serra, A. Tani, L. Zarri, "Matrix Converter Modulation Strategies: A New General Approach Based on Space-Vector Representation of the Switch State", *IEEE Transactions on Industrial Electronics*, Vol 49, No 2, pp 370-381, April 2002.
- [2.20] L. Helle, K. B. Larsen, A. H. Jorgensen S. Munk-Nielsen, "Evaluation of Modulation Schemes for Three-Phase to Three-Phase Matrix Converters", *IEEE Transactions on Industrial Electronics*, Vol 51, No. 1, pp 158-171, February 2004.
- [2.21] M. V. M. Villaça, A. J. Perrin, "A soft switched direct frequency changer", in *Proceedings of IEEE Industry Applications Society Annual Meeting*, pp 2321-2326, 1995.
- [2.22] J. G. Cho, G. H. Cho, "Soft switched matrix converter for high frequency direct Ac-to-AC power conversion", in *Proceedings of European Power Electronics Conference*, Florence (Italy), pp 4196-4201, 1991.
- [2.23] C. Klumpner, P. Nielsen, I. Boldea, F. Blaabjerg, "A new matrix converter-motor (MCM) for industry applications", in *Proceedings IEEE Industry Applications Society Annual Meeting*, Vol 3, pp 1394-1402, October 2000.
- [2.24] C. L. Neft, "AC Power Supplied Static Switching Apparatus Having Energy Recovery Capability", *U.S. Patent 4 697 230*, 1987.
- [2.25] J. Holtz, W. Lotzkat, "Controlled AC drives with ride-through capability at power interruption", *IEEE Transactions on Industry Applications*, Vol 30, pp 1275-1283, September/October 1994.
- [2.26] C. Klumpner, I. Boldea, F. Blaabjerg, "Short term ride-through capabilities for direct frequency converters", in *Proceedings of IEEE Power Electronics Specialists Conference*, Vol 1, pp 235-241, June 2000.

- [2.27] K-B. Lee, F. Blaabjerg, "A Non-Linearity Compensation Method for a Matrix Converter Drive", *IEEE Power Electronics Letter*, Vol 3, No1, pp 19-23, March 2005.
- [2.28] Yaskawa Corporation, "A motor drive responding to environmental needs: Matrix Converter. Varispeed AC", *EZZ020326 – No. U050601*, January 2006.
- [2.29] O. Simon, J. Mahlein, M. N. Muenzer, M. Bruckmann, "Modern Solutions for Industrial Matrix-Converter Applications", *IEEE Transactions on Industrial Electronics*, vol 49, No. 2, pp 401-406, April 2002.
- [2.30] F. Blaabjerg, P. Thøgersen, "Adjustable Speed Drives. Future Challenges and Applications", *4<sup>th</sup> International Power Electronics and Motion Control Conference*, Vol 1, pp 36-45, 2004.
- [2.31] G. Towers, "Analysis of a Matrix Converter Driven Electro-Mechanical Actuator for an Aircraft Rudder", *IEEE Power Electronics Society – United Kingdom and Republic of Ireland Chapter, One Day Seminar on Matrix Converters*, The University of Nottingham, November 17<sup>th</sup> 2004.
- [2.32] P. W. Wheeler, J. Clare, L. de Lillo, K. Bradley, M. Aten, C. Whitley, G. Towers, "A Reliability Comparison of a Matrix Converter and an 18-pulse Rectifier for Aerospace Applications", *12<sup>th</sup> International Power Electronics and Motion Control Conference*, pp 496-500, Aug 2006.
- [2.33] P. Snary, B. Bhangu, C. M. Bingham, D. A. Store, N. Schofield, "Matrix Converter for Sensorless Control of PMSMs and other auxiliaries on Deep-Sea ROVs2", *IEE Proceedings – Electric Power Applications*, Vol 152, No. 2, pp 382-392, March 2005.
- [2.34] T. F. Podlesak, H. Singh, "On the Feasibility of a 1 MW inverter in less than a cubic meter volume for vehicle applications", in *Proceedings 30<sup>th</sup> Intersociety Energy Conversion Engineering Conference*, Orlando (United States), pp 479-484, August 1995.
- [2.35] P. W. Wheeler, J. C. Clare, L. Empringham, K. G. Kerris, T. Podlesak, "A Matrix Converter for Military All-Electric Vehicle Applications", in *Proceedings All Electric Combat Vehicles Conference*, June 2003.
- [2.36] L. Guyer, "Going Green. Hybrid Stake Claims: Demand Grows for Vehicles Once Considered Quirky", *WARD'S Dealer Business*, pp 46-47, May 2006.
- [2.37] A. Emadi, K. Rajashekara, S. S. Williamson, S. M. Lukic, "Topological Overview of Hybrid Vehicular Power System Architectures and Configurations", *IEEE Transactions on Vehicular Technology*, Vol 54, No. 3, pp 763-770, May 2005.

- [2.38] S. M. Barakati, M. Kazerami, X. Chen, "A New Wind-Turbine Generation System Based on Matrix Converters", in *Proceedings of IEEE Power Engineering Society General Meeting*, pp 2083-2089, June 2006.
- [2.39] T. Podlesak, D. Katsis, P. W. Wheeler, J. C. Clare, L. Empringham, M. Bland, "A 150 kVA vector-controlled matrix converter induction motor drive", *IEEE Transactions on Industry Applications*, Vol 41, No. 3, pp 841-847, May/June 2005.
- [2.40] D. Katsis, P. W. Wheeler, J. C. Clare, P. Zanchetta, "A Three-phase Utility Power Supply based on the Matrix Converter", in *Proceedings of 39<sup>th</sup> Industry Applications Society Annual Meeting*, Vol 3, pp 1447-1451, 3-7 October 2004.
- [2.41] D. Casadei, G. Serra, A. Tani, "The Use of Matrix Converters in Direct Control of Induction Machines", *IEEE Transactions on Industrial Electronics*, Vol 48, No. 6, pp 1057-1064, December 2001.
- [2.42] K-B. Lee, F. Blaabjerg, "Reduced-order Extended Luenberger Observer Based Sensorless Vector Control Driven by Matrix converter with Nonlinearity Compensation", *IEEE Transactions on Industrial Electronics*, Vol 53, No. 1, pp 66-75, February 2006.
- [2.43] R. Hoadley, "Harmonic Mitigation in AC Drives", *Control Engineering*, pp 55-60, September 2006.
- [2.44] J. W. Kolar, T. M. Wolbank, M. Schrod, "Analytical Calculation of the RMS Current Stress on the DC-link capacitor of voltage DC-link PWM Converter System", in *Proceedings 9<sup>th</sup> International Conference on Electrical Machines and Drives*, pp 81-89, September 1999.
- [2.45] B. K. Bose, "Power Electronics and AC Drives". *Prentice-Hall*. ISBN 0-13-686882-7. 1986.
- [2.46] J. Vithayathil, "Power Electronics. Principles and Applications". *McGraw Hill Series in Electrical and Computer Engineering*. ISBN 0-07-067555-04. 1995.
- [2.47] M. Liserre, C. Klumpner, F. Blaabjerg, V. G. Monopoli, A. Dell'Aquila, "Evaluation of Ride-Through Capability for an Active Front-End Adjustable Speed Drive under Real Grid Conditions", in *Proceedings 30<sup>th</sup> Annual Conference of the Industrial Electronics Society*, Vol 2, pp 1688-1693, Nov 2004.
- [2.48] M. Liserre, F. Blaabjerg, S. Hansen, "Design and Control of an LCL filter based Three-Phase Rectifier", in *Proceedings of Industry Applications Society Annual Meeting 2001*, Vol 1, pp 299-307, 2001.
- [2.49] H.A. Toliyat, G.B. Kliman, "Handbook of Electric Motors", *CRC Press 2004 Ed 2* – ISBN 0824741056

- [2.50] S. R. Bowes, Y-S. Lai, "The Relationship between Space-Vector Modulation and Regular-sampled PWM", *IEEE Transactions on Industrial Electronics*, vol 44, N°5, Oct 1997.
- [2.51] D. G. Holmes, B.P. McGrath, "Opportunities for Harmonic Cancellation with Carrier-Based PWM for Two-level and Multi-level Cascaded Inverters", *IEEE Transactions on Industry Applications*", Vol 37, no2, pp 574-582, March/April 2001.
- [2.52] S. R. Bowes, D. Holliday, "Optimal Regular-Sampled PWM Inverter Control Techniques", *IEEE Transactions on Industrial Electronics*, vol 54, No3, pp 1547-1559, June 2007

## IRON LOSSES IN SOFT MAGNETIC MATERIALS: A SURVEY

---

### **3.1 Introduction**

In electrical machinery, laminated steels are subjected to cyclic magnetisation. Successful research on physics of matter and electromagnetism described magnetisation in crystalline structures as a dynamic rearrangement of domains. Energy is dissipated within the soft magnetic material, which leads to the so-called iron losses. Novel concepts (domain wall dynamics, magnetic viscosity) were incorporated to classical knowledge on electromagnetism (Maxwell's Equations, eddy-currents) in idealised models in an attempt to describe, quantify and predict iron losses in electrical steels subjected to sinusoidal magnetising conditions.

The expansion of fast-switching Pulse-Width-Modulated [PWM] converter-fed induction motors in industrial applications resulted in an increase in iron losses in non-oriented steel. Non-sinusoidal induction implies low/high order harmonics, which cause minor loops and an increase in frequency-dependent losses (classical eddy-currents, anomalous). Loss distribution in complex geometries of stator/rotor cores has become easier, as advances in finite element modelling and improved knowledge of rotational magnetisation have been accomplished. More recently, new formulation of iron loss analysis have been proposed for a more straightforward use in engineering applications. The impact of iron losses on the overall efficiency of a variable speed drive has also been estimated. The review presented in this chapter aims at providing the reader with an overall perspective on research carried out on iron losses in soft magnetic materials.

### **3.2 Fundamentals of Losses in Ferromagnetic Materials**

#### **3.2.1 Weiss Domains**

Electrons have a magnetic dipole moment along their spin axis. In ferromagnetic materials below the Curie temperature, groups of individual atomic moments align themselves parallel to each other in regions without applying an external field. A magnetisation vector, of specific magnitude and orientation, is associated to every microscopic region of material. The so-called Weiss domains, of which the existence was predicted by the French physicist Pierre-Ernest Weiss in 1907, are commonly known as magnetic domains. The boundaries between them are classified as Bloch walls when magnetic moments in the transition layer are normal to the plane of the material.

### **3.2.2 Crystalline Structure**

Ferromagnetic materials, such as silicon-iron alloys are polycrystalline materials. The solid matter is divided into many crystallites or grains, where atoms are ordered following a three-dimensional, regular pattern without any structural discontinuity. The interface between crystallites is known as grain boundary. Grain boundaries can be explained by the collision of two grains which grow in different directions to cause planar defects and dislocations (Vito Volterra, 1905). When the orientation of individual grains is random, the material is defined as isotropic. This property is required in non-oriented steels, which need to conduct radial and tangential flux in cores of rotating machines. Conversely, transformers are static machines where high anisotropy is needed by grain-oriented steels to conduct unidirectional flux in limbs and yokes. This can be accomplished in the manufacturing process by cold rolling (to reduce misalignment from grain to grain), magnetic annealing or application of tensile stress (to obtain a common easy axis of magnetisation).

### **3.2.3 Physics of Magnetisation**

Should no external field be applied, the net magnetisation of a volume of ferromagnetic material is very small. Nevertheless, when a positive field is applied, magnetic domains within the material re-orient themselves parallel to the direction of the field. The ferromagnetic material is then magnetised. By applying a negative field (in the opposite direction), ferromagnetic materials can be demagnetised to a high degree as a consequence of their low coercivity. However, due to the phenomenon of magnetic hysteresis, the material

tends to remain magnetised. The lag between flux density  $B$  and magnetic field strength  $H$  becomes apparent when the material approaches saturation (fig. 3.1)

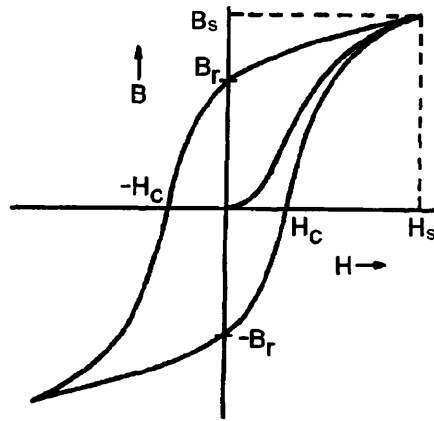


Fig. 3.1. Simplified B-H curve with  $B_s$  (induction at saturation),  $H_s$  (magnetic field at saturation) and  $B_r$  (retentivity),  $H_c$  (coercive field)

Alternating flux may be conducted in ferromagnetic materials by two mechanisms: domain rotation and domain-wall motion. Both mechanisms can be reversible or irreversible [3.1]. In reversible processes, potential energy is cyclically stored and released by the lattice. However, in irreversible processes, thermal energy is dissipated in the material as the lattice is excited during each flux-reversal cycle. When domain rotation occurs, individual magnetic moments rotate within the domain in order to overcome anisotropy forces and become aligned with the applied field. In laminated steel, irreversible domain-wall motion is the main mechanism explaining magnetisation under alternating fields. Magnetic moments rotate within the domain, but this rotation is accompanied by movement of the wall. Initially, the configuration of Weiss domains is an answer to minimisation of the magneto-static energy of the system. Local internal fields around crystalline imperfections are therefore ideal points for the creation of domains. Their value is critical to determine the remanence or retentivity, which measures how difficult reverting magnetisation from an initial saturated state is.

### 3.2.4 Domain Wall Motion

Once an alternating field is applied, domain wall motion takes place until the volume of material is magnetised and domain walls become stable. Motion of  $180^\circ$  Bloch walls is illustrated in fig. 3.2.

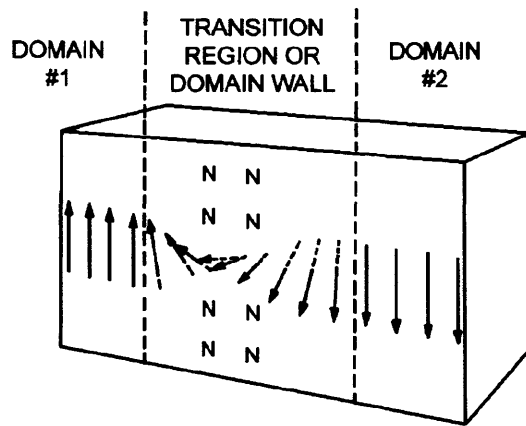


Fig. 3.2. Transition layer between two  $180^\circ$  anti-parallel domains [3.3]

The general motion equation of a plane domain-wall motion in ferromagnetic materials is provided in (3.2).  $x(t)$  is the displacement of the wall,  $\beta$  is a damping coefficient and  $k$  is a stiffness parameter linked to elastic forces.  $M_s$  is the magnetisation vector at saturation.  $H$  is the applied field.

$$m_w \ddot{x} + \beta \dot{x} + kx = \lambda \vec{M}_s \cdot \vec{H} \quad (3.2)$$

$m_w$  is the domain wall mass per unit area (equal to zero when acceleration is neglected). The coefficient  $\beta$  describes damping per unit area of domain wall. In the case of ferromagnetic materials, damping is mainly due to eddy-currents ( $\beta_e$ ). In thin laminations (less than 25 $\mu$ s) or in high resistivity ferrites, the relaxation contribution ( $\beta_r$ ) is dominant. The adimensional term  $\lambda$  is characteristic of the domain wall type (equal to 2 for  $180^\circ$  domain walls).

Inhomogeneities within the material oppose the propagation of domain walls that remain pinned until sufficient energy is provided to overcome the obstacle. The magnetic viscosity phenomenon, which occurs when the required unpinning energy is supplied thermally, is well explained by  $N_g$  [3.2]. When the wall gets detached collectively from several pinning sites, domain wall pinning is of weak nature. Should the wall detach itself in a pin-by-pin fashion, the phenomenon is known as strong pinning. The ultimate position of the deformed wall before unpinning and its final location after getting detached define the activation volume analytically described for both weak and strong pinning models. The general expression of the magnetic viscosity is given in (3.4).

$$S = \frac{-kT\chi_{irr}}{dE/dH} \quad (3.4)$$

Where  $kT$  is the Boltzmann constant,  $\chi_{irr}$  the irreversible susceptibility,  $E$  [J.mol<sup>-1</sup>] is the activation energy and  $H$  [A.m<sup>-1</sup>] is the applied magnetic field.

### **3.3 Modelling Losses in Soft Magnetic Materials**

#### **3.3.1 Dynamic component**

Based upon Faraday's Law of Induction, classical eddy-current losses in ferromagnetic laminations of thickness were deduced analytically. Nevertheless, the calculation was only valid if linearity between magnetic field and induction (both sinusoidal quantities), isotropy and homogeneous permeability of the medium were accepted. Structural inhomogeneities, which affect motion of Weiss domain walls and cause discontinuous permeability in the volume of material, were not considered. As a result of idealising the magnetic material, it was soon revealed that classical eddy-current losses were somewhat smaller than the subtraction of static hysteresis loss from total measured losses. This phenomenon was defined in scientific terms as the eddy-current anomaly [3.4].

In a discussion on losses in magnetic steel sheet, Stewart acknowledged that the variation of losses and permeability in ferromagnetic materials subjected to alternating excitation in power applications (high flux densities and power frequencies) was yet to be thoroughly investigated [3.4]. While research on domain structure was underway, Stewart suggested that domain wall dynamics were, at least, partly responsible for the excess loss in steels in the power frequency range. Furthermore, the author raised awareness in his introduction on the very theoretical assumption of linearity between flux density and magnetic field. It was reported that consideration of non-linearity between the two quantities in real materials could lead to a better understanding of anomalous losses. Stewart briefly reviewed the assumption of constant permeability across the cross sectional area of the laminated material. Non-uniform permeability was pointed out as an essential phenomenon in ferromagnetic laminations, owing to its influence on induced eddy-currents and dynamic energy losses. Although it is very difficult to evaluate their individual contribution, domain

wall dynamics, non-uniform permeability and non-linearity between magnetic field and flux density are related to excess losses.

### **3.3.2 Pry and Bean model: rigid domain walls**

Pry and Bean proposed a particular form of eddy current loss analysis [3.5]. Their model was based on parallel, longitudinal  $180^\circ$  domains, whose magnetisation lay in the plane of the lamination. These equally-spaced domains of the same dimensions were limited by Bloch walls perpendicular to the plane of the lamination. The model proposed by Pry and Bean assumed that, at sufficiently low frequencies and high magnetic fields, domain walls could be considered planar and rigid. However, at this early stage, the authors suggested that that wall bowing due to pinning was not be neglected for high values of magnetising frequency. Although it relied on idealisation of the material, the model proposed by Pry and Bean was a significant milestone in the study of eddy-current losses in ferromagnetic laminations. In their discussion, Pry and Bean emphasised that the effect of increasing magnetising frequency on domain wall bowing had yet to be for in the determination of classical and excess eddy-current losses in ferromagnetic laminations. It was pointed out that the model proposed would yield reasonable accuracy in the analysis of energy losses in laminated 3 % grain-oriented steel. However, it was derived from their conclusions that the investigation of frequency-dependent losses in electrical steel sheets had to be taken further, in order to cover a broader range of materials including non-oriented steel.

### **3.3.3 Anomalous losses**

Alberts et al carried out experimental work to confirm that discrete domain configuration at a micro-structural level played an essential role in losses in magnetised, laminated steel [3.6]. Firstly, the temperature was raised up to the Curie temperature in order to alter domain wall spacing while maintaining the polycrystalline structure of iron. The influence of temperature on domain size in the sample was assumed to be equivalent to that of a single crystal. A reduction of anomalous losses by a factor of eight, while the temperature was varied from normal conditions to the Curie temperature, was proved experimentally. Furthermore, it was confirmed that experimental excess losses were smaller than the predicted under Pry and Bean theory. The strong dependence of the anomaly factor (discrepancy between measured and sum of calculated static and classical eddy-current

losses) on the magnetising frequency of the applied field at room temperature was highlighted. While at the lowest frequencies, experimental anomaly factor values of up to 65 were observed, frequencies close to 2 kHz lead to maximum values of four approximately

Mazzetti correlated Bloch walls and energy losses in silicon-iron grain-oriented steel [3.7]. When the applied field is varied continuously, changes in flux density are discontinuous. By assuming regular movement of the walls, there is no plausible explanation for irreversible jumps observed throughout the B-H loop. The author suggested that the separation of magnetic losses into hysteretic and dynamic components is artificial. Owing to the Barkhausen effect [3.8], the independence of static hysteresis on magnetising frequency is questioned. The study of anomalous or excess losses, which result from subtracting the sum of well-defined static hysteresis and classical eddy-current components from measured losses, was the main focus of the proposed study. The mismatch between these two quantities confirms that an anomaly factor had to be considered in the analysis of loss in silicon-iron alloys.

Celasco et al [3.8] continued the work initiated by Mazetti in [3.7]. Bloch walls dynamics were established as a key concept in the quantification of excess losses in 3% grain-oriented silicon-iron alloys. The paper studied the effect of domain wall spacing on losses per cycle in a commonly used alloy in industrial transformers. The variation with magnetising frequency of experimental and calculated losses, in accordance with classical and Pry & Bean theories, is also presented (fig. 3.3). It was concluded that higher domain wall spacing accounted for a maximum increase in losses of 35% at 30 Hz magnetising frequency, but the effect of this parameter on losses in the steel was attenuated at higher frequencies. It was underlined that Pry and Bean model showed strong dependence of calculated losses on domain boundary spacing, which was not in agreement with experimental results.

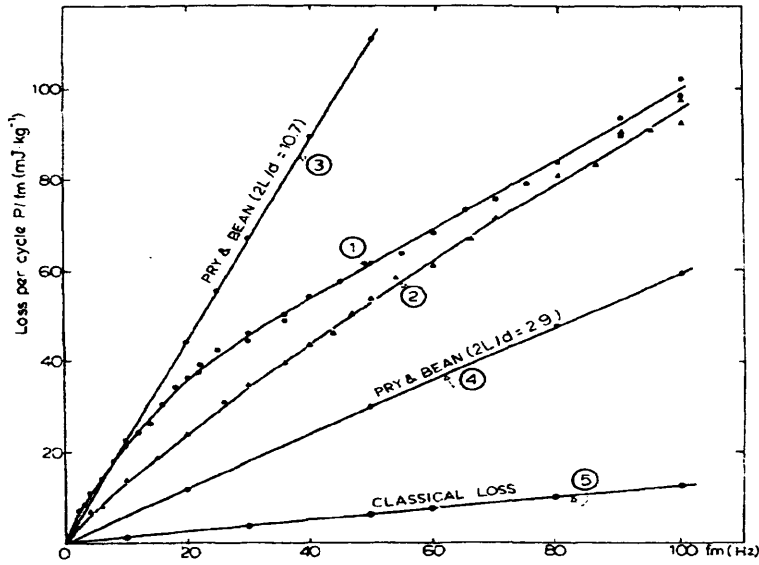


Fig. 3.3. Variation of predicted and measured frequency-dependent losses with magnetising frequency in 3% grain-oriented steel [3.8]

### 3.3.4 Domain Wall Bowing

By introducing the concept of a segmented wall (fig. 3.4), Bishop [3.9] investigated the influence of severe wall bowing on a significant decrease in the eddy-current losses, as calculated in accordance with Pry and Bean theory.

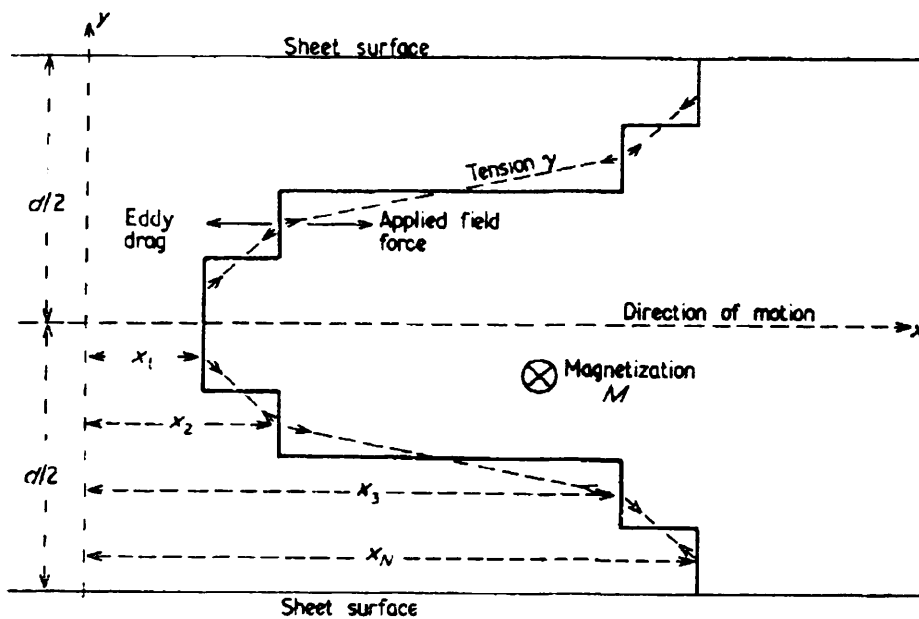


Fig. 3.4. Segmented domain wall subjected to bowing [3.9]

Due to eddy-currents in the magnetic material, the magnetisation is lower at the centre of the lamination than on the surface. Owing to the flux created by these eddy-currents, change in magnetisation is faster on the surface, which explains faster domain wall motion than in the centre of the lamination. As a result, the domain wall suffers from bowing (fig 3.5). The assumption of rigid, plane walls subjected to finite displacement is proved to be inadequate. Although the author's study focuses on isolated  $180^\circ$  Bloch walls, the investigation was a good contribution to a better understanding of domain wall dynamics. By introducing sinusoidal variation of the mean wall displacement  $x$  of amplitude  $\beta$  and reduced frequency  $W$ , the movement of the wall is induced by the external applied field but opposed by an eddy-current counter-field. Bishop proved that the energy loss associated with each wall is of different nature to that caused by classical eddy-currents. It was acknowledged that supplementary energy was needed by the domain boundary to overcome inhomogeneities [3.9]. The variation of energy loss per wall with magnetising frequency of a triangular waveform is given for a rigid, plane model, as postulated by Pry and Bean. Results are compared with losses incurred by a segmented wall subjected to severe bowing (fig. 3.5).

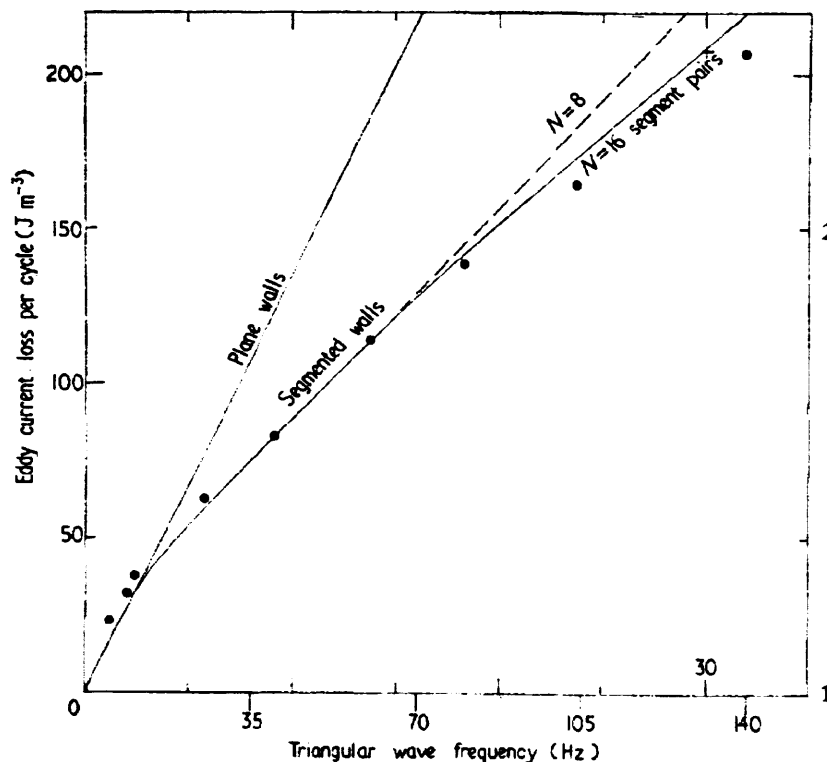


Fig. 3.5. Variation of eddy-current losses with fundamental frequency in a triangular magnetising waveform [3.9]

### 3.3.5 Statistical Approach by Bertotti

It was not until the beginning of 1980s that Bertotti developed the statistical theory of eddy-current losses, which reported that anomalous or excess losses were a consequence of the interaction between the applied magnetic field and eddy-current counter-fields impeding domain wall motion within the inhomogeneous micro-structure of the material. A more detailed discussion on the statistical approach to the problem of eddy-current losses was presented in [3.10].

#### 3.3.5a. Concept

According to Bertotti, magnetisation is a space-time stochastic process that consists of a random sequence of elementary magnetisation changes, caused by sudden, localised jumps of domain wall segments in the material. Based upon on the Barkhausen effect, which causes domain wall motion to be discontinuous, Bertotti identified domain structure dynamics as a key concept in the evaluation of losses in ferromagnetic sheets. Firstly, the sum of the loss incurred by every wall segment throughout the material in a localised jump is accounted for by the hysteresis loss, which is independent of the magnetising frequency. When jumps occur simultaneously, magnetisation changes take place in the material and frequency-dependent eddy-currents are induced. From Bertotti's point of view, the classical eddy-current component can be calculated by assuming statistically independent jumps in the magnetisation process.

Bertotti introduced the concept that individual jumps of domain wall segments were space and time correlated events. Eddy-currents were induced. Due to the superposition of those currents, which were determined by the space-time correlation of the jumps originating them, dynamic losses exceeded the classical term in the ferromagnetic material. The theoretical description of this correlation is founded on the transition amplitude  $M(\Delta r, \Delta t)$  which defines the way in which two subsequent jumps occur at a distance  $\Delta r$  with a time delay  $\Delta t$ . The function  $F$  introduced in [3.11] is highlighted as a direct link between losses in the material and magnetisation dynamics at a microscopic scale (3.5).

$$P = P_{hys} + P_c + F\{M(\Delta r, \Delta t)\} \quad (3.5)$$

At this stage, the challenge for Bertotti was to give physical meaning to the transition amplitude  $M(\Delta r, \Delta t)$  by taking into account parameters such as domain structure, magnetising frequency or flux density.

### 3.3.5b - Experimental Validation

Bertotti undertook an investigation [3.11], where losses per cycle in samples of several soft ferromagnetic materials (including grain-oriented and non-oriented 3% silicon-iron alloys) were measured experimentally under sinusoidal conditions. Several laminations were grouped in order to perform standard measurement of iron losses by the Epstein frame. Bertotti rationalised separation of losses into static hysteresis, classical eddy-current and excess losses as a valid hypothesis. When materials subjected to sinusoidal excitation are magnetised at a very low frequency, domain walls overcome inhomogeneities without bowing. In these quasi-static conditions, the energy necessary to achieve domain boundary motion in a medium with impurities or crystalline defects is known as static hysteresis. It depends on the level of induction and micro-structural properties of the material, but is assumed to be independent of the frequency and waveshape of the magnetising waveform. The author measured the static hysteresis loss, which is quantified by the area of the  $B$ - $H$  loop, for different materials. Classical eddy-current losses were calculated, based on idealisation of soft magnetic material (isotropy, homogeneous permeability, linearity between magnetic field and induction), by solving Faraday's Law of Induction in ferromagnetic laminations.

Bertotti was then in a position to estimate excess or anomalous losses, by simply subtracting the addition of measured static hysteresis and calculated classical eddy-current losses from total measured losses. The author introduced a general, analytical equation relating anomalous losses to peak magnetisation, magnetising frequency, conductivity of the material and cross-sectional area of the sample. A constant, dimensionless coefficient  $G$  was explicitly calculated. The intrinsic magnetic field  $V_o$  [ $A \cdot m^{-1}$ ] characterises the statistical distribution of local coercive fields for a specific material [3.11]. It is stated to be independent of peak flux magnetisation. Fiorillo et al extended the separation model proposed by Bertotti to ferromagnetic laminations under non-sinusoidal magnetising conditions [3.12]. The separation model proposed by Bertotti has been accepted for two

decades. Its main strength is that it acknowledges well-established physical concepts of magnetism.

Uniform flux distribution in thick laminations of non-oriented steel is not a valid hypothesis owing to eddy-current shielding effect. This phenomenon is emphasised in materials with an increasingly low silicon content that lowers resistivity. Since the applied field responsible for magnetising steel in induction machines is created by pulsating voltages, harmonic distortion in the kilo-Hertz range in the flux density spectrum must be incorporated to the study of efficient magnetisation. Eddy-current shielding at high frequencies has an influence on harmonic core losses. The breakdown of those into static hysteresis, classical eddy-currents and excess losses would then be modified. Moreover, constant air gap flux has to be maintained in rotating machines to develop the required mechanical torque. It is not uncommon that machine cores are then brought to a magnetising state close to saturation. In these conditions, non-linearity between magnetic field and induction becomes apparent and the assumption of linearity between the two quantities is largely inadequate. The estimation of real eddy-current losses, as inferred from the classical view, is inaccurate. It has to be highlighted at this stage that the permeability of the material is not explicitly represented in the separation model proposed by Bertotti.

### 3.3.6 Linear frequency-dependence of anomalous losses

Fish et al investigated the frequency dependence of core losses in 6.5% Si – Fe steel [3.13]. It was reported that the assumption of the constant number of active magnetic objects in non-oriented ferromagnetic laminations leads to a linear variation of anomalous losses with classical eddy-current losses ( $P_{exc} \propto B_p^2 f^2$ ), as postulated by Pry and Bean. By pointing out that a certain number of magnetic objects - group of neighbouring interacting domain walls [3.13] - may be active without applying an external field, the authors questioned the proportionality of anomalous losses to  $B_p^{3/2} f^{3/2}$ , as concluded by Bertotti. The complexity inherent to magnetisation processes, which is affected by material properties (purity, anisotropy, grain size, domain wall spacing), dimensional characteristics of the sample (thickness) and magnetising conditions (temperature, frequency, peak flux density), recommends a more cautious look on the analysis of iron losses carried out by Bertotti. Fish et al reported experimental results that confirmed the linear dependence of anomalous losses

on  $B_p^2 f^2$  [3.13]. This conclusion emphasised that the theory proposed by Pry and Bean was more adequate than Bertotti's approach for this type of material.

### 3.3.7 Domain Wall Interaction

Bishop elaborated a study, where excess losses derived from an equally-spaced domain wall model, as used by Pry and Bean theory, were calculated for different ratios of domain width to lamination thickness [3.14]. Analytical results are compared to those obtained by a model with random domain wall width. The author justifies his study by presenting this particular model as a more realistic approach to domain structure in real materials. Based on this hypothesis, domain boundaries do not progress at an identical speed within the material. On the contrary, motion of each individual wall is determined by its interaction with already magnetised, neighbouring domains. It is illustrated that the anomaly factor in laminations is underestimated by Pry and Bean theory, especially at high ratios of mean wall spacing to thickness [3.14]. Moreover, Bishop casts a critical view on the statistical approach by highlighting that the interaction of simultaneously active magnetic objects would yield smaller anomalous losses than predicted by Bertotti.

### 3.3.8 Dynamic Hysteresis Model

Zirka et al elaborated a dynamic hysteresis model based on magnetic viscosity in conducting ferromagnetic laminations [3.15]. Firstly, the model is founded on the characteristic curve linking flux density  $B_i$  to applied field  $H_{st}(B_i)$  for an individual node  $i$  of the grid. The solution to the associated differential equation is obtained by a static hysteresis model. After that, the dynamic hysteresis model computes the time lag between  $B_i$  and applied field  $H_i$  (3.6).

$$\frac{dB_i(t)}{dt} = r(B_i) |H_i(t) - H_{i,st}(B)|^v \times \text{sgn}(H_i(t) - H_{i,st}(B)) \quad (3.6)$$

The term  $r(B_i)$  is the dynamic magnetic resistivity, which controls the shape of the dynamic loop. The coefficient  $v$  defines time and frequency characteristics of the model. The coefficient  $r(B_i)$  is critical to the development of the model. Its calculation is related to the concept of the magnetisation vector, rotating under the only influence of the applied field. The expression of flux derivative without considering any nodal values is incorporated in

(3.7), where  $\gamma$  [ $\text{C.kg}^{-1}$ ] is the gyro-magnetic ratio,  $\alpha$  a damping coefficient and  $B_s$  [T] the magnetic induction at saturation.

$$\frac{dB(t)}{dt} = B_s(t) \times \frac{\gamma\alpha}{1 + \alpha^2} \left( 1 - \left[ \frac{B(t)}{B_s(t)} \right]^2 \right) \times (H(t) - H_{st}) \quad (3.7)$$

The correlation of (3.6) and (3.7) appears unclear, as it is the coefficient  $\nu$  that plays a key role in the implementation of the dynamic hysteresis model proposed by the authors. An expression of the applied field as the sum of static and dynamic components is derived. By adding up the term  $[H_i dB_i / dt]$  associated to each node in the grid and integrating the result over one magnetising cycle, the authors obtain an analytical expression for static  $W_{st}$  and frequency-dependent  $W_{dyn}$  components of the total hysteresis loss  $W_h$  (3.8).

$$\begin{aligned} W_h(t) = W_{st}(t) + W_{dyn}(t) = & \int_0^{T/2} \left[ \sum_{i=0}^N H_{i,st}(t) \frac{dB_i(t)}{dt} \right] dt \\ & + 2 \int_0^{T/2} \left[ \sum_{i=0}^N \left( \frac{1}{r(B_i)} \frac{dB_i(t)}{dt} \right)^\nu \frac{dB_i(t)}{dt} \right] dt \end{aligned} \quad (3.8)$$

Classical eddy-current losses were calculated according to the conventional equation and by static and dynamic hysteresis solvers, respectively. The addition of the three components was then compared to total losses resulting from independent integration of the dynamic  $B - H$  loop [3.16]. One of the interesting conclusions of the study is that the calculated static hysteresis loss by the dynamic model showed almost constant behaviour at 1.5T peak flux density. Nonetheless, an increase in losses in two non-oriented steels (silicon content 5.5%, 6.5% - resistivity 0.735  $\mu\Omega\text{m}$ ; 0.824  $\mu\Omega\text{m}$  - thickness 0.1mm) of 50% was observed, over the 0 to 600 Hz magnetising frequency range at lower levels of induction (0.5 T; 1.0 T). Moreover, it was confirmed by the authors that a suitable choice of the parameter  $\nu$  (equal to 2) yielded a variation of excess losses with  $B_p^{3/2} f^{1/2}$ , in agreement with the prediction made by Bertotti. The use of a dynamic model was accountable for higher total losses (anomalous losses) and a redistribution of its three components. Although the dynamic hysteresis model proposed is certainly a powerful tool, little comment is offered on the

impact that thickness and/or resistivity of laminations, of grain-oriented or non-oriented steel, would have on an accurate separation of losses.

### ***3.4 Distorted Magnetising Conditions***

For many decades, research on modelling and predicting iron losses in electrical steels focussed on magnetisation under sinusoidal excitation. The analysis of loss mechanisms under purely sinusoidal flux density was a first step in order to understand physical phenomena, such as eddy-currents and domain wall motion. Furthermore, transformers, which consist in laminated cores of grain-oriented steel, were subjected to sinusoidal voltage. Due to their important role played in generation and distribution of electricity, research aiming at a more efficient magnetisation of commercial steel under sinusoidal conditions included revision of physics of magnetism, improved knowledge on material properties and theoretical description of energy losses.

Constant changes in industry were made possible by significant advances in semiconductor technology. Solid-state smaller and more reliable devices dealt successfully with higher currents. These devices were then used to produce frequency converters that fed well-established induction machines at variable frequency. Improved control of processes and potential energy savings were identified as strongly beneficial to industry applications [3.17]. Carrier-based Pulse-Width-Modulation, which compared the sinusoidal reference signal to a triangular waveform, was accountable for generating the logic signals controlling every individual semiconductor. This modulation scheme [3.17], that has remained extremely popular in industry due to its simplicity, is performed at frequencies in the kilo-Hertz range (1 kHz – 10 kHz). In these conditions, pulsating voltage applied to primary windings of induction machines create distorted flux density waveforms. The harmonic content in low, medium and high frequency ranges affects the performance of laminated steel, present in stator and rotor cores of asynchronous machines. As a result, iron losses increase. The negative effect that distorted induction, as originated by fast-switching PWM converters, had on such an increase started to be investigated.

#### **3.4.1 Minor Loops**

Magnetisation happens under non-continuous induction due to flux reversals. While it is being magnetised (demagnetised), the material suffers from a demagnetisation (magnetisation) instant that is visible on the dynamic  $B$ - $H$  loop by the means of a minor loop (fig. 3.6). As a consequence of the presence of minor loops, the area of the  $B$ - $H$  loop that results from the integration of  $B$  over  $H$  over one magnetising cycle increases.

Lavers et al highlighted the negative effect of minor loops on iron losses in laminations of grain-oriented steel [3.18]. The authors measured losses in laminations of grain-oriented steel of thicknesses 0.356 mm and 0.635 mm in the 1.0 – 2.0T peak flux density range. The controlled induction waveform at 60 Hz magnetising frequency contained low order harmonics (3<sup>rd</sup>, 5<sup>th</sup>, 7<sup>th</sup>, 9<sup>th</sup> and 11<sup>th</sup>).

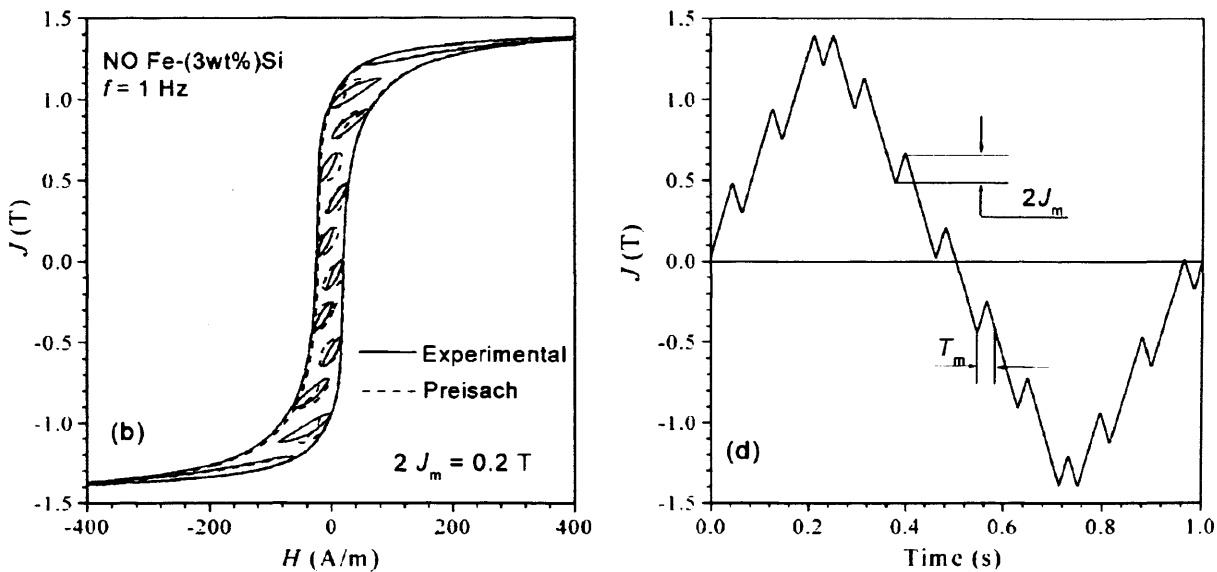


Fig. 3.6.  $B$ - $H$  loop with minor loops caused by flux reversals in the induction wave-shape [3.18]

The experimental measurement of losses ( $W_{dist}$ ) in the samples was also carried out under purely sinusoidal conditions ( $W_{sine}$ ). Firstly, the authors introduced a correcting factor of calculated classical eddy-current losses under sinusoidal conditions to estimate eddy-current losses under distorted excitation (3.8). The terms  $B_p$ ,  $B_1$  and  $B_n$  refer to peak flux density, fundamental and harmonic (order  $n$ ) component, respectively.

$$W_{ec,dist}(B_p) = W_{ec,sin}(B_p) \times \left( \frac{B_1}{B_p} \right)^2 \sum_n \left( \frac{nB_n}{B_1} \right)^2 \quad (3.9)$$

In analogy to eddy-current losses, Lavers et al introduce a correcting factor to account for the effect of minor loops on hysteresis losses. The authors point out the magnitude, phase angle and order of flux harmonic components as essential parameters in the estimation of losses caused by minor loops. Flux harmonics in the kilo-Hertz range, as found in stator cores of PWM converter-fed asynchronous machines, are reported by the authors to cause higher number of flux reversals of larger amplitude. Moreover, the occurrence of flux reversals  $\Delta B_n$  at a particular stage of the cycle, along with the magnetisation state reached by the material ( $B_p$ ), strongly affects the shape of the minor loop. Although the study presented is limited to low order, odd harmonics, it is a simple and instructive view on minor loop phenomenon. Nonetheless, Lavers et al only considered the influence of flux reversals on total losses in terms of their separate effect on two components (hysteresis, eddy-currents). It is expected that minor loops would have an effect on domain wall dynamics.

Rupanagunta et al studied the influence of the third harmonic, of given amplitude and phase angle, on iron losses in three C-cores of laminated 3% Si grain-oriented steel [3.19]. In order to determine the position, size and number of minor loops, static and dynamic B-H loops, under sinusoidal excitation at 60 Hz and 180 Hz, had to be measured experimentally. The calculations were made by accepting that hysteresis loss was proportional to magnetising frequency. Eddy-currents were assumed proportional to the effective induced voltage in the secondary windings. The range of peak flux densities was 1.0 – 1.8 T. It was interesting to note how the authors established experimentally the critical magnitude of the third harmonic necessary to the appearance of two minor loops. The authors analysed the energy losses in the transformer cores in terms of hysteresis and (eddy-current + minor loop) losses.

### **3.4.2 Effect of PWM Supply on Iron Losses**

#### **3.4.2a - Modulation index**

Boglietti et al started the study of the effect of pulsating voltage typical of Pulse-Width-Modulated [PWM] inverters on iron losses in laminated cores of induction motors under the no-load test [3.20]. Isolating with accuracy iron losses from resistive, mechanical and stray load losses in inverter-fed asynchronous machines is a complicated task. However,

the trend shown in [3.20] highlighted that lower modulation indices were accountable for higher core losses in the whole range of magnetising frequencies and peak induction values. Presumably due to the complexity of carrying out experimental measurements in the real machine, the variation of losses with the electromotive force in the stator, not peak flux density, is presented.

### 3.4.2b - Switching frequency

Following the study focused on modulation index, Boglietti et al introduced PWM switching frequency to the analysis of power losses in soft magnetic materials [3.21]. After describing PWM theoretical concept, the authors measured losses in laminated grain-oriented and non-oriented Si-Fe alloys, of respective thicknesses 0.3 mm and 0.5 mm at 50 Hz magnetising frequency. Peak flux density lied between 1.0 and 1.7 T while PWM switching frequency was varied in the range 1 – 20 kHz. At a constant modulation index equal to 0.9, it was shown that power losses in both materials were reduced when the switching frequency increased from 1 kHz to 5 kHz. However, it was revealed that losses in the two electrical steels were approximately constant in the range 5 – 20 kHz. The drop in losses observed in the low segment of switching frequencies was more pronounced at higher induction levels in the grain-oriented alloy (20-24%). Losses in laminations of non-oriented Si-Fe alloy were less sensitive to such a variation of switching frequency (10-14%).

As a first step in the analysis of the influence of PWM switching frequency, the conclusions reported by Boglietti et al are remarkable. Nonetheless, the authors do not take into account in [3.21] that losses in electrical steels subjected to PWM supply are defined by the correlation of fundamental frequency, switching frequency and modulation index. The performance of Si-Fe alloys while, for instance, switching frequency is varied from 1 kHz to 5 kHz, would be affected by the selected values of modulation index and fundamental frequency. Despite introducing an analytical equation for total eddy-current losses that included non-uniform flux distribution across the lamination, the sensitivity of losses in grain-oriented steel to variations of PWM switching frequency, higher than in non-oriented steel, is not clearly explained.

### 3.4.2c - Analysis of losses

Boglietti et al extended their research to the effect of PWM excitation on the breakdown of iron losses [3.22]. Laminations (0.5 mm thick) of non-oriented steel (2.5% Si) were considered in the analytical and computational (Finite Element Method) study, where total losses predicted by FEM were compared to experimental results. On another hand, the distribution of losses (classical eddy-current; hysteresis + excess) performed is compared with the prediction by the computational technique. The results were obtained for a constant 50 Hz magnetising frequency. Selected modulation indices were 0.45 and 0.9, PWM switching frequency range was 1 kHz – 10 kHz and peak flux density was varied between 0.8 T and 1.6 T. The magnetising frequency was kept constant and equal to 50 Hz. The analysis carried out by the authors [3.22] confirmed that the only component significantly affected by variations of PWM switching frequency and modulation index was the classical eddy-current losses. The variation in PWM parameters affects the harmonic spectrum of flux density, which modifies the sideband pattern around high frequency clusters and thus domain wall bending. It was illustrated that the sum of hysteresis and anomalous losses appeared to be approximately constant. Furthermore, the analysis showed good agreement with the analytical predictions by Fiorillo and Novikov.

Owing to non-realistic assumptions on the soft magnetic material (isotropy, linearity between magnetic field and flux density), any conclusion linked to eddy-current losses, as calculated in the classical theory, has to be drawn with care. It is well-known that, due to the presence of high harmonics, the flux density waveform is not smooth. As a consequence, excess losses, which depend on domain wall dynamics, would be somewhat affected by PWM supply of different modulation index and switching frequency. On another hand, the effect of distorted induction on non-uniform flux distribution across the lamination was acknowledged by the authors. Under PWM supply, harmonic characteristics of the flux density waveform are defined by modulation index and switching frequency. Nonetheless, their effect needs to be somehow correlated to the fundamental frequency.

This negative effect was attributed to higher  $dv/dt$  rates which increased eddy-current losses in the soft magnetic material. Although the experimental work is conclusive, the authors do not comment on the way classical eddy-current and anomalous components share the reported rise in losses. It was recommended that keeping as high a value of modulation index as possible would result in more efficient magnetisation of grain-oriented and non-oriented steel. Whenever possible in order to comply with power limitations of the inverter, this is explained by better harmonic quality in the voltage applied to stator windings.

Since losses in the induction motor at the no-load test are plotted versus applied voltage to stator windings, it is difficult to conclude on which type of material (grain-oriented or non-oriented Si-Fe alloy) was mostly affected by PWM modulation index.

#### 3.4.2d - Impact of full and half-bridge inverter topologies

Swan et al carried out an interesting analysis of the influence of two different types of PWM waveforms, typical of full and half-bridge inverters, on iron losses in grain-oriented steel [3.23]. The magnetising frequency considered in the measurement of losses under the two distorted excitations was 50 Hz. In the case of a full-bridge inverter, the recorded induction was a multi-step waveform consisting of periods of null values of  $dB/dt$ , followed by flux variations of the same sign during one half cycle limited by peak values. On the other hand, the induction typical of a half-bridge inverter suffered from flux reversals throughout the magnetising/demagnetising cycle.

The increase in losses, due to harmonic distortion caused by the first PWM supply, was significantly lower, when compared to the negative effect the second type of voltage had on the material. Moreover, variations in the number of controlled  $dB/dt$  variations per cycle (number of pulses) had opposite effects in the two cases considered. A reduction in the number of pulses was beneficial for harmonic losses (full-bridge inverter excitation). On the contrary, a better behaviour of the material was reported when the number of pulses in half-bridge inverter excitation was increased. This results in the appearance of more minor loops, but of smaller size due to more moderate flux reversals. Dynamic B-H loops for both half and full-bridge PWM inverters are illustrated in fig. 3.7.

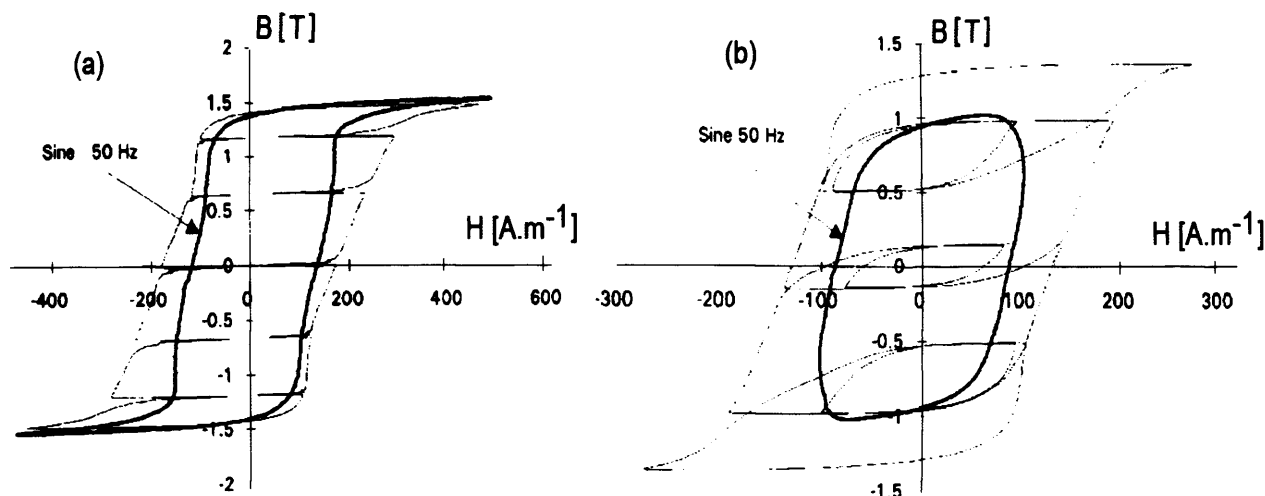


Fig. 3.7. Dynamic B-H loops under voltage by (a) full-bridge (b) half-bridge inverter [3.23]

### 3.4.3 Magnetisation under square wave voltage

Moses et al investigated the effect of square and sinusoidal magnetising excitation on losses in 0.5 mm thick laminations of non-oriented silicon-free steel by the means of the standard Epstein test [3.24]. Selected values of peak flux density were 0.5 T, 1.0 T and 1.5 T. The magnetising frequency was varied between 25 Hz and 400 Hz. While sinusoidal voltage creates sinusoidal flux density of changing  $dB/dt$ , square excitation leads to triangular induction characterised by constant  $dB/dt$  over each one of the two half cycles. The increase of up to 20 % under sinusoidal induction can only be explained by the influence of flux derivative  $dB/dt$  on classical eddy-current and excess losses. The absence of silicon in the samples suggests an important role played by excess losses, especially at low magnetising frequencies. The results reported by the authors suggest movement of domain boundary without acceleration/deceleration as favourable to a more efficient magnetisation of the steel.

As continuation to previous work on non-sinusoidal magnetising conditions, Moses et al studied the negative impact of PWM supply on non-oriented steel in a broad range of magnetising frequencies and inductions [3.25]. One of the important conclusions to be drawn from the investigation is the need for careful selection of the parameters defining magnetising conditions in the standard Epstein test. Although this point is less relevant in PWM flux density waveforms (harmonically distorted in the high frequency range), it was emphasised that selecting peak flux density or fundamental peak flux density yielded

contradictory results on measured iron losses under sine and square excitation. This was caused by significant low order harmonic distortion in flux density waveforms. Iron losses in 0.5 mm thick laminations of two different silicon iron alloys, of respective silicon content 1.8 % and 0.3 %, were measured under square and sinusoidal conditions at 1.0 T peak flux density. The magnetising frequency was varied in the range 25 - 400 Hz. It was revealed that energy losses in the alloy of lowest resistivity were increased by nearly 120 % at 400 Hz. Although no comparative results under selected PWM supply conditions were given, the silicon content appeared as an influential parameter in the assessment of losses in thick laminations of non-oriented steel.

### 3.4.4 High frequency flux harmonics

Son et al covered an investigation of the impact of high flux harmonics on laminated non-oriented steel, subjected to arbitrary magnetising excitation along rolling and transverse directions [3.26]. Firstly, the authors synthesised controlled induction waveforms at given frequency (below 3 kHz) and amplitude. Separate losses in the material were measured under sinusoidal induction at respective frequencies [ $f_o$ ;  $f_h$ ] and amplitudes [ $B_m$ ;  $\Delta B_m$ ]. The addition of the two terms was then compared to losses measured when the superposition of both sine waves in phase was the magnetising excitation. The authors justified the relevance of their study by introducing the negative effect that complex geometries in stator cores of rotating machines had on harmonic characteristics of the induction. Moreover, Son et al highlighted that the prediction of losses under distorted magnetising conditions was difficult to achieve in non-oriented steels, especially at high induction along the rolling direction. The mismatch between measured and predicted losses questioned the adequacy of superposing flux harmonics in the assessment of core losses. Moreover, their presence in the kilo-Hertz range was pointed out as a key element affecting domain wall motion and induced eddy-currents within the material.

### 3.4.5 Stator / Rotor Core of Induction Machines

#### 3.4.5a - Loss increase under PWM Supply

In order to assess the impact of typical PWM pulsating excitation applied to stator windings on core losses, Boglietti et al performed the no-load test in a machine consisting of

a slot-less rotor, without windings and driven by a synchronous motor at the nominal speed [3.27]. The authors also supplied the induction motor with square voltage, which would correspond to PWM excitation of infinitely high modulation index. The core losses obtained from this experiment, based on an analytical energy balance, were compared with the results of an equivalent test in a commercial induction machine with a wound rotor core. Due to harmonic distortion of flux density introduced by stator and rotor teeth, a higher value of core losses was found in the conventional machine. Owing to the complexity of measuring the current flowing in rotor windings, high accuracy in the results was difficult to accomplish. Nonetheless, it was shown that the negative effect of PWM excitation on losses in laminated electrical steel of induction machines was enhanced by the complex geometry of stator and rotor cores. On the other hand, iron losses were not significantly affected under square wave excitation. It can be derived that the influence of core geometry would be attenuated as the PWM modulation index is increased. Although the experimental procedure presented by the authors was useful, no information on critical PWM parameters (modulation index, switching frequency) of the voltage produced by the inverter was given. These would be the key to relating the increase in core losses reported by the authors with the harmonic quality of the excitation feeding primary windings in the asynchronous machine.

#### 3.4.5b - Loss distribution in teeth and yoke

Following the analysis of core losses under PWM conditions, Cester et al selected two different types of PWM voltage excitation (3-level, 5-level) to describe measured respective voltages in yoke and teeth of the stator core [3.28]. While the switching frequency was kept constant (2.9 kHz), the modulation index was varied in order for the inverter to produce 50 %, 75 % and 100 % of the nominal voltage. First of all, core losses in the induction machine were measured in the three conditions. The level of induction in yoke and teeth was measured experimentally and respective voltage wave-shapes recorded. The authors then measured iron losses in laminations of non-oriented steel and thickness (0.65 mm), as used in the stator core of the machine, by the standard Epstein frame. Ideal and measured PWM waveforms (3-level; 5-level) were used to magnetise the samples at an identical peak induction, as given by experimental measurements, in yoke and teeth, respectively. The specific loss obtained for the two parts of stator geometry were weighted according to their relative mass in the stator core, and added. Loss predictions were compared to experimental measurements.

Although important differences were reported, it was highlighted that using real PWM waveforms in the Epstein frame test yielded better accuracy. Higher modulation indices lead to reduced relative increases in loss when sinusoidal excitation was taken as a reference. Induction levels in the teeth were higher than in the yoke and, at nominal voltage, magnetising states close to saturation in the teeth were reached. Nevertheless, the complexity of isolating iron losses from resistive, stray load, windage and friction losses means that the method proposed by the authors may be more accurate than reflected on [3.28]. It is acknowledged by Cester et al that a more accurate description of flux distribution inside stator core implemented by computational methods could be used to validate their approach.

### 3.4.5c - Introduction of finite element analysis

Chevalier et al continued the work initiated by Cornut et al [3.29]. Induction waveforms at stator teeth and yoke of an asynchronous machine were measured and recorded. Iron losses in laminations of non-oriented steel, of the same material and thickness as used in the induction machine, were measured by the standard Epstein frame test at various peak flux densities. The induction waveform in this preliminary test was triangular with controlled  $dB/dt$  rate. The authors then obtained three-dimensional surfaces that related induction  $B(t)$  and flux derivative  $dB(t)/dt$  to the magnetic field  $H(t)$  for different values of peak induction  $B_p$ . The method reported is interesting, since it explicitly acknowledged non-linearity between induction and magnetic field strength in the prediction of major B-H loops. Induction waveforms measured in teeth and yoke were associated to the standard triangular waveform that provided their best description. Once the three parameters (induction as a function of time,  $db/dt$  rate and peak flux density) were introduced, the field was obtained to determine specific losses in several volumes of material.

Finite element [FEM] methods are used to solve partial differential equations in a pre-determined number of points constituting a mesh. As a result of solving electromagnetic differential equations, flux density and applied field distributions in complex geometries of stator and rotor cores are obtained and losses in the mass of steel can be calculated analytically. The small error reported between computed and experimentally measured losses confirmed in this case the good accuracy of the approach. The conclusions reaffirmed that

losses in the stator yoke were lower than in the teeth, where saturation was reached. Moreover, rotor core losses accounted for one third of the stator losses. They were mainly concentrated in regions close to the teeth [3.29]. Non-linearity between induction and magnetic field was given special attention in this paper. Results from the standard Epstein test with a computational method were successfully blended to describe flux distribution within the machine and visualise rotational magnetisation in the stator yoke. Nonetheless, the adequacy of finite element methods to solve electromagnetic problems in rotating machines is determined, not only by its accuracy, but also by required time and computing resources. This is especially true when induction waveforms found in PWM inverter-fed induction motors are strongly distorted in the high frequency range. In these conditions, reaching high accuracy could be more problematic.

### **3.5 Rotational Magnetisation**

From a physical perspective, this phenomenon is explained by rotation of magnetic domains aiming at an alignment with an external applied field of alternating amplitude and changing orientation. Due to planar rotation of the flux vector in specific regions of the stator core, such as the root of teeth and inner portions of the yoke, iron losses in those volumes of material are higher than under the presence of purely alternating flux. Respective rotational fluxes in a mild steel sample, one grain-oriented steel and a point in a T-joint of a transformer were measured by Moses et al in [3.30]. The study revealed that magnetic flux maintained constant amplitude and rotated at a constant angular velocity in the mild steel sample. However, variation in both amplitude and angular velocity were observed in the 0.11mm silicon-iron alloy. This phenomenon, which was caused by the presence of a third-harmonic (150 Hz) flux component that rotates in the opposite direction to the fundamental flux component, results in highly localized losses in points of the T-joint of the three-phase three-limb transformer.

Moses continued his analysis of aspects related to calculation and measurement of losses in electrical machines due to rotational magnetisation in [3.31]. The discrepancy in measured rotational losses by the means of magnetic sensors or a thermometric method was emphasised. The importance of using an appropriate equation that accounted for axis ratio  $a$  (ratio to localised instantaneous peak flux density in the transverse direction ( $b_y$ ) to localised instantaneous peak flux density in the rolling direction ( $b_x$ ) of the specimen) in rotational loss

calculation was highlighted. The terms  $h_x$  and  $h_y$  refer to localised instantaneous applied field in transverse and rolling directions, respectively.  $\delta$  [ $\text{kg.m}^{-3}$ ] is the density of the specimen and  $T$  [s] is the period of magnetization. The term  $P_{\text{tot}}$  [ $\text{W.kg}^{-1}$ ] is the value of specific total losses in the material

$$P_{\text{tot}} = \frac{a}{T\delta} \int_0^T \left( h_x \frac{db_x}{dt} + h_y \frac{db_y}{dt} \right) dt + \frac{1-a}{Td} \int_0^T \left( h_x \frac{db_x}{dt} \right) dt \quad (3.13)$$

Although reasonable agreement was agreed in grain-oriented 3.2% Si-Fe steel, the assumption of taking AC losses as the addition of losses in transverse and rolling direction was confirmed as a completely inadequate hypothesis in a 2.7% non-oriented Si Fe steel (50 Hz; 0.5 T - 1.7 T). This conclusion was reinforced for low axis ratios and high induction. Two techniques of localised flux measurement (search coil and needle probe) were analysed by Loisos et al [3.32]. The search coil method requires drilling in the specimen which induces stresses in the steel and affects the measurement. The needle probe technique, which relies upon a non-destructive measurement procedure, is undermined by sensitivity to noise interferences and error due to the presence of electrical vertical field. The two methods yielded similar peak flux density measurements at 0.6 T, 1.0 T and 1.5 T (50 Hz) in grain-oriented and non-oriented steel. In rotational loss measurements, several coils or probes must be installed to cover a specific volume of the material. A modified probe technique was proposed in [3.32] to compensate for the error derived from the proximity of measuring probes.

### 3.6 Iron Loss Calculation

#### 3.6.1 Classical Steinmetz Equation

Chen et al [3.33] carried out a review of two methods of separation of losses based upon the classical Steinmetz equation (3.26) and the statistical approach postulated by Bertotti (3.27).

$$P_s = k_h f B_p^n + k_e B_p^2 f^2 \quad (3.26)$$

$$P_s = k_h f B_p^n + k_e B_p^2 f^2 + k_a B_p^{3/2} f^{3/2} \quad (3.27)$$

Whereas the first one only considers static hysteresis and frequency-dependent eddy-current component, Bertotti introduces in the equation the anomalous loss, which is related to magnetisation dynamics. Classical eddy-current losses are calculated based on several assumptions (linearity between magnetic field and induction, sinusoidal nature of quantities). Therefore, they do not account for actual eddy-current losses in the magnetic material. Should these be calculated accurately by the means of a coefficient  $k_e$  dependent on induction and frequency, the analysis of losses in two terms (static hysteresis and non-classical real eddy-current components) would be an equally valid hypothesis.

Firstly, the authors gathered information on energy losses in different materials at various peak flux densities. Data used were based on characteristic curves obtained by the manufacturer under sinusoidal magnetisation. The authors then determined the analytical coefficients in Steinmetz and Bertotti's equations. At low magnetising frequency, the losses predicted by the two formulas were in good agreement with characteristic curves provided by the manufacturer for each material at low magnetising frequency. When this parameter was increased to a value of 400 Hz, reasonable accuracy in the prediction could only be reached below 1.0 T peak flux density. Chen et al concluded that the coefficients  $n$ ,  $k_h$  and  $k_e$  had to vary with magnetising frequency. The authors based their study on the coefficient  $k_a$  being constant and independent of frequency. Since excess losses derive from domain wall motion at a micro-structural level, it was expected that different magnetising frequencies would affect not only  $k_e$ , but also  $k_a$ .

In order to improve accuracy in the prediction of core losses in a broad range of materials at high frequencies and induction, Chen et al replaced the parameter  $n$  in the static hysteresis loss component by a quadratic function of peak flux density ( $a+bB_p+cB_p^2$ ). Although predicted losses were coincident with characteristic values provided by the manufacturer, no explanation of the parameter ( $a+bB_p+cB_p^2$ ), which accounts for changes in the dynamic  $B$ - $H$  loop [3.33], is presented. Despite the absence of discussion on the applicability of their method to harmonically distorted induction conditions, the authors underlined some of the weaknesses of the separation model postulated by Bertotti.

### **3.6.2 Engineering Approach**

Boglietti et al proposed an engineering approach on the prediction of iron losses in soft magnetic materials subjected to arbitrary voltage supply [3.34]. Owing to the thorough investigation carried out, the paper written by the authors is certainly instructive. First of all, the range of thicknesses of laminated material, along with the selected non-oriented steels, is representative of what is commonly used in stator and rotor cores of asynchronous machines. Secondly, the authors based their method on standard measurements on the Epstein frame under sinusoidal conditions. By using these results, Boglietti et al succeeded in defining the coefficients in the equation that separated total losses into three components: static hysteresis, classical eddy-currents and anomalous losses. Nonetheless, the authors revealed that anomalous losses could not be reliably quantified from the standard Epstein test. As a result, their investigation only considered static hysteresis and frequency-dependent (global) eddy-current losses.

In the first method proposed by the authors, total losses in non-oriented steel subjected to PWM voltage excitation could be predicted with reasonable accuracy from preliminary measurements under sinusoidal conditions at various peak flux densities and magnetising frequencies. Owing to the complexity of iron loss analysis, Boglietti et al confirmed that preliminary measurements under selected PWM conditions (modulation index, switching frequency) were necessary to analyse the distribution of losses under identical supply in terms of hysteresis and eddy-current losses. The harmonic distortion of the supply voltage is encapsulated by the ratio of root mean square values  $\xi$  [3.34]. The quality of the voltage waveform applied to primary windings appears as essential to iron loss analysis. The investigation, which does not consider minor loops or establish the relative weight of excess losses, highlights that loss prediction in non-oriented Si-Fe alloys is a complex task. The empirical approach presented, which may not fully describe the problem from a physical perspective, predicts losses in alloys of low-medium Si content satisfactorily. The accuracy is somewhat affected at high induction in laminations of larger thickness and lower resistivity.

### ***3.7 Efficiency in a PWM inverter-fed motor: an overview***

Green et al presented a full analysis of experimental losses in a 2.1 kW induction motor under grid and PWM inverter supply [3.35]. The values obtained were then compared to the results provided by finite element analysis. Owing to the study of stator/rotor copper and iron losses at various load regimes, the paper was found interesting as an overview on the problem of efficiency in low-power induction motors commonly used in industrial

applications. Due to experimental inaccuracy incurred while isolating conventional Joule and core losses from mechanical and stray load losses, some discrepancy between computed and measured losses was observed. As reported by the authors, precise measurement of electric power originated by pulsating voltages and currents, as produced by PWM inverters with switching frequency in the kilo-Hertz range, is difficult to accomplish. Moreover, meshing complex geometries of stator and rotor cores with excessive accuracy compromises the computational efficiency of the finite element analysis carried out. Therefore, a reasonable error was justified.

By applying a pulsating voltage to the primary windings, total core losses under sinusoidal conditions were increased by nearly 50 % in the machine. It was by the far the most sensitive component affected by harmonic distortion introduced by the PWM inverter. Iron losses represented between 35-40 % of the variable speed drive (inverter + motor) at light load. At full load, the same losses only accounted for 15-20 % of the global losses. Although hysteresis losses increased by 5 % approximately, rises of 40 % and 35 % were observed in classical eddy-current and anomalous losses, respectively. From these results, it can be concluded that efficient magnetisation of laminated electrical steel has the most positive impact on the overall efficiency of the speed drive at light loads. The finite element analysis revealed that iron loss density was found highest in stator teeth tips. When the rotor core was under investigation, the largest power loss density was localised in slot bridges. It was important to notice that high harmonics in the switching frequency cluster had a considerable effect on localised losses in the rotor [3.35].

On the other hand, copper losses in stator windings and rotor bars were arguably the most important component at light load (40-45 %) and full load (70-75 %). Nevertheless, their value was not significantly affected by distorted voltage. It is important to highlight the relevance of semiconductor losses in the frequency converter, which increased losses by 10-15 % [3.35]. The study proposed by Green et al points out which conditions give iron losses in PWM inverter-fed induction motors a prominent role in the global efficiency of the system. It can also be deduced that iron losses could be proportionally larger if the induction machine is supplied at higher frequencies than 50 Hz. Although the higher PWM modulation index required by constant  $V/f$  control would ensure reasonable harmonic quality, distorted voltage wave-shapes would still be responsible for increased core losses within the machine.

As motor nominal power increases, the efficiency is improved noticeably. While efficiency in an IE3 class, fully-loaded induction motor (1.1 kW) reaches only 82.7%, a value of 90.2% is attained in an 11 kW motor [3.36]. Iron losses become proportionally larger at high speed and low load.

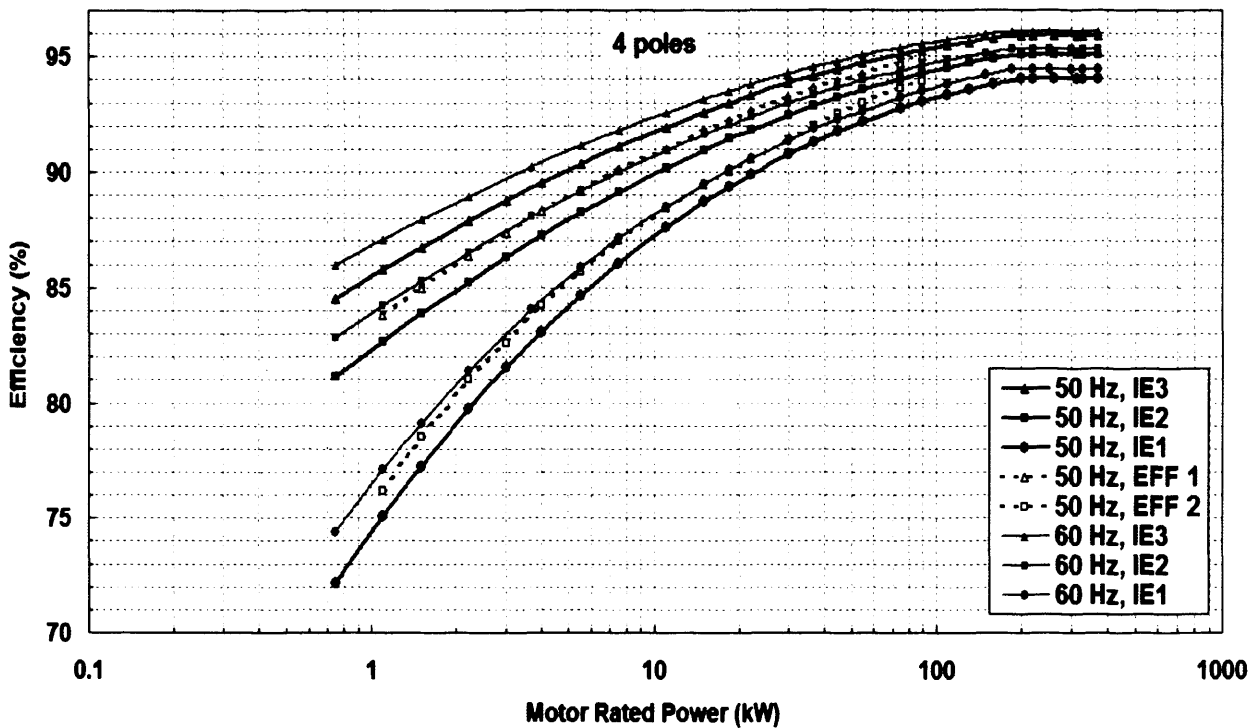


Fig 3.8. Efficiency [%] for 4-pole induction motors of different rated power [3.38]

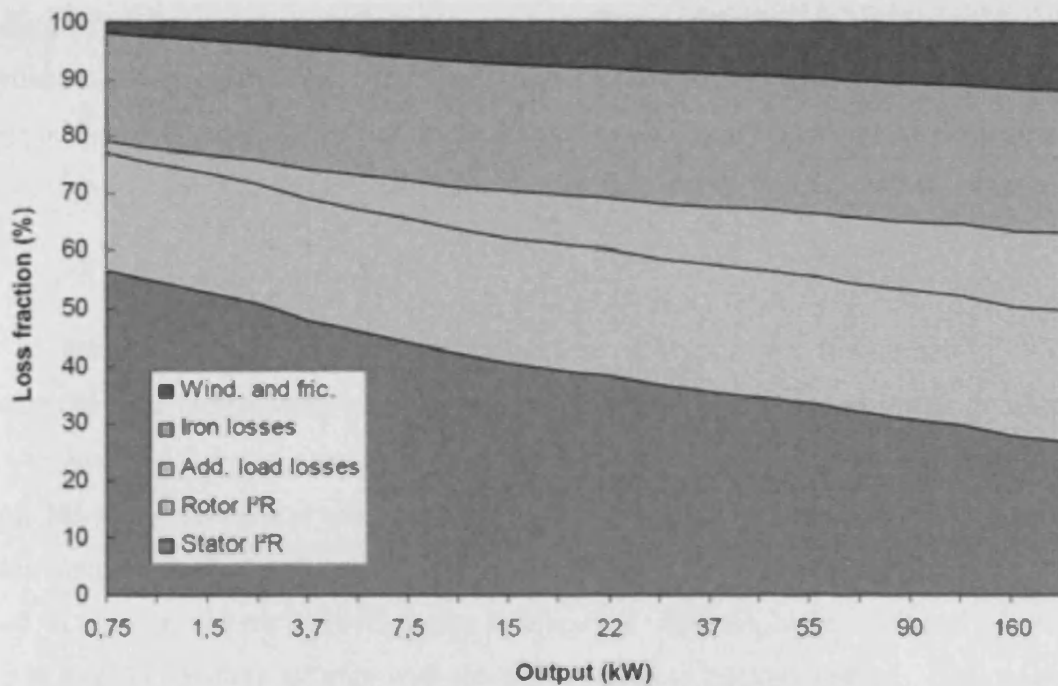


Fig 3.9. Fraction of resistive (stator + rotor), iron, windage, friction and stray load losses in fully-loaded 4-pole induction motors of different rated power [3.38]

### 3.8 Summary

Electrical steels are characterised by a crystalline structure. Regions of the material where no lattice structural discontinuity exists constitute grains. When the direction of these is random, the steel is identified as non-oriented and used to manufacture stator cores in rotating machines. When grains are aligned in a given direction, the steel is known as grain-oriented and used to manufacture transformer cores. Individual atomic moments in non-oriented steels are aligned without applying an external field in microscopic volumes called Weiss domains. When the applied field changes direction, domains are reoriented in order to align themselves with the field. A time lag between flux density and applied field occurs in the material.

This phenomenon, which is known as magnetic hysteresis, is accompanied by irreversible energy losses (iron losses) caused mainly by domain wall motion. This is theoretically described by the means of a differential equation in an analogy with dynamic motion of a mechanical system. Iron losses were initially analysed as the sum of static hysteresis and classical eddy-current losses (Steinmetz). Experimental work confirmed that the addition of these two terms was always somewhat lower than measured losses. This discrepancy, which was defined scientifically as the anomaly factor, led to the consideration

of a third term (excess losses) in iron loss analysis. Pry and Bean were the first to propose an analytical model in order to quantify the so-called excess losses. The approach was based on the hypothesis that domain walls could be assumed to be rigid and planar at sufficiently low magnetising frequencies. Results proved this modelling concept valid for 3% grain oriented steel.

Further experimental work underlined the influence that the alteration of micro-structure (through temperature variation) in electrical steel had on excess losses. Furthermore, total iron losses in the steel were confirmed to increase with larger domain wall spacing, even though this phenomenon was attenuated for high magnetising frequencies. A model based on random domain wall distance (and not equally-spaced domain walls) was presented by Bishop as a more realistic approximation to electrical steels. A highest anomaly factor was found in steel laminations of high wall spacing distance to thickness ratios. Bishop went on to analyse magnetisation by the means of a segmented wall concept in contrast with the rigid and planar wall model proposed by Pry and Bean. As a result of counter-flux created by internal eddy-currents, domain wall motion was found faster in the surface of steel laminations than at its centre. Bertotti described magnetisation as a sequence of localised jumps of domain wall segments in the material. The sum of the losses incurred in every jump was identified as static hysteresis losses. Under the hypothesis that these jumps are statistically independent, classical eddy-current losses were calculated. However, Bertotti stated that localised domain wall jumps were in fact space and time correlated events to yield super-imposed eddy-currents explaining excess (also called anomalous) losses. Through experimental loss measurements in laminations of grain-oriented and non-oriented steel, Bertotti succeeded in finding a law relating excess losses to the product of  $(Bf)^{3/2}$  and an empirically-defined coefficient intimately related to the distribution of local coercive fields.

After analysing iron losses under sinusoidal magnetising conditions, the impact that low order flux harmonics had on total losses under magnetisation in electrical steels became relevant. As a result of harmonic distortion in the low range, minor loops caused by flux reversals in the induction wave-shape increase total losses. Lavers introduced an empirical method to quantify eddy-current losses under distorted magnetising conditions based upon harmonic flux amplitude and eddy-current losses under sinusoidal conditions in grain oriented steel. Advances in semiconductor technology in the seventies enabled the use of fast switching frequency converters in industrial motor drives. The analysis of iron losses in non-oriented steels under harmonic-distorted voltage in the high frequency range was undertaken

by Boglietti et al. The effect of variations in parameters in PWM control (such as modulation index and switching frequency) on losses in laminated steel was measured in Epstein frame or in induction motors at no-load conditions. Other studies focussed on different inverter topologies (full and half-bridge) that lead to different flux density waveforms and thus different iron losses in the ferromagnetic material.

The impact of high flux harmonics on losses in laminated non-oriented steel in rolling and transverse directions was also studied. Recorded inverter voltage waveforms (instead of ideally generated wave-shapes) were used to feed Epstein frame set-ups. Several studies founded upon FEM computational methods analysed iron losses in stator cores of complex geometry. Knowledge on flux density distribution in steel cores and quantification of rotational magnetisation contribute to better machine design and a more cost-effective selection of material. While saturation is commonly reached in tooth tips and bases, very low induction is observed in the yoke. Moses highlighted the complexity of rotational magnetisation phenomena as well as its impact on accurate loss measurement and prediction. In regions of rotating machines but specially in T-joints of transformer cores (high anisotropy of grain-oriented steel), the magnetic flux is not only alternating but also changing direction, which causes additional losses in localised regions.

Awareness on energy consumption in common applications (fans, pumps) has boosted the use of variable-speed drives built around an induction motor and a fast-switching frequency converter. The prediction of iron losses under pulsating voltage supply has regained a major role in industry and academia. An engineering approach based upon Bertotti's statistical approach was proposed. The method introduced harmonic quality of the magnetising voltage waveform explicitly as an influential factor on iron loss calculation. While good accuracy when compared to experimental measurements was found at low frequencies, a larger discrepancy was observed in thick laminations with low resistivity and high induction. A comparison between Bertotti and Steinmetz (only hysteresis and classical eddy-current components) predicting methods was introduced to highlight again good agreement at low magnetising frequencies but noticeable mismatch at high induction and frequency. It was concluded that the coefficients in Steinmetz equation to quantify eddy-current and hysteresis losses would need to be frequency-dependent.

To capitalise on the benefits of variable-speed control requires a thorough analysis of efficiency and composition of motor losses at variable speed and load. A system-oriented perspective is to be coupled with solid expertise of AC-AC conversion topologies and modulation strategies. At the same time, this goal may not be achieved without combining engineering knowledge with scientific understanding of iron losses in electrical steels by the means of analytical methods, loss measurement (Epstein frame, real motors) and finite-element computation. Knowledge on flux density distribution in steel cores and quantification of rotational magnetisation contribute to better machine design and a more cost-effective selection of material.

## References

- [3.1] J. B. Goodenough, "Summary of Losses in Magnetic Materials", *IEEE Transactions on Magnetics*, Vol 38, No 5, Part 2, pp 3398-3408, September 2002.
- [3.2] D. Jiles, "Introduction to Magnetism and Magnetic Materials", *Chapman & Hall*, March 1991, ISBN – 10 0412386305.
- [3.3] D. H. L. Ng, C. C. H. Lo, P. Gaunt, "Magnetic Viscosity and Activation Volume in Domain Wall Pinning", *IEEE Transactions on Magnetics*, Vol 30, No 6, pp 4854-4856, Nov 1994.
- [3.4] K. H. Stewart, "Losses in Electrical Sheet Steel", *Proceedings of the institution of Electrical Engineers*, Vol 97, pp 121-125, 1950.
- [3.5] R. H. Pry, C. P. Bean, "Calculation of the Energy Loss in Magnetic Sheet Materials Using a Domain Model", *Journal of Applied Physics*, Vol 29, No 3, pp 532-533, March 1958.
- [3.6] L. Alberts, B. J. Shepstone, "The Influence of Temperature on the Eddy-Current Anomaly Factor", *Proceedings of the Physical Society*, Vol 75, No 4, pp 539-542, April 1960.
- [3.7] P. Mazetti, "Bloch Walls Correlation and Losses in Ferromagnets", *IEEE Transactions on Magnetics*, Vol 14, No 5, pp 758-763, November 1978.
- [3.8] M. Celasco, A. Masoero, P. Mazetti, A. Stepanescu, "Optical Study of the Bloch Walls Dynamics during the Magnetisation Process of Fe-Si Grain-oriented Laminations under Controlled Induction Waveforms", *IEEE Transactions on Magnetics*, Vol 18, No 6, pp 1475-1477, November 1982.
- [3.9] J. E. L. Bishop, "The Analysis of Eddy-current Limited Magnetic Domain Wall Motion, including Severe Bowing and Merging", *Journal of Physics D: Applied Physics*, Vol 6, pp 97-115, 1973.
- [3.10] G. Bertotti, "A General Approach to the Problem of Eddy-Current Losses", *Journal of Magnetism and Magnetic Materials*, Vol 41, pp 253-260, 1984.
- [3.11] G. Bertotti, "General Properties of Power Losses in Soft Ferromagnetic Materials", *IEEE Transactions on Magnetics*, Vol 24, No 1, January 1988.
- [3.12] F. Fiorillo, A. Novikov, "An Improved Approach to Power Losses in Magnetic Laminations under Nonsinusoidal Induction Waveforms", *IEEE Transactions on Magnetics*, Vol 26, No 5, pp 2904-2910, September 1990.

- [3.13] G. E. Fish, C. F. Chang, R. Bye, "Frequency Dependence of Core Loss in Rapidly Quenched Fe - 6.5% Si wt", *Journal of Applied Physics*, Vol 64, pp 5370-5372, November 1988.
- [3.14] J. E. L. Bishop, "Eddy Current Interaction Loss of Randomly Distributed Magnetic Domain Walls with Speeds in Field Equilibrium", *IEEE Transactions on Magnetics*, Vol 26, No 5, September 1990.
- [3.15] S. E. Zirka, Y. I. Moroz, P. Marketos, A. J. Moses, "A Viscous-Type Dynamic Hysteresis Model as a Tool for Loss Separation in Conducting Ferromagnetic Laminations", *IEEE Transactions on Magnetics*, Vol 41, No 3, pp 1109-1111, March 2005.
- [3.16] S. E. Zirka, Y. I. Moroz, P. Marketos, A. J. Moses, D. C. Jiles "Measurement and Modeling of B-H loops and Losses of High Silicon Non-Oriented Steels", *IEEE Transactions on Magnetics*, Vol 42, No 10, pp 3177-3179, Oct 2006.
- [3.17] H. H. Huffman, "Introduction to Solid-State Adjustable Speed Drives", *IEEE Transactions on Industry Applications*, Vol 26, No 4, pp 671-678, July/Aug 1990.
- [3.18] J. D. Lavers, P. P. Biringer, H. Hollitscher, "A Simple Method of Estimating Minor Loop Hysteresis Loss in Thin Laminations", *IEEE Transactions on Magnetics*, Vol 14, No 5, pp 386-389, September 1978.
- [3.19] P. Rupanagunta, J. H. Hsu, W. F. Weldon, "Determination of Iron Core Losses under the Influence of the Third Harmonic Flux Component", *IEEE Transactions on Magnetics*, Vol 27, No2, pp 768-777, March 1991.
- [3.20] A. Boglietti, P. Ferraris, M. Lazzari, F. Profumo, "Effects of Different Modulation Index on the Iron Losses in Soft Magnetic Materials Supplied by PWM Inverter", *IEEE Transactions on Magnetics*, Vol 29, No 6, pp 3234-3236, November 1993.
- [3.21] A. Boglietti, P. Ferraris, M. Lazzari, M. Pastorelli, "Change of the Iron Losses with the Switching Supply Frequency in Soft Magnetic Materials Supplied by PWM Inverter", *IEEE Transactions on Magnetics*, Vol 31, No 6, pp 4250-4252, November 1995.
- [3.22] A. Boglietti, M. Chiampi, M. Repetto, O. Bottauscio, D. Chiarabaglio, "Loss Separation Analysis in Ferromagnetic Sheets under PWM Inverter Supply", *IEEE Transactions on Magnetics*, Vol 34, No 4, pp 1240-1242, July 1998.
- [3.23] J. P. Swan, O. Walti, T. Belgrand, "Influence of PWM Waveform Parameters on the Breakdown of Harmonic Losses in Electrical Steels", *Journal of Magnetism and Magnetic Materials*, Vol 160, pp 31-32, July 1996.

- [3.24] A. J. Moses, J. Leicht, "Power Loss of Non-Oriented Electrical Steel under Square Wave Excitation", *IEEE Transactions on Magnetics*, Vol 37, No 4, pp 2737 – 2739, July 2001.
- [3.25] A. J. Moses, J. Leicht, P. Anderson, "Characterising Electrical Steels under Complex Magnetising Conditions", *Journal of Magnetism and Magnetic Materials*, vol 254-255, pp 54-56, January 2003.
- [3.26] D. Son, J. D. Sievert, Y. Cho, "Core Loss Measurement including Higher Harmonics of Magnetic Induction in Electrical Steel", *Journal of Magnetism and Magnetic Materials*, Vol 160, pp 65-67, July 1996.
- [3.27] A. Boglietti, P. Ferraris, M. Lazzari, "Induction Motor Iron Loss Measurement with a Static Converter Supply Using a Slotless Rotor Bench", *IEEE Transactions on Magnetics*, Vol 30, No 6, pp 4599-4601, November 1994.
- [3.28] C. Cester, A. Kedous-Lebouc, B. Cornut, "Iron Loss under Practical Working Conditions of a PWM Powered Induction Motor", *IEEE Transactions on Magnetics*, Vol 33, No 5, pp 3766-3768, September 1997.
- [3.29] T. Chevalier, A. Kedous-Lebouc, B. Cornut, C. Cester, "Estimation of Loss in an Induction Motor Fed with Sinusoidal Supply using a Finite Element Software and a New Approach to Dynamic Hysteresis", *IEEE Transactions on Magnetics*, Vol 35, No 5, pp 3400-3402, September 1999.
- [3.30] A. J. Moses, "Measurement of Rotating Flux in Silicon Iron Laminations", *IEEE Transactions on Magnetics*, Vol MAG-9, pp 651-654, Dec 1973.
- [3.31] A. J. Moses, "Rotational Magnetization Problems in Experiments and Theoretical Studies of Electrical Steels and Amorphous Magnetic Materials", *IEEE Transactions on Magnetics*, vol 30, No 2, pp 902-906, Mar 1994.
- [3.32] G. Loisos, A. J. Moses, "Critical Evaluation and Limitations of Localised Flux Density Measurements in Electrical Steel", *IEEE Transactions on Magnetics*, vol 37, No 4, pp 2755-2757, July 2001
- [3.33] Y. Chen, P. Pillay, "Improved Formula for Lamination Core loss Calculations in Machines Operating with High Frequency and High Flux Density Excitation", *37<sup>th</sup> Annual Meeting of the Industry Applications Society*, Vol 2, pp 759-766, 13-18 October 2002.
- [3.34] A. Boglietti, A. Cavagnino, M. Lazzari, M. Pastorelli, "Predicting Iron Losses in Soft Magnetic Materials: An Engineering Approach", *IEEE Transactions on Magnetics*, vol 39, no 2, pp 981-989, March 2003.

- [3.35] T. C. Green, C. A. Hernandez-Aranburo, A. C. Smith, "Losses in Grid and Inverter Supplied Induction Machine Drives", *IEE Proceedings on Electrical Power Applications*, vol 150, No 6, pp 712-724, November 2003.
- [3.36] A. T. De Almeida, F. J. T. E Ferreira, J. A. C. Fong, C. U. Brunner, "Electrical Motor Standards, Ecodesign and Global Market Transformation", *European Centre for Power Electronics Seminar. "Towards Energy Gain and Savings. Emerging Drives and Generator Systems"*, Warsaw (Poland), 15-16 April 2008.

## LOSSES IN STEEL LAMINATIONS: EXPERIMENTAL PROCEDURE

---

Laminations of three grades of non-oriented steel (M470-50A, M530-50A and M700-65A) were tested in the Epstein frame and a single strip tester under pulsating magnetising signals, typical of matrix and two-level DC-link converters. Special attention is devoted to the description of Space-Vector-Modulated [SVM] matrix and DC-link Pulse-Width-Modulated [PWM] converters, which provided respective line-neutral and line-line voltage signals used to magnetise laminated steel in the Epstein frame.

Following the analysis of the output voltage regulation function of the DC-link converter and its correlation to PWM modulation index, a computational technique for generating line-line voltages (typical of direct/indirect AC-AC converters) in MATLAB-SIMULINK environment is introduced. The experimental set-up related to loss measurement in steel laminations subjected to PC-generated signals in the single strip tester is also described. Experimental inaccuracy in Epstein frame and single strip testers is analysed.

### **4.1 Electrical steel characterisation**

#### **4.1.1 Laminations**

Losses in twenty four laminations of three grades of fully-processed non-oriented steel (M470-50A, M530-50A and M700-65A) provided by Cogent Steel Ltd. are measured in Epstein and single strip testers. Non-oriented steel grades (M400-50A to M700-65A) are recommended in laminated cores of medium-sized rotating machines of nominal power up to 15 kW. Average weight  $m$  [g] was measured by an Avery Berkel balance. The dimensions (length  $L$  ; width  $\omega$  ; thickness  $d$  in mm). Physical properties of the laminations (resistivity  $\rho$  [ $\mu\Omega$  cm]; silicon content Si\_wt [%]; typical applied field  $H_p$  [A/m] at peak induction 1.0 T, 1.3 T and 1.5 T), which were measured by the manufacturer (Cogent Steel Ltd) are provided in table 4.1.

Table 4.1. Dimensions and properties of M470-50A, M530-50A and M700-65A laminations

	m [g]	L x w x d [mm]	$\rho$ [ $\mu\Omega$ cm]		Si wt %	$H_p$ [A/m]		
			typ	meas		1.0T	1.3T	1.5T
M470-50A	35.0	305 x 30 x 0.50	39	30.2	1.28	146	284	1100
M530-50A	32.2	280 x 30 x 0.50	36	29.0	1.21	147	282	1080
M700-65A	46.4	305 x 30 x 0.65	30	25.0	0.73	167	265	688

#### 4.1.2 25 cm Epstein frame

The Epstein frame (used to measure iron losses reported in § 5.3) can be described as an ideal transformer where primary windings are supplied by the magnetising current that energises the core of laminated steel. The strips tested are assembled in a 25 cm square and have double-lapped joints. In the experimental measurement, 24 steel laminations of the three materials are arranged in a 6-layer configuration. Both primary (magnetising) and secondary windings consist of four, series connected, coils, of respective total number of turns  $N_1 = 700$  and  $N_2 = 700$ . Values of resistances ( $R_1$ ;  $R_2$ ) and inductances ( $L_1$ ;  $L_2$ ) of primary and secondary windings measured using a TENMA 72-6634 LCR meter are presented in table 4.2. Fig 4.9 shows the Epstein frame

Table 4.2. Resistance and inductance in Epstein frame windings

Resistance		Inductance	
$R_1$ [ $\Omega$ ]	$R_2$ [ $\Omega$ ]	$L_1$ [mH]	$L_2$ [mH]
1.2	5.3	3.4	6.2

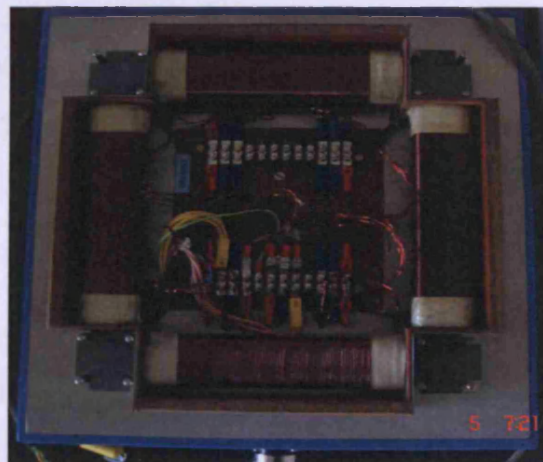


Fig. 4.1. 25 cm Epstein frame

### 4.1.3 Single strip tester

Power losses in M470-50A, M530-50A and M700-65A laminations were measured in the single strip tester (fig. 4.2) and results are given in §5.4. The strip of steel tested is inserted in a slot of cross-sectional area  $31 \times 3 \text{ mm}^2$  located in the centre of two coaxial coils (240 mm length) of  $N_1 = 220$  turns and  $N_2 = 224$  turns. The magnetic circuit is closed by two U-shaped yokes of laminated iron shown in fig 4.2. Primary and secondary coil winding resistances were measured by the TENMA 72-6634 LCR meter to be  $0.7 \Omega$ . Magnetising ( $L_1$ ) and secondary ( $L_2$ ) windings inductances were measured to be  $169 \mu\text{H}$  and  $352 \mu\text{H}$  respectively



Fig. 4.2. Single strip tester

The measurement of iron losses in laminations in Epstein or single strip testers is a valid experimental procedure due to controllability of significant parameters (frequency, peak flux density, type of magnetising waveform), flexibility (use of samples of different material and geometries) and standardisation. Nonetheless, magnetisation in motor laminations is a much more complex phenomenon and is intimately linked to machine construction and operating conditions (leakage flux around copper windings causing additional eddy-current losses, multidirectional flux leading to rotational losses, variation of physical quantities with temperature).

A comprehensive analysis of iron losses in steel laminations requires not only measurement in standard test benches [Epstein and single strip testers] but must be complemented by power loss measurements in a real rotating machine (introduced in chapter 6). Solid theoretical understanding of physics behind magnetisation is always necessary for an in-depth analysis of the results in either standard or real machine set-ups.

## **4.2 Power converters and auxiliary equipment**

### **4.2.1 Frequency Converters**

#### 4.2.1a - Matrix Converter

The three-phase matrix converter (fig. 4.3) prototype used in the experimental study consists of a Field Programmable Gate Array [FPGA] board (level 4), a Digital Signal Processor [DSP] board (level 3) and gate driver board (level 2) to control semi-conducting devices inserted on the power board (level 1). Three voltage and current transducers are incorporated into the power board, along with a clamp circuit. A heat sink (level 0) is used to cool the device. The DSP board is independently supplied (0; +5V) and energises all components mounted on the FPGA board. The DSP executes the SVM control algorithm and conveying nine logic signals to the FPGA, which implements the four-step semisoft commutation and generates eighteen logic signals for as many individual Insulated Gate Bipolar Transistors [IGBTs]. A 24V DC-DC converter located on the FPGA board ensures that IGBTs, current and voltage transducers are supplied accordingly (-15V; +15V). The gate driver board with independent supply (0; +5V) forwards eighteen control signals associated to the IGBTs in a EUPEC EconoMAC module configuration (FM35R12KE3), specially designed for matrix converters and based upon nine bidirectional switches (§A.3). IGBTs may function at a maximum collector emitter voltage 1200V and maximum collector current 55A, which result in a total power rating for the module of 7.5 kW. A three-phase input filter of resistances ( $56\ \Omega$ ) and inductances (1H) connected in parallel, is provided on the input side to the direct AC-AC converter to ensure soft-switching operation. Fig. 4.3 shows the matrix converter prototype used in the experimental study.

#### 4.2.1b – DC-link Converter

The three-phase indirect DC-link converter used in this first part of the study is the TOSHIBA TOSVERT VF-A3 (400V - 0.75kW) transistor inverter. Supplied at 50 Hz and 380 – 415V between phases, the output frequency range in this converter is 0.5 Hz - 400 Hz. The maximum switching frequency is 3 kHz. Power ratings are defined by maximum apparent power and current (RMS) capabilities of 2kVA and 2.5A, respectively. Fig. 4.4 illustrates the DC-link converter used.



Fig. 4.3. Matrix converter prototype [PEMC Group – The University of Nottingham, UK]



Fig. 4.4. DC-link indirect converter [TOSHIBA –TOSVERT VF-A3]

## 4.2.2 Auxiliary equipment

### 4.2.2a – Power analyser

The power analyser used in the measurement of iron losses is the VOLTECH PM3000A (§A.4). Characterised by a wide bandwidth (0.1Hz to 10MHz), this three-channel universal power analyser achieves measurement of active and apparent power with a basic accuracy of 0.05%. Apart from determining RMS and rectified mean values of voltages and currents, this power analyser integrates power and current over precise periods of time. Fig. 4.5 shows the VOLTECH PM3000A analyser.

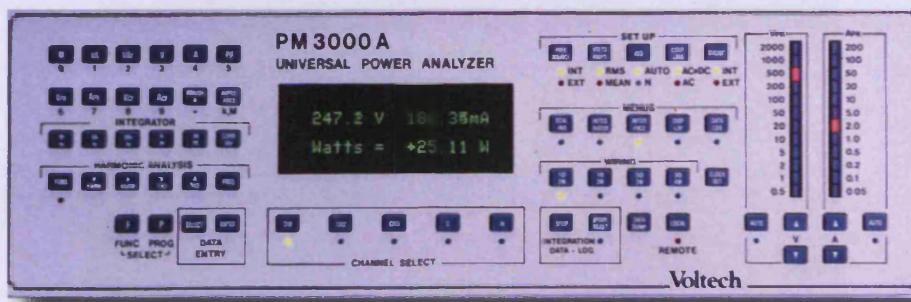


Fig 4.5. Universal power analyser (VOLTECH PM3000A)

### 4.2.2b – Signal generator

The signal generator used for the storage of line-line voltages, typical of matrix and two-level PWM converters, is the TGA 1230 model from THURLBY THANDAR INSTRUMENTS (§A.5). Any arbitrary waveform can be defined with up to 4096 vertical points and from 4 to 65,536 horizontal points. A maximum of 50 waveforms may be stored in non-volatile RAM memory. Fig. 4.6 illustrates the TTI TGA 1230 signal generator.

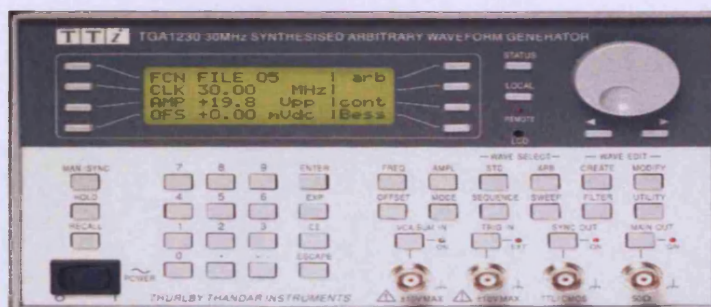


Fig. 4.6. TTI TGA 1230 signal generator

#### 4.2.2c – Digital oscilloscope

The digital oscilloscope used to monitor and store flux density curves and voltages during the experimental work is the YOKOGAWA DL716 16-channel digital oscilloscope [4.1]. Characterised by a maximum sampling rate per channel of 200 kS/s, this oscilloscope has a time-axis accuracy of  $\pm 0.005\%$ . Its mathematical functions allow on-line multiplication, addition, differentiation and integration of any input signal, of which the RMS value can be visualised. Waveforms may be saved to a floppy disk or transferred to a PC via a serial cable (RS-232). Fig. 4.7 shows the YOKOGAWA DL716 digital scope.

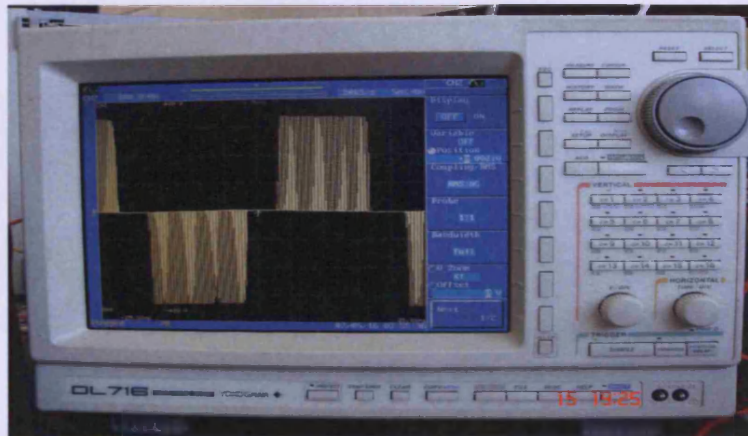


Fig. 4.7. Digital oscilloscope (YOKOGAWA DL716) under operation

#### 4.2.2d – Power amplifier

The power amplifier connected to the signal generator was the BK Electronics MXF 900 MOSFET amplifier (§A.6). Based upon two main toroidal transformers and independent power supplies (associated to as many channels) and a fan cooling system, the maximum power rating per channel is 450W. Power frequency bandwidth ranges from 1Hz to 50kHz. The input sensitivity for signal amplification is 775mV. Fig. 4.8 shows the BK Electronics MXF 900 amplifier.



Fig. 4.8. BK Electronics MXF 900 power amplifier

## 4.2.2e – Multi-meters

The multi-meters (fig 4.9) used to measure the resistance and inductance of windings in Epstein and single strip testers, asynchronous motors and variable transformers are:

- CLARKE CDM 50 multimeter
- TENMA 72-6634 LCR meter
- HEWLETT PACKARD 34401A digital multimeter



Fig. 4.9. Multimeters CLARKE, TENMA and HEWLETT PACKARD

## 4.2.2f – Variable transformers

The first three-phase variable transformer (A) was used as a regulator of the power supplied by the grid network to the three-phase matrix converter. Due to power limitations in order to avoid damage of semi-conducting devices, the experimental prototype could not be subjected to a line-line voltage above  $190 V_{RMS}$ . The second variable transformer (B) was used to regulate the power supplied by the grid to two asynchronous machines (introduced in chapter 5) of respective nominal powers 0.75 kW and 2.2 kW. The two variable transformers are shown in Fig. 4.10.



Fig. 4.10. Three-phase variable transformers A and B

Values of phase-neutral and phase-phase resistances on input and output sides of the two variable transformers were measured by a CLARKE CDM 50 multimeter. They are given in table 4.3. The inductance in the windings, measured by TENMA 72-6634 LCR meter, was found to be negligible in both transformers.

Table 4.3. Resistance of primary / secondary windings of variable transformers A and B

R ( $\Omega$ )	input		output	
	A	B	A	B
Phase-neutral	0.7	1.3	0.2	2.4
Phase-phase	1.2	4.4	0.4	9.4

### 4.3 Losses under pulsating excitation (Epstein frame)

#### 4.3.1 Line-neutral matrix converter signals

Losses in M470-50A, M530-50A and M700-65A laminations subjected to line-neutral output voltage produced by a three-phase matrix converter were measured in the 25 cm Epstein frame at 50 Hz, 100 Hz and 200 Hz magnetising frequency  $f$  [Hz] and 1.0 T, 1.25 T and 1.5 T peak flux density  $B_p$ . SVM sampling frequency was set to 2.5 kHz; the output

voltage transfer ratio set to the maximum value ( $\sqrt{3}/2$ ). The experimental set-up is shown in Fig. 4.11.

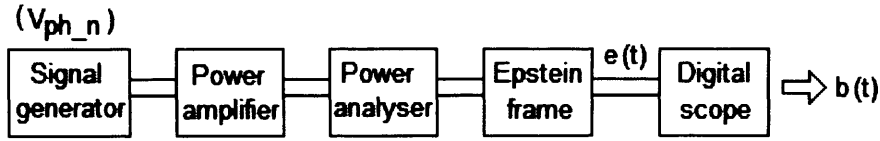


Fig. 4.11. Experimental set-up for iron loss measurement in Epstein frame

The matrix converter, under grid supply via a variable transformer (A), was loaded with a bank of  $100\ \Omega$  resistances (Fig 4.12). The RMS value of line-line output voltage was monitored by the digital oscilloscope. The power flowing to the converter from the variable transformer was increased until  $50\ V_{RMS}$  were reached.

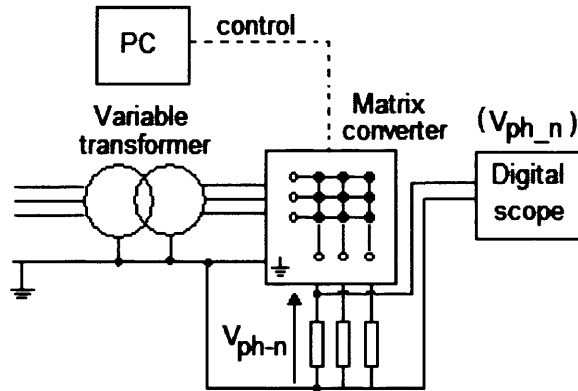


Fig. 4.12. Preliminary set-up to obtain characteristic voltage waveforms (matrix converter)

At this stage, line-neutral output voltage waveforms were recorded at three different frequencies: 50 Hz, 100 Hz and 200 Hz. Characteristic line-neutral voltage waveforms from the experimental AC-AC converter prototype were uploaded and stored in the signal generator. Steel laminations were then energised in the Epstein frame via the power amplifier connected to the signal generator. The induced voltage  $e(t)$  was integrated and divided by  $(N_2 S)$ , where  $N_2 = 700$  is the number of turns of the secondary windings of the Epstein frame and  $S$  is the cross-sectional area of the mass of steel (section 4.1.2). The output voltage from the power amplifier was varied until peak-peak magnitude of flux density was equal to  $(2B_p)$ . Total active power  $P_a$  [W] and RMS magnetising current  $(I_{RMS})$  were calculated from measured values of energy [Wh] and  $I \times \Delta t$  [Ah] given by the integrating function of the power analyser over a period of 1 min. After subtracting the term  $(R_1 I_{RMS}^2)$  associated to Joule losses in primary windings from  $P_a$ , iron losses  $P$  [W] were divided by the active mass

of steel, which was calculated as documented in the British Standard (BS EN 60404-2) for iron loss measurement [4.1].

The accuracy in active power measurements (table 4.4) was estimated upon specifications of the manufacturer of VOLTECH PM3000A power analyser for the three magnetising frequencies.

Table 4.4. Accuracy in active power measurements as % of the reading

f [Hz]				
50	100	200	2500	1000
±0.4%	±0.4%	±0.4	±1.0%	±1.5%

The accuracy in current measurements by the VOLTECH PM3000A power analyser is given for various peak-peak current ranges in table 4.5.

Table 4.5. Accuracy in current measurements as a % of the reading

Peak-peak current range [A]			
0 – 0.5	0.5 – 1.0	1.0 – 2.0	2.0 – 5.0
±0.075%	±0.1%	±0.15%	±0.3%

### 4.3.2 Line-line DC-link converter signals

The DC-link converter (TOSHIBA TOSVERT VF-A3) was supplied by the grid (415 V between phases; 50 Hz). PWM switching frequency was set equal to 2.5 kHz. The output frequency was set to 50 Hz, 100 Hz and 200 Hz. Any parameters defining the operation of the converter had to be set manually by accessing the control panel. In measurements carried out in academic research, ideal PWM waveforms are described by the modulation index  $m_i$  (§2.4.2). In the converter used in this experimental study, the Output Voltage regulation function  $OV$  [%] is the parameter that regulates how much energy is drawn from the DC-link during operation. In most cases, no detail on this function is disclosed by inverter manufacturers. Apart from being seen as sensitive information, it is believed to be not particularly relevant to common industrial use in variable speed drives.

Therefore, an equivalence between the output voltage regulation function  $OV$  [%] and modulation index  $m_i$  had to be established prior to loss measurement. Ideal PWM waveforms associated to line-line square-modulated voltages in real indirect DC-link

converter were generated by the computational method described in section 4.4. Fundamental frequencies were 50 Hz, 100 Hz and 200 Hz for a constant value of switching frequency (2.5 kHz). The modulation index  $m_i$  was varied in the range 0.2 – 1.0. Fast Fourier Transform [FFT] analysis of the generated signals was performed by DAY POST PROCESSOR in ANSOFT-SIMPLOER environment. Fig. 4.13 and fig. 4.14 illustrate the variation of Total Harmonic Distortion  $THD$  [%] and form factor  $FF$  with modulation index  $m_i$  at 50 Hz.

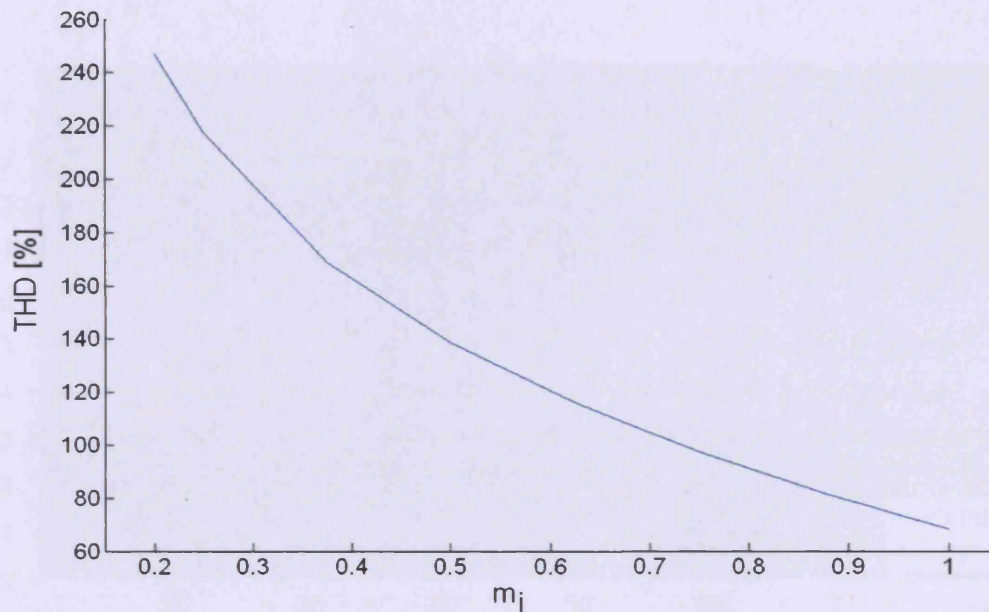


Fig. 4.13. Variation of  $THD$  [%] with modulation index  $m_i$  in PC-generated line-line two-level PWM converter signals (50Hz)

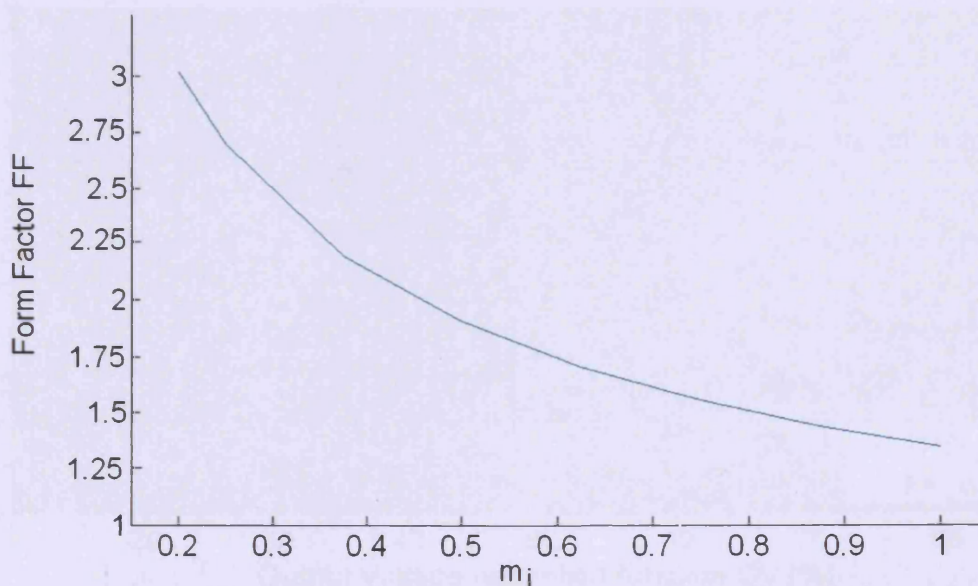


Fig. 4.14. Variation of form factor  $FF$  with modulation index in PC-generated line-line two-level PWM converter signals (50Hz)

Line-line voltages produced by the DC-link converter at values of  $OV$  [%] in the range 20 % - 90 %, switching frequency 2.5 kHz and fundamental frequency 50 Hz, 100 Hz and 200 Hz were recorded under no-load conditions.  $THD$  and form factor values of these signals were calculated in DAY POST PROCESSOR. Based upon the results obtained, a relation of equivalence between modulation index  $m_i$  and  $OV$  [%] function was established at 50 Hz, 100 Hz and 200 Hz (Fig. 4.15, fig 4.16 and fig 4.17).

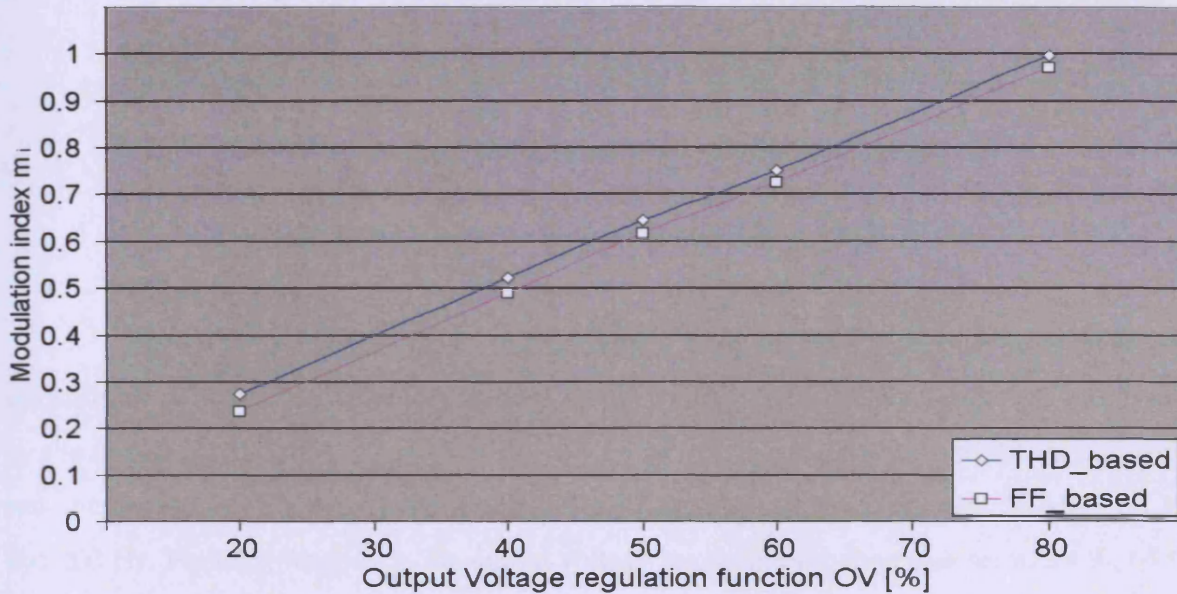


Fig. 4.15. Correlation between  $OV$  [%] and  $m_i$  (50 Hz)

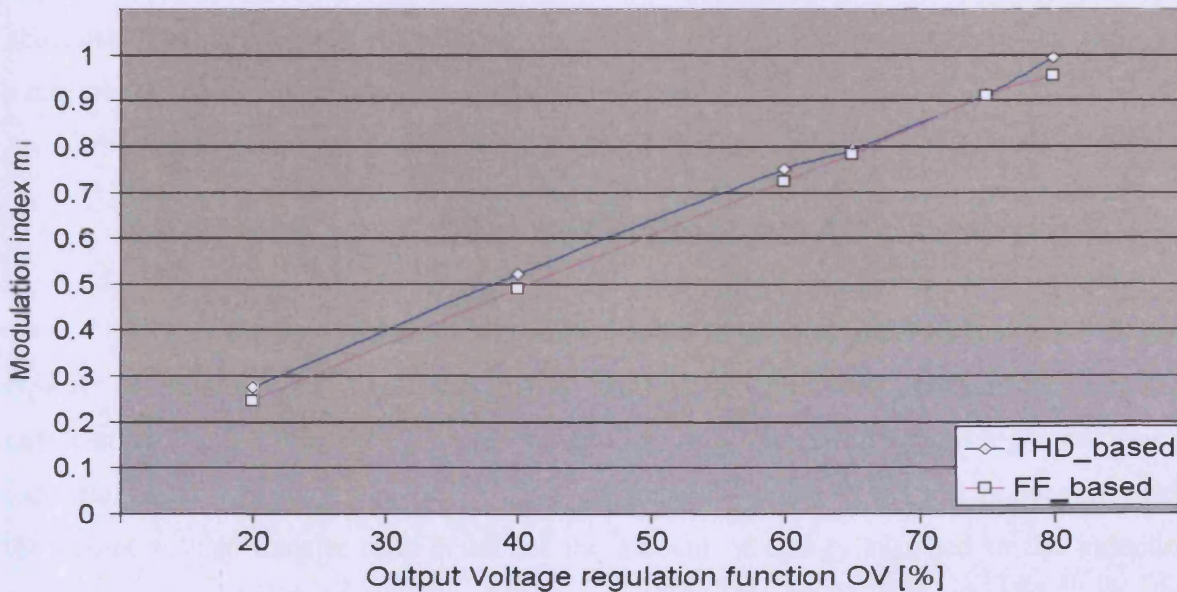


Fig. 4.16. Equivalence between  $OV$  [%] and  $m_i$  (100 Hz)

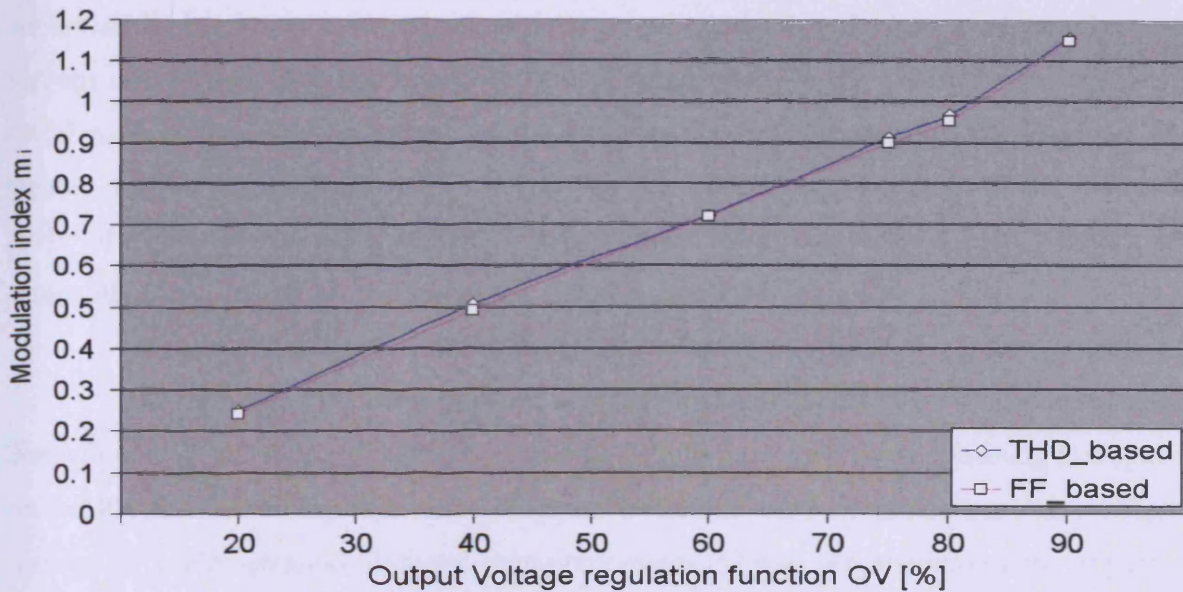


Fig. 4.17. Equivalence between  $OV$  [%] and  $m_i$  (200Hz)

The DC-link converter was loaded with a bank of  $100\ \Omega$  resistances via variable transformer A. The RMS value of line-line output voltage from the converter was monitored by the digital oscilloscope. The power flowing to the converter from the variable transformer was increased until  $50\ V_{RMS}$  were reached. Output frequencies selected were 50 Hz, 100 Hz and 200 Hz. For each frequency, the output voltage regulation function was set to 39 %, 65 % and 81 %. It was estimated to within  $\pm 1.5\%$  accuracy that those values were equivalent to modulation indices 0.5, 0.8 and 1.0. Characteristic line-line output voltage waveforms from the TOSHIBA TOSVERT VF-A3 were recorded. They were uploaded and stored in the signal generator. Steel laminations were then energised in the Epstein frame via the power amplifier connected to the signal generator as described in section 4.3.1.

#### 4.4 Modelling of direct and indirect AC-AC converters

A computational technique was implemented in order to generate line-line voltages, typical of matrix and two-level PWM converters. Important parameters affecting characteristics of line-line voltages were varied in a range associated to working conditions in industrial variable speed drives (low-to-medium nominal power). In the matrix converter case, the output voltage transfer ratio  $q$  defines the amount of energy supplied to the induction machine. The maximum value  $q_{max} = \sqrt{3}/2$  is normally linked to the regime of the induction motor of highest rotational speed. High values of SVM sampling frequency (around 10 kHz)

are desirable, but losses in the eighteen active semi-conducting devices must be taken into account due to their negative impact on global efficiency. In the DC-link converter case, PWM modulation index ( $m_i$ ) regulates the amount of energy taken from the DC-link. The highest modulation index (at least equal to unity) is linked to the regime of the induction motor of highest rotational speed. Switching frequencies in the range 1 kHz – 8 kHz are commonly found in low-to-medium power variable speed drives (below 15 kW).

Although the PWM technique adopted for simulation and loss measurement throughout this PhD thesis is based upon natural sampling, it is worth emphasizing that space-vector PWM is nowadays the most common technique used in motor control owing to easiness of implementation in digital signal processors (§2.4.2). An analysis of the impact of four PWM modulation techniques on voltage and load current harmonic distortion is featured in §2.4.2 as a complement to the research work undertaken.

As introduced in chapter 5, these four parameters [ voltage transfer ratio and SVM sampling frequency (matrix) – PWM modulation index and switching frequency (DC-link converter) ] have a critical effect on harmonic distortion and form factor of output voltages that feed the rotating machine. Since the number of high clusters and sideband harmonic pattern vary, frequency spectra (1 kHz – 22.5 kHz) are strongly affected by their value.

#### 4.4.1 Matrix converter

Space-Vector-Modulation [SVM] algorithm (§A.7) was programmed in an S-function [4.2] in the MATLAB-SIMULINK environment (Fig. 4.19). The language used was C-language. The instantaneous representation of three-phase sine 50 Hz input voltages  $\{U_A U_B U_C\}$  and sine reference output voltages in a stationary frame ( $\alpha - \beta$  coordinates) was calculated under defined output voltage transfer ratio  $q$ , output frequency  $f$  and relative phase angle  $\varphi$ . The four signals were then conveyed to a SIMULINK block.

The latter contains the S-function where the SVM algorithm is implemented at a selected sampling frequency  $f_s$ . Nine logic signals  $[S_{Aa} \dots S_{Cc}]$  defining the duty cycle of each one of the nine bidirectional switches in the direct AC-AC converter topology were generated and introduced to a 9x9 duty cycle matrix  $[D]$ . The post-multiplication of  $[D]$  by a 3x1 input voltage vector  $\{U_A U_B U_C\}$  gives three phase-neutral output voltage signals  $\{U_a U_b U_c\}$ . By subtracting phase-neutral voltages accordingly, line-line output voltages  $\{U_{ab} U_{bc} U_{ca}\}$  were

generated (Fig. 4.18). Those signals were eventually sampled at a rate  $T_i$  and saved, along with associated time values, to an Excel file from MATLAB workspace. Fig. 4.19 shows line-line output voltage typical of a three-phase matrix converter at  $f = 50\text{Hz}$ , sampling frequency  $f_s = 5\text{ kHz}$ ,  $\varphi = 0$  and output voltage transfer ratio  $q = \sqrt{3}/2$ .

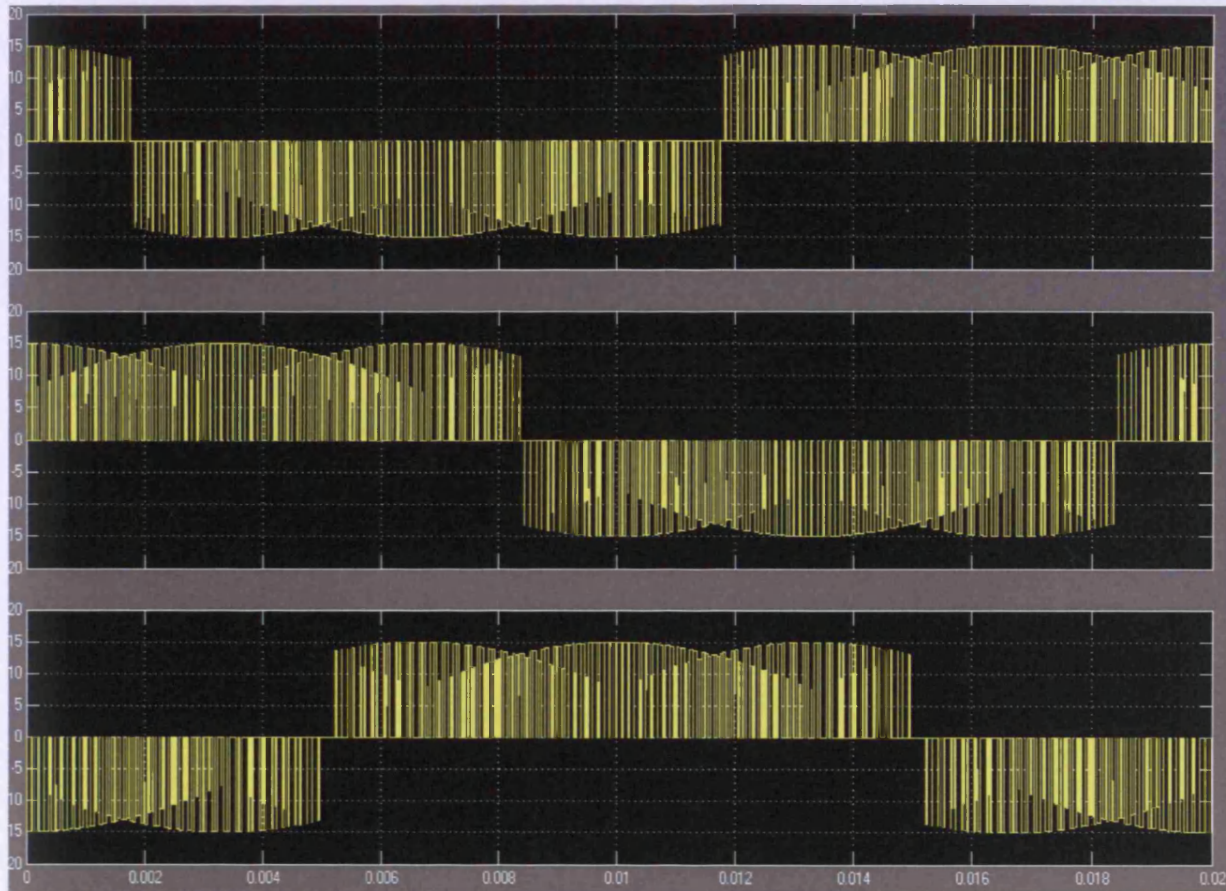


Fig. 4.18. Line-line output voltages in a three phase matrix converter (50 Hz)

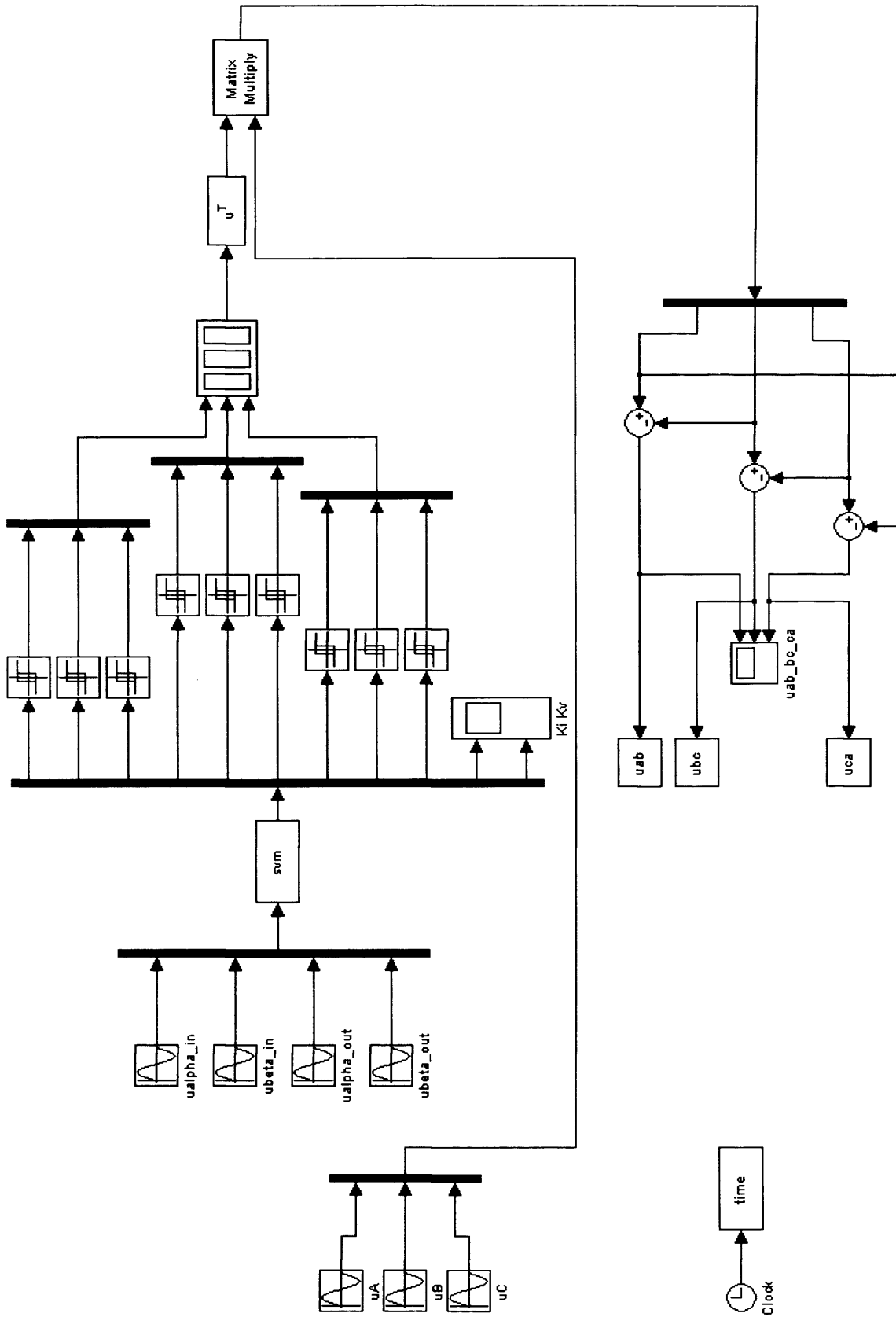


Fig. 4.19. Matlab-Simulink model used to generate matrix converter voltages

#### 4.4.2 Two-level DC-link converter

Pulse-Width-Modulation [PWM] algorithm was programmed in an S-function [4.2] in the the MATLAB-SIMULINK environment (Fig. 4.21). The language used was C-language. Three-phase sine 50 Hz input voltages  $\{U_{cm,A} U_{cm,B} U_{cm,C}\}$  of amplitude  $m_i$  and offset 0.5 were defined as reference signals. A triangular waveform of amplitude unity, offset 0.5 and frequency  $f_{sw}$  was defined as the carrier signal. Both signals were conveyed to a SIMULINK block, which implemented PWM comparison to establish the state of each one of the six ideal switches in analogy to a full-bridge inverter. The algorithm was executed at a selected sampling rate defined by the user in the menu Simulation Parameters. Once the logic state of the six switches was inserted in a duty cycle matrix, a final equation adjusted output voltages consistently with the value of DC-link voltage (fig. 4.20). Those signals are eventually sampled at a rate  $T_i$  and saved, along with associated time values, to an Excel file from MATLAB workspace. Fig.. 4.21 shows line-line output voltage typical of a two-level DC-link PWM converter at  $f = 50\text{Hz}$ , switching frequency  $f_{sw} = 5 \text{ kHz}$ , and modulation index  $m_i = 1$ .

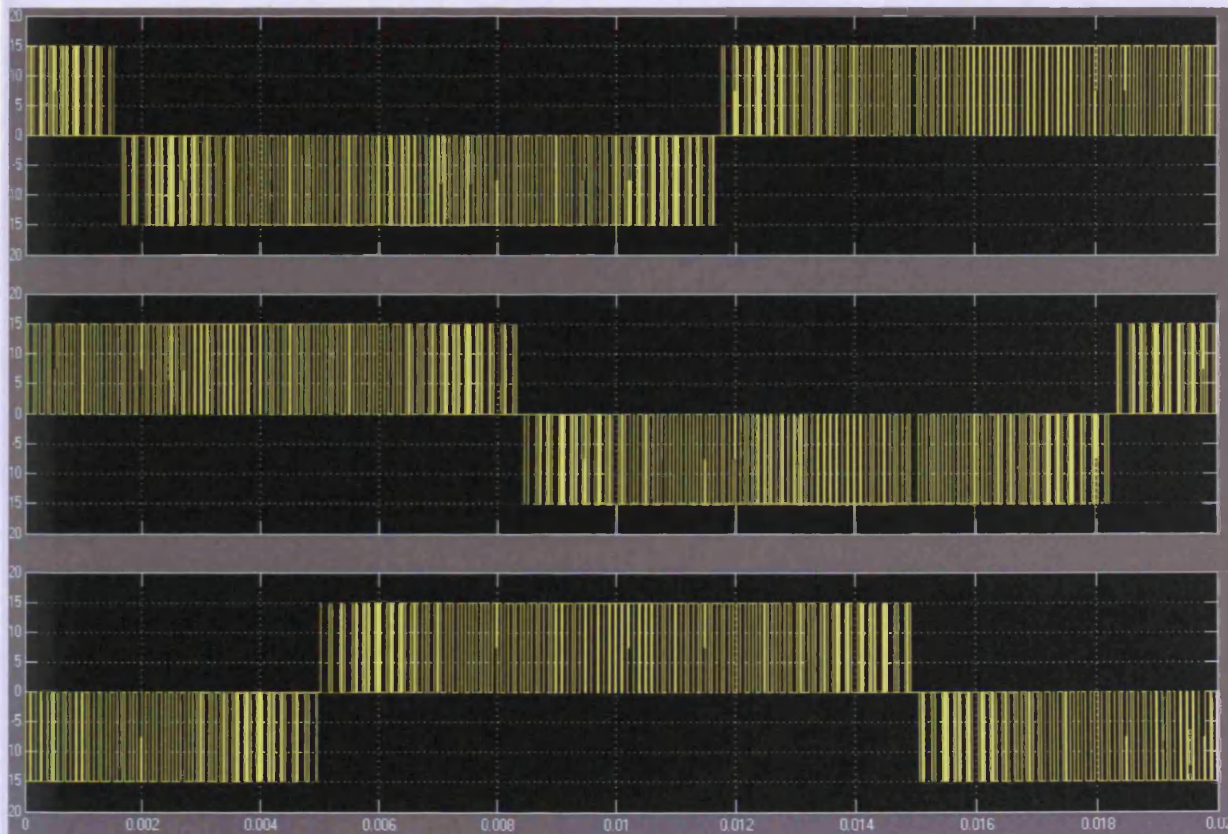


Fig 4.20. Line-line output voltages in a two-level DC-link PWM converter (50Hz)

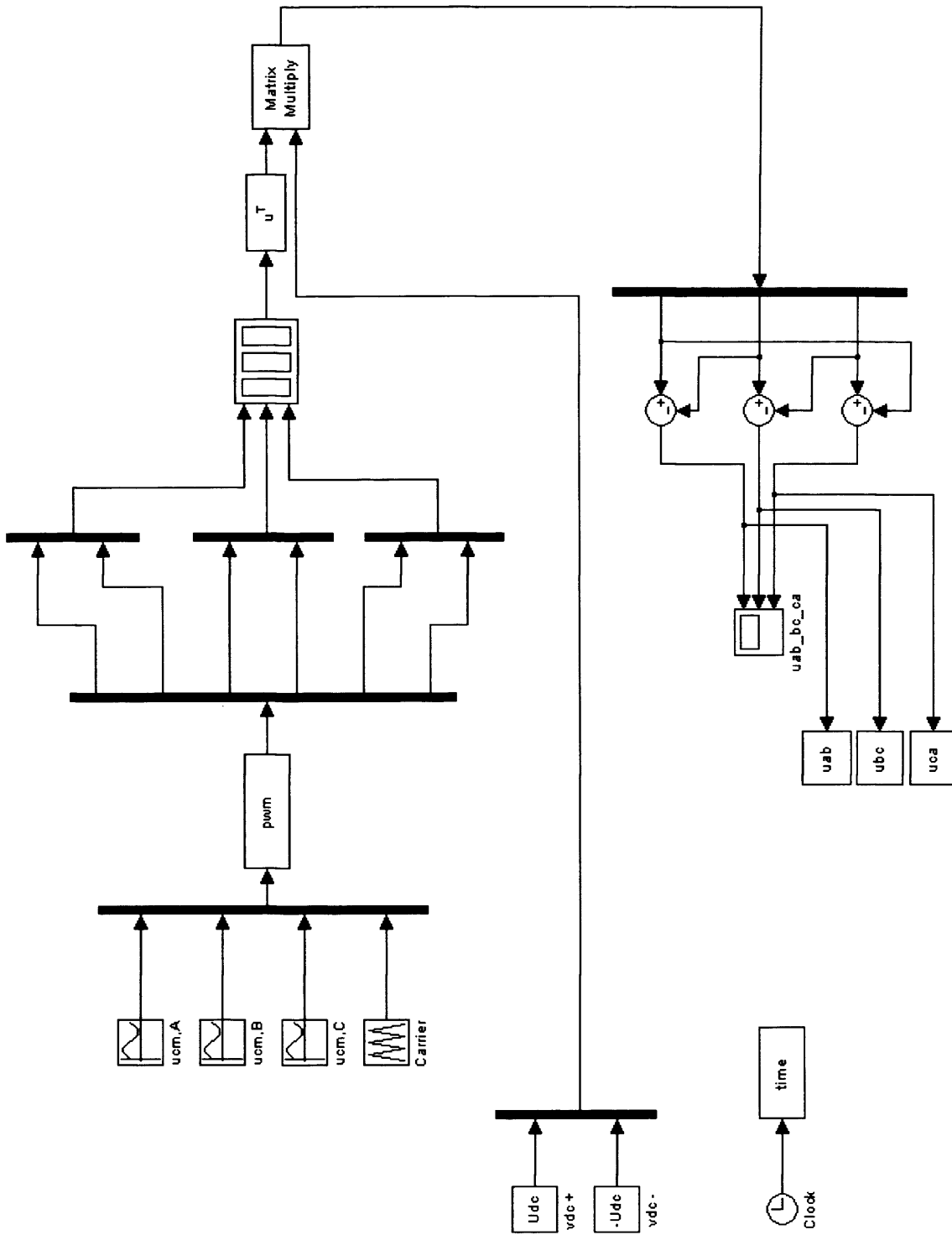


Fig. 4.21. Matlab-Simulink model used to generate voltages produced by a two-level PWM converter

### 4.5 Losses under pulsating excitation (Single Strip tester)

Line-line matrix converter voltages at 50 Hz, 100 Hz and 200 Hz are generated as described in the computational technique (§ 4.4.1). Three values of sampling frequency  $f_s$  (2.5 kHz, 5 kHz and 10 kHz) are selected. The output voltage transfer ratio  $q$  is maintained constant at the maximum value  $\sqrt{3}/2$ . The relative phase angle between input and output voltages is kept constant ( $\varphi=0$ ). Line-line voltages as produced by a two-level PWM indirect converter are generated at 50 Hz, 100 Hz and 200 Hz as described in the computational technique (§ 4.4.2). A constant value of switching frequency  $f_{sw} = 5$  kHz is selected. Modulation indices chosen were 0.5, 0.8 and 1.0.

These line-line voltage waveforms are uploaded and stored in the signal generator. Steel laminations are then energised in the single strip tester via the power amplifier connected to the signal generator. The induced voltage  $e(t)$  is integrated and divided by  $(N_2 S)$  by the digital oscilloscope. The number of turns of the secondary windings of the single strip tester is  $N_2 = 224$  and  $S$ , the cross-sectional area of the lamination under test. The output voltage from the power amplifier is varied until peak-peak magnitude of flux density is equal to  $(2B_p)$ . Total active power  $P_a$  [W] and RMS value of magnetising current ( $I_{RMS}$ ) are calculated from measured values of energy [Wh] and  $I \times \Delta t$  [Ah] given by the integrating function of the power analyser over a period of 1 min. After subtracting the term  $(R_1 I_{RMS}^2)$  associated to Joule losses in primary windings from  $P_a$ , iron losses  $P$  [W] are divided by the mass of the strip of steel, previously measured by an Avery Berkel balance.

Losses in five different laminations of each material (M470-50A, M530-50A and M700-65A) subjected to line-line voltages typical of the two converters are measured at 1.5T peak flux density at an identical value of SVM sampling frequency (matrix) and PWM switching frequency of 5 kHz. Selected magnetising frequencies are 50 Hz, 100 Hz and 200 Hz. Secondly, the impact of SVM sampling frequency on losses in the same five laminations of the three grades is measured under line-line voltage excitation, typical of matrix converter. Peak flux density is maintained at 1.5 T. The selected values of sampling frequency are 2.5 kHz, 5 kHz and 10 kHz. The three magnetising frequencies chosen are 50 Hz, 100 Hz and 200 Hz. In the two experiments, the output voltage transfer ratio  $q$  is equal to  $\sqrt{3}/2$  in the matrix converter case. PWM modulation indices are 0.5, 0.8 and 1.0.

Loss measurements in the Epstein frame and single strip testers are accomplished in a frequency range from 50Hz to 200Hz while peak flux density is within the 1.0 – 1.5T interval. For the sake of completeness and optimum utilisation of set-up for experimental validation of theoretical loss modelling approach, frequency and induction ranges are taken as broad as possible. However, steel laminations would not be subjected simultaneously to high induction at a very high magnetising frequency in a variable speed drive.

When a motor rotates at a speed well above its base value, iron losses in the stator core increase dramatically. Subsequently, more energy has to be extracted from the DC-link in the frequency converter, the value of which must remain above a safe value to avoid collapsing the power electronics circuit. Due to internal over-heating, the rise in iron losses compromises motor reliability and reduces the lifetime of the machine significantly. While in robust induction motors copper winding insulation will be mainly affected, large temperatures have a devastating effect on permanent-magnet used in servomotors in applications (robotics, machine tools) as the magnetic material may suffer from irreversible demagnetization.

In order to prevent these problems, a field weakening strategy is accomplished when the rotor must operate at higher speeds than the base value (traction, electric vehicle, machine tool applications). The latter is determined based on inverter voltage and current ratings and machine parameters such as stator and stator transient inductances [4.3]. The principle behind this technique consists in reducing the flux in inverse proportion to the increasing rotor speed. Although the torque is reduced, the output power is maintained constant.

#### ***4.6 Analysis of experimental inaccuracy***

Line-line voltage waveforms of matrix and two-level DC-link converters are sampled at a variable rate depending on the fundamental frequency. The wave-shapes uploaded to the signal generator (§4.2.2b) are described by 20,000 points. While a sampling period of 1 $\mu$ s was associated to 50Hz, respective values of 0.5 $\mu$ s and 0.25 $\mu$ s were chosen for 100Hz and 200Hz. The digitised waveform stored in the memory is transferred to the digital-to-analog converter at the maximum sampling rate of 30MHz. The vertical resolution of the signal generator is limited to 12 bits, which means that the output analogue signal is a quantised signal with 4096 discrete voltage levels to introduce some inaccuracy in the final

signal. The power amplifier (§4.2.2d) has a minimum sensitivity of 775mV. Any voltage below this threshold can not be amplified by the device based upon toroidal transformers.

Generation of line-line voltage typical of an indirect DC-link converter for iron loss measurement is not affected by intrinsic inaccuracy in signal generation and power amplification (bipolar signals with an additional zero-level – fig 4.21). However, exact reproduction of typical voltages of a matrix converter is more challenging owing to co-sinusoidal amplitude modulation (fig. 4.19). Due to the absence of some pulses of low amplitude, total harmonic distortion in the magnetising signal feeding the single strip tester is somewhat modified (slightly higher low order harmonics).

Specific iron losses  $p_{fe}$  [ $W.kg^{-1}$ ] were determined based on experimental measurement of total absorbed active power  $P_0$  [W], RMS current  $I_{rms}$  [A], winding resistance  $R[\Omega]$  and mass  $m_{fe}$  [kg] of steel laminations in single strip and Epstein testers.

$$p_{fe} = \frac{P_0 - RI_{rms}^2}{m_{fe}} \quad (4.1)$$

Measurement of active power and RMS current by the PM3000A power analyser (§ 4.2.2b) have respective accuracies  $\varepsilon_P = 0.3\%$  (of the read value) and  $\varepsilon_I = 0.15\%$  (of the read value). The winding resistance was measured to within  $\pm 0.15\%$ . In the analysis introduced in this subsection, the inaccuracy of the Avery Berkel balance is considered negligible. Then, the maximum error  $\Delta p_{fe,real}$  [ $W.kg^{-1}$ ] in iron loss measurement can be described as a function of experimental inaccuracy in measured physical quantities

$$\Delta p_{fe,real} = \frac{(1+\varepsilon_P)P_0 - (1-\varepsilon_R)(1-\varepsilon_I)^2(RI_{rms}^2)}{m_{fe}} - \frac{P_0 - RI_{rms}^2}{m_{fe}} \approx \frac{\varepsilon_P P_0 + (2\varepsilon_I + \varepsilon_R)(RI_{rms}^2)}{m_{fe}} \quad (4.2)$$

In practice, power and current values were integrated over period  $\Delta t$  [sec] (equal to one minute) and then divided by time. This procedure was adopted in order to ensure repeatability in the recorded values. In order to estimate errors ( $\varepsilon_{int,P}$ ;  $\varepsilon_{int,I}$ ) in power and current measurements derived from integration, a normally distributed random signal (of null mean value) was generated in Matlab-Simulink environment during 60 seconds. The variance was adjusted to a value equal to 0.01 in order to generate the signal in fig 4.22. The rectified mean value of the random signal was then calculated by the mean value block in Simulink (averaging period of 5sec)

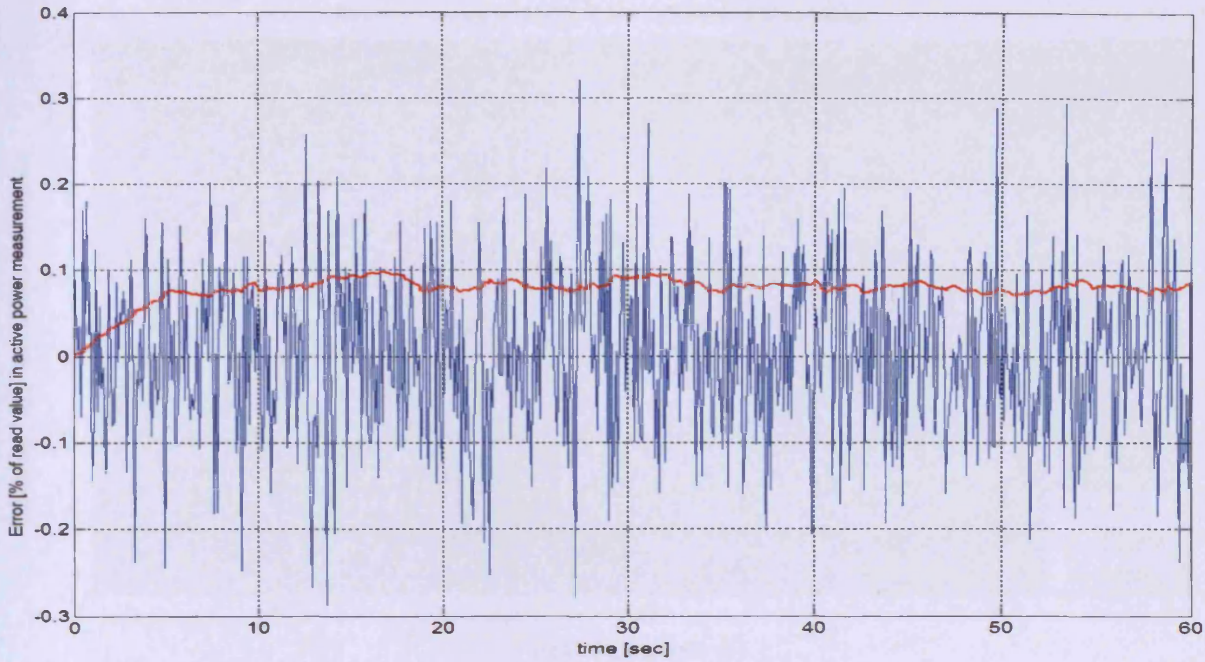


Fig. 4.22. Variation of random signal (blue) and its rectified mean value (red) over one minute

Respective values of  $(\varepsilon_{\text{int},P}; \varepsilon_{\text{int},I})$  equal to (0.08%; 0.04%) were found and then used to accuracy calculation in iron loss measurement.

$$\Delta p_{fe,real} \approx \frac{\varepsilon_{\text{int},P} (\text{int}(P_0) / \Delta t) + (2\varepsilon_{\text{int},I} + \varepsilon_R) \left[ R [\text{int}(I_{rms}) / \Delta t]^2 \right]}{m_{fe}} \quad (4.3)$$

$$\varepsilon_{fe} [\%] = 100 \frac{\Delta p_{fe,real}}{P_{fe}} \quad (4.4)$$

The inaccuracy in iron loss measurement with the Epstein frame tester is shown in fig 4.23 – fig 4.25 for laminations of the three steel grades (M470-50A, M530-50A and M700-65A)

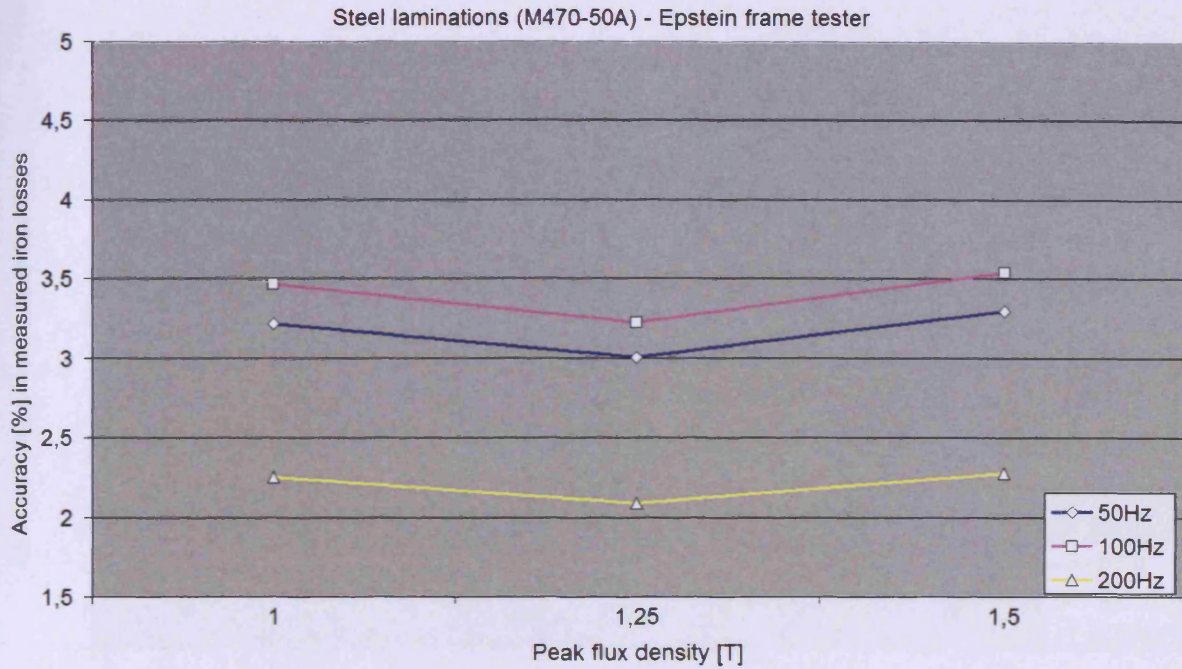


Fig. 4.23. Accuracy [%] in measurement of iron losses in M470-50A laminations (Epstein tester)

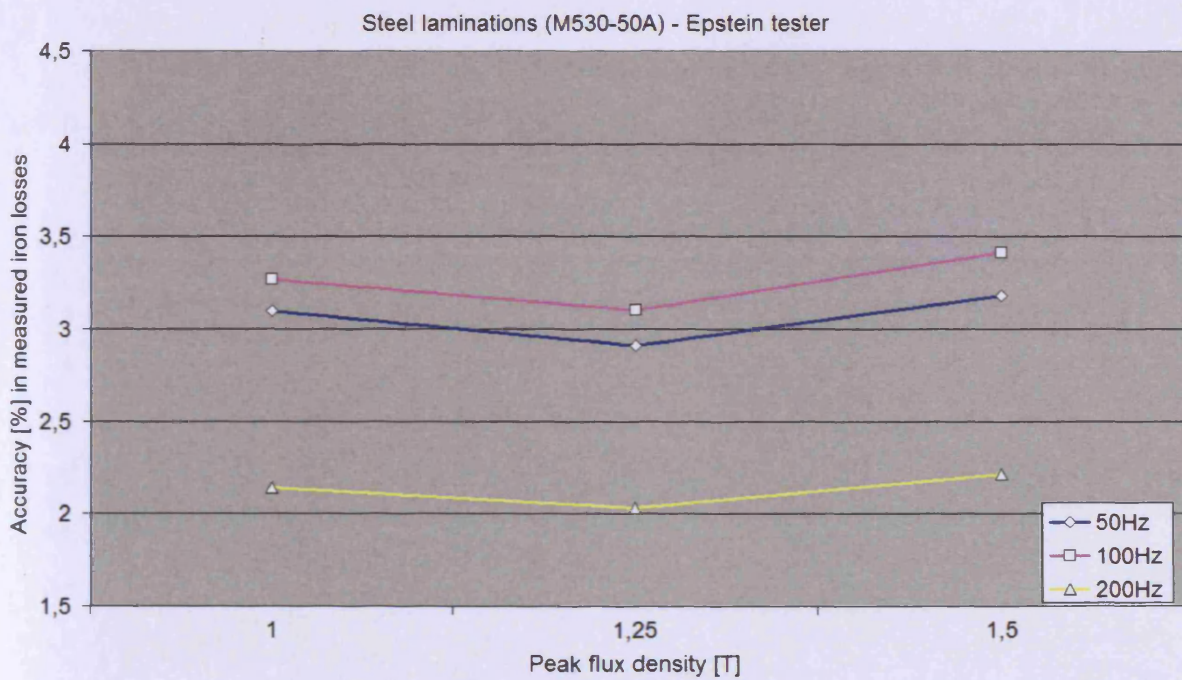


Fig. 4.24. Accuracy [%] in measurement of iron losses in M530-50A laminations (Epstein tester)

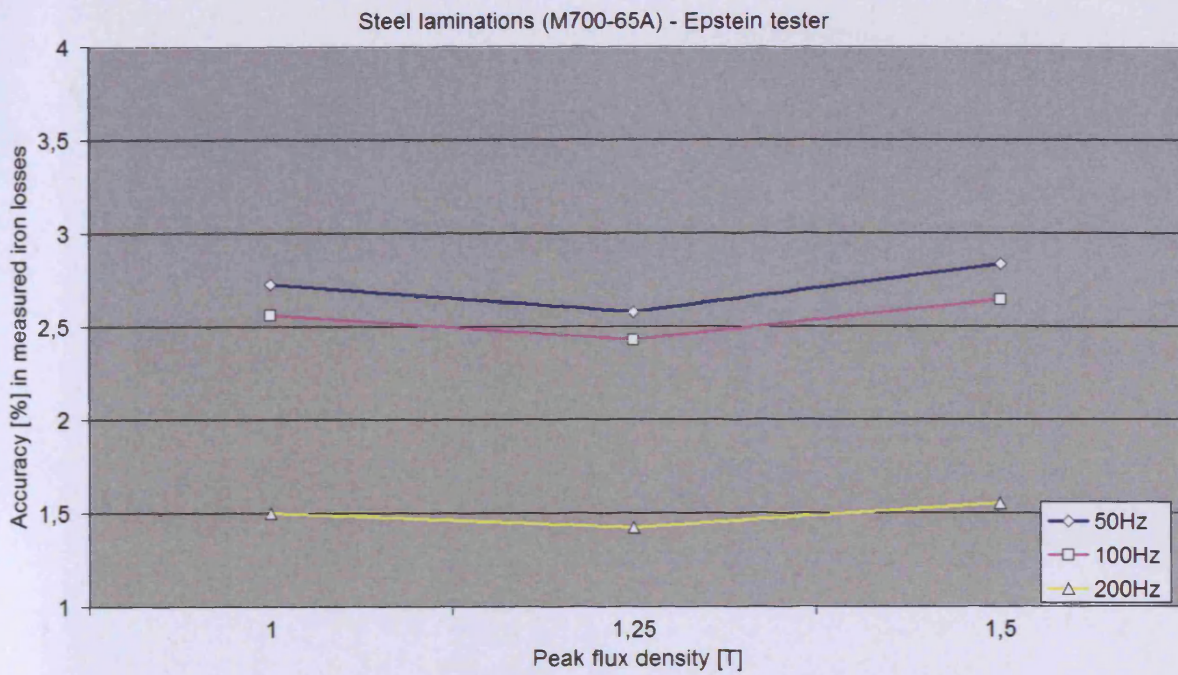


Fig. 4.25. Accuracy [%] in measurement of iron losses in M700-65A laminations (Epstein tester)

Fig 4.26 –fig 4.28 illustrate the variation of error [%] in measured iron losses in M470-50A, M530-50A and M700-65A laminations by the means of the single strip tester.

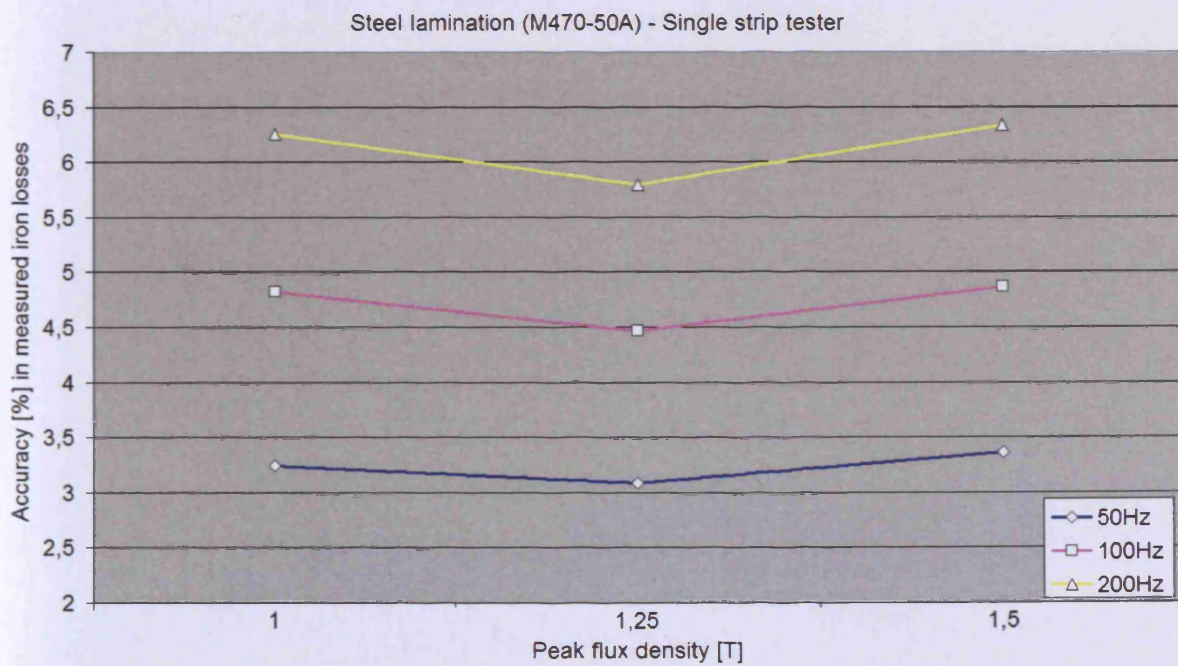


Fig. 4.26. Accuracy [%] in measurement of iron losses in M470-50A laminations (single strip tester)

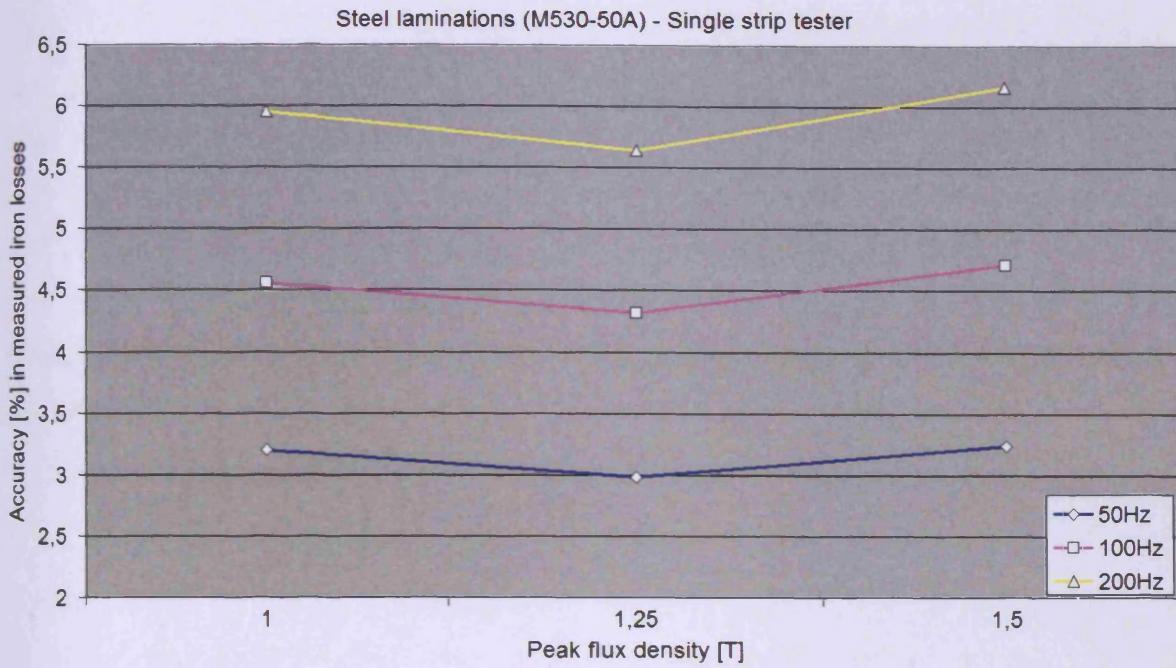


Fig. 4.27. Accuracy [%] in measurement of iron losses in M530-50A laminations (single strip tester)

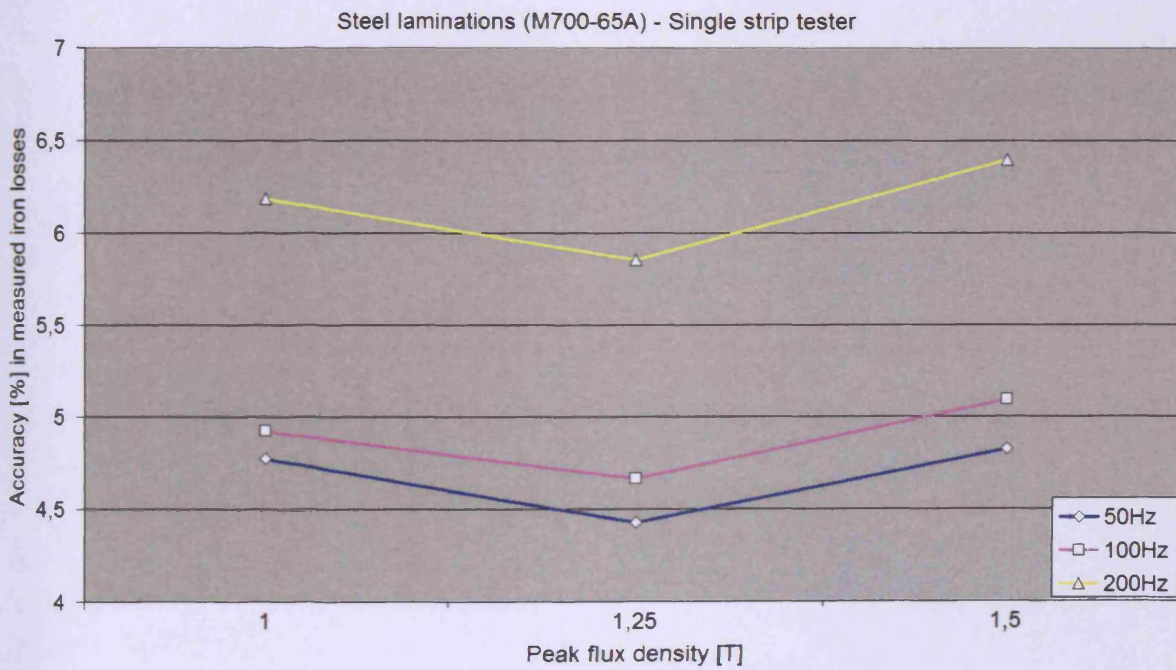


Fig. 4.28. Accuracy [%] in measurement of iron losses in M700-65A laminations (single strip tester)

## **References**

- [4.1] N. Yoshihisa, T. Yukihiro, Y. Chiaki, "DL716 Scope", *Yokogawa Technical Report. English Edition*, pp 1-14, 2000.
- [4.2] The Mathworks, "Simulink: Simulation and Model-Based Design. Writing S-functions in C", Chapter 3, pp 1-52, <http://www.mathworks.com/products/matlab/>, 2004.
- [4.3] S. h. Kim et al, "Maximum Torque Control of an Induction Machine in the Field Weakening Region", *Annual Meeting of the IEEE Industry Applications Society*, pp 401-407, Oct 1993.

## MAGNETISATION OF LAMINATED STEEL UNDER MATRIX CONVERTER SUPPLY: RESULTS AND DISCUSSION

---

Losses in M470-50A, M530-50A and M700-65A laminations subjected to matrix converter supply are measured at various peak flux densities and magnetising frequencies. They are complemented in the study by measured losses under PWM conditions. Non-linearity between applied field and induction as well as eddy-current shielding effect are discussed and incorporated into a novel analytical model for iron loss prediction in laminated steel. The effect of line-neutral matrix converter excitation on the performance of non-oriented steel in the Epstein frame is investigated along with the role played by modulation index on efficient magnetisation under PWM conditions. The impact of optimum line-line matrix converter voltage on losses in steel laminations is measured in a single strip tester and compared to values obtained under ideal PWM signals.

Total harmonic distortion of flux density curve and induced voltages, as well as their form factor, are analysed. Attention is given to the influence of sideband patterns of clusters in the frequency spectrum (1 kHz – 22.5 kHz) on losses in laminations of the three Si-Fe alloys. The distribution of harmonic components below 22.5 kHz was modified in matrix converter voltages, as Space-Vector-Modulation [SVM] sampling frequency is varied between 2.5 kHz – 10 kHz. Subsequent changes in losses in steel laminations are measured in a single strip tester.

### ***5.1 Energy flux: Poynting vector***

The geometry of a steel lamination of steel is characterised by its thickness  $d$  [m], width  $a$  [m] and length  $l$  [m]. The  $y$ -axis is aligned vertically across the lamination while the  $z$ -axis is aligned horizontally. The origin of the  $xyz$  coordinate system is located at the geometrical centre of the lamination (see fig. 5.1). It is assumed that the distribution of silicon is homogeneous so that resistivity remains constant within the volume of material.

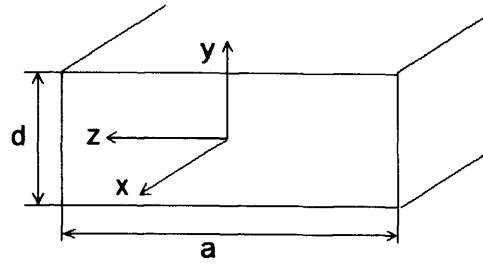


Fig. 5.1. System of coordinates and dimensions in a lamination of steel.

Under uniaxial magnetisation conditions, peak flux density has only one component  $B_x = B(y)$  in the  $x$ -direction, which is assumed constant along the  $z$ -direction ( $\partial B_x / \partial z = 0$ ). This component decreases with increasing distance from the surface of the lamination. Its maximum value, found on the surface, is defined as  $B_s$ . From Maxwell's equations, the component of the electrical field in the  $y$ -direction  $E_y$ , and its gradient with the  $z$ -coordinate ( $\partial E_y / \partial z$ ) is equal to zero. By introducing the constitutive relation of the material, it is accepted that peak magnetic field has only one component  $H_s$  in the  $x$ -direction given by  $B_s = \mu \cdot H_s$ . The absolute permeability  $\mu$  of the material is a scalar equal to  $(\mu_0 \mu_r)$ , where  $\mu_0$  is the permeability of free space ( $4\pi \times 10^{-7} \text{ Wb} \cdot \text{A}^{-1} \cdot \text{m}^{-1}$ ) and  $\mu_r$  the relative permeability of the material. At low frequencies, the displacement current is negligible. The electrical field in the  $z$  direction ( $E_z$ ) can then be written as in (5.1)

$$E_z(y) = -\frac{\partial H(y)}{\partial y} \quad (5.1)$$

The variation of peak flux density with distance  $y$  to the centre of the lamination is given by (5.2)

$$B(y) = B_s \left[ \frac{\cosh(\beta \cdot y)}{\cosh(\beta \cdot d/2)} \right] \quad (5.2)$$

$\beta$  is the propagation constant of the material while  $f$  and  $\rho$  are magnetising frequency [Hz] and resistivity of the material [ $\Omega \cdot \text{m}^{-1}$ ], respectively. Its value is defined in (5.3).

$$\beta = \sqrt{\frac{\omega \mu}{\rho}} = \sqrt{\frac{2\pi \cdot f \cdot \mu}{\rho}} \quad (5.3)$$

The  $z$ -component of the electrical field  $E_z$  can be calculated as in (5.4)

$$E_z(y) = -\rho \cdot \beta \cdot H_s \left[ \frac{\sinh(\beta \cdot y)}{\cosh(\beta \cdot d/2)} \right] = (-\sqrt{\alpha \mu \rho}) \cdot H_s \left[ \frac{\sinh(\beta \cdot y)}{\cosh(\beta \cdot d/2)} \right] \quad (5.4)$$

Since peak magnetic field  $H_s$  can be written as  $H_s = B_s / \mu$  based upon the constitutive relation of the material, Poynting vector  $\vec{S}$ , which gives the magnitude and direction of power flux per unit area [ $\text{W} \cdot \text{m}^{-2}$ ] associated to the electromagnetic field, is calculated as the cross-product of electrical field and flux density (5.5).

$$|\vec{S}| = |\vec{E} \times \vec{H}| = \frac{|\vec{E} \times \vec{B}|}{\mu} = \frac{|E_z| \cdot |B|}{\mu} \quad (5.5)$$

The modulus of Poynting vector  $|\vec{S}|$  can be described as a function of the distance  $y$  from the centre of the lamination (5.6).

$$|\vec{S}| = \frac{\sqrt{\alpha \mu \rho}}{\mu} \cdot B_s \cdot \left[ \frac{\sinh(\beta \cdot y)}{\cosh(\beta \cdot d/2)} \right] \cdot \left[ \frac{\cosh(\beta \cdot y)}{\cosh(\beta \cdot d/2)} \right] \quad (5.6)$$

Equation (5.6) will be used in sections 5.1.1 and 5.1.2 to calculate power flux per unit area under the hypotheses of linearity and non-linearity between magnetic field and induction.

### 5.1.1 Poynting vector and eddy-current losses

In the study introduced in section 5.1, the lamination of steel is assumed to be an ideal conductor. Since no magnetic domains are present, the only losses incurred in the material are eddy-current losses  $P_{ec}$  (hysteresis losses  $P_{hyst} = 0$ ). Iron losses in a steel lamination, which were divided into hysteresis and eddy-current components (5.7), were calculated based upon Poynting vector [5.1]. The vector  $\vec{s}$  is the instantaneous Poynting vector (5.8) and  $A$  is the area of Gaussian surface normal to  $\vec{s}$ .

$$P_{hyst} + P_{ec} = -\frac{1}{T} \int_0^T \int_A \vec{s} \cdot \vec{dA} \cdot dt = -\frac{1}{T} \int_0^T \vec{\nabla} \cdot \vec{s} \cdot dt \quad (5.7)$$

$$|\vec{s}| = |\vec{S}(y)| \cdot f_s(t) = |\vec{S}| \cdot f_s(t) \quad (5.8)$$

From the energy-conservation law or Poynting's theorem (5.9),

$$\frac{du}{dt} + \vec{J} \cdot \vec{E} = -\vec{\nabla} \cdot \vec{s} \Rightarrow \frac{du}{dt} + \frac{J^2}{\sigma} = -\vec{\nabla} \cdot \vec{s} \quad (5.9)$$

The vector  $\vec{J}$  [A.m<sup>-2</sup>] is the current density and  $u$  [J.m<sup>-3</sup>] is the electromagnetic energy density in the material. From (5.9), it is derived after integration of left and right-hand terms over the fundamental period (5.10).

$$\frac{1}{T} \int_0^T du + \frac{1}{T} \int_0^T \frac{J^2}{\sigma} dt = -\frac{1}{T} \int_0^T \vec{\nabla} \cdot \vec{s} \cdot dt \Rightarrow \frac{1}{T} \int_0^T du + P_{ec} = -\frac{1}{T} \int_0^T \vec{\nabla} \cdot \vec{s} \cdot dt \quad (5.10)$$

By identifying (5.7) and (5.10) and considering  $P_{hyst} = 0$ , an expression for instantaneous eddy-current losses  $p_{ec}(y, t)$  can be written (5.11).

$$p_{ec}(y, t) = \int_0^t \vec{\nabla} \cdot \vec{s} \cdot dt = \int_0^t \int_A |\vec{S}| \cdot f_s(t) \cdot dA \cdot dt = \int_0^t \int_{-l/2}^{l/2} \int_{-a/2}^{a/2} |\vec{S}(y)| \cdot dz \cdot dx \cdot f_s(t) dt \quad (5.11)$$

Instantaneous eddy-current losses  $p_{ec}(y, t)$  at a given point depend on the distance  $y$  to the centre of the lamination. However, an average value of eddy-current losses  $P_{ec\_mean}$  [W] across the thickness can be introduced (5.12) to define  $p_{ec}(t)$  as an independent function of  $y$ .

$$p_{ec}(t) = P_{ec\_mean} \cdot f_{ec}(t) \quad (5.12)$$

For that purpose, an average value  $S_{mean}$  [W.m<sup>-2</sup>] of the modulus of Poynting vector over the thickness of the lamination is also calculated in (5.13).

$$S_{mean} = \frac{1}{d} \int_{-d/2}^{d/2} |\vec{S}| \cdot dy = \frac{\Gamma}{d} \quad (5.13)$$

By combining (5.11) and (5.12), expressions for  $P_{ec\_mean}$  and  $f_{ec}(t)$  are obtained in (5.14) and (5.15).

$$P_{ec\_mean} = \left( \frac{al}{d} \right) \times \Gamma \quad (5.14)$$

$$f_{ec}(t) = - \int_0^t f_s(t) dt \quad (5.15)$$

## 5.1.2 Linearity between magnetic field and induction

Typical peak values of magnetic field were provided by the steel manufacturer at various peak flux densities in the range 0.1 T – 1.6 T under sinusoidal conditions and 50 Hz [5.2]. Dimensions and physical properties of the laminations were given in section 4.1.1. In

this section, linearity between magnetic field and flux density is assumed in the peak flux density range (0.1T – 1.6T). Values of relative permeability (associated to peak flux densities 1.05T, 1.15T and 1.25T, respectively) were selected for each one of the materials for a fundamental frequency of 50 Hz (table 5.1).

Table 5.1. Relative permeability at  $B_{s,lin} = 1.05 \text{ T} - 1.15 \text{ T} - 1.25 \text{ T}$  (linear assumption)

Case	A	B	C
$B_{s,lin} \text{ [T]}$	1.05	1.15	1.25
M470-50A	5451	4829	4035
M530-50A	5413	4842	4060
M700-65A	4765	4621	4179

The variation of coefficient  $\Gamma$  (5.14) with peak flux density is shown in fig. 5.2 for three different permeability values in M470-50A, M530-50A and M700-65A laminations at 50 Hz (table 5.1). Under the assumption of linearity between magnetic field and induction assumption (section 5.1.2), the term will be referred as  $\Gamma_{lin}$ . In section 5.1.3, the same term will be referred as  $\Gamma_{non,lin}$ .

As surface peak flux density  $B_s$  increases, the power associated to the electromagnetic field increases in the three materials. However, the rise calculated at  $B_s = 1.5 \text{ T}$  is more acute in M470-50A (+36.5 %) and M530-50A (+34.4 %) than in M700-65A (+18.1 %). Whereas relative permeability drops by 26.0 % (M470-50A) and 25.0 % (M530-50A) between cases A and C, this reduction is only 12.2 % in the steel with lower resistivity (M700-65A). The propagation of the electromagnetic field is more favourable in the thinner alloys with higher resistivity (M470-50A and M530-50A). For case A, values of  $\Gamma_{lin}$  are 33.0 % (M470-50A) and 35.1 % (M530-50A) lower than in M700-65A ( $B_s = 1.6 \text{ T}$ ). When case C is studied, the decrease in  $\Gamma_{lin}$  values is reduced to 21.8 % (M470-50A) and 25.5 % (M530-50A). Linearity between magnetic field and induction has been commonly accepted in eddy-current loss calculations. However, a careful selection of the value of relative permeability that describes this linear relation must be ensured.

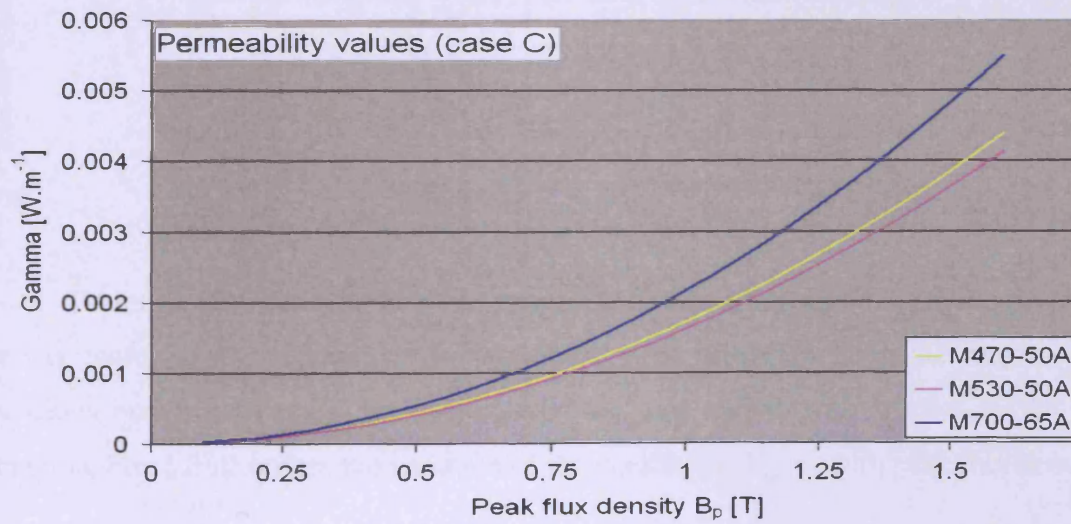
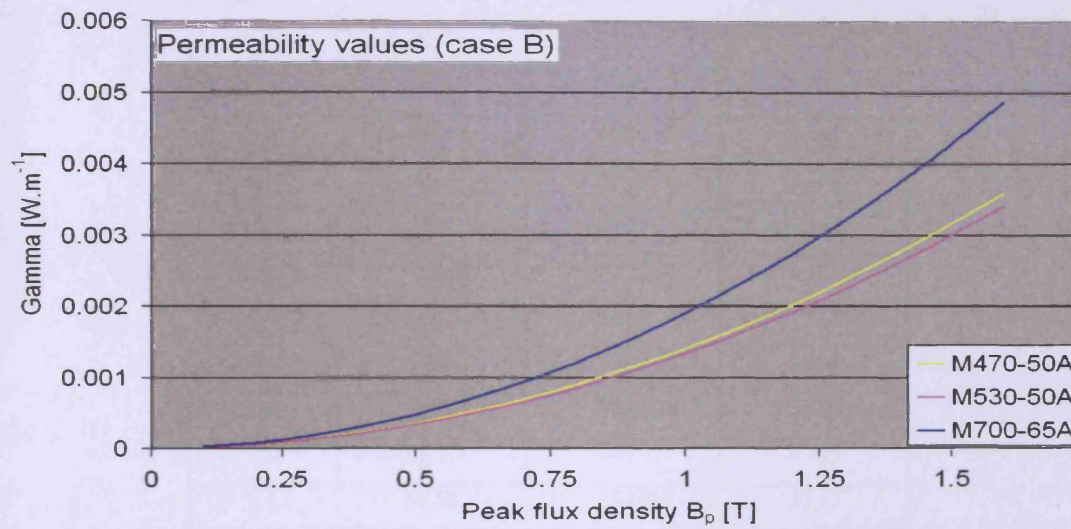
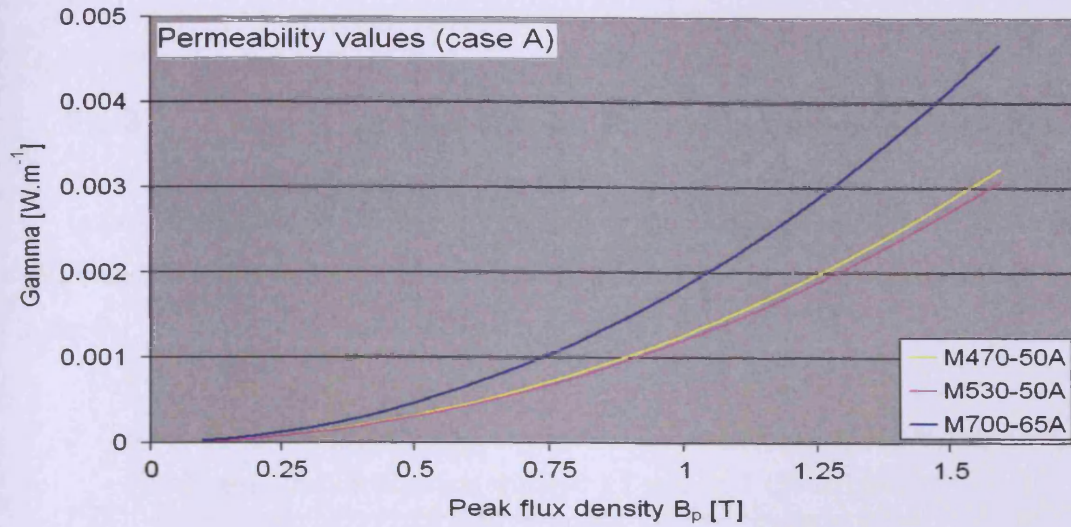


Fig 5.2. Variation of the coefficient  $\Gamma_{lin}$  with peak flux density (linear assumption) in steel laminations for three constant values of relative permeability

### 5.1.3 Non-linearity between magnetic field and induction

In this subsection, the energy flux linked to the electromagnetic field in M470-50A, M530-50A and M700-65A laminations is studied for a set of relative permeability values [5.2] in the 0.1 T – 1.6 T peak flux density range (table 5.2).

Table 5.2. Relative permeability for M470-50A, M530-50A and M700-65A for peak surface induction within 0.1 T and 1.6 T (50 Hz) [5.2]

$B_s$ [T]	M470-50A	M530-50A	M700-65A
0.1	1631	1545	1386
0.2	2456	2337	2100
0.3	3213	3076	2725
0.4	3863	3719	3248
0.5	4411	4265	3684
0.6	4862	4727	4421
0.7	5206	5064	4721
0.8	5441	5305	4935
0.9	5552	5426	5552
1.0	5451	5413	4765
1.1	5149	5149	4732
1.2	4569	4591	4526
1.3	3643	3668	3904
1.4	2345	2370	2940
1.5	1085	1105	1735
1.6	447	456	781

Therefore, non-linearity between magnetic field and induction is taken into account to reflect more realistic conditions in laminated steel subjected to cyclic magnetisation. Dimensions and resistivity of the laminations are not varied with respect to the linear assumption. Fig. 5.3 illustrates the variation of the coefficient  $\Gamma_{non,lin}$  with peak flux density.

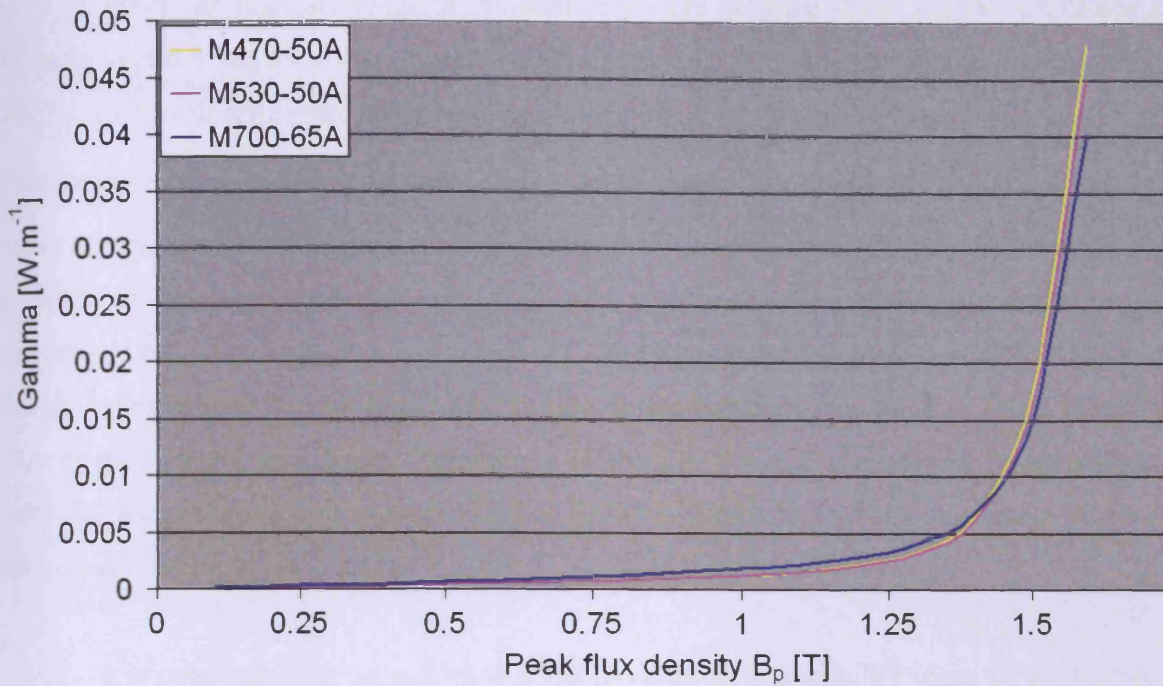


Fig 5.3. Variation of the coefficient  $\Gamma_{non,lin}$  with peak flux density in steel laminations

Results confirm that in the 0.1T – 1.4T peak flux density range, M470-50A and M530-50A are more energetically favourable to the propagation of the electromagnetic field. Nonetheless, owing to non-linearity between applied field and induction in these two alloys of higher silicon content (table 5.2), M700-65A appeared as a better material for conducting electromagnetic field beyond 1.4 T peak flux density. A look at fig. 5.2 and fig. 5.3 reveals that non-linearity between  $H$  and  $B$  must be considered in order to draw effective conclusions on energy considerations in laminated non-oriented steel subjected to alternating magnetising conditions. Eddy-current losses, which are strongly affected by the correlation of physical (resistivity) and magnetic (permeability) properties of the material, will be miscalculated if the non-linear relation between magnetic field and induction is not taken into account.

Fig. 5.4 show the discrepancy  $R$  [%] in the calculation of the term  $\Gamma$  when non-linearity between magnetic field and flux density is not considered (5.16). Furthermore, the importance of the value of relative permeability used in the description of linearity between  $H$  and  $B$  is also highlighted.

$$R = \frac{\Gamma_{non,lin} - \Gamma_{lin}}{\Gamma_{lin}} \times 100 \quad (5.16)$$

When the highest values of permeability were selected (case A), the amplitude of Poynting vector is highly underestimated at low induction (0.1 T – 0.6 T) and high induction (1.3 T – 1.6 T). Nevertheless, the linear assumption between  $H$  and  $B$  yields values of  $\Gamma_{lin}$  in a close range (-7 % - +15 %) to values of  $\Gamma_{non,lin}$  for peak flux density within 0.7 T – 1.2 T. The inaccuracy in the calculation is comparable in the three materials. When the lowest values of permeability were selected (case C), the amplitude of Poynting's vector is still underestimated at low induction (0.1 T – 0.5 T) and high induction (1.4 T – 1.6 T). However, a slight improvement by the linear assumption is observed in the 1.2 T – 1.4 T induction range at the expense of a larger discrepancy in the 0.5 T – 1.2 T range. A better accuracy under the linear assumption is reached in M700-65A laminations with the largest thickness and lowest resistivity.

It is concluded that selection of a lower value of permeability (case C) in the linear assumption would yield a more accurate description of energy flux in Si-Fe steel throughout the magnetising range. This derives from the fact that alternating magnetisation at 1.6T peak flux density (for instance) implies that the material is magnetised / demagnetised every cycle throughout the induction range [0.0 T - 1.6 T]. When the thickness  $d$  [m] of the material is taken into account under a linear relation between  $H$  and  $B$  (5.14), calculated average eddy-current losses  $P_{ec\_mean}$  are reduced by 16 % (M470-50A) and 13 % (M530-50A) with respect to losses incurred in M700-65A. In case C, the drop in mean eddy-current losses is reduced to 3 % (M470-50A) while virtually identical values were obtained in M530-50A. When non-linearity between magnetic field and induction is acknowledged,  $P_{ec\_mean}$  values remain lower in the thinner alloys (M470-50A and M530-50A) for peak flux density below 1.3 T approximately. However, as induction increases above this limit, average eddy-current losses become lower in the thicker alloy with lower resistivity (M700-65A).

Non-linearity between  $H$  and  $B$  is strongly influential on eddy-current losses in laminated steel. Losses are higher in thick laminations with lower resistivity for induction values below 1.3 T. However, they are lower than in much thinner laminations with higher resistivity for induction values above 1.3 T. The classical equation for the calculation of eddy-current losses (2.13) must be used with care due to its inadequacy for high induction.

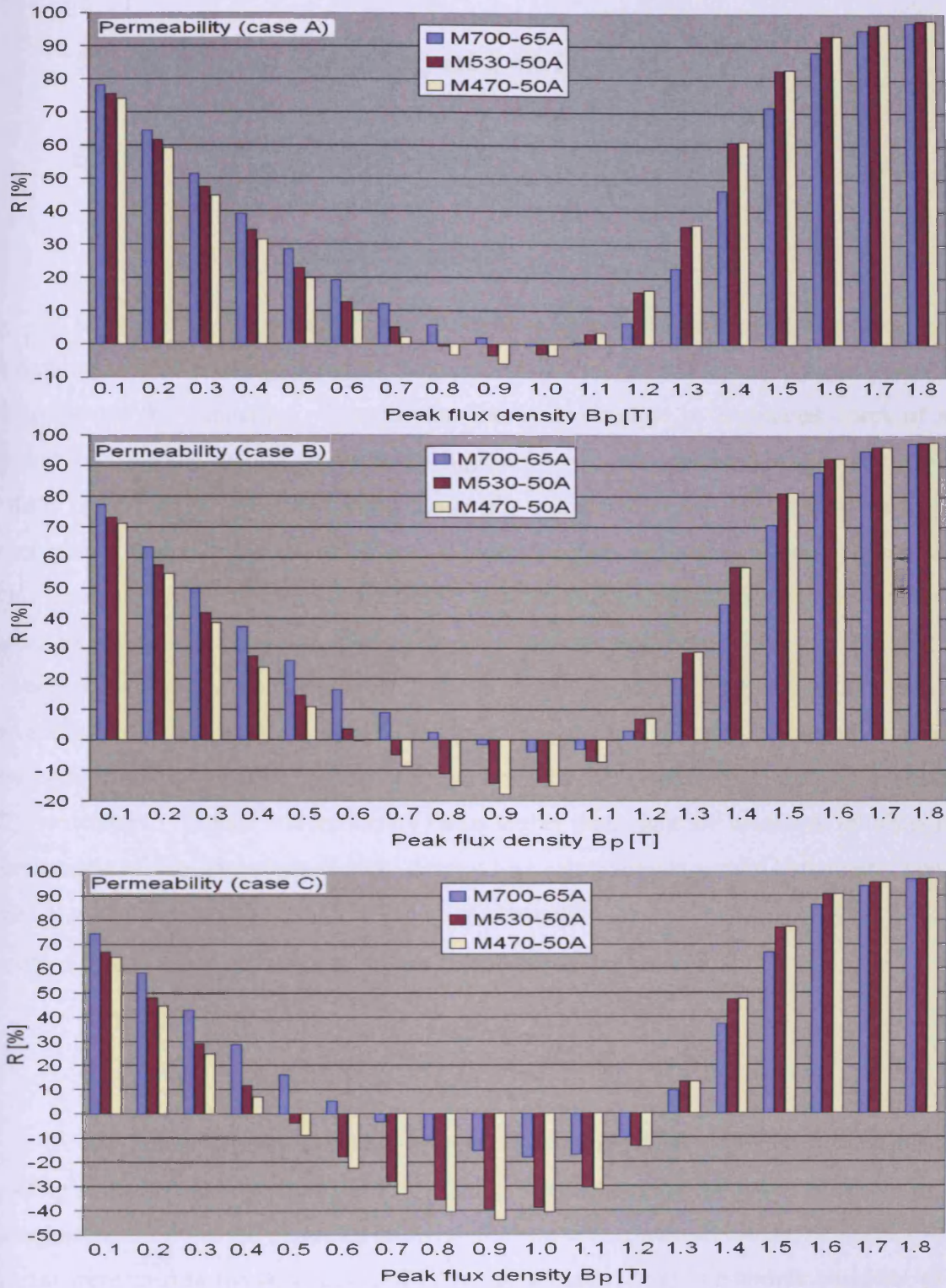


Fig 5.4 Variation of  $R$  [%] values with peak flux density in cases A, B and C.

## 5.2 Analytical Modelling of iron Losses

### 5.2.1 Eddy-current losses

#### 5.2.1a. Classical approach

Eddy-current losses in laminated steel have been calculated for many decades under the assumptions of linearity between magnetic field and induction and constant peak flux density across the lamination. This idealisation is inadequate in laminated cores of non-oriented steel used in rotating machines for high induction. As explained in chapter 3, the sum of static hysteresis  $P_h$  and eddy-current losses  $P_{ec}$  calculated under the classical was always found smaller than total measured losses. A more accurate evaluation of eddy-current losses within laminated steel could lead to a better understanding and quantification of anomalous losses. In order to accomplish this goal, eddy-current shielding effect and non-linearity between  $H$  and  $B$  must be considered. Voltage supply produced by pulse-width-modulated converters causes flux harmonics in the medium frequency range (around clusters at the first three or four multiples of the switching frequency). In low power speed drives (less than 20 kW), switching to fundamental frequency ratios higher than eight are common. In this context, superposition of flux harmonics in eddy-current loss calculation is a valid hypothesis. Specific classical eddy-current losses  $P_{ec}$  [W/kg] in a lamination of steel of resistivity  $\rho$  [ $\Omega \cdot m$ ], density  $\delta$  [ $kg \cdot m^{-3}$ ] and thickness  $d$  [m] are calculated as in (5.17) [5.3].

$$P_{ec} = \frac{\pi^2 d^2}{6\rho\delta} \sum_{n=1} B_n^2 f_n^2 \quad (5.17)$$

A derivation of classical eddy-current losses from Maxwell's equations by using Poynting's vector was introduced in [5.4]. Under the assumption of linear permeability and homogeneous nature of the magnetic material, the two curl equations (see eq (2.4) and (2.5) in §2.2.1a) were used in the description of Poynting's vector. Due to isotropic character of the material, the vectors of flux density  $B(t)$  and field intensity  $H(t)$  are assumed to be colinear, as well as current density  $J(t)$  and electrical potential  $E(t)$  [5.4]. Poynting's vector is then integrated over the volume of material to calculate the energy flow. The resultant term consists in a first term (time integral of  $HdB$ ) linked to hysteresis losses and a second term (integral of  $J^2(t)/\sigma$ ) associated to classical eddy-current losses.

The final calculation of this term is accomplished by solving a differential equation where the curl of the curl of the current density vector ( $\nabla^2 J(t)$ ) of sinusoidal amplitude is given as the product of its gradient over time ( $\partial J / \partial t$ ) and a constant  $K = (\omega\sigma\mu)$  where  $\omega$  is the electrical pulsation [ $\text{rad}\cdot\text{s}^{-1}$ ],  $\sigma$  the conductivity [ $\text{S}\cdot\text{m}^{-1}$ ] of the material and  $\mu$  its absolute permeability. The amplitude of the current density vector in a lamination follows an hyperbolic law and is dependent on respective ratios of width and thickness over skin depth. The expression is simplified under the hypotheses that both ratios are considerable smaller than unity [5.4]. Moreover, Faraday's line integral of the electrical potential over the contour of the lamination is accomplished to express current density  $J_0$  [ $\text{A}\cdot\text{m}^{-2}$ ] at the boundaries as a function of maximum peak flux density.

### 5.2.1b. Eddy-current shielding effect

Non-constant flux density across the thickness of the lamination reaches its minimum value in the centre. Flux harmonics suffer from reduced penetration into the material due to a shielding effect caused by peripheral eddy-currents. This phenomenon is emphasised at higher frequencies and in alloys with low resistivity. Alternating flux harmonics of higher amplitude are linked to increased resistive losses due to the flow of eddy-currents. Eddy-current losses in steel laminations increase with thickness, relative permeability and conductivity. The equation used to define flux density variation across the laminations is given below for a harmonic component of amplitude  $B_{s,n}$  at the surface (5.18 – 5.19).

$$\beta_n = \sqrt{\frac{\omega_n \cdot \mu}{\rho}} = \sqrt{\frac{2\pi \cdot f_n \cdot \mu_0 \mu_r}{\rho}} \quad (5.18)$$

$$\alpha(y, f_n) = \frac{B_n(y)}{B_{s,n}} = \sqrt{\frac{1 + \cosh(2 \cdot \beta_n \cdot y)}{1 + \cosh(\beta_n \cdot d)}} \quad (5.19)$$

The distribution of flux density harmonics at various harmonic frequencies  $f_n$  is shown across M470-50A, M530-50A and M700-65A laminations (fig. 5.5 - fig. 5.7). The fundamental peak induction values  $B_s$  considered were 1.0 T, 1.25 T and 1.5 T. Respective values of relative permeability were obtained from manufacturer's specifications on the three materials (50 Hz) [5.2].

Table 5.3. Relative permeability at 1.0 T, 1.25 T and 1.5 T in three materials [5.2]

	1.0 T	1.25 T	1.5 T
M470-50A	5451	4106	1085
M530-50A	5413	4130	1105
M700-65A	4765	4215	1735

As its frequency  $f_n$  increases, the penetration of the  $n^{th}$  flux harmonic is attenuated due to eddy-current shielding effect. This physical phenomenon, which can be described in terms of peripheral flow of eddy-currents, is more prominent at high frequencies and in laminations of larger thickness and lower resistivity (M700-65A). As relative permeability in the three materials decreases, the flux density distribution across the lamination is less influenced by the eddy-current shielding effect. A term  $k(f_n)$ , which incorporates the impact of thickness, resistivity and relative permeability in the three materials (5.20), will be therefore incorporated to the calculation of eddy-current losses (5.21).

$$k(f_n) = \left[ \frac{d - \int_{-d/2}^{+d/2} \alpha(y, f_n) \cdot dy}{d} \right]^2 \quad (5.20)$$

$$P_{ec} = \frac{\pi^2 d^2}{6\rho\delta} \sum_{N=1} B_n^2 f_n^2 \cdot [1 + k(f_n)] \quad (5.21)$$

(5.21) is used in the analysis of measured losses in M470-50A, M530-50A and M700-65A laminations subjected to line-neutral and line-line voltage excitation typical of matrix and DC-link converters, respectively. These results are introduced in § 5.3, § 5.4 and § 5.5. The variation of the coefficient  $k$  with flux harmonic frequency in M470-50A, M530-50A and M700-65A laminations is shown in fig. 5.8.

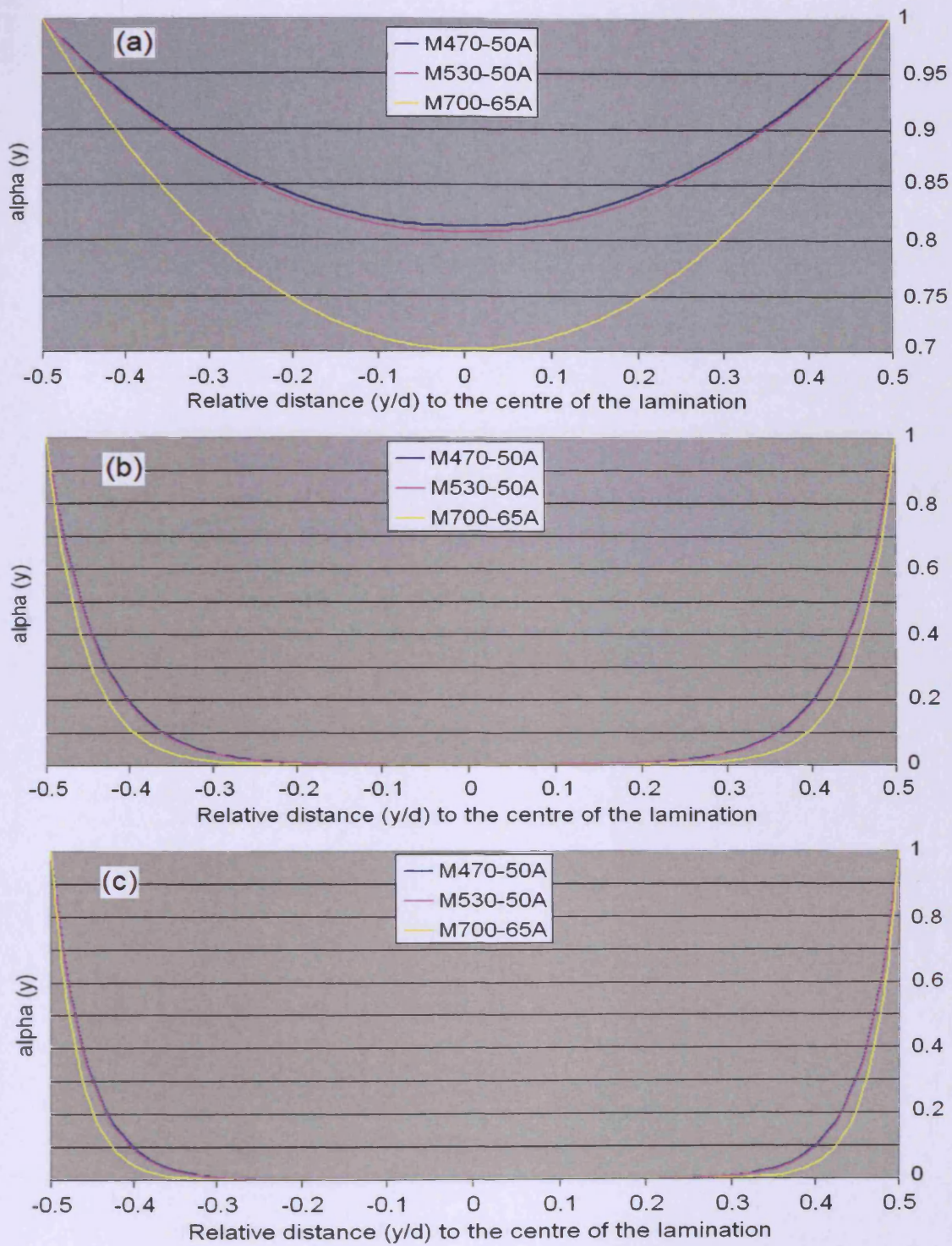


Fig. 5.5  $\alpha(y/d)$  in M470-50A, M530.50A and M700-65A laminations at  $B_s = 1.0$  T

(a)  $f_n = 50$  Hz – (b)  $f_n = 7.5$  kHz – (c)  $f_n = 15$  kHz

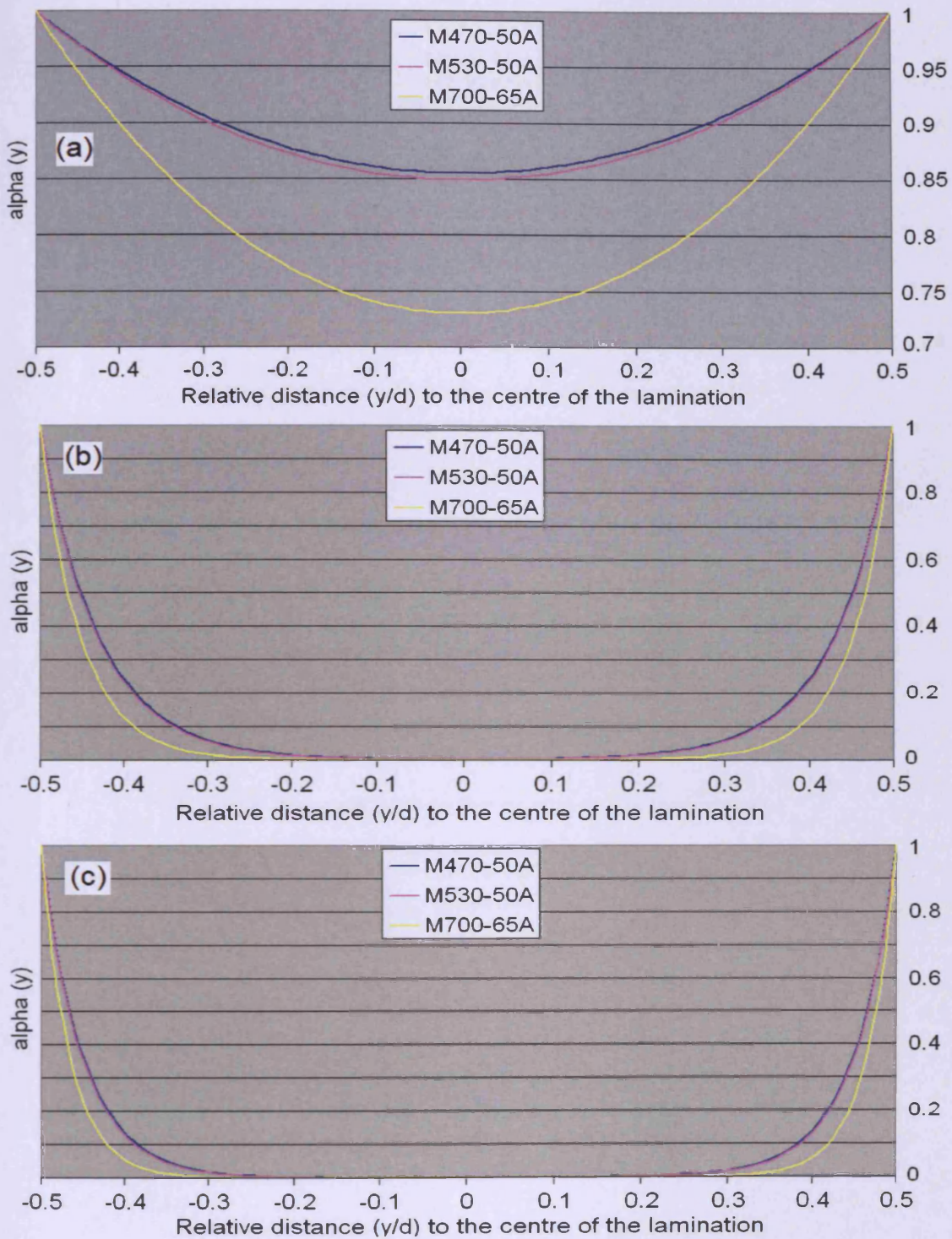


Fig. 5.6.  $\alpha(y/d)$  in M470-50A, M530-50A and M700-65A laminations at  $B_s = 1.25$  T

(a)  $f_n = 50$  Hz – (b)  $f_n = 7.5$  kHz – (c)  $f_n = 15$  kHz

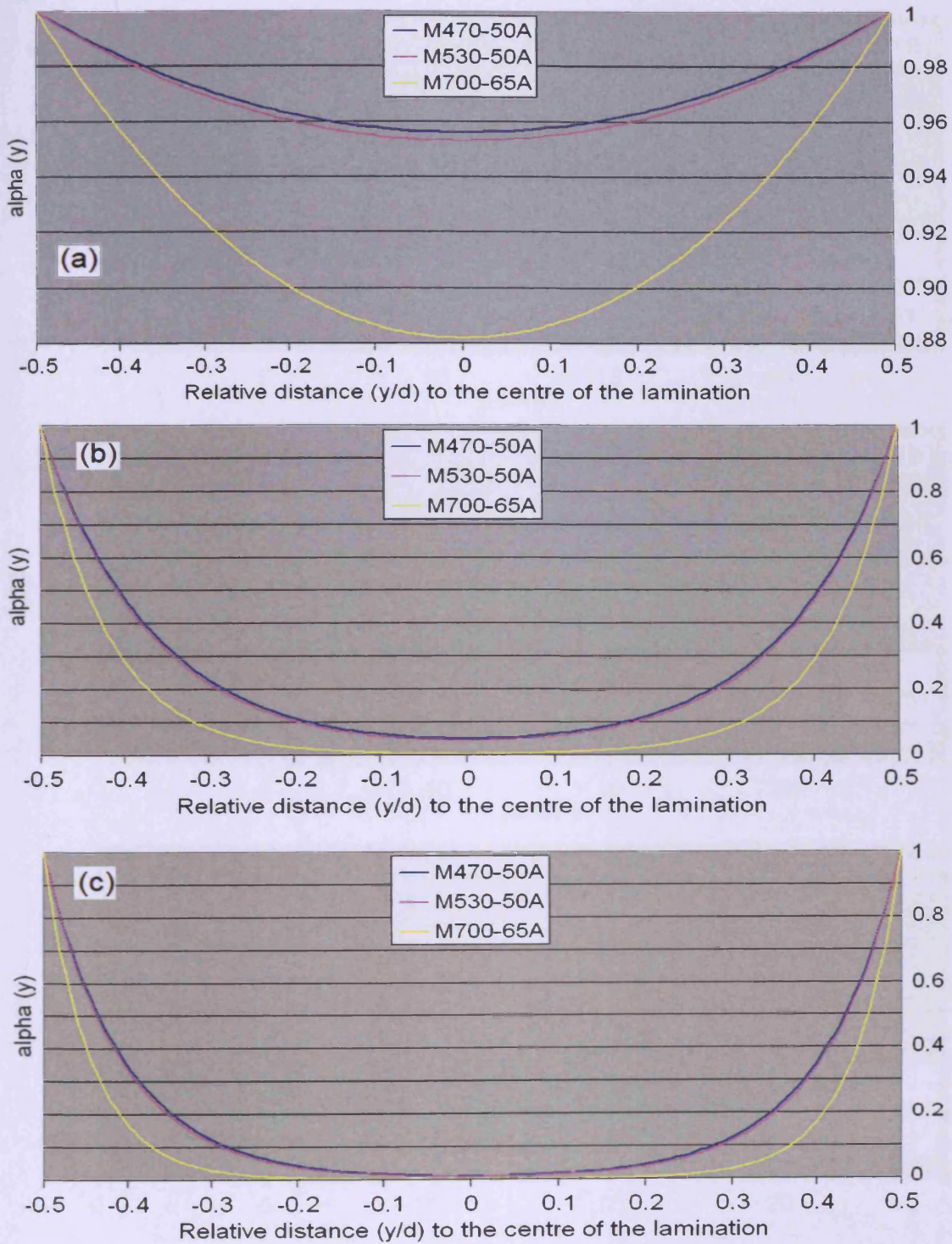


Fig. 5.7.  $\alpha(y/d)$  in M470-50A, M530.50A and M700-65A laminations at  $B_s = 1.5$  T

(a)  $f_n = 50$  Hz – (b)  $f_n = 7.5$  kHz – (c)  $f_n = 15$  kHz

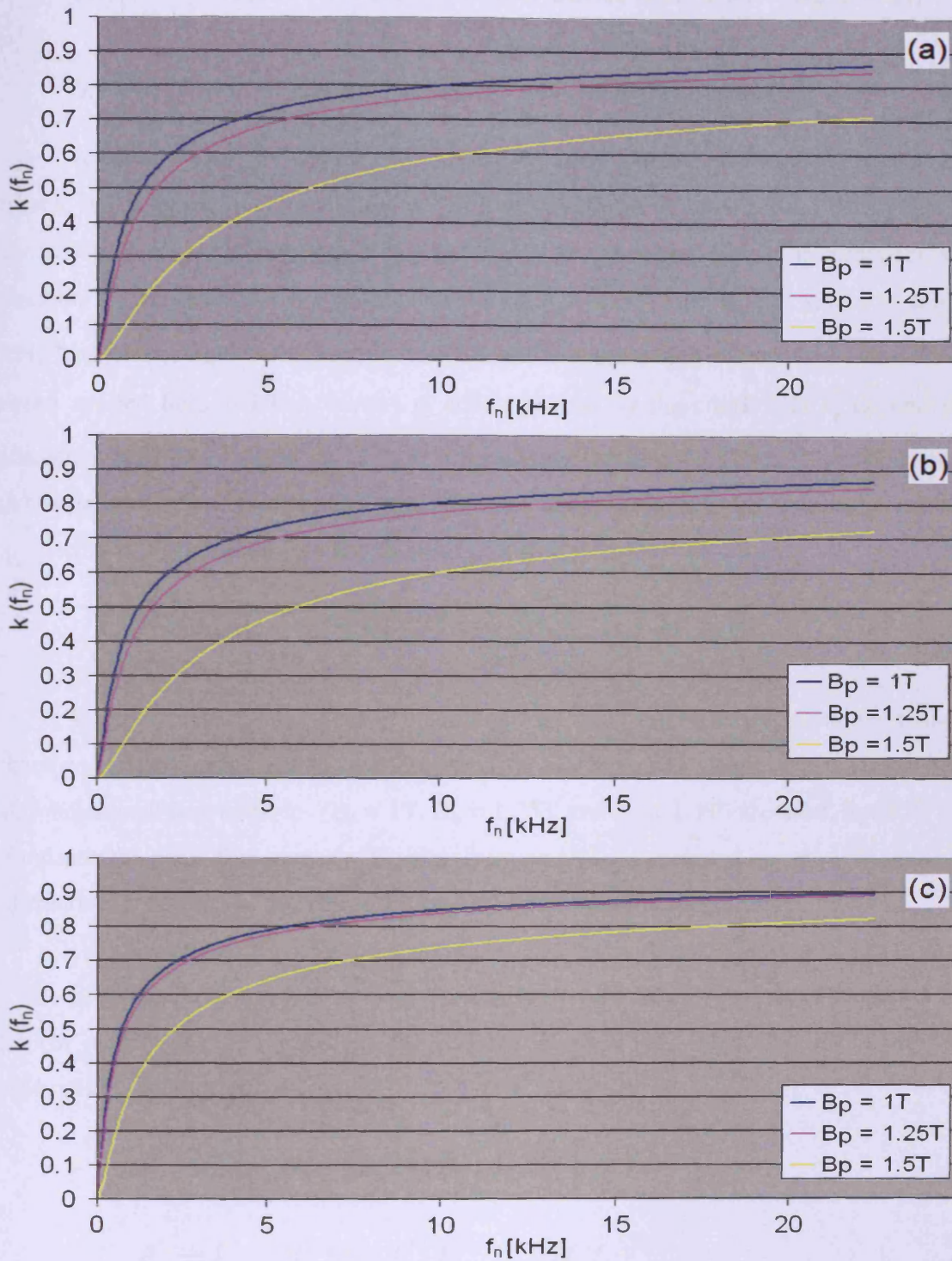


Fig 5.8. Variation of  $k$  with harmonic frequency  $f_n$  at 1.0 T, 1.25 T and 1.5 T in  
 (a) M470-50A – (b) M530-50A – (c) M700-65A laminations

## 5.2.2 Iron loss model (non-linearity and shielding effect)

### 5.2.2a. Non-linearity and eddy-current shielding effect

A new model for estimating losses in laminations of electrical steels under harmonic-rich magnetisation is introduced in this PhD thesis. Total specific losses  $P$  [ $\text{W.kg}^{-1}$ ] in the material are divided into hysteresis and eddy-current losses. Shielding effect across the lamination is accounted for by the coefficient  $k(f_n)$  (§ 5.2.1b).  $B_n$  [T] refers to the flux density harmonic component at the  $n^{\text{th}}$  multiple of the magnetising frequency  $f_1$ . Non linearity between applied field and flux density is accounted for by the coefficient  $k_e^*$  dependent on fundamental peak flux density  $B_1$  [T] and magnetising frequency  $f_1$ [Hz]. The coefficient  $k_h^*$ , which is independent of fundamental peak flux density and magnetising frequency, is defined by properties of the material (grain size, purity, porosity)

$$P = k_h^* B_1^2 f_1 + k_e^*(B_1; f_1) \sum_{n=1} B_n^2 f_n^2 [1 + k(f_n)] \quad (5.22)$$

In order to determine the coefficients  $k_h^*$  and  $k_e^*$ , measured losses under sinusoidal magnetising conditions for three frequencies ( $f_a = 50$ ,  $f_b = 100$  and  $f_c = 200$  Hz) and three peak fundamental flux densities ( $B_a = 1\text{T}$ ,  $B_b = 1.25\text{T}$  and  $B_c = 1.5\text{T}$ ) are used. Specific losses at fundamental peak flux density  $B_a$  and frequency  $f_c$  is denoted as  $P_{ac}$  [ $\text{W.kg}^{-1}$ ]. The mathematical procedure to determine the two analytical parameters consists in:

Step 1: selecting a fundamental peak flux density ( $B_a$  for instance) and solve a two unknown system for two selected frequencies ( $f_a$  and  $f_b$ ). Thus, an initial hysteresis coefficients  $k_{a(ab)}^*$  is calculated.

$$P_{aa} = k_{a(ab)}^* B_a^2 f_a + k_e^*(B_a; f_a) (B_a f_a)^2 \quad (5.23)$$

$$P_{ab} = k_{a(ab)}^* B_a^2 f_b + k_e^*(B_a; f_b) (B_a f_b)^2 \quad (5.24)$$

$$k_{a(ab)}^* = \frac{\begin{vmatrix} P_{aa} & B_a^2 f_a^2 \\ P_{ab} & B_a^2 f_b^2 \end{vmatrix}}{\begin{vmatrix} B_a^2 f_a & (B_a f_a)^2 \\ B_a^2 f_b & (B_a f_b)^2 \end{vmatrix}} \quad (5.25)$$

Step 2: while maintaining identical peak flux density ( $B_a$ ), two new equation systems are defined for selected frequencies ( $f_a$  and  $f_c$ ) and ( $f_b$  and  $f_c$ ). Thus, two hysteresis coefficients  $k_{b(ac)}^*$  and  $k_{a(bc)}^*$  are determined.

Step 3: the procedure described in steps 1 and 2 is executed for the second value of fundamental peak flux density ( $B_b$ ). Then, the hysteresis coefficients  $k_{b(ab)}^*$ ,  $k_{b(ac)}^*$  and  $k_{b(bc)}^*$  are calculated.

Step 4: the procedure described in steps 1 and 2 is executed for the third value of fundamental peak flux density ( $B_c$ ). Then, the hysteresis coefficients  $k_{c(ab)}^*$ ,  $k_{c(ac)}^*$  and  $k_{c(bc)}^*$  are calculated.

Step 5: once the hysteresis coefficients associated to the nine operating conditions are determined, an average value  $k_h^*$  is calculated as follows:

$$k_h^* = \frac{\sum_{j,m,n=a..b..c} k_{j(mn)}^*}{9} \quad (5.26)$$

Step 6: by substituting the hysteresis loss coefficient by the calculated value  $k_h^*$ , the equation describing specific total losses  $P_{aa}$  at fundamental peak flux density  $B_a$  and frequency  $f_a$  can now be solved to determine  $k_e^*(B_a, f_a)$

$$k_e^*(B_a, f_a) = \frac{P_{aa} - k_h^*(B_a^2 f_a)}{(B_a f_a)^2} \quad (5.27)$$

Step 7: the remaining eight equations are solved in an identical manner to obtain the eddy-current loss coefficient  $k_e^*$  for every measured point.

The values of hysteresis and eddy-current coefficients  $k_h^*$  and  $k_e^*(B, f)$  are introduced in tables 5.4 – 5.6 for the three materials under study (M470-50A, M530-50A, M700-65A).

Table 5.4 Eddy-current coefficient  $k_e^*$  in M470-50A laminations

	$B_a = 1T$	$B_b = 1.25T$	$B_c = 1.5T$
$f_a = 50Hz$	0.000128	0.000166	0.000114
$f_b = 100Hz$	0.000111	0.000160	0.000124
$f_c = 200Hz$	0.000103	0.000152	0.000173

Table 5.5 Eddy-current coefficient  $k_e^*$  in M530-50A laminations

	$B_a = 1T$	$B_b = 1.25T$	$B_c = 1.5T$
$f_a = 50Hz$	0.000197	0.000188	0.000111
$f_b = 100Hz$	0.000160	0.000183	0.000133
$f_c = 200Hz$	0.000139	0.000175	0.000193

Table 5.6. Eddy-current coefficient  $k_e^*$  in M700-65A laminations

	$B_a = 1T$	$B_b = 1.25T$	$B_c = 1.5T$
$f_a = 50Hz$	0.000280	0.000233	0.000188
$f_b = 100Hz$	0.000232	0.000249	0.000137
$f_c = 200Hz$	0.000222	0.000269	0.000336

The value of the hysteresis coefficient  $k_h^*$  for the three materials under study is introduced in table 5.7

Table 5.7. Hysteresis coefficient  $k_h^*$  in the three materials

	$k_h^*$
M470-50A	0.023198
M530-50A	0.025935
M700-65A	0.032375

### 5.2.2b. Statistical approach by Bertotti

Specific losses  $P$  [ $W.kg^{-1}$ ] in laminations of electrical steel under harmonic-rich magnetising conditions are commonly estimated following the statistical approach proposed by Bertotti. Based on his theory, losses in the electrical steel can be decomposed into static hysteresis, classical eddy-current and anomalous losses (section.....).

$$P = k_h B_1^2 f + k_e \sum (B_n f_n)^2 + k_a \sum (B_n f_n)^{3/2} \quad (5.28)$$

The eddy-current coefficient  $k_e$  is calculated based upon the thickness of the lamination  $d$  [m], resistivity  $\rho$  and density  $\delta$  of the material.

$$k_e = \frac{\pi^2 d^2}{6\rho\delta} \quad (5.29)$$

Hysteresis and anomalous coefficients ( $k_h$  and  $k_a$ ) must be calculated analytically with experimentally measured losses ( $P_a$  and  $P_b$ ) under sinusoidal conditions at a frequency  $f$  [Hz] (often 50Hz) and two fundamental peak flux densities ( $B_a$  and  $B_b$ ).

$$P_a = k_h B_a^2 f + k_e (B_a f)^2 + k_a (B_a f)^{3/2} \quad (5.30)$$

$$P_b = k_h B_b^2 f + k_e (B_b f)^2 + k_a (B_b f)^{3/2} \quad (5.31)$$

By solving the system of two unknowns and two equations, hysteresis and anomalous loss coefficients are easily determined.

$$k_h = \frac{\begin{vmatrix} P_a - k_e (B_a f)^2 & (B_a f)^{3/2} \\ P_b - k_e (B_b f)^2 & (B_b f)^{3/2} \end{vmatrix}}{\begin{vmatrix} B_a f & (B_a f)^{3/2} \\ B_b f & (B_b f)^{3/2} \end{vmatrix}} \quad (5.32)$$

$$k_a = \frac{\begin{vmatrix} P_a - k_e (B_a f)^2 & (B_a f)^{3/2} \\ P_b - k_e (B_b f)^2 & (B_b f)^{3/2} \end{vmatrix}}{\begin{vmatrix} B_a f & (B_a f)^{3/2} \\ B_b f & (B_b f)^{3/2} \end{vmatrix}} \quad (5.33)$$

Hysteresis, classical eddy-current and anomalous loss coefficients for the three materials under study are introduced in table.....

Table 5.8. Hysteresis, classical eddy-current and anomalous losses associated to the three materials(Bertotti's statistical approach)

	$k_h$	$k_e$	$k_a$
M470-50A	0.015269	0.000178	0.000429
M530-50A	0.016294	0.000185	0.0006
M700-65A	0.010680	0.000361	0.00165

### 5.3 Line-neutral supply (matrix converter)

#### 5.3.1 Total power losses

Specific power losses in M470-50A, M530-50A and M700-65A laminations subjected to matrix converter (line-neutral) and two-level PWM converter (line-line) were measured as described in section 4.3. Results are showed in fig. 5.9, fig. 5.10 and fig. 5.11. As expected, losses in laminations of the three non-oriented steels were highest under low modulated PWM ( $m_i = 0.5$ ). Line-neutral voltage excitation produced by the matrix converter ensured the most efficient magnetisation of the three materials over peak flux density (1.0 T – 1.5 T) and fundamental frequency (50 Hz – 200 Hz) ranges.

Owing to highest resistivity and lower thickness, losses in M470-50A laminations were less affected by the pulsating waveform selected as magnetising signal. On the contrary, the impact of the applied voltage on the performance of M700-65A laminations was more prominent due to larger thickness and lowest resistivity. As a consequence of these two properties, strips of this material suffered from increased eddy-current losses.

The ratio  $\lambda$  [%] is defined for the three materials subjected to distorted magnetising conditions (matrix – PWM 0.8 – PWM 0.5) at various peak flux densities (1.0 – 1.25 – 1.5T) and magnetising frequencies (50 – 100 – 200 Hz). Losses under PWM  $m_i = 1.0$  are taken as a reference in the calculation (5.34). As an example, (5.34) illustrates the value of the index  $\lambda$  [%] associated to losses in laminations subjected to matrix converter excitation.

$$\lambda_{mx} [\%] = \frac{P_{mx} - P_{PWM\ 1.0}}{P_{PWM\ 1.0}} \cdot 100 \quad (5.34)$$

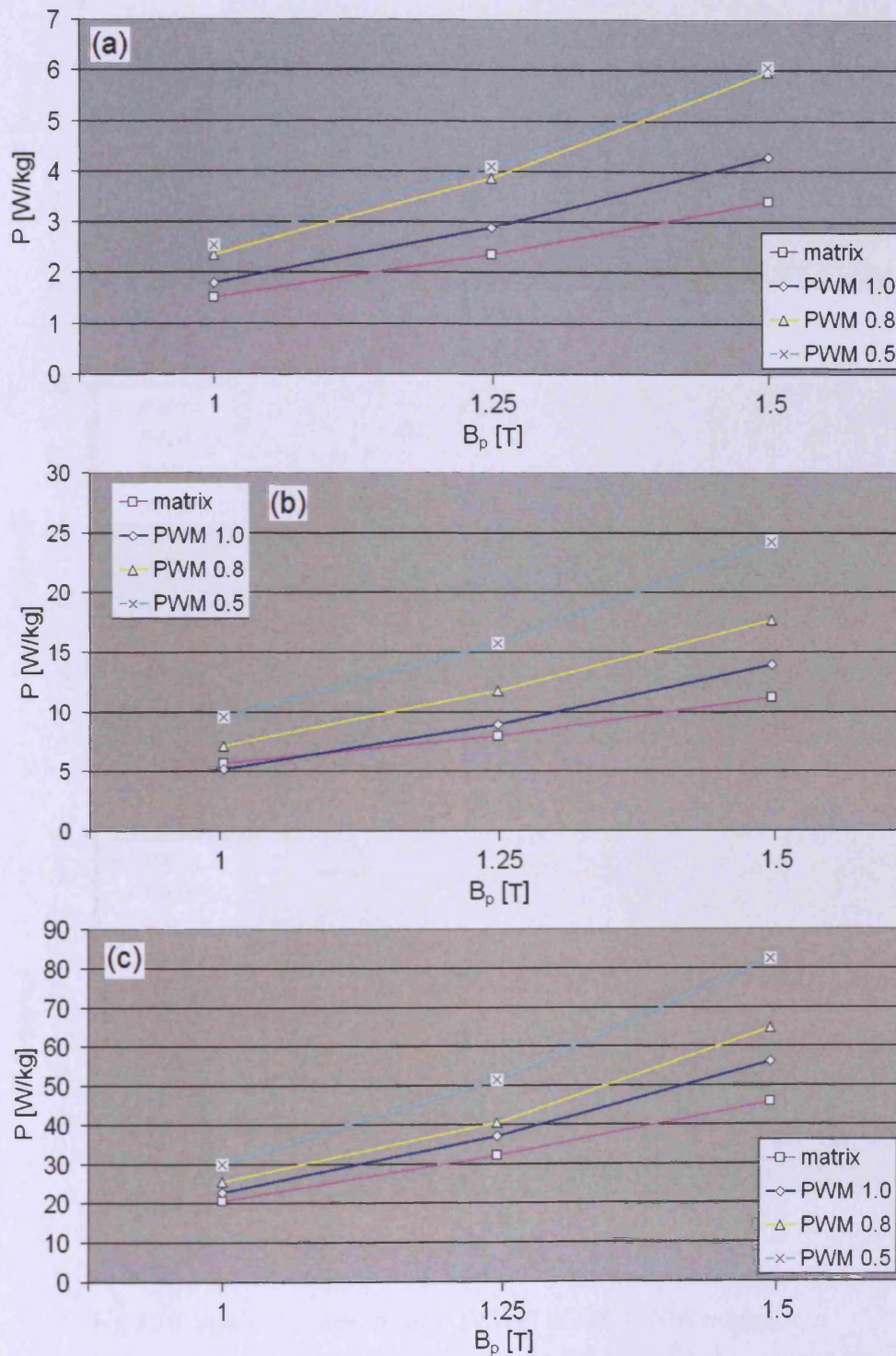


Fig 5.9. Specific power losses  $P$  [W/kg] in M470-50A subjected to matrix and two-level PWM excitation at (a) 50 Hz – (b) 100 Hz – (c) 200 Hz

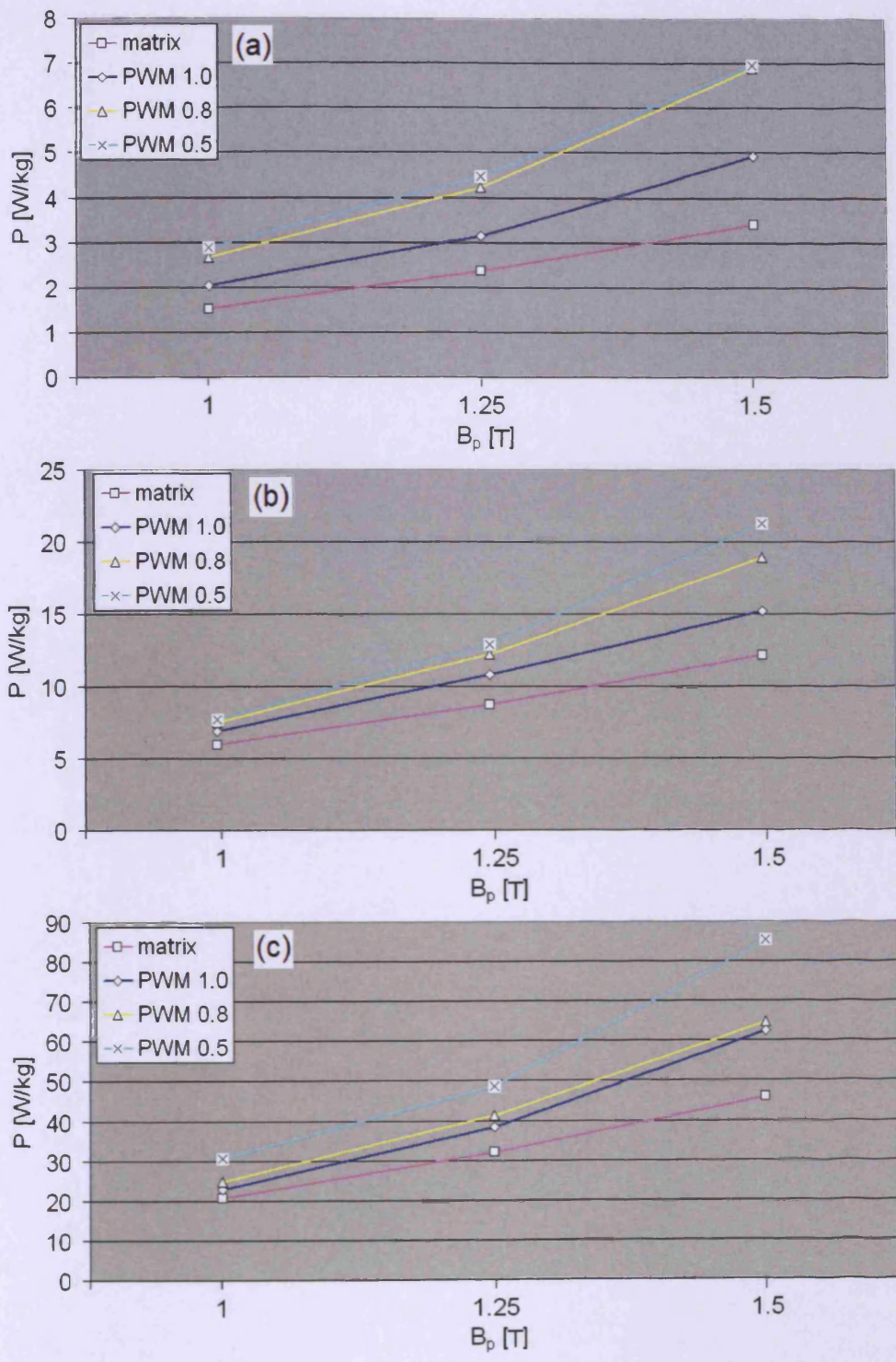


Fig 5.10. Specific power losses  $P$  [W/kg] in M530-50A subjected to matrix and two-level PWM excitation at (a) 50 Hz – (b) 100 Hz – (c) 200 Hz

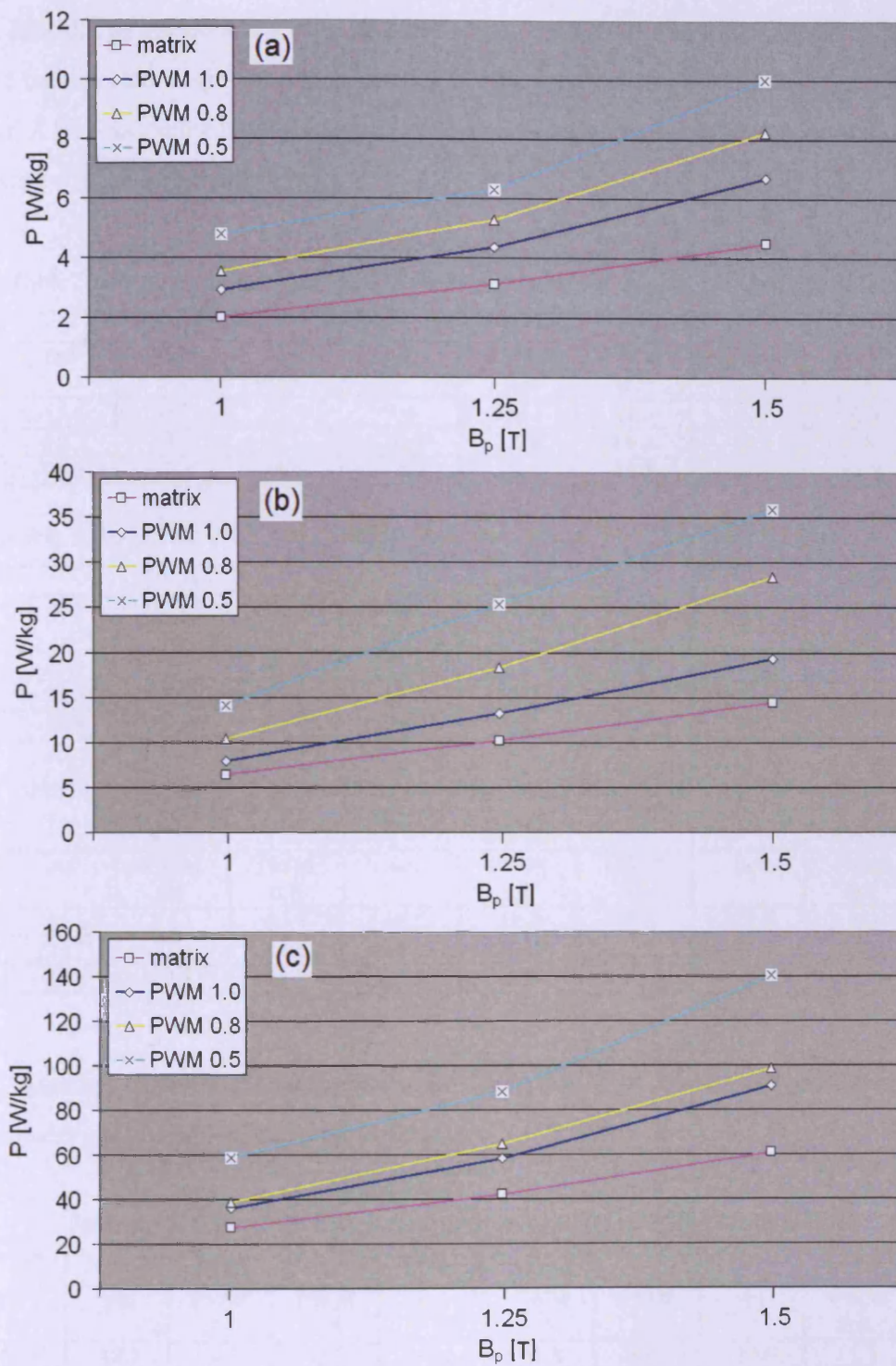


Fig 5.11. Specific power losses  $P$  [W/kg] in M700-65A subjected to matrix and two-level PWM excitation at (a) 50 Hz – (b) 100 Hz – (c) 200 Hz

Results of measured losses in M470-50A, M530-50A and M700-65A laminations subjected to distorted magnetising conditions are summarised in table 5.9 – 5.11. Calculated values of  $\lambda$  [%] associated to matrix converter and two-level PWM ( $m_i = 0.8$ ;  $m_i = 0.5$ ) magnetising signals are presented.

Table 5.9. Values of  $\lambda$  [%] in M470-50A laminations at 50 Hz, 100 Hz and 200 Hz

	50 Hz			100 Hz			200 Hz		
	mx	PWM 0.8	PWM 0.5	mx	PWM 0.8	PWM 0.5	mx	PWM 0.8	PWM 0.5
1.0T	-15.6	31.2	41.7	9.4	36.7	84.6	-9.6	10.9	30.6
1.25T	-18.3	33.7	41.9	-10.8	32.4	76.4	-13.7	8.8	38.5
1.5T	-20.3	39.3	41.6	-19.7	26.4	73.5	-18.3	14.8	46.6

Table 5.10. Values of  $\lambda$  [%] in M530-50A laminations at 50 Hz, 100 Hz and 200 Hz

	50 Hz			100 Hz			200 Hz		
	mx	PWM 0.8	PWM 0.5	mx	PWM 0.8	PWM 0.5	mx	PWM 0.8	PWM 0.5
1.0T	-25.1	31.4	41.9	-13.8	9.2	11.6	-9.6	9.3	34.2
1.25T	-24.8	34.1	41.6	-19.5	13.2	19.4	-16.6	7.4	26.5
1.5T	-30.8	39.7	41.4	-19.9	24.7	39.9	-26.6	3.4	36.5

Table 5.11. Values of  $\lambda$  [%] in M700-65A laminations at 50 Hz, 100 Hz and 200 Hz

	50 Hz			100 Hz			200 Hz		
	mx	PWM 0.8	PWM 0.5	mx	PWM 0.8	PWM 0.5	mx	PWM 0.8	PWM 0.5
1.0T	-31.6	21.1	64.9	-18.7	31.2	78.5	-24.3	7.2	62.0
1.25T	-28.7	21.4	44.5	-23.1	38.5	92.4	-27.4	10.9	50.9
1.5T	-33.0	22.8	49.3	-25.0	47.6	86.5	-32.8	8.9	54.5

Average values  $\bar{\lambda}$  [%] calculated over the peak flux density range (1.0 – 1.5 T) for the three materials are presented in table 5.12.

Table 5.12. Values of  $\bar{\lambda}$  [%] in laminations at 50 Hz, 100 Hz and 200 Hz

	50 Hz			100 Hz			200 Hz		
	mx	PWM 0.8	PWM 0.5	mx	PWM 0.8	PWM 0.5	mx	PWM 0.8	PWM 0.5
M470-50A	-18.1	34.7	41.8	-7.0	31.8	80.5	-13.9	11.5	34.6
M530-50A	-24.9	32.7	41.7	-16.6	11.2	15.5	-13.1	8.3	30.4
M700-65A	-30.1	21.3	54.7	-20.9	34.8	85.5	-25.9	9.1	56.5

Line-neutral voltage excitation produced by a three phase matrix converter under optimal conditions ( $q = \sqrt{3}/2$ ) was confirmed as a better magnetising waveform than line-line voltage, produced by a two-level indirect PWM converter at modulation index equal to

unity. This beneficial effect on losses was particularly emphasised at 50 Hz in the three silicon–iron alloys. Amongst the three grades of non-oriented steel under study, M700-65A was most efficiently magnetised by matrix converter excitation. Nevertheless, results in the three materials showed that line-line PWM excitation ( $m_i = 1.0$ ) improved as magnetising signal when fundamental frequency changed from 50 Hz to 100 Hz and 200 Hz.

### 5.3.2 Eddy-current losses

Eddy-current losses in the three materials were calculated according to equation (5.21). Results are presented in fig. 5.12, fig. 5.13 and fig. 5.14 for M470-50A, M530-50A and M700-65A laminations at peak flux densities 1.0 T, 1.25 T and 1.5 T. Magnetising frequencies were 50 Hz, 100 Hz and 200 Hz. Lower losses  $P$  [W/kg] in steel laminations subjected to matrix converter supply can be explained by a reduction in the eddy-current component  $P_{ec}$  [W/kg]. Line-neutral voltage excitation from the matrix converter was confirmed as a more favourable signal than line-line voltage from two-level PWM converter at a modulation index of unity, especially at the highest frequency (200 Hz) in M700-65A laminations (table 5.5). High values of total specific losses in the laminations subjected to low modulated PWM magnetising signal resulted from the negative impact that the pulsating voltage applied to energise the steel had on the eddy-current component of loss.

The ratio  $\lambda_{ec}$  [%] is calculated for M470-50A, M530-50A and M700-65A laminations subjected to distorted magnetising signals (matrix – PWM 0.8 – PWM 0.5) as in (5.35). The term of eddy-current losses under PWM ( $m_i = 1.0$ ) signal is used as a reference in the calculations. Results are given in table 5.13 – 5.15.

$$\lambda_{ec, mx} [\%] = \frac{P_{ec, mx} - P_{ec, PWM\ 1.0}}{P_{ec, PWM\ 1.0}} \cdot 100 \quad (5.35)$$

Table 5.13. Values of  $\lambda_{ec}$  [%] in M470-50A laminations at 50 Hz, 100 Hz and 200 Hz

	50 Hz			100 Hz			200 Hz		
	mx	PWM 0.8	PWM 0.5	mx	PWM 0.8	PWM 0.5	mx	PWM 0.8	PWM 0.5
1.0T	-15.1	30.1	116.4	-9.7	27.2	125.2	-7.1	29.1	110.2
1.25T	-15.5	30.2	119.0	-12.0	27.4	129.2	-10.3	30.5	116.7
1.5T	-15.5	28.0	111.2	-12.1	26.2	125.3	-12.2	31.3	116.9

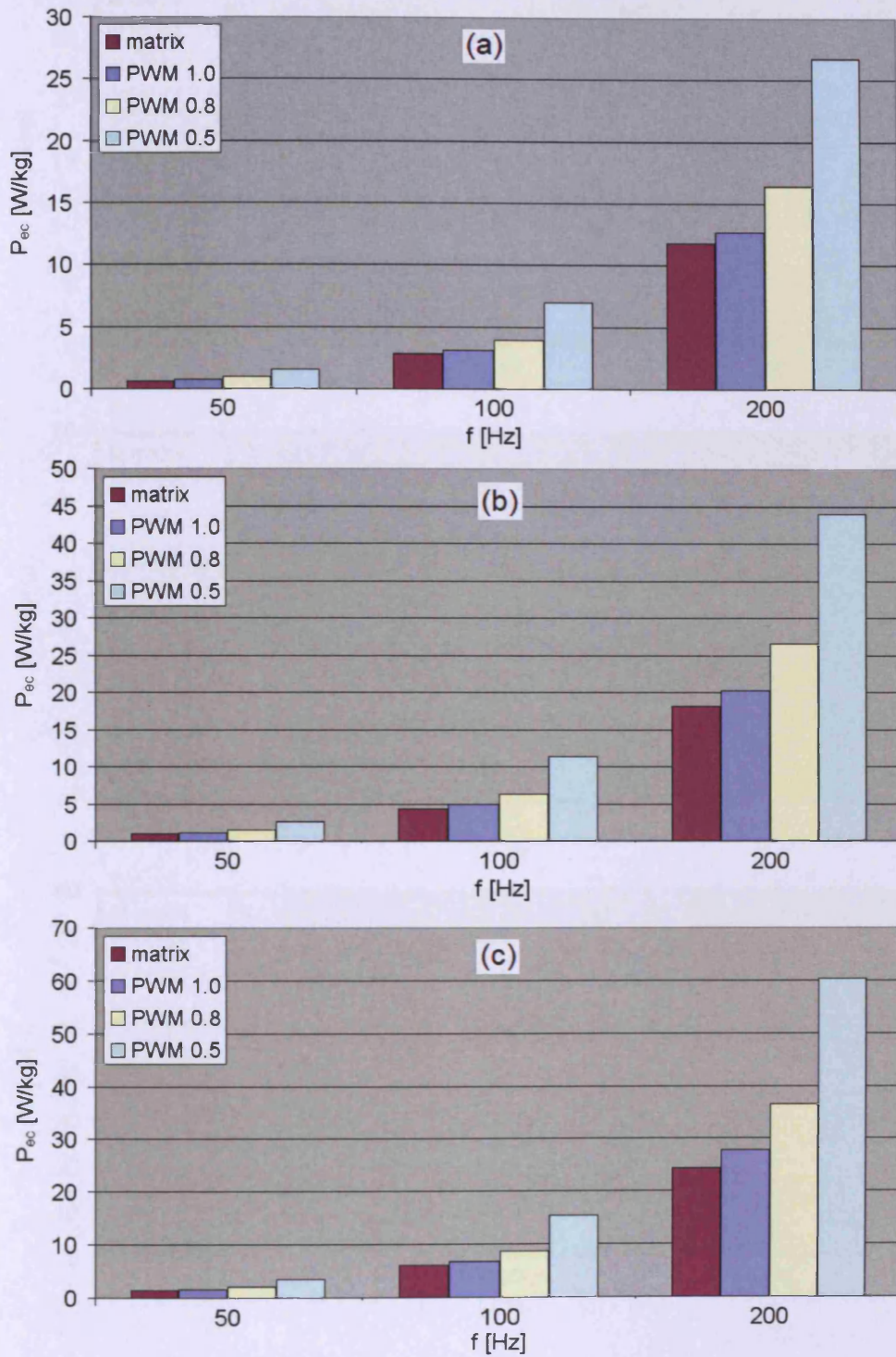


Fig 5.12. Specific eddy-current losses  $P_{ec}$  [W/kg] in M470-50A laminations at 50, 100 and 200 Hz and (a)  $B_p = 1.0$  T – (b)  $B_p = 1.25$  T – (c)  $B_p = 1.5$  T

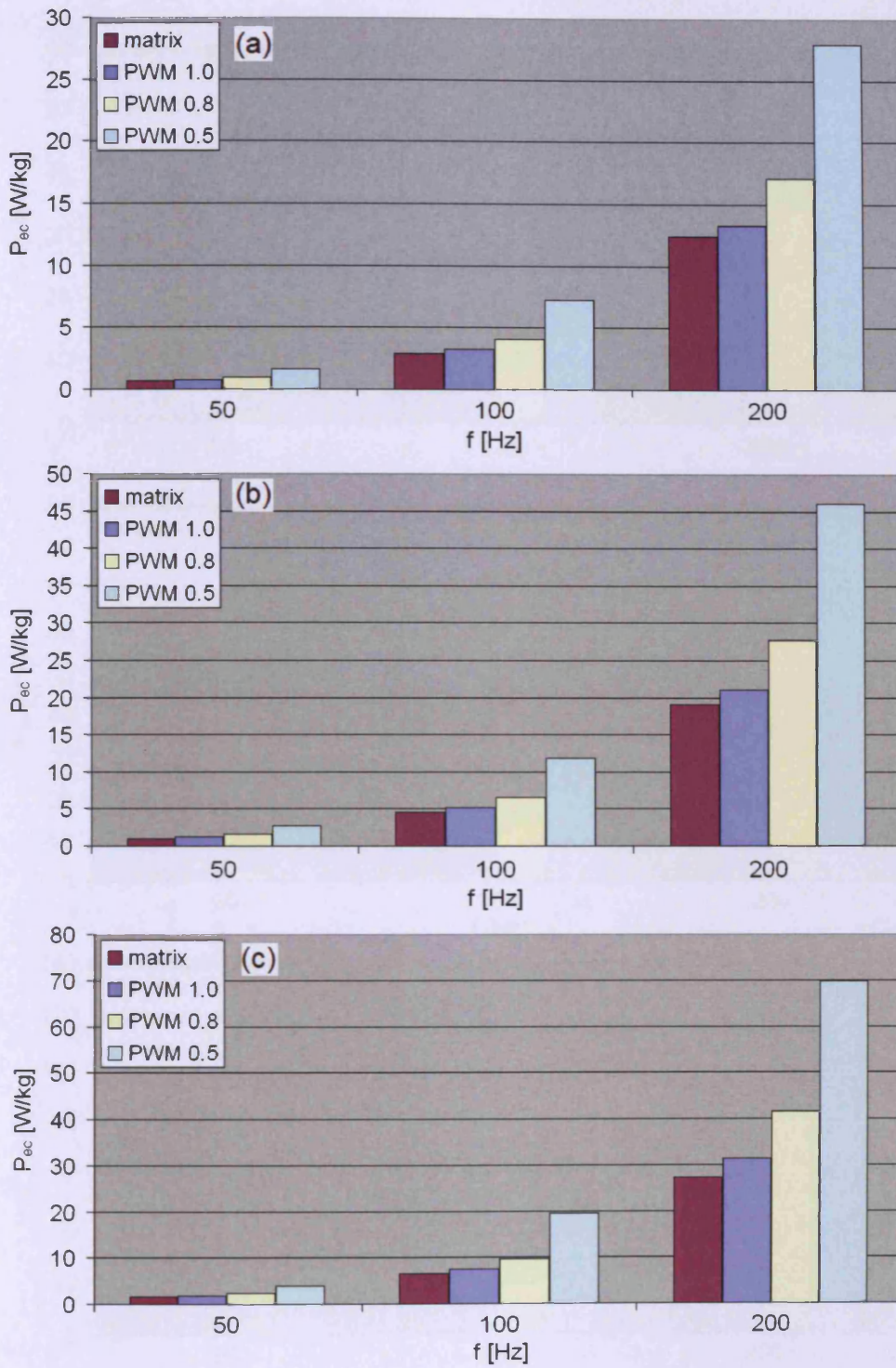


Fig 5.13. Specific eddy-current losses  $P_{ec}$  [W/kg] in M530-50A laminations at 50, 100 and 200 Hz and (a)  $B_p = 1.0$  T – (b)  $B_p = 1.25$  T – (c)  $B_p = 1.5$  T

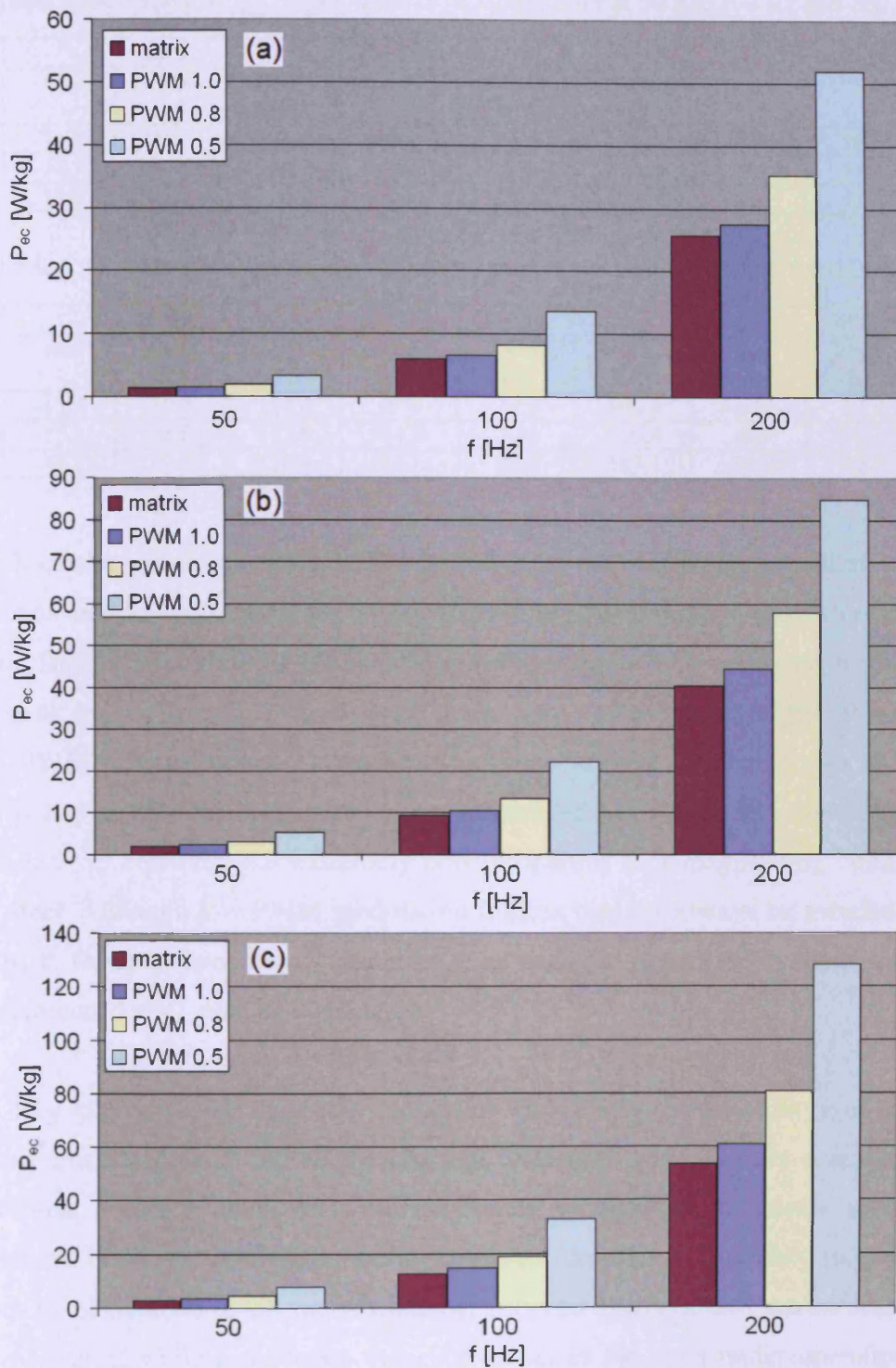


Fig 5.14. Specific eddy-current losses  $P_{ec}$  [W/kg] in M700-65A laminations at 50, 100 and 200 Hz and (a)  $B_p = 1.0$  T – (b)  $B_p = 1.25$  T – (c)  $B_p = 1.5$  T

Table 5.14. Values of  $\lambda_{ec}$  [%] in M530-50A laminations at 50 Hz, 100 Hz and 200 Hz

	50 Hz			100 Hz			200 Hz		
	mx	PWM 0.8	PWM 0.5	mx	PWM 0.8	PWM 0.5	mx	PWM 0.8	PWM 0.5
1.0T	-14.5	30.3	117.1	-9.9	24.8	125.1	-6.8	28.6	109.8
1.25T	-15.7	30.6	119.0	-11.7	27.6	129.6	-9.5	31.3	118.0
1.5T	-16.9	29.8	120.2	-13.4	28.2	158.3	-13.1	32.6	122.7

Table 5.15. Values of  $\lambda_{ec}$  [%] in M700-65A laminations at 50 Hz, 100 Hz and 200 Hz

	50 Hz			100 Hz			200 Hz		
	mx	PWM 0.8	PWM 0.5	mx	PWM 0.8	PWM 0.5	mx	PWM 0.8	PWM 0.5
1.0T	-15.0	30.1	117.6	-9.6	24.9	106.4	-6.5	27.9	88.0
1.25T	-15.9	31.0	122.0	-11.6	27.4	110.4	-8.9	30.1	90.8
1.5T	-16.8	30.3	120.8	-13.6	27.9	123.1	-12.3	32.7	110.2

It can be seen from tables 5.13 – 5.15 that, as the magnetising frequency increased, the reduction in eddy-current losses achieved by line-neutral matrix converter excitation is mitigated. This fact reinforces line-line PWM voltage ( $m_i = 1.0$ ) produced by the DC-link inverter as an improved magnetising signal when values of frequency higher than 50 Hz are selected. PWM modulation index is confirmed as an influential factor on losses in M470-50A, M530-50A and M700-65A laminations. Low modulated ( $m_i = 0.5$ ) line-line voltage from a two-level indirect converter has extremely poor properties as a magnetising voltage of non-oriented steel. Although low PWM modulation indices can not always be avoided in control algorithms in variable speed drives (chapter 6), its negative impact on dynamic eddy-current losses in laminated steel must be considered.

Key physical and magnetic properties (resistivity, permeability) of silicon-iron alloys have a critical impact on the composition of losses. It is generally accepted that high silicon content, which reduces eddy-current losses, is desirable to ensure more efficient magnetisation. However, brittleness and a significant drop in permeability impose practical limitations to the addition of silicon. A trade-off between magnetic and mechanical properties has to be reached, while a moderate value of losses in the steel under operation must be guaranteed. In order to elaborate a full analysis on the suitability of a specific grade of non-oriented steel for laminated cores in induction motors, the influence of magnetising voltages produced by various frequency converters on the composition of losses should also be taken into account.

The proportion of eddy-current losses [%] in M470-50A, M530-50A and M700-65A laminations subjected to distorted magnetising conditions is illustrated in fig. 5.15. Selected fundamental frequencies are 50 Hz, 100 Hz and 200 Hz. Results shown on the graph are an average of the three values obtained at peak flux densities 1.0 T, 1.25 T and 1.5 T, respectively. In the alloy with the highest resistivity (M470-50A), the flow of eddy-currents is attenuated so that resistive losses in the material are lower. On the contrary, static hysteresis and anomalous loss components become proportionally larger. The composition of losses in the intermediate alloy (M530-50A) revealed a similar pattern to the one observed in M470-50A laminations. Nonetheless, as resistivity is reduced, the proportion of the eddy-current component of loss is increasingly affected by the magnetising voltage. It is worth emphasising that in this grade, the proportion of eddy-current losses under matrix converter excitation is larger (5 - 7 %) than under PWM ( $m_i = 1.0$ ) excitation in the 50 – 200 Hz frequency range. The analysis of the composition of losses in M700-65A laminations confirmed that matrix and PWM ( $m_i = 1.0$ ;  $m_i = 0.8$ ) voltage excitation lead to significant proportions of eddy-current losses when compared to values reported in the two previous alloys. In M700-65A laminations, the proportion of eddy-current losses calculated under matrix converter excitation was significantly larger than under PWM ( $m_i = 1.0$ ) excitation in the 50 – 200 Hz frequency range.

Accuracy in the calculation of eddy-current, static hysteresis and anomalous losses in soft magnetic materials remains a very challenging task. Furthermore, high flux harmonics, which are inherited from pulsating magnetising signals typical of AC-AC converters, add a new dimension of complexity to the problem. The analytical equations, which define the composition of iron losses, should then take into account harmonic distortion in flux frequency spectra, along with flux penetration across laminated steel.

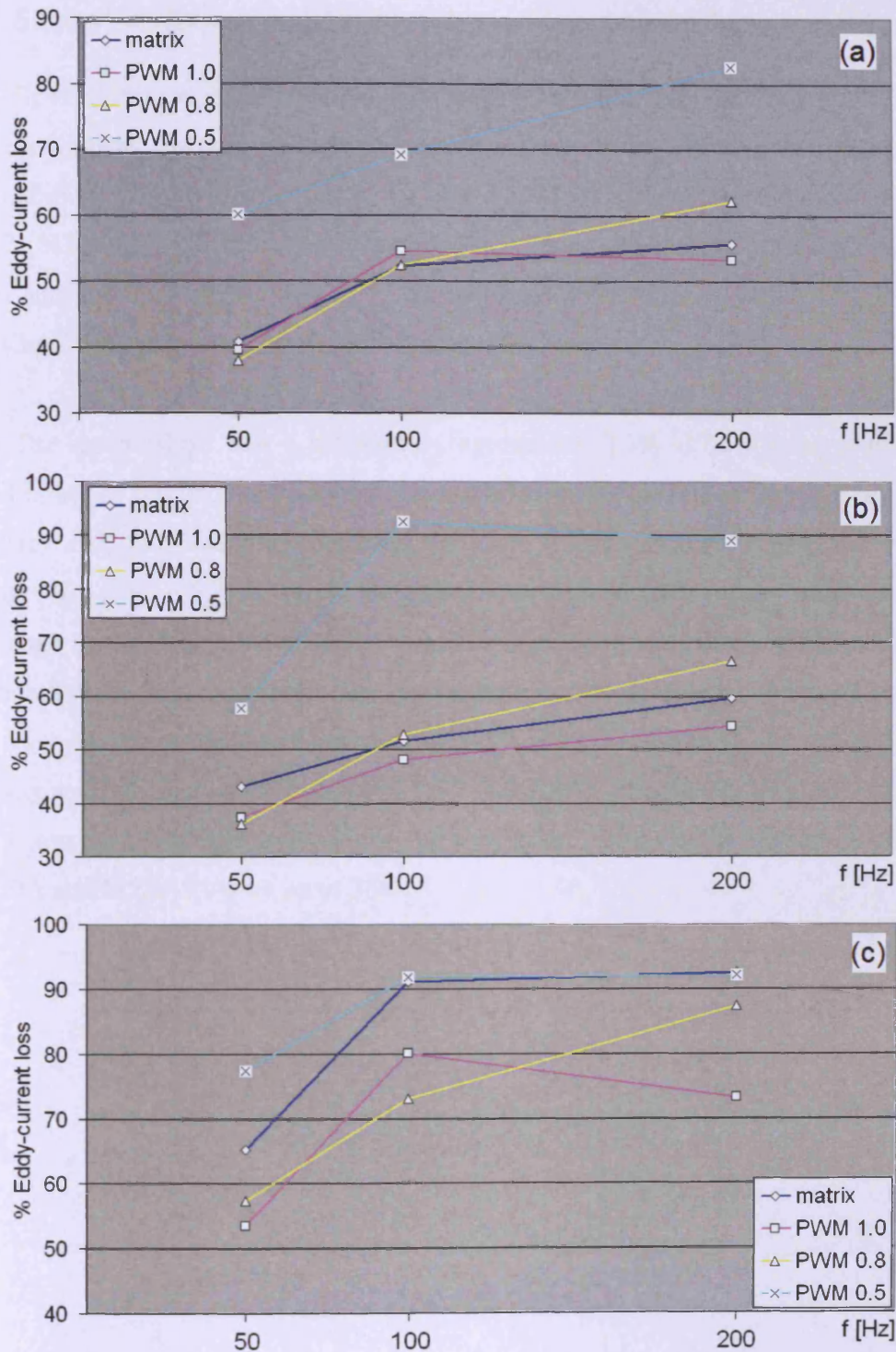


Fig 5.15. Eddy-current component [%] at  $B_p = 1.5$  T and 50, 100 and 200 Hz in  
 (a) M470-50A – (b) M530-50A – (c) M700-65A laminations

### 5.3.3 Experimental benchmarking of iron loss model

Results of measured and calculated losses by the methods described in §5.2.2a (non-linear + eddy-current shielding – denoted as NL+SE) and in §5.2.2b (Bertotti) are introduced in figs. 5.16-5.19 (M470-50A laminations), figs. 5.20-5.23 (M530-50A laminations) and figs. 5.24-5.27 (M700-65A laminations). Magnetising voltage waveforms were typical of matrix converter and two-level back-to-back PWM inverter at modulation indices unity, 0.8 and 0.5. Magnetising frequencies were 50 Hz, 100 Hz and 200 Hz.

The results show that a satisfactory agreement (15% -17.5%) was found between estimated losses by the two methods and measured losses for two magnetising frequencies (50 and 100Hz) and two peak flux densities (1T and 1.25T) in M470-50A and M530-50A laminations (fig 5.17 – 5.24). While Bertotti's approach yielded results of power losses in similar range to the new method at the lowest magnetising frequency (50Hz), the NL+SE approach improved loss estimation by approximately 5% at 100Hz under all magnetising voltage wave-shapes in the lower alloys (M470-50A and M530-50A). As fundamental peak flux density and frequency increased up to 1.5T and 200Hz, the results obtained indicated that Bertotti's approach under-estimated iron losses in the alloys with higher silicon content (M470-50A and M530-50A) by up to 35%.

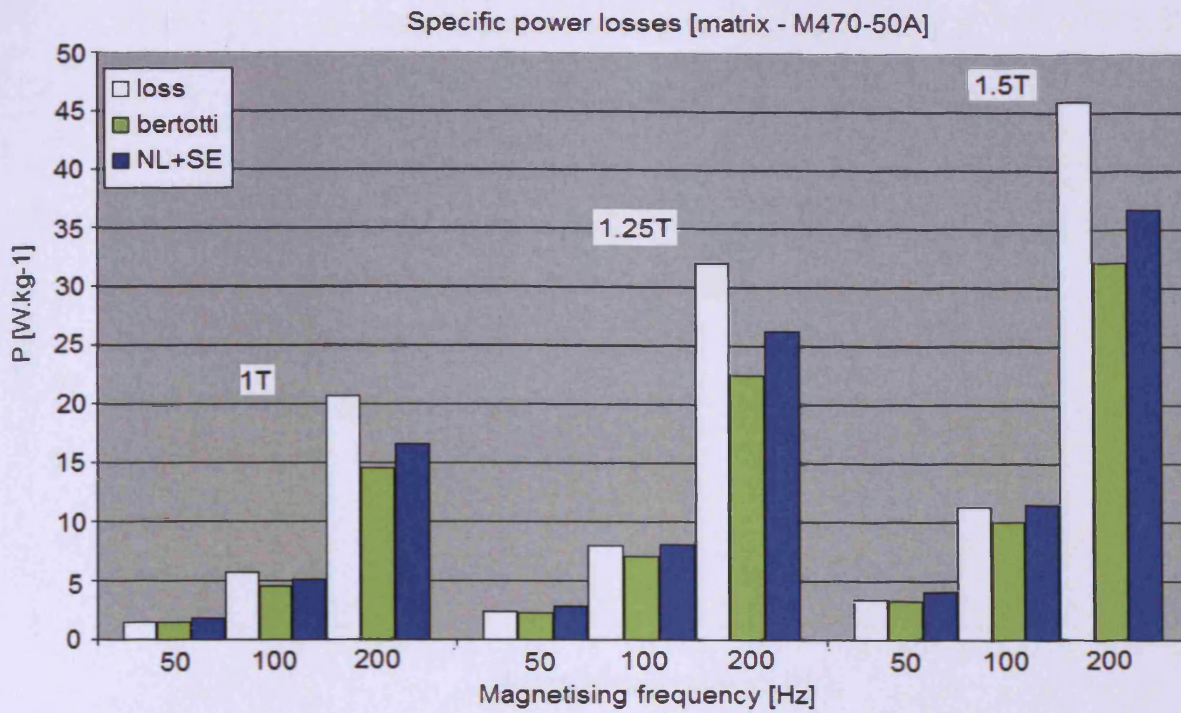


Fig 5.16 Measured and estimated losses according to Bertotti's approach and the new method in M470-50A laminations under matrix converter magnetizing conditions

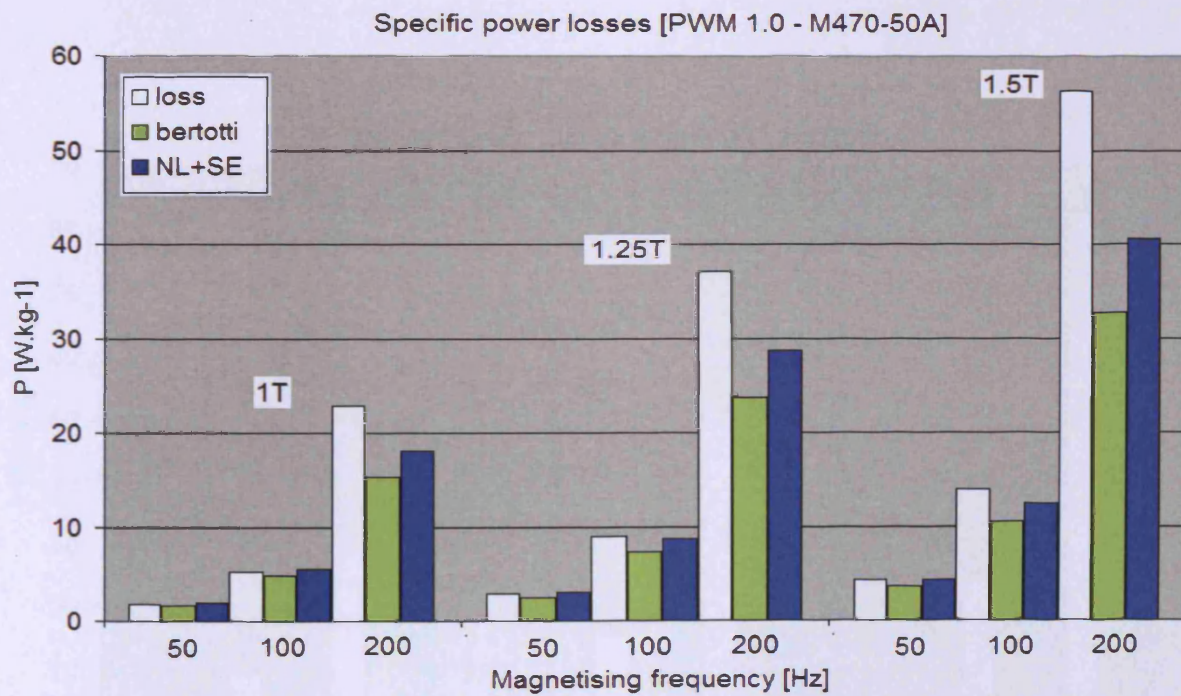


Fig 5.17 Measured and estimated losses according to Bertotti's approach and the new method in M470-50A laminations under PWM (1.0) magnetizing conditions

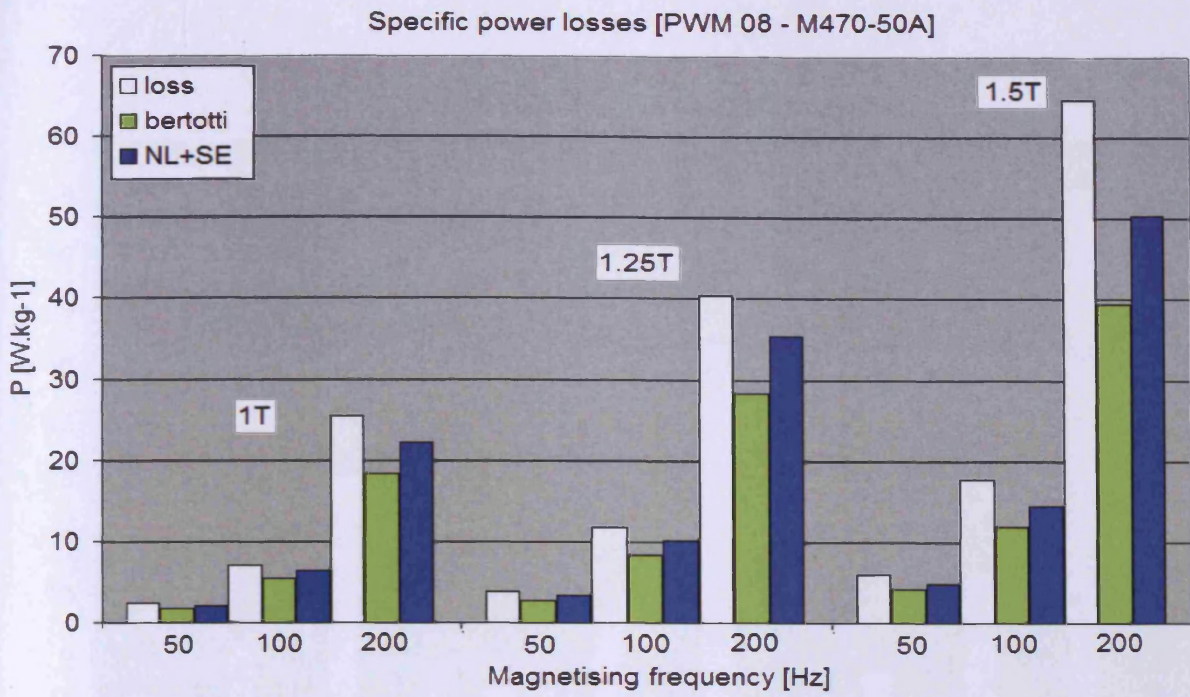


Fig 5.18. Measured and estimated losses according to Bertotti's approach and the new method In M470-50A laminations under PWM (0.8) magnetizing conditions

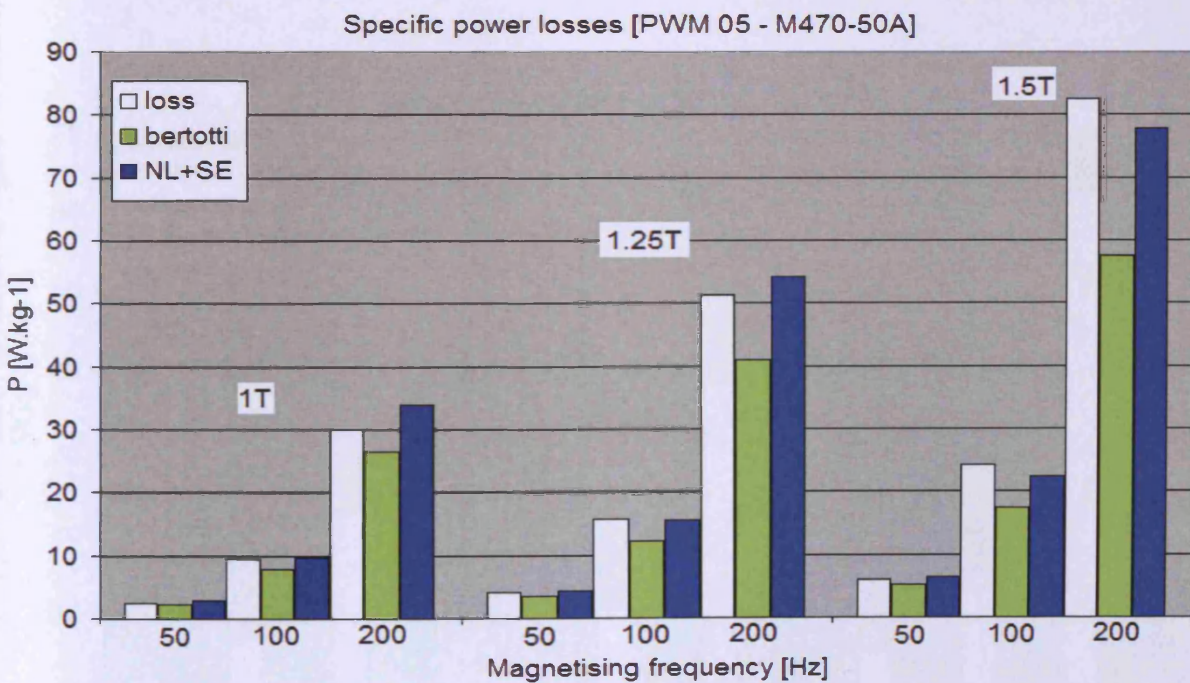


Fig 5.19. Measured and estimated losses according to Bertotti's approach and the new method In M470-50A laminations under PWM (0.5) magnetizing conditions

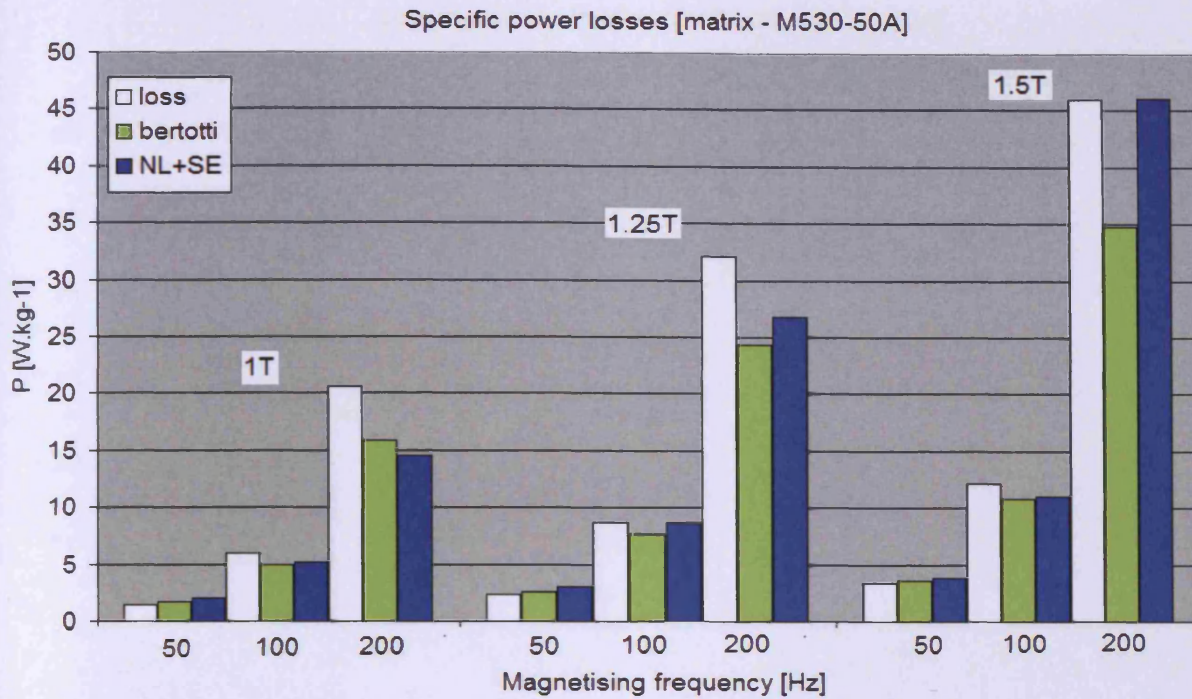


Fig 5.20 Measured and estimated losses according to Bertotti's approach and the new method in M530-50A laminations under matrix converter magnetizing conditions

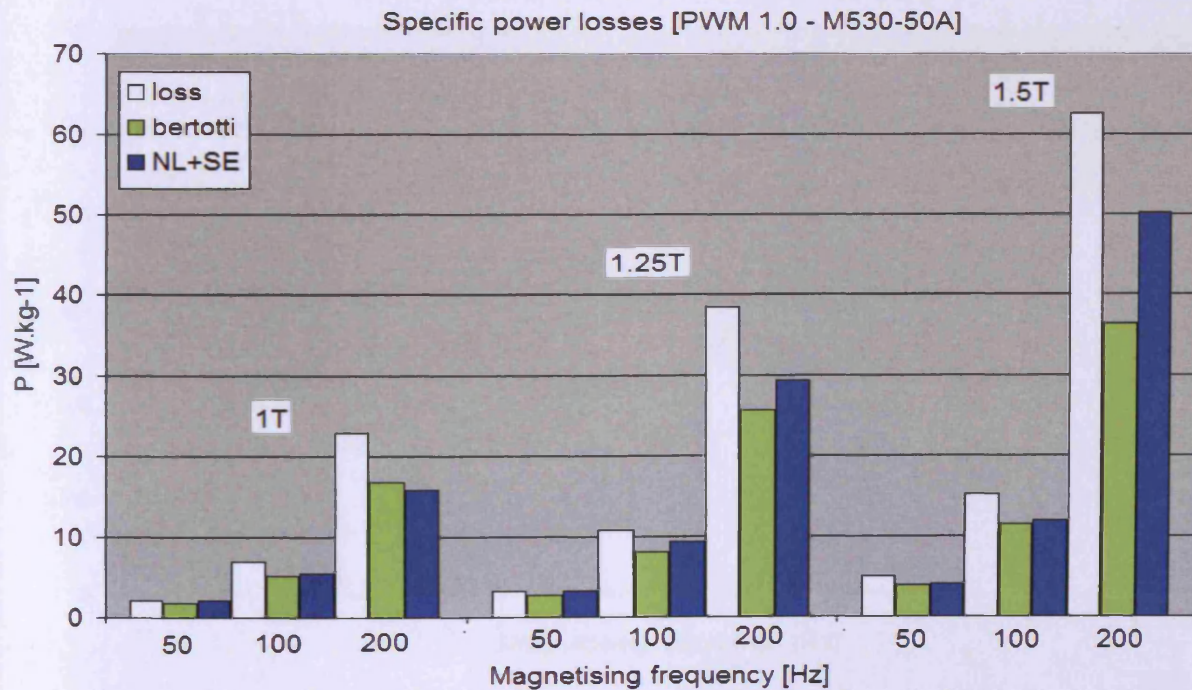


Fig 5.21. Measured and estimated losses according to Bertotti's approach and the new method in M530-50A laminations under PWM (1.0) magnetizing conditions

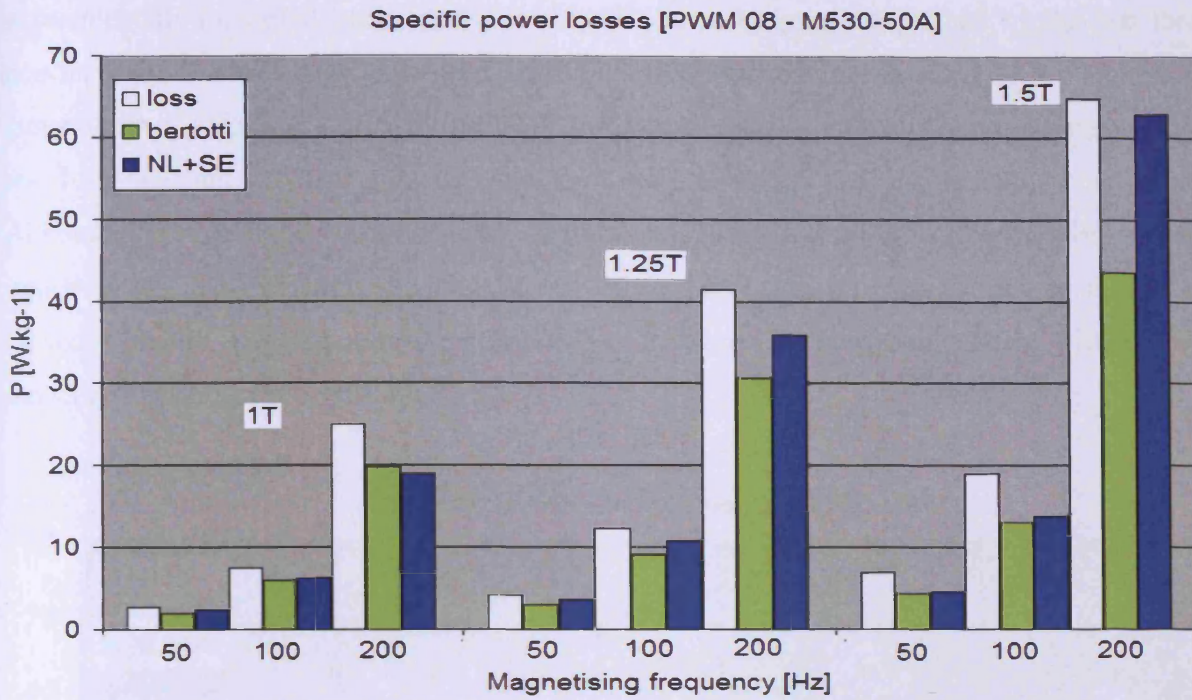


Fig 5.22. Measured and estimated losses according to Bertotti's approach and the new method in M530-50A laminations under PWM (0.8) magnetizing conditions

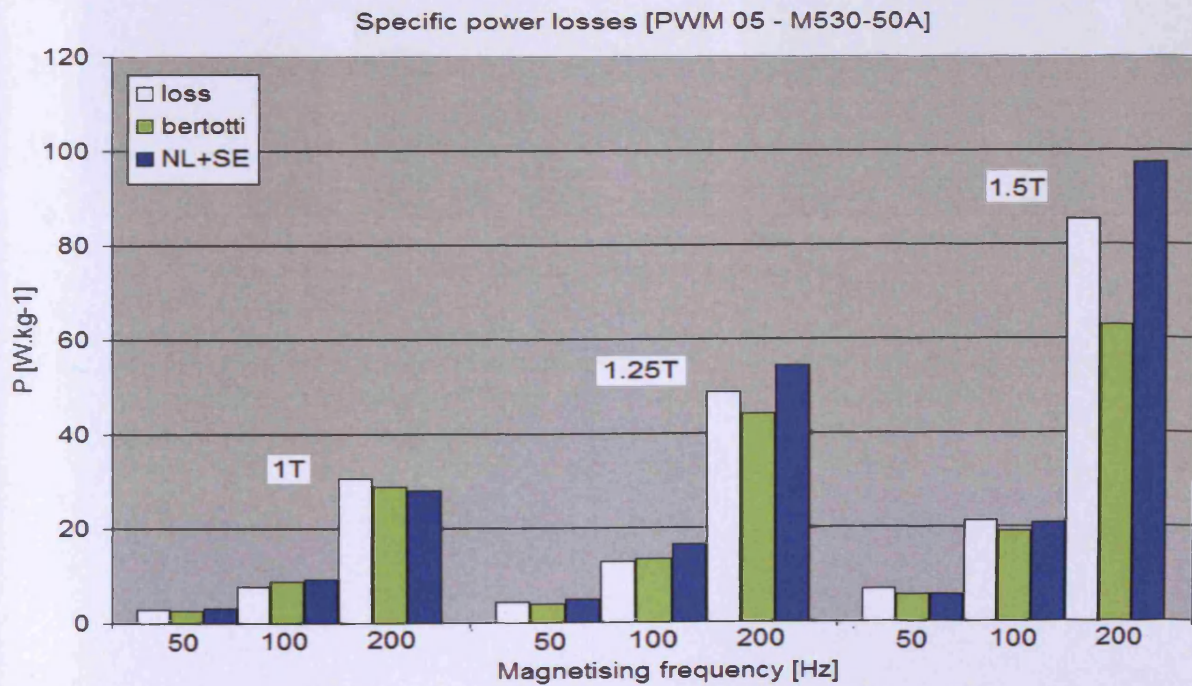


Fig 5.23. Measured and estimated losses according to Bertotti's approach and the new method in M530-50A laminations under PWM (0.5) magnetizing conditions

The discrepancy between calculated losses based upon Bertotti's formula and experimentally measured losses in the lower alloys can be partly explained by the fact that non-linearity between magnetic field and induction is most pronounced at 1.5T in thin laminations of electrical steel with high silicon content. The anomalous loss component may not fully account for this phenomenon in these materials and magnetising conditions. Although the same trend was noticed in identical magnetising conditions, the NL+SE method improved loss quantification significantly (by 10%). More accurate loss estimation may then be accomplished by accounting for non-linearity in the eddy-current calculation with a peak induction-dependent coefficient  $k_e^*$ .

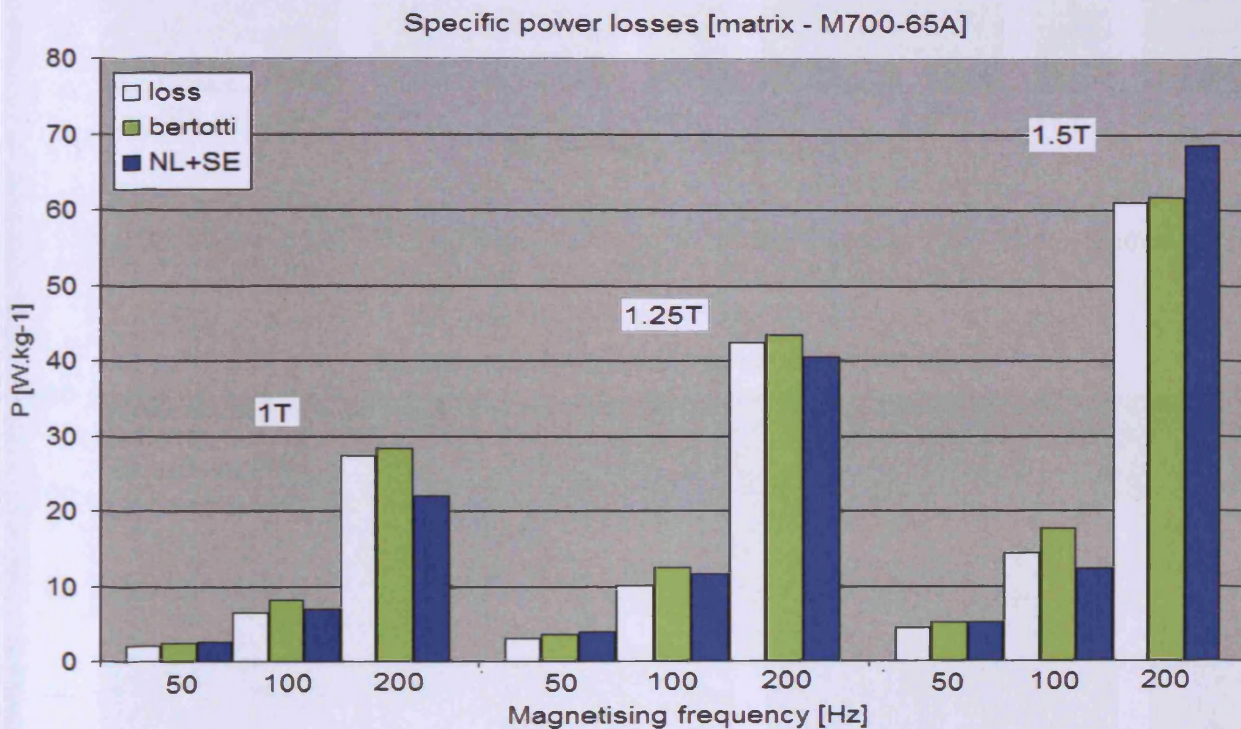


Fig 5.24. Measured and estimated losses according to Bertotti's approach and the new method in M700-65A laminations under matrix converter magnetizing conditions

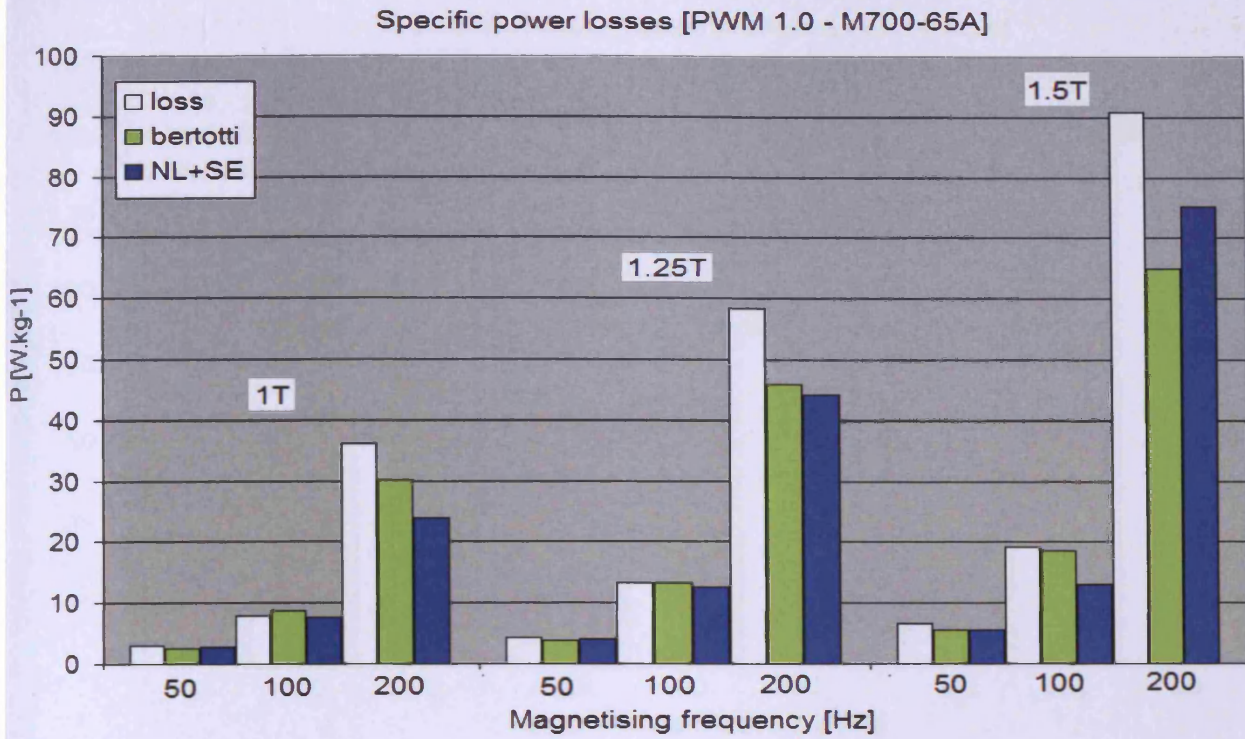


Fig 5.25. Measured and estimated losses according to Bertotti's approach and the new method in M700-65A laminations under PWM (1.0) magnetizing conditions

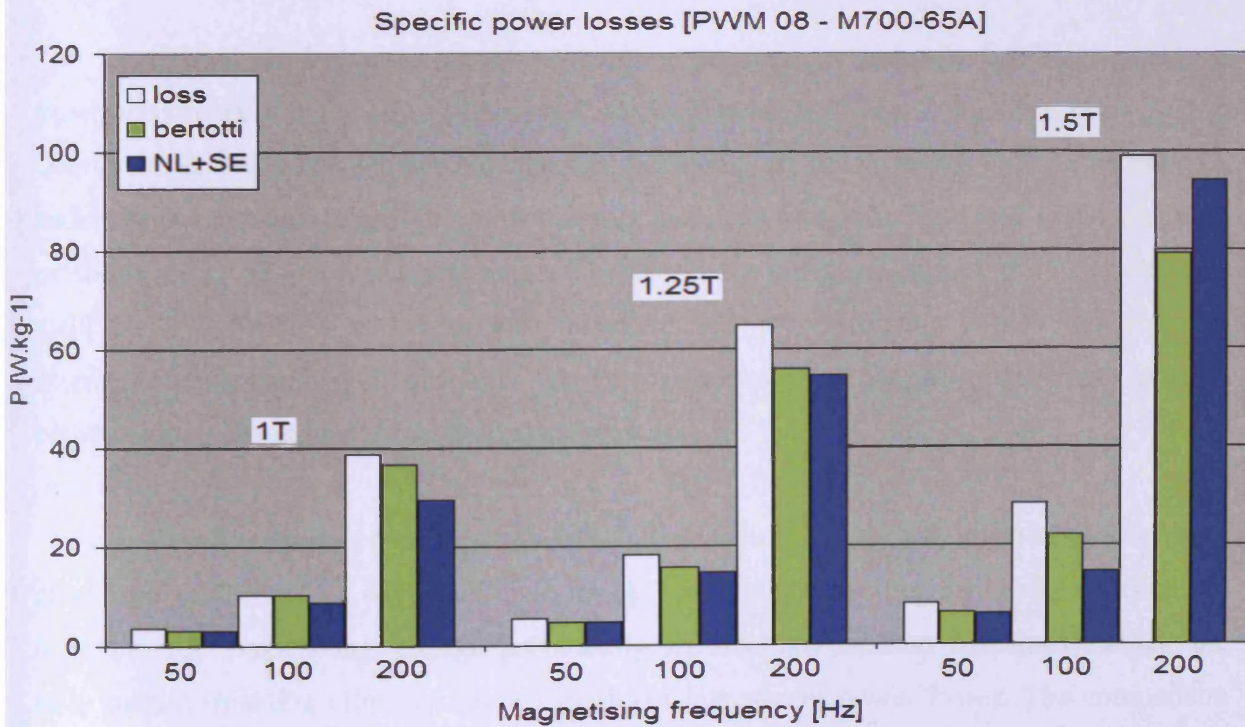


Fig 5.26. Measured and estimated losses according to Bertotti's approach and the new method in M700-65A laminations under PWM (0.8) magnetizing conditions

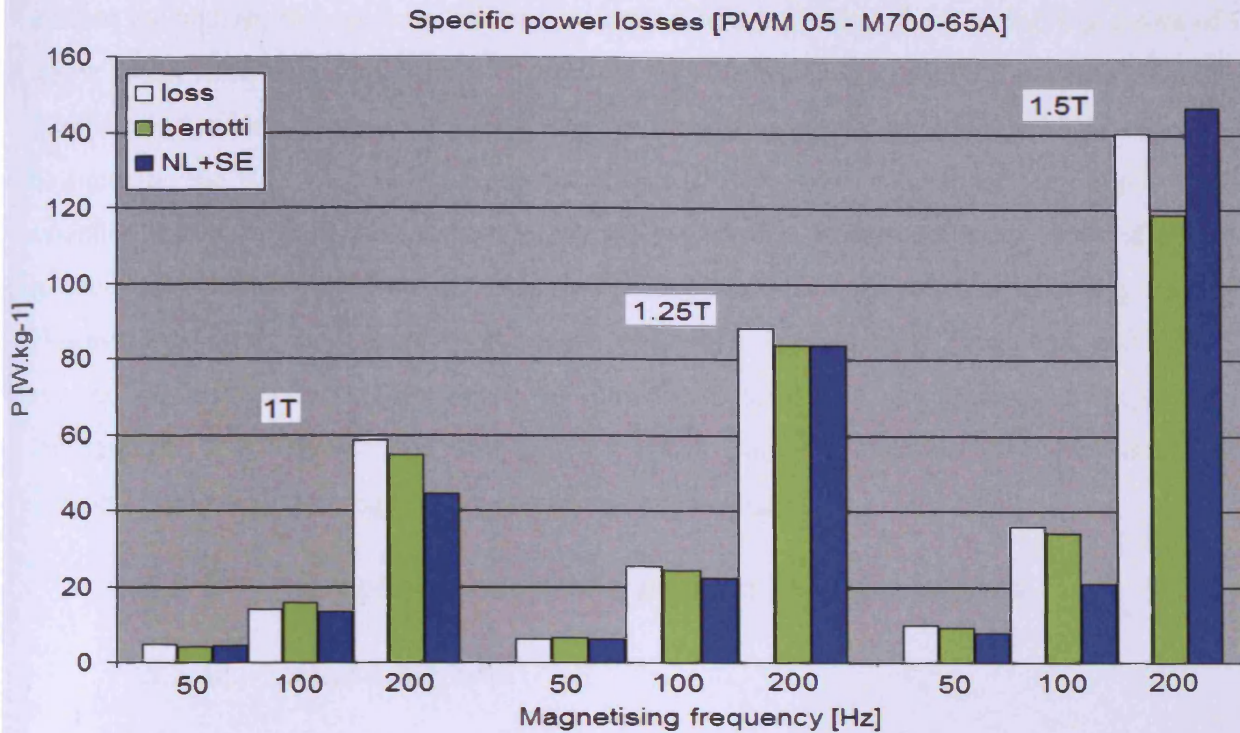


Fig 5.27 Measured and estimated losses according to Bertotti's approach and the new method in M700-65A laminations under PWM (0.5) magnetizing conditions

Overall, the best agreement between the two methods and experimentally measured losses was observed in the alloy with lowest silicon content and largest thickness (M700-65A). Owing to relatively low silicon content, the behaviour of the material used in M700-65A under magnetisation is consistent with linearity between magnetic field and induction in an extended induction and frequency range. Therefore, the approach proposed by Bertotti may yield better agreement as far as loss quantification is concerned. In this material, the anomalous loss component accounts for the inadequacy of the assumption of linearity between induction and magnetic field satisfactorily.

Results introduced in fig 5.24 – 5.27 reveal that the NL+SE method ensures very good loss prediction in M700-65A. In thick laminations of this material (subjected to harmonic-rich magnetising voltage particularly in the high-medium frequency range), the eddy-current shielding effect causes a significant increase in power losses. The comparison with measured losses proves that the NL+SE accounts for the eddy-current shielding effect in an adequate manner. In the two methods for loss estimation introduced in this section, analytical calculation of loss coefficients plays a non-negligible role in the accuracy for loss prediction. Due to the limited amount of data normally used to quantify loss coefficients in

Bertotti's equation, the accuracy in loss prediction is more affected by measuring errors of losses under sinusoidal conditions. However, the method proposed by Bertotti demands limited effort in comparison with the NL+SE method proposed in this PhD thesis. In order to be accurate, the NL+SE method requires measured losses under sinusoidal conditions in an extended induction and frequency range. By the same token, some additional time and effort is needed to define the parameter  $k(f_n)$  which accounts for eddy-current shielding effect. However, physical phenomena (non-linearity between applied field /induction and eddy-current shielding effect) that occur in laminated steel are accounted for explicitly. Furthermore, it is believed that iron losses a broad range of electrical steels subjected to different non-sinusoidal magnetising conditions can be analysed

### 5.3.4 Sideband harmonic pattern in high clusters

#### 5.3.4a - Matrix Converter

The line-neutral voltage produced by a three phase matrix converter (§ 4.2.1) under Space-Vector-Modulation [SVM] has specific characteristics that make its waveshape completely different to that of line-line voltage produced by a DC-link Pulse-Width-Modulated [PWM] converter. Fig. 5.28 illustrates line-neutral voltages produced by a matrix converter prototype.

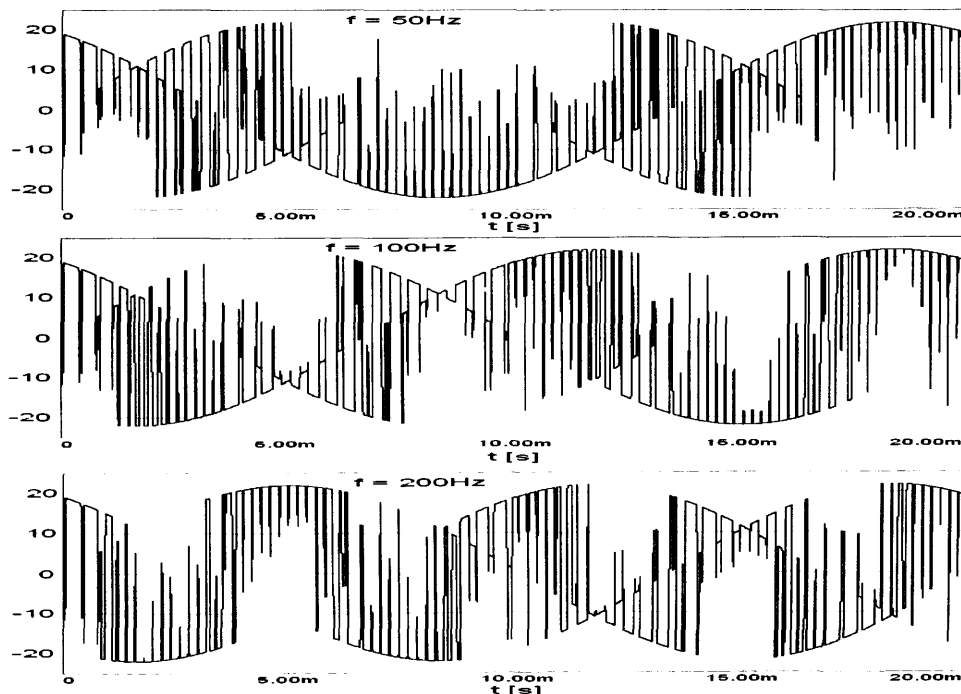


Fig 5.28. Line-neutral voltage from matrix converter at 50 Hz, 100 Hz and 200 Hz

The line-neutral voltage from a matrix converter is a superposition of three pulsating signals of relative phase angle  $120^\circ$  and cosinusoidally-modulated amplitude. Line-line voltage produced by a two-level DC-link converter is a pulsating signal, the amplitude of which is modulated by an alternating square waveform. As a consequence of the different amplitude-modulation, sideband harmonics in clusters located at multiple frequencies of SVM sampling (matrix converter) or PWM switching frequency (two-level DC-link converter) are spread following a specific pattern.

In line-neutral voltage typical of matrix converter, the spread of these harmonic components is enhanced and eventually contributes towards a smoother flux density curve. The harmonic spectrum of induced voltages is therefore relevant to the analysis of iron losses in laminated steel, as it is related to flux density. Fig. 5.29 show the harmonic spectrum of experimental induced voltages at peak flux density 1.5 T and respective frequencies 50 Hz, 100 Hz and 200 Hz in M700-65A laminations subjected to matrix converter supply (line-neutral) produced by a real prototype (§ 4.2.1). *THD* [%] of each voltage is also provided.

It can be seen that spreading of sideband harmonics maintains a moderate height of clusters, which are located at multiples of SVM sampling frequency (2.5 kHz). At 50 Hz magnetising frequency, low order harmonics are not significant. Nonetheless, as magnetising frequency increases to 100 Hz and 200 Hz, low order harmonics at multiple frequencies of 50 Hz (mainly 150 Hz) become comparable to the height of high clusters. The reason for this phenomenon is that, owing to the absence of decoupling in three-phase direct AC-AC conversion topology, output line-neutral voltages in matrix converters inherit harmonic components at multiple frequencies of input frequency (equal to grid frequency 50 Hz).

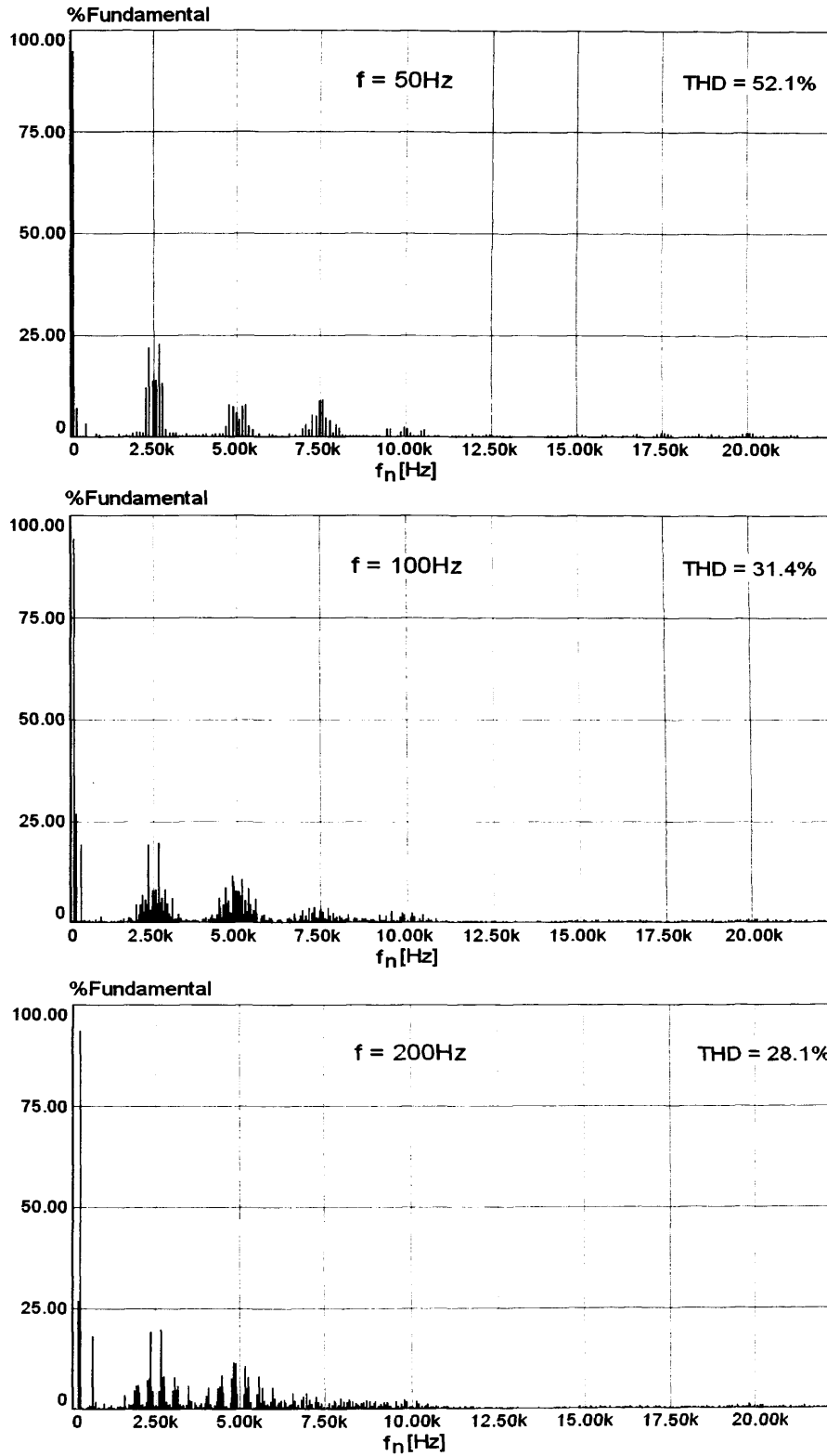


Fig 5.29. Harmonic spectra of induced voltages and associated  $THD$  [%] under line-neutral matrix converter excitation (50 Hz, 100 Hz, 200 Hz)

Low order harmonics in voltages produced by the AC-AC converter are inherited by the flux density. When those harmonics are inferior to the fundamental frequency, they are defined as subharmonics. They lead to magnetising cycles with different maximum induction. Although losses in the steel can be reduced when the material is magnetised to a higher level during one cycle and then magnetised to a lower level in the next cycle, induction with a high content of subharmonics is not desirable in induction motors. Since the air gap flux is different at every cycle, the torque developed by the rotating machine under operation will not be constant. Performance and mechanical stability of the system could be compromised. Harmonic spectra of magnetic induction are shown in fig. 5.30 for identical conditions and the same material. *THD* [%] of associated flux density curves is also given at 50 Hz, 100 Hz and 200 Hz magnetising frequency.

It can be seen from the spectra that high clusters are spread and their negative effect on losses in laminated steel mitigated. However, due to significant low order harmonics, harmonic distortion in flux density curves at 100 Hz and 200 Hz under line-neutral matrix converter supply increases noticeably. In order to assess whether an alternating waveform suffers from distortion in the low or high frequency range, frequency-weighted Total Harmonic Distortion *fwTHD* [%] (2.34) can be used. For M470-50A, M530-50A and M700-65A laminations subjected to line-neutral matrix converter magnetising conditions, values of *fwTHD* [%] of the induction are introduced in table 5.11 at 50 Hz, 100 Hz and 200 Hz magnetising frequency and 1.5T peak flux density.

Table 5.16. *fwTHD* [%] values of flux density in laminations at 1.5 T peak flux density

	50 Hz	100 Hz	200 Hz
M470-50A	1.1	15.7	60.3
M530-50A	0.9	16.0	59.0
M700-65A	0.8	14.9	58.1

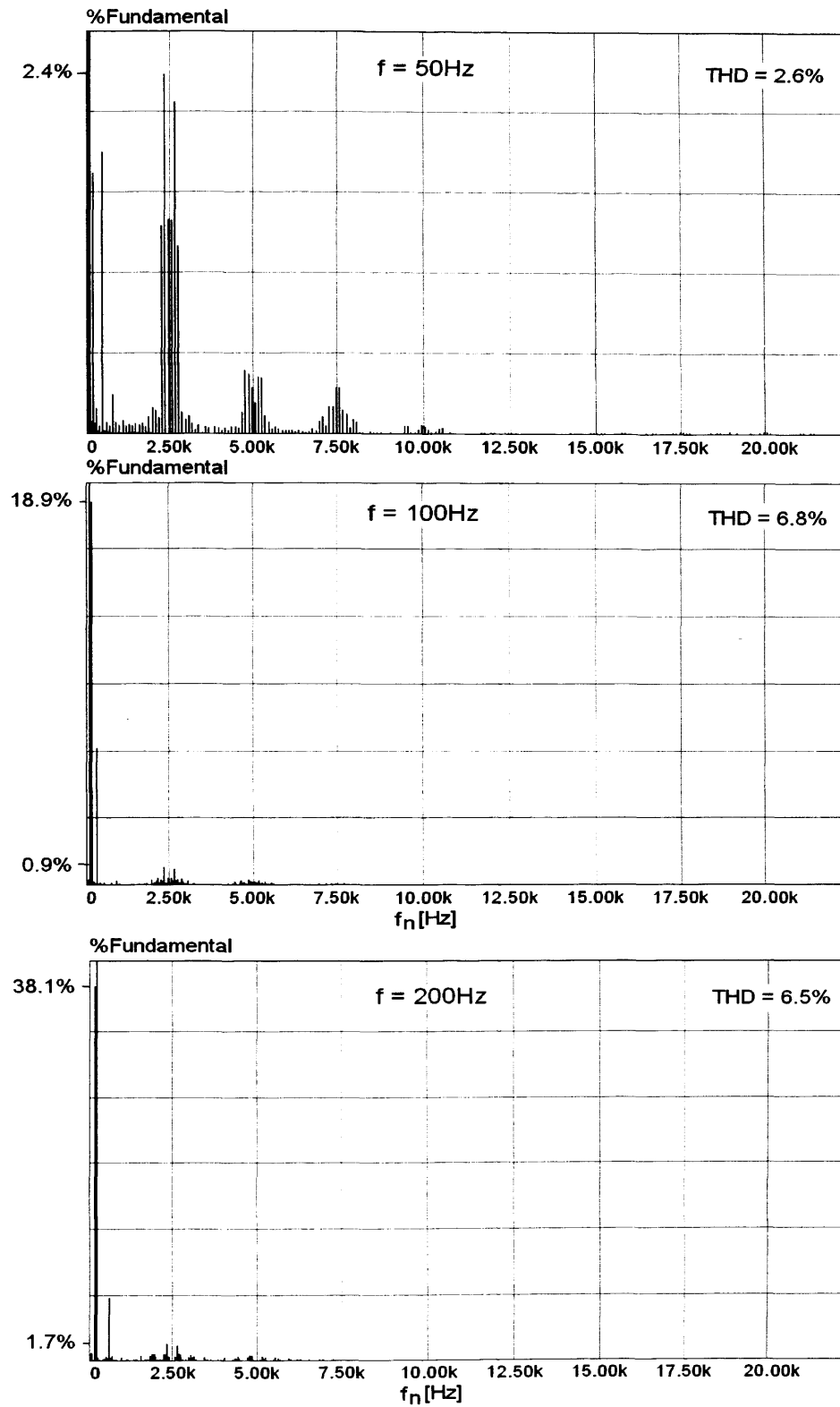


Fig. 5.30. Harmonic spectra of induction and associated *THD* [%] under line-neutral matrix converter excitation (50 Hz, 100 Hz, 200 Hz)

As the frequency increases, the rise in low order harmonic content in the flux density curve is highlighted by a significant increase of  $f_wTHD$  [%] in laminations of the three materials. The form factor  $FF$  (2.35) is also a useful parameter in the evaluation of the quality of a given waveform. It is defined as the ratio of RMS to rectified mean values. For M470-50A, M530-50A and M700-65A laminations subjected to line-neutral matrix converter magnetising conditions, values of form factor of the induction are introduced in table 5.17 at 50 Hz, 100 Hz and 200 Hz magnetising frequency and 1.5T peak flux density.

Table 5.17. Form factor values of flux density in laminations at 1.5T peak flux density.

	50 Hz	100 Hz	200 Hz
M470-50A	1.075	1.079	1.083
M530-50A	1.082	1.078	1.079
M700-65A	1.074	1.082	1.080

### 5.3.4b - DC-link Converter

In two-level PWM DC-link converter, line-line voltages are pulsating signals of amplitude modulated by an alternating square waveform (fig. 5.20). Harmonic spectra of induced voltages at 50 Hz, 100 Hz and 200 Hz are shown for M700-65A laminations at 1.5 T peak flux density in fig. 5.31 – 5.33. PWM modulation indices are 0.5, 0.8 and 1.0. Values of  $THD$  [%] are also provided.

Spreading of sideband harmonics in high clusters is not as prominent as in line-neutral voltage typical of a three-phase matrix converter (fig. 5.30). Clusters, which are located at multiple frequencies of PWM switching frequency, are higher, especially at low modulation index. The first cluster (2.5 kHz) in spectra of induced voltages under PWM magnetising signals is higher for the three modulation indices (0.5, 0.8, and 1.0) than under optimum matrix converter supply ( $q = \sqrt{3}/2$ ). This explains why eddy-current losses under typical line-neutral excitation of matrix converters are reduced. Moreover, an increase in  $m_i$  attenuates the difference between frequency spectra characteristic of DC-link and direct AC-AC converters. Magnetic induction under two-level PWM supply can be described as a multi-step waveform associated to a sequence of periods of acceleration and deceleration affecting domain wall motion during magnetisation.

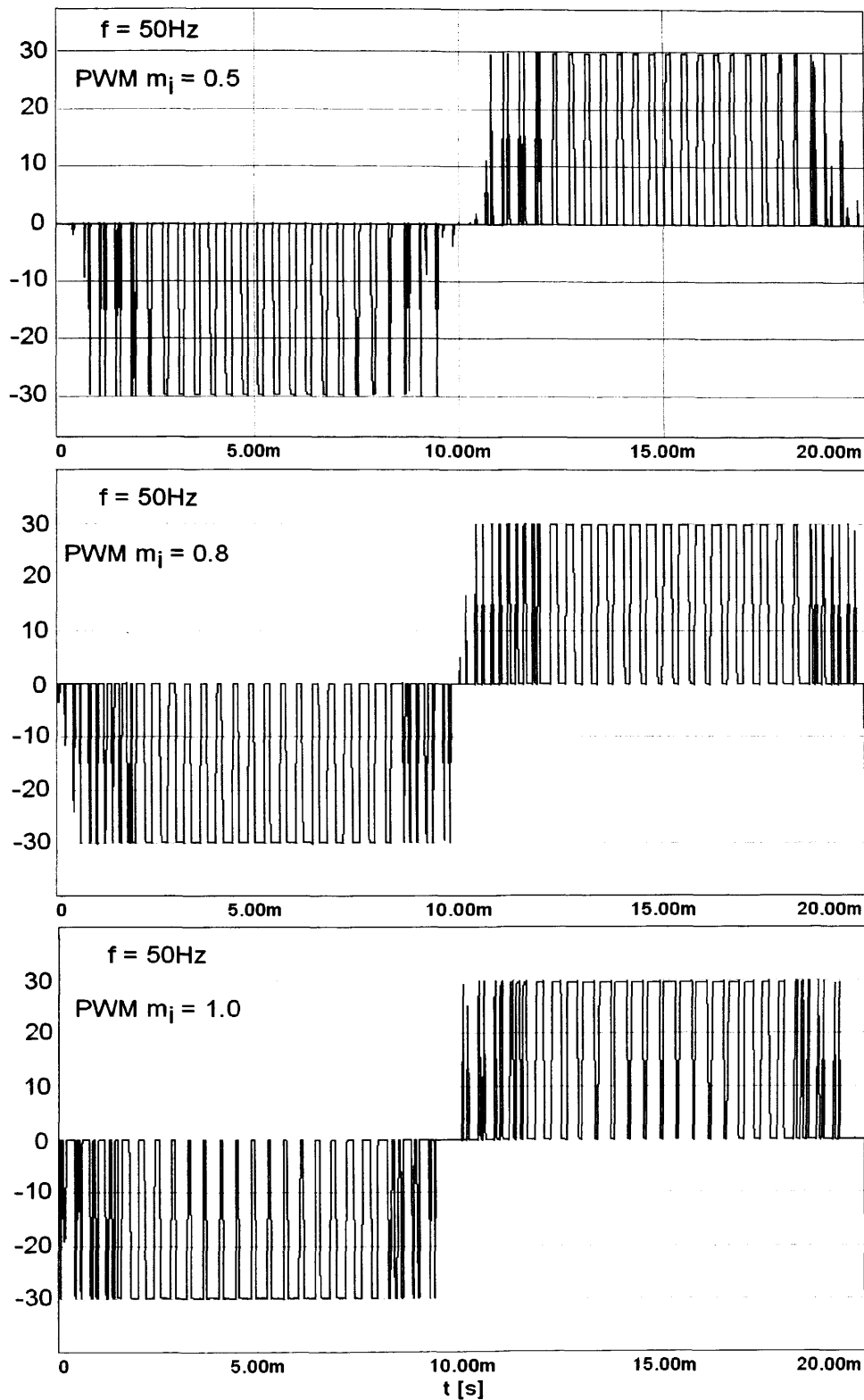


Fig 5.31. Line-line voltages produced by DC-link converter (§4.4.2) under Pulse-Width-Modulation and modulation indices 0.5, 0.8 and 1.0

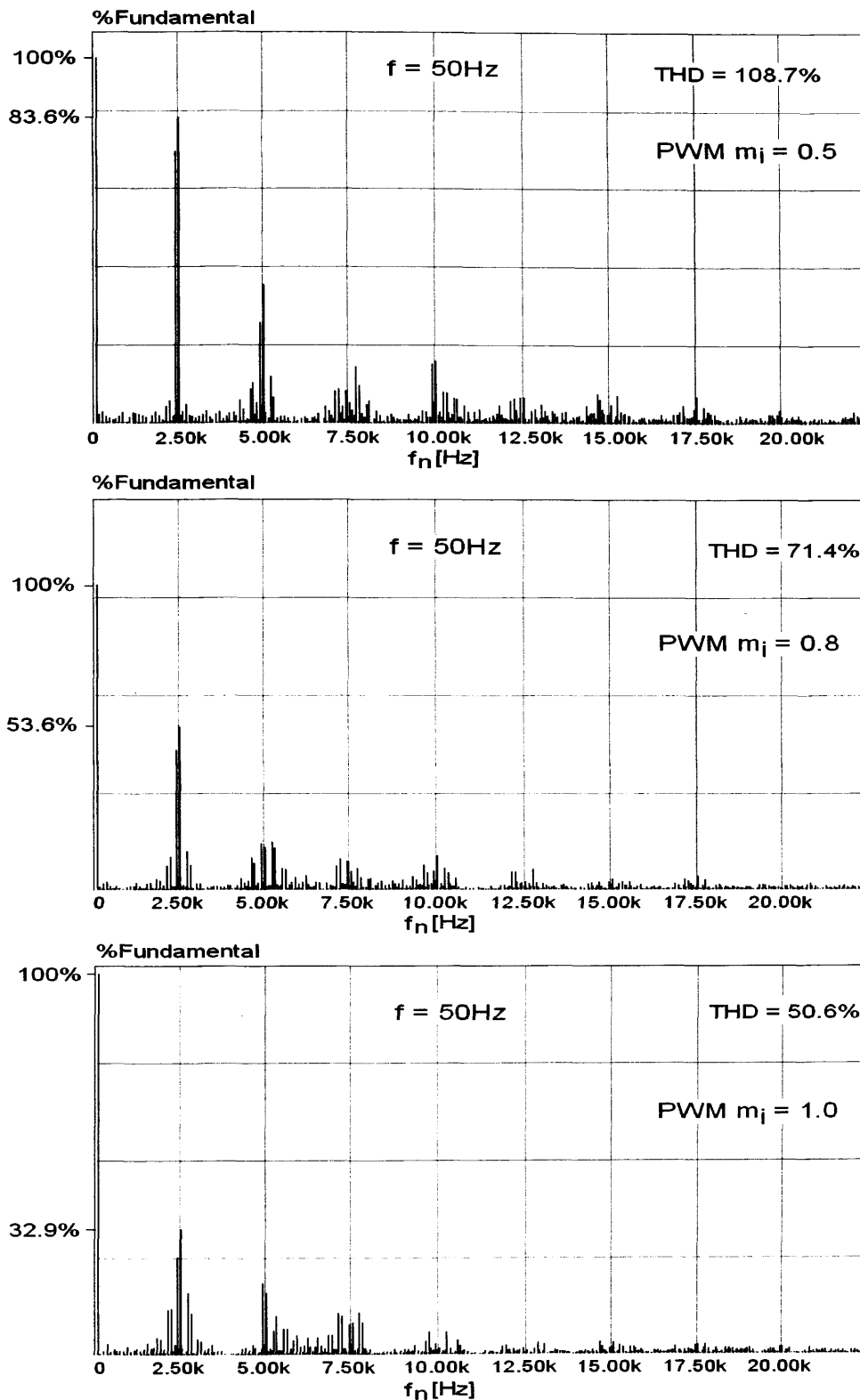


Fig. 5.32. Harmonic spectra of induced voltages under DC-link converter (§4.4.2) excitation for modulation indices 0.5, 0.8 and 1.0 ( $f = 50$  Hz)

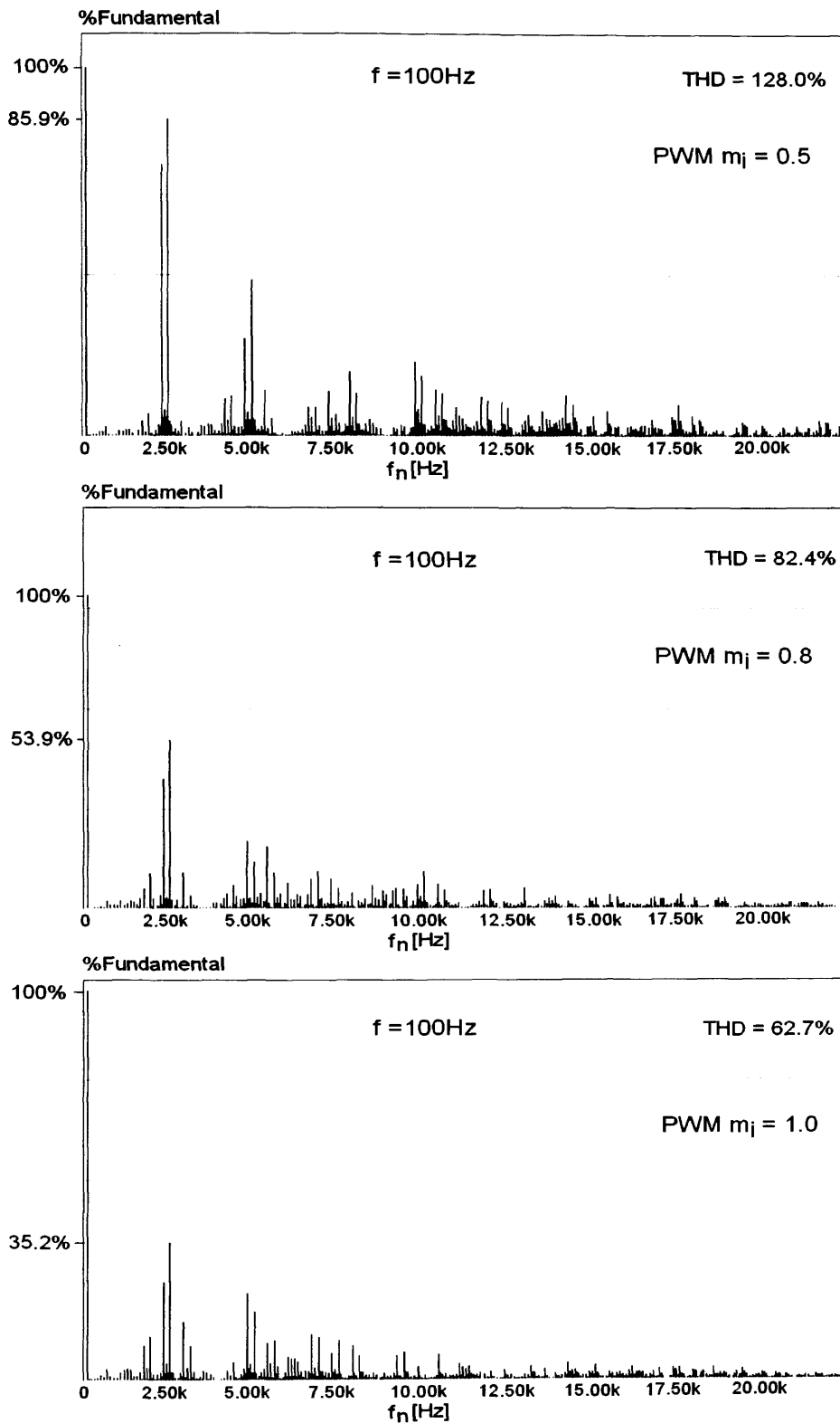


Fig. 5.33. Harmonic spectra of induced voltages under two-level PWM converter (§4.4.2) excitation for modulation indices 0.5, 0.8 and 1.0 ( $f = 100\text{ Hz}$ )

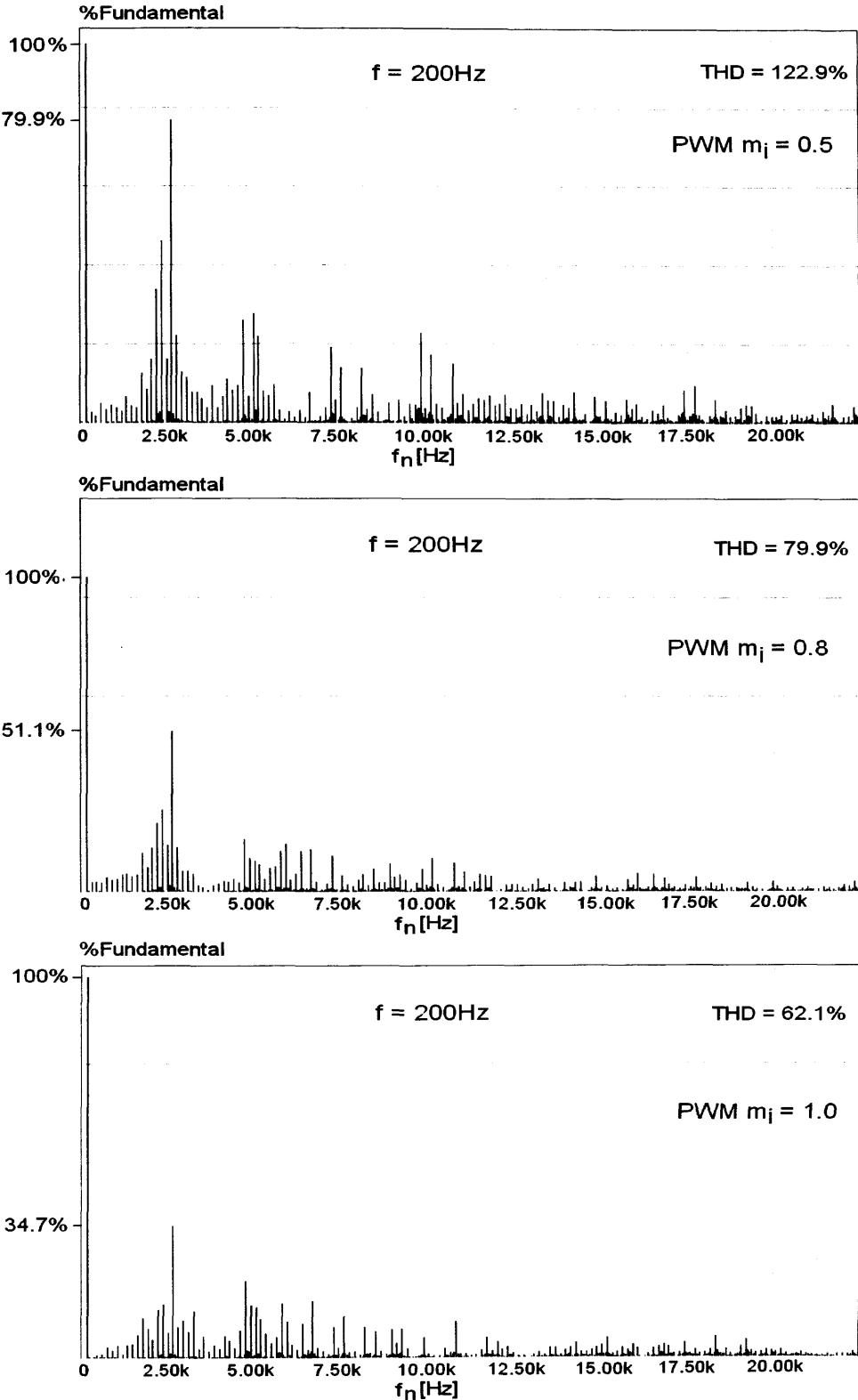


Fig. 5.34. Harmonic spectra of induced voltages under two-level PWM converter (§ 4.4.2) excitation for modulation indices 0.5, 0.8 and 1.0 ( $f = 200\text{ Hz}$ )

One cycle of magnetic induction under line-line PWM voltage excitation is illustrated in fig. 5.35 – 5.37. As can be seen from the graphs, the non-sinusoidal nature of induction wave-shapes becomes more apparent for higher magnetising frequencies. The width of pulses in line-line voltages is proportionally closer to the fundamental period. It was confirmed on the graphs that modulation index equal to unity yielded a smoother and more sinusoidal flux density curve in the 50 – 200 Hz fundamental frequency range.

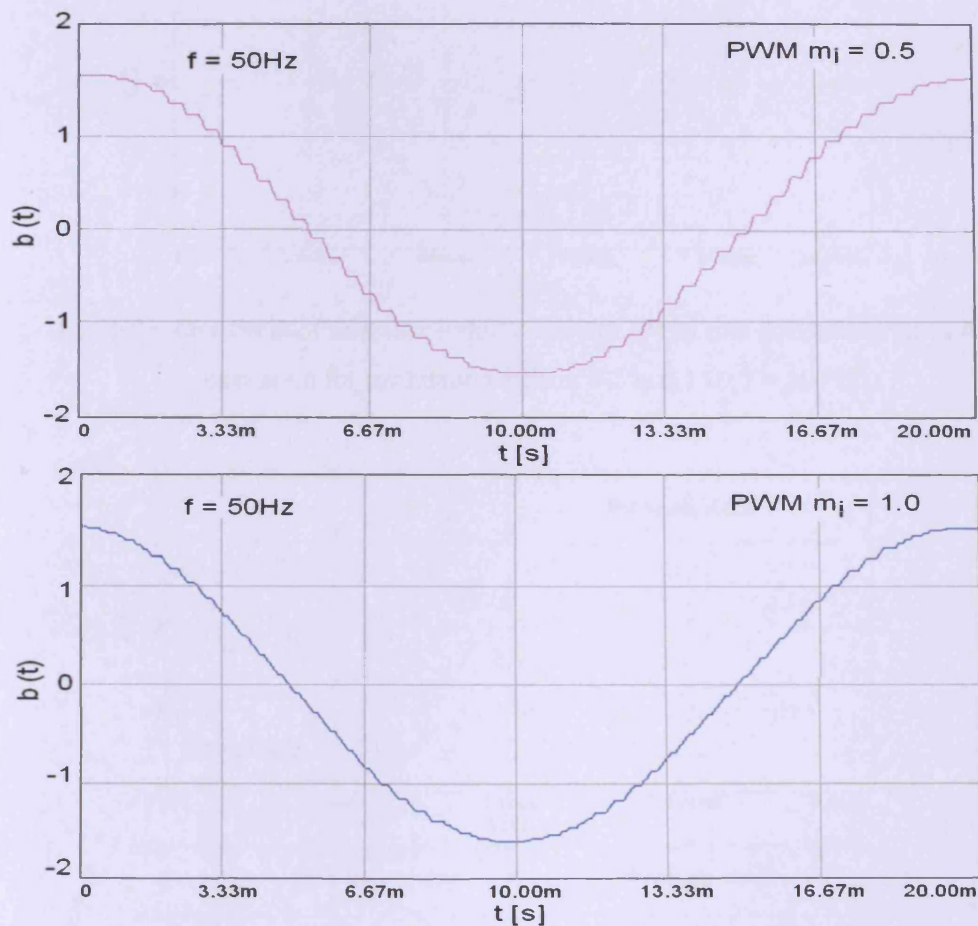


Fig. 5.35. One cycle of magnetic induction under PWM line-line converter (§ 4.4.2) excitation for modulation indices 0.5 and 1.0 ( $f = 50\text{ Hz}$ )

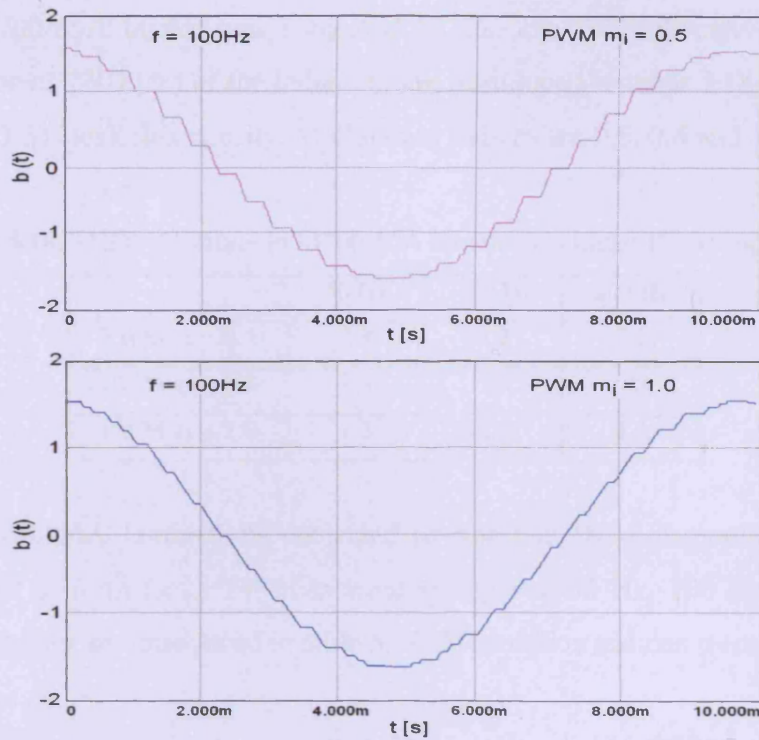


Fig. 5.36. One cycle of magnetic induction under PWM line-line converter (§ 4.4.2) excitation for modulation indices 0.5 and 1.0 ( $f = 100 \text{ Hz}$ )

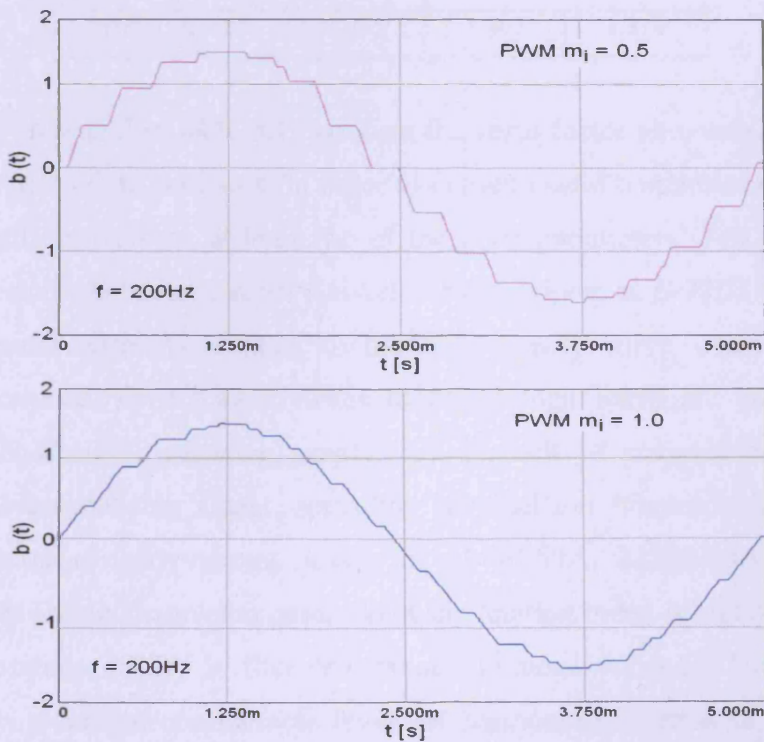


Fig. 5.37. One cycle of magnetic induction under PWM line-line converter (§ 4.4.29) excitation for modulation indices 0.5 and 1.0 ( $f = 200 \text{ Hz}$ )

For M700-65A laminations subjected to line-line DC-link converter magnetising conditions, values of *THD* [%] of the induction are introduced in table 5.18 at 50 Hz, 100 Hz and 200 Hz and 1.5T peak flux density. Modulation indices are 0.5, 0.8 and 1.0.

Table 5.18. *THD* [%] values in M700-65A laminations under PWM supply (1.5 T)

	50 Hz	100 Hz	200 Hz
PWM $m_i = 0.5$	2.8	4.9	7.1
PWM $m_i = 0.8$	1.8	3.0	4.7
PWM $m_i = 1.0$	1.3	2.4	3.3

For M700-65A laminations subjected to line-line DC-link converter magnetising conditions, values of form factor *FF* of induced voltages at 50 Hz, 100 Hz and 200 Hz and 1.5T peak flux density are introduced in table 5.19. Modulation indices were 0.5, 0.8 and 1.0.

Table 5.19. *THD* [%] values in M700-65A laminations under PWM supply (1.5T)

	50 Hz	100 Hz	200 Hz
PWM $m_i = 0.5$	1.741	1.851	1.800
PWM $m_i = 0.8$	1.392	1.457	1.447
PWM $m_i = 1.0$	1.275	1.327	1.314

Results presented in table 5.18 confirm the form factor as a sensitive parameter to variations of PWM modulation index. In order to extract useful conclusions on the harmonic quality of a specific waveform, at least two of the three parameters (*THD*, *fwTHD* or form factor) must be studied. In the matrix converter case, a look at *fwTHD* values reveals an important low order harmonic content in the flux density curve when the magnetising frequency is increased. Form factor values highlight high harmonic quality of voltages induced under line-neutral pulsating supply. As a result of cosinusoidal modulation of amplitude in the magnetising signal, spreading of sideband harmonics contributes to an important reduction of eddy-current losses in M470-50A, M530-50A and M700-65A laminations. In the DC-link converter case, PWM modulation index is highlighted as a critical parameter to harmonic quality in flux density and induced voltages. Too low a value of modulation index results in considerable levels of harmonic distortion in the medium-high frequency range (beyond 1 kHz). Due to decoupling between input and output in DC-link converters, multiple harmonics of 50 Hz are not inherited by flux density curve or induced voltages. In spite of the negative impact of high clusters of flux harmonics on losses in

laminated steel, the effective decoupling carried out by the electrolytic capacitor strengthens the position of indirect converters as AC-AC links in variable speed drives.

## **5.4 Line-line supply (matrix converter)**

### **5.4.1. Total Power Losses**

Losses in M470-50A, M530-50A and M700-65A laminations subjected to sinusoidal and line-line supply, typical of matrix (§4.4.1) and two-level PWM (§4.4.2) converters, were measured in a single strip tester (§ 4.5) at 1.5 T peak flux density and 50 Hz, 100 Hz and 200 Hz. In the matrix converter case, an optimum value of voltage transfer ratio  $q = \sqrt{3}/2$  was selected. As for the indirect converter, selected PWM modulation indices  $m_i$  were 0.5, 1.0 and 1.2. SVM sampling (matrix) and PWM switching frequencies were set to a constant value of 5 kHz. Measured power losses in M470-50A, M530-50A and M700-65A laminations are given in fig. 5.38. Results confirmed low modulated PWM ( $m_i = 0.5$ ) line-line voltage as the less favourable magnetising signal in the 50 – 200 Hz frequency range for the three materials. Numerous and narrow pulses in the magnetising voltage cause a non-smooth flux derivative waveform characterized by repeated positive and negative peaks. Flux reversals accompanying this phenomenon during magnetisation of the samples result in higher eddy-current and anomalous losses.

When over-modulated PWM excitation was selected to energise M470-50A and M700-65A laminations, measured power losses were similar to those obtained under PWM voltage at modulation index equal to unity. A reduction in losses in M530-50A laminations at 100 Hz and 200 Hz was ensured by over-modulated PWM signal. The use of over-modulation in PWM control of DC-link converters is not uncommon. One of the main reasons that support this practice is the need to extract high levels of energy from the electrolytic capacitor in order to maximise shaft power in the rotating machine. Nevertheless, when the modulation index increases, line-line voltages produced by two-level DC-link converters lose its pulsating nature and get closer to an ideal alternating square waveform. Although the presence of flux harmonics in high clusters is naturally reduced by this change in the magnetising voltage, low order harmonics characteristic of ideal square waveform are inherited by the flux density curve. The potential decrease in iron losses achievable by reduced high harmonic distortion is then partially offset by low order harmonic distortion. Depending on the phase angle of these components [5.5], a variable amount of supplementary energy linked to iron losses is required to reach an identical level of magnetisation in the steel.

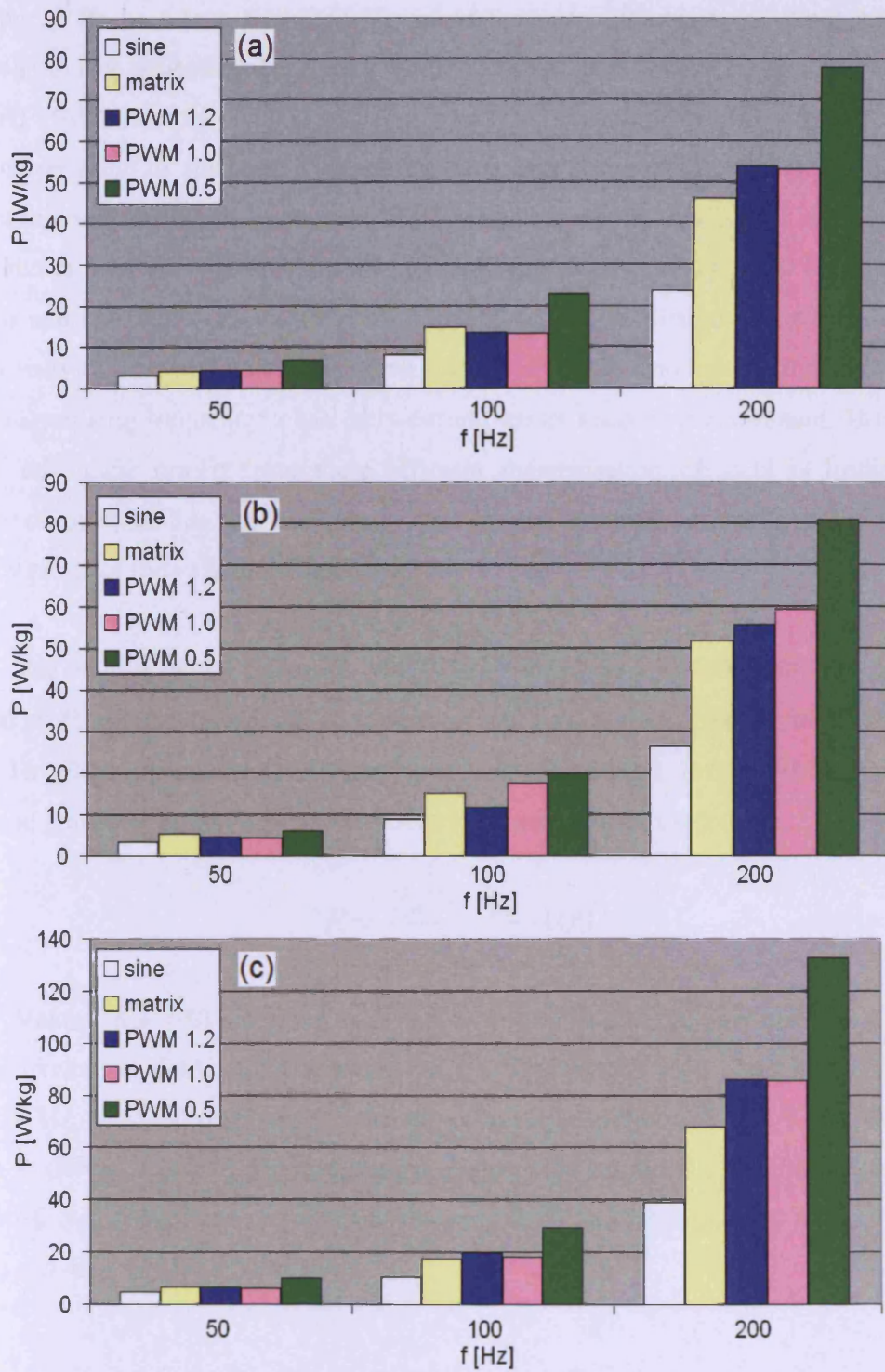


Fig. 5.38. Specific power losses at 1.5 T peak flux density and 50 Hz, 100 Hz and 200 Hz in  
 (a) M470 – 50A – (b) M530 – 50A – (c) M700 – 65A laminations  
 subjected to line-line matrix converter and two-level PWM excitation

Line-line matrix converter excitation ensured more efficient magnetisation than PWM supply ( $m_i = 1.2; 1.0$ ) at 200 Hz magnetising frequency in the three materials. In opposition to line-neutral voltage, this type of signal has similar characteristics to high modulated PWM line-line voltages in terms of total harmonic distortion and form factor. Although spreading of sideband flux harmonics is still accomplished under line-line supply typical of three-phase matrix converters, its beneficial impact on total losses in laminated steel is mitigated at low and intermediate magnetising frequencies (50 Hz, 100 Hz) where static hysteresis and anomalous losses are predominant. In thick laminations of silicon-iron alloys of low resistivity, line-line matrix converter excitation yields a noticeable reduction of losses at high magnetising frequency when eddy-current losses become predominant. However, the potential advantage drawn from more efficient magnetisation of steel is limited by the selection of material for the laminated core of the induction motor and by the output frequency range of the variable speed drive.

The increment in losses in M470-50A, M530-50A and M700-65A laminations subjected to distorted magnetising conditions at 1.5 T peak flux density and 50 Hz, 100 Hz and 200 Hz was calculated in (5.20) for line-line matrix and two-level PWM signals. Losses in the three grades under sinusoidal conditions  $P_{sin}$  were used as a reference.

$$R = \frac{P_{dist} - P_{sin}}{P_{sin}} \cdot 100 \quad (5.35)$$

Values of  $R$  [%] are given in fig. 5.39. In M470-50A laminations, line-line matrix converter excitation yielded inferior losses by 33.1 % (PWM  $m_i = 1.2$ ) and 30.5% (PWM  $m_i = 1.0$ ) at 200 Hz. In M530-50A laminations, the decrease in losses was 14.4 % (PWM  $m_i = 1.2$ ) and 28.1 % (PWM  $m_i = 1.0$ ). Under identical magnetising conditions, line-line voltage typical of direct AC-AC converter ensured lower losses in M700-65A laminations by 46.9 % (PWM  $m_i = 1.2$ ) and 46.4 % (PWM  $m_i = 1.0$ ).

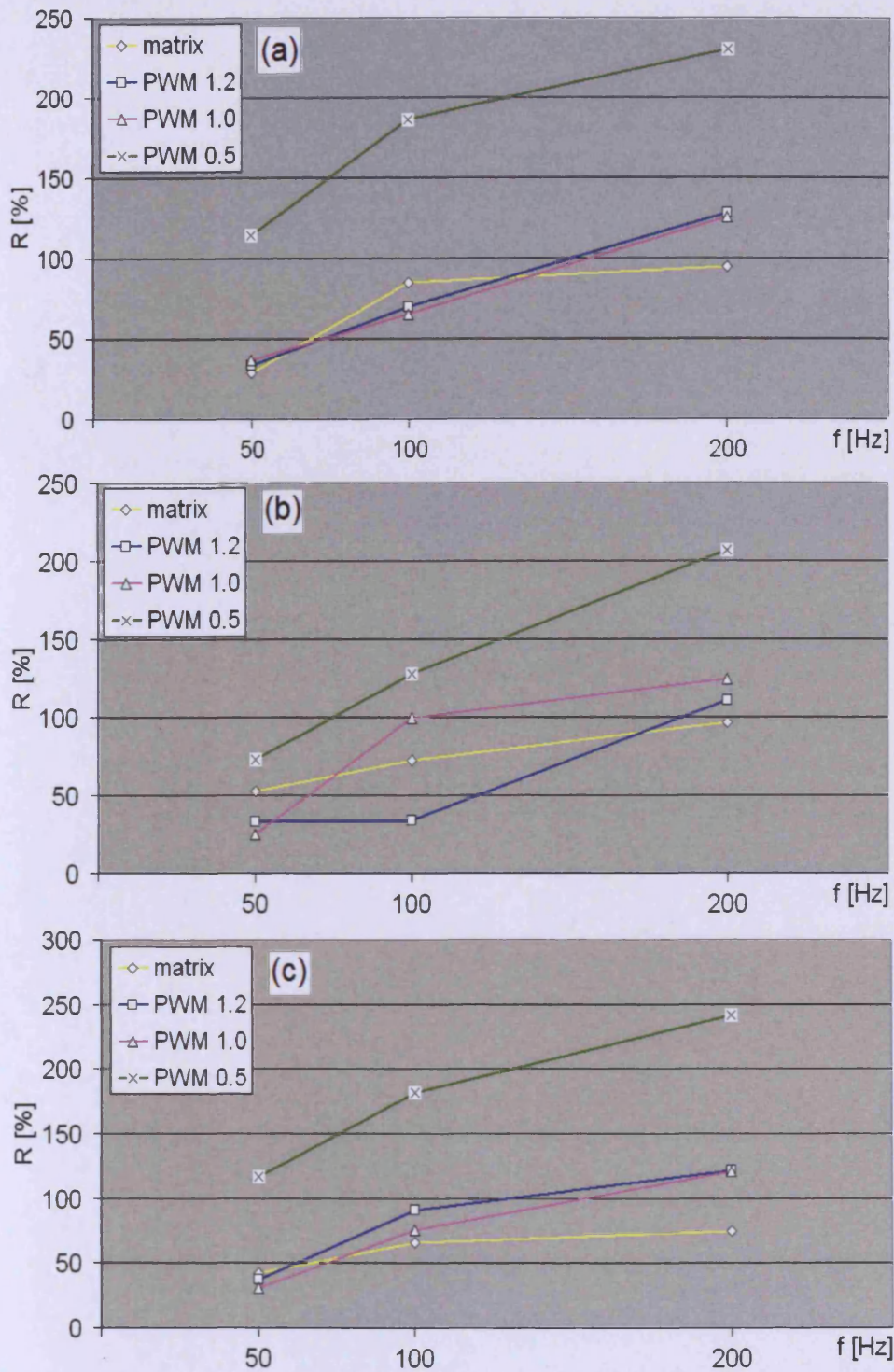


Fig. 5.39. Incremental losses  $R$  [%] under line-line matrix and two-level PWM converter supply with respect to sinusoidal conditions (1.5 T peak flux density)  
 (a) M470-50A – (b) M530-50A – (c) M700-65A laminations

### 5.4.2 Harmonic distortion and form factor

Fig. 5.40 and fig. 5.41 illustrate typical line-line voltages of matrix and two-level PWM converters, respectively. Identical waveforms were used to magnetise M470-50A, M530-50A and M700-65A laminations at 1.5T peak flux density and 50 Hz, 100 Hz and 200 Hz. Wave-shapes of line-line voltages produced by matrix converters have more similarities with voltages produced by an indirect DC-link converter.

Although cosinusoidal modulation of amplitude in half-cycles of the alternating wave-shape is clearly seen in the direct AC-AC converter case, *THD* [%] and form factor values of the same order as linked to high modulated PWM signals ( $m_i = 1.2$ ; 1.0) were expected. Values of *THD* and form factor in induced voltages at 1.5 T peak flux density and 50 Hz, 100 Hz and 200 Hz, are introduced in tables 5.20 – 5.22 for M470-50A, M530-50A and M700-65A laminations.

Table 5.20. *THD* and form factor values in M470-50A laminations (1.5T peak flux density)

	matrix		PWM $m_i = 1.2$		PWM $m_i = 1.0$		PWM $m_i = 0.5$	
	THD	FF	THD	FF	THD	FF	THD	FF
50 Hz	59.6	1.257	55.9	1.262	64.8	1.329	132.6	1.837
100 Hz	34.9	1.250	54.0	1.265	63.1	1.313	129.6	1.811
200 Hz	24.2	1.241	54.5	1.258	62.8	1.306	125.4	1.772

Table 5.21. *THD* and form factor values in M530-50A laminations (1.5T peak flux density)

	matrix		PWM $m_i = 1.2$		PWM $m_i = 1.0$		PWM $m_i = 0.5$	
	THD	FF	THD	FF	THD	FF	THD	FF
50 Hz	59.0	1.259	55.3	1.263	65.1	1.325	131.7	1.837
100 Hz	34.2	1.252	54.9	1.260	63.7	1.317	128.5	1.809
200 Hz	24.4	1.243	53.9	1.253	62.5	1.307	125.1	1.776

Table 5.22. *THD* [%] and form factor values in M700-65A laminations (1.5 T peak flux density)

	matrix		PWM $m_i = 1.2$		PWM $m_i = 1.0$		PWM $m_i = 0.5$	
	THD	FF	THD	FF	THD	FF	THD	FF
50 Hz	58.7	1.258	54.9	1.265	65.8	1.323	131.4	1.830
100 Hz	33.9	1.245	54.1	1.269	63.3	1.312	128.2	1.801
200 Hz	24.3	1.242	53.8	1.253	62.5	1.307	125.2	1.779

From the tables above, it is highlighted that form factor values in induced voltages under matrix converter supply ( $q = \sqrt{3}/2$ ) are similar to those associated to over-modulated PWM conditions ( $m_i = 1.2$ ). Results indicate that line-neutral voltage has better characteristics as magnetising signal than line-line voltage in direct AC-AC converter. Form factor values introduced in this section are in the proximity of 1.25 while values reported in § 5.3.3 were close to 1.09. In opposition to line-neutral voltages, line-line supply typical of a matrix converter showed a more uniform pattern (independent of fundamental frequency) when THD values were analysed. The presence of subharmonics was strongly reduced due to the change in the wave-shape. This type of supply appears as more suitable to the operation of the asynchronous machine in industrial variable speed drives. However, an analytical study on motor efficiency under these two different supplies is introduced in chapter 7.

Table 5.23 provides *THD* [%] and *fwTHD* [%] of the flux density curve when M470-50A, M530-50A and M700-65A laminations were subjected to line-line matrix converter excitation at 1.5 T peak flux density and 50 Hz, 100 Hz and 200 Hz.

Table 5.23. *THD* [%] and *fwTHD* [%] of induction (1.5T peak flux density)

	50 Hz		100 Hz		200 Hz	
	<i>THD</i>	<i>fwTHD</i>	<i>THD</i>	<i>fwTHD</i>	<i>THD</i>	<i>fwTHD</i>
M470-50A	0.37	0.04	0.33	0.43	0.47	3.18
M530-50A	0.34	0.04	0.33	0.40	0.48	3.23
M700-65A	0.30	0.03	0.32	0.40	0.46	3.12

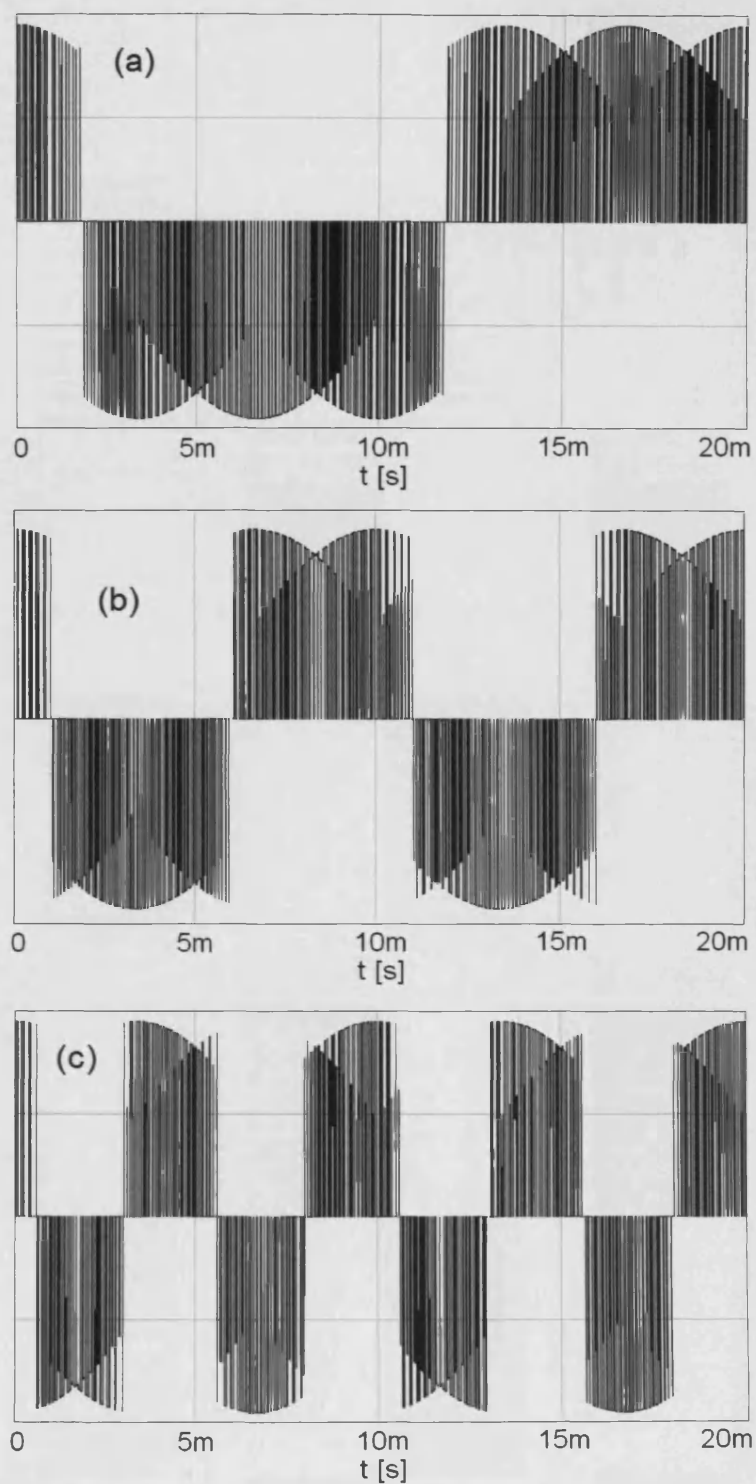


Fig 5.40. Line-line voltage of a three-phase matrix converter at 5 kHz SVM sampling frequency  
 (a) 50 Hz – (b) 100 Hz – (c) 200 Hz

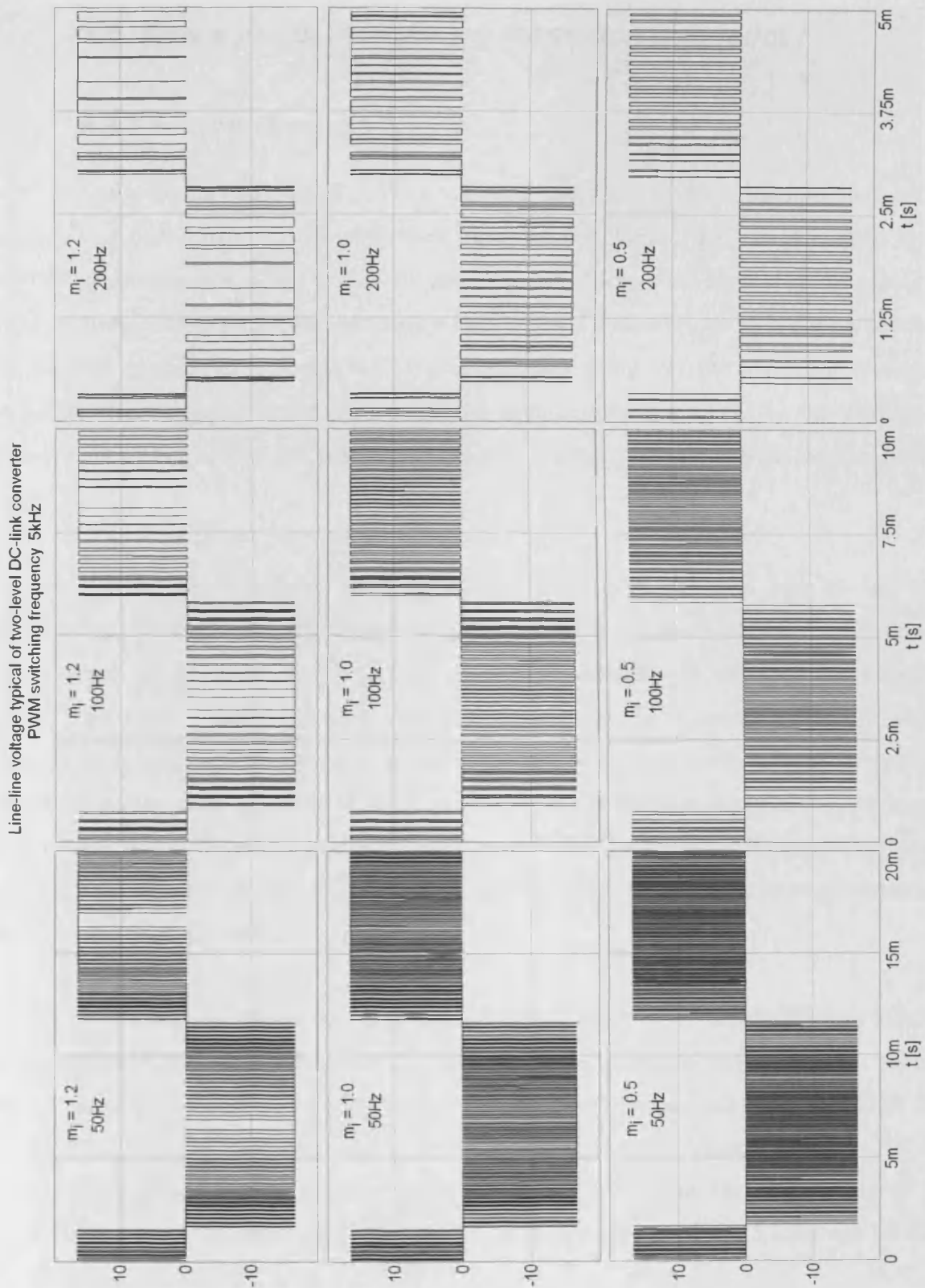


Fig 5.41. Typical line-line voltage of a two-level PWM converter at 5 kHz switching frequency

Fundamental frequencies: 50 Hz – 100 Hz – 200 Hz

Modulation indices: 0.5 – 1.0 – 1.2

## **5.5 Space vector modulation [sampling frequency]**

### **5.5.1 Total losses**

Space-Vector-Modulation [SVM] was established as the most suitable modulation technique in three-phase matrix converters more than a decade ago. Implemented by a Digital-Signal-Processor [DSP] at a given sampling frequency  $f_s$ , the algorithm associated to SVM is more complicated than elementary carrier-based Pulse-Width-Modulation [PWM]. The need for engineering expertise in DSP programming, along with the requirement of more performant technology in electronic boards, has maintained basic PWM as the most cost-effective choice for control of commercial DC-link converters in the low-to-medium power range.

When SVM algorithm is executed, the duty cycle of each one of the nine bidirectional switches is defined for one sampling period (§ 2.3.6). Every switching element remains then turned on or off for periods of time considerably shorter than the sampling period. As a result, voltage signals produced by matrix converters consist of narrow pulses [5.6]. Harmonic distortion derived from the pulsating nature of these voltages is strongly dependent on the ratio of width of those pulses to one fundamental cycle defined by the output frequency. It is easily understood that the ratio of SVM sampling frequency to output frequency determines, not only harmonic quality of voltages, but also the number, shape and distribution of high clusters in frequency spectra.

When line-line matrix converter voltages at 50 Hz, 100 Hz and 200 Hz are selected as magnetising signals, it is anticipated that selected SVM sampling frequencies will have an impact on the performance of the soft magnetic material. Losses in M470-50A, M530-50A and M700-65A laminations subjected to line-line voltage supply, typical of direct AC-AC converters, are measured in a single strip tester (§ 4.5) at 1.5 T peak flux density and 50 Hz, 100 Hz and 200Hz. SVM sampling frequencies selected were 2.5 kHz, 5 kHz and 10 kHz. Results are presented in fig. 5.42.

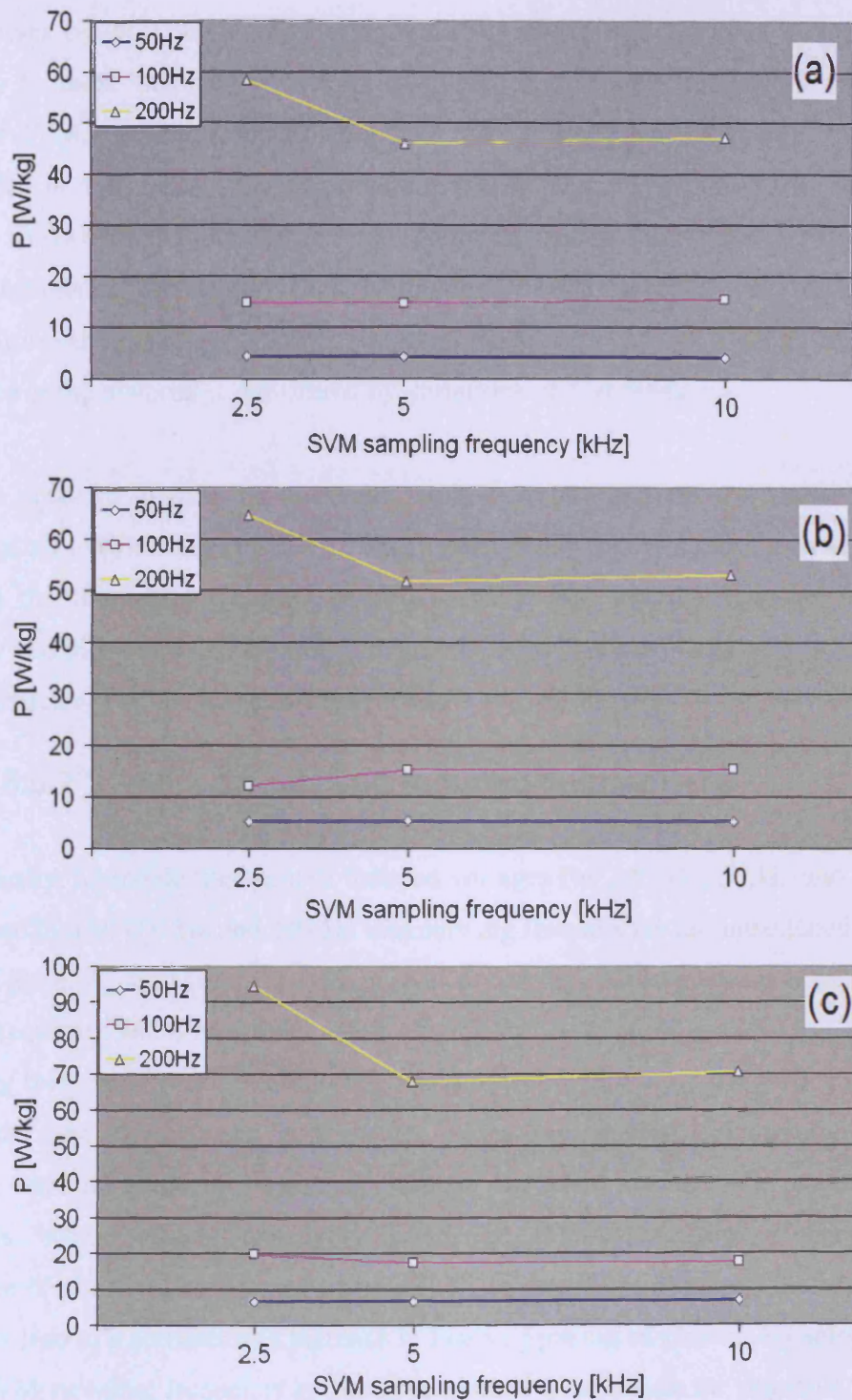


Fig. 5.42. Variation of specific power losses  $P$  [W/kg] with SVM sampling frequency in  
 (a) M470 – 50A – (b) M530 - 50A – (c) M700 – 65A laminations  
 subjected to line-line matrix converter supply (1.5 T peak flux density)

At 200 Hz magnetising frequency, losses in M470-50A, M530-50A and M700-65A laminations are affected by SVM sampling frequency. When  $f_s$  is equal to 2.5 kHz, a higher value of losses by 27.0 % (M470-50A), 24.7 % (M530-50A) and 39.5 % (M700-65A) in comparison to those obtained at 5 kHz is found. In the alloy of highest resistivity, the variation of SVM sampling frequency does not have a significant impact on losses at 50 Hz and 100 Hz. In the grade with intermediate silicon content (M530-50A), losses remain constant at 50 Hz while a moderate increase accompany the rise in  $f_s$  from 2.5 kHz to 5 kHz at 100 Hz magnetising frequency. Thick laminations of the material with lowest resistivity benefited from an increase of SVM sampling frequency (2.5 to 5 kHz) at 100Hz. The performance of the material is not altered by variations of  $f_s$  at 50Hz.

In order to analyse these results, eddy-current losses in the three materials are calculated at all magnetising conditions. Since peak flux density is close to a saturating state (1.5T) and the frequency spectrum of flux density and induced voltages is completely changed by variations in SVM sampling frequency, eddy-current losses will play an important role in the efficiency of the magnetising process.

### 5.5.2 Flux density and induced voltage

Firstly, harmonic spectrum of induced voltages for 2.5 kHz, 5 kHz and 10 kHz SVM sampling and 50 Hz, 100 Hz and 200 Hz magnetising frequencies are introduced in fig. 5.43 – 5.45 for M700-65A laminations at 1.5T peak flux density. Clusters were lowest when SVM sampling frequency had a maximum value of 10 kHz. At  $f_s$  equal to 2.5 kHz, an increase in magnetising frequency from 50 to 200 Hz was not accompanied by a significant reduction in height of the first two clusters. Furthermore, spreading of sideband harmonics at 200 Hz causes the medium frequency range (1 kHz to 10 kHz) to be fully covered by active components, which affects negatively losses in the laminations. Depending on the combination of phase angles associated to each component in this range, the superposition of components lead to a considerable increase in losses. Spacing of clusters by selecting a higher value of SVM sampling frequency is therefore needed to attenuate the negative influence that enhanced spreading of sideband harmonics in line-line matrix converter signals has on the performance of the steel.

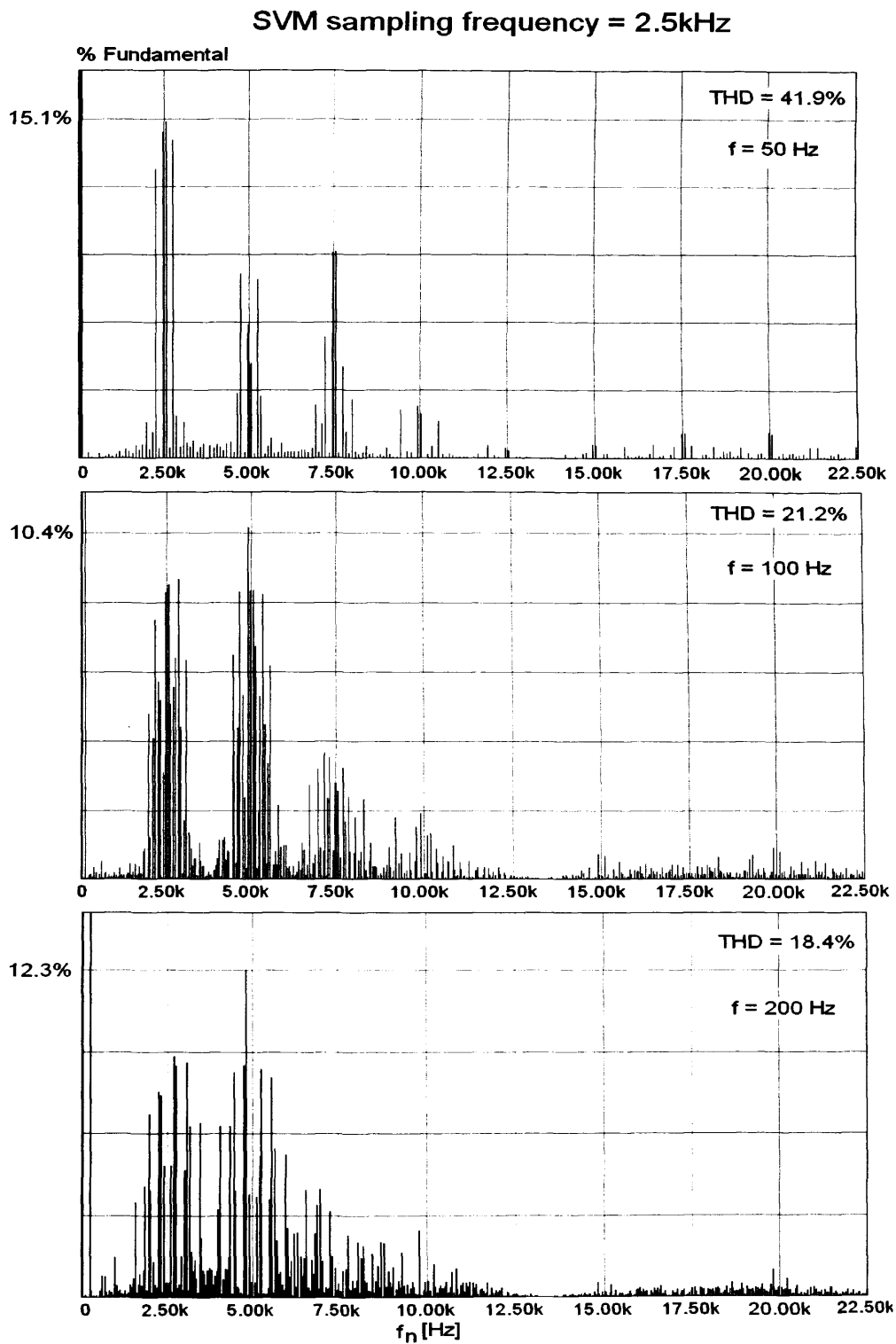


Fig 5.43. Harmonic spectra of induced voltages produced by the matrix converter (§ 4.4.2) and  $THD$  [%] at 50 Hz, 100 Hz and 200 Hz and 2.5 kHz sampling frequency in M700 – 65A laminations (1.5 T peak flux density)

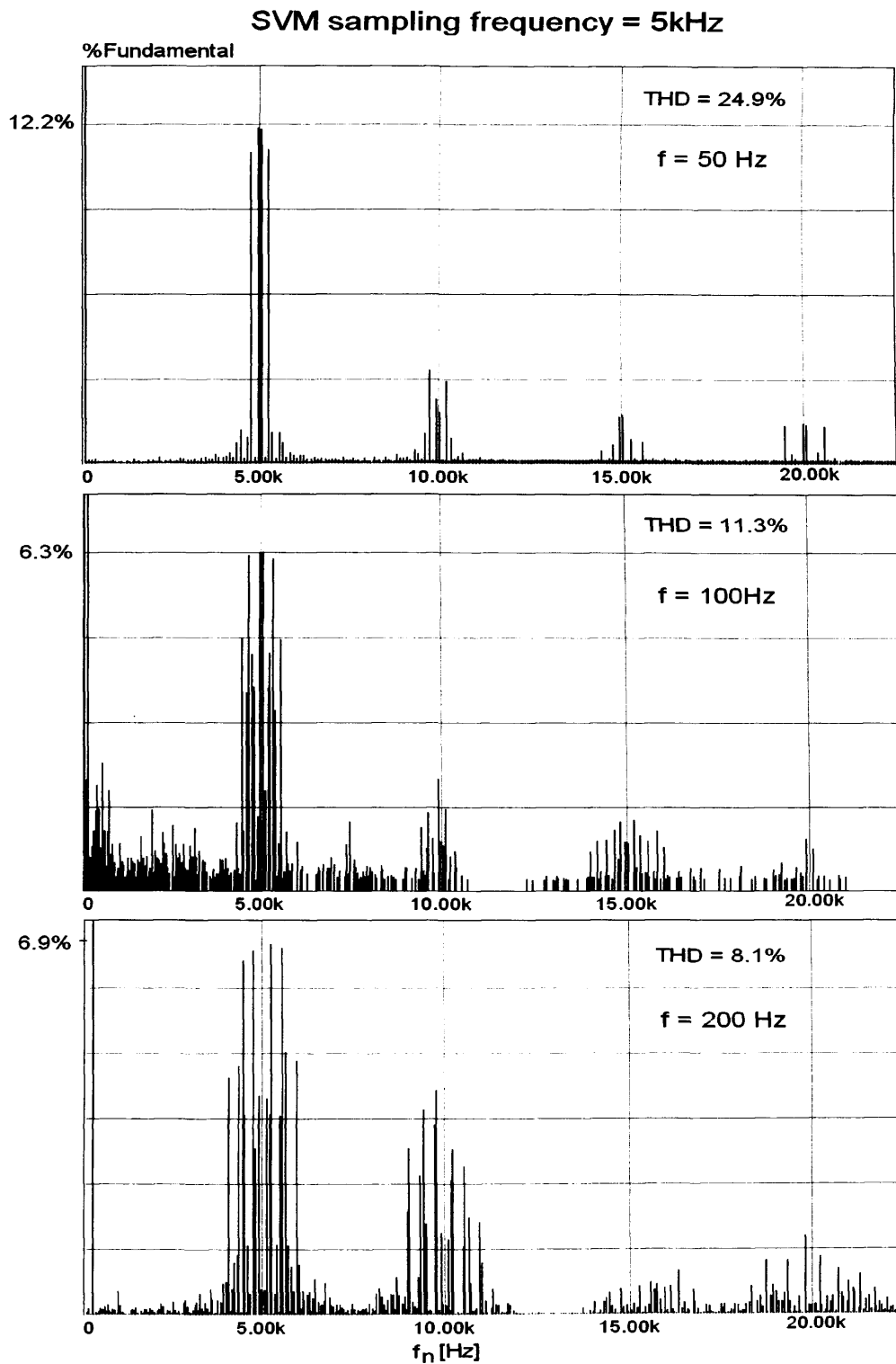


Fig 5.44. Harmonic spectra of induced voltages produced by the matrix converter (§ 4.4.2) and *THD* [%] at 50 Hz, 100 Hz and 200 Hz and 5 kHz sampling frequency in M700 – 65A laminations (1.5 T peak flux density)

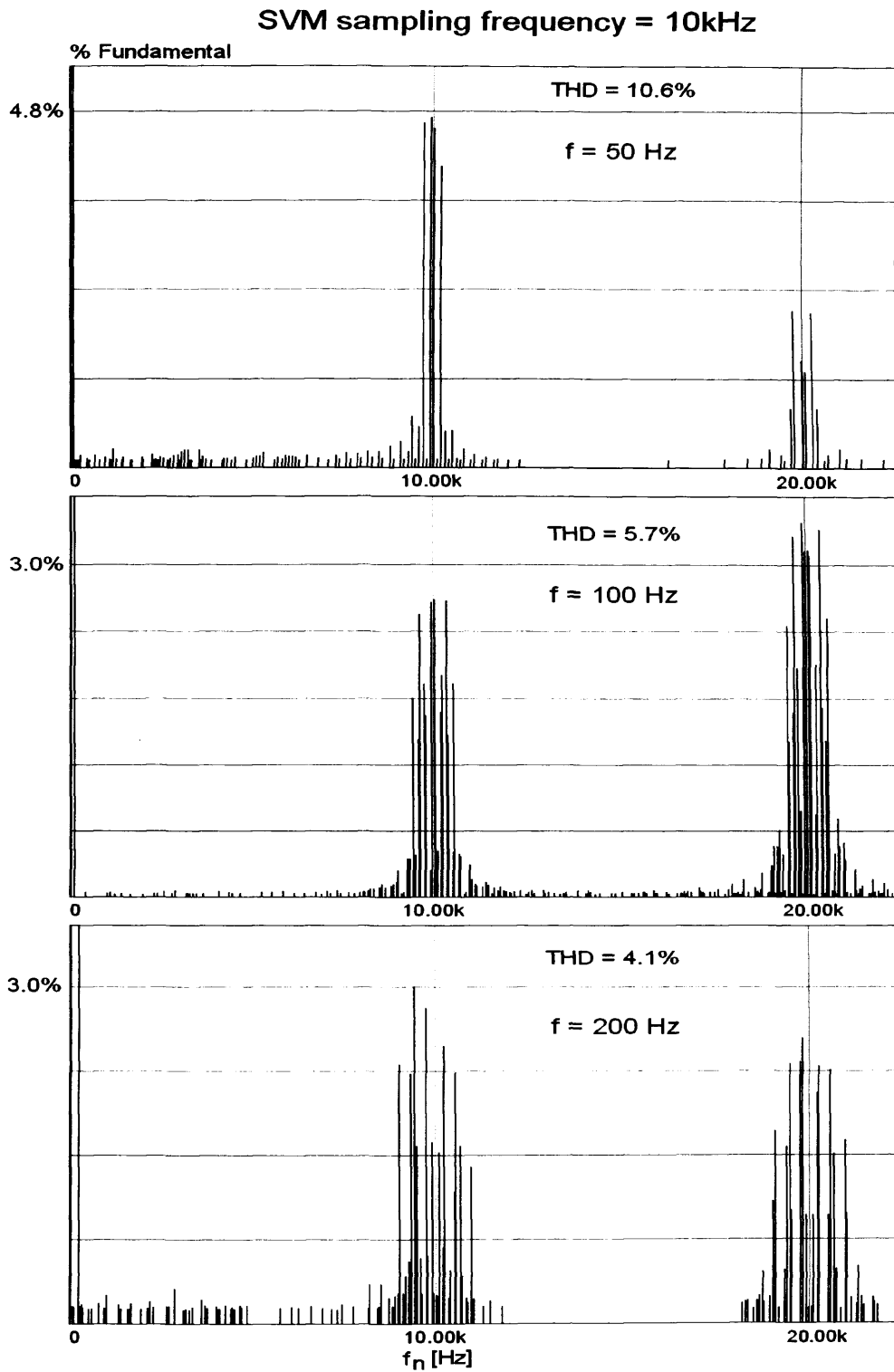


Fig 5.45. Harmonic spectra of induced voltages produced by the matrix converter (§ 4.4.2) and *THD* [%] at 50 Hz, 100 Hz and 200 Hz and 10 kHz sampling frequency in M700 – 65A laminations (1.5 T peak flux density)

Following harmonic spectra of induced voltages, one cycle of associated flux density curves at 50 Hz, 100 Hz and 200 Hz magnetising frequency and 2.5 kHz, 5 kHz and 10 kHz SVM sampling frequency are introduced in fig. 5.46. Flux density curves at 50 Hz can be described as very smooth waveforms at all SVM sampling frequencies. The moderate improvement in the performance of the steel derived from selecting a highest SVM sampling frequency (10 kHz) must be considered along with the collateral effect that such value of  $f_s$  would have on semiconductor losses in the matrix converter. Although core losses in laminated steel may be reduced, it is important to consider the beneficial impact of this reduction on global efficiency in the variable speed drive.

As discussed earlier, a highest value of SVM sampling frequency becomes mandatory when 200 Hz is selected as magnetising frequency, not only to reduce the number of high clusters, but to ensure proper spacing between them. Flux density curves are affected by discontinuities that disrupt domain wall motion during the magnetising process and increase dynamic losses in the laminations. These periods of acceleration and deceleration become proportionally longer as the fundamental cycle gets reduced. A noticeable improvement in the smoothness of the flux density curve was observed at 200 Hz magnetising and 10 kHz SVM sampling frequencies. Values of *THD* [%] associated to flux density curves in M700-65A laminations are introduced in table 5.24 at 50 Hz, 100 Hz and 200 Hz magnetising frequency. SVM sampling frequencies were 2.5 kHz, 5 kHz and 10 kHz. Peak flux density was equal to 1.5 T.

Table 5.24. *THD* [%] in M700-65A laminations  
at 2.5 kHz, 5 kHz and 10 kHz SVM sampling frequency (1.5T peak flux density)

	SVM sampling frequency		
	2.5 kHz	5 kHz	10 kHz
50 Hz	0.67	0.34	0.17
100 Hz	0.69	0.33	0.19
200 Hz	1.18	0.48	0.23

An increase in magnetising frequency from 50 Hz to 200 Hz lead to a rise in *THD* of 76.1% at  $f_s = 2.5$  kHz. Increases by 41.1 % and 35.2 % were reported for respective SVM sampling frequencies 5 kHz and 10 kHz.

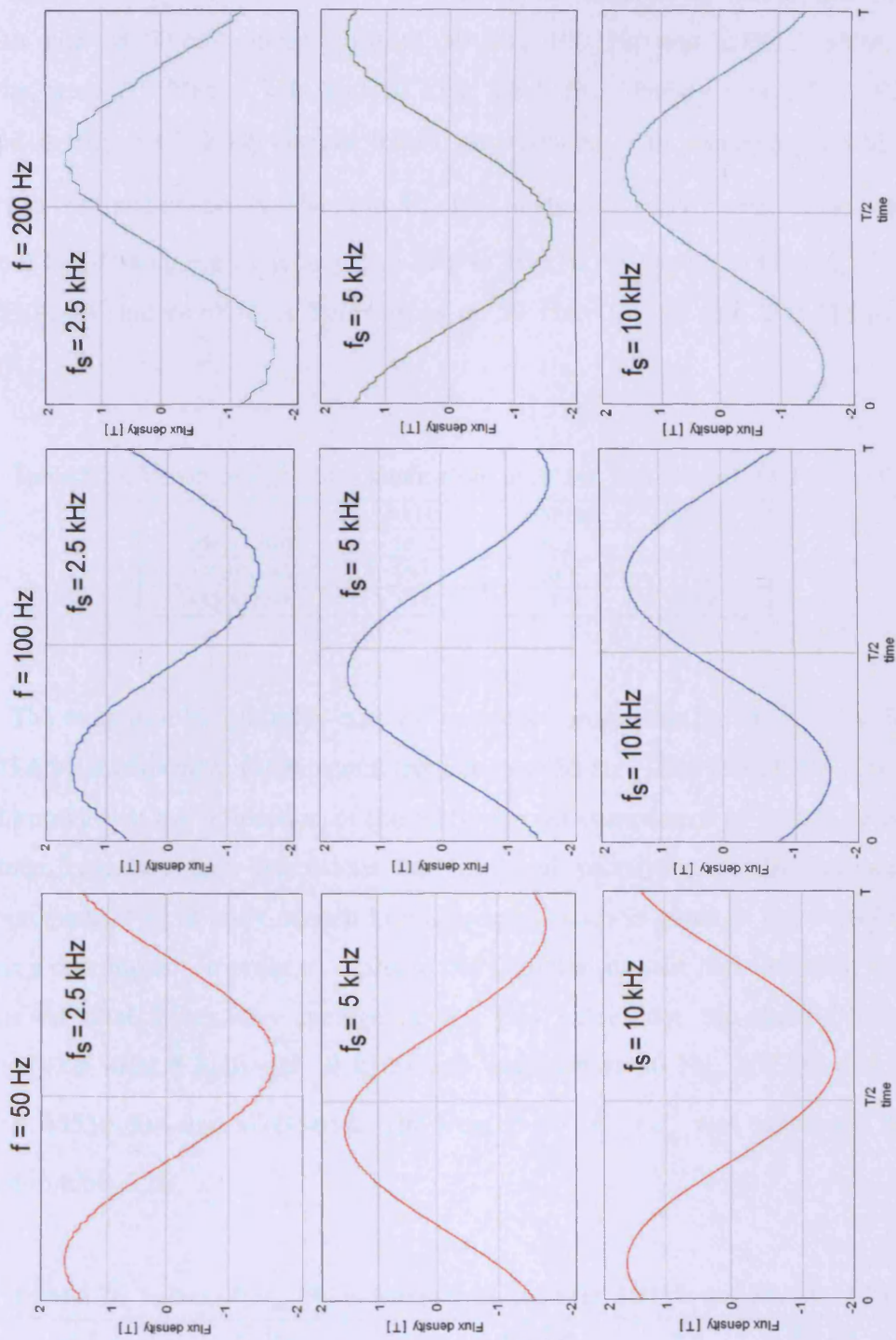


Fig 5.46. One cycle of induction in M700-65A subjected to line-line matrix converter excitation

Magnetising frequency: 50 Hz, 100 Hz and 200 Hz

SVM sampling frequency: 2.5 kHz, 5 kHz and 10 kHz

### 5.5.3 Eddy-current losses

Specific eddy-current losses were calculated [§5.2.1a eq (5.17)] for M470-50A, M530-50A and M700-65A laminations at 50 Hz, 100 Hz and 200Hz. SVM sampling frequencies were 2.5 kHz, 5 kHz and 10 kHz. Peak flux density was 1.5 T. Results are introduced in fig. 5.47. Eddy-current losses are reduced with increasing SVM sampling frequency in the three materials. The drop  $\nu_{ec}$  [%] in specific eddy-current losses caused by a variation of SVM sampling frequency (2.5 kHz to 10 kHz) is shown in table 5.25 for M470-50A, M530-50A and M700-65A laminations at 50 Hz, 100 Hz and 200 Hz magnetising frequency.

Table 5.25. Values of  $\nu_{ec}$  [%] in laminations at 50 Hz, 100 Hz and 200 Hz (1.5T)

	50 Hz	100 Hz	200 Hz
M470-50A	16.7	9.3	10.0
M530-50A	15.9	10.8	11.6
M700-65A	15.6	11.6	11.4

The reduction [%] in eddy-current losses is comparable in M470-50A, M530-50A and M700-65A at respective fundamental frequencies (50 Hz, 100 Hz and 200 Hz). However, it is well known that the proportion of the eddy-current component of loss is determined by magnetising frequency and dimensions and physical properties of the laminations. The relative weight  $R_{ec}$  [%] of eddy-current losses to total losses is given in fig. 5.48 for identical magnetising conditions. In order to evaluate the potential impact that lowering eddy-current losses has on total losses, the average of  $R_{ec}$  [%] values for the three SVM sampling frequencies (2.5 kHz, 5 kHz and 10 kHz) was obtained at 50 Hz, 100 Hz and 200 Hz in M470-50A, M530-50A and M700-65A. The term  $\Delta_{ec} = R_{ec} \cdot \nu_{ec}$  was calculated. Results are introduced in table 5.26.

Table 5.26. Values of  $\nu_{ec}$  [%] in laminations at 50 Hz, 100 Hz and 200 Hz (1.5T)

	50 Hz		100 Hz		200 Hz	
	$\overline{R_{ec}}$	$\Delta_{ec}$	$\overline{R_{ec}}$	$\Delta_{ec}$	$\overline{R_{ec}}$	$\Delta_{ec}$
M470-50A	31.3	5.2	35.9	3.3	43.9	4.4
M530-50A	26.9	4.3	41.8	4.5	43.4	5.0
M700-65A	40.6	6.3	62.8	7.3	62.0	7.1

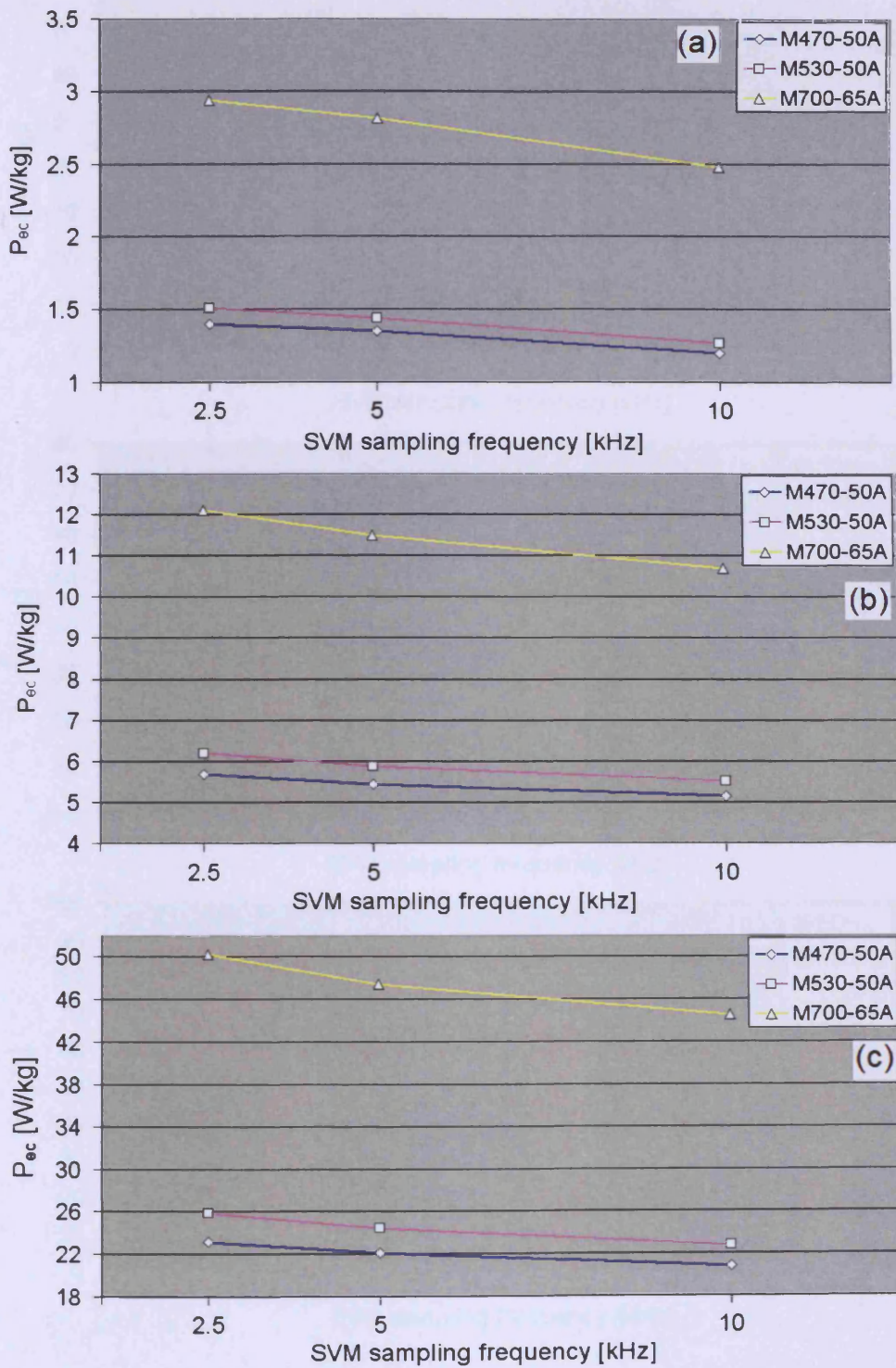


Fig. 5.47. Variation of specific eddy-current losses  $P_{ec}$  [W/kg] in M470-50A, M530-50A and M700-65A laminations subjected to line-line matrix converter excitation at 1.5 T peak flux density and magnetising frequencies (a) 50 Hz – (b) 100 Hz – (c) 200 Hz

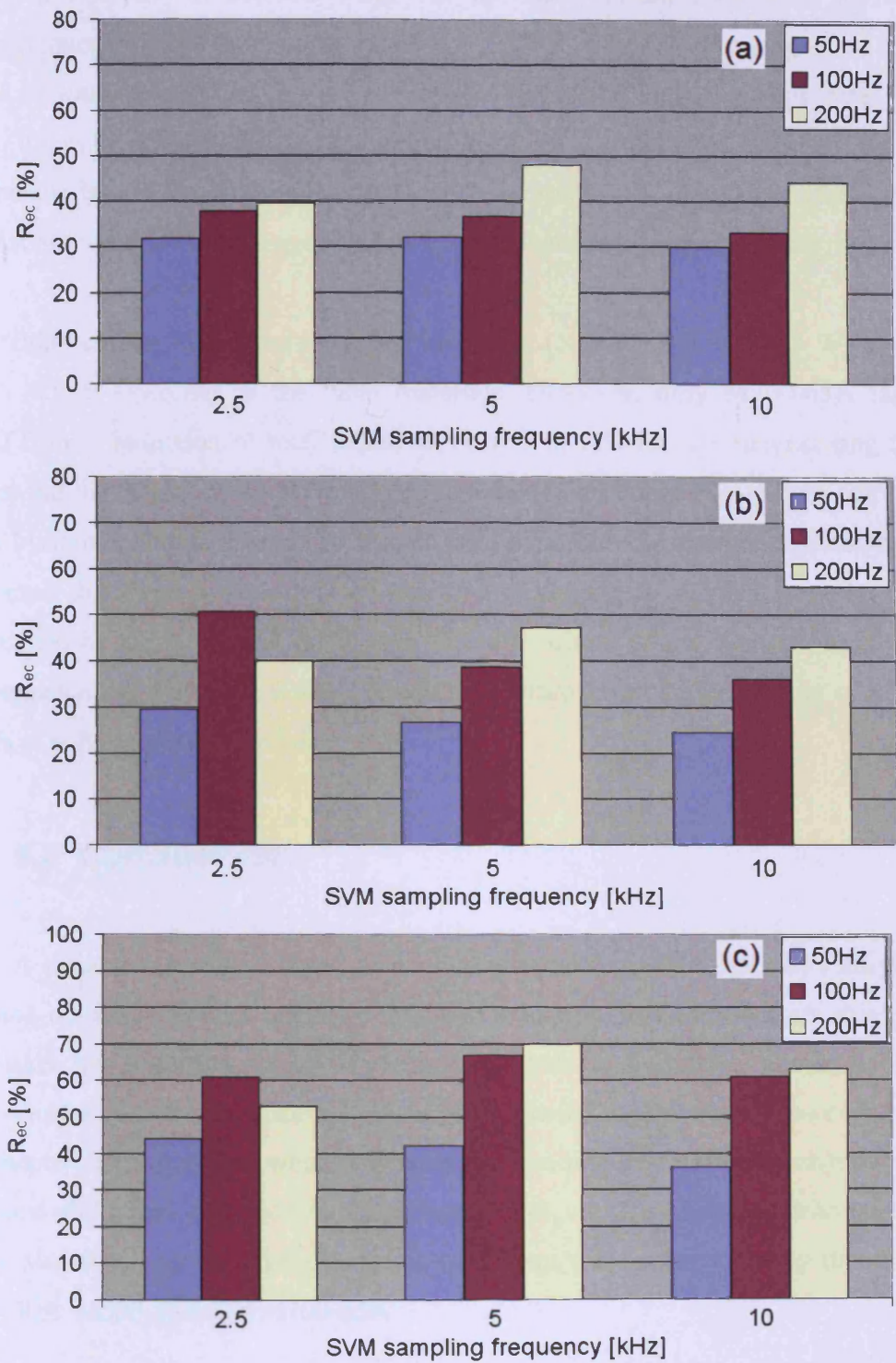


Fig. 5.48. Proportion  $R_{ec}$  [%] of eddy-current losses in M470-50A, M530-50A and M700-65A laminations subjected to line-line matrix converter excitation at 1.5 T peak flux density and magnetising frequencies (a) 50 Hz – (b) 100 Hz – (c) 200 Hz

The decrease in absolute values of the eddy-current component at high SVM sampling frequency in the three materials (4.4 % - 5.0 % - 7.1 %) is accompanied by a larger reduction of total losses (19.3 % - 17.8 % - 25.5 %) at the highest magnetising frequency (200Hz). It can be concluded that maintaining sufficiently high SVM sampling frequency is equally beneficial to eddy-current and dynamic hysteresis losses, due to smoother flux density curves that are more favourable to domain wall motion during the magnetising process.

Eddy-current losses were reduced at 50 Hz (5.2 % - 4.3 % - 6.3 %) and 100 Hz (3.3 % - 4.5 % - 7.3 %) in the three materials. However, only M700-65A laminations benefited from a reduction of total losses of 11.6 % at 100 Hz. As magnetising frequency decreases and the resistivity of the material increases, eddy-current losses are converted into losses of hysteretic nature, inherent to domain wall dynamics during the magnetising process. It is believed that these losses are more sensitive to variations in SVM sampling frequency than predicted by any analytical calculation of eddy-current losses. Recent studies point out micro-magnetism as a decisive field of research to improve the understanding of magnetising processes in soft magnetic materials.

## **5.6 Conclusions**

A theoretical analysis based on Poynting vector revealed that physical phenomena such as non-linearity (between magnetic field and induction) and eddy-current shielding effect must be taken into in the calculation of eddy-current losses. An analytical model for iron loss prediction under pulsating excitation (typical of fast-switching converter) has been introduced in this chapter. The approach, which accounts for non-linearity between magnetic induction and applied field and eddy-current shielding effect and has been benchmarked against Bertotti's statistical approach, showed good agreement with experimentally measured losses in M470-50A, M530-50A and M700-65A

Line-neutral voltages produced by three-phase matrix converters have properties (lower form factor, spreading of sideband harmonics in high clusters) which make them a more favourable magnetising signal than line-line voltage produced by two-level PWM DC-link converters. High PWM modulation indices improve the magnetising capability of line-line voltage of indirect converters considerably. On the contrary, low indices must be avoided whenever possible to prevent excessive core losses. Due to changes in their wave-shape that

lead to higher values of form factor, line-line voltage, typical of matrix converters, could effectively ensure better magnetisation of non-oriented steel at the highest magnetising frequency. However, the absence of subharmonics (present in line-neutral signals at different frequency than 50 Hz) makes line-line voltage an operational form of supply of asynchronous motors and features matrix converters as potential candidates for AC-AC links in variable speed drives. The requirement for sufficiently high values of SVM sampling frequency in matrix converter control was emphasised at high magnetising frequency. Iron losses in strips of the three materials subjected to line-line matrix converter excitation were decreased as a result. The analysis of iron losses was based upon harmonic spectra, total harmonic distortion and form factor of flux density curves and induced voltages.

## References

- [5.1] N. Burais, "Iron Losses Calculations in Non-oriented Steel Plate", *IEEE Transactions on Magnetics*, Vol 6, pp 2257 – 2579, November 1981.
- [5.2] Cogent Power Ltd, "Non-Oriented Fully Processed Steel", November 2002.
- [5.3] J. Gyselinck, L. Vandeveldel, J. Melkebeck, P. Dular, F. Henrotte, W. Legros, "Calculation of Eddy-Currents and Associated Losses in Electrical Steel Laminations", *IEEE Transactions on Magnetics*, Vol 35, N°3, pp 1191-1194, May 1999.
- [5.4] J. Barranger, "Hysteresis and Eddy-Current Losses of a Transformer Lamination viewed as an Application of the Poynting Theorem", *National Aeronautics and Space Administration (NASA)*, Nov 1965.
- [5.5] A. J. Moses and G. H. Shirkoohi, "Importance of Harmonic Phase Angle in Prediction of Iron Loss under Distorted Magnetisation", *Physica Scripta*, Vol 39, pp 523–525, 1989.
- [5.6] D. Casadei, G. Serra, A Tani, L. Zarri, "Matrix converter Modulation Strategies: A New General Approach Based on Space-Vector Representation of the Switch State", *IEEE Transactions on Industrial Electronics*, Vol 49, N°2, pp 370 – 381, April 2002.

## POWER CONSUMPTION IN DC-LINK CONVERTER-FED INDUCTION MOTORS: AN EXPERIMENTAL STUDY

---

The first step in the study of speed drives is a good understanding of the operation of standard converters and their role as suppliers of squirrel-cage induction motors. A broad range of DC-link converters are commercially available for the low power range. Knowledge of their performance and functionality is necessary to make a cost-effective selection of the most suitable converter for each induction motor. Nominal power of the rotating machine and desired frequency range of operation are important aspects that must be taken into consideration. In this chapter, the use of two DC-link converters (Toshiba – ABB) to feed two squirrel-cage induction motors (nominal power 0.75 kW and 2.2 kW) within the 50 Hz – 200 Hz frequency range is investigated. A method, based on measured power consumption in the four experimental speed drives, is presented in order to establish the relation between modulation index (inverter control) and core magnetisation.

### ***6.1 Description of goal and methodology***

#### **6.1.1 Motivation**

In this chapter, a method which combines measurements and analysis of two induction motors under supply by two commercial frequency converters is described. The goal of the method introduced is to establish the analytical relation between average peak flux density in the stator core of laminated steel (commonly used in induction motors) and modulation index in Pulse-Width-Modulation [PWM] based control. The procedure may be applied to induction motors in a broader power range. Although it is mainly focussed on induction motors (often used in industry applications), the approach described may also be applied to synchronous or Permanent-Magnet [PM] motors. Owing to higher efficiency combined to higher price, these motors are only used in 10% of the cases where power above 10MW (mining, marine applications) and constant rotational speed are required. Industrial robot applications rely upon PM servomotor applications as power density and low weight are paramount. As the reader will appreciate throughout the chapter, an adequate equivalent

circuit would be then required along with an estimation algorithm for losses in the magnet material (often NdFeB).

In pumps and fans applications in the low voltage range (less than 1000V across the DC-link), variable speed drives [VSD] have been highlighted as a suitable technical solution to replace throttled systems to regulate fluid flow. In order to fulfil this goal, a commercial VSD of competitive price is preferred. Since no significant requirements on dynamic performance or torque ripple exist, a two-level back-to-back converter (passive rectifier) operating in open-loop is satisfactory. The potential for energy savings (up to 30%) is at its highest when the motor rotating the pump or the fan works at full load only at limited periods of peak demand. In the remaining time, the motor is operated at partial load. In this particular condition, iron losses in the stator core become proportionally larger when compared to Joule losses in copper windings. Then, the control of average peak flux density in the mass of steel (iron losses) and load current (Joule losses) through an externally accessible parameter (such as modulation index) is an interesting feature for industrial users.

The method proposed is of particular interest for companies in power and automation technologies (ABB, Siemens, General Electric....) with motor and drive business divisions in which combined expertise in machine design and motor control is natural. In such companies, an integrated system (power converter + motor) is often offered. Therefore, detailed knowledge on the motors in the product port-folio contributes towards a very good accuracy of the approach documented in this chapter. For small drive manufacturers without a motor division, the purchase of several motors from different suppliers would be then needed to carry out experimental work. Thus, the relation between induction and control parameters can be established internally. Another alternative consists in exploring university relations and use academic resources for external consultancy.

### **6.1.2 Methodology**

#### 6.1.2a. Electrical parameter identification of the induction motor

The first step in the implementation of the method is motor characterization. Based upon specifications given by the motor supplier [nominal torque / speed, nominal slip, efficiency and power factor], direct measurement of stator resistance ( $R_1$ ) and leakage inductance ( $L_1$ ) with a multimeter and a locked rotor test, the equivalent circuit associated to

## CHAPTER 6: POWER CONSUMPTION – DC-LINK CONVERTER-FED MOTORS

the induction motor is solved analytically (fig 6.1). The assumption made for solving the analytical system of equations is that the modulus of the rotor impedance  $|Z_2'|$  is proportional to the modulus of the stator impedance  $|Z_1|$  by a factor  $K$  which is determined through the locked rotor test. The use of the equivalent circuit for analysis of induction motors is a well established method that yields satisfactory results. When the emphasis is purely on motor control, the resistance in the magnetizing branch is often neglected as the motor is expected to run at full load most of the time. In order to capitalise on the potential for energy savings, the motor is expected to run at partial load on a more frequent basis. Under these conditions, iron losses become proportionally larger and the resistance in the magnetizing branch must be considered.

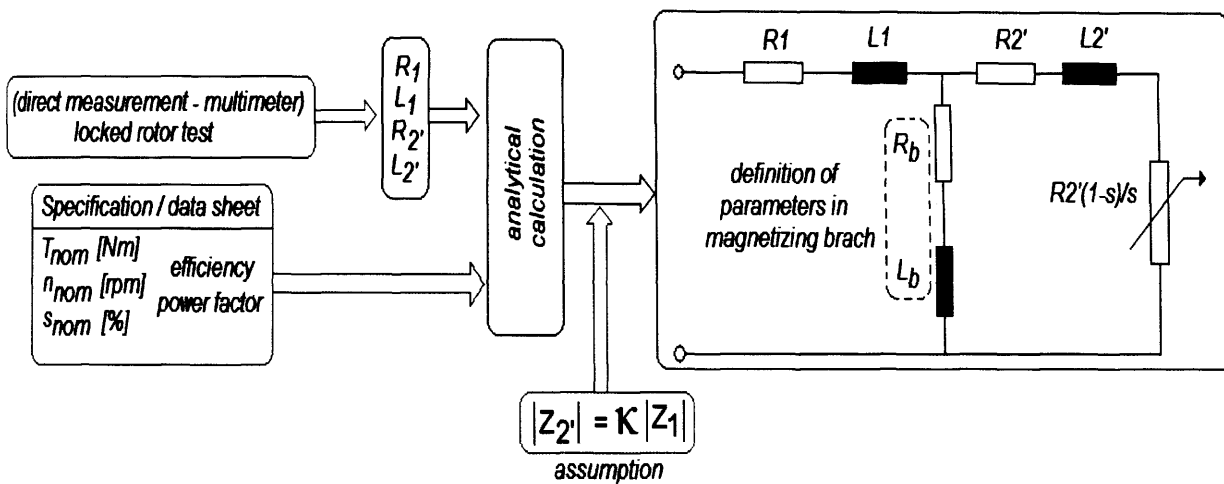


Fig 6.1 Graphic description of motor characterization

Parameters in the equivalent circuit are normally assumed constant. This is strictly true when the current has only one frequency component equal to the fundamental. In reality, the current flowing through copper windings of two-level PWM is harmonic distorted. From a theoretical perspective, a new set of motor parameters would then be required for each harmonic frequency in the load current. Thus, the equivalent circuit linked to each harmonic frequency should be fed separately by the voltage component of identical harmonic frequency.

The method proposed in this chapter aims at reaching a trade-off between satisfactory description of physical phenomena in the motor and pragmatism to establish the relation between peak flux density and modulation index. For this reason, an equivalent circuit with constant parameters is used throughout the analysis.

### 6.1.2b. Harmonic characterization of line-line voltage (two-level converter)

Once the induction motor for the experimental approach has been characterised, an inverter of suitable power ratings must be selected. By accessing the manual, frequency range and output voltage function can be identified. In the case of the Toshiba inverter used for the purpose of this PhD thesis, the output voltage regulation function is intimately linked to the PWM modulation index. Prior to experimental work, a simple simulation model is used to obtain line-line voltages (typical of two-level back-to-back converters) for a sufficiently broad range of modulation indices and electrical frequencies (50 – 75 – 100 – 150 ... 200Hz). Then, two parameters of the voltage (such as form factor and THD) directly related to the harmonic characteristics of the wave-shape must be calculated. This task should be executed for a reasonable number of modulation indices, since linear interpolation will give satisfactory results. The calculation of the RMS value of the voltage is also required. Digital oscilloscopes that monitor voltages have powerful built-in features that allow RMS calculation. Post processing of line-line voltages from a source file (Excel) may be executed with a variety of tools. Day Post Processor [Ansoft Simplorer] was the software tool selected for this PhD work. A Matlab-Simulink model was used to generate line-line voltages. The model that generates line-line voltages should include at least two different PWM modulation schemes. Due to easy implementation in a digital signal processor, space-vector PWM has become the most common modulation strategy and is preferred over natural sampled PWM. However, the relation between space-vector and other PWM schemes (symmetrical/asymmetrical regular sampled PWM) is well described theoretically.

### 6.1.2c. No-load measurements in the induction motor

No-load measurements in the induction motor fed by the frequency converter are carried out for a given number of electrical frequencies. Line-line voltages as well as their RMS values must be recorded by a digital oscilloscope for every measuring case. The active power  $P$  [W], the apparent power  $S$  [VA] and the RMS value of the current flowing to the induction motor must be measured by the means of a power analyser. Once the measurements are completed and experimental data transferred to an Excel file, the variation of active power, apparent power and RMS current with RMS line-line voltage is plotted for each electrical frequency (50 – 75 – 100...200 Hz). Furthermore, a Fast Fourier Transform [FFT] analysis must be performed to obtain form factor and THD for each experimentally measured line-line voltage wave-shape. By accessing the reference curves generated in a simulating environment,

the relation between the RMS values of measured voltages indices for each electrical frequency and subsequent PWM modulation indices is easily obtained. Therefore, RMS load current, and active / apparent powers absorbed by the induction motor are mapped to a PWM modulation index (fig 6.2).

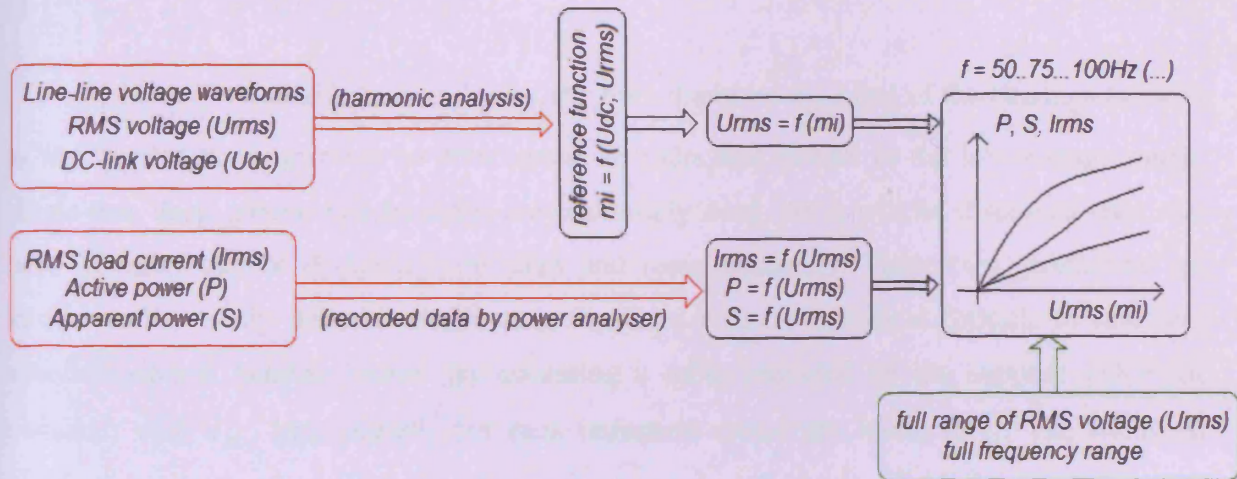


Fig 6.2 Graphic description of no-load measurement in the induction motor

#### 6.1.2.d. Loss segregation

The losses measured in the induction motor under no-load conditions consist of mainly four components: Joule losses in copper windings ( $P_1$ ), losses caused by mechanical friction in the bearings ( $P_{frict}$ ), windage losses ( $P_{wind}$ ) and losses in the stator core of laminated steel ( $P_{fe}$ ). Stray load losses ( $P_{stray}$ ), which are also incurred, reach their highest value at full load conditions. In the measurements performed, the motor was unloaded and  $P_{stray}$  assumed to be negligible. Since iron losses must be extracted from total measured losses, the three loss components ( $P_{wind}$ ,  $P_{frict}$ ,  $P_1$ ) must be quantified analytically and subtracted from measured losses.

The calculation of Joule losses in copper windings is straightforward by knowing the stator resistance  $R_1$  [ $\Omega$ ] and the RMS load current  $I_{RMS}$  [A].

$$P_1 = 3R_1 I_{RMS}^2 \quad (6.1)$$

Nonetheless, some inaccuracy may be introduced by taking the value of cold stator resistance  $R_0$  [ $\Omega$ ] at reference temperature  $\theta_0$  [ $^{\circ}\text{C}$ ] instead of the resistance at the winding temperature  $\theta_1$  [ $^{\circ}\text{C}$ ]. As tests needed for the experimental approach are run, temperature in motor copper windings may increase substantially. An increase in winding temperature from

20°C to 70°C would result in an increase in stator resistance of approximately 19.5%. In order to reduce the inferred inaccuracy, measurements for each point were run every fifteen minutes.

$$R_1 = R_0(1 + \alpha(\theta_1 - \theta_0)) \quad (6.2)$$

In order to quantify friction losses, the bore diameter  $d_{bore}$  [m] of the bearings (as well as the type of bearing) must be determined. In induction motors in the low voltage range, single-row deep groove ball bearings are commonly used. As it will be discussed later, the bore diameter can be deduced from shaft and rotor diameters. These two parameters are known and/or easily determined. Bearing suppliers give an analytical formula to calculate speed-dependent bearing losses. By accessing a table provided by the supplier (SKF for instance) with  $d_{bore}$  [m], suitable for each induction motor are found [6.1]. The frictional moment  $M_{frict}$  [Nm] in the bearings is calculated as a function of the static bearing load  $C$  [N].  $\tau$  is a friction coefficient for single row deep groove ball bearings. Then, losses caused by mechanical friction in bearings are obtained for a given rotational speed  $n$  [rpm]

$$P_{frict} = M_{frict} \times \frac{2\pi}{60} n = \left( \frac{1}{2} \tau * P_{dyn} d_{bore} \right) \times \frac{2\pi(1-s)n_s}{60} = \frac{\pi}{60} \mu(0.1C) d_{bore} \times (1-s)n_s \quad (6.3)$$

Windage losses result from the friction of the enclosed fan that ensures internal motor cooling with air. This loss component is mainly dependent on rotational speed but is influenced by air physical properties (temperature, viscosity). Their value for several speeds synchronous speeds targeted during the measurements is also calculated analytically based on [6.2].

#### 6.1.2e. Calculation of the mass of the stator core of laminated steel

In order to establish the relation between peak flux density and PWM modulation index, the mass  $m_{fe}$  [kg] of the stator core must be estimated as accurately as possible without compromising the pragmatism of the method. Data such as shaft diameter  $d_{shaft}$  [m] and external dimensions are well documented in the catalogue advertised by the motor supplier. In industry applications without specific requirements on weight or power density, cast iron squirrel cage induction motors are the straightforward choice. External motor dimensions (length  $L_{ext}$  [m], diameter  $d_{ext}$  [m]) are therefore normalised for all power ranges.

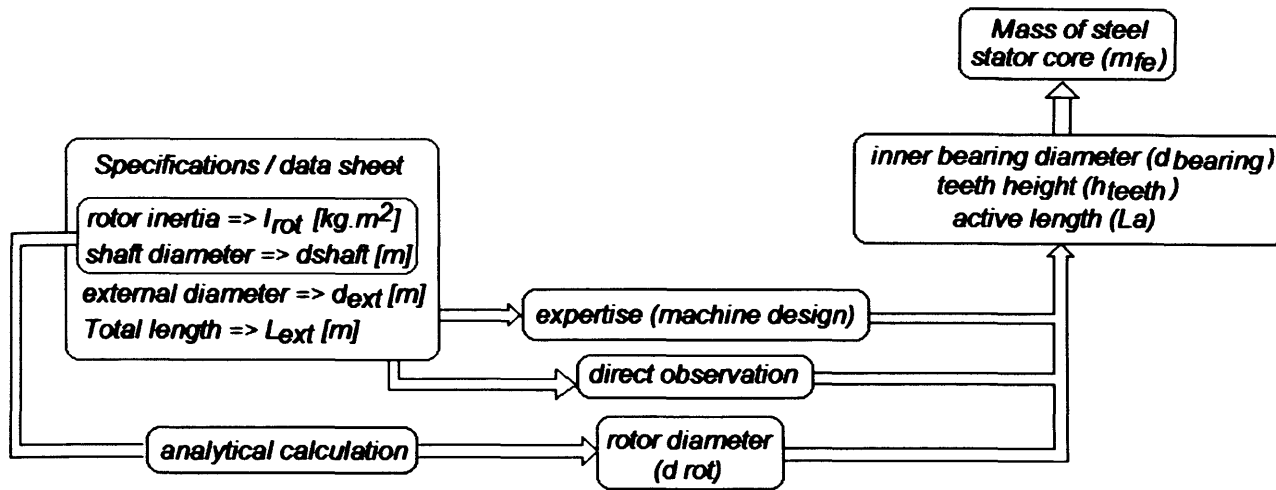


Fig 6.3 Calculation of the mass of steel in the stator core

Based on parameters such as  $d_{\text{shaft}}$ ,  $L_{\text{ext}}$  and  $d_{\text{ext}}$ , engineers with expertise in machine design can deduce geometry parameters [bore diameter, active length  $L_a$  [m] and teeth height / width] required for mass calculation. Alternatively, the motor can be opened and information obtained by direct observation. Rotor inertia  $I_{\text{rot}}$  [kg.m<sup>2</sup>] is known from the technical data sheet given by the motor supplier. By describing the rotor as a hollow cylinder of internal diameter  $d_{\text{shaft}}$  [m] and active length  $L_a$  [m], an analytical formula is used to determine the rotor diameter  $d_{\text{rot}}$  [m].  $\delta$  [kg.m<sup>-3</sup>] is the density of steel (7750 kg.m<sup>-3</sup>).

$$I_{\text{rot}} = \frac{m_{\text{rot}}}{2} \left[ \frac{d_{\text{rot}}^2}{4} + \frac{d_{\text{shaft}}^2}{4} \right] = \frac{\pi}{2} \left[ \frac{d_{\text{rot}}^2}{4} - \frac{d_{\text{shaft}}^2}{4} \right] L_a \delta \times \left[ \frac{d_{\text{rot}}^2}{4} + \frac{d_{\text{shaft}}^2}{4} \right] = (\pi \times L_a \delta) \times \left[ \frac{d_{\text{rot}}^4}{32} - \frac{d_{\text{shaft}}^4}{32} \right] \quad (6.4)$$

$$d_{\text{rot}} = \sqrt[4]{d_{\text{shaft}}^4 + \frac{32I_{\text{rot}}}{\pi L_a \delta}} \quad (6.5)$$

The area of the cross-section of the stator core is calculated as the sum of two terms. The first term corresponds to the area of hollow circle of external diameter  $d_{\text{ext}}$  [m] and internal diameter  $d_x$  [m]. The magnitude  $d_x$  [m] denotes the base teeth diameter. The second term is calculated as a fraction ( $\lambda$ ) of a hollow circle of external diameter  $d_x$  [m] and internal diameter  $d_{\text{rot}}$  [m]. The normalised stator core mass ( $m_{\text{fe}}^*$ ) is illustrated (fig. 6.4) for three values of the ratio ( $d_{\text{rot}} / d_{\text{ext}}$ ) (0.5, 0.575 and 0.625) and two values of  $\lambda$  (1/2 and 1/3).

$$m_{\text{fe}}^* = \left[ 1 + \frac{(\lambda - 1)d_x^2 - \lambda d_{\text{rot}}^2}{d_{\text{ext}}^2} \right] \quad (6.6)$$

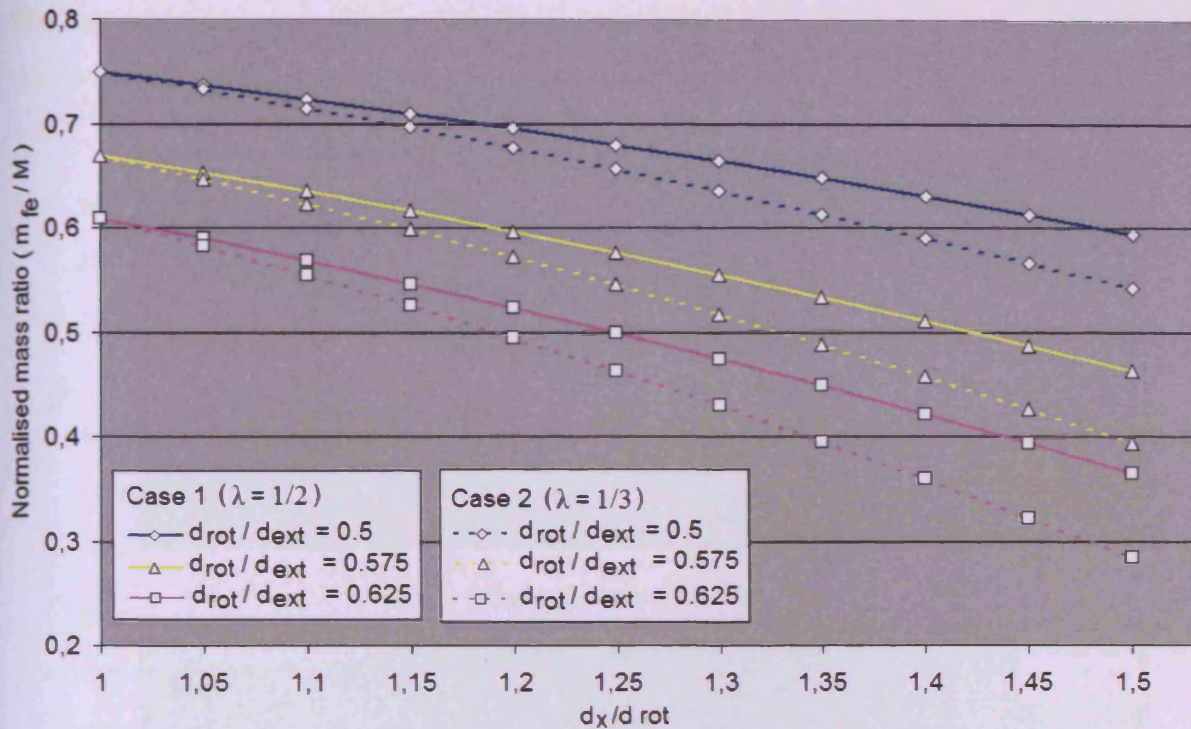


Fig 6.4. Variation of normalised mass ratio ( $m_{fe}^*$ ) with base teeth diameter ( $d_x$ )

By accessing such a graph a value of  $\lambda$  and the ratio of rotor to external diameter, the normalised mass ration  $m_{fe}^*$  is defined and used for estimating the mass of the stator core as given in (x.x). The term  $M$  is the mass of a cylinder of external diameter  $d_{ext}$  [m] and length  $L_a$  [m]

$$m_{fe} = M \times m_{fe}^* = \frac{\pi d_{ext}^2}{4} (L_a \delta) \times m_{fe}^* \quad (6.7)$$

#### 6.1.2f. Determination of specific apparent power losses in the stator core

Once iron losses ( $P_{fe}$ ) for each measured point are extracted analytically from total losses, specific power losses  $p_{fe}$  [W.kg<sup>-1</sup>] are calculated as the ratio of  $P_{fe}$  to the stator core mass  $m_{fe}$ . By using the parameters ( $R_b$ ;  $L_b$ ) in the magnetizing branch of the equivalent circuit, specific apparent power losses  $s_{fe}$  [VA.kg<sup>-1</sup>] are determined in (6.8)

$$s_{fe} = \frac{P_{Fe}}{\cos \left[ \tan^{-1} \left( \frac{2\pi \times f \times L_b}{R_b} \right) \right]} \quad (6.8)$$

The variation of specific apparent power  $s_{fe}$  [VA.kg<sup>-1</sup>] with peak flux density in M400-50A and M680-50A was obtained from a steel supplier [6.3] at 50 Hz, 100 Hz and 200

Hz magnetising frequencies (fig 6.5). These two grades of non-oriented steel are within the recommended reference range for low power induction motors [6.3].

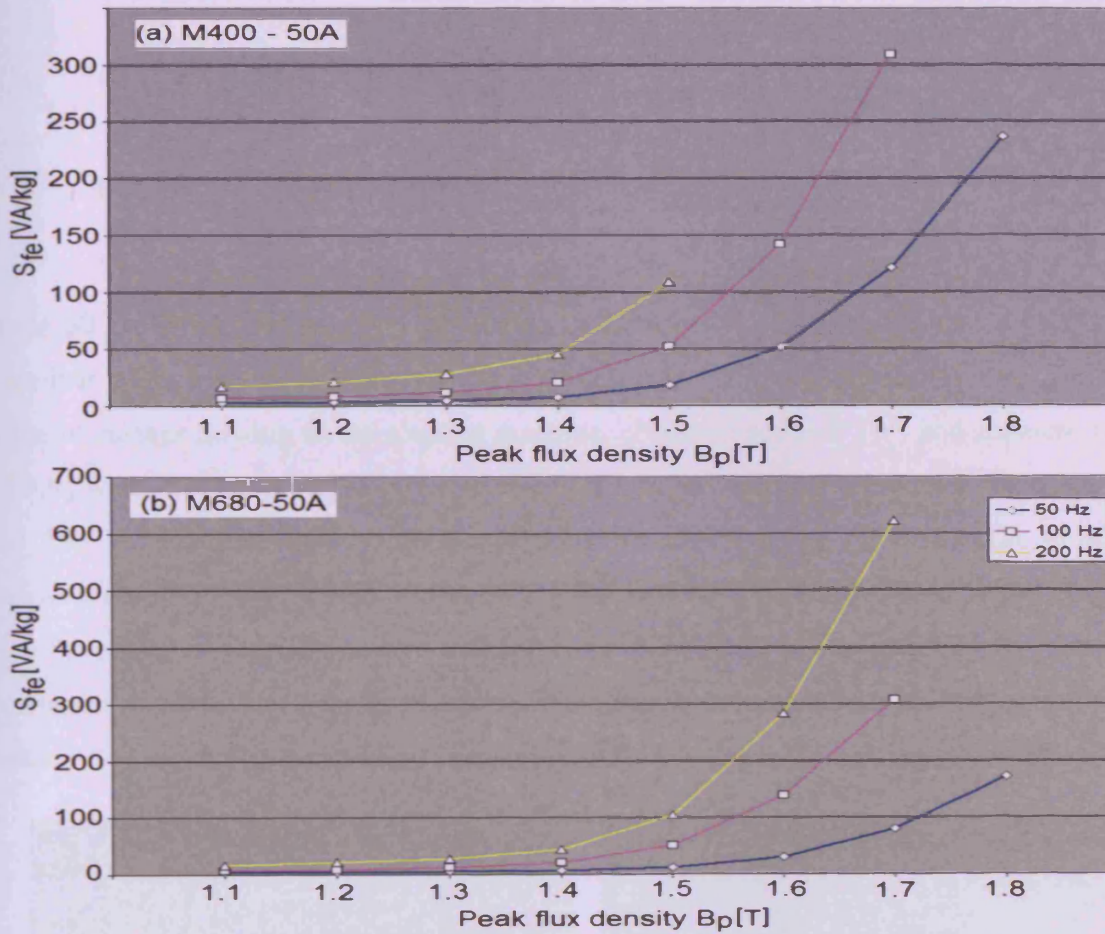


Fig 6.5. Variation of specific apparent power  $s_{Fe}$  [VA/kg] with peak flux density  
 (a) M400-50A (b) M680-50A

The importance of identifying the grade of steel used in the stator core must be emphasized. Because the selection of the material remains crucial to ensure profitability and satisfy customer requirements on quality, motor suppliers are usually reluctant to reveal the referred steel grade. This hurdle may be overcome in companies with motor and drives divisions, where technical information can be shared. On the contrary, small drive manufacturers could find it more difficult to access such technical data without relying upon research groups or external consultants with established knowledge on electrical steels. Increasing demands on energy efficiency in low voltage induction motors (IEC classes) in the last ten years has favoured non-oriented steels with lower losses thanks to lower lamination thickness and higher silicon content. By accessing the graph (fig 6.x) with values

of  $s_{fe}$  (table 6.9), the average peak flux density in the mass of laminated steel is obtained for every measured point associated to a given electrical frequency and modulation index.

## 6.2 Experimental procedure

### 6.2.1 Test bench

Motors A and B (§ 6.2.2) were energised under no-load conditions by the three-phase 50 Hz sinusoidal supply via variable transformer B (§ 4.2.2) connected to the grid. Line-line voltage and its RMS value were monitored by the digital oscilloscope. The RMS value of current flowing to the rotating machine, absorbed active  $P$  [W] and apparent power  $S$  [VA] were measured by the power analyser. Line-line voltages were set to between 50 V and 250 V and their RMS value recorded by the digital scope (§ 4.2.2). The un-loaded motors were fed by TOSHIBA TOSVERT VF-A3 (§ 6.2.3a). The ABB ACS 140 converter was then used to supply motors A and B (§ 6.2.3b). Fig. 6.6 and fig. 6.7 show the experimental set-up for measurements under the four combinations of DC-link converter and motor.



Fig. 6.6. Experimental set-up with TOSHIBA VF-A3 inverter

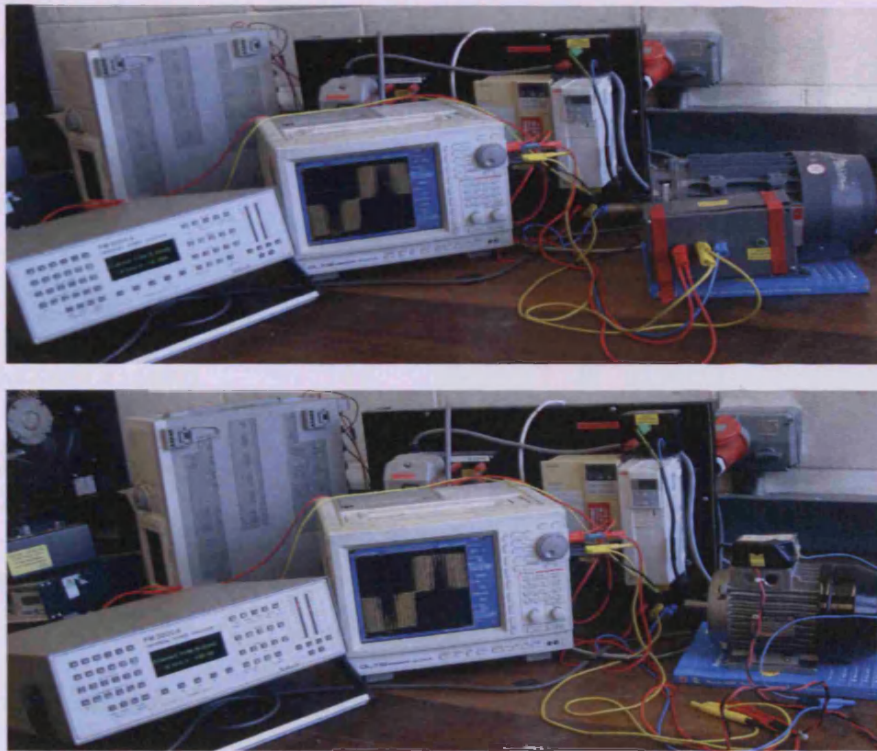


Fig. 6.7. Experimental set-up with ABB ACS 140 inverter

### 6.2.2 Induction motors

Motor A is a squirrel-cage three-phase induction motor (fig. 6.8). Its main characteristics are listed in table 6.1. Resistance and inductance of stator windings were measured by a HP multimeter and a TENMA 72 - 6634 LCR meter, respectively (§ 4.2.2).

Table 6.1. Characteristics of motor A

CLARKE Motor type 80B/4	
Nominal power [kW]	0.75
Nominal voltage [V] – (Δ – Y)	230 - 400
Nominal current [A] – (Δ – Y)	3.4 – 2.0
Connection of stator windings	Δ
Synchronous speed [rpm]	1500
Nominal slip $s_{nom}$ [%]	5.33
Stator resistance per phase $R_1$ [ $\Omega$ ]	9.6
Leakage inductance $L_1$ [mH]	46.4

Fig. 6.8. Induction motor A



Motor B is an induction motor of nominal power 2.2 kW. Its main parameters are introduced in table 6.2. Resistance and inductance of stator windings were measured by the multimeter and impedance meter used for motor A (§ 4.2.2).

Table 6.2. Characteristics of motor A

Fig. 6.9. Induction motor B

Brook Crompton Parkinson AC motor	
Nominal power [kW]	2.2
Nominal voltage [V] – (Δ – Y)	240 – 415
Nominal current [A] – (Δ – Y)	8.5 – 4.9
Connection of stator windings	Y
Synchronous speed [rpm]	1500
Nominal slip $s_{nom}$ [%]	5.33
Stator resistance per phase $R_1$ [ $\Omega$ ]	3.5
Leakage inductance $L_1$ [mH]	14.2.



Both motors were supplied under sinusoidal voltage (50 Hz) via variable transformer A (§4.2.2) at an RMS line-line voltage  $U_{lock}$  of 200V. The shaft of the two induction motors was locked while the RMS current  $I_{lock}$  [A] was measured by the multimeter (§.4.2.2). The rotor impedance  $|Z_2'|$  [ $\Omega$ ] is calculated based on experimental measurements as the product of stator impedance  $|Z_1|$  and a factor  $\kappa$ .

$$|Z_1 + Z_2'| = |Z_1 + \kappa Z_1| = \frac{U_{lock}}{\sqrt{3}I_{lock}} \quad (6.9)$$

$$\kappa = \frac{U_{lock}}{\sqrt{3}I_{lock} \sqrt{(R_1^2 + (\omega L_1)^2)}} - 1 \quad (6.10)$$

Table 6.3. Experimental measured voltages and currents in the locked rotor test

	$U_{lock}$ [V]	$I_{lock}$ [A]	$ Z_1 $ [ $\Omega$ ]	$\kappa$
Motor A	200.9	4.2	17.45	0.583
Motor B	200.2	17.1	5.67	0.192

The parameters defining the equivalent circuit of motors A and B are given in table 6.4

Table 6.4. Equivalent circuit parameters for the motors A and B

	$R_1$ [ $\Omega$ ]	$L_1$ [mH]	$R_2'$ [ $\Omega$ ]	$L_2'$ [ $\Omega$ ]	$R_b$ [ $\Omega$ ]	$L_b$ [mH]
Motor A	9.6	46.4	5.6	27.8	162.0	382
Motor B	3.5	14.2	0.7	2.7	94.5	221

### 6.2.3 DC-link converters

#### 6.2.3a - TOSHIBA TOSVERT VF-A3

A description of this converter is given in § 4.2.1. When rotational speed of the motor increases, more power must be extracted from the DC-link. This is accomplished by adjusting the Output Voltage regulation function  $OV$  [%]. Throughout the experimental work carried out,  $OV$  [%] was varied between 20 % and 100 %. Four output frequencies were selected for measurements of power consumption in motors A and B under supply by the TOSHIBA inverter: 50 Hz, 75 Hz, 100 Hz and 150 Hz. The PWM switching frequency was set to 3 kHz. The correlation between  $OV$  and  $U_{RMS}$  [V] supplied to motor A is given in table 6.5 for 50 Hz, 75 Hz, 100 Hz and 150 Hz.

Table 6.5. Correlation between  $OV$  [%] and  $U_{RMS}$  [V] (TOSHIBA – motor A)

OV[%]	20	30	35	40	45	50	55	60	65	70	75	80	85	90
50 Hz	204	252	276	299	317	338								
75 Hz	201	253		297	315	336	353	369	387	400	417			
100 Hz	202	252		295		333	347	365	383	398	412			
150 Hz								360	377	394	411	425	442	458

As the output frequency increases, more power is required to reach the desired rotational speed. As reactance in copper windings increases with frequency, higher voltage is needed to provide the required magnetising currents. Iron losses in laminated steel subjected to cyclic magnetisation increase with frequency. This demands more energy to maintain the air-gap flux density that ensures rotation of the shaft. This is accomplished by increasing  $OV$  values in the TOSHIBA inverter manually via the control panel. On the other hand, excessive power can not be supplied to the motor at low output frequency since the TOSHIBA inverter is internally protected against such resulting over-currents. The correlation between  $OV$  values and line-line voltage  $U_{RMS}$  [V] supplied to motor B is given in table 6.6 for 50 Hz, 75 Hz and 100 Hz.

Table 6.6. Correlation between  $OV$  [%] and  $U_{RMS}$  [V] (TOSHIBA – motor B)

OV	30	35	40	45	50	55	60	65	70	75
50 Hz	253	279	302	321	340					
75 Hz			297	315	335	369	386	398	416	
100 Hz					333	351	368	383	399	412

#### 6.2.3b - ABB ACS 140 – Standard 400 V series

This frequency converter (fig. 6.10) is used to supply the two induction motors in the nominal power range 0.12 kW – 2.2 kW. Its nominal ratings are listed in table 6.7.

Table 6.7. Characteristics of ABB ACS 140

Nominal power load [kW]	0.75	2.2
Input voltage [V]	380 – 480	
Cont output current (4 kHz)	2.0	4.9
Max output current (4 kHz)	3.0	7.4
Cont output current (16 kHz)	1.5	3.7
Max output current (16 kHz)	2.2	5.4
Switching frequency [kHz]	4 – 8 – 16	
Output frequency [Hz]	0 – 300	

Fig 6.10. ABB ACS 140



Throughout the work with the ABB ACS 140 converter, seven output frequencies were selected [50 – 75 – 100 – 125 – 150 – 175 – 200 Hz]. Three series of measurements were made at each frequency. Series A were associated with reference rotational speed 1500 rpm (50 Hz) while series B and C corresponded to reference values of 3000 rpm (100 Hz) and 3750 rpm (125 Hz), respectively. Measurements with motor B were made for the three series A, B and C. PWM switching frequency was set to 4 kHz. By selecting different speed reference, modulation indices assigned to every output frequency in the control algorithm of the converter are modified (fig 6.11). In series A (1500 rpm), the modulation index is already above unity (1.9) at 50 Hz. On the contrary, a very low modulation index (0.4) is assigned to 50 Hz in series B to 1500 rpm. Over-modulation only takes places when the selected speed is at least 3000 rpm. The method followed to establish the correlation between frequency and modulation index is based on values of *THD* and form factor of recorded line-line voltages produced by the converter. These values were used to access the graphs in § 4.3.2 to estimate the modulation index.

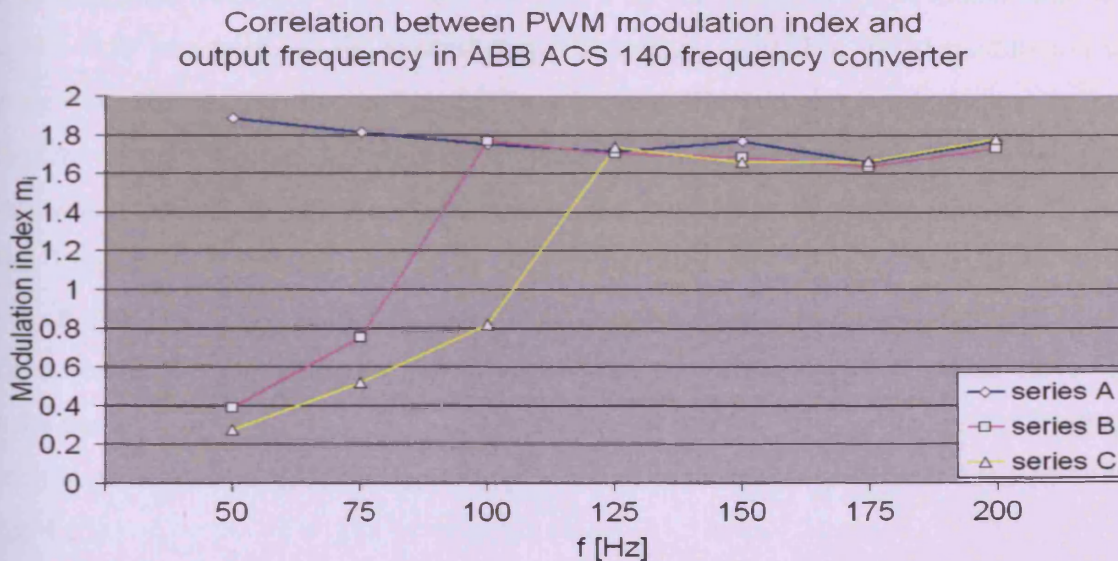


Fig. 6.11. Frequency variation of modulation index

### 6.2.4 Power consumption [TOSHIBA converter supply]

#### 6.2.4a – Motor A

The RMS current was measured for several values of  $OV$  [%] in the TOSHIBA inverter (fig. 6.12). Measured apparent power  $S$  [VA] and active power  $P$  [W] consumed by motor A are illustrated in fig. 6.13.

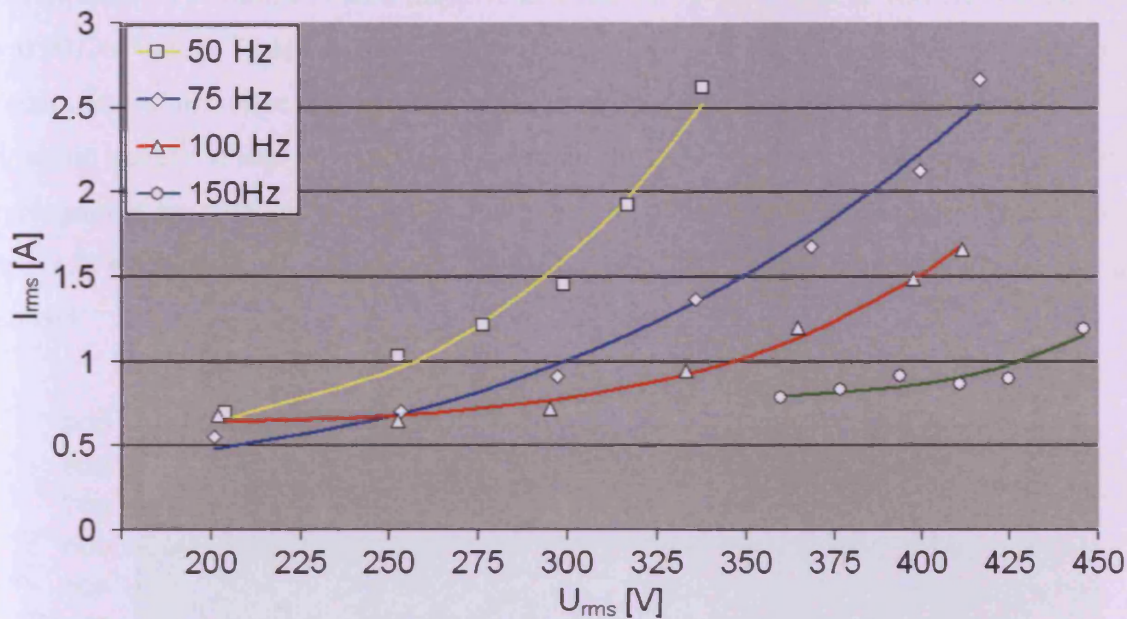


Fig. 6.12. Variation of RMS current with line-line voltage in motor A supplied by TOSHIBA inverter

PWM modulation indices at 50 Hz are within the 0.25 – 0.6 range approximately. At intermediate frequency (75 Hz and 100 Hz), a broader range of PWM modulation indices (0.25 – 0.9) was used. At the highest output frequency (150 Hz), PWM modulation index range was reduced to within the range 0.7 – 1.15. Line RMS current was highest at the lowest frequency, and lowest at the highest frequency, for RMS voltages above 250 V (fig. 6.8). This was expected since, for a given voltage, the impedance of copper windings increases with frequency. Moreover, current at 50 Hz increases more steeply with RMS line-line voltage than at 150 Hz. Increases in PWM modulation indices in the low range (0.25 – 0.9) are more effective in raising the power supplied by the inverter. As  $OV$  values move higher in the modulation index range (0.7 – 1.15), the rate of increase in electrical power feeding the machine is attenuated, along with the improvement in harmonic quality of line-line voltages (fig. 4.13).

When the output frequency increases (50 to 100 Hz) in the 200 to 300V range, the voltage drop in stator winding reactance increases while moderate losses are incurred in winding and iron loss resistances. When voltage increases beyond 300V and a high frequency (100 Hz) is maintained, copper losses  $P_{cu}$  and iron losses  $P_{fe}$  increase and the motor acts closer to a resistive load. The evolution of power factor indicates that the proportion of  $P_{cu}$  increases more steeply at 50 and 75 Hz than at 100 and 150 Hz. Consequently,  $PF$  values (which improve at a rate of 0.0033 / Volt at 100 Hz) increase only by 0.0013 / Volt at 75 Hz. In the frequency range 75 – 100 Hz, rotational speed of the motor remains in a close range that allows similar modulation indices in inverter control. Although harmonic quality in line-line voltages is similar, the increase in 25 Hz of supply frequency is accompanied by a better natural filtering effect by phase winding reactance that yields less harmonic-rich currents. Associated harmonic iron and copper winding losses are then reduced.

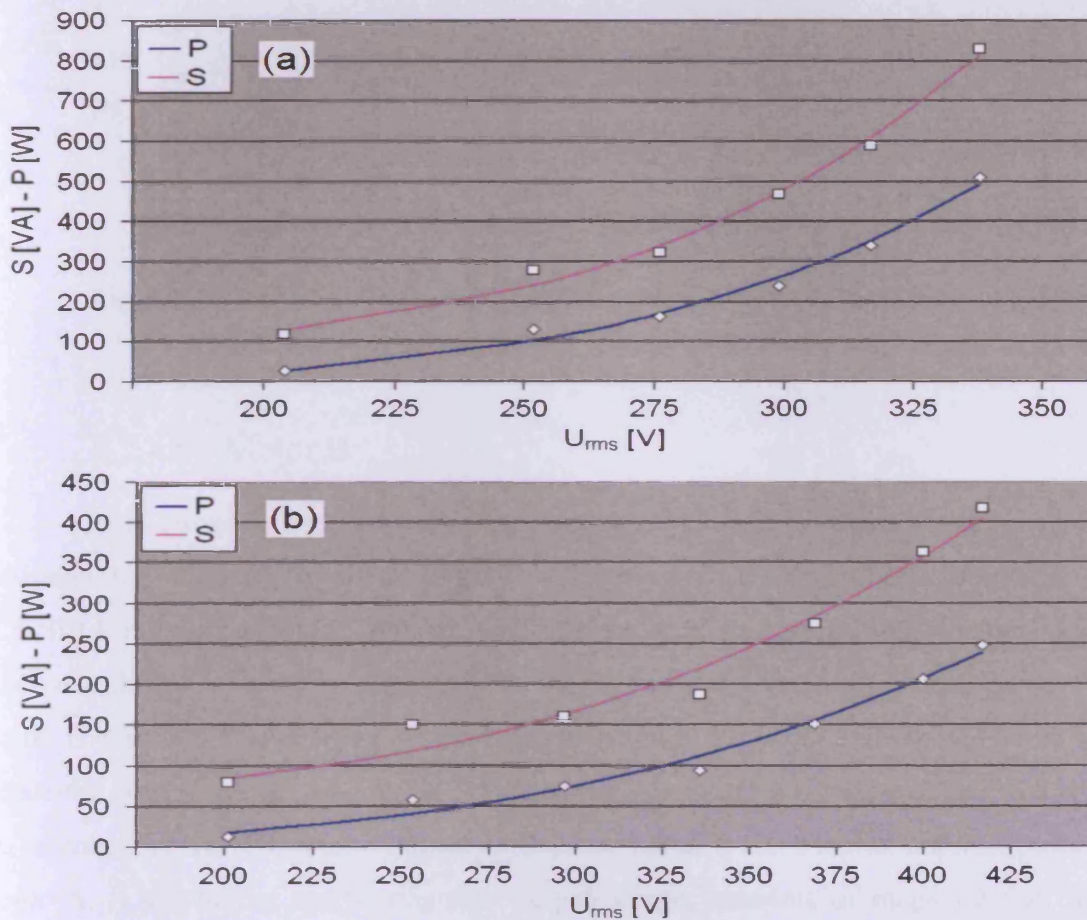


Fig. 6.13a. Variation of apparent and active power consumed with line-line voltage in motor A under supply by TOSHIBA inverter at (a) 50 Hz – (b) 75 Hz

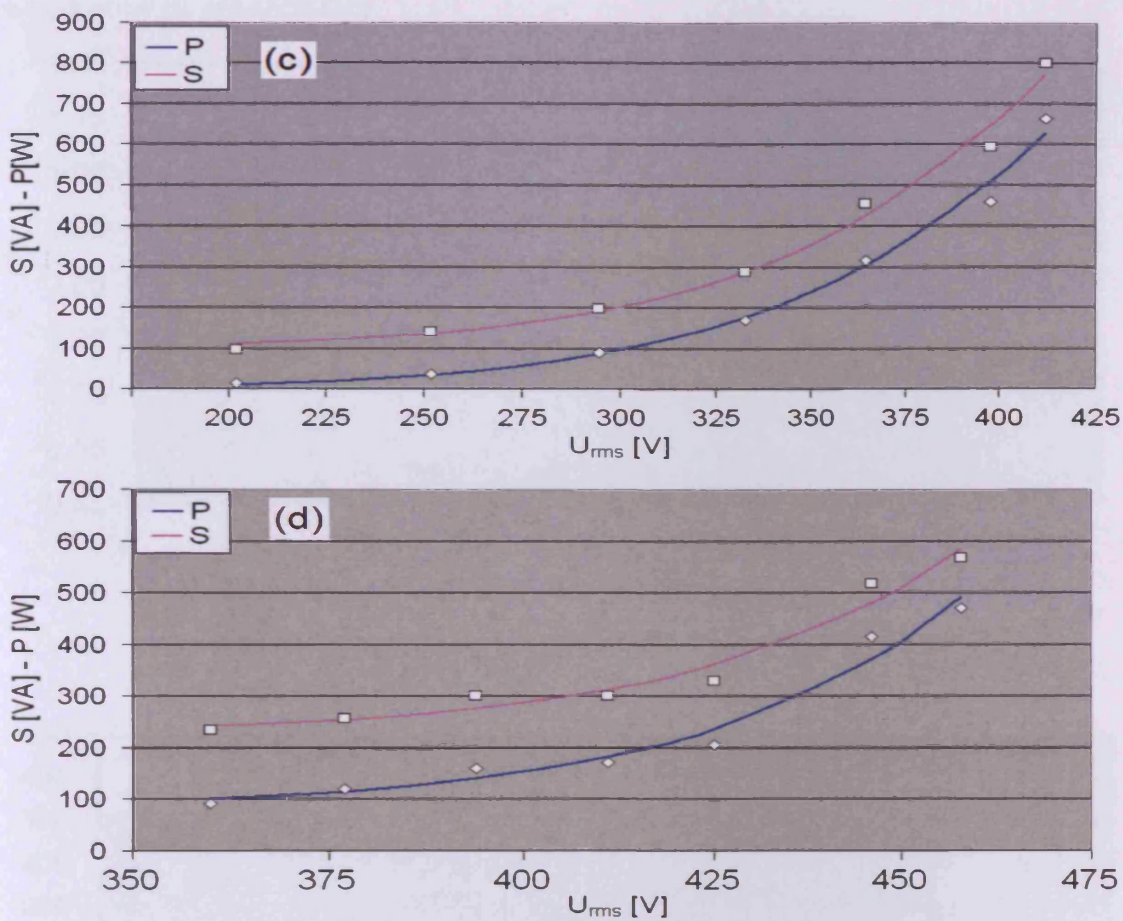


Fig. 6.13b. Variation of apparent and active power consumed with RMS voltage in motor A under supply by TOSHIBA inverter at (c) 100 Hz – (d) 150 Hz

### 6.2.4b – Motor B

RMS currents (fig. 6.14) along with apparent power  $S$  [VA] and active power  $P$  [W] consumed by motor B (fig. 6.14 and 6.15) were measured for several  $OV$  [%] values in the TOSHIBA inverter at 50, 75 and 100 Hz. The variation in current with voltage (fig 6.14) exhibits a similar trend at the three frequencies. Due to lower values of leakage inductance in motor B (table 6.1 and 6.2), the reactance does not reach as high values with supply frequency as in motor A. As a result, RMS current is less affected by the output frequency of the converter in motor B than in motor A. Because motor B has a higher nominal power than motor A, it has higher electromagnetic torque. Larger amounts of magnetic flux than in motor A need to be conducted through the air gap between stator and rotor cores. The magnetising inductance must be sufficiently high to maintain the required air-gap flux

density. On the other hand, the phase winding resistance is lower in motor B than in motor A since high currents are necessary.

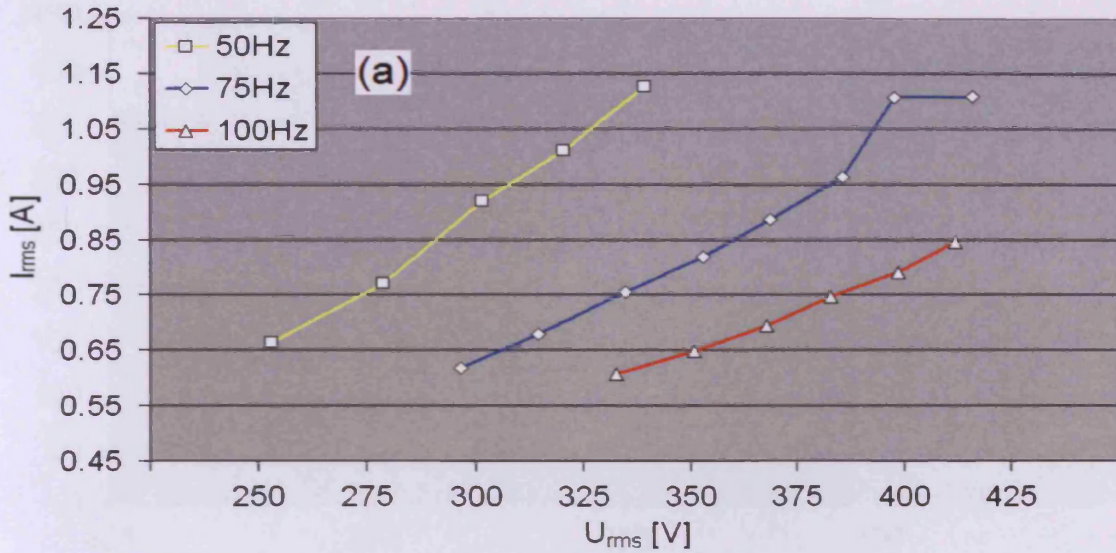


Fig. 6.14. RMS current in motor B under supply by TOSHIBA inverter

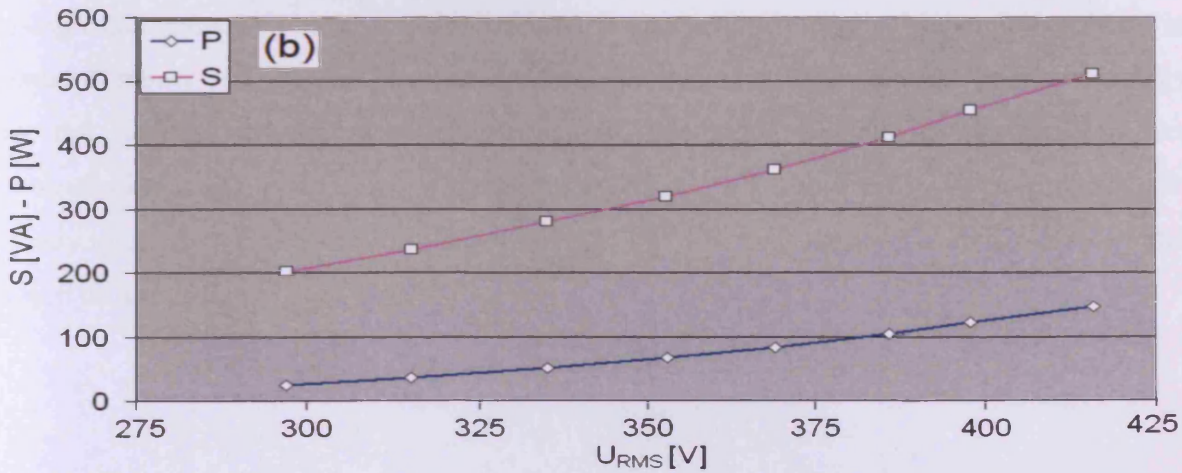
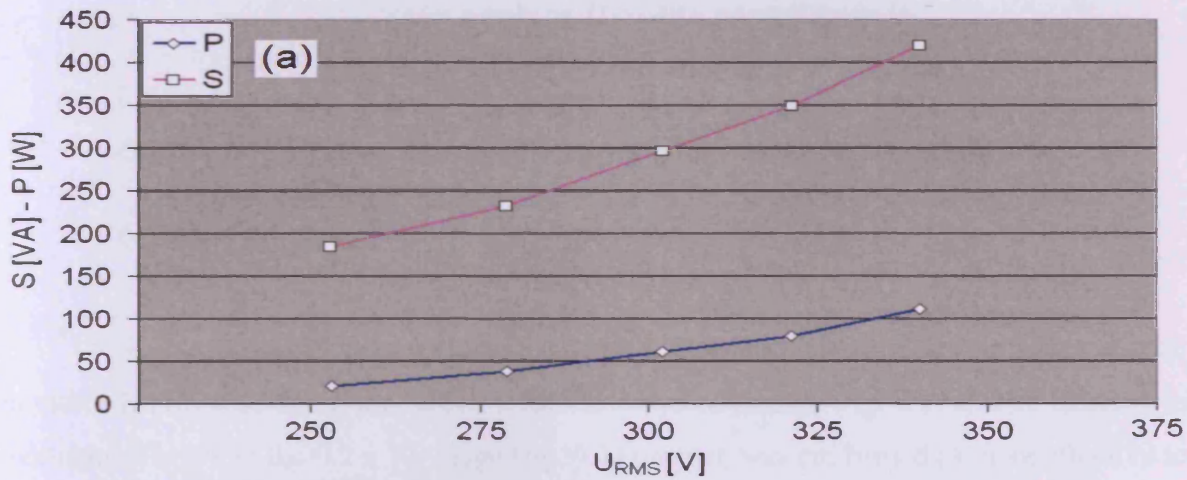


Fig. 6.15. Apparent and active power consumed by motor B under supply by TOSHIBA inverter at (a) 50 Hz – (b) 75 Hz

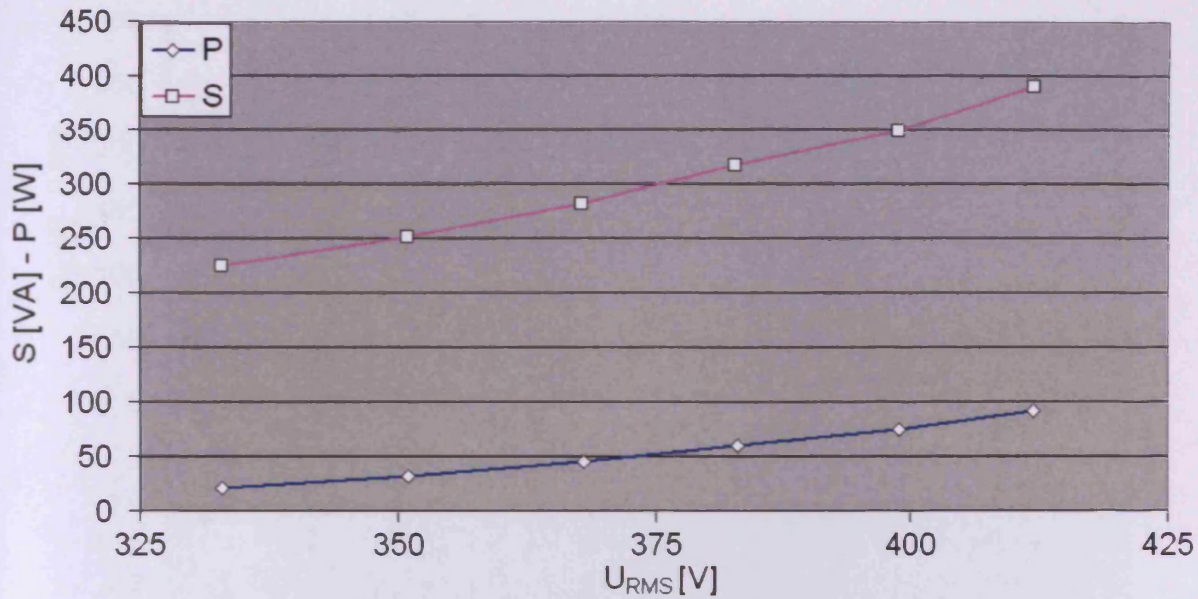


Fig. 6.16. Apparent and active power consumed by motor B under supply by TOSHIBA inverter at 100 Hz

## 6.2.5 Power consumption [ABB converter supply]

### 6.2.5a – Motor A

Active power increases more steeply with frequency (2.05 W/Hz) in motor A than in motor B (1.65 W/Hz) in the 50 Hz – 100 Hz frequency range (fig. 6.17a). The increase in modulation index in the 0.2 – 1.0 range (fig. 6.11), which was confirmed as more effective to rising rotational speed in the smaller machine, is also accompanied by higher power factor in motor A below 100 Hz. Because line-line over-modulated voltages provide sufficient energy for the smallest rotating machine to reach to maximum rotational speed, active power consumption was slowed down in motor A beyond 125 Hz (fig. 6.17a). On the contrary, the steady increase in active power consumption until 175 Hz was required to raise the rotational speed of motor B.

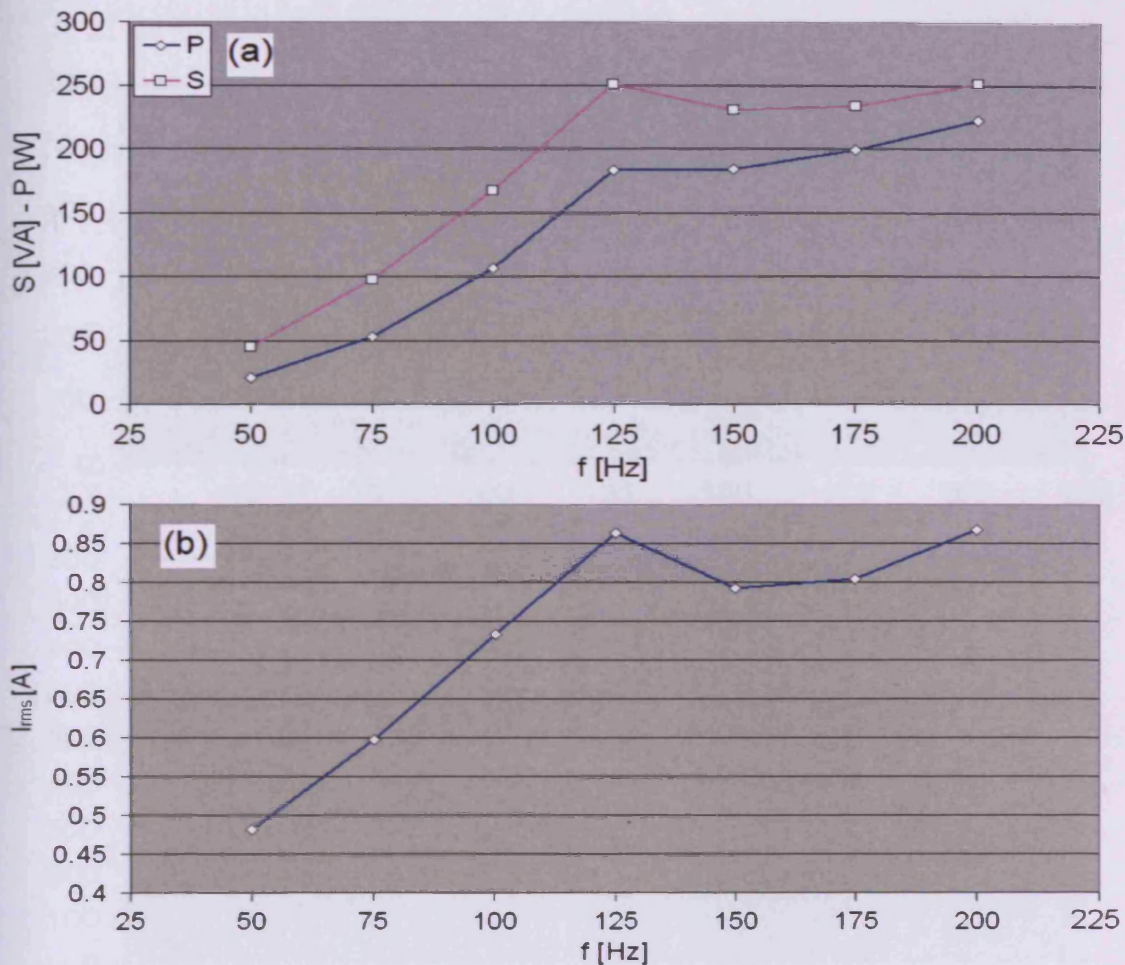


Fig 6.17. (a) Active power P [W] and apparent power S [VA] - (b) RMS current in motor A supplied by the ABB ACS 140 converter

### 6.2.5b – Motor B

Apparent power  $S$  [VA], active power  $P$  [W] and RMS current were measured in motor B while fed by the ABB ACS 140 converter at frequencies between 50 Hz and 200 Hz (fig. 6.18 and fig 6.19). The importance of adjusting the reference of rotational speed in the control of the converter can be seen from fig. 6.18 and fig. 6.19. When a value of 1500 rpm is selected (series A), maximum apparent and active power are consumed at 50 Hz. In series B and C, respectively, values of reference rotational speed are 3000 rpm and 3750 rpm. It can be seen that, by making this choice, maximum power consumption by the induction machine is delayed until 100 Hz and 125 Hz were selected manually via the control panel. This is

caused by the fact that PWM modulation indices higher than unity in the control algorithm are assigned to the 100 Hz – 175 Hz frequency range (fig. 6.12).

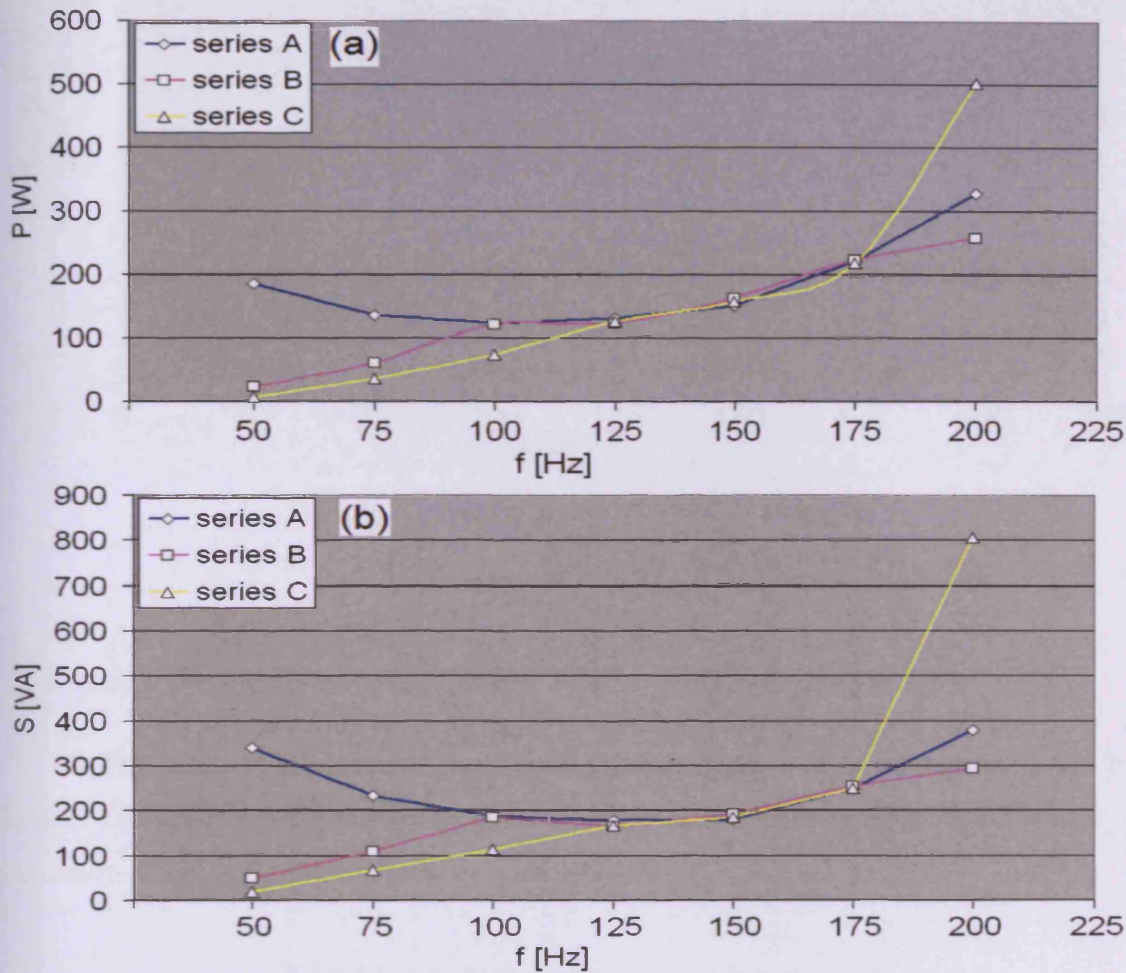


Fig 6.18. Frequency variation of (a) active – (b) apparent power consumed by motor B with frequency under supply by the ABB ACS 140 converter

The variation of line current with frequency (fig 6.19) followed a similar trend as active and apparent power (fig. 6.18). The use of lower PWM modulation indices in series B and C in the low frequency range (50 Hz – 75 Hz) was accompanied by lower values of power factor. When PWM modulation indices were assigned in a comparable range (over-modulation) in the three series of measurements, similar values of power factor were found. The use of low modulation indices leads to narrow pulses in line-line voltages of reduced width (fig. 5.20). Due to filtering by leakage inductances, the already low RMS supply voltage is reduced even further. This reduces active power transfer from the inverter to the motor.

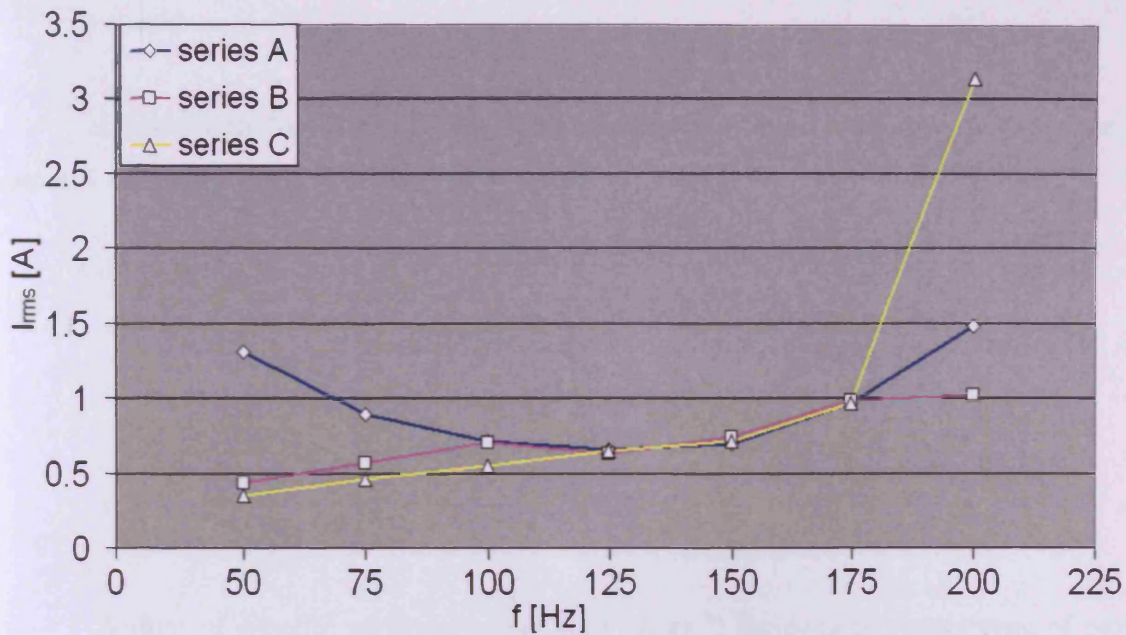


Fig 6.19. Frequency variation of (a) RMS current in motor B under supply by the ABB ACS 140 converter

### 6.3 Peak flux density vs. PWM modulation index

The geometrical parameters required to characterize induction motors A and B are listed in table 6.8. Values of  $\lambda=1/2$  and  $(d_x / d_{rot}) = 1.4$  were selected for the analytical calculation of stator core mass (6.6).

Table 6.8. Geometry parameters of induction motors a and B

	$d_{shaft}$ [m]	$d_{rot}$ [m]	$d_{ext}$ [m]	$d_{rot}/d_{ext}$	$d_x/d_{rot}$	$I$ [ $kg \cdot m^{-2}$ ]	$La$ [mm]	$m_{fe}$ [kg]
Motor A	19	66.5	125	0.532	1.4	0.0021	101.6	9.66
Motor B	28	90.5	160	0.565	1.4	0.0069	136.5	11.22

The characteristics of deep groove single row ball bearings (SKF 61910) and (SKF 16012) used in induction motors are shown in table 6.9

Table 6.9. Deep groove single row bearings used in motors A and B

	$d_{bore}$ [mm]	$C$ [kN]	$M_{frict}$ [N.mm]
SKF 61910 (motor A)	50	14.6	54.8
SKF 16012 (motor B)	60	20.8	93.6

Losses in motors A and B caused by mechanical friction in the two bearings used in motors A and B are given in table 6.10.

Table 6.10. Power losses in motors A and B caused by mechanical friction in bearings

n [rpm]	1500	2250	3000	4500
$P_{frict}$ [W] (A)	17.2	25.8	34.4	51.6
Bearing type (A)	SKF 61910			
$P_{frict}$ [W] (B)	29.5	44.3	59.0	68.5
Bearing type (B)	SKF 16012			

Values of specific apparent power  $s_{fe}$  [VA.kg<sup>-1</sup>] losses in the stator core of motors A and B under supply by the Toshiba inverter are given in table 6.11 and table 6.12 for four electrical frequencies (50, 75, 100 and 150 Hz)

Table 6.11. Specific apparent power  $s_{fe}$  [VA/kg] in motors A and B (Toshiba inverter)

f [Hz]	50				75		
$m_i$	0.45	0.50	0.57	0.63	0.5	0.63	0.74
$s_{fe}$ [VA/kg] (A)	41.6	60.2	81.0	114.3	16.95	22.2	48.4
$s_{fe}$ [VA/kg] (B)	5.9	10.6	14.6	21.20	2.6	9.1	17.2

Table 6.12. Specific apparent power  $s_{fe}$  [VA/kg] in motors A and B (Toshiba inverter)

f [Hz]	100				150					
$m_i$	0.63	0.74	0.85	0.92	0.85	0.92	0.97	1.16	1.50	1.85
$s_{fe}$ [VA/kg] (A)	60.1	113.7	162	236	67.7	72.3	87.1			
$s_{fe}$ [VA/kg] (B)	2.1	9.4	18.1	23.2				6.1	9.3	22.3

By accessing the graph in fig 6.6, peak flux density in motor stator core is obtained under the hypothesis that M400-50A is the grade of steel used to manufacture the stator. The relation between peak flux density and PWM modulation index in Toshiba inverter control is illustrated in fig 6.20 and fig 6.21. In the two induction motors studied, it was found that the relation between flux density and modulation index is nearly linear.

Motor A

(a)  $B_p (m_i) = 0.6513m_i + 1.3062$  (50Hz) (6.11)

(b)  $B_p (m_i) = 0.5873m_i + 1.0389$  (75Hz) (6.12)

(c)  $B_p (m_i) = 0.4904m_i + 1.1046$  (100Hz) (6.13)

(d)  $B_p (m_i) = 0.4138m_i + 1.1154$  (150Hz) (6.14)

Motor B

(a)  $B_p (m_i) = 0.9177m_i + 0.9385$  (50Hz) (6.15)

(b)  $B_p (m_i) = 0.6407m_i + 1.0014$  (75Hz) (6.16)

(c)  $B_p (m_i) = 0.3532m_i + 0.9608$  (100Hz) (6.17)

(d)  $B_p (m_i) = 0.6662m_i + 0.0622$  (150Hz) (6.18)

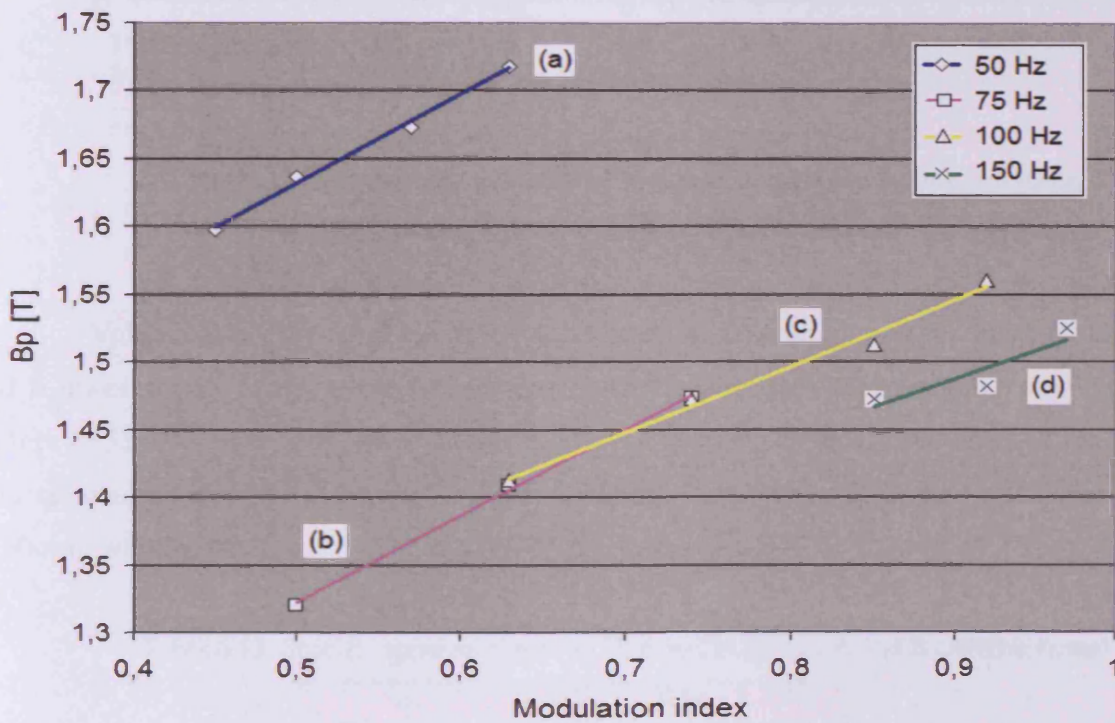


Fig 6.20. Relation between average peak flux density and modulation index in motor A under supply by Toshiba inverter

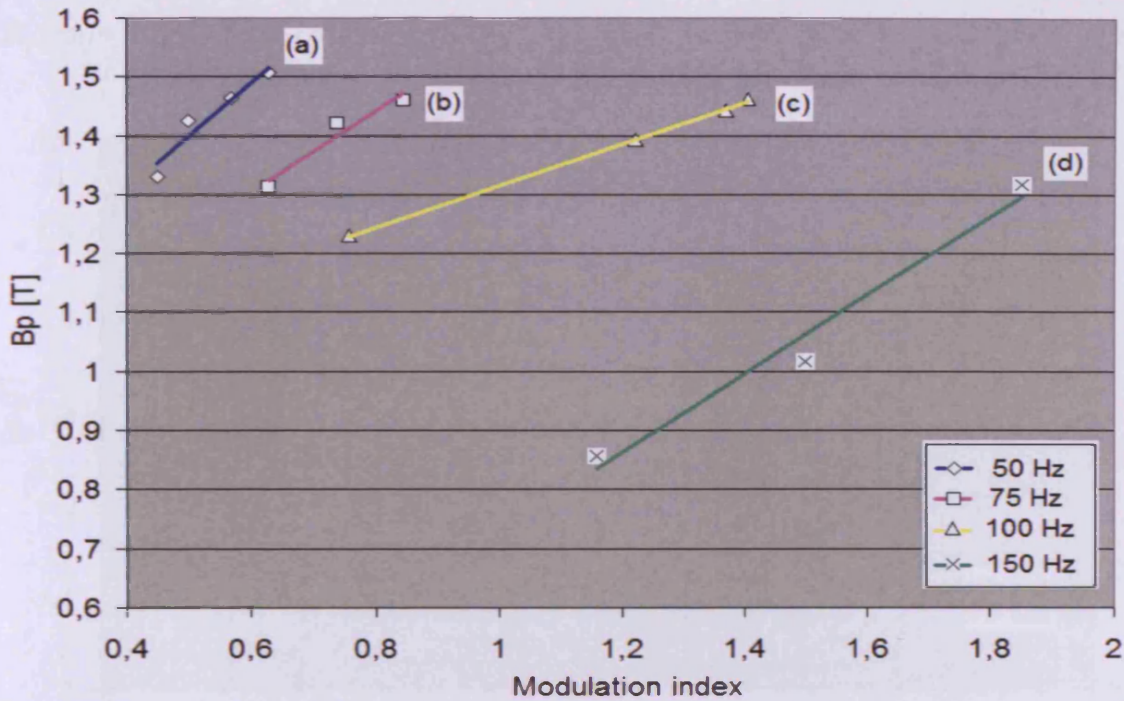


Fig 6.21. Relation between average peak flux density and modulation index in motor B under supply by Toshiba inverter

Values of specific apparent power  $s_{fe}$  [VA.kg<sup>-1</sup>] losses in the stator core of motors A and B under supply by the ABB ACS 140 are provided in table 6.13 for three modulation indices (0.52, 0.82 and 1.66) associated to electrical frequencies of 75, 100 and 150 Hz. The data selected correspond to series C of measurements in which a reference rotor speed of 2750 rpm was chosen.

Table 6.13. Specific apparent power  $s_{fe}$  [VA/kg] in motors A and B (ABB inverter)

$m_i$	0.52	0.82	1.66
$s_{fe}$ [VA/kg] (A)	16.8	41.7	87.6
$s_{fe}$ [VA/kg] (B)	6.3	14.3	57.2

By following the same procedure than the one used under Toshiba inverter supply, values of apparent specific iron losses  $s_{fe}$  [VA.kg<sup>-1</sup>] were obtained and then linked to peak flux density values (fig 6.6). Finally, the relation between average peak flux density in stator cores of motors A and B and PWM modulation index in ABB ACS140 converter control was

established (fig 6.22). The analytical relation between these two magnitudes was found logarithmic as shown below.

Motor A

Motor B

(a)  $B_p (m_i) = 0.0862 \ln(m_i) + 1.4739$  (6.19)

(b)  $B_p (m_i) = 0.2974 \ln(m_i) + 1.3423$  (6.20)

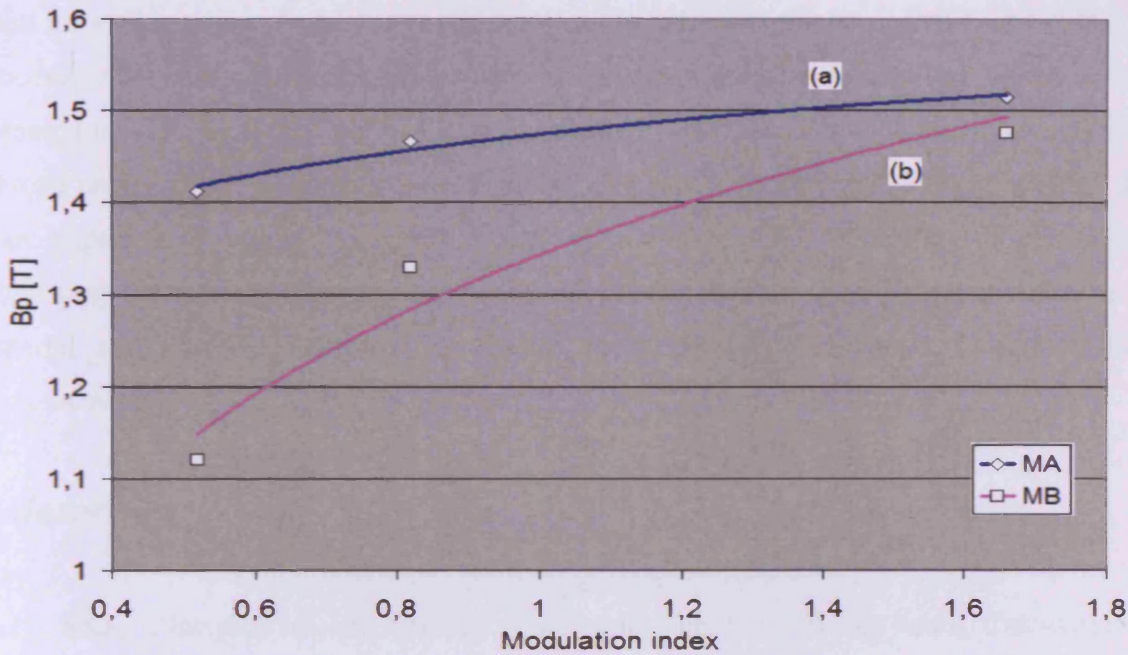


Fig 6.22. Relation between average peak flux density and modulation index in motors A and B under supply by ABB ACS 140 converter

### 6.4 Conclusions

A method to establish the relation between average peak flux density ( $B_p$  [T]) in the stator core of two induction motors [0.75kW and 2.2kW] and PWM modulation index ( $m_i$ ) for two frequency converters [Toshiba VF-A3 and ABB ACS140] has been introduced in this chapter. The approach, which requires experimental power loss measurements under no-load conditions, is founded on loss segregation and analysis based upon motor equivalent circuit. A linear relation between  $B_p$  and  $m_i$  was obtained for four electrical frequencies (50, 75, 100 and 150 Hz) when the two motors were fed by the Toshiba converter. In this case, the modulation index was set manually for each experimental case. A logarithmic relation between  $B_p$  and  $m_i$  was found when the two motors were fed by the ABB ACS140 converter. Here, the reference rotor speed was the only parameter set by the user. A built-in function assigned a value of modulation index to the desired rotational speed for each experimental case.

The method proposed combines pragmatism (well-known motor theory, technical data given by the supplier) and consideration of real physical phenomena (experimental measurements, motor internal geometry) in the machine. The procedure described may eventually contribute to adding a feature in variable speed drives [VSD] where an optimum point for a wide range of operating conditions can be selected in fan or pump-based industrial processes. By being able to estimate iron and copper losses satisfactorily, energy saving potential in VSD industrial systems may be fulfilled. The approach, which can be applied in a broad power range, is suitable for companies with power technology business strategy that share expertise in motor design and control. At the same time, the method is particularly interesting for academic departments in electrical engineering with on-going research on material and power electronics that could act as external consultants for small drive manufacturers

## **References**

- [6.1] SKF, “Interactive Engineering Catalogue. Product Tables and Calculations”, [www.skf.com](http://www.skf.com).
- [6.2] Y. Suzuki, A . Koyanagi, M. Kobayashi, R. Shimada, “Novel Applications of the Flywheel Energy Storage System”, *Elsevier - Energy*, Vol 30, pp 2128 – 2143, 2005.
- [6.3] Cogent Surahammar Bruks AB. 73531 - Surahammar (Sweden).

## DIRECT AC-AC CONVERSION TOPOLOGY: AN ANALYTICAL VIEW ON SPEED DRIVES

---

Line-neutral voltages produced by three-phase matrix converters are characterised by spreading of sideband harmonics in high clusters due to cosinusoidal modulation of amplitude. Moreover, their low form factor enhances their position as magnetising signals of non-oriented steel. However, they inherit subharmonics at multiples of the line frequency, which compromises their applicability in variable speed drives. In terms of magnetisation of non-oriented steel, line-line voltages from matrix converters are more efficient than those produced by two-level DC-link converters at high frequencies.

The proportion of iron losses in induction motors within the low nominal power range (below 15 kW) depends on motor characteristics and load conditions. Modulation and control strategies in the regulation of supplied energy by the frequency converter must be equally taken into account. In small machines often subjected to continuous full load, Joule losses in stator windings and aluminium bars are predominant. Nevertheless, partial load conditions result in core losses in laminated steel becoming proportionally larger. The impact of line-neutral and line-line voltages, typical of matrix and two-level DC-link converters, on efficiency in two commercial squirrel-cage induction motors (3 kW – 15 kW) is analysed and discussed for various load conditions in the 50 Hz – 200 Hz frequency range. The influence of Y –  $\Delta$  winding configuration, the ratio of Joule to iron losses are also investigated.

### ***7.1 Analytical procedure***

#### **7.1.1 Voltages typical of matrix and DC-link converters**

Line-neutral and line-line voltages, typical of three-phase matrix and two-level DC-link converters were generated by the computational technique described in §4.4 at 50 Hz, 100 Hz and 200 Hz. In the DC-link converter case, line-neutral voltages were defined as a bipolar signal. Space-Vector-Modulation [SVM] and PWM switching frequency were set equal to 2.5 kHz in respective modulation strategies for matrix and indirect converters. The PWM modulation scheme analysed in this chapter is carrier-based with natural sampling. Due to easiness of implementation in digital signal processors, space-vector PWM is nowadays

commonly in motor control. A brief overview on PWM modulation schemes, as well as their influence on current harmonic distortion in the 15kW motor (table 7.1) under two-level converter supply, was introduced in §2.4.2.

The control strategy adopted in the study was constant ratio of supplied voltage to frequency. Therefore, maximum output voltage transfer ratio  $q_{\max} = \sqrt{3}/2$  in the control of matrix converter was associated to 200 Hz. Values of  $(q_{\max} / 4)$  and  $(q_{\max} / 2)$  were selected for 50 Hz and 100 Hz, respectively. In the DC-link converter case, the maximum modulation index  $m_{\max} = 1$  was associated to 200 Hz. Values of  $(m_{\max} / 4)$  and  $(m_{\max} / 2)$  were selected for 50 Hz and 100 Hz, respectively. The difference in total harmonic distortion between line-line and line-neutral voltages, typical of matrix and two-level DC-link converters, is shown in fig 7.1 for the range of voltage transfer ratios ( $q/q_{\max} = 0.25$  to 1.0) and modulation indices ( $m/m_{\max} = 0.25$  to 1.0) under study. Selected frequencies were 50 Hz, 100 Hz and 200 Hz.

Total Harmonic Distortion *THD* [%] in line-line voltages produced by the matrix converter was between 8.4 % and 11.5 % lower than in voltages generated by a two-level DC-link converter. Line-neutral voltages, typical of the matrix converter, are considerably less distorted than bipolar signals produced by the DC-link converter. As the width of pulses decreases with voltage transfer ratio ( $mx$ ) || modulation index (PWM), line-neutral signals typical of the direct AC-AC converter take advantage of cosinusoidal modulation of amplitude while *THD* in bipolar voltages from the DC-link converter increases sharply. However, the operation of induction motors is determined by the flow of three-phase currents. The applied voltage generated by the frequency converter, along with motor characteristics and load, determines harmonic quality of load currents and therefore the efficiency of the transformation of electrical energy into mechanical energy.

### 7.1.2 Squirrel-cage induction motors

Information on two commercial squirrel-cage induction motors, of respective nominal power 3 kW and 15 kW, are specified in §A.8. Characteristics of the two machines are summed up in table 7.1.

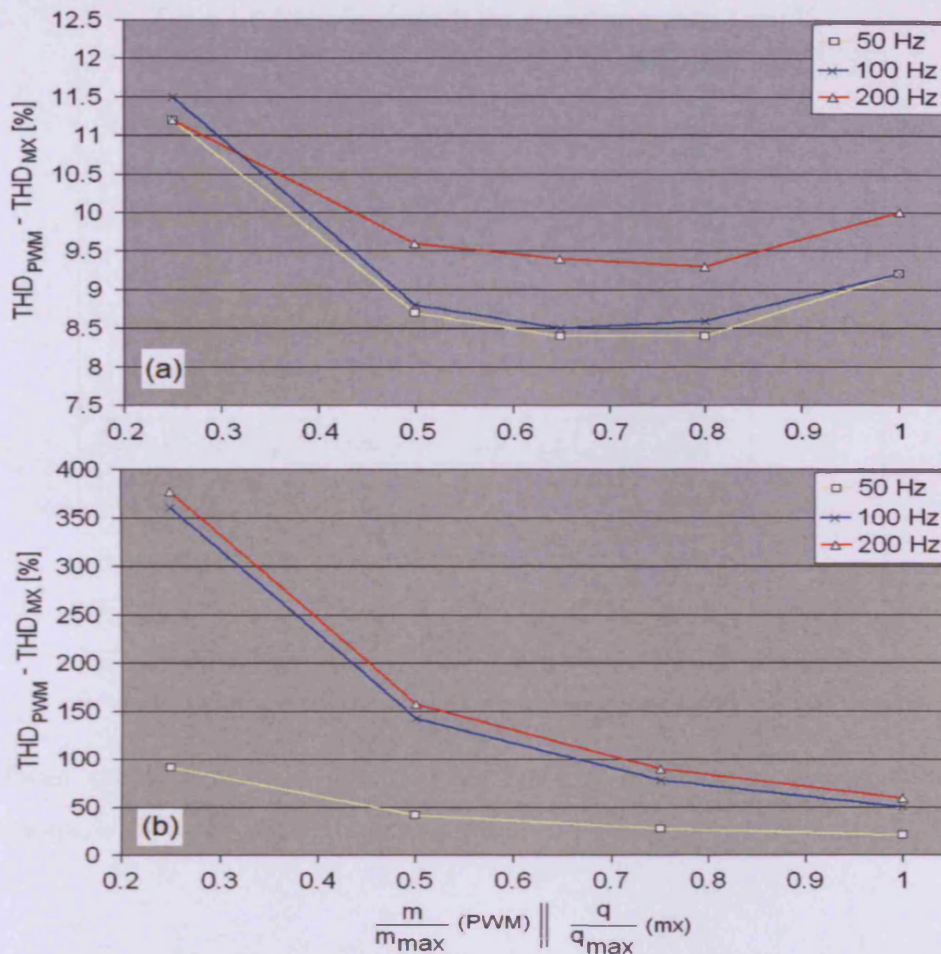


Fig 7.1. Difference in  $THD$  [%] between DC-link and matrix converter  
 (a) line-line - (b) line-neutral voltages

In order to determine the equivalent circuit ( fig 7.2) of the two three-phase asynchronous machines, a system of nine unknowns must be solved.

- stator resistances  $R_1$  [ $\Omega$ ]
- stator leakage inductance  $L_1$  [H]
- rotor resistances  $R_2'$  [ $\Omega$ ]
- rotor leakage inductance  $L_2'$  [H]
- iron loss resistance  $R_0$  [ $\Omega$ ]
- magnetising inductance  $L_0$  [H]
- rotor current  $I_u$  [A]
- equivalent resistance at nominal conditions  $R_{eq}$  [ $\Omega$ ]
- equivalent reactance at nominal conditions  $X_{eq}$  [ $\Omega$ ]

Table 7.1. Specifications of the induction motors I and II

	Motor I	Motor II
Nominal power $P_u$ [kW]	15	3
Synchronous speed $n_s$ (rpm)	1500	
Number of poles (2p)	4	
Connection	Y	
Nominal voltage $V_N$ [V]	$415/\sqrt{3}$	
Nominal current $I_N$ [A]	28	6.48
Ratio of start-up to nominal current $I_S / I_N$	6.8	5.5
Nominal torque $T_N$ [Nm]	98.0	20.0
Ratio of start-up to nominal current $T_S / T_N$	3.0	2.5
Nominal slip $s_{nom}$ [%]	2.67	4.67
Power factor ( $\cos \varphi$ )	0.89	0.77

From specifications on the induction motors provided by the manufacturer, the equivalent impedance and rotor current at nominal conditions can be determined (7.1) - (7.2) - (7.3).

$$R_{eq} = \frac{V_N}{I_N} \cdot \cos \varphi \quad (7.1)$$

$$X_{eq} = \frac{V_N}{I_N} \cdot \sin \varphi \quad (7.2)$$

$$I_u = \sqrt{\frac{P_u}{3R_2 \frac{1-s_{nom}}{s_{nom}}}} \quad (7.3)$$

Two different expressions of the voltage drop  $V_0$  [V] across the magnetising branch at nominal conditions can be written when  $R_{eq}$  and  $X_{eq}$  are introduced (7.4) - (7.5).

$$V_0(I) = \sqrt{(R_{eq} - R_1)^2 + (X_{eq} - X_1)^2} \cdot I_N \quad (7.4)$$

$$V_0(II) = \sqrt{\left(\frac{R_2'}{s_{nom}}\right)^2 + (X_2')^2} \cdot I_u \quad (7.5)$$

By substituting  $R_{eq}$ ,  $X_{eq}$  and  $I_u$  by their value in equations (7.4) and (7.5), a new equation can be written as a function of stator and rotor impedances (7.6).

$$\delta(R_1, L_1, R_2', L_2') = V_0(I) - V_0(II) = 0 \quad (7.6)$$

At start-up conditions, the laminated core is completely demagnetised. Therefore, no current flows through the magnetising branch. Start-up current ( $I_s$ ) and torque ( $T_s$ ) in the induction motor at nominal voltage and frequency are known from specifications provided by the manufacturer. The rotor resistance can be then obtained from (7.7)

$$R_2' = \frac{T_s \omega}{3I_s^2} = \frac{T_s (2\pi)n_s}{60(3I_s^2)} \quad (7.7)$$

In small squirrel-cage induction motors, leakage inductance in stator and rotor are often assumed equal in order to simplify the analysis of the performance of the motor. Under the assumption  $X_1 = X_2'$ , the module of the stator impedance  $Z_1$  can be written as in (7.8)

$$|Z_1| = \sqrt{\left(\frac{V_N}{I_s}\right)^2 - (R_2'^2 + X_1'^2)} \quad (7.8)$$

By expressing  $X_1$  as a function of  $R_1$ , the term  $\delta$  becomes a function of the unique variable  $R_1$ . After calculating the values of stator resistance  $R_1$  and inductance  $L_1$ , iron loss resistance  $R_0$  and magnetising inductance  $L_0$  can be calculated by introducing equivalent

impedance  $\underline{Z}_{eq}$ , stator impedance  $\underline{Z}_1$  and rotor impedance  $\underline{Z}_u = \frac{R_2'}{s_{nom}} + j \cdot X_2'$  in the

definition of  $\underline{Z}_0$  (7.9)

$$\underline{Z}_0 = \frac{1}{\frac{1}{\underline{Z}_{eq} - \underline{Z}_1} - \frac{1}{\underline{Z}_u}} \quad (7.9)$$

Parameters of the per-phase equivalent circuit (fig 7.2) of the two squirrel-cage induction motors are listed in table 7.2.

Table 7.2. Parameters of the equivalent circuit in motors I and II

	$P_N$ [kW]	$R_1$ [ $\Omega$ ]	$R_2'$ [ $\Omega$ ]	$L_1$ [mH]	$R_0$ [ $\Omega$ ]	$L_0$ [mH]
Motor I	15	0.85	0.41	1.8	8.7	28.3
Motor II	3	5.25	2.06	8.2	2.7	157.9

The per phase equivalent circuit (fig. 7.2) is a common method for motor analysis. However, machine impedances vary with harmonic frequency. When the motor is supplied by a frequency converter, the method relying upon a single equivalent circuit has intrinsic inaccuracies (§6.2.1a) that can be overcome by creating an adapted circuit for each harmonic frequency following an Fast Fourier Transform [FFT] decomposition of the supply voltage.

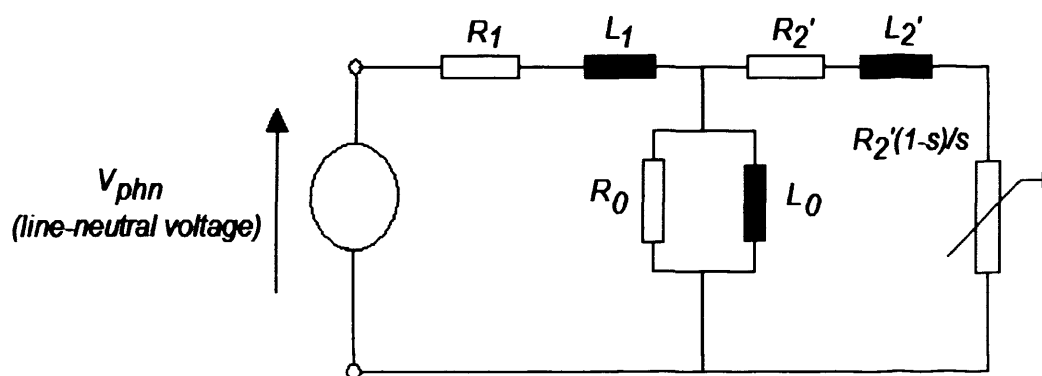


Fig 7.2. Per-phase equivalent circuit of the induction motor

The ratio of slip to the nominal value was varied in the range 20 % - 100 % in analogy to variable load conditions in the two induction machines. The amplitude of line-line voltages typical of matrix and two-level DC-link converters was equal to 415 V. Based on this hypothesis, line-neutral voltages were calculated from line-line signals. Firstly, line-neutral voltages typical of matrix and two-level DC-link converters were applied to the equivalent circuit of the two induction motors. A common neutral connection for frequency converters and Y-wound stator windings was introduced. Secondly, Y-connection in stator windings of the two induction machines was then changed to  $\Delta$ -connection. The first step was to adjust the amplitude of line-neutral voltages  $V_{\Delta}$ . The criterion used was to maintain constant the amplitude of apparent power absorbed by the two machines under  $\Delta$  and Y connections.

Then, line-line voltage  $U_{\Delta}$  were calculated and applied to the equivalent circuit of impedance  $(2/3) \cdot Z_{eq}$ . Calculations are illustrated in (7.10), (7.11) and (7.12).

$$S_{\Delta} = \sqrt{3} \cdot U_{\Delta} \cdot \frac{U_{\Delta}}{(2/3) \cdot Z_{eq}} = 3 \cdot V_Y \cdot \frac{V_Y}{Z_{eq}} = S_Y \quad (7.10)$$

$$\frac{\sqrt{3}}{2} \cdot U_{\Delta}^2 = V_Y^2 \quad (7.11)$$

$$V_{\Delta} = V_Y \cdot \sqrt{\frac{2}{3\sqrt{3}}} \quad (7.12)$$

Prior to calculation of power components, load current  $I_L(s)$ , current in iron loss resistance and magnetising inductance branches  $I_{0,R0}(s)$ ;  $I_{0,L}(s)$  and rotor current  $I_{rot}(s)$  were calculated as a function of slip  $s$  in the two induction machines. Then, Joule losses in stator windings  $P_{st}(s)$  and rotor aluminium bars  $P_{rot}(s)$  were calculated, along with iron losses  $P_{Fe}(s)$  and mechanical power  $P_{mec}(s)$ , as a function of slip  $s$  in the two induction machines (7.13) – (7.16).

$$P_{st} = 3 \cdot R_1 \cdot I_L^2 \quad (7.13)$$

$$P_{rot} = 3 \cdot R_2' \cdot I_{rot}^2 \quad (7.14)$$

$$P_{Fe} = 3 \cdot R_0 \cdot I_{0,R0}^2 \quad (7.15)$$

$$P_{mec} = 3 \cdot R_2' \frac{1-s}{s} \cdot I_{rot}^2 \quad (7.16)$$

Efficiency  $\eta$  [%], which gives the proportion of mechanical power available to the machine after dissipation of resistive and iron losses, is calculated in (7.17) in this investigation. Although shaft power will be reduced by within 2 % - 4 % due to windage and friction losses, this term is a good indicator on the quality of the transformation of electrical into mechanical energy under supply typical of matrix and two-level DC-link converters.

$$\eta = 100 \cdot \frac{P_u}{P_u + P_{st} + P_{rot}} \quad (7.17)$$

Special attention in this investigation was given to the variation of the ratio  $\chi_{Fe}$  of iron to resistive losses with slip in the two induction motors (7.18)

$$\chi_{Fe} = 100 \cdot \frac{P_{Fe}}{P_{st} + P_{rot}} \quad (7.18)$$

Two induction motor configurations ( $\Delta$  and Y) are considered in the simulating platform object of this chapter. Fig 7.3 introduces the induction motor as three dipoles associated to as many phases in converter supply. In the so-called  $\Delta$ -configuration, the motor windings are connected forming a delta while the line-line voltage (typical of matrix and two-level Dc-link converters) is applied to each dipole. In the so-called Y-configuration, the end windings (a,b and c) of the three dipoles are interconnected to the single neutral point n, forming a star thereof. The neutral point of the frequency converter is linked to the single neutral point n. Thus, motor and converter share common neutral point while line-neutral voltages (typical of matrix and two-level Dc-link converters) are applied to each one of the three motor dipoles.

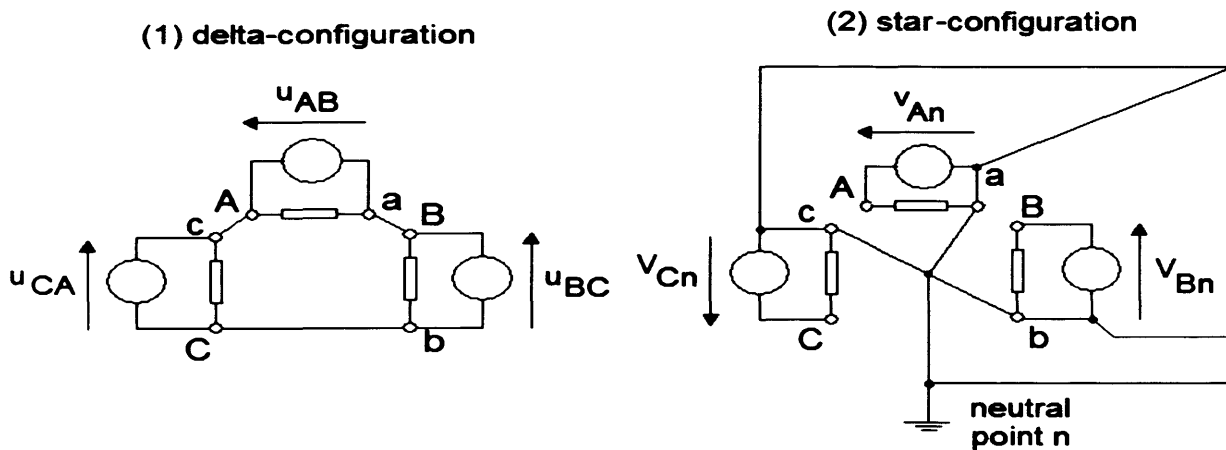


Fig 7.3.  $\Delta$  and Y configurations for simulating platform

## 7.2 Efficiency $\eta$

Efficiency in motors I and II are calculated under line-neutral and line-line supply from matrix and two-level DC-link converters. Y and  $\Delta$  are the winding configurations selected in line-neutral and line-line voltage excitation, respectively. Results are provided in fig. 7.4 and fig. 7.5, respectively.

### 7.2.1 Line-neutral voltage (Y - configuration)

The difference in efficiency  $\Delta\eta = \eta_{mx} - \eta_{DC-link}$  between matrix and DC-link converters under line-neutral supply is calculated for the two Y-wound induction motors at variable load conditions. Results are shown in Table 7.5.

Table 7.3. Difference in efficiency in motors I and II caused by line-neutral supply from matrix or DC-link converters

Motor I							
Load [%]	37.5	46.8	56.2	65.5	74.9	84.3	100
50 Hz	5.4	5.4	5.3	4.8	4.4	3.4	3.3
100 Hz	1.2	1.1	0.9	0.7	0.7	0.3	0.5
200 Hz	-0.4	-0.4	-0.3	-0.3	-0.3	-0.5	-0.2
Motor II							
Load [%]	32.1	42.8	53.5	64.2	74.9	85.6	100
50 Hz	10.5	11.0	11.0	10.3	9.4	8.5	7.5
100 Hz	2.3	2.2	2.0	1.8	1.5	1.3	1.0
200 Hz	-0.5	-0.5	-0.3	-0.3	-0.3	-0.2	-0.2

Matrix converter ensures higher efficiency in the two motors at 50 Hz and 100 Hz. As the load is increased, such improvement is mitigated. On the contrary, the two-level DC-link converter under PWM yields a slightly more efficient performance of both asynchronous machines at 200Hz in the 30 % - 100 % loading range. At low modulation indices (below 0.85), line-neutral PWM voltage waveforms are noticeable more distorted than matrix converter voltages (fig 7.1). When maximum indices are reached for  $m_i$  and  $q$  in PWM and matrix converters, similar THD values are observed. Nonetheless, sub-harmonics at multiple frequencies of 50Hz appear in matrix converter voltages to reduce significantly the output shaft power and thus efficiency. Line-neutral supply, typical of matrix converters, favours more efficient operation of the machine with smallest nominal power (3 kW) in the 50 Hz – 100 Hz frequency range. Efficiency in the two machines is less affected by the supply frequency under line-neutral supply typical of a matrix converter. On the contrary, efficiency

in the two motors fed by bipolar voltages, as produced by two-level DC-link converter, is considerably affected by the same parameter. In identical conditions, matrix converter ensures a more uniform performance of the machines, in terms of efficiency, in the 50 Hz – 200 Hz frequency range.

### 7.2.2 Line-line voltage ( $\Delta$ - configuration)

The difference in efficiency  $\Delta\eta = \eta_{mx} - \eta_{DC-link}$  between matrix and DC-link converters under line-line supply is calculated for the two  $\Delta$ -wound induction machines at variable load conditions. Results are shown in table 7.6.

Table 7.4. Difference in efficiency in motors I and II caused by line-line supply from matrix or DC-link converters

Motor I							
Load [%]	37.5	46.8	56.2	65.5	74.9	84.3	100
50 Hz	0.2	0.3	0.4	0.1	0.2	0.4	0.3
100 Hz	0.1	0.1	0.1	0.0	0.1	0.0	0.0
200 Hz	-0.2	-0.1	-0.2	-0.1	0.0	-0.1	0.0
Motor II							
Load [%]	32.1	42.8	53.5	64.2	74.9	85.6	100
50 Hz	0.4	0.7	0.4	0.2	0.1	0.2	0.2
100 Hz	0.3	0.2	0.2	0.2	0.1	0.1	0.0
200 Hz	0.1	0.1	0.1	0	0	0.1	0

Due to similar harmonic quality in line-line voltages, typical of matrix and two-level DC-link converters (§5.4.2), the performance of the two motors is characterised by comparable values of efficiency (fig 7.10). Nevertheless, matrix converters yield slightly higher efficiency at 50 Hz and 100 Hz. As reported for line-neutral supply case, such improvement is enhanced in the motor with lowest nominal power (3 kW), but attenuated by an increase in loading conditions. Efficiency in motor I (15 kW) is not significantly affected by line-line frequency converter supply. Values of efficiency within a 3 % - 4 % range are found throughout all load conditions. The best performance of this motor is observed at full load and 200 Hz, when efficiency reaches 75 %. On the contrary, efficiency in motor II (3 kW) is noticeably lower at 50 Hz, but increases rapidly with frequency. In opposition to motor I, an optimum efficiency (78 %) is reached at 80 % - 82 % load. As a result of larger resistance in stator windings, the potential increase in available mechanical power expected from higher currents is offset by higher Joule losses in stator windings. Under line-neutral supply, maximum efficiency (84 %) in motor I is reached at 100 Hz and full load. The maximum efficiency (86 %) in motor II is found at 200 Hz and 75 % load.

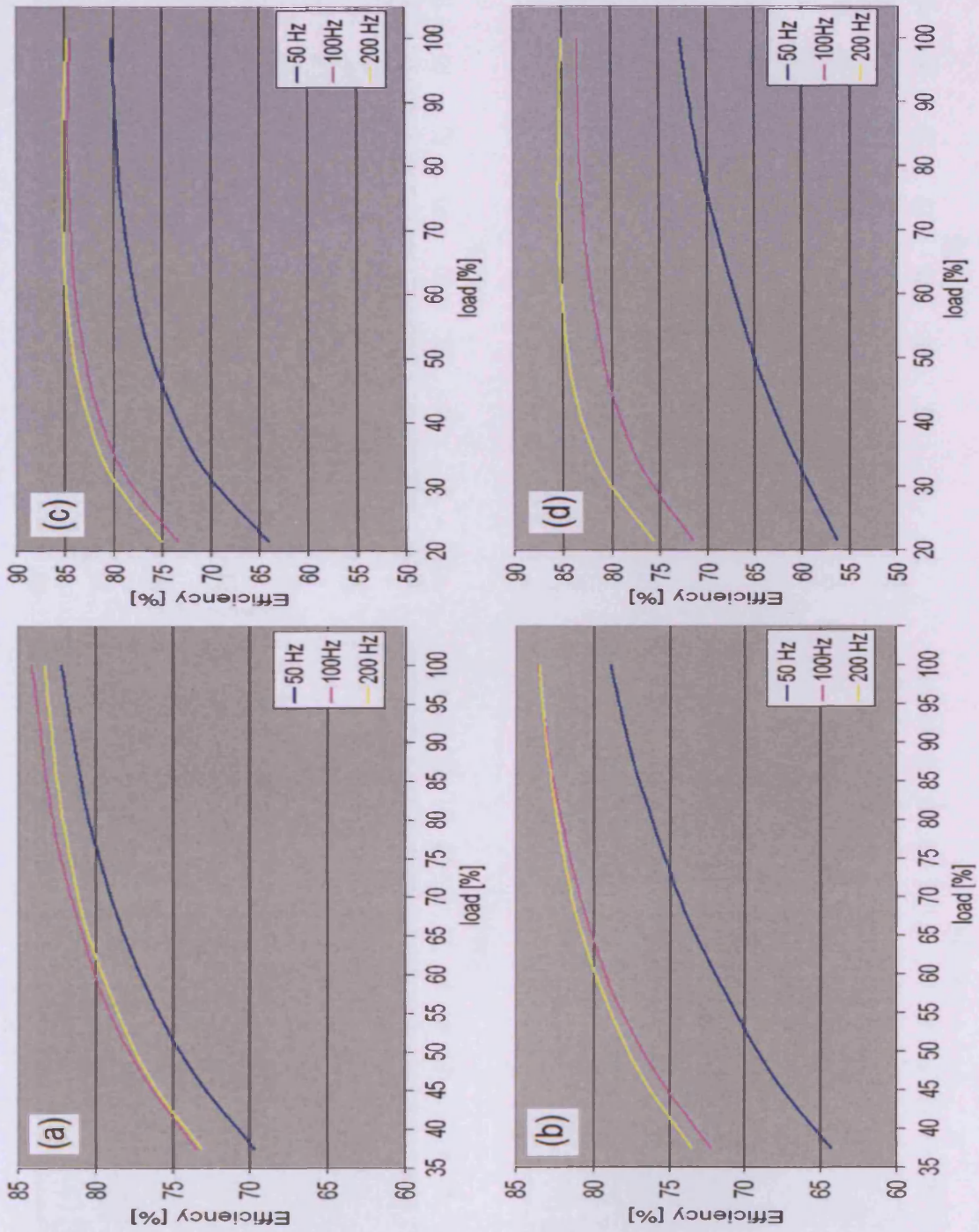


Fig 7.4. Efficiency in star-connected (line-neutral supply)

=> motor I fed by (a) matrix - (b) two-level DC-link converter  
 => motor II fed by (c) matrix - (d) two-level DC-link converter

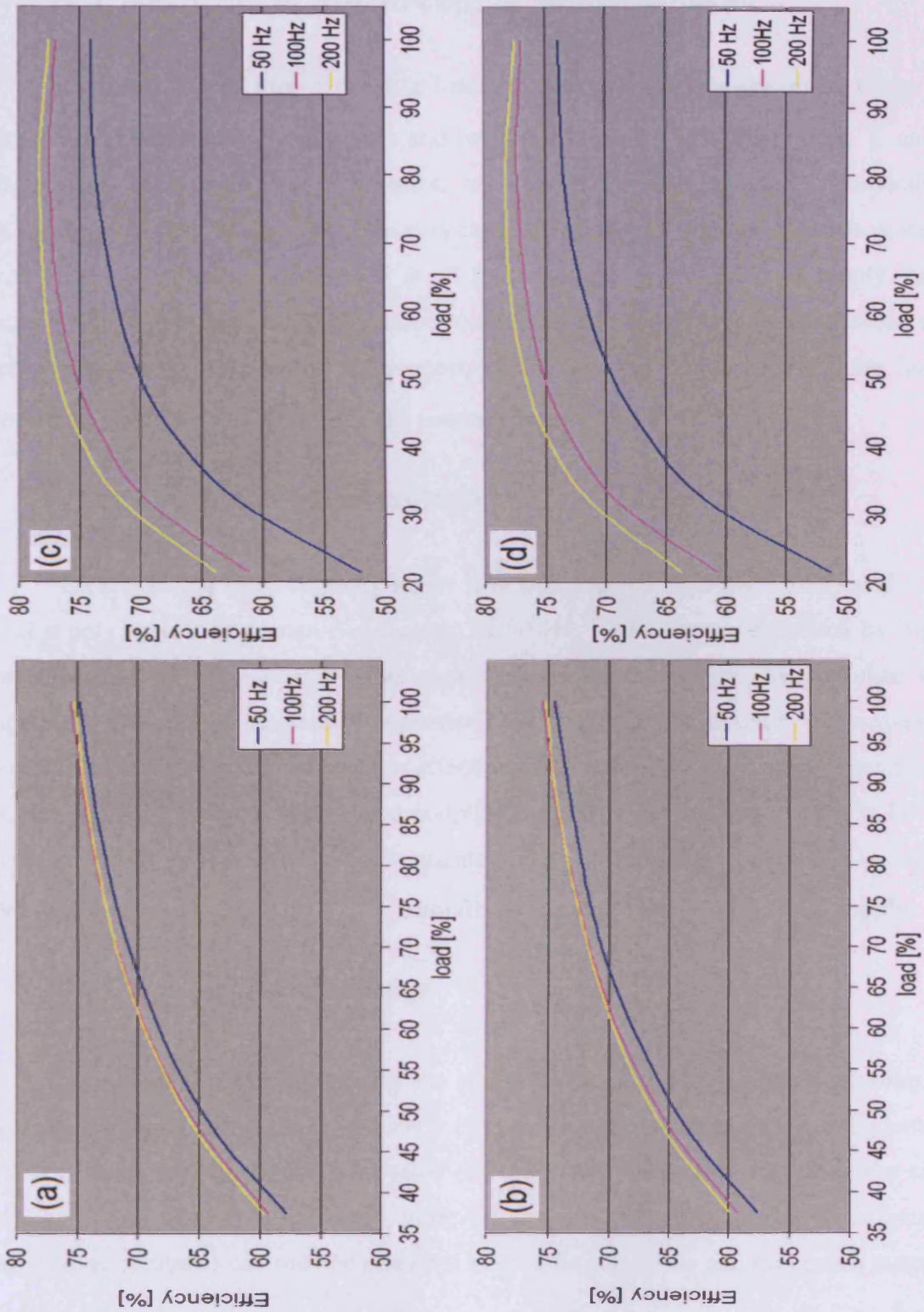


Fig 7.5. Efficiency in delta-connected (line-line supply)  
 => motor I (a) matrix - (b) two-level DC-link  
 => motor II (c) matrix - (d) two-level DC-link

### 7.3 Ratio $\chi_{Fe}$ of iron to copper winding losses

The ratio  $\chi_{Fe}$  of iron to resistive losses in motors I and II is calculated under line-neutral and line-line supply from matrix and two-level DC-link PWM converters. Y and  $\Delta$ -configurations are selected for line-neutral and line-line voltage excitation, respectively. Results are provided in fig. 7.6. As expected, the ratio of iron to resistive losses is approximately 70 % lower in motor II at all frequencies under all types of supply. Larger induction motors are characterised by more voluminous and heavier cores of laminated steel, which explains why iron losses are proportionally larger in motor I. When the load is increased, the ratio  $\chi_{Fe}$  is reduced in the two machines.

#### 7.3.1 Line-neutral voltage

Losses have a proportionally larger iron component in the two motors under line-neutral supply typical of a matrix converter. At 50 Hz, load currents, generated by bipolar voltages produced by two-level DC-link converter, are more harmonic distorted than when compared to currents in the matrix converter case (fig. 7.2). As frequency increases, the appearance of subharmonics reduces the effective RMS value of load currents generated by the direct AC-AC converter. Owing to decoupling between input and output sides in DC-link converters, levels of current flow are maintained with increasing frequency in indirect converters. As a result, the ratio  $\chi_{Fe}$  is naturally lower under line-neutral PWM supply.

#### 7.3.2 Line-line voltage

As reported in several parts of the study, harmonic quality in line-line voltages is comparable in direct and indirect frequency converters and not affected by the fundamental frequency. Therefore, RMS and *THD* value of load currents remain within a similar range. Moreover, it has been confirmed that more efficient magnetisation of laminated steel by matrix converter signals can only be achieved in specific conditions and for certain materials. These remarks are confirmed by the results shown in fig 7.6, where ratios  $\chi_{Fe}$  for the two machines under line-line supply from both converters are very similar at all load conditions. When the winding configuration in the motors is changed from (line-neutral supply - Y) to (line-line supply -  $\Delta$ ), the composition of losses is less affected under matrix converter than under two-level DC-link converter supply at 50 Hz and 100 Hz. This indicates that a more flexible use of direct AC-AC converters as suppliers of squirrel-cage induction motors can be

implemented. If the design of an induction machine relies on laminations of specific thickness and material to minimise iron losses, a change in the connection converter – motor will remain consistent with initial considerations under matrix converter supply.

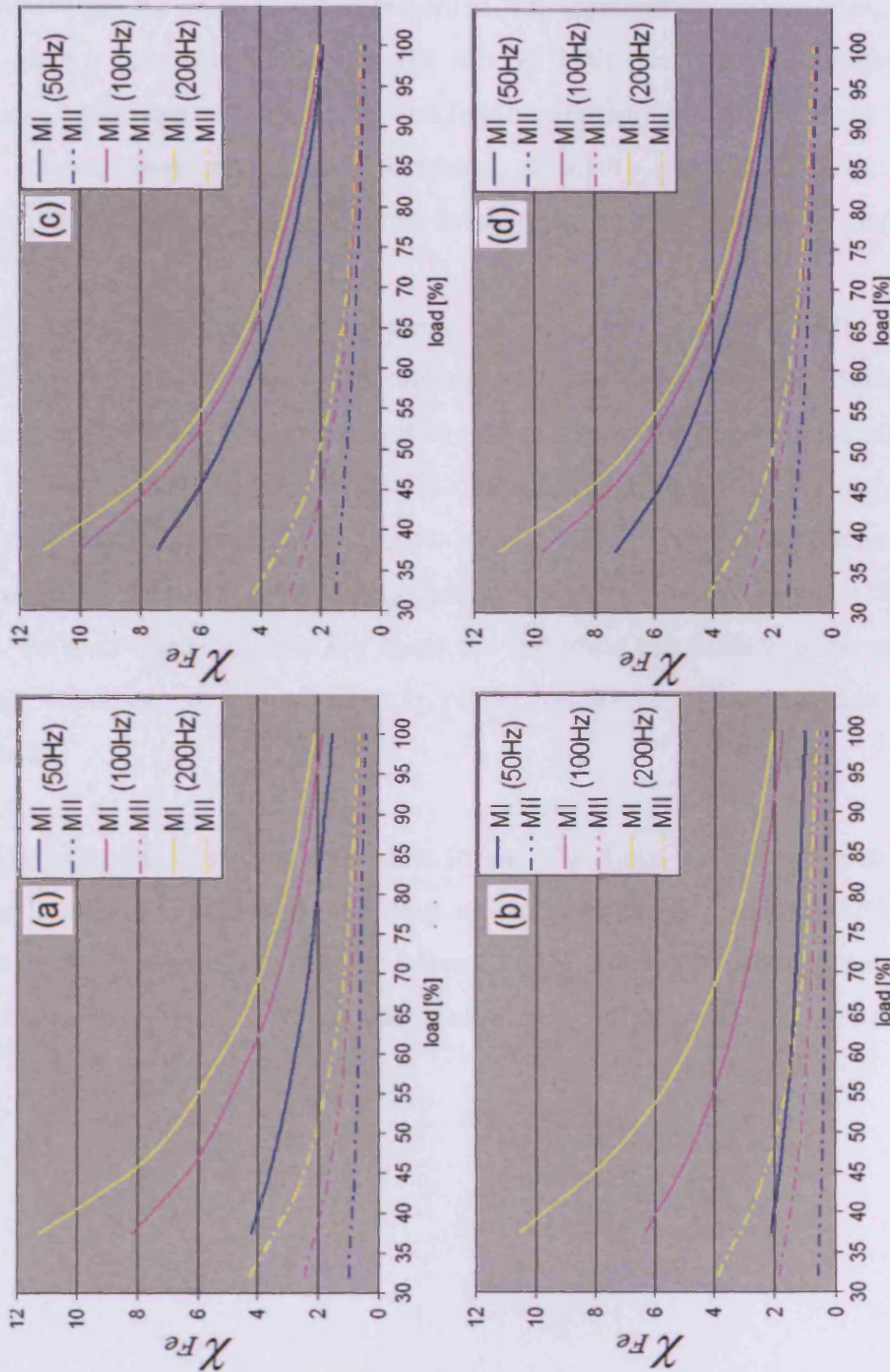


Fig 7.6. Ratio of iron to copper winding losses in  
 ❖ Y-connected motors fed by (a) matrix - (b) two-level DC-link converter  
 ❖  $\Delta$ -connected motors fed by (c) matrix - (d) two-level DC-link converter

## **7.4 Conclusions**

A general view on the applicability of matrix conversion topology to variable speed drives in the low power range has been presented. The influence of voltage wave-shape on the efficiency of two induction motors (3 kW and 15 kW) has been highlighted. Y and  $\Delta$ -configurations have been considered, so that line-neutral and line-line voltages were directly applied to generate load currents in both motors. Available mechanical power and ratio of iron to resistive losses under matrix and two-level converter supply have also been studied.

Motor performance is very similar at the highest frequency (200 Hz), when voltage harmonic distortion is lowest due to the selection of highest output transfer ratio (matrix) and modulation index (PWM). Matrix converters ensure similar or better motor efficiency than two-level DC-link converters under all the studied conditions. As far as efficiency is concerned, significant improvements (up to 10%) were observed under line-neutral matrix converter supply at 50Hz and partial loads (below 60%). Owing to the absence of voltage sub-harmonics, the motor benefits from low harmonic distortion that leads to lower iron losses. At this loading condition, this component is proportionally larger or comparable to copper winding losses.

The potential of matrix converters for AC-AC links in low power drives is offset today by high engineering costs derived from sophisticated control strategy and larger number of semiconductors. Nonetheless, reduced volume and absence of DC-link in matrix converters will remain important assets to attract industrial interest and promote commercialisation in the future.

**References**

- [7.1] G. Petrovic, T. Kilic, B. Terzic, "Sensorless speed detection of squirrel-cage induction machines using stator neutral point voltages", *Mechanical Systems and Signal Processing*, in press, June 2008.
- [7.2] M.E.K. Oumaamar, A. Khezzar, M. Bourchema, H. Razik, R. N. Andriamala, L. Baghli, "Neutral voltage analysis for broken rotor bars detection in induction motors using Hilbert transform phase", *42<sup>nd</sup> Annual Meeting of the Industry Applications Society*, pp 1940-1947, 23-27 Sept 2007.
- [7.3] Y.J. Wang, "An analytical study on steady-state performance of an induction motor connected to unbalanced three-phase voltage", *Power Engineering Society Winter Meeting*, Vol 1, pp 159-164, 23-27 Jan 2000.
- [7.4] M. Morimoto, "Reduction of high frequency leakage current from PWM inverter-motor system at the Integrated Grounding System", *Applied Power Electronics Conference and Exposition*, 19-23 Mar 2006.

## CONCLUSION – FUTURE WORK

---

### **Conclusions**

In this PhD thesis, two physical phenomena (non-linearity between applied field and induction as well as shielding effect) and their impact on eddy-current loss calculation have been analysed. A theoretical study based upon Poynting's vector revealed that lower mean eddy-current losses are obtained in alloys with lower silicon content and larger thickness above 1.4T peak flux density. A novel analytical model for iron loss calculation in laminated non-oriented steel has been introduced. The approach (denoted as NL+SE), which analyses losses into two components (static hysteresis and eddy-current terms) and accounts for non-linearity between  $B$  and  $H$  and shielding effect, has been experimentally benchmarked against calculated (based upon Bertotti's statistical approach) and measured losses in three non-oriented steel grades (M470-50A, M530-50A, M700-65A).

As one of the main innovations in the research work described throughout this PhD thesis, voltages typical of direct AC-AC (matrix) converters have been characterised as magnetising signals of laminated non-oriented steel through iron loss measurements. The study is complemented with iron loss measurements under typical voltages of two –level DC-link pulse-width-modulated (carrier-based PWM) inverters. While Bertotti's and NL+SE model approximate losses in M470-50A and M530-50A within 15% (below 1.25T peak flux density and 50Hz magnetising frequency), losses estimated by the new model show 10% better agreement with experimental values than the statistical approach which under-estimated losses at 200Hz magnetising frequency and 1.5T peak flux density. The discrepancy between predicted losses based upon Bertotti's formula and experimental values can be partly explained by the fact that non-linearity between magnetic field and induction is most pronounced at 1.5T in thin laminations of electrical steel with high silicon content.

Both methods of iron loss prediction under pulsating voltage excitation proved good agreement with experimentally measured losses in M700-65A laminations in which non-linearity between  $B$  and  $H$  is attenuated due to lower silicon content. However, the increased importance of eddy-current shielding (particularly at high magnetising frequency in thick laminations) was well accounted for by the NL+SE method. As far as the magnetising signal

was concerned, the NL+SE method yielded the best accuracy in loss estimation when matrix and PWM pulsating voltages (modulation indices 0.8 and 0.5) were considered. When modulation index equals unity, the voltage becomes closer to a square signal as the number of pulses decreases. As a result, the phase angle of flux harmonics (not considered in the two approaches) is more influential on iron losses. The relation between determination of parameters used in the analytical formulas and accuracy in loss prediction has also been highlighted.

When compared to losses under two-level DC-link converter excitation, measured iron losses in Epstein frame or single strip testers were reduced by up to 32 % (M700-65A), 25 % (M530-50A) and 18 % (M470-50A) under line-neutral matrix converter excitation (50 Hz). Due to spreading of sideband harmonics in high flux clusters, eddy-current losses were reduced by between 15 % and 10 %. The smoothness of flux density wave-shapes contributed to reducing anomalous losses in the three materials. Line-line matrix supply only ensured significant respective decreases in iron losses by 30 % and 45 % in M530-50A and M700-65A laminations (200 Hz). As illustrated in the PhD thesis written, line-line voltages from matrix and two-level PWM converters have closer properties (total harmonic distortion, form factor) which makes them equally good as magnetising signals of non-oriented steel at low frequency (below 100Hz). As the magnetising frequency increases, the benefit of a segmented co-sinusoidal envelop in line-line voltages generated by the matrix converter when compared to square envelop (DC-link converter) is enhanced. The attenuation in voltage derivative ( $dv/dt$ ) in fundamental cycles with less number of pulses still reinforces matrix converter line-line voltages as more suitable magnetising signals.

An increase from 2.5 kHz to 10 kHz in space-vector modulation sampling frequency reduced eddy-current losses by up to 7% in the three grades magnetised under line-line matrix converter supply. This beneficial effect leads to a maximum drop in total losses of 12% in M700-65A laminations (200 Hz). Owing to an envelope of co-sinusoidal nature in matrix converter voltages, sideband flux harmonics in clusters located at multiples of the switching frequency are spread. When the ratio of SVM sampling to fundamental frequency is high, sideband harmonics are sufficiently confined and no superposition occurs. However, should this ratio decrease below a certain threshold (approximately fifteen), a phenomenon of superposition of sideband flux harmonics takes place to increase losses in the steel. A higher SVM sampling frequency is then clearly beneficial.

In order to expand the theoretical and experimental work carried out experimentally on laminated non-oriented by the means of established techniques (Epstein frame and single strip tests), a method to establishing the link between average peak flux density in the stator core of two induction motors (0.75kA and 2.2kW) to PWM modulation index has been developed. The approach presented, which capitalises on technical information available on commercial motors as well as on established analysis of rotating machines, aims at combining pragmatism and scientific insight. While supported by no-load measurements in the two motors under supply by two converters [Toshiba VF-A3 and ABB ACS140], the approach mainly targets drives manufacturers which can add new functionality to motion control by knowing how the modulation index affects average peak flux density, and thus iron losses.

Such a feature, which is also scalable to induction motors in a broader power range, can contribute to capitalise on the energy saving potential of industrial applications based upon variable speed drives [VSD] technology. A linear relation between  $B_p$  and  $m_i$  was obtained for four electrical frequencies (50, 75, 100 and 150 Hz) when the two motors were fed by the Toshiba converter. In this case, the modulation index was set manually for each experimental case. A logarithmic relation between  $B_p$  and  $m_i$  was found when the two motors were fed by the ABB ACS140 converter. The method proposed, which requires expertise in motor control and knowledge on iron loss, can be implemented in power technology providers with combined business and development strategies in drives and machines. The approach described is of value to academic departments or research groups in electrical engineering that can provide scientific depth in both areas and act as consultants.

A simulation platform has been built to elaborate a system view on two induction motors of respective nominal powers 3kW and 15kW fed by direct AC-AC (matrix) and DC-linked based to-level PWM converter. Although the work reported is based on carrier-based naturally sampled PWM, three alternative pulse width modulation strategies (asymmetric regular sampled PWM, symmetric regular sampled PWM and space-vector PWM) are considered to enrich the analysis and give a brief overview on the singularities of each modulation scheme. Furthermore, an analytical procedure for parameter identification in the induction motors founded on technical data by the motor supplier is featured. Special attention has been given to the proportion of iron to resistive losses in copper windings in a speed range within 1500 rpm and 4500 rpm and torque conditions ranging from 30% to full load. Efficiency as well as output power analysed.

The system approach to matrix converter-fed induction motor drive described in the final chapter of this PhD thesis reveals that electrical efficiency in star-wound machines with accessible neutral can be improved by 0.5% at medium speed (3000 rpm) and full-load. However, sub-harmonics in matrix converter voltages reduced the output power developed by the motor at rotational speed associated to different frequencies than 50 Hz. Efficiency in delta-wound induction motors were found to be within a similar range in the two converter cases. Iron losses are proportionally larger at high speed and low load. While the ratio of iron to resistive losses reached a value of two in the 15kW motor at 50% load and high speed (6000 rpm), it was found close to 0.5 at full load and low speed (1500 rpm).

Apart from no DC-link operation and increased power density, the maximum benefit from line-neutral matrix converter supply can be drawn in industry applications where star-wound induction motors with accessible neutral point operate at partial load and low-to-medium speed range. When delta-wound induction motors are considered, matrix converters offer the same functionality as two-level DC-link converters as AC-AC links. In order to capitalize on potential energy savings derived from reduced iron losses under line-line supply, matrix converters must be used in drives in the 50 to 100 kW range. Thus, proportionally larger iron losses in motors operating at high speed under variable load will be reduced.

### ***Future work***

In the final stages of this PhD thesis, the influence of anisotropy on losses in non-oriented steel has been studied. It is believed that the use of statistical distributions in the description of magnetisation of non-oriented steel is an interesting research path that can be explored further. This thesis has placed emphasis on iron losses under matrix converter supply. A global view of the drive has been undertaken to contextualise iron losses in the system consisting of converter and motor. A preliminary study on the impact of load current harmonic distortion on AC copper losses in matrix converter-fed induction motors has been presented. The assessment of direct AC-AC conversion topology in terms of motor efficiency and performance requires further analysis of skin and proximity effects in induction motors of different nominal power, size and slot design.

Co-simulation techniques (integration of a converted finite-element model used for machine design in a circuit simulator [SimPowerSystems Mathworks – Ansoft Simplorer – Dymola] ) can prove to be very useful in the study of the performance of variable speed drives. By ensuring a better physical description of the machine, essential information required to improving machine analytical models can be extracted. As a result, equivalent circuit with harmonic voltage frequency-dependent parameters may be built. Thus, the impact of design on losses in inverter (two-level, multi-level, matrix) supplied rotating machines would be investigated.

# APPENDIX

---

IRON LOSSES IN NON-ORIENTED STEEL  
SUBJECTED TO MATRIX AND DC-LINK  
CONVERTER SUPPLY.  
AN EXPERIMENTAL AND ANALYTICAL STUDY  
ON VARIABLE SPEED DRIVES.

---

BY JUAN SAGARDUY OCHOA DE ERIBE

THESIS FOR THE DEGREE  
OF DOCTOR OF PHILOSOPHY (PhD)

OCTOBER 2009

## APPENDIX

---

### **A1. Publications**

- A1.1. J. Sagarduy, A.J. Moses, F.J. Anayi, “ Eddy-Current Losses in Electrical Steels Subjected to Matrix and Classical PWM Excitation Waveforms”, *IEEE Transactions on Magnetics*, Vol 42, No 10, pp 2818-2820.

# Eddy Current Losses in Electrical Steels Subjected to Matrix and Classical PWM Excitation Waveforms

Juan Sagarduy, Anthony J. Moses, and Fatih J. Anayi

Wolfson Centre for Magnetics, Cardiff School of Engineering, Cardiff University, Cardiff CF24 3AA, U.K.

Iron losses due to flux harmonics in stator cores of pulswidth-modulation [PWM] inverter-fed induction motors have a major effect on system efficiency. Novel direct ac-ac matrix converters involve no dc-link function and enable adjustment of power factor. This paper presents experimental results of magnetic losses in two nonoriented electrical steels magnetized under different excitation, characteristic of PWM, and matrix converters. Results show the beneficial effect of a specific voltage supply (phase-to-neutral) from matrix converters on the performance of electrical steels. Iron losses in laminations excited by matrix converter waveforms were up to 30% lower than that under PWM excitation due to reduced eddy-current losses.

**Index Terms**—Eddy-current losses, matrix converters, nonoriented steels, pulswidth-modulation (PWM).

## I. INTRODUCTION

MATRIX converters are promising candidates for ac-ac links because of their near-to-sinusoidal voltage output [1]. Classical pulswidth-modulation (PWM) ac-dc-ac converters are commonly used, but the distorted voltage output characteristic of nonsinusoidal excitation increases magnetic losses in machine cores [2]–[4]. While the effect of the variation of parameters in PWM supply on core losses has been thoroughly investigated [5], [6], the performance of electrical steels under matrix converter excitation is yet unknown.

In this paper, synchronized carrier-based PWM based on the suboscillation method [7] is used in the control of a back-to-back converter. In the case of a three-phase matrix converter space-vector-modulation (SVM) is used. At high pulse number values as investigated here (60, 30, 15 for 50, 100, 200 Hz, respectively, at switching frequency 3 kHz), synchronized SVM and suboscillation PWM techniques are equivalent [7] and lead to a similar harmonic distortion factor of the voltage produced by the converter.

Total iron losses per cycle in soft magnetic materials can be separated into static hysteresis loss, dynamic anomalous loss, and classical eddy-current loss component. Static hysteresis loss, caused by micro eddy-currents due to domain wall pinning of impurities and defects, depends on material properties such as grain size, orientation, homogeneity, and internal stress. The dynamic loss, which is frequency-dependent, is related to losses caused by domain wall motion and rotation during magnetization. The classical eddy-current loss can be calculated provided assumptions, such as linearity between local  $B$  and  $H$  within the lamination and sinusoidal nature of quantities, are made. However, a better accuracy in the estimation of the classical eddy-current losses requires the consideration of nonlinearity in soft magnetic materials.

## II. THEORETICAL BASIS

A lamination of steel (width  $a$  [m]; thickness  $d$  [m]) of conductivity  $\sigma$  [S.m<sup>-1</sup>] and absolute permeability  $\mu$  is magnetized

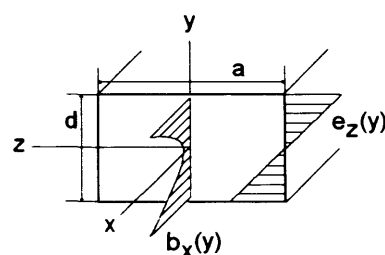


Fig. 1. Lamination of steel under uniaxial magnetization.

under sinusoidal excitation at a frequency  $f$  and a peak value of flux density  $B_p$  (see Fig. 1). The flux density  $b$  has one only component in the  $x$  direction, which is assumed constant in the  $z$  direction ( $\partial b_x / \partial z = 0$ ). From Maxwell's electric field equation [7], it is derived that  $e_y = 0 = \partial e_y / \partial z$  and  $\sigma \cdot e_z = -\partial h_x / \partial y$  (the displacement-current is neglected at low  $f$ ).

By introducing the constitutive relation of the material  $b = \mu \cdot h$  into Maxwell's equation as derived from Ampere's Law [8], the flux density  $b_x(y)$  and the electric field  $e_z(y)$  across the lamination are defined by (1) and (2). The peak value of flux density is set equal to  $B_p$  in the surface of the lamination and its variation in the center of the lamination equal to zero

$$b_x(y) = B_p [\cos(\beta \cdot y) / \cos(\beta \cdot d/2)] \quad (1)$$

$$e_z(y) = B_p \sqrt{\mu\omega/\sigma} [\sin(\beta \cdot y) / \cos(\beta \cdot d/2)] \quad (2)$$

$$\beta = \sqrt{\omega\sigma\mu} = \sqrt{2\pi f\sigma\mu_0\mu_r}. \quad (3)$$

After solving the differential equations [9] to determine  $e_z$  and  $h_x$ , Poynting's vector is calculated and integrated along the boundary of the eddy-current space [10].

Due to the assumption of nonhysteretic behavior of the material (no magnetic energy stored), the result obtained represents the eddy current losses [W/m] induced in the cross-sectional area of the lamination by time-varying excitation.

## III. NUMERICAL ANALYSIS OF EDDY-CURRENT LOSSES

### A. Linear/Nonlinear Assumption

The eddy-current losses in laminations of nonoriented electrical steel (M470-50 A and M700-65 A), with respective thicknesses 0.5 mm and 0.65 mm, were calculated based upon

TABLE I  
VARIATION OF  $R$  WITH PEAK FLUX DENSITY IN LAMINATIONS  
OF M470-50 A AND M700-65 A

M47050A	0.643	0.692	0.779	0.958	1.433	2.988
M70065A	0.653	0.676	0.708	0.779	0.946	1.438
Bp[T]	1.0	1.1	1.2	1.3	1.4	1.5

Maxwell's equations assuming linear ( $Pa$ ) and nonlinear ( $Pb$ ) behavior. For the two materials, the conductivity was  $10^8/39$  and  $10^8/30$  S.m<sup>-1</sup>, respectively, the frequency of the sinusoidal excitation was 50 Hz. For each value of peak flux density in the case of nonlinear behavior, the correspondent value of peak magnetic field was taken from a catalogue of industrial fully-processed steels [11]. In the linear region of the BH curve (below 1.0 T), the relative permeability calculated for M470-50 A and M700-65 A was 4974 and 4325, respectively. Table I shows the variation of  $R = (Pb/Pa)$  with the peak value of induction  $Bp$ . It can be seen that at 1.0 T, the eddy-current losses are overestimated by 35.7% and 34.7% by the linear approach in M470-50 A and M700-65 A, respectively. However, at 1.5 T, the linear method accounts for an underestimation of the eddy-current losses of 199% and 44% in both materials, respectively.

Due to the dependence of the eddy-current phenomenon on the fundamental frequency of magnetization  $f$ , the assumption of linear behavior under sine excitation for high values of  $f$  also leads to an inaccurate estimation. The disparity of the results derived from the two approaches is reinforced in laminations of steel subjected to pulsating waveforms of voltage excitation, with a high-order harmonic content. The skin effect in laminations of steel [12] can be taken into account below 1.3 T, reduce the calculated value of the losses, and improve the accuracy of the linear method. However, above 1.3 T, the skin effect may contribute to an even larger inaccuracy, as the materials approach saturation and nonlinearity becomes apparent. Therefore, in this paper, the calculation of the eddy-current losses at 1.5 T will be based upon the linear approach and neglect the skin effect. Nonetheless, an additional term  $k$  will be considered in order to compensate for the above-mentioned underestimation.

In laminations of electrical steels magnetized under sine excitation where  $B_{in}$  and  $B_p$  are peak values of flux density in the center of the lamination and on the surface, respectively, the variation of the ratio  $B_{in}/B_p$  with distance  $y$  from the center of the lamination [13] is given by

$$\alpha(y, f) = \frac{B_{in}}{B_p} = \sqrt{\frac{1 + \cosh(2\beta y)}{1 + \cosh(\beta d)}} \quad (4)$$

Under pulsating forms of voltage excitation, the flux density  $b$  across the lamination can be decomposed into sinusoidal harmonic components of amplitude  $B_n$  and frequency  $f_n$ . In this paper, the calculation of the specific eddy-current losses  $Pe$  is performed as given in (5) and neglects harmonics above  $f_n = 12$  kHz. The density of the material is  $\delta$  [kg/m<sup>3</sup>] and the factor  $k$  is given in (6)

$$Pe = \frac{\pi^2 \sigma \cdot d^2}{6\delta} \sum_{n=1} [1 + k(f_n)] B_n^2 f_n^2 \quad (5)$$

TABLE II  
VARIATION OF  $k$  [%] WITH FREQUENCY  $f_n$  OF THE  $n$ th HARMONIC  
COMPONENT IN M470-50 A AND M700-65 A

$f_n$ [Hz]	50	750	1250	4500	9000	12000
M47050A	0.05	6.08	11.76	36.36	50.84	56.25
M70065A	0.64	31.92	46.79	79.57	90.06	93.12

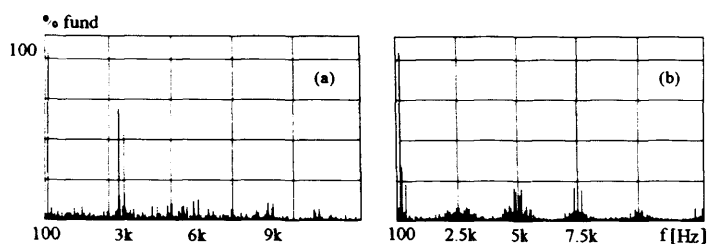


Fig. 2. Harmonic spectrum of voltage waveforms. (a) PWM. (b) Matrix.

$$k(f_n) = (1/d^2) \cdot \left[ d - \int_{-d/2}^{+d/2} \alpha(y, f_n) dy \right]^2 \quad (6)$$

#### IV. EXPERIMENTAL RESULTS AND DISCUSSION

Nonoriented electrical steels samples (thickness 0.5 and 0.65 mm, respectively; width 30 mm, length 306 mm) were selected for measurement and calculation of their eddy-current loss components. M470-50 A is a 2.5% silicon steel ( $\rho = 39 \mu\Omega$  cm;  $\delta = 7700$  kg/m<sup>3</sup>;  $\mu_r = 1120$ ), and M700-65 A is a 1.8% silicon steel ( $\rho = 30 \mu\Omega$  cm;  $\delta = 7750$  kg/m<sup>3</sup>;  $\mu_r = 1570$ ). Table II shows the variation of calculated values of  $k(f_n)$  with the frequency  $f_n$  for the two materials.

Prior to magnetic testing of the steel samples, the output voltages of a prototype 7.5-kW matrix converter and a classical PWM converter (Toshiba-Transistor Inverter TOSVERT VF-A3 400 V - 0.75 kW) were measured and stored in a signal generator (TTi - TGA 30 MHz). Fig. 2 shows the harmonic spectrum of the voltage waveforms produced by a PWM (a) (phase-to-phase, modulation index 0.8, and switching frequency 3 kHz) and matrix converter (b) (phase-to-neutral, output voltage ratio  $(\sqrt{3}/2)$ , and sampling frequency 2.5 kHz).

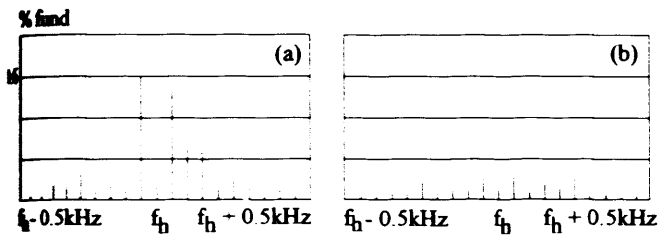
Whereas in PWM voltage waveforms harmonics are found at the switching frequency, the absence of a unique switching frequency in matrix converters leads to a different spectrum (see Fig. 2). Furthermore, the presence of spread sideband harmonics results in a reduction of the peak of clusters in the envelope of the harmonic spectrum corresponding to the matrix excitation. 306 mm  $\times$  30 mm strip samples were magnetized in a single strip tester and their power loss measured using a power analyzer (Voltech - PM3000 A). The loss was measured when sinusoidal voltage and voltages of the same waveshapes as the stored PWM and matrix signals were used to energize the magnetizing coil. The flux density in each case was monitored by integrating the induced voltage in a secondary coil. Table III shows the measured loss ( $Pt$ ) under the three conditions in the two materials at three values of fundamental frequency, each at a peak flux density of 1.5 T.

Under the worst conditions, the loss under matrix and PWM waveforms was 46.1% and 64.3% higher than that under sine

TABLE III

MEASURED LOSS (Pt) AND CALCULATED EDDY-CURRENT LOSS (Pe) [W/kg] IN LAMINATIONS OF (a) M470-50 A(a) AND (b) M700-65 A

f [Hz]	50		100		200	
	Pt	Pe	Pt	Pe	Pt	Pe
Exc (a)	2.92	0.77	10.08	3.09	31.41	12.42
Matrix (a)	3.41	0.89	11.21	4.77	45.96	15.59
PWM (a)	4.77	1.27	14.13	7.25	51.70	22.30
Exc (b)	3.96	1.69	11.80	6.88	37.97	28.71
Matrix (b)	4.49	2.00	14.43	9.89	60.96	36.46
PWM (b)	6.58	3.06	22.73	18.4	79.08	55.80

Fig. 3. Amplitude of a harmonic component of flux density at 1.5 T under (a) matrix voltage excitation and (b) PWM voltage excitation at a high frequency  $f_h$ .

conditions in the high silicon steel and 60.5% and 108.3%, respectively, in the low silicon steel. The higher losses can be attributed to the higher harmonic components in the flux density waveform in the PWM voltage condition, as shown in Fig. 3.

Table III also shows the eddy-current loss calculated from the loss associated with each harmonic component, based on the spectrum of flux density, was calculated. It is relevant to highlight that the eddy current component under PWM excitation was up to 86% higher than when supplied by a matrix converter signal at 100 Hz. This was due to redistribution (see Fig. 2) and spreading (see Fig. 3) of harmonics in the frequency spectrum. Nevertheless, subharmonics in phase-to-neutral voltage waveforms of the matrix converter, which are intrinsic to the frequency conversion, appear at 100 and 200 Hz. Therefore, the effect of a substantial reduction in the eddy-current component on the total loss is mitigated, probably caused by saturation of the static BH loop.

## ACKNOWLEDGMENT

The authors would like to thank Prof. J. C. Clare and Dr. P.W. Wheeler at the University of Nottingham for providing the matrix converter used in the experimental study.

## REFERENCES

- [1] G. P. W. Wheeler, J. Rodriguez, J. C. Clare, L. Empringham, and A. Werstein, "Matrix converters: A technology review," *IEEE Trans. Ind. Electron.*, vol. 49, no. 2, pp. 276–288, Apr. 2002.
- [2] A. J. Moses, "Loss prediction in electrical steel laminations and motor cores," *Steel Res. Int.*, vol. 76, 2005.
- [3] E. Barbisio, F. Fiorillo, and C. Ragusa, "Predicting loss in magnetic steels under arbitrary induction waveform and with minor hysteresis loops," *IEEE Trans. Magn.*, pt. 1, vol. 40, no. 4, pp. 1810–1819, Jul. 2004.
- [4] A. Boglietti, A. Cavagnino, M. Lazzari, and M. Pastorelli, "Predicting iron losses in soft magnetic materials with arbitrary supply: An engineering approach," *IEEE Trans. Magn.*, pt. 2, vol. 39, no. 2, pp. 981–989, Mar. 2003.
- [5] A. Boglietti, P. Ferraris, M. Lazzari, and M. Pastorelli, "Change of the iron losses with the switching supply frequency in soft magnetic materials supplied by PWM inverter," *IEEE Trans. Magn.*, pt. 2, vol. 31, no. 6, pp. 4250–4252, Nov. 1995.
- [6] A. Boglietti, P. Ferraris, M. Lazzari, and F. Profumo, "Effects of different modulation index on the iron losses in soft magnetic materials supplied by PWM inverter," *IEEE Trans. Magn.*, pt. 2, vol. 29, no. 6, pp. 3234–3236, Nov. 1993.
- [7] J. Holtz, "Pulsewidth modulation. A survey," *IEEE Trans. Ind. Electron.*, vol. 39, no. 5, pp. 410–420, Oct. 1992.
- [8] J. D. Kraus, "Electromagnetics," in *Electrical Engineering Series*, 4th ed. New York: McGraw-Hill, 1991.
- [9] W. E. Boyce and R. Di Prima, *Elementary Differential Equations and Boundary Value Problems*, 2nd ed. New York: Wiley, 1969.
- [10] A. Krawczyk and J. A. Tegopoulos, "Numerical modeling of eddy currents," in *Monographs in Electrical & Electronic Engineering No. 32*. Oxford, U.K.: Oxford Science, 1993.
- [11] Cogent Power Ltd., *Electrical Steel Non-Oriented Fully Processed*, Nov. 2002.
- [12] J. Gyselinck, L. Vandeveld, J. Melkebeek, P. Dular, F. Henrotte, and W. Legros, "Calculation of eddy current and associated losses in electrical steel laminations," *IEEE Trans. Magn.*, pt. 1, vol. 35, no. 3, pp. 1191–1194, May 1999.
- [13] D. O'Kelly, "Flux penetration in a ferromagnetic material including hysteresis and eddy-current effects," *J. Phys. D: Appl. Phys.*, vol. 5, no. 1, pp. 203–213, Jan. 1972.

Manuscript received March 9, 2006 (e-mail: Sagarduychoadeeribe1@Cardiff.ac.uk).

A1.2. J. Sagarduy, A.J. Moses, "Impact of Sideband Harmonic Pattern on Losses in Laminated Non-Oriented Steels", *Journal of Magnetism and Magnetic Materials*, Vol 320, e614-618, April 2008.

## Impact of sideband harmonic pattern on losses in laminated non-oriented steel

Juan Sagarduy<sup>a,\*</sup>, Anthony J. Moses<sup>b</sup>

<sup>a</sup>ABB Corporate Research, Electrical Machines and Intelligent Motion Group, Västerås 721 78, Sweden

<sup>b</sup>Wolfson Centre for Magnetics, Cardiff School of Engineering, Cardiff CF24 3AA, UK

Available online 10 April 2008

Losses in laminated non-oriented steel under the effect of two high harmonic clusters, caused by voltage excitation typical of two-level pulse-width modulated (PWM) DC-link and space-vector modulated (SVM) matrix converters, were analyzed. The predicting method used, which incorporates anisotropy of loss  $K_a$  and grain size  $g_s$ , describes the magnetizing process within the steel by the means of a statistical distribution. Results are then compared to losses determined by Bertotti's model. The two methods confirmed that the effect of sideband harmonics in the kilohertz range can reduce harmonic losses by up to 40% at low power frequencies.

© Elsevier B.V. All rights reserved.

Keywords: Non-oriented steel; Iron loss; Sideband flux harmonics; Matrix converter

### Introduction

The growth of developing economies has resulted in a steady increase in the worldwide demand for steel [1]. In India, Mittal reported that 22% of their production was used by industrial and mechanical machinery markets. In Japan, identical market accounted for 15.5% of the domestic consumption [3]. Large synchronous motors are used in power generation and industry applications. These motors are more efficient than three-phase induction motors, essential in industrial fans and pumps. Considerable energy savings are achievable by incorporating variable speed drives and replacing throttle-based flow control [4]. Induction motors are then supplied by fast-switching frequency converters, which cause flux harmonics in the kilohertz range. The rise in core losses contributes to overheating, which compromises reliability, motor lifespan and requires cooling of the motor by a fan. The location of flux clusters is defined by pulse-width modulated (PWM) switching or space-vector modulated (SVM) sampling frequency ( $f_{sw}$ ), sideband harmonic clusters are characteristic of the AC–AC power conversion

topology [5]. Losses in laminated steel are analyzed in terms of static hysteresis, classical eddy-current and anomalous losses [6]. More recently, the concept of magnetic viscosity has been introduced to loss prediction under PWM supply [7].

Non-oriented steels are a complex structure of grains of irregular shape, size and orientation. Grain size is an influential factor on permeability and losses in non-oriented steel. It is strongly affected by the annealing process. A study predicted the optimum grain size in laminated steel for various magnetizing frequencies [8]. The impact of silicon content and grain texture was investigated based upon artificial neural networks [9]. Hot rolling conditions were underlined as key elements to the performance of Si–Fe alloys [10]. High permeability and isotropy are required for the steel, while cyclic magnetization should be accomplished with minimum losses. In practice, non-oriented steels are not fully isotropic. The performance of non-oriented steel with different anisotropy was experimentally studied. The investigation confirmed that losses in identical alloys, but provided by different manufacturers, were affected by the disparity in their anisotropic characteristics [11].

In this paper, the impact of two clusters (A and B) of flux harmonics centered at  $f_{sw} = 2.5$  kHz (Fig. 1) on losses in

\*Corresponding author. Tel.: +46 73 06 07 808; fax: +46 21 32 32 12.

E-mail address: [juan.sagarduy@se.abb.com](mailto:juan.sagarduy@se.abb.com) (J. Sagarduy).

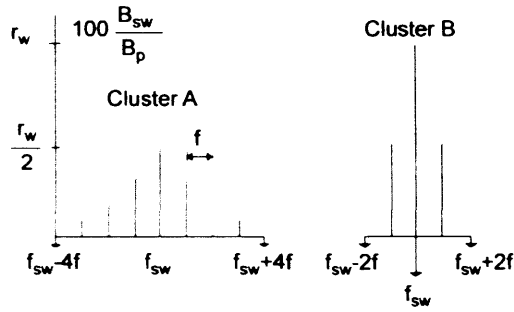


Fig. 1. Clusters A and B of high flux harmonics ( $r_w = 2.5\%$ ).

Eqs. (4) and (5)

$$\dot{\delta}_{dw}(y, t) = \left( \frac{g_s}{2B_{sat}(n_{dw} - 1)} \right) \frac{\partial B(y)}{\partial y} \sin(\omega t) \quad (4)$$

$$\delta_{dw}(y, t) = \left( \frac{-g_s}{2\omega B_{sat}(n_{dw} - 1)} \right) \frac{\partial B(y)}{\partial y} \cos(\omega t) \quad (5)$$

The energy loss per grain  $W_{loss}$  (J) dissipated by friction exerted on domain walls is expressed as a function of specific power losses  $P_{sin}$  (W/kg) under sinusoidal conditions [12], frequency  $f$ , thickness  $d$  and density  $\rho$  (kg/m<sup>3</sup>). This equation is used to determine the viscous coefficient  $\beta$ :

$$W_{loss} = \beta \int_0^{1/f} \dot{\delta}_{dw} \delta_{dw} dt = \frac{P_{sin}(g_s^2 d) \rho}{n_{dw} f} \quad (6)$$

When flux harmonics are present, instantaneous flux density  $b_{harm}(y, t)$  is analyzed as a sum of  $n$  harmonics of amplitude  $B_{s,n}$  at the surface of the grain:

$$b_{harm}(y, t) = \sum_{n=1}^n B_n(y) \sin(\omega_n t) \quad (7)$$

$$B_n(y) = \sum_{n=1}^n B_{s,n} \sqrt{\frac{\cosh(2p_n y) + \cos(2p_n y)}{\cosh(p_n d) + \cos(p_n d)}} \quad (8)$$

The conductivity of the steel is assumed constant in the steel. The relative permeability of the material is obtained from manufacturer's specifications on M400-50A [12]. The principle of superposition of harmonics is applied (flux harmonics  $B_n$  are assumed to be in phase with the fundamental component). From Eqs. (7) and (8), displacement and velocity of domain walls are calculated in a Matlab M-file. Harmonic losses in each grain of the material can therefore be defined for given frequency and peak flux density  $B_s$ .

### 2.1. Poisson statistical distribution

Prior to the calculation of harmonic losses, the contribution of grains to net magnetization (and hence their flux density) must be established. Poisson statistical distribution [13] was used to describe the magnetizing process in non-oriented steel with  $A = 10^3$  and  $k(\theta) = A(\theta + 90)/180$ . The probability function  $f(\theta, \lambda)$  is given in Eqs. (9) and (10)

$$f(k(\theta), \lambda) = \frac{e^{-\lambda} \lambda^{k(\theta)}}{k(\theta)!} \quad (9)$$

$$\lambda = \frac{\alpha}{g_s K_a f} \quad (10)$$

The term  $\alpha$  is taken equal to 4.5 in this first approach to modeling losses under harmonic-rich induction. The function  $f(\theta)$  was calculated for  $K_a = 9\%$  and two grain sizes (100–125  $\mu\text{m}$ ) at three magnetizing frequencies (50–100–200 Hz). Three populations of grains  $R_1$ ,  $R_2$  and

M400-50A are investigated in the 50–200 Hz frequency range. While cluster A is associated to low-modulated ( $m_i = 0.65$ ) two-level DC-link converter supply, cluster B is linked to optimum matrix converter excitation ( $q = \sqrt{3}/2$ ).  $B_1$  is the fundamental peak flux density and  $B_{sw}$  the amplitude of the harmonic component at  $f_{sw} = 2.5$  kHz.

## 2. Analysis of losses in non-oriented steel

The steel is analyzed in terms of identical prismatic grains  $G_i$  of square base ( $g_s \times g_s$ ) and height  $d$ , where  $d$  (m) is the thickness of the M400-50A lamination. The orientation of every grain with respect to the rolling direction is equal to  $\theta_i$ . The associated induction is a vector  $b_i$  in the plane of the lamination. The volume of material contained in an individual grain is divided into bar-like 180° domains ( $n_{dw}$  = number of domain walls per grain). The material is cyclically magnetized through domain wall motion. A force  $F_r$ , proportional to the velocity of the walls and a viscous coefficient  $\beta$ , opposes its movement and accounts for the total energy dissipated in the material during the magnetizing process. The flux density across the height of every grain is given by  $b(y, t) = B(y) \sin(\omega t)$ , where  $\omega = 2\pi f$  and  $f = (\mu\sigma\omega)^{1/2}$ :

$$B(y) = B_s \sqrt{\frac{\cosh(2p y) + \cos(2p y)}{\cosh(p d) + \cos(p d)}} \quad (1)$$

The gradient of the instantaneous magnetization  $m(y, t)$  can be written in terms of permeability of free space  $\mu_0$ , relative permeability of the material  $\mu_r$  and flux density  $b$ :

$$\left( \frac{\mu_r - 1}{\mu_0 \mu_r} \right) \times \frac{\partial b}{\partial y} = \frac{\partial m}{\partial y} = n_{dw} K_\delta \dot{\delta}_{dw} \quad (2)$$

When saturation is reached at the surface of the grain [ $B(d/2) = B_{sat}$ ], the displacement of every domain wall is given in Eq. (3). The coefficient  $K_\delta$  is then calculated:

$$\dot{\delta}_{dw} \left( \frac{d}{2} \right) = \frac{g_s}{2(n_{dw} - 1)} = \frac{B_{sat}}{n_{dw} K_\delta} \left( \frac{\mu_{r,sat} - 1}{\mu_0 \mu_{r,sat}} \right) \quad (3)$$

When the relative permeability of the material ( $\mu_r$ ;  $\mu_{r,sat}$ ) is very high compared to unity, the velocity and displacement of domain walls along the thickness of the grain is given as

... were defined within the steel based on Poisson statistical distribution. In  $R_1$  where  $(\sqrt{3}/2 < f(\theta)/f(\theta = 0) < 1)$ ,  $X_1$  grains reach  $B_{R1} = (2\sqrt{3}/3)B_{max}$  as surface peak flux density. In  $R_2$  where  $(2/3 < f(\theta)/f(0) < \sqrt{3}/2)$ ,  $X_2$  grains reach  $B_{R2} = B_{max}$ . In  $R_3$ , where  $(f(\theta)/f(0) < 2/3)$ ,  $X_3$  grains reach  $B_{R3} = (4\sqrt{3}/9)B_{max}$ .  $X_1$ ,  $X_2$  and  $X_3$  are accumulated probabilities related to groups  $R_1$ ,  $R_2$  and  $R_3$  as given by Eq. (11). Values are shown in Table 1:

$$X_i = \int_{R_i} f(\lambda, \theta) d\theta \quad (11)$$

In the three cases, an increase in frequency resulted in a higher contribution to net magnetization by grains closely aligned with the applied field. When frequency was raised and size was lowest, grains with intermediate orientation (RF) played the main part in the magnetizing process. On the contrary, grains with higher degree of misalignment with the applied field ( $R_3$ ) reduced their impact on global magnetization. When the grain size was largest, grains in the second group ( $R_2$ ) saw their contribution to net magnetization reduced while grains in  $R_1$  (closely aligned with the applied field) and  $R_3$  (more closely oriented in the transverse direction) played the main role.

Once  $X_1$ ,  $X_2$  and  $X_3$  were calculated, maximum induction  $B_{max}$  in the steel is given by Eq. (12). Values of  $B_{max} = (B_{max} B_1)$  are shown in Table 2 for two grain sizes (10 and 125  $\mu\text{m}$ ):

$$B_{max} = \frac{B_1}{(2\sqrt{3}/3)X_1 + X_2 + (4\sqrt{3}/9)X_3} \quad (12)$$

In the three magnetizing frequencies, an increase in grain size had a major impact on the ratio  $r_{max}$ . The calculation of losses associated to the three grain populations requires information on the permeability of the steel at peak inductions ( $B_{R1}$ ,  $B_{R2}$  and  $B_{R3}$ ) and specific power losses under sine conditions at 50, 100 and 200 Hz. They must be further obtained from experimental measurements, or

Table 1  
Values of  $X_1$ ,  $X_2$  and  $X_3$  at 50, 100 and 200 Hz

f (Hz)	$K_a = 9^\circ$					
	$g_s = 10^{-4} \text{ m}$			$g_s = 1.25 \times 10^{-4} \text{ m}$		
	$R_1$	$R_2$	$R_3$	$R_1$	$R_2$	$R_3$
50 Hz	0.0266	0.3830	0.5904	0.0297	0.4239	0.5464
100 Hz	0.0376	0.4287	0.5337	0.0421	0.3653	0.5926
200 Hz	0.0532	0.4522	0.4946	0.0595	0.3465	0.5940

Table 2  
Ratio  $(B_{max} B_1)$  at 50, 100 and 200 Hz

f (Hz)	$g_s = 10^{-4} \text{ m}$		$g_s = 1.25 \times 10^{-4} \text{ m}$	
	$R_1$	$R_2$	$R_1$	$R_2$
50 Hz	1.1580	1.1381	1.1381	1.1381
100 Hz	1.1326	1.1478	1.1478	1.1478
200 Hz	1.1181	1.1461	1.1461	1.1461

provided by the steel manufacturer. Research on loss prediction in non-oriented steel under harmonic-rich induction is often confronted to limited available data on commercial steel grades in frequency and induction ranges, even under sinusoidal conditions.

### 3. Results and discussion

In laminated cores of rotating machines, very high levels of induction (close to saturation) are reached in specific regions (teeth bases and tips) while other parts (yoke) reach much lower flux density (less than 1.0 T). In this paper, harmonic core losses in M400-50A are therefore calculated at an intermediate value  $B_1 = 1.2 \text{ T}$  that can be associated to the total mass of steel in a real machine. The number of domain walls per grain was constant ( $n_{dw} = 5$ ).

#### 3.1. Model incorporating anisotropy and grain size

With information on physical/magnetic properties and typical loss of M400-50A under sinusoidal conditions, a curve C linking harmonic losses caused by clusters A and B to frequency was obtained in the 0.5–1.7 T induction range. Selected magnetizing frequencies were 50, 100 and 200 Hz. Anisotropy of loss  $K_a$  and grain size  $g_s$  were 9% and 100  $\mu\text{m}$ , respectively. With calculated values of  $(B_{R1}, X_1)$ ,  $(B_{R2}, X_2)$  and  $(B_{R3}, X_3)$  shown in Table 3, harmonic core losses associated to the three populations of grains ( $\Delta R_1, \Delta R_2, \Delta R_3$ ) are obtained from curve C. Table 4 shows values of harmonic losses at 1.0, 1.3 and 1.5 T. The increment  $\Delta W_{Fe}$  (%) in iron losses in the M400-50A lamination is given in Eq. (13):

$$\Delta W_{Fe} (\%) = (X_1 \Delta R_1 + X_2 \Delta R_2 + X_3 \Delta R_3) \quad (13)$$

Table 3  
Definition of the three populations of grains ( $X_1, X_2, X_3$ ) and their associated magnetising states ( $B_{R1}, B_{R2}, B_{R3}$ )

	$B_{R1}$ (T)	$X_1$	$B_{R2}$ (T)	$X_2$	$B_{R3}$ (T)	$X_3$
50 Hz	1.594	0.0266	1.380	0.3830	1.063	0.5904
100 Hz	1.570	0.0376	1.359	0.4287	1.046	0.5337
200 Hz	1.550	0.0532	1.342	0.4522	1.033	0.4946

Table 4  
Harmonic losses (%) caused by clusters A and B in M400-50A at 1.0, 1.3 and 1.5 T and 50, 100 and 200 Hz magnetizing frequency

	$B_1$ (T)	Harmonic losses (%)		
		1.0	1.3	1.5
50 Hz	Cluster A	48.5	22.3	4.3
	Cluster B	77.7	35.4	6.9
100 Hz	Cluster A	39.5	18.2	3.4
	Cluster B	72.5	34.1	6.5
200 Hz	Cluster A	16.2	7.5	1.3
	Cluster B	25.8	12.5	2.6

3.2. Bertotti's model

Harmonic core losses in M400-50A subjected to flux harmonics (clusters A and B) were predicted by Bertotti's model [14].

Based on known total losses ( $W_s$ ) under sine conditions at 50, 100 and 200 Hz [12], coefficients  $K_h$  and  $K_a$  were calculated for 1.2 T ( $K_h = 0.0164$  and  $K_a = 8.6 \times 10^{-4}$ ). The proportion of eddy-current and anomalous losses in M400-50A is given in Table 5. Static hysteresis per cycle was assumed constant and independent of harmonic distortion in the flux density. Classical eddy-current loss (term 2) is defined by thickness  $d$  (m), conductivity  $\sigma$  (S/m) and density  $\rho$  (kg/m<sup>3</sup>) of the lamination.

Respective increments  $\Delta W_e$  and  $\Delta W_a$  of classical eddy-current and anomalous losses were calculated analytically for clusters A and B. They were then used to establish global harmonic losses in M400-50A. Results obtained from the two methods are presented in Figs. 2 and 3.

The proposed model confirmed that the two flux harmonics clusters A and B had a moderate impact on harmonic core losses (10.4% and 16.8%) at 200 Hz. On the contrary, spreading of sideband harmonics ensured by cluster A was proven strongly beneficial to magnetization of M400-50A at (50 Hz; 100 Hz). Core losses increased by (31.3%; 25.3%) under cluster A compared to (49.9%; 46.9%) under cluster B.

Results obtained from Bertotti's model underlined the beneficial effect of cluster A at 50 Hz (57% harmonic losses compared to 81.7% under cluster B). A lower rise in core losses (25.4%) was ensured by cluster A at 100 Hz when compared to 31.4% associated to cluster B. However, very similar increases (11.10–10.9%) in magnetic losses were reported under clusters A and B, respectively.

Table 5  
Classical eddy-currents and anomalous loss components in M400-50A at 1.2 T and 50, 100 and 200 Hz

% Of total loss	50 Hz	100 Hz	200 Hz
Eddy-current	22.4	34.4	47.9
Anomalous	19.7	21.4	21.0

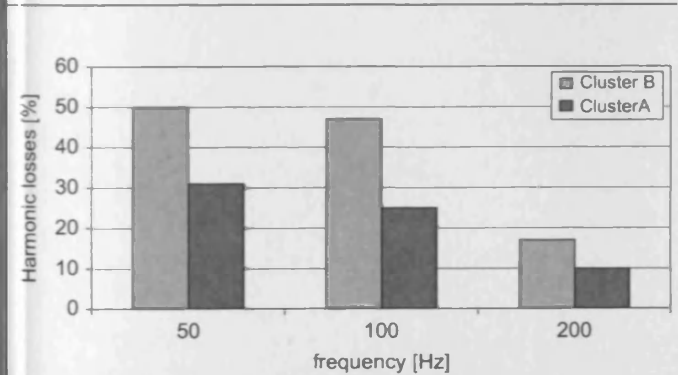


Fig. 2. Harmonic core losses  $\Delta W_{Fe}$  (%) caused by clusters A and B (predicted from Poisson model based on anisotropy and grain size).

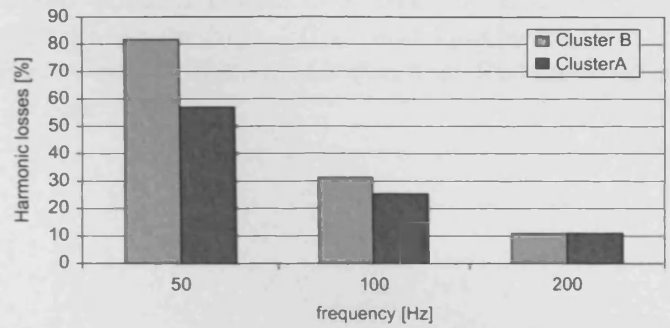


Fig. 3. Harmonic core losses  $\Delta W_{Fe}$  (%) caused by clusters A and B (predicted by Bertotti's model).

Although the two approaches highlighted the same trend, some discrepancy in the results was observed. Due to the physical complexity of non-oriented steel, a more accurate description of the magnetizing process would need breaking down the total number of grains into more than three groups. Grains of different size throughout the material consist of variable number of domain walls, which in addition may change with frequency. This would affect the calculation of losses associated to every group of grains. Nonetheless, a certain degree of abstraction will always be necessary to combine pragmatism and accuracy of loss prediction to a satisfactory physical description of non-oriented steel.

4. Conclusion

The AC-AC conversion topology, along with the modulation strategy, has a direct impact on losses in laminated steel commonly used in rotating machines. SVM matrix converters ensured spreading of sideband harmonics in high flux clusters. Two predicting methods, based on anisotropy of loss and grain size (1) and Bertotti's separation model (2), confirmed that spreading of harmonics in the kilohertz range can reduce harmonic core losses by up to 40% at low power frequencies.

References

- [1] International Iron and Steel Institute, World Steel in Figures.
- [2] Arcelor-Mittal, ArcelorMittal Fact Book 2006, July 2007.
- [3] Nippon Steel Corporation, Iron and Steel Statistics, 2006.
- [4] A. De Almeida, et al., Variable Speed Drives for Electric Motor Systems, Save II Programme, 2000, pp. 1–105.
- [5] Sagarduy, et al., IEEE Trans. Magn. 42 (10) (2006) 2818.
- [6] G. Bertotti, et al., JMMM 112 (1–3) (1992) 146.
- [7] S. Zirka, et al., IEEE Trans. Magn. 42 (9) (2006) 2121.
- [8] M.F. de Campos, et al., JMMM 301 (1) (2006) 91.
- [9] A. Chaudhury, et al., JMMM 313 (1) (2007) 21.
- [10] J. Hunady, et al., JMMM 304 (2) (2006) E620.
- [11] S. Tumanski, et al., JMMM 254/255 (2003) 50.
- [12] Cogent Power, Non-Oriented Fully-Processed Steel, November 2002.
- [13] K. Bury, Statistical Distributions in Engineering, Cambridge University Press, 1999 ISBN 0-521-63506-3.
- [14] G. Bertotti, Hysteresis in Magnetism for Physicists, Material Scientists and Engineers, Academic Press, 1998 ISBN 012093270-9.

- A1.3. J. Sagarduy, A.J. Moses, "Copper Winding Losses in Matrix Converter-Fed induction Motors: a Study Based on Skin Effect and Conductor Heating, *39<sup>th</sup> IEEE Power Electronics Specialists Conference*, Rhodes (Greece), pp 3192 -3198, 16-20 June 2008.

# Copper Winding Losses in Matrix Converter-Fed Induction Motors: A Study Based on Skin Effect and Conductor Heating

Juan Sagarduy\* and Anthony J Moses\*\*

\* Electrical Machines and Motion Control Group, ABB Corporate Research, Västerås, Sweden

\*\* Wolfson Centre for Magnetics, Cardiff University, Cardiff, United Kingdom

**Abstract**— The potential for increasing electrical efficiency in two induction motors (nominal power 15kW and 3kW) under space-vector modulated [SVM] matrix converter-supply is analysed. Skin effect losses in stator copper conductors can be reduced by up to 1.5% at medium speed when compared to losses under DC-link carrier-based PWM two-level converter excitation. The investigation, which uses the thermal network technique to account for internal heating, reveals that the beneficial effect of line-line matrix converter supply on iron losses must be considered to capitalize on energy saving potential of low-power variable-speed drives built around asynchronous motors.

## I. INTRODUCTION

Potential energy savings are achieved by using variable speed drives for control of rotating machines [1]. In this context, squirrel-cage induction motors in the 0.75 to 30 kW range are to play an essential role in the near future. Due to their overwhelming presence in widespread applications (pumps, fans, air conditioning, refrigeration) enhanced by the growth of major economies (China, India), induction motors (and their interaction with fast-switching frequency converters) have gained recent attention. As a result of being exposed to permanent full load operation, Joule losses in copper windings lead to overheating. In order to ensure reliability and guarantee a minimum lifespan, a cooling fan has to be incorporated. While design based upon sinusoidal conditions remains a very pragmatic approach, the impact of current ripple and flux harmonics on efficiency and thermal stress in internal parts of the motor must be taken into account. Increasing awareness on power consumption, which will be accompanied by more strict requirements on motor efficiency, may result in higher engineering costs for motor suppliers. Nonetheless, understanding of AC-AC power conversion topologies, modulation techniques and control methods is undoubtedly the way ahead to maintain a competitive market position. Carrier-based Pulse-Width-Modulated [PWM] DC-link converters are well established as a low-cost solution for AC drives. However, their operation depends on temperature-sensitive electrolytic capacitors that require proper cooling. Furthermore, their lifespan is compromised by DC current ripple, which must be mitigated by an inductor. Space-Vector-Modulated [SVM] three-phase matrix converters are direct AC-AC links, where input and output phases are connected via three bidirectional switches (two IGBT and anti-parallel diodes in back-to-back configuration) [2]. Due to

reduction in weight and volume (absence of DC-link) and possible power factor control, matrix converters have been confirmed as suitable candidates for AC drives [3][4] specially in aerospace and military applications [5]. Research aiming at improving the operation of matrix converters has been carried out successfully [6]. Robustness against input voltage disturbances [7], analysis of line currents [8], improved modulation and control [9][10][11][12] and increased output voltage transfer ratio [13] can be cited as the most recent points of interest. The beneficial effect of voltages produced by matrix converters on losses in non-oriented steel has already been investigated. As a result of spreading of sideband harmonics in the kilohertz range, a more efficient magnetization of steel thanks to reduced eddy-current and anomalous losses is accomplished [14]. The correlation between load current ripple and SVM control in matrix converters has been studied [15]. However, the impact of direct AC-AC converter supply on copper winding losses in low-power induction motors at various load conditions is yet unknown and presented here. The paper, which looks into skin effect in conductors, discusses potential improvements in motor efficiency by using matrix converters instead of classical two-level DC-link converters.

The thermal network technique [TNT] [16] is used to determine the effect of an increase in effective AC frequency (due to harmonic current distortion) on stator winding temperature. For that purpose, a simplified lumped parameter circuit with five masses (chassis, copper windings, steel core, rotor, shaft) and two components of losses (Joule losses in the copper and iron losses in the steel) was considered. Conductive (radial direction), convective and irradiative heat transfer to the ambient was accounted for in the thermal model of the induction motors.

## II. ANALYTICAL PROCEDURE

### A. Motor characterisation

Based on specifications provided by the manufacturer [17] (table I), the equivalent circuit of two squirrel-cage induction motors of nominal power 15 kW and 3 kW (table II) was calculated.

TABLE I. CHARACTERISTICS OF THE TWO INDUCTION MOTORS UNDER STUDY

	Pu [kW]	ns [rpm]	In [A]	Ist/In	cos φ	s <sub>nom</sub> [%]
Motor I	15	1500	28	6.8	0.89	4.67
Motor II	3	1500	6.48	5.5	0.77	2.67

The number of pole pairs  $p$  and nominal voltage  $V_{nom}$  [V] in the two induction motors are 4 and  $415/\sqrt{3}$  V, respectively.

TABLE II. PARAMETERS OF THE EQUIVALENT CIRCUIT IN MOTORS I AND II

	$R_1 = R_2$ [Ω]	$L_1 = L_2$ [mH]	$R_0$ [Ω]	$L_0$ [mH]
Motor I	0.27	1.8	79.6	70.1
Motor II	2.10	8.2	760.2	182.6

From specifications given by the motor supplier, basic information on motor I (M2AA 160L) and motor II (M2AA 100LB) such as diameter  $d_{sh}$  [mm] and axial length  $L_{sh}$  [mm] of the shaft, inertia  $I_{rot}$  [kgm<sup>2</sup>] and active length  $L_a$  [mm] were extracted.

TABLE III. DATA ON INDUCTION MOTORS I AND II

	dsh [mm]	$I_{rot}$ [kgm <sup>2</sup> ]	$L_a$ [mm]	$L_{sh}$ [mm]
motor I	42	0.091	250	604
motor II	28	0.0082	172	403

If the geometry of the rotor is analysed as a hollow cylinder of internal diameter  $d_{sh}$ , the diameter  $d_{rot}$  [m] of the rotor is obtained (2) where  $\delta$  [kg.m<sup>-3</sup>] is the density of the steel used to manufacture the rotor.

$$d_{rot} = \sqrt{d_{sh}^4 + \frac{16I_{rot}}{L_a \pi \delta}} \quad (2)$$

The four magnitudes ( $d_{sh}$ ,  $L_{sh}$ ,  $I_{rot}$ ,  $L_a$ ) along with information on stator slots (§ I.D), insulation layer (material and thickness) are required to calculate the mass of chassis, core, windings, rotor and shaft and define thermal resistances and capacitances in the thermal network associated to squirrel-cage asynchronous motors I and II.

### B. Motor Loading and Control Strategy

The slip was kept at its nominal value  $s_{nom}$  [%]. Typical line-voltages of two-level DC-link and matrix converters [ $U_{pk} = 415V$ ] were generated in Matlab – Simulink environment (§A2), as respective PWM and SVM algorithms for a given switching (PWM) / sampling (SVM) frequency  $f_w = 5$  kHz were implemented in an S-function. Three fundamental frequencies  $f$  [Hz] were selected: 50 Hz, 100 Hz and 200 Hz. In the DC-link converter case, the maximum modulation index ( $m_{i,max} = 1.0$ ) was associated to 200 Hz. In the matrix converter case, the maximum output voltage transfer ratio  $q_{max} = \sqrt{3}/2$  was equally associated to 200 Hz. A constant V/f control was implemented to ensure that (3) remained valid at 50 and 100 Hz.

$$\frac{q}{q_{max}} = \frac{m_i}{m_{i,max}} \quad (3)$$

### C. Harmonic Analysis of Load Currents

Load currents were recorded at different slip values [as % of nominal] (§A3) and Fast Fourier Transform [FFT] analyses carried out by Day Post Processor in Ansoft – Simplorer environment. Total Harmonic Distortion  $THD$  [%] of load currents in motors I and II are presented in §A1 for matrix and two-level indirect converter supply at 50, 100 and 200 Hz and different load conditions. For  $m_{i,max}$  and  $q_{max}$  (200 Hz),  $THD$  values in a similar range were found. However, the matrix converter reduced  $THD$  in load currents at 50 Hz (by up to 0.5% in motor I). The largest decreases in  $THD$  were observed in motors I (1.7%) and motor II (1.2%) for  $(m_i/m_{i,max}) = (q/q_{max}) = 1/2$  (100 Hz). When they are produced by fast-switching AC-AC converters, load currents are characterized by an effective frequency  $f_{AC,harm}$  (higher than the fundamental frequency), which depends on harmonic distortion in the kilohertz range and is directly related to current ripple (4). The coefficient  $\xi$  lies in the 0 – 0.2 range.

$$f_{AC,harm} = f + \frac{(f_w \times THD) + (f \times 100)}{100 + THD} \times \xi \quad (4)$$

### D. Skin and Proximity Effect in Copper Windings

In order to use the value of effective AC frequency required to quantify skin and proximity effect in copper windings, some preliminary calculations must be accomplished for the two motors to obtain the diameter of conductors. The number of conductors per slot per phase  $n_{cond}$  can be written as in (5).  $N_1$  is the number of equivalent turns per pole per phase,  $c_s$  is the connection factor (= 1 for Y-connection; =  $\sqrt{3}$  for delta connection),  $q$  is the number of slots per pole per phase and  $f_{w1}$  the winding factor [18].

$$n_{cond} = \text{int} \left( \frac{N_1 c_s}{q f_{w1}} \right) \quad (5)$$

The term  $N_1$  is given in (6) as a function of peak phase voltage  $V_{pk}$  [V], active length  $L_a$  [m] of the motor, the air-gap diameter  $D$  [m], the nominal supply frequency  $f$  [Hz] and the air-gap flux density  $B_a$  (1.1T).

$$N_1 = \frac{V_{pk}}{\sqrt{2} \pi L_a D f B_a} \quad (6)$$

The phase winding resistance  $R_1$  [ohm] and diameter of copper conductor  $d_{cu}$  [m] are then linked in (7) where  $L_1$  [m] is the half value of average conductor length and  $\rho$  [ $\Omega.m^{-1}$ ] the resistivity of copper.

$$d_{cu} = \sqrt{\frac{4\rho L_a p q n_{cond}}{\pi R_1 c_s^2}} \quad (7)$$

If (5) is introduced in (7), the definition of the copper winding diameter  $d_{cu}$  [m] may be found in (8)

$$d_{cu} = \sqrt{\frac{2\rho L_a p N_1}{f_{w1} R_1 c_s \pi}} \quad (8)$$

An initial value of  $f_{w1} = 0.965926$  was assumed from assigned value of pitch length  $y_{sp} = 6$ . Then, several iterations were carried out based on the equations presented above until a coherent and similar value of winding factor was found in motors I and II. Motor I was characterized by  $d_{cu} = 2.54$  mm (AVG 10),  $f_{w1} = 0.836331$ , 21 conductors per slot and total conductor length 82.70 m. Motor II was characterized by  $d_{cu} = 1.45$  mm (AWG 15),  $f_{w1} = 0.824931$ , 51 conductors per slot and total conductor length 201.6 m.

Proximity effect losses between copper conductors can be calculated as in (7) [19].

$$P_{prox} = \frac{\rho d_{cu} \sqrt{\pi}}{2d_p} H_{max}^2 G\left(\frac{\rho d_{cu} \sqrt{\pi}}{2d_p}\right) = \rho x H_{max}^2 G(x) \quad (9)$$

The skin depth  $d_p$  [m] at frequency  $f$  [Hz] is given in (8) where  $\mu \approx \mu_0$  is the absolute permeability of copper.

$$d_p = \sqrt{\frac{\rho}{\pi f \mu}} \quad (10)$$

The function  $G(x)$  is defined in (9).

$$G(x) = \frac{\sinh x - \sin x}{\cosh x + \cos x} \quad (11)$$

Although the calculation of  $G(x)$  at a given frequency is straightforward, the quantification of proximity effect losses requires a numerical value of magnetic applied field  $H_{rms}$  [A.m<sup>-1</sup>]. For this purpose, two slot shapes (trapezoidal, semicircular) were considered in the study presented in this paper. The area of slots in motors I ( $A_{slot} = 109$  mm<sup>2</sup>) and motor II ( $A_{slot} = 101.2$  mm<sup>2</sup>) was known based upon number of conductors and winding factor  $f_{w1}$ . By assuming a reasonable ratio of upper and lower slot width, the trapezoidal slot in motor I was defined by ( $w_1 = 7.79$  mm,  $w_2 = 6.23$  mm,  $h = 15.54$  mm) while in motor II dimensions were ( $w_1 = 6.89$  mm,  $w_2 = 8.62$  mm,  $h = 13.05$  mm). The semi-circular slot shape was characterized by  $w_1 = 6.46$  mm,  $d = 8.08$  mm and  $h = 15.54$  mm (motor I) while in motor II dimensions of the slot were  $w_1 = 7.23$  mm,  $w_2 = 9.03$  mm and  $h = 13.05$  mm.

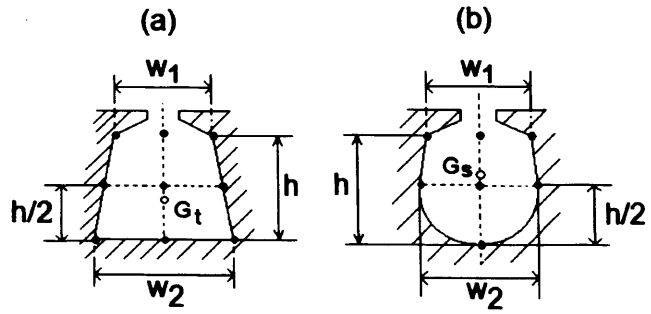


Fig. 1. Discrete distribution of the mass of copper in stator slot with (a) trapezoidal – (b) semicircular shape

A discrete distribution of the mass of copper (fig. 1) within the slot was taken as the hypothesis to determine the RMS value of applied field as a function of load RMS current. Whereas 9 points were selected for the trapezoidal slot design, 7 points were chosen in the semicircular slot shape. Then, the total applied field  $H_{rms}$  was calculated as the sum of the applied field caused by current flowing in node  $i$  ( $\omega_i * I_{max}$ ) located at a distance  $\beta_i$  [m] of the geometrical barycentre ( $G_i$ ,  $G_s$ ) of the slot.

$$H_{rms} = \sum_{i=1}^{7 \text{ or } 9} \frac{\omega_i I_{rms}}{2\pi\beta_i} \quad (12)$$

$$\sum_{i=1}^{7 \text{ or } 9} \omega_i = 1 \quad (13)$$

The sum of skin and proximity effect losses  $P_{AC}$  [W] can be written as in (11) [19].

$$P_{AC} = P_{skin} + P_{prox} = \frac{\rho I_{rms}^2}{\sqrt{2} d_p d_{cu}} F(x) \quad (14)$$

The function  $F$  is defined in (12)

$$F(x) = \frac{\sinh 2x + \sin 2x}{\cosh 2x - \cos 2x} \quad (15)$$

#### E. Thermal network of the motor

Firstly, an appropriate number of elements and nodes represented in the thermal network must be chosen (fig. 2). Five components (cast iron chassis, non-oriented laminated steel core, copper windings, steel hollow rotor and cylindrical shaft) are selected in the study. Every one of the five masses is linked to a single node in this simplified thermal network (fig. 2). A capacitance  $C_{th}$  [J.K<sup>-1</sup>] was associated to each node.  $V$  [m<sup>3</sup>] is the volume of the element and  $c_p$  [J.K<sup>-1</sup>.Kg<sup>-1</sup>] is the specific heat capacity of the material used for the element.  $\lambda$  [W.m<sup>-1</sup>.K<sup>-1</sup>] is the thermal conductivity of the material,  $t$  [m] is the length of the heat flow path and  $A$  [m<sup>2</sup>] the area normal to radial heat flow.

$$C_{th} = mc_p = \delta V c_p \quad (16)$$

$$R_{th} = \frac{t}{A\lambda} \quad (17)$$

The thermal resistance between copper windings and stator core must be given special attention due to the impact that the insulation layer has on internal heat dissipation in the motor. Since the area and perimeter of slots and winding factor are known from previous calculations, the thickness  $t_{ins}$  [m] and area  $A_{ins}$  [m<sup>2</sup>] of slot (Nomex  $\lambda = 0.143 \text{ W.m}^{-1}.\text{K}^{-1}$ ) and conductor insulation (varnished isonol-51  $\lambda = 0.44 \text{ W.m}^{-1}.\text{K}^{-1}$ ) is obtained from (18) and (19).  $\Gamma_{slot}$  [m] is the perimeter of the slot.

$$t_{ins} = \frac{A_{slot}(1 - f_{w1})}{\Gamma_{slot}} \quad (18)$$

$$A_{ins} = \Gamma_{slot} L_a \quad (19)$$

The external convection on the chassis of the motor is ensured by a fan which forces air flow linearly all over the total axial length of the motor [20]. Due to the presence of cooling fins, the effective cooling area subjected to convection must be estimated by the product of the idealized geometry of the motor (prism) and an amplifying factor  $f_{conv}$ . In order to define the convection coefficient  $\alpha$  [W.m<sup>2</sup>.K<sup>-1</sup>], two axial fans A250 and A160 (respectively) were selected. The air linear velocity  $v_{air}$  [m.s<sup>-1</sup>] was calculated to the rotational speeds (1400 rpm, 2800 rpm and 5600 rpm) associated to supply frequencies 50 Hz, 100 Hz and 200 Hz.

TABLE IV. LINEAR AIR VELOCITY [M.S<sup>-1</sup>] ON MOTOR SURFACE

n [rpm]	A250	A160
1400	3.78	3.70
2800	7.56	7.40
5600	15.11	14.79

Thus, the fluid flow over the motor surface can be identified as laminar or turbulent. Therefore, a proper definition of the Nusselt number is ensured. Forced convection over four flat plates of corrected area was the hypothesis made to access empirical equations [21].

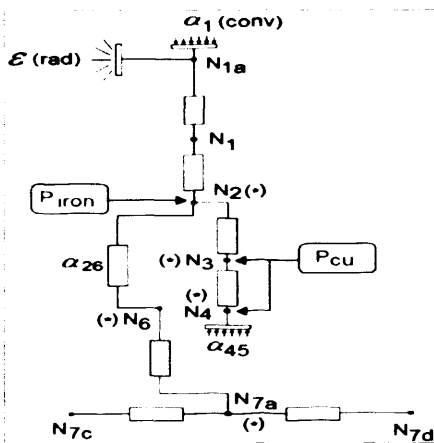


Fig 2. Thermal network of the induction motor (\*) node with thermal capacitance.

Total losses  $P_j$  [W] in copper windings (DC + AC) and iron losses  $P_{fe}$  [W] in the mass of steel stator core are heat sources in the thermal network (fig. 2). From basic information on the geometry of the motor, the mass of the stator core was calculated. An average fundamental peak flux density equal to 1.5T was taken for the analysis. Although some parts of the core (tooth tip, base) are subjected to magnetic saturation (1.6 – 1.8T), induction in the yoke is noticeably lower (1.1 – 1.3T). A common non-oriented steel grade (M400-50A) was selected for determining iron losses [22].

### III. RESULTS AND DISCUSSION

The applied field within the slot due to current flow in copper windings was calculated for the two slot shapes. Results of  $H_{mean}$  [A.m-1] and  $I_{mean}$  [A] are introduced in table V for the trapezoidal slot design, which yielded a reduction of proximity effect losses by 8.9% and 27.6% in motors I and II, respectively.

TABLE V. MEAN APPLIED FIELD AND LOAD CURRENT IN MOTORS I AND II (TRAPEZOIDAL SLOT)

f [Hz]	Motor I		Motor II	
	I <sub>mean</sub> [A]	H <sub>mean</sub> [A.m-1]	I <sub>mean</sub> [A]	H <sub>mean</sub> [A.m-1]
50	6.21	10417	1.45	6862
100	11.55	19371	2.47	11660
200	21.14	35461	4.40	20780

Then, total copper winding losses  $P_j$  [W] and their breakdown into DC losses, skin and proximity effect components [  $\eta_{dc}$ [%];  $\eta_{sk}$ [%];  $\eta_{prox}$ [%] ] was then calculated in the two induction motors at nominal slip and three rotational speeds linked to 50 Hz, 100 Hz and 200 Hz (table VI).

TABLE VI. VALUE AND REPARTITION OF AC LOSSES IN DC, SKIN AND PROXIMITY EFFECT LOSSES

Motor I				
f [Hz]	$P_j$ [W]	$\eta_{dc}$ [%]	$\eta_{sk}$ [%]	$\eta_{prox}$ [%]
50	12.9	50.2	49.0	0.8
100	44.4	49.9	46.5	3.6
200	148.9	49.6	36	14.4
Motor II				
f [Hz]	$P_j$ [W]	$\eta_{dc}$ [%]	$\eta_{sk}$ [%]	$\eta_{prox}$ [%]
50	5.5	50.4	49.4	0.2
100	15.8	50.0	49.1	0.9
200	50.1	49.9	46.6	3.5

Proximity effect losses increase with current and supply frequency. This phenomenon is more prominent in motor I with highest nominal power (15 kW) and larger copper diameter ( $d_{cu} = 2.54$  mm). In the motor with lowest nominal power (3kW), a moderate increase in the proportion of proximity effect losses was observed. Skin effect losses  $P_{sk}$  [W], which were determined as the subtraction of proximity effect losses (9) from AC losses (14), were calculated for different effective harmonic frequencies associated to 1400 rpm, 2800 rpm and 5600 rpm in motors I and II. These were taken as the addition of the fundamental frequency (50; 100 and 200) and an increment between 0 Hz (sinusoidal conditions) and 50 Hz. Then, (DC + skin effect) losses, as well as iron losses, were fed to thermal network implemented in the multi-engineering package Dymola. The rise in stator

inding temperature  $\Delta\theta_{wdg}$  [°C] when the motor reached steady state while operating at nominal slip was recorded (table VII) and used to obtain the new value of phase winding resistance  $R_{ac,harm}$  [ohm] (fig. 3 and fig. 4).

TABLE VII.  $\Delta\theta_{wdg}$  [°C] FOR DIFFERENT INCREMENT IN AC HARMONIC FREQUENCY [Hz] IN MOTOR I

$\Delta f_{ac,harm}$ [Hz]	f [Hz]		
	50 Hz	100 Hz	200 Hz
12.5	0.07	0.42	3.39
25	0.15	0.91	7.38
37.5	0.25	1.46	12.12
50	0.36	2.11	17.81

the effective harmonic frequency  $f_{ac,mx}$  [Hz] and  $f_{ac,pwm}$  [Hz] under matrix and two-level DC-link PWM converters line-line voltage supply was calculated for  $\alpha=0.1$  in (4). For that purpose, load current Total Harmonic Distortion [THD] was obtained for load currents in motors I and II under V/f control strategy described in § I.A. Values of  $\Delta f_{mx-pwm} = f_{ac,mx} - f_{ac,pwm}$  are given in table VIII.

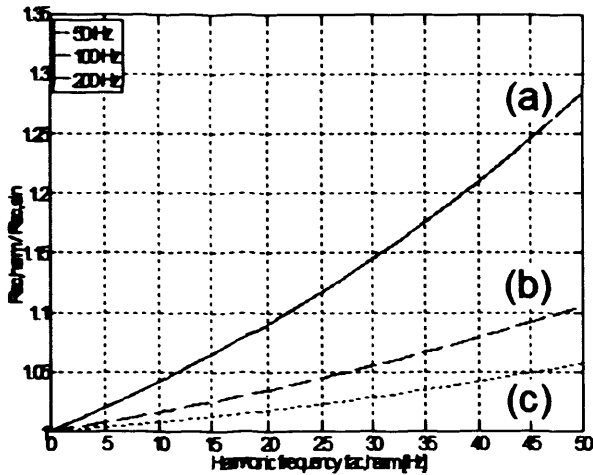


Fig 3. Variation of the ratio of harmonic to sinusoidal AC resistance with increase in effective AC frequency (motor I) (a) 200 Hz – (b) 100 Hz – (c) 50 Hz

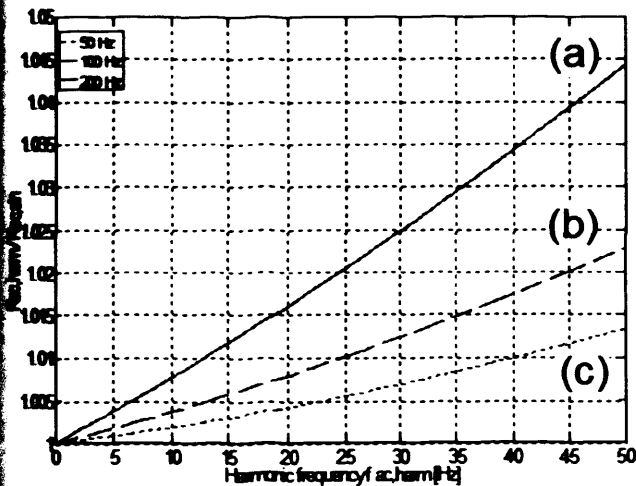


Fig 4. Variation of the ratio of harmonic to sinusoidal AC resistance with increase in effective AC frequency (motor II) (a) 200 Hz – (b) 100 Hz – (c) 50 Hz

TABLE VIII. DIFFERENCE IN AC HARMONIC FREQUENCY [Hz] IN LOAD CURRENTS IN MOTORS I AND II UNDER MATRIX AND TWO-LEVEL DC-LINK CONVERTER SUPPLY

f [Hz]	Motor I		Motor II	
	$f_{ac,pwm}$	$\Delta f_{mx-pwm}$	$f_{ac,pwm}$	$\Delta f_{mx-pwm}$
50	70.8	-2.8	66.1	-1.4
100	138.6	-6.6	132.4	-5.4
200	230.8	+0.5	229.9	+0.4

Line-line matrix converter supply allowed a reduction in load current THD at base frequencies 50 and 100 Hz in the two induction motors. A very similar value of effective harmonic frequency in the two motors under supply by direct and DC-link converter was noted at 200 Hz. By accessing the graphs with  $f_{ac,pwm}$  [Hz] and  $\Delta f_{mx-pwm}$  [Hz] the reduction in  $\Delta R_{ac}$  [%] in copper winding resistance (due to reduction in skin effect losses under matrix converter supply) were determined. Values for the two motors studied are presented in table IX.

TABLE IX. REDUCTION IN AC COPPER WINDING RESISTANCE  $\Delta R_{ac}$  [%] IN MOTORS I AND II UNDER MATRIX CONVERTER SUPPLY

	Motor I	Motor II
50 Hz	-0.28	-0.02
100 Hz	-1.46	-0.26
200 Hz	+0.26	+0.04

Copper winding losses are mostly reduced by using the matrix converter at 100 Hz base frequency in the 15kW induction motor. Very similar values of copper winding losses were observed at 50 and 200 Hz in motors I and II. However, the impact of AC-AC converter supply on electrical efficiency of the motor also depends on the ratio  $\gamma_{cu}$  [%] of stator winding losses to input power (table IX). Once this information is obtained, conclusions on the potential benefit of matrix converters in AC drives regarding efficiency can be drawn (table X).

TABLE X. FRACTION OF STATOR COPPER WINDING LOSSES  $\gamma_{cu}$  [%] AND EFFICIENCY IMPROVEMENT  $\Delta\eta$  [%] IN MOTORS I AND II UNDER MATRIX CONVERTER SUPPLY

f	Motor I		Motor II	
	$\gamma_{cu}$ [%]	$\Delta\eta$ [%]	$\gamma_{cu}$ [%]	$\Delta\eta$ [%]
50 Hz	3.3	+0.0092	7.4	+0.0015
100 Hz	3.2	+0.047	6.4	+0.017
200 Hz	3.1	-0.0081	6.0	-0.0024

An increase  $\Delta\eta$  [%] in efficiency by 0.05% and 0.02% (as fraction of input power) was reached in motors I and II at one frequency (100 Hz) associated to a medium speed of 2800 rpm. This is possible thanks to a reduction in skin effect losses in stator copper windings. However, marginal changes in motor electrical efficiency were observed in both induction motors at lowest (1400 rpm) and highest (5600 rpm) speeds.

#### IV. CONCLUSIONS

A very good understanding of physical concepts explaining losses in electrical machines is necessary to analyze the impact of frequency converter topologies on power consumption and efficiency in commonly used asynchronous motors. Knowledge on power electronics, control and machine design is to be coupled with thermal analysis of the motor at variable speed conditions. The study presented in this paper reveals that matrix converters can contribute to improve efficiency in a 15kW motor (by up to 0.05%) at medium speed by

reducing AC copper losses in stator windings. Nevertheless, it is believed that more substantial improvement in induction motor efficiency may be reached in the 100 to 200 kW range. Then, higher harmonic quality in line-line voltages produced by matrix converters) may lead to minimizing iron and Joule losses (stator and rotor) in asynchronous motors commonly used in industrial applications with significant energy saving potential.

#### ACKNOWLEDGMENT

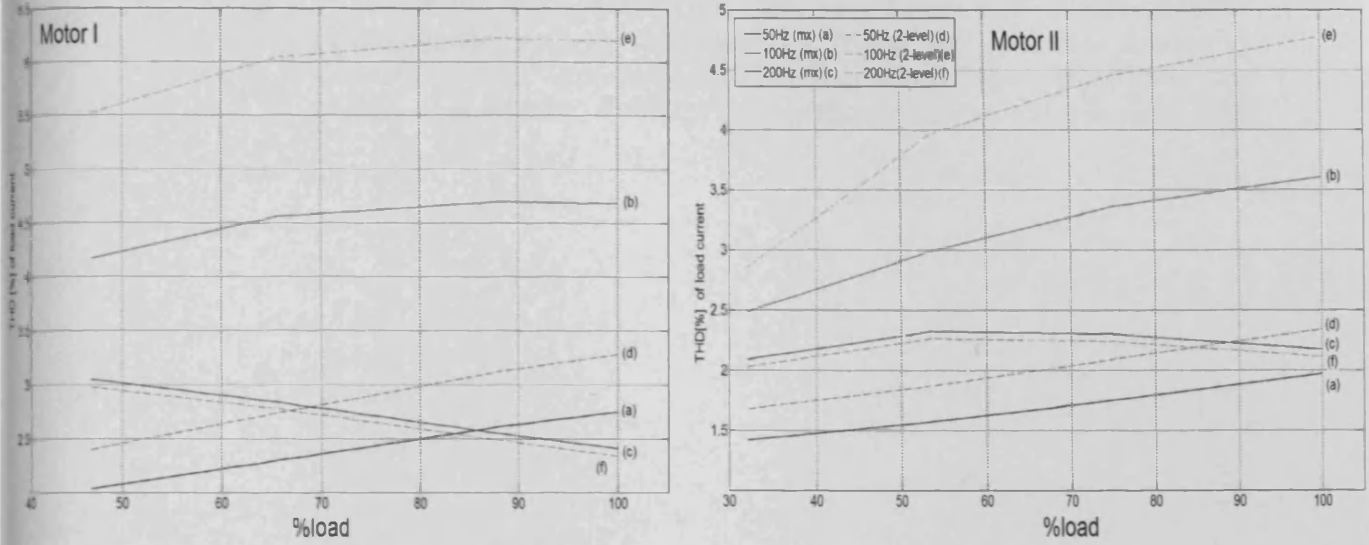
The authors would like to thank Prof. J. Clare and Dr. P. Wheeler at the PEMC group (The University of Nottingham, UK) for their knowledge on matrix converters.

#### REFERENCES

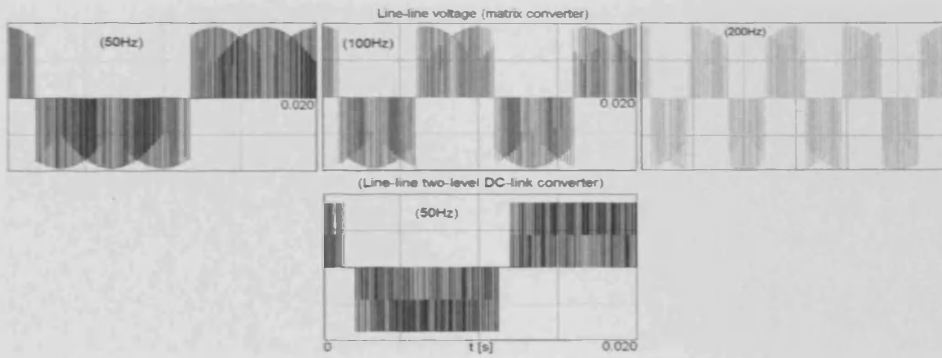
- [1] A. De Almeida, F. J. T. E. Ferreira, P. Fonseca, B. Chretien, H. Falkner, J. C. C. Reichert, M. West, S. B. Nielsen, D. Both, "Variable speed drives for electric motor systems", *Save II Programme 2000*, pp 1-105, 2000.
- [2] P.W. Wheeler, J. Rodriguez, J.C. Clare, L. Empringham, A. Weinstein, "Matrix converters: a technology review", *IEEE Transactions on Industrial Electronics*, Vol 49, No 2, pp 276-288, April 2002.
- [3] J. Lettl, "Matrix converter induction motor drive", *12th International EPE-PEMC*, pp 787-792, August 2006.
- [4] T. Podlesak, D. Katsis, P.W. Wheeler, J.C. Clare, L. Empringham, M. Bland, "A 150 kVA vector-controlled matrix converter induction motor drive", *IEEE Transactions in Industry Applications*, Vol 41, Issue 3, pp 841-847, May-June 2005.
- [5] De Lillo L, Empringham L, Wheeler P, Clare J, Bradley K, "A 20kW matrix converter drive system for an electro-mechanical actuator", *European Conference on Power Electronics and Applications*, 11-14 sept 2005.
- [6] C. Klumpner, F. Blaabjerg, "Short term braking capability during power interruptions for integrated matrix converter motor drives", *IEEE Transactions on Power Electronics*, Vol 19, No2, pp 303-311, March 2004.
- [7] Sato I, Itoh J, Ohiguchi H, Odaka A, Mine H, "An improvement method of matrix converter under input voltage disturbances", *IEEE Transactions on Power Electronics*, Vol 22, No1, pp 132-138, Jan 2007.
- [8] D. Casadei, Ghirelli M, Serra G, Tani A, Zarri L, "Theoretical and experimental analysis of the line current in matrix converters", *12th International EPE-PEMC Conference*, Portoroz (Slovenia), pp 781-786, Aug 2006.
- [9] D. Casadei, G. Serra, A Tani, L. Zarri, "Matrix converter modulation strategies: a new general approach based on space-vector representation of the switch state", *IEEE Transactions on Industrial Electronics*, Vol 49, No 2, pp 370-381, April 2002.
- [10] Young-Doo Y, Seung-Ki S, "Carrier-based modulation technique for matrix converters", *IEEE Transactions on Power Electronics*, Vol 21, No6, pp 1691-1703, November 2006.
- [11] Kyo-Beum L, Blaabjerg F, "A non-linearity compensation method for a matrix converter drive", *IEEE Power Engineering Letters*, Vol 3, No1, pp 19-23, March 2005.
- [12] Hara H, Yamamoto E, Jun-Koo K, Kume T, "Improvement of output voltage control performance for low-speed operation of matrix converter", *IEEE Transactions on Power Electronics*, Vol 20, No 6, pp 1372-1378, November 2005.
- [13] C. Klumpner, "A hybrid indirect matrix converter immune to unbalanced voltage supply, with reduced switching losses and improved voltage transfer ratio", *21st IEEE Applied Power Electronics Conference and Exposition*, 19-23 March 2006.
- [14] J. Sagarduy, A.J. Moses, F.J. Anayi, J. Clare, P.W. Wheeler, "Matrix vs PWM converters: iron losses under pulsating forms of voltage excitation", *37th Power Electronics Specialist Conference*, pp 2247-2252, June 2006.
- [15] D. Casadei, G. Serra, A. Tani, L. Zarri, "A space-vector-modulation strategy for matrix converters minimizing the RMS value of the load current ripple", *32nd Annual Conference on Industrial Electronics (IECON)*, pp 2757-2762, Nov 2006.
- [16] P. H. Mellor, D. Roberts and D.R. Turner, "Lumped Parameter Thermal Model for Electrical Machines of TEFC Design", *IEE Proceedings on Industry Applications*, Vol 138, No 5, pp 205 – 218, Sept 1991.
- [17] ABB Motors. "Totally enclosed squirrel-cage three-phase motors with aluminum frame. Protection (IP55). Cooling (IC411). Insulation Class F. Temperature Rise Class B".
- [18] Chandur Sadarangani, "Electric Machines. Design and Analysis of Induction and Permanent Magnet Motors", Kungs Tekniska Högskolan Stockholm, ISBN 91-7170-627-5, Aug 2000.
- [19] X. Nan, C. R. Sullivan, "An Improved Calculation of Proximity Effect in High-Frequency Windings of Round Conductors", *IEEE Power Electronics Specialists Conference*, Vol 2, pp 853 – 860, June 2003.
- [20] G. Spindler, "AC cooling fans. Series A25089 and A16062", www.sofasco.com.
- [21] J. P. Holman, "Heat Transfer", *McGraw Hill Mechanical Engineers Series, 7th Edition*, ISBN 0-07-112644-9, 1992.
- [22] Cogent Steels Ltd, "Non-Oriented Steel. Fully-Processed". November 2002.

APPENDIX A1.

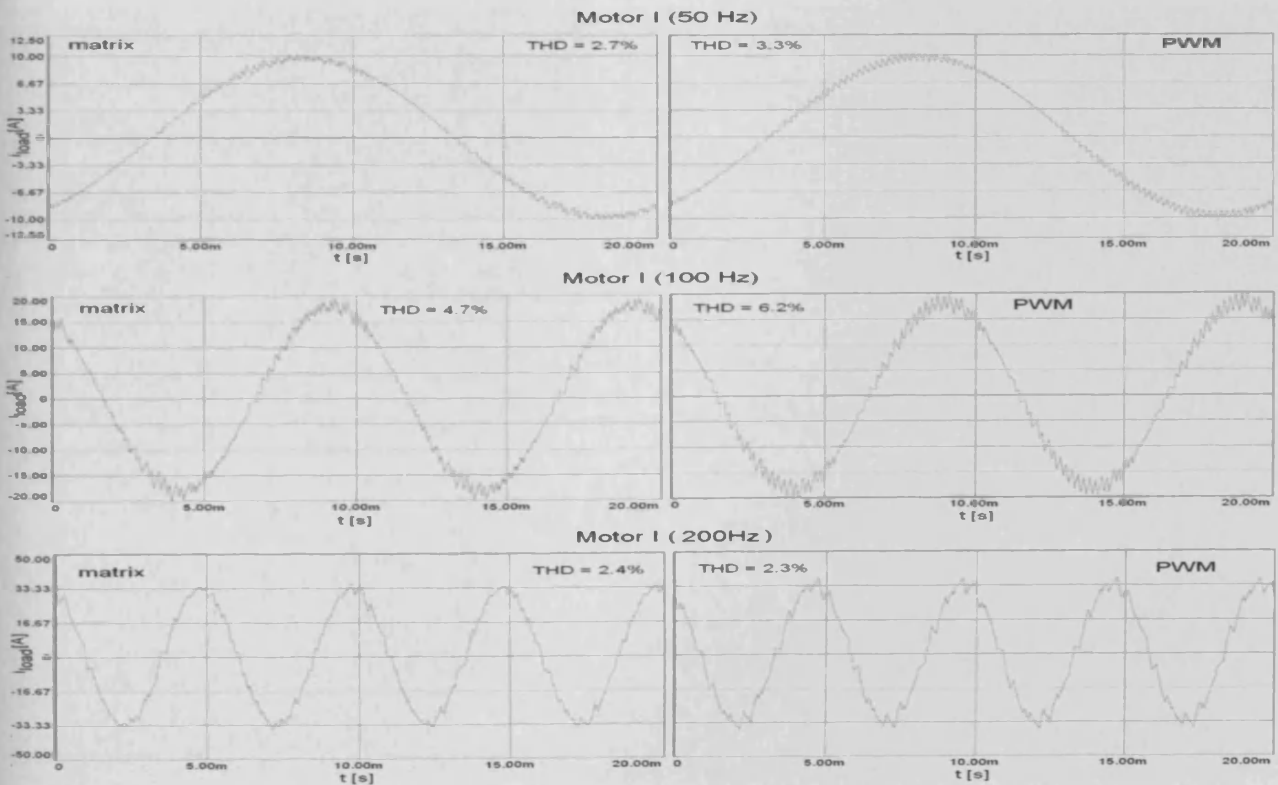
Total Harmonic Distortion of load current in motors I and II at various load conditions and frequencies under supply by matrix and 2-level DC-link converters



APPENDIX A2.



APPENDIX A3.



- A1.4. J. Sagarduy, A.J. Moses, F.J. Anayi, J. Clare, P.W. Wheeler, "Iron Losses under Voltage Excitation by Novel and Classical Frequency Converters", *12<sup>th</sup> International Conference on Power Electronics and Motion Control EPE-PEMC*, Portoroz (Slovenia), pp 131-136, Aug 2006.

# Iron Losses Under Voltage Excitation by Novel and Classical Frequency Converters

Juan Sagarduy<sup>1</sup>, Anthony J. Moses<sup>1</sup>, Fatih J. Anayi<sup>1</sup>, Jon Clare<sup>2</sup>, Patrick W. Wheeler<sup>2</sup>

<sup>1</sup>Wolfson Centre for Magnetics, Cardiff University, United Kingdom

<sup>2</sup>Power Electronics and Machines Control Group, The University of Nottingham, United Kingdom

**Abstract**— Iron losses due to flux harmonics in stator cores of Pulse-Width-Modulation [PWM] back-to-back inverter-fed induction motors have a major effect on system efficiency. A new generation of direct ac-ac matrix converters offer important advantages over classical frequency converters such as absence of bulky and temperature sensitive dc-links and possible adjustment of power factor. The paper presents experimental results of magnetic losses in three non-oriented electrical steels magnetised under different types of voltage excitation. Characteristic waveforms of real 3x3 matrix converter and PWM inverter under various modulation indices were recorded and used by a signal generator feeding a Single Strip Tester [SST] used to measure iron loss. Harmonic distortion, contribution of high frequency components and sideband effect were analysed. Influence of flux density curve as well as form factor of voltage excitation were also investigated.

## I. INTRODUCTION

Indirect frequency converters have been key elements in Adjustable Speed Drives [ASD] for many decades. In order to improve efficiency in rotating machines, primary windings in asynchronous motors are subjected to pulsating voltage excitation, typical of back-to-back converters, at variable frequency. As a cheap and mature technology based upon a simple PWM strategy, indirect converters remain very popular in industry. Nonetheless, latest developments in direct AC-AC conversion, along with continuous improvements in power semiconductor technology, reinforce the role played by matrix converters in specific applications, where reduced volume at high temperature conditions and effective bidirectional flow are paramount [1][2][3]. This paper investigates the unknown effect of voltage excitation produced by a real matrix converter on the performance of non-oriented steel, commonly used in small and medium-sized induction motors. Moreover, a comparison with iron losses under supply from a commercial back-to-back PWM converter is also presented.

### A. Iron Losses

Flux harmonics in stator cores of conventional induction motors cause iron losses in non-oriented electrical steels, which can be analysed in terms of static hysteresis, eddy-current and anomalous loss [4] as given

in (1), where  $f$  is the frequency of magnetisation and  $K_h$ ,  $K_e$  and  $K_a$  are coefficients defining static hysteresis, eddy current and dynamic hysteresis (anomalous) loss respectively.

$$\frac{P_s}{f} \left[ \frac{W}{kg} \right] = K_h + K_e f + K_a f^{0.5} \quad (1)$$

Static hysteresis loss per cycle, which depends on characteristics of the material such as purity, an isotropy or composition, is assumed to be independent of frequency. Classical eddy-current loss, which is caused by internal currents opposed to flux density variation, and anomalous loss, which results from micro-eddy currents linked to domain wall motion during magnetisation, are frequency dependent and hence increase significantly when the time variation of flux density is non-sinusoidal [5][6][7]. Flux harmonics in the kilohertz range, which are caused by pulsating timevarying voltage excitation waveforms typical of frequency converters, can cause a larger increase in eddy current loss in the magnetic core materials [8]. Heat is dissipated in stator cores as iron losses increase.

### B. Frequency Converters

Matrix converters can be considered as  $n \times n$  direct ac-ac converters. For  $n=3$ , three input phases provided with a LC filter are connected to the load through nine bidirectional switches (Fig 1).

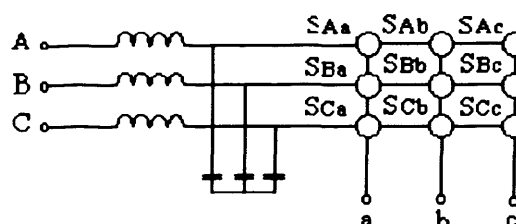


Fig. 1. Topology of a 3x3 matrix converter.

Each consists of two anti-parallel IGBTs in a common-collector back-to-back configuration and is controlled by logic signals from a Field Programmable Gate Array [FPGA], which implements the four-steps

emi-soft current-direction based commutation. Fatal short or open circuits between input phases are consequently avoided [9]. A Digital Signal Processor [DSP] executes the control algorithm and implements Space Vector Modulation [SVM]. Input current and output voltage reference phase vectors rotate at a given angular frequency. Depending on their position within six sectors at each sampling time, a pattern, in which the duty cycles of the bidirectional switches are calculated, is selected [10]. Sampling frequency  $f_s$  of execution of SVM algorithm is fixed; this should not be confused with the switching frequency  $f_w$  of semiconductors. Implementation of four-step commutation is carried out after nine logic signals are conveyed to the FPGA. This enables control of eighteen individual IGBTs. Since no intermediate dc-link is present, a clamp circuit is therefore required to deal with input power disturbances and ensure ride-through capability [11].

Classical back-to-back converters perform ac-ac conversion in two stages: rectification and inversion. A dc-link, between an active (semiconductors) or passive (diodes) rectifier and inverter, is an essential element in this topology. Synchronized carrier-based Pulse-Width-Modulation [PWM] based on the suboscillation method [12] is commonly used in the control of back-to-back converter owing to its simplicity. Space-Vector-Modulation (SVM) may also apply as a modulation strategy. Nonetheless, at high pulse number values as investigated here (60; 30; 15 for 50; 100; 200 Hz respectively at switching frequency 3 kHz), synchronised SVM and suboscillation PWM techniques are equivalent [12] and lead to similar harmonic distortion factor of the voltage produced by the converter. The most important parameters in carrier-based suboscillation PWM method are modulation index  $[m_i]$  defined in equation (2), where  $A_{ref}$  and  $A_c$  are the amplitude of reference and carrier signals, and switching frequency (carrier signal). Its influence on the harmonic behavior of voltage waveforms in PWM inverters will be discussed later.

$$m_i = \frac{A_{ref}}{A_c} \quad (2)$$

## II. THEORETICAL BASIS

Harmonic analysis of voltage waveforms produced by frequency converters requires the definition of frequency weighted Total Harmonic Distortion [ $f_wTHD$ ], given in equation (3) where  $v_1$  and  $v_n$  are components corresponding to fundamental and  $n^{th}$  order frequency.

In order to evaluate sideband effect on the  $k^{th}$  high order harmonic, the concept of  $f_wTHD$ , introduced by equations (4a) and (4b), is used. Each pair of side harmonics is assigned order  $j$  and the bandwidth of analysis is defined by the order  $j_{max}$  of the maximum side frequency considered (with the software used to carry out FFT in this investigation, the resolution  $\Delta f$  is 25Hz).

$$f_wTHD(k^{th} \text{ harm}) = \frac{\frac{v_k}{k} + \sum_{-j_{max}}^{j_{max}} \frac{v_j}{|j|}}{v_1} \times 100 \quad (4a)$$

$$j = \frac{f_j - f_k}{\Delta f} \quad (4b)$$

The Form Factor [FF] is also important when assessing waveforms. It is defined in terms of Root Mean Square and Rectified Mean values, is given in equation (5).

$$FF = \frac{v_{rms}}{v_{rectmean}} = \frac{\sqrt{\frac{1}{T} \int_0^T v^2(t) dt}}{\frac{1}{T} \int_0^T |v(t)| dt} \quad (5)$$

## III. EXPERIMENTAL SETUP

A 7.5kW matrix converter prototype was connected to a 3 phase 50Hz supply through a variable transformer and loaded with resistances. The output voltage between phase and neutral (phn) was measured and recorded by means of a digital oscilloscope, (Yokogawa- Digital scope DL716 16CH). A PWM converter, (Toshiba- Transistor Inverter TOSVERTVF-A3 400V- 0.75kW), was connected to a 3 phase delta-wound induction motor, (Clarke Motor Type80B/4). The output voltage regulation function was used to obtain line-to-line (phph) waveforms at different modulation indices. The fundamental frequency of the converter outputs was varied between 50Hz and 200Hz. Typical experimental matrix output voltage waveforms at  $f=50\text{Hz}$ ,  $f=100\text{Hz}$  and  $f=200\text{Hz}$  are shown in Fig2a, 2b and 2c. Output voltage waveform of an indirect ac-dc-ac converter is shown in Fig 3.

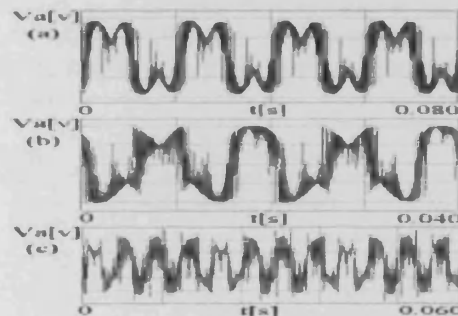


Fig.2. Typical matrix converter output voltage waveforms at (a) 50Hz- (b) 100 Hz - (c) 200 Hz.

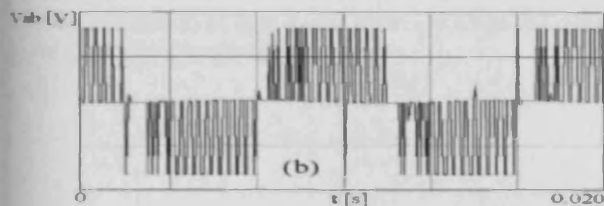


Fig. 3. Line-to-line PWM output voltage waveform at 100 Hz.

306x30mm, 280x30mm, 306x30mm strips of three electrical steels (M470-50A; M530-50A; M700-65A) of thicknesses 0.50, 0.50 and 0.65mm were selected. Table I shows typical physical properties of these grades [13] [14].

TABLE I.

RELATIVE PERMEABILITY (AT 1.5T, 50HZ), DENSITY, RESISTIVITY AND SILICON CONTENT OF THREE ELECTRICAL STEELS.

EN10106	$\mu_r$	$d$ [kg/dm <sup>3</sup> ]	$\rho$ [ $\mu\Omega.cm$ ]	Si [%]
M470-50A	1120	7.70	39	2.5
M530-50A	1150	7.70	36	2.2
M700-65A	1570	7.75	30	1.75

The Single Strip Tester [SST] was connected to a signal generator (TTi - TGA 30MHz) and power amplifier (BK Electronics MXF 900) as shown in Fig. 4.

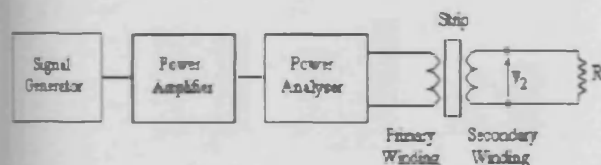


Fig. 4. Setup for measurement of magnetic losses in single strip specimens.

The signal generator was programmed to output the same voltage waveshape as the actual converters. The power loss of the material in the SST was measured by a power analyzer, (Voltech - PM3000A). The process was repeated for the three materials under phn (matrix) and phph (PWM) voltage waveforms. Modulation indices of unity, 0.8 and 0.5 were chosen under PWM excitation. The peak flux density,  $B_m$ , was set between 1.0T and 1.5T. It was estimated that the iron loss could be measured to within  $\pm 2.5\%$ .

#### IV. RESULTS

Iron losses of the three batches of material were measured while the SST was supplied with forms of voltage excitation, typical of real matrix and PWM converter, at three fundamental frequencies [50; 100; 200Hz]. Fig. 5 shows the variation of specific power loss  $P$ , [W/kg] with peak flux density in the M470-50A material at a fundamental magnetization frequency of 50Hz under PWM [ $m_i=0.5$ ; 0.8; 1], matrix and sinusoidal excitation.

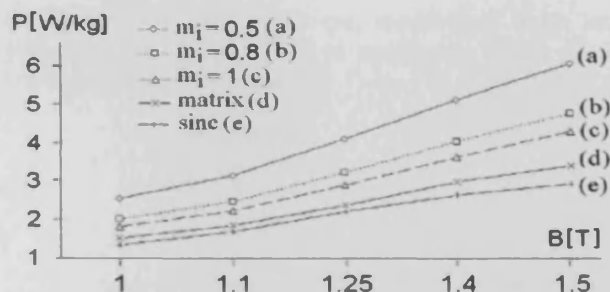


Fig. 5. Variation of specific power loss with flux density B[T] at fundamental frequency of magnetization  $f = 50\text{Hz}$  (M470-50A).

Fig. 6 shows the ratio ( $P_{PWM} / P_{sine}$ ) of power loss under PWM excitation (modulation index  $m_i=1$ ;  $m_i=0.5$ ) to that of loss under sinusoidal excitation for materials M530-50A and M700-65A. M470-50A showed similar behaviour to that of M530-50A. It is interesting to note that the relative loss increase with the lower modulation index is much higher in the M530-50A material than in the thicker steels whose hysteresis component of loss would probably be larger.

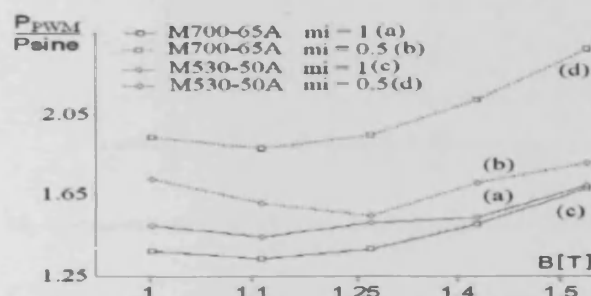


Fig. 6. Variation of ratio ( $P_{PWM} / P_{sine}$ ) with peak flux density at 50Hz under  $m_i=1$ ;  $m_i=0.5$  in M530-50A and M700-65A.

Fig. 7 shows the ratio, ( $P_{matrix} / P_{sine}$ ), of power loss under matrix converter excitation over power loss under sinusoidal excitation for different inductions. The deterioration in loss here is very similar in all three materials accounting for the experimental accuracy apart from the increased ratio in the lowest loss material at low flux density

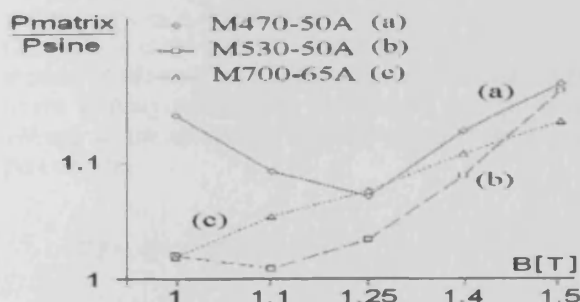


Fig. 7. Variation of ratio ( $P_{matrix} / P_{sine}$ ) with flux density B[T] at 50Hz in the three materials.

The reduction of loss under matrix voltage waveform as the ratio  $r$  [%] is given by:

$$r[\%] = \frac{P_{PWM} - P_{matrix}}{P_{PWM}} \times 100 \quad (6)$$

Fig.8 shows how  $r$  varies with frequency in the three materials when the modulation index under PWM was 0.8. At the highest frequency, the loss reduction under matrix condition is small and similar in the two thinner materials. However, at the lowest frequency, the reduction in all materials is similar, perhaps because harmful eddy current loss component is relatively lower in each material.

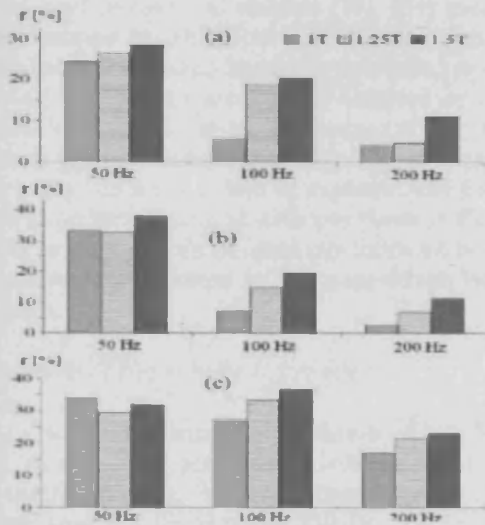


Fig.8. Variation of  $r$  with flux density and frequency for three non-oriented steels (a)M470-50A (b) M530-50A (c) M700-65A.

## V. DISCUSSION

### A. Effect of PWM Modulation Index

Fig.5 verifies that lower modulation index causes higher loss. This is a well known phenomenon [8][15] due to the noticeably higher harmonic distortion. While low order components change the general shape of the B-H loop, high order flux harmonics lead to the appearance of non-desired minor loops on the B-H curve [16][17]. Both phenomena cause higher losses in electrical steels. Table II shows the variation of  $ov$ [%], the output voltage regulation function of the PWM inverter used, with the frequency weighted harmonic distortion and the modulation index.

TABLE II.  
VARIATION OF MODULATION INDEX WITH OUTPUT VOLTAGE REGULATION FUNCTION

$ov$ [%]	20	30	40	50	60	70
$m_i$	0.43	0.63	0.77	0.85	0.98	1.03

Fig.9 shows the variation of frequency-weighted harmonic distortion of output voltage waveform, in the

PWM inverter used, with the modulation index  $m_i$ . Reduction of  $fwTHD$  [%] is noticeable when  $m_i$  is increased between 0.5 and 0.8.

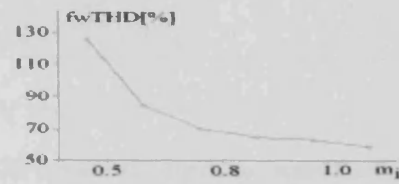


Fig.9. Variation of  $fwTHD$  [%] with modulation index in output voltage waveforms typical of the inverter used.

Fig.10 shows the harmonic spectrum of PWM voltage waveforms at 50 Hz of magnetising frequency for values 30% and 70% of the output voltage regulation function of the inverter. As can be seen in Fig.10, low modulation index sharpens the shape of each cluster of high frequency harmonics. This is believed to have a harmful effect on eddy current losses within the material.

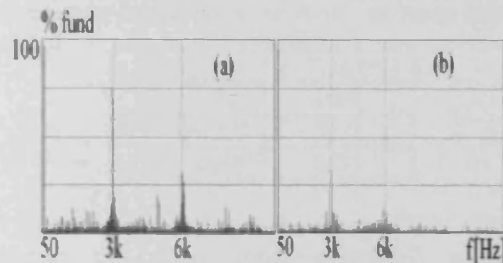


Fig.10. Harmonic spectrum of PWM voltage waveforms at  $f = 50$  Hz (a)  $m_i = 0.63$  - (b)  $m_i = 1.03$ .

M530-50A has the lowest proportion of eddy current loss due to its high hysteresis component. In low alloy non-oriented steel, such as the M700-65A, the hysteresis loss accounts for 30-60% of the total loss, classical eddy current loss accounts for 40-60% and the anomalous loss is 10-20%. In thinner, high alloy material, the hysteresis component is relatively higher, which conforms with the low effect of flux harmonics as shown in Fig.6.

### B. Smoothness of Flux Density Curve

Magnetic flux density  $B[t]$  is related to induced voltage  $e(t)$ , in a search coil or secondary winding as in (7). Here  $N$  is the number of secondary turns,  $A$  the cross section of the sample,  $v(t)$  the voltage excitation supplied to the primary winding by the inverter,  $e(t)$  the induced voltage in the secondary winding and  $B(t)$  the magnetic flux density.

$$e(t) = NA \frac{dB(t)}{dt} \Leftrightarrow B(t) = \frac{1}{NA} \int e(t) dt \quad (7)$$

In this paper, integration of primary voltage excitation  $v(t)$  was carried out for matrix and PWM converters so this will not be identical to the flux density waveform but it is a good indicator of waveshape. The result is given in Fig.11.

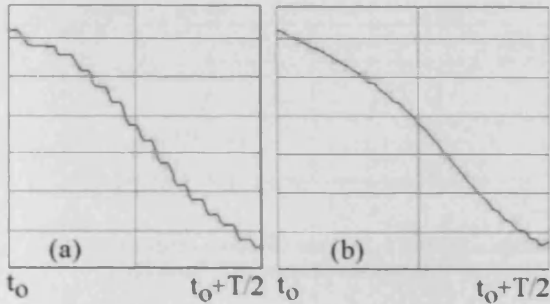


Fig. 11. Integral of  $v(t)$  over half a cycle under different voltage excitations at 100 Hz fundamental frequency  
(a)-PWM  $m_i=0.8$  (b) matrix converter

The loss in electrical steel is fundamentally caused by domain wall motion and rotation [18]. It is assumed that magnetisation in which  $dB(t)/dt$  is continuous and sinusoidal has low dynamic hysteresis compared to other waveforms [5]. The loss can also be assumed as being approximately proportional to the square of the mean domain wall velocity within a material. This is obviously a complex function but it would be expected that domain walls in a material magnetised with waveform in Fig. 11a are subject to short periods of inactivity followed by high velocity movement indicated by the steps which lead to higher losses.

### C. Distribution of High Order Harmonics

Fig. 12 shows the harmonic spectrum of the PWM [ $m_i=0.8$ ] (line-to-line) and matrix converter (line-to-neutral) output voltages. Switching frequency for PWM is 3kHz and sampling frequency in SVM is 2.5kHz.

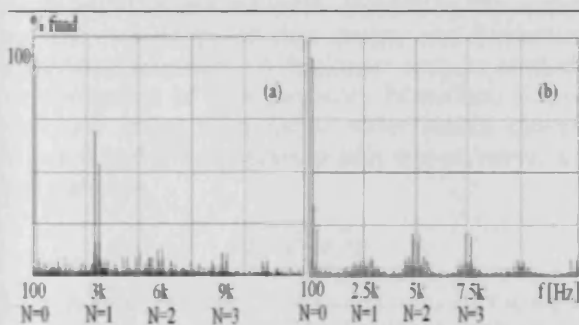


Fig. 12 Harmonic spectrum of voltage waveforms  
(a)-PWM  $m_i=0.8$  (b) - matrix

The first high order harmonic present in pulsating waveforms strongly affects eddy current losses. As can be seen in Fig. 12, the distribution of harmonic envelopes in the matrix converter waveform is different in the PWM waveform and this probably mitigates their effect on losses. In PWM converters, the harmonic due to the switching frequency has the highest amplitude, which is believed to have a serious harmful impact on iron loss. Table III presents  $f_wTHD$  [%] due to each cluster of high order  $N$  (Fig 14) for matrix (ph-ph) and PWM (ph-ph) [ $m_i=0.8$ ] waveforms.

TABLE III.  
 $f_wTHD$  [%] DUE TO HIGH FREQUENCIES, EACH IN A BANDWIDTH OF  $\pm 1$ KHZ

N	0	1	2	3
Matrix	18.3	14.5	27.1	16.2
PWM	11.1	51.3	22.8	19.9

### D. Nature of Matrix Converter Waveform

When the input and output frequencies are the same, the matrix converter generates a periodic waveform of period  $T=1/f$  between phase and neutral. In this case, even harmonics are negligible and the form factor [FF](6) has a strong impact on the magnetizing conditions. Table IV shows  $f_wTHD$  [%] due to the first ten even harmonics in phase-to-neutral voltage waveforms of matrix converter with input frequency of 50Hz and output frequencies of 50 Hz, 100 Hz and 200Hz (Fig. 2a-c).

TABLE IV.  
 $f_wTHD$  [%] DUE TO THE FIRST TEN EVEN HARMONICS IN TYPICAL MATRIX CONVERTER WAVEFORMS FOR THE THREE OUTPUT FREQUENCIES

Waveform	$f_wTHD$ [%]
$V_{phn5050}$	0.89
$V_{phn50100}$	2.73
$V_{phn50200}$	5.73

Table V shows the form factor [FF] of voltage waveforms of matrix (phase-to-neutral) and PWM (phase-to-phase) converters [ $m_i=1; 0.8; 0.5$ ].

TABLE V.  
FORM FACTOR IN TYPICAL MATRIX (PH-N) AND PWM (PH-PH) WAVEFORMS AT 50 HZ

matrix	PWM $m_i=1$	PWM $m_i=0.8$	PWM $m_i=0.5$
1.06	1.39	1.74	2.37

In PWM converters, the amplitude of line-to-line voltages is modulated by a square waveform whereas, in matrix converters, line-to-neutral voltages result from the superposition of three cosinusoidal amplitude-modulated signals, which are a consequence of the contribution of input voltages  $V_A$ ,  $V_B$ , and  $V_C$  to phase-to-neutral voltage  $V_{pn}$  (phase p) when active switches are  $S_{Ap}$ ,  $S_{Bp}$  and  $S_{Cp}$  (Fig. 1). This affects the sideband effect in pulsating waveforms, defined by harmonic characteristics of the modulating waveform [19]. Due to cosinusoidal modulation, matrix converters enhance sideband effects for medium and high order harmonics (Fig. 12), which leads to a reduction of magnetic losses. Fig. 13 shows distribution of sideband harmonics of order  $n$  around the switching frequency component [ $f_0=5$ kHz] for ideal waveforms with square and cosinusoidal amplitude modulation where the width of pulses is constant and equal to 0.5.

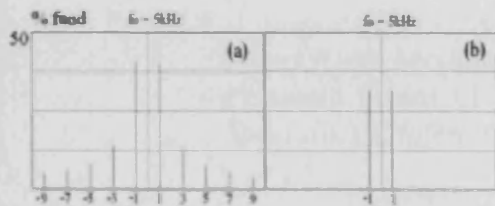


Fig. 13. Sideband harmonics around  $f_0 = 5\text{kHz}$  in amplitude modulation (a)-square (b)-cosinusoidal.

Fig. 14 presents sideband values for a high frequency  $fh$  component in real phase-to-phase (PWM  $m_i=0.8$ ) and phase-to-neutral (matrix) voltage.

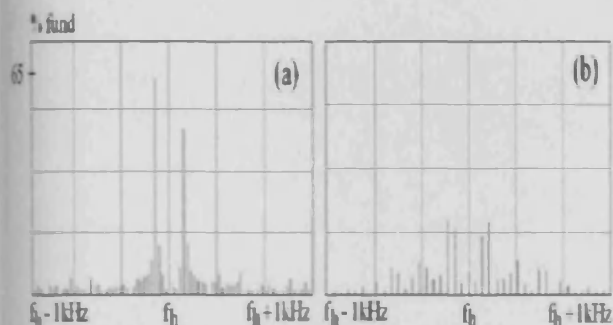


Fig. 14. Sideband harmonic components around a high frequency component of large amplitude (a)-PWM  $m_i=0.8$ (b)-matrix.

## VI. CONCLUSION

Losses in three electrical steels magnetised under typical matrix converter voltage supply was between 38% and 5% lower than when magnetised under PWM waveforms. The loss reduction depends on the material, thickness, magnitude of flux density and fundamental magnetising frequency. A harmonic analysis confirmed that distribution of high frequency harmonics, sideband effect and lower form factor under matrix converter excitation lead to a reduction in eddy current losses in the three materials.

## REFERENCES

- [1]. T. Podlesak, D. Katsis, P.W. Wheeler, J.C. Clare, L. Empringham, M. Bland, "A 150 kVA vector-controlled matrix converter induction motor drive", IEEE Transactions in Industry Applications, Vol 41, Issue 3, pp 841-847, May-June 2005.
- [2]. P. Snary, B. Bhangu, C.M. Bingham, D.A. Store, N. Schofield, "Matrix Converters for sensorless control of PMSMs and other auxiliaries on deep-sea ROVS", IEE Proceedings - Electric Power Applications, Vol 152, Issue 2, pp 382-392, March 2005.
- [3]. D. Katsis, P.W. Wheeler, J.C. Clare, P. Zanchetta, "A three-phase utility power supply based on the matrix converter", 39th IAS Annual Meeting- Industry Applications Conference, Vol 3, pp 1447-1451, 3-7 Oct 2004.
- [4]. G. Bertotti, "General Properties of Power Losses in SoftFerromagnetic Materials", IEEE Transactions on Magnetics, Vol 24, Issue 1, pages 621-630, January 1988.
- [5]. A. Boglietti, P. Ferraris, M. Lazzari, F. Profumo, "Iron losses in magnetic materials with six-step and PWM inverter supply [induction motors]", IEEE Transactions on Magnetics, Vol 27, Issue 6, Part 2, pages 5334-5336, November 1991.
- [6]. A.J. Moses, J. Leicht and Phil Anderson, "Iron Losses in Electrical Machines excited by Non-sinusoidal Voltages", Power Electronics, Machines and Drives, Conference Publication No 487, 16-18 April 2002.
- [7]. T.C. Green, C.A. Hernandez-Aramburo, A.C. Smith, "Losses in grid and inverter supplied induction machines drives", Electric Power Applications, IEE Proceedings, Vol 150, Issue 6, pages 712-724, November 2003.
- [8]. D. Son, J.D. Sievert and Y. Cho, "Core loss measurements including higher harmonics of magnetic induction in electrical steel", Journal of Magnetism and Magnetic Materials, Vol 160, pages 65-67, July 1996.
- [9]. P.W. Wheeler, J. Rodriguez, J.C. Clare, L. Empringham, A. Weinstein, "Matrix Converters: a Technology Review", IEEE Transactions on Industrial Electronics, Vol 49, Issue 2, pages 276-288, April 2002.
- [10]. D. Casadei, G. Serra, A. Tani, L. Zarri, "Matrix converter modulation strategies: a new general approach based on space-vector representation of the switch state", IEEE Transactions on Industrial Electronics, Vol 49, Issue 2, pages 276-288, April 2002.
- [11]. C. Klumpner, F. Blaabjerg, "Experimental evaluation of ride-through capabilities for a matrix converter under short power interruptions", IEEE Transactions on Industrial Electronics, Vol 49, Issue 2, pages 276-288, April 2002.
- [12]. J. Holtz, "Pulsewidth Modulation. A Survey", IEEE Transactions on Industrial Electronics, vol 39, No 5, December 1992.
- [13]. Cogent. SIR Gruppen Sweden. "Non-Oriented Fully Processed Electrical Steels". 2002
- [14]. Philip Beckley, "Electrical steels for rotating machines", The Institution of Electrical Engineers. London. 2002
- [15]. J. P. Swan, O. Walti, T. Belgrand, "Influence of PWM Waveforms on the Breakdown of Harmonic Losses in Electrical Steels", Journal of Magnetism and Magnetic Materials, Vol 160, pages 31-32, July 1996.
- [16]. B.F. Phelps, D.L. Atherton, "Pinning and minor loops in an inclusive model of ferromagnetic hysteresis", IEEE Transactions on Magnetics, Vol 37, Issue 1, Part 2, pages 517-521.
- [17]. A. Al-Rasheed and M. El-Hilo, "Modelling of major and minor hysteresis loops in particulate systems", Journal of Physics D: Applied Physics, Vol 38, No 7, pages 840-845, April 2000.
- [18]. J. B. Goodenough, "Summary of losses in magnetic materials", IEEE Transactions on Magnetics, Vol 38, Issue 5, Part 2, pages 3398-3408, 2002.
- [19]. C. Louis Cuccia, "Harmonics, Sidebands and Transients in Communication Engineering as studied by the Fourier and Laplace analyses". McGraw Hill. Electrical and Electronic Engineering Series. 1952.

- A1.5. J. Sagarduy, A.J. Moses, F.J. Anayi, J. Clare, P.W. Wheeler, "Matrix vs Pulse-Width-Modulation Frequency Converters. Iron Losses under Pulsating Forms of Voltage Excitation", *37<sup>th</sup> IEEE Power Electronics Specialists Conference*, Jeju island (South Korea), 16-20 June 2006.

# Matrix vs Pulse-Width-Modulation Frequency Converters. Iron Losses under Pulsating Forms of Voltage Excitation.

Juan Sagarduy, Anthony J. Moses, Fatih J. Anayi  
Wolfson Centre for Magnetics - Cardiff University  
Queen's Buildings - Newport Road  
Cardiff C24 3AA - United Kingdom  
Email: [Sagarduyochoadee@Cardiff.ac.uk](mailto:Sagarduyochoadee@Cardiff.ac.uk)

Jon Clare, Patrick W. Wheeler  
Power Electronics, Machines and Control Group  
The University of Nottingham  
Nottingham NG7 2RD - United Kingdom  
Email: [jon.clare@nottingham.ac.uk](mailto:jon.clare@nottingham.ac.uk)

**Abstract**— A Single Strip Tester was used to measure iron losses in laminations of non-oriented electrical steel magnetised under typical supply of a 2-level PWM (line-to-line) and three-phase matrix converter (line-to-neutral). Results show the beneficial effect of the harmonic characteristics of voltage excitation produced by direct ac-ac converters on the performance of soft magnetic material, commonly used in laminated stator cores of induction motors.

## I. INTRODUCTION

### A. Iron losses

Non-oriented electrical steels used in the stator core of conventional induction motors cause iron losses, which can be analysed in terms of static hysteresis, eddy-current and anomalous loss [1] as given in (1) where  $f$  is the frequency of magnetisation and  $K_h$ ,  $K_e$  and  $K_a$  are coefficients defining static hysteresis, eddy current and dynamic hysteresis (anomalous) loss respectively.

$$P_s \left[ \frac{W}{kg} \right] = K_h f + K_e f^2 + K_a f^{1.5} \quad (1)$$

While static hysteresis loss (*term1*) mainly depends on the characteristics of the magnetic material, eddy-current (*term2*) and anomalous losses (*term3*) are frequency dependant and hence increase significantly when the time variation of flux density is non-sinusoidal [2][3][4]. Flux harmonics in the kilohertz range, which are caused by pulsating time varying voltage excitation waveforms characteristic of frequency converters, can cause a larger increase in eddy current loss in the magnetic core materials [5]. Heat is dissipated in stator cores as iron losses increase.

While the performance of laminated cores subjected to PWM excitation has been investigated [2][4], the impact of matrix converter excitation on iron losses in electrical machines is yet unknown. Since direct ac-ac conversion technology is ready to challenge classical inverters in several applications such as ship propulsion, aerospace [6], this paper studies the effect of matrix converter supply on core losses in three commonly used non-oriented steels.

### B. Frequency converters

Matrix converters can be considered as  $n \times n$  direct ac-ac converters. For  $n=3$ , three input phases provided with a LC filter are connected to the load through nine bidirectional switches (Fig 1).

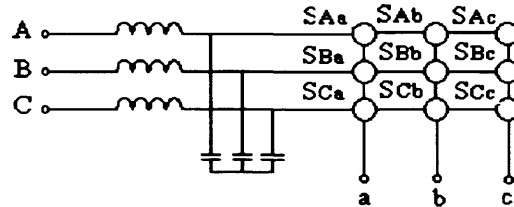


Fig 1 Topology of a 3x3 matrix converter

Each consists of two anti-parallel IGBTs in a common-collector back-to-back configuration and is controlled by logic signals from a Field Programmable Gate Array [FPGA], which implements the four-step semi-soft current-direction based commutation. Fatal short or open circuits between input phases are consequently avoided [7]. A Digital Signal Processor [DSP] executes the control algorithm for the load and implements Space Vector Modulation [SVM]. Input current and output voltage reference phase vectors rotate at a given angular frequency. Depending on their position within six sectors at each sampling time, a pattern, in which the duty cycles of the bidirectional switches are calculated, is selected [8]. Sampling frequency  $f_s$  of execution of SVM algorithm is fixed; this should not be confused with the switching frequency  $f_w$  of semiconductors. Implementation of the four-step commutation is carried out after nine logic signals are conveyed to the FPGA. This enables control of eighteen individual IGBTs. Since no intermediate dc-link is present, a clamp circuit is therefore required to deal with input power disturbances and ensure ride-through capability [9].

Classical Pulse-Width-Modulated [PWM] converters perform ac-ac conversion in two stages: rectification and inversion. A dc-link, between rectifier and inverter, is an essential element in this topology.

The most important parameter in PWM waveforms is the modulation index [ $m_i$ ] defined in (2), where  $A_{ref}$  and  $A_c$  are the amplitude of reference and carrier signals. Its influence on the harmonic behaviour of waveforms in PWM inverters will be discussed later.

$$m_i = \frac{A^{ref}}{A^c} \quad (2)$$

## II. THEORETICAL ANALYSIS OF WAVEFORMS

Harmonic analysis of voltage waveforms produced by frequency converters requires the definition of frequency weighted Total Harmonic Distortion [ $fwTHD$ ], given in (3) where  $v_1$  and  $v_n$  are components corresponding to fundamental and  $n^{th}$  order frequency.

$$fwTHD [\%] = \frac{\sum \left[ \frac{v_n}{n} \right]}{v_1} \times 100 \quad (3)$$

In order to evaluate sideband effect on the  $k^{th}$  high order harmonic, the concept of  $fwTHD$ , introduced by (4a-b), is used. Each pair of side harmonics is assigned order  $j$  and the bandwidth of analysis is defined by the order  $j_{max}$  of the maximum side frequency considered (with the software used to carry out FFT in this investigation, the resolution  $\Delta f$  is 25Hz).

$$fwTHD(k^{th} \text{ harm}) = \frac{\frac{v_k}{k} + \sum_{-j_{max}}^{j_{max}} \frac{v_j}{|j|}}{v_1} \times 100 \quad (4a)$$

$$j = \frac{f_j - f_k}{\Delta f} \quad (4b)$$

The Form Factor [FF] is also important when assessing waveforms. It is defined in terms of Root Mean Square and Rectified Mean values, is given in (5).

$$FF = \frac{v_{rms}}{v_{rectmean}} = \frac{\sqrt{\frac{1}{T} \int_0^T v^2(t) dt}}{\frac{1}{T} \int_0^T |v(t)| dt} \quad (5)$$

## III. EXPERIMENTAL PROCEDURE

The three-phase matrix converter prototype used in the experimental study consists of one FPGA board, one

DSP board, a gate driver board, power system and heat sink. The DSP board, independently supplied (0; 5V), provides the supply to the FPGA board, executes SVM control algorithm and conveys nine duty cycles to the FPGA. Responsible for carrying out the four-step semisoft commutation and generating eighteen logic signals for as many individual Insulated Gate Bipolar Transistor [IGBT], the FPGA board ensures, by the means of a 24V DC-DC converter, that IGBTs, current and voltage transducers are supplied accordingly (-15; +15V). The gate driver board with independent supply (0; +5V) forwards the control signals to the power module. The latter is the EUPEC EconoMAC module (FM35R12KE3), specially designed for matrix converters and based upon nine bidirectional switches [10], which consist of IGBT-antiparallel diode in a back-to-back configuration. IGBTs may function at a maximum collector emitter voltage 1200V and maximum collector current 55A [11], which result in a total power rating for the module of 7.5kW. Fig 2 shows the matrix converter prototype used in the study.



Fig 2. Three-phase 7.5kW matrix converter

The matrix prototype described above was connected to a 3 phase 50 Hz supply through a variable transformer and loaded with resistances as shown in Fig 3.

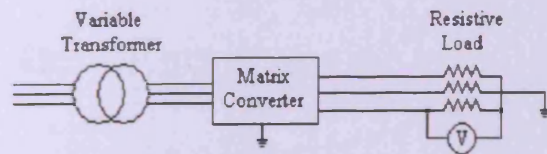


Fig 3. Experimental setup [matrix converter]

The output voltage between phase and neutral (phn) was measured and recorded by means of a digital oscilloscope, (Yokogawa - Digital scope DL716 16CH). A PWM converter, (Toshiba - Transistor Inverter TOSVERT VF-A3 400 V - 0.75 kW), was connected to a 3 phase delta-wound induction motor, (Clarke Motor Type 80B/4). The output voltage regulation function

was used to obtain line-to-line (phph) waveforms at different modulation indices. The fundamental frequency of the converter outputs was varied between 50Hz and 200Hz. Typical experimental matrix and PWM output voltage waveforms at  $f=100\text{Hz}$  are shown in Fig 4.

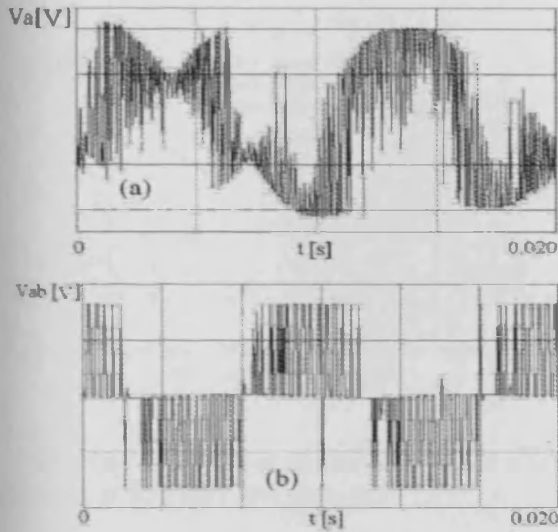


Fig 4. Typical voltage waveforms at 100 Hz in (a) - matrix converter (b) - PWM

(306x30mm; 280x30mm; 306x30mm) strips of three electrical steels (M470-50A; M530-50A; M700-65A) of thicknesses (0.50, 0.50 and 0.65 mm) were selected. Table I shows typical physical properties of these grades [12][13].

Table I. Relative permeability (at 1.5T, 50Hz), density, resistivity and Silicon content of three electrical steels

EN10106	$\mu_r$	$d$ [ $\text{kg}/\text{dm}^3$ ]	$\rho$ [ $\mu\Omega.\text{cm}$ ]	Si [%]
M470-50A	1120	7.70	39	2.5
M530-50A	1150	7.70	36	2.2
M700-65A	1570	7.75	30	1.75

The Single Strip Tester [SST] was connected to a signal generator (TTi - TGA 30MHz) and power amplifier (BK Electronics MXF 900) as shown in Fig 5.

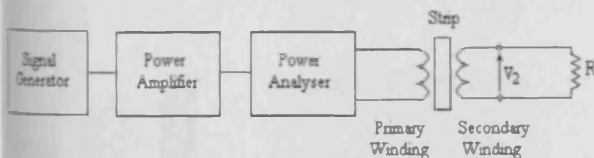


Fig 5. Setup for measurement of magnetic losses in single strip specimens

The signal generator was programmed to output the same voltage waveshape as the actual converters. The

power loss of the material in the SST was measured by a power analyzer, (Voltech - PM3000A). The process was repeated for the three materials under phn (matrix) and phph (PWM) voltage waveforms. Modulation indices of unity, 0.8 and 0.5 were chosen under PWM excitation. The peak flux density,  $B_m$ , was set between 1.0T and 1.5T. It was estimated that the iron loss could be measured to within  $\pm 2.5\%$

#### IV. RESULTS AND DISCUSSION

Iron losses of the three batches of material were measured while the SST was supplied with forms of voltage excitation, typical of real matrix and PWM converter, at three fundamental frequencies [50; 100; 200Hz]. Fig 6 shows the variation of specific power loss  $P_s$  [W/kg] with flux density  $B$  in the M470-50A material at a fundamental magnetisation frequency of 50Hz under PWM [ $m_i=0.5$ ; 0.8; 1], matrix and sinusoidal excitation.

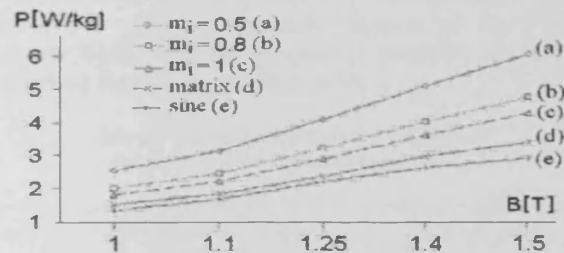


Fig 6 Variation of specific power loss with flux density  $B$  at fundamental frequency of magnetisation of  $f=50\text{Hz}$  (M470-50A)

Fig 7 shows the ratio ( $P_{PWM}/P_{sine}$ ) of power loss under PWM excitation (modulation index  $m_i=1$ ;  $m_i=0.5$ ) to that of loss under sinusoidal excitation for materials M530-50A and M700-65A. M470-50A showed similar behaviour to that of M530-50A. It is interesting to note that the relative loss increase with the lower modulation index is much higher in the M530-50A material than in the thicker steels whose hysteresis component of loss would probably be larger.

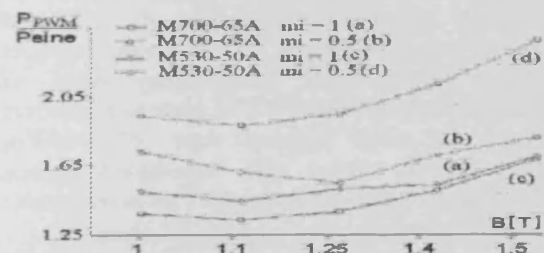


Fig 7 Variation of ratio ( $P_{PWM}/P_{sine}$ ) with flux density  $B$  at 50Hz under  $m_i=1$ ;  $m_i=0.5$  in M530-50A and M700-65A

Fig 8 shows the ratio, ( $P_{matrix}/P_{sine}$ ), of power loss under matrix converter excitation over power loss under sinusoidal excitation for different inductions. The deterioration in loss here is very similar in all three materials accounting for the experimental accuracy apart from the increased ratio in the lowest loss material at low flux density.

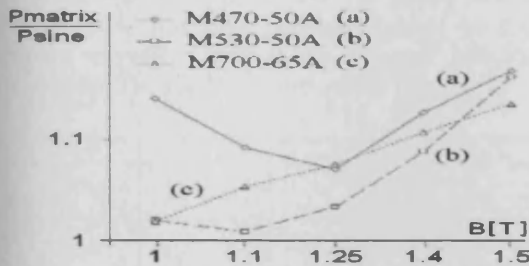


Fig 8 Variation of ratio ( $P_{matrix}/P_{sine}$ ) with flux density  $B$  [T] at 50 Hz in the three materials

We define the reduction of loss under matrix voltage waveform as the ratio  $r$  [%] given by:

$$r[\%] = \frac{P_{PWM} - P_{matrix}}{P_{PWM}} \times 100 \quad (6)$$

Figures 9-11 show how  $r$  varies with frequency in the three materials when the modulation index under PWM was 0.8. At the highest frequency, the loss reduction under matrix condition is small and similar in the two thinner materials. However, at the lowest frequency, the reduction in all materials is similar, perhaps because harmful eddy current loss component is relatively lower in each material.

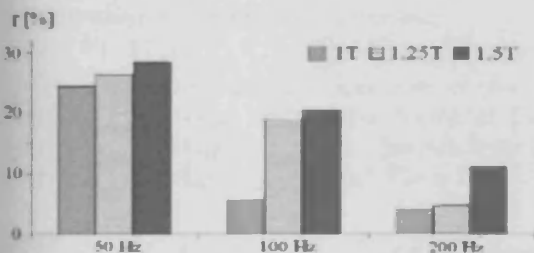


Fig 9. Variation of  $r$  with flux density and frequency (M470-50A)

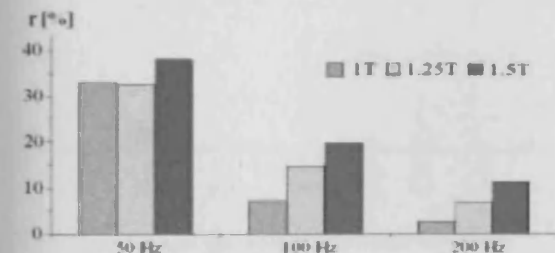


Fig 10. Variation of  $r$  with flux density and frequency (M530-50A)

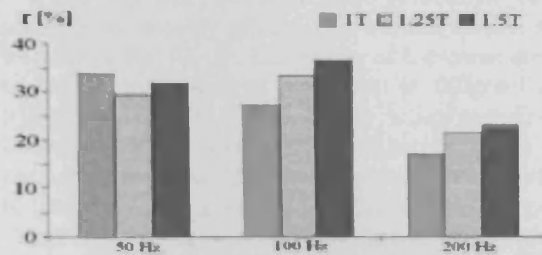


Fig 11. Variation of  $r$  with flux density and frequency (M700-65A)

#### A. Effect of PWM modulation index

Fig 5 verifies that lower modulation index causes higher loss. This is a well known phenomenon [5][14] due to the noticeably higher harmonic distortion. While low order components change the general shape of the B-H loop, high order flux harmonics lead to the appearance of non-desired minor loops on the B-H curve [15][16]. Both phenomena cause higher losses in electrical steels. Table II shows the variation of  $ov$  [%], the output voltage regulation function of the PWM inverter used, with the frequency weighted harmonic distortion and the modulation index

Table II. Variation of fwTHD [%] with  $mi$  and corresponding voltage regulation function

$ov$ [%]	20	30	40	50	60	70
$mi$	0.43	0.63	0.77	0.85	0.98	1.03
$fwTHD$ [%]	126.3	84.6	70.3	64.8	63.2	59.2

M530-50A has the lowest proportion of eddy current loss due to its high hysteresis component. In low alloy non-oriented steel, such as the M700-65A, the hysteresis loss accounts for 30-60% of the total loss, classical eddy current loss accounts for 40-60% and the anomalous loss is 10-20%. In thinner, high alloy material, the hysteresis component is relatively higher, which conforms with the low effect of flux harmonics as shown in Fig 7. It can be seen that in M530-50A and M700-65A the loss under matrix converter waveform rises with flux density but not as rapidly as occurs under PWM (Fig 7), presumably because of the smaller harmonic content in the matrix converter waveform. The better performance under matrix converter waveform compared to PWM waveform (at  $mi=0.8$ ) is significant for each material under all measured magnetic conditions. This is due to the different combination of harmonics present in each case.

#### B. Smoothness of flux density curve

Magnetic flux density  $B$  [T] is related to induced voltage  $e$  (t), in a search coil or secondary winding as in equation (9). Here  $N$  is the number of secondary turns,  $A$  the cross section of the sample,  $v$  (t) the voltage

excitation supplied to the primary winding by the inverter,  $e(t)$  the induced voltage in the secondary winding and  $B(t)$  the magnetic flux density.

$$e(t) = NA \frac{dB(t)}{dt} \Leftrightarrow B(t) = \frac{1}{NA} \int e(t) dt \quad (9)$$

In this paper, integration of primary voltage excitation  $v(t)$  was carried out for matrix and PWM converters so this will not be identical to the flux density waveform but it is a good indicator of waveshape. The result is given in Fig 12.

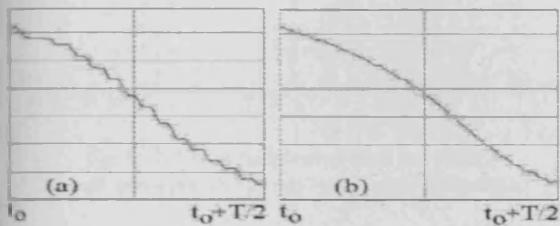


Fig 12. Integral of  $v(t)$  over half a cycle under different voltage excitations at 100 Hz fundamental frequency (a) - PWM  $m_i=0.8$  (b) matrix converter

The loss in electrical steel is fundamentally caused by domain wall motion and rotation [17]. It is assumed that magnetisation in which  $dB(t)/dt$  is continuous and sinusoidal has low dynamic hysteresis compared to other waveforms [2]. The loss can also be assumed as being approximately proportional to the square of the mean domain wall velocity within a material. This is obviously a complex function but it would be expected that domain walls in a material magnetised with waveform in Fig 11a are subject to short periods of inactivity followed by high velocity movement indicated by the steps which lead to higher losses.

### C. Distribution of high order harmonics

Fig 13 shows the harmonic spectrum of the PWM [ $m_i=0.8$ ] (line-to-line) and matrix converter (line-to-neutral) output voltages. Switching frequency for PWM is 3kHz and sampling frequency in SVM is 2.5kHz.

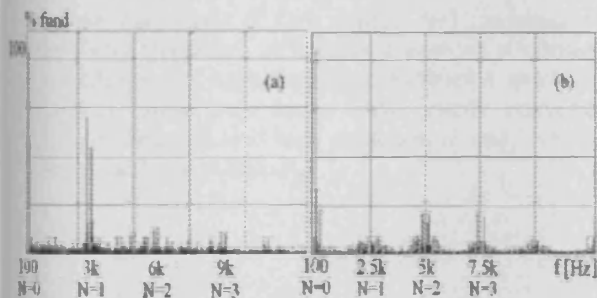


Fig 13. Harmonic spectrum of voltage waveforms (a) - PWM  $m_i=0.8$  (b) - matrix

The first high order harmonic present in pulsating waveforms strongly affects eddy current losses. As can be seen in Fig 12, the distribution of harmonic envelopes in the matrix converter waveform is different in the PWM waveform and this probably mitigates their effect on losses. In PWM converters, the harmonic due to the switching frequency has the highest amplitude, which is believed to have a serious harmful impact on iron loss. Table III presents  $f_wTHD$  [%] due to each cluster of high order  $N$  (Fig 12) for matrix (ph-ph) and PWM (ph-ph) [ $m_i=0.8$ ] waveforms.

Table III.  $f_wTHD$  [%] due to high frequencies, each in a bandwidth of  $\pm 1$ kHz

N	0	1	2	3
Matrix	18.3	14.5	27.1	16.2
PWM	11.1	51.3	22.8	19.9

### D. Nature of matrix converter waveform

When the input and output frequencies are the same, the matrix converter generates a periodic waveform of period  $T = 1/f$  between phase and neutral. In this case, even harmonics are negligible and the form factor [FF] (6) has a strong impact on the magnetising conditions. Table IV shows  $f_wTHD$  [%] due to the first ten even harmonics in phase-to-neutral voltage waveforms of matrix converter with input frequency of 50Hz and output frequencies of 50 Hz, 100 Hz and 200Hz.

Table IV.  $f_wTHD$  [%] due to the first ten even harmonics in typical matrix converter waveforms for the three output frequencies

Waveform	$f_wTHD$ [%]
$V_{phn5050}$	0.89
$V_{phn50100}$	2.73
$V_{phn50200}$	5.73

Table V shows the FF of voltage waveforms from matrix (phase-to-neutral) and PWM (phase-to-phase) converters [ $m_i=1; 0.8; 0.5$ ].

Table V. FF in typical matrix (ph-n) and PWM (ph-ph) waveforms at 50 Hz

matrix	PWM $m_i = 1$	PWM $m_i = 0.8$	PWM $m_i = 0.5$
1.06	1.39	1.74	2.37

In PWM converters, the amplitude of line-to-line voltages is modulated by a square waveform whereas, in matrix converters, line-to-neutral voltages result from the superposition of three cosinusoidal amplitude-modulated signals, which are a consequence of the contribution of input voltages  $V_A$ ,  $V_B$ , and  $V_C$  to phase-to-neutral voltage  $V_{pn}$  (phase p) when active switches are  $S_{Ap}$ ,  $S_{Bp}$  and  $S_{Cp}$  (Fig 1). This affects the sideband effect in pulsating waveforms, defined by harmonic characteristics of the modulating waveform [18]. Due to

cosinusoidal modulation, matrix converters enhance sideband effects for medium and high order harmonics (Fig 13), which leads to a reduction of magnetic losses. Fig 14 shows distribution of sideband harmonics of order  $n$  around the switching frequency component [ $f_0=5\text{kHz}$ ] for ideal waveforms with square and cosinusoidal amplitude modulation where the width of pulses is constant and equal to 0.5.

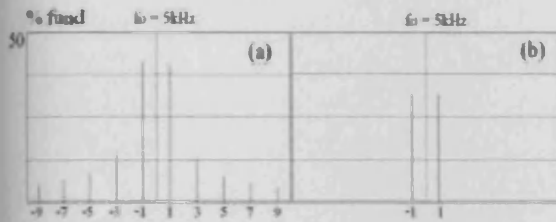


Fig 14. Sideband harmonics around  $f_0 = 5\text{kHz}$  in amplitude modulation in (a) - square (b) - cosinusoidal

Fig 15 presents sideband values for a high frequency,  $f_h$ , component in real phase-to-phase (PWM  $m_i=0.8$ ) and phase-to-neutral (matrix) voltage.

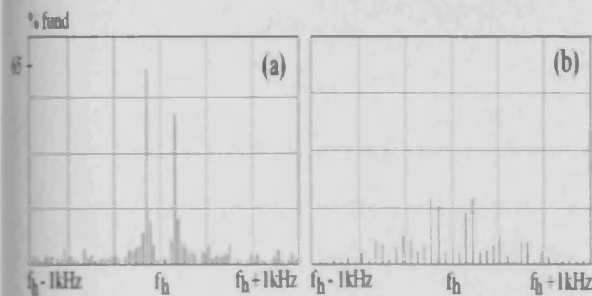


Fig 15. Sideband harmonic components around a high frequency component of large amplitude (a) - PWM  $m_i=0.8$  (b) - matrix

## V. CONCLUSION

The loss of three electrical steels magnetised under typical matrix converter voltage supply was between 38% and 5% lower than when magnetised under PWM waveforms. The loss reduction depends on the material, thickness, magnitude of flux density and fundamental magnetising frequency. A harmonic analysis confirmed that distribution of high frequency harmonics, sideband effect and lower form factor under matrix converter excitation probably lead to a reduction in eddy current losses in the three materials.

## REFERENCES

- [1] G. Bertotti, "General Properties of Power Losses in Soft Ferromagnetic Materials", IEEE Transactions on Magnetics, Vol 24, Issue 1, pp 621-630, January 1988.
- [2] A. Boglietti, P. Ferraris, M. Lazzari, F. Profumo, "Iron losses in magnetic materials with six-step and PWM inverter supply [induction motors]", IEEE Transactions on Magnetics, Vol 27, Issue 6, Part 2, pp 5334-5336, November 1991.
- [3] A.J. Moses, J. Leicht and Phil Anderson, "Iron losses in electrical machines excited by non-sinusoidal voltages", Power Electronics, Machines and Drives, Conference Publication No 487, 16-18 April 2002.
- [4] T.C. Green, C.A. Hernandez-Aramburo, A.C. Smith, "Losses in grid and inverter supplied induction machines drives", Electric Power Applications, IEE Proceedings, Vol 150, Issue 6, pp 712-724, November 2003.
- [5] D. Son, J.D. Sievert and Y. Cho, "Core loss measurements including higher harmonics of magnetic induction in electrical steel", Journal of Magnetism and Magnetic Materials, Vol 160, pp 65-67, July 1996.
- [6] P. Snary, "Matrix Converters for Sensorless Control of PSMs Propulsion Thrusters on Deep-Sea ROVs". G. Towers, "Analysis of a Matrix Converter Driven Electro-Mechanical Actuator for an Aircraft Rudder". IEEE United Kingdom & Republic of Ireland One Day Seminar on Matrix Converters, University of Nottingham (UK), November 17<sup>th</sup> 2004.
- [7] P.W. Wheeler, J. Rodriguez, J.C. Clare, L. Empringham, A. Weinstein, "Matrix Converters: a Technology Review", IEEE Transactions on Industrial Electronics, Vol 49, Issue 2, pp 276-288, April 2002.
- [8] D. Casadei, G. Serra, A. Tani, L. Zarri, "Matrix converter modulation strategies: a new general approach based on space-vector representation of the switch state", IEEE Transactions on Industrial Electronics, Vol 49, Issue 2, pp 276-288, April 2002.
- [9] C. Klumpner, F. Blaabjerg, "Experimental evaluation of ride-through capabilities for a matrix converter under short power interruptions", IEEE Transactions on Industrial Electronics, Vol 49, Issue 2, pp 276-288, April 2002.
- [10] M. Hornkamp, M. Loddenkoetter, M. Muenzer, O. Simon, M. Bruckmann, "EconoMAC: the first all-in-one IGBT module for matrix converters", Power Conversion Intelligent Motion (PCIM) Conference, Nuremberg, June 2001.
- [11] EUPEC Infineon Technologies AG, "Eupec IGBT Modules", Datenblatt FM35R12KE3, February 2001.
- [12] Cogent. SIR Gruppen Sweden. "Non-Oriented Fully Processed Electrical Steels". 2002
- [13] Philip Beckley, "Electrical steels for rotating machines", The Institution of Electrical Engineers, London. 2002
- [14] J. P. Swan, O. Walti, T. Belgrand, "Influence of PWM Waveforms on the Breakdown of Harmonic Losses in Electrical Steels", Journal of Magnetism and Magnetic Materials, Vol 160, pp 31-32, July 1996.
- [15] B.F. Phelps, D.L. Atherton, "Pinning and minor loops in an inclusive model of ferromagnetic hysteresis", IEEE Transactions on Magnetics, Vol 37, Issue 1, Part 2, pp 517-521.
- [16] A. Al-Rasheed and M. El-Hilo, "Modelling of major and minor hysteresis loops in particulate systems", Journal of Physics D: Applied Physics, Vol 38, No7, pp 840-845, April 2000.
- [17] J. B. Goodenough, "Summary of losses in magnetic materials", IEEE Transactions on Magnetics, Vol 38, Issue 5, Part 2, pp 3398-3408, 2002.
- [18] C. Louis Cuccia, "Harmonics, Sidebands and Transients in Communication Engineering as studied by the Fourier and Laplace analyses". McGraw Hill. Electrical and Electronic Engineering Series. 1952.

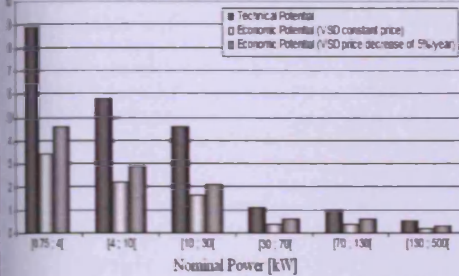
- A.1.6. J. Sagarduy, A.J. Moses, F.J. Anayi, "Effect of AC-AC Conversion Topology on Separation of Losses in Si-Fe Steel", *10<sup>th</sup> Joint Magnetism and Magnetic Materials / Intermag Conference*, Baltimore (US), 7-11 Jan 2007.

# Effect of AC-AC Conversion Topology on Separation of Losses in Si-Fe Steel

Juan Sagarduy Anthony J. Moses Fatih J. Anayi

Wolfson Centre for Magnetics – Cardiff University SagarduychoadeeribeJ@Cardiff.ac.uk

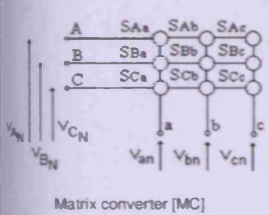
Potential energy savings by 2015 [TWh] in the tertiary sector by power range



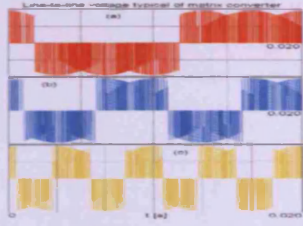
Variable Speed Drives [VSD]  
 - Asynchronous machine  
 - Frequency converter  
 → Commonly used in industry/tertiary sector  
 [Fans; Pumps; Air Compressors; Conveyors]

Technical & Economical Potential for Energy Savings in the tertiary sector  
 [VSD applied to induction motors  
 Nominal Power = 0.75 – 30 kW]

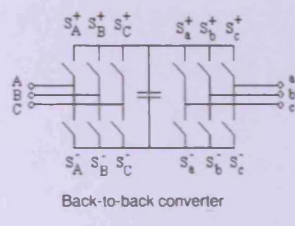
Objectives  
 (1) Losses in non-oriented steel (typically used in stator cores of induction machines) subjected to line-line matrix converter supply  
 (2) Contribution to standardisation of iron loss measurement under distorted excitation [direct AC-AC converter]  
 (3) Effect of supply of higher harmonic quality on total energy losses and frequency-dependent components [validation by conventional model]



Matrix converter [MC]



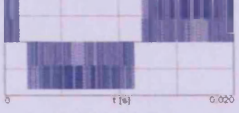
Line-to-neutral voltage (matrix converter) at  $f_s = 5$  kHz and  $f$  equal to 50 Hz (a), 100 Hz (b) 200Hz (c)  
 Maximum output voltage transfer ratio  $\sqrt{3}/2$



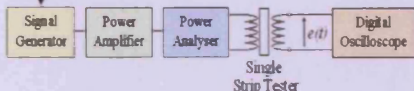
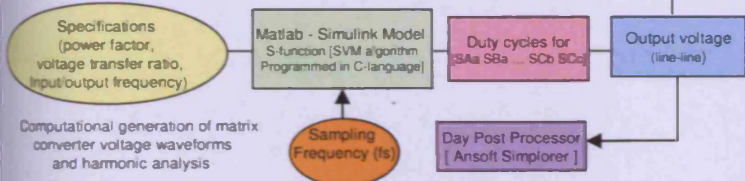
Back-to-back converter

Pulse Width Modulation [PWM]

- Modulation index (m)
- Switching frequency ( $f_s$ )



Line-to-line voltage in 2-level PWM inverter at  $f_w = 5$  kHz and  $f = 50$  Hz ( $m = 1$ )



Experimental setup for iron loss measurement

Increment  $R$  [%] of energy losses caused by distorted excitation where  $W_{e(dist)}$  and  $W_{e(sine)}$  are measured specific energy losses [J/kg]  

$$R = 100 \cdot [W_{e(dist)} - W_{e(sine)}] / W_{e(sine)} \quad (1)$$

Definition of the factor  $D$  related to Total Harmonic Distortion  $THD$  [%] in the induced voltage where  $E_n$  and  $E_1$  refer to harmonic (order  $n$ ) and fundamental components respectively  

$$THD [\%] = 100 \cdot \sqrt{\sum_{n=2}^{\infty} E_n^2} / E_1 \quad E = E_1 \sqrt{1 + (THD/100)^2} = E_1 \cdot D$$

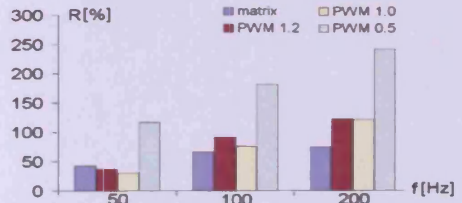
Repartition of losses [static hysteresis - classical eddy current - anomalous loss] based upon harmonic distortion inherent to frequency converter supply

$$W_s = W_H + (4\pi^2 B_1^2) k_e F_o + (2\pi B_1)^{3/2} k_a F_o \quad (4)$$

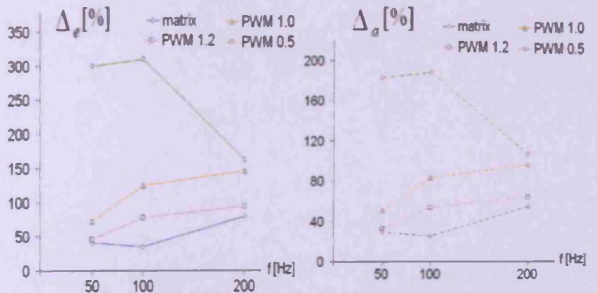
$$F_e = f D^2 \quad F_o = f^{1/2} D^{3/2} \quad (5)$$

Increment  $\Delta_{e-a}$  [%] of frequency-dependent components of loss caused by harmonic distortion resulting from frequency conversion topology  

$$\Delta_{e-a} = 100 \cdot [F_{e-a(dist)} - F_{e-a(sine)}] / F_{e-a(sine)} \quad (6)$$



Increment of measured energy losses at 50, 100 and 200 Hz under matrix and PWM ( $m = 0.5 - 1.0 - 1.2$ ) voltage excitation



Calculated increment of classical eddy-current loss  $\Delta_e$  [%] and anomalous loss  $\Delta_a$  [%] in laminations subjected to voltage excitation typical of matrix and back-to-back PWM frequency converters

## Conclusions

- (1) Improvement of harmonic quality of voltage excitation by MC
- (2) Reduction of calculated frequency-dependent losses [50 – 200 Hz]
- (3) Highest impact of classical eddy-current / anomalous loss reduction on total energy losses → highest magnetising frequency (200Hz)
- (4) Effect of non-linearity between  $b(f)$  – magnetic field  $h(f)$  and harmonic spectrum of induced voltage on coefficients  $k_e$  and  $k_a$  to be taken into account

- A.1.7. A.J. Moses, J. Sagrduy, “Impact of PWM and matrix converters on performance of Electrical Steel”, *UK Magnetics Society Seminar on Developments in Magnetic Materials*, QinetiQ Farnborough (UK), 25 April 2006.

# Impact of PWM and Matrix converters on performance of electrical steel

A J Moses and J Sagarduy  
Wolfson Centre for Magnetics  
School of Engineering - Cardiff University

Pulse width modulation (PWM) voltage supplies are common in electrical drive systems and already matrix converters are being claimed to be a long term cheaper and more efficient alternative in many applications. This presentation will review the impact of both on magnetic losses in electrical steel. It is well known that losses can increase by 30 % or more under PWM conditions but how will matrix converters compare? Additional losses are due to flux harmonics caused by the PWM voltage waveform and it is well known that these can be minimised by appropriate material selection and choice of PWM waveform. The presentation will cover measurement and prediction of such losses and show the impact of good and bad combinations of material and voltage supply on system performance.

## I. Introduction

Induction motors have been the workhorse of industry for several decades. Also called AC asynchronous motors, they are based upon a stator core consisting of insulated laminations of non-oriented electrical steel (0.3-3.0 % Si, thickness 0.5-0.65 mm), where an alternating magnetic flux is created by three-phase currents flowing in the copper primary windings. Soft magnetic materials used to manufacture stator cores must have low power loss and high permeability. The linkage flux causes current to flow in aluminium conductor bars, interconnected by end rings in the most common squirrel cage rotor. The presence of magnetic flux and current leads to the appearance of the magneto-motive force, accountable for the rotation of the rotor. In Variable Speed Drives (VSD), induction motors function as prime movers for pumps, fans etc. In common VSD systems, the rotating machine is supplied by a variable frequency converter. Therefore, the system efficiency is not only affected by the efficiency of the motor, but also by the efficiency of the power converter.

## II. Frequency converters

Two-level Pulse-Width-Modulated (PWM) converters are the primary choice nowadays in VSD. The principle of frequency conversion rests on the connection of a three-phase rectifier connected to an inverter by the means of a DC-link (Fig. 1). While passive rectifiers are attractive to industry thanks to their low cost, active rectifiers (semiconductor + diode in antiparallel configuration) enable bidirectional flow. The two critical parameters in PWM for the analysis of iron loss are modulation index ( $m_i$ ) and switching frequency ( $f_w$ ). As a result of being a cheap and mature technology and ensuring effective decoupling between rectifier and inverter, PWM converters are commonly used. Nonetheless, the impossibility of adjusting power factor (passive rectifier), high levels of harmonic distortion and a strong dependence on bulky and temperature-sensitive DC-links, which require a reliable cooling system, make them less attractive.

Matrix converters can be considered as 3x3 direct ac-ac converters. Three input phases provided with a LC filter are connected to the load through nine bidirectional switches (Fig. 1).

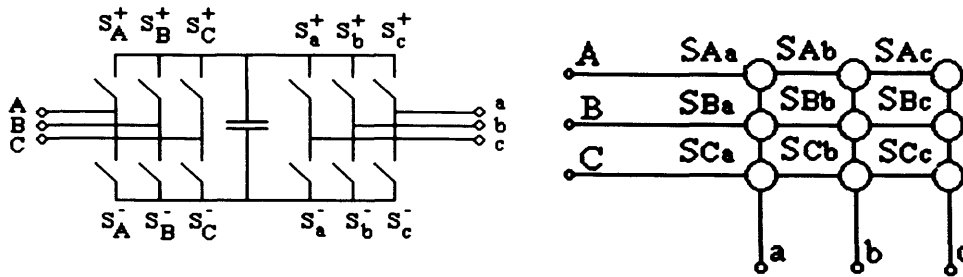


Fig. 1. Topology of three phase converters (a) 2-level PWM - (b) matrix

Each bidirectional switch consists of two anti-parallel IGBTs in a common-collector back-to-back configuration and is controlled by logic signals from a Field Programmable Gate Array [FPGA]. Fatal short or open circuits between input phases must be avoided. The control of a matrix converter is shown in Fig. 2.

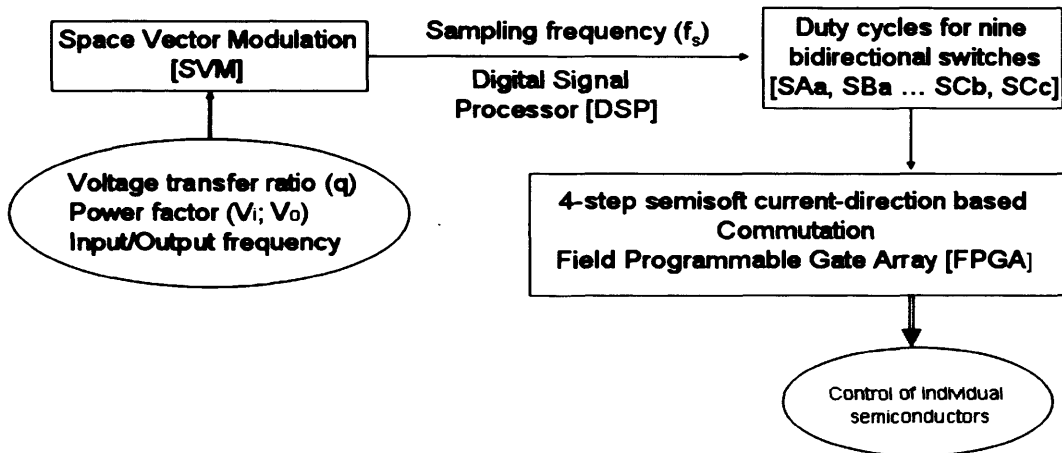


Fig. 2. Basic control of a three-phase matrix converter

Since no intermediate dc-link is present, a clamp circuit is therefore required to deal with input power disturbances and ensure ride-through capability. Typical matrix converter line-to-neutral (phn) and line-to-line (p-ph) voltage waveforms at 50; 100 and 200 Hz, which were obtained in a Matlab – Simulink based model [4], are given in Fig. 3.

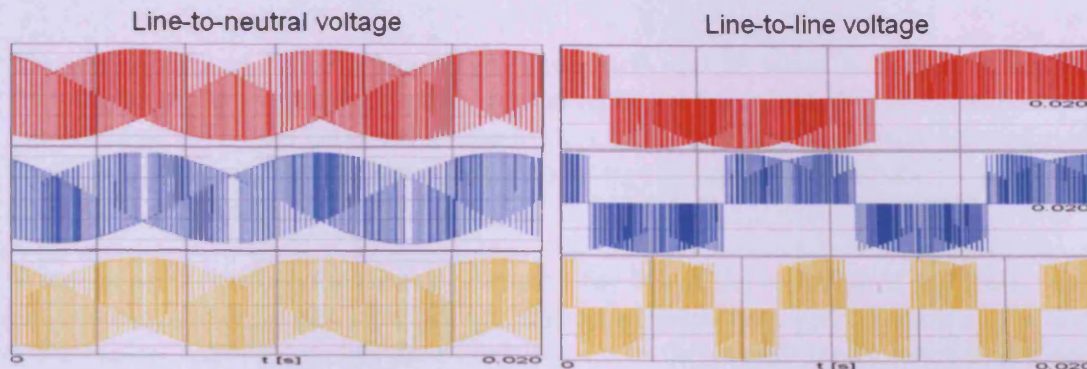


Fig. 3. Voltage waveforms typical of a three-phase converter

Despite limited voltage transfer ratio ( $\sqrt{3}/2$ ), higher number of semiconductors and complexity of control, matrix converters are already challenging PWM converters relying upon possible adjustment of power factor and integrability with the motor (absence of DC-link). For high values of  $f_s$  and  $f_w$  (beyond 10 kHz), PWM converters show reduced switching losses in semiconductors [5], certainly caused by a higher number of IGBT/MOSFETs in the matrix converter. Nevertheless, in small or medium power applications, converter losses are negligible when compared to the total motor losses at regimes close to full load.

### III. Induction motor

Losses in a motor can be split in two categories:

Load-independent losses include iron losses in the laminated stator core, windage and friction losses. Load-dependent losses include stator / rotor resistive losses and stray load losses. Each is briefly analysed here but special attention is devoted to iron losses in the stator core.

Iron loss may comprise 25% of the total losses at full load but more than 50% at half load. It results directly from the magnetisation of the ferromagnetic material in the stator core and is dependent of the voltage applied to the primary windings but almost independent from the shaft load.

The well-known and assumed separation model of iron losses [static hysteresis, classical eddy-current and dynamic hysteresis or anomalous loss components] by Bertotti [6] is still highly controversial and further work is needed to fully understand the physical behaviour of magnetic materials. Static hysteresis is greatly affected by material properties such as homogeneity, isotropy and purity it is believed to be frequency-independent. Classical eddy-current loss, which is affected by resistivity and thickness of the lamination, and dynamic hysteresis loss, which is believed to be dependent on domain structure, depend, not only on the fundamental frequency of magnetisation, but also on flux harmonics. In fast switching converters such as PWM and matrix converters, harmonic characteristics of the supply voltage applied to the windings are intimately related to the harmonic distortion of the flux density curve.

The assumption of linear relationship between B and H, along with their sinusoidal time variation, has yielded the conventional equation for calculation of classical eddy-current losses [7]. It is certain that due to non-linearity in the B-H curve in conditions close to saturation, this equation leads to a significant underestimation of classical eddy-current losses.

Windage and friction losses are accountable for 5% of the total loss at full load. Stator and rotor resistive losses in windings and aluminium bars predominant at full load (35% stator - 25% rotor) but their contribution to the overall inefficiency at low load is comparable to the iron loss. Stray load losses, which are manifested by abnormal heating, drop of torque and acceleration/retardation effects, are caused by flux leakage within the machine. Most relevant in varying torque or frequent start regimes, stray load losses, account for 10% of the total loss at full load, and should be considered in the study of efficiency in VSD drives.

#### IV. Experimental procedure and discussion

Ph-n voltage waveforms produced by a three-phase 7.5 kW matrix converter prototype and ph-ph voltage waveforms produced by a PWM inverter were recorded. These waveshapes were stored in a signal generator used to energise (via a power amplifier) 0.5 mm thick laminations of M470-50A grade non oriented steel samples of dimensions 306mmx30mm in a Single Strip Tester. Three values (50; 100; 200 Hz) of fundamental frequency and values of peak flux density in the range 1.0-1.5T were selected to magnetise the batches of material. The iron loss in laminations under sinusoidal, matrix ( $f_s = 2.5$  kHz) and PWM ( $m_i = 0.5; 0.8; 1 \parallel f_w = 3$  kHz) were measured by the means of a power analyser. Fig. 4a gives the ratio of reduction of specific iron losses in laminations of the M470-50A under matrix converter excitation when compared to PWM supply at  $m_i = 0.8$ . Fig. 4b shows the variation of core losses with peak flux density for different types of excitation (sine, PWM, matrix).

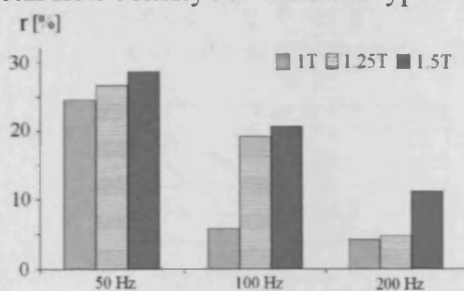


Fig. 4a. Reduction of core losses [%]

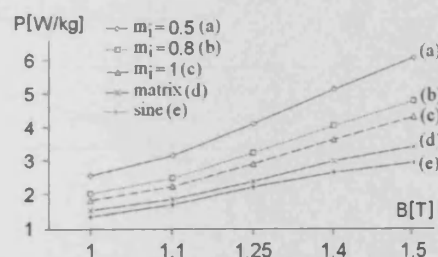


Fig. 4b. Variation of loss with peak flux density

The PWM supply results in higher core losses than matrix excitation. Above all, the lowest modulation index in PWM resulted in the highest form factor ( $FF$ ) and the highest frequency-weighted harmonic distortion ( $fwTHD$ ) in the primary voltage [8]. While high  $FF$  results in a higher amount of energy necessary to reach the magnetising value of peak field strength, high harmonic distortion in the supply voltage leads to remanent high order components in the flux density curve, accountable for minor loops and responsible for increased classical eddy-current loss. Under matrix converter excitation, sideband harmonics associated to each high order component in the harmonic spectrum feature a broader cluster than under PWM, which reduces the penetration in the ferromagnetic material and has a negative impact on losses. Fig. 5 shows sideband harmonics associated to a high order component. They correspond to the harmonic spectrum of the voltage produced by (a) PWM inverter ( $mi = 0.8$ ) and (b) matrix converter.

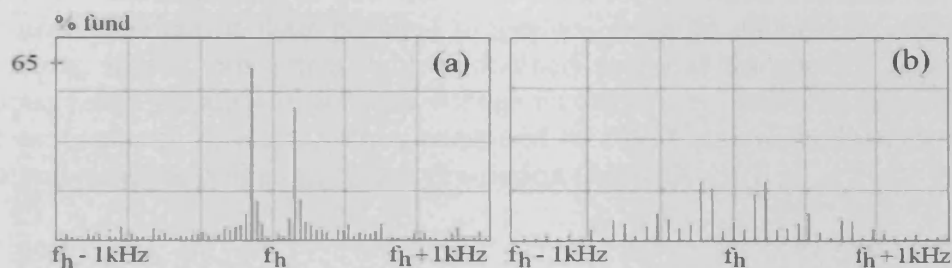


Fig. 5. Sideband harmonics in the primary voltage produced by (a) PWM  $mi = 0.8$  – (b) matrix

It is interesting to note that the flux density curve under matrix excitation was smoother than under PWM excitation, especially at low modulation indices. It is believed that a smoother profile will enable continuous domain wall motion inside the material and mitigate the negative effect of discontinuity events on the anomalous loss during magnetisation. Fig. 6 shows flux density curve under excitation typical of (a) PWM  $mi = 0.8$  and (b) matrix converter during half-cycle.

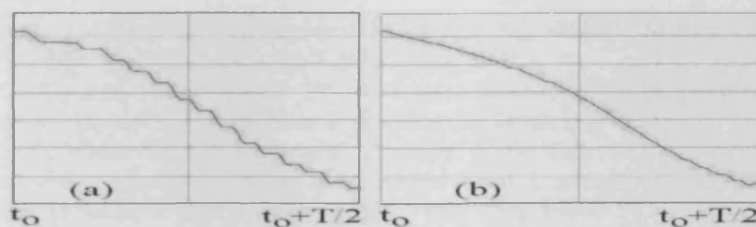


Fig. 6. Flux density curve under (a) PWM  $mi = 0.8$  – (b) matrix converter

The variation of losses at constant peak flux density with fundamental frequency was studied under matrix and PWM excitation ( $m_i = 0.8$ ). Due to the topology of direct ac-ac converters and the absence of decoupling between input and output, voltage waveforms produced by matrix converters inherit subharmonics multiple of 50 Hz. These components, intrinsic to the frequency conversion, distort the static B-H loop and affect the performance of the steel at fundamental frequencies other than 50 Hz. Therefore, the beneficial effect of sideband harmonics and lower form factor on the iron loss is mitigated.

## V. Conclusion

In the age of system optimisation, increasing the efficiency of commonly used adjustable speed drives is significant, since energy savings with financial implications might arise. Developments of new materials used for industrial applications, with a better understanding of their physical properties, must be coupled to expertise in engineering. Matrix converters, with undoubted potential for specific applications (aerospace, ship propulsion), generate voltage waveforms of beneficial characteristics, to the performance of steels. When compared to PWM at low modulation indices, matrix converters appear as an attractive solution for VSD.

## References

- [1] P.W. Wheeler, J. Rodriguez, J.C. Clare, L. Empringham, A. Weinstein, "Matrix Converters: a Technology Review", *IEEE Transactions on Industrial Electronics*, Vol 49, Issue 2, pp 276-288, April 2002.
- [2] D. Casadei, G. Serra, A. Tani, L. Zarri, "Matrix converter modulation strategies: a new general approach based on space-vector representation of the switch state", *IEEE Transactions on Industrial Electronics*, Vol 49, Issue 2, pp 276-288, April 2002.
- [3] C. Klumpner, F. Blaabjerg, "Experimental evaluation of ride-through capabilities for a matrix converter under short power interruptions", *IEEE Transactions on Industrial Electronics*, Vol 49, Issue 2, pp 276-288, April 2002.
- [4] J. Sagarduy, A.J. Moses, F.J. Anayi, J. Clare, P.W. Wheeler, "Computational Technique for Modelling of Frequency Converters and Analysis of Generated Waveforms", *6<sup>th</sup> International Conference on Computational Electromagnetics (CEM)* in Aachen (Germany), pp 171-172, April 2006.
- [5] P.W. Wheeler, J. Clare, L. Empringham, M. Apap, M. Bland, "Matrix Converters", *Power Engineering Journal*, Vol 16, Issue 6, pp 273-282, Dec 2002.
- [6] G. Bertotti, "General Properties of Power Losses in Soft Ferromagnetic Materials", *IEEE Transactions on Magnetics*, Vol 24, Issue 1, pp 621-630, January 1988.
- [7] J. Gyselinck, L. Vandeveld, J. Melkebeek, P. Dular, F. Henrotte and W. Legros, "Calculation of Eddy Current and Associated Losses in Electrical Steel Laminations", *IEEE Transactions on Magnetics*, Vol 35, Issue 3, Part 1, pages 1191 - 1194, May 1999.
- [8] J. Sagarduy, A.J. Moses, F.J. Anayi, J. Clare, P.W. Wheeler, "Matrix vs. PWM Frequency Converters. Iron Losses under Pulsating Forms of Voltage Excitation", accepted for publication in *IEEE Power Electronics Specialist Conference (PESC)*, Jeju (South Korea), June 2006.

- A.1.8. J. Sagarduy, A.J. Moses, F.J. Anayi, J. Clare, P. Wheeler, "Computational Technique for Modelling of Frequency Converters and Analysis of Generated Waveforms", *6<sup>th</sup> International Conference on Computational Electromagnetics*, Aachen (Germany), 4-6 April 2006.

# Computational Technique for Modelling of Frequency Converters and Analysis of Generated Waveforms

Mr. Juan Sagarduy Ochoa de Eribe<sup>1</sup>

Prof. Anthony J. Moses<sup>1</sup>

Dr. Fatih J. Anayi<sup>1</sup>

Prof. Jon Clare<sup>2</sup>

Dr Patrick W. Wheeler<sup>2</sup>

<sup>1</sup>Wolfson Centre for Magnetics. Cardiff School of Engineering. Queen's Buildings - The Parade. Cardiff CF24 3AA. United Kingdom. E-mail: [SagarduychoadeeribeJ@Cardiff.ac.uk](mailto:SagarduychoadeeribeJ@Cardiff.ac.uk)

<sup>2</sup>Power Electronics and Machines Control Group. School of Electrical and Electronic Engineering. The University of Nottingham. Nottingham NG7 2RD. United Kingdom. E-mail: [Jon.Clare@nottingham.ac.uk](mailto:Jon.Clare@nottingham.ac.uk)

## Abstract

Iron losses due to flux harmonics in stator cores of Pulse-Width-Modulation [PWM] inverter-fed induction motors have been highlighted recently as having a major effect on system efficiency. A new generation of direct ac-ac matrix converters offer important advantages over classical frequency converters such as absence of bulky and temperature sensitive dc-link, adjustment of power factor and nearly sinusoidal input/output current.

The method proposed here, using S-functions in a Matlab-Simulink environment, and Day Post Processor in Ansoft Simplorer, aims for a thorough analysis of output voltage waveforms of PWM inverters and 3x3 matrix converters under Space Vector Modulation [SVM]. After a brief introduction to frequency converters, the paper describes the new method and presents voltage waveforms along with analytical results of their harmonic characteristics. It is believed that as well as high processing speed and limited computational effort, this technique will provide the academic and research community with a better understanding of waveform characteristics of novel and classical ac-ac converters.

## 1 Introduction

Flux harmonics in stator laminations of inverter-fed induction motors increase iron losses by up to 30% [1]. In order to account for such losses in machines supplied by PWM or matrix converters, an efficient method of analysis of excitation waveforms is needed. This paper introduces a computational technique by which this can be efficiently carried out.

Matrix converters can be considered as  $n \times n$  direct ac-ac converters. For  $n=3$ , three input phases provided with a LC filter are connected to the load through nine bidirectional switches. These consist of two anti-parallel IGBTs in a common-collector back-to-back configuration and are controlled by logic signals from a Field Programmable Gate Array [FPGA], which implements the four-step semi-soft current-direction based commutation. Fatal short or open circuits between input phases are consequently avoided [2].

A DSP executes the control algorithm for the load and generates nine logic signals to be processed by the FPGA. Implementation of the four-step commutation results in signals for control of individual IGBTs. In SVM the input current and output voltage reference phase vectors rotate at a given angular frequency.

Depending on their position within six sectors at each sampling time, a pattern, in which duty cycles for bidirectional switches are calculated, is selected [3].

Classical frequency converters perform ac-ac conversion in two stages: rectification and inversion. A DC-link between rectifier and inverter is therefore necessary. Characteristic parameters in PWM are modulation index [mi] and frequency ratio [mf].

## 2 Computational Method

The modulation strategy applied to the converter was implemented as a C-language program to create an S-function, computer language description of a Simulink block [4]. Furthermore, a template was used as a basis to write the specific algorithm. The file \*.c was stored in the same directory along with the Simulink application \*.mdl and compiled as a MEX-file.

Classical blocks provided the S-function inserted in the Simulink model with input and desired output reference voltages from the matrix converter. The modulation algorithm was executed at a frequency, defined within the Simulink application or by means of a user-defined parameter, in order to generate nine duty cycles. Logic signals for six switches in a PWM

inverter were determined in a similar fashion by implementing PWM strategy. A matrix equation [2] calculates the output voltage pulsating waveforms. Available data is then saved to an excel file.

The DAY Post Processor package was used to enable an extensive, accurate and instantaneous analysis of any waveform to be performed [5]. A FFT algorithm was used to obtain form factor (FF) and Total Harmonic Distortion (THD) shown by equations (1) and (2).

$$FF = \frac{V_{rms}}{V_{rectmean}} \quad (1)$$

$$THD.[\%] = 100 \times \frac{\sqrt{\sum_{n=2}^{\infty} V_n^2}}{V_1} \quad (2)$$

Figure 1 shows the analysis of typical PWM and matrix converter waveforms.

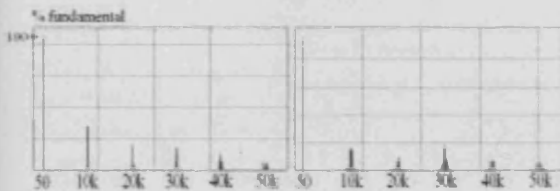


Fig 1 Harmonic spectrum of line-to-line voltages [PWM  $m_i = 1$  (left) - Matrix Converter (right)]

Complete characterisation of the waveforms gives information such as form, crest and ripple factors and RMS / rectified mean values. Integration, derivation and filtering are often required for suppression of high order harmonics in pulsating waveforms.

### 3 Results

Figures 2 and 3 show ideal waveforms at  $f = 50\text{Hz}$  generated by perfect  $3 \times 3$  matrix converter under SVM and the output voltage from a PWM inverter [ $m_i = 1$ ] is also shown. The switching frequency is  $10\text{kHz}$ .

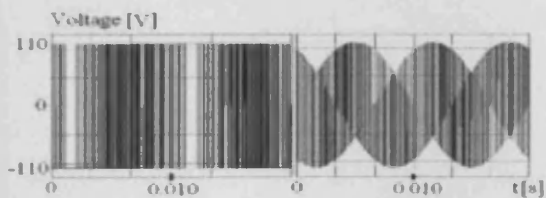


Fig 2 Phase-neutral voltage [PWM (l) - Matrix (r)]

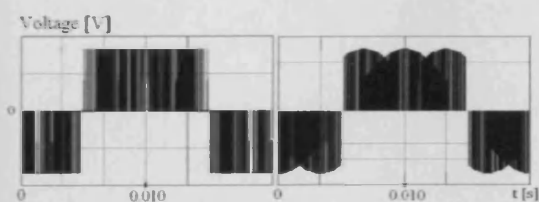


Fig 3 Phase-phase voltage [PWM (l) - Matrix (r)]

Analytical results corresponding to line-to-line voltages are given in Table 1. In the matrix converter, THD is lower, which is expected to result in lower magnetic losses in stator cores [1].

	SVM	PWM <sub>1</sub>	PVM <sub>0.75</sub>	PWM <sub>0.5</sub>
THD [%]	57.8	67.7	96.9	137.6
FF	1.292	1.347	1.555	1.905

Table 1 THD (%) and form factor (FF) of voltage waveforms by matrix / PWM inverter [ $m_i = 1$ ;  $m_i = 0.75$ ;  $m_i = 0.5$ ]

The THD is lower in the matrix converter waveform because of the enhanced side-band harmonic effects at high frequencies as shown in Figure 4.

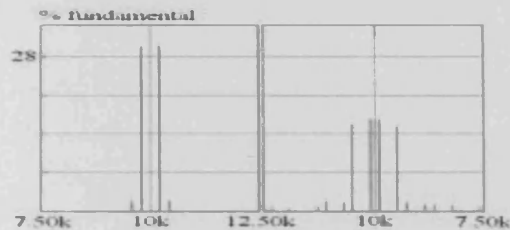


Fig 4 Harmonic spectrum

THD<sub>10kHz</sub> [PWM || Matrix] = 45.05% || 29.99%

### 4 Conclusion

The computational technique presented can analyse the performance of novel matrix converters and classical PWM inverters. Furthermore, it is suitable for recording waveforms sent to signal generators, key elements in the study of magnetic losses under new forms of voltage excitation.

### 5 References

- [1] Moses A.J: Loss Prediction in Electrical Steel Laminations and Motor Cores. Steel Research Int. 76, 2005.
- [2] Wheeler, P.W et al. IEEE Trans. on Ind. Electronics, vol 49, (2), April 2002.
- [3] Casadei D. et al. IEEE Trans. on Ind. Electronics, vol 49, (2), April 2002.
- [4] Simulink. Simulation and Model-Based Design. Chapter 3: Writing S-functions in C. The Mathworks.
- [5] Ansoft Corporation - Simplorer™ version 7.0. DAY Post Processor.

- A.1.9. A.J. Moses, F. Anayi, J. Sagarduy, S. Zurek, “Additional Losses in Inverter-Driven Electrical Machines”, *2<sup>nd</sup> International Workshop on Magnetism and Metallurgy*, Freiberg (Germany), 21-23 June 2006.

# Additional Losses in Inverter Driven Electrical Machines

A. J. Moses, F. Anayi, J. Sagarduy and S. Zurek  
Wolfson Centre for Magnetics  
School of Engineering  
Cardiff University  
Newport Road,  
Cardiff, CF24 3AA  
Wales, United Kingdom

## Summary

There is a growing use of inverter fed induction motors in industrial drives and greater consciousness of their energy efficiency. Pulse width modulation (PWM) supplies are very common and there is increasing interest in matrix converters. The harmful effect of low modulation index in PWM systems is well documented but the effect of switching frequency is not so well known. This paper summarises some present knowledge of the effect of such parameters on losses in non-oriented steels of various compositions and thicknesses and shows the effect of harmonics on the hysteresis, eddy current and excess components of power loss. Some approaches to modelling or predicting the additional losses are demonstrated. The apparent benefits of matrix converters over PWM approaches due to the different voltage harmonic spectrum are quantified.

## 1. Introduction

Interest in energy efficiency is higher today than it has been for several years. The largest use of electrical energy is for driving industrial motors of which there are over ten million operating in the UK alone. A fully loaded motor will typically consume electrical energy within its first 30 days of operation costing as much as its purchase price. An 11 kW motor costing £500 for example can consume over £50 000 worth of electricity over a ten year operating life [1]. The iron loss of a high efficiency motor with  $\eta \sim 85\%$  at full load would consume around £1500 of electricity in such a motor. In a typical variable drive system, a motor may operate at reduced speed for much of its life where the efficiency will normally be much lower so the fiscal value of the losses will be much higher.

Motor efficiency referred to above is based on sinusoidal voltage operation but when the machine is energised by an electronically produced voltage of variable magnitude and frequency the iron loss may increase by 20 % or more [2]. If the motor speed is reduced by varying the voltage wave shape, increased flux harmonics in the stator laminations of such inverter fed induction motors increase iron loss up to 30 % [3]. Due to their low cost and high reliability, Pulse-Width-Modulated (PWM) supplies have been commonly used in drive systems for thirty years, even though the high harmonic distortion of the voltage waveforms produced adversely affects efficiency.

After nearly fifteen years of research, matrix converters have become a reality in power electronics. While classical PWM inverters perform AC-AC conversion in two stages (rectification-inversion) and a bulky DC-link is required, matrix converters are based on direct frequency conversion. Main advantages of this novel topology are adjustment of power factor, reduced volume, convenient integration into the drive electronics and nearly sinusoidal input/output current. A better harmonic spectrum, along with improved form factor and lower total harmonic distortion of characteristic voltage waveforms, may lead to a significant reduction of iron loss in the electrical steel laminations which form induction motor cores.

This paper focuses on additional losses in electrical steels due to flux harmonics typical of those occurring in induction motors stator cores. There are many approaches to modelling loss mechanisms or predicting loss even under sinusoidal magnetisation. Although it is not highlighted in this paper, it should be noted that in practice predictions of loss increase under PWM excitation will be compounded by effects of stress, temperature, geometrical and building factors as well as rotational flux [4].

## 2. Loss measurements under Distorted Flux conditions

For unidirectional magnetisation of a strip of electrical steel, the instantaneous energy loss,  $P$ , under distorted flux can be written as

$$P = \sum_n 0.5 \cdot \omega_n \cdot B_n \cdot H_n \cdot \sin(\phi_{bh}) \quad (1)$$

Where  $n$  is the harmonic number,  $\omega = 2\pi f$ , is the fundamental frequency,  $B_n$  and  $H_n$  are the peak values of the  $n$ -th harmonic components of flux density and field and  $\phi_{bh}$  is the phase angle between them. When material is to be magnetised under flux density waveforms characteristic of PWM voltages, it is necessary to have an accurate and reliable means of controlling the  $b$  waveform. The waveform can be expressed as

$$b = \sum_{n=1}^n n \cdot B_n \cdot \sin(n \cdot \omega \cdot t + \varphi_n) \quad (2)$$

Where  $\varphi_n$  is the phase angle of the  $n$ -th harmonic. All the terms in equations (1) and (2) are experimentally accessible; instantaneous values of  $b$  and  $h$  are normally deduced from EMFs induced in search coils wound around a sample to detect  $db/dt$  and surface mounted  $h$  sensors to detect  $h$  or  $dh/dt$ . In practical PWM waveforms, values of  $n$  up to more than 500 need to be considered for accurate measurement or loss prediction.

In order to ensure the reproducibility the measurements of magnetic properties under such conditions, measurements need to be carried out under controlled magnetising conditions. Currently, only measurements under sinusoidal flux density are standardised. However, the increasing range of magnetising conditions in magnetic cores of real devices raises the need for standardised measurements under non-sinusoidal conditions.

The arbitrary waveforms are difficult to control by analogue electronic circuits widely used in the past, but the computerised systems equipped with digital feedback

algorithms can easily provide arbitrary magnetisation with frequencies ranging from 0.01 Hz to 40 kHz and flux density up to 2.0 T [5]. Figure 1 shows typical characteristics of a non-oriented electrical steel magnetised under controlled PWM excitation.

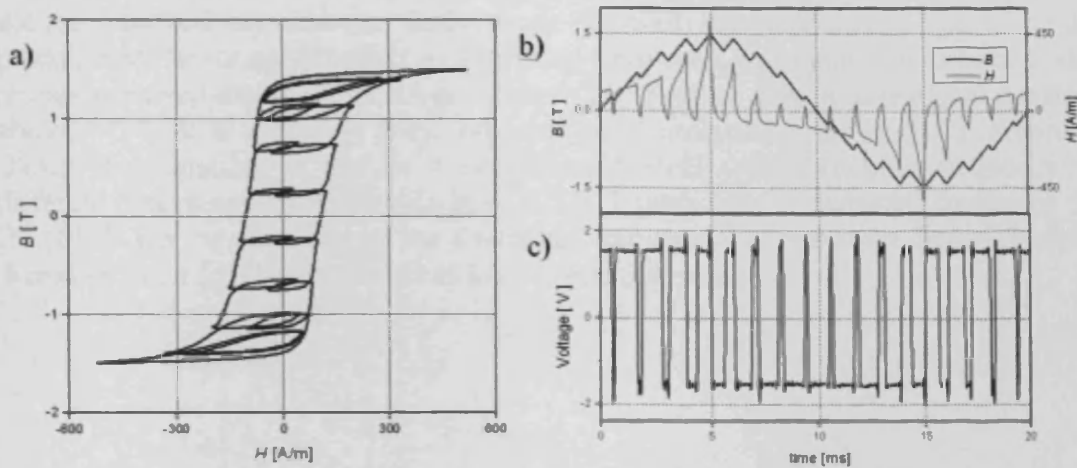


Figure 1. Non-oriented low silicon electrical steel, 0.5 mm thick, magnetised in an Epstein frame under controlled PWM excitation at 50 Hz, 1.5 T: (a)  $B$ - $H$  loop, (b) corresponding  $B$  and  $H$  waveforms, and (c) voltage waveform proportional to  $dB/dt$ .

There is a growing need for a unified method of measurements of magnetic properties under such arbitrary magnetising conditions. The accuracy of the measurements in the Epstein frame or Single Sheet Tester cannot be guaranteed for arbitrary magnetisation. Since the control of magnetising waveforms is no longer an issue, full attention should be focused on developing a robust and versatile magnetising system, which would be universally recognised for use in the characterisation of soft magnetic materials under arbitrary magnetising conditions.

Figure 2 shows a typical set of characteristics indicating the harmful effect of decreasing modulation index on loss in non-oriented steel [6]. Although the designer of PWM inverters may choose a high modulation index for normal operation, in many speed control applications it may be low over a wide range of the duty cycle [3].

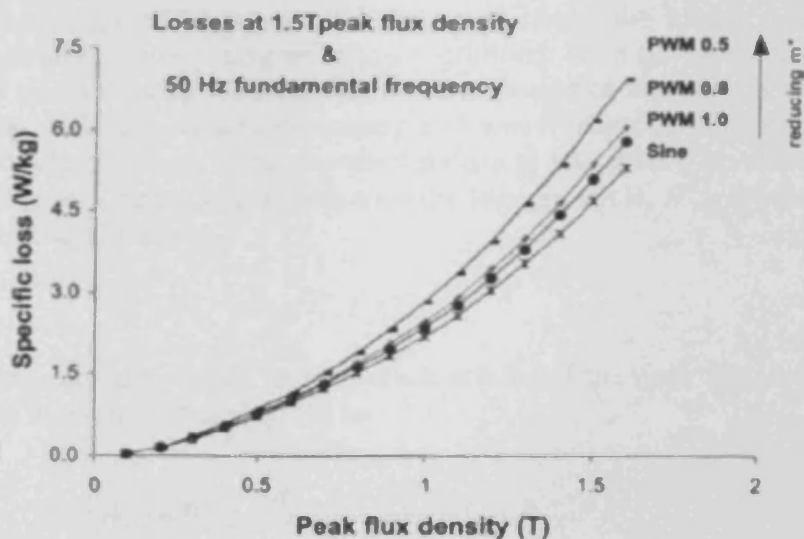


Figure 2. Variation of specific loss with modulation index ( $m^*$ ) in typical non-oriented steel [6]

The effect of switching frequency of the carrier voltage in PWM supplies is not so conclusively known. Early work showed the modulation index is the predominant factor so the effect of switching frequency was mainly neglected. Some research showed that over the range 1 kHz to 20 kHz loss may be considered constant above 45 kHz in electrical steel and iron based amorphous material [7]. Figure 3 shows the variation of loss in a non-oriented steel with switching frequency at different percentage modulation indices at 1.3 T peak and fundamental frequency 50 Hz [8]. It can be seen that as the switching frequency increases the harmful effect decreases but it is relatively worst at low modulation index.

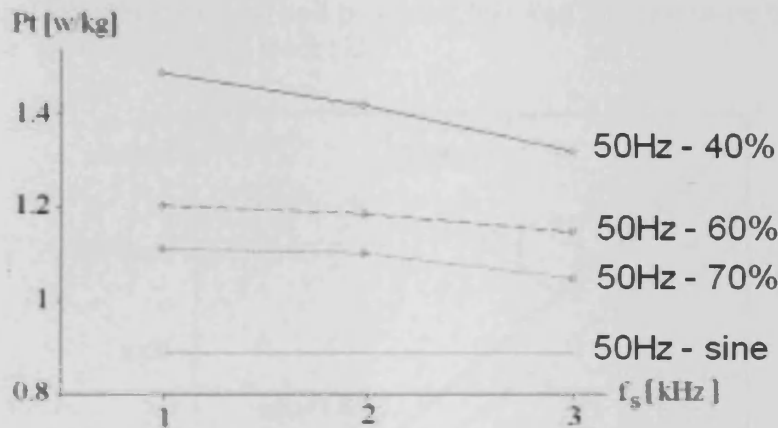


Figure 3. Variation of iron loss ( $P_t$ ) with switching frequency ( $f_s$ ) in grain-oriented electrical steel at 1.3 T, 50 Hz fundamental frequency [8].

### 3. Loss Prediction under Distorted Flux waveforms

Despite attempts over several decades there is still no recognised physical model for predicting the dynamic  $B$ - $H$  loop and hence the loss of electrical steel laminations under arbitrary magnetisation conditions. By a physical model we mean one capable of accounting for magnetic domain structures not only in explaining the loss variation with flux density, frequency and wave shape but also in predicting it. The most popular approach is the so-called statistical loss theory developed to explain the fact that under sinusoidal magnetisation the loss per cycle,  $W_{tot}$ , for the majority of materials is close to the law

$$W_{tot} = C_0 + C_1 \cdot f + C_2 \cdot f^{0.5} \quad (3)$$

Where constants  $C_0$ ,  $C_1$  and  $C_2$  are functions of the peak flux density. This is often written in the form based on [9] as

$$W_{tot} = W_{hyst} + \frac{d^2 \cdot \pi^2 \cdot B_m^2}{6 \cdot \rho} + C_3 \cdot B_m^{1.5} \cdot f^{0.5} \quad (4)$$

Where  $d$  is the thickness of the lamination,  $\rho$  is the material resistivity and  $C_3$  is a fitting parameter. Equation (4) applies to non-oriented and grain-oriented materials although they have quite different domain structures. The second term is the well known low frequency limit of the eddy current loss calculated from Maxwell's equation for a homogeneous material with no domain structure and a linear dependence of  $B$  on  $H$ .

This approach is capable of use for studying magnetisation processes in general under non-sinusoidal  $B$  conditions and it is convenient for being incorporated into circuit simulators. The model error is very low, lying within that of the measurements used to set it up for a given material or to validate it. It can be used to examine and study the three components of loss and demonstrates a frequency dependence of hysteresis and skin effect phenomena at high induction where the usual skin effect is almost absent [10]. Figure 4 shows the calculated variation of loss components with frequency of a non-oriented, 0.30 mm thick, 1.8 % silicon steel [11]. The agreement between measured and predicted loss can be seen to be close and it is found likewise in other grades of steel [11].

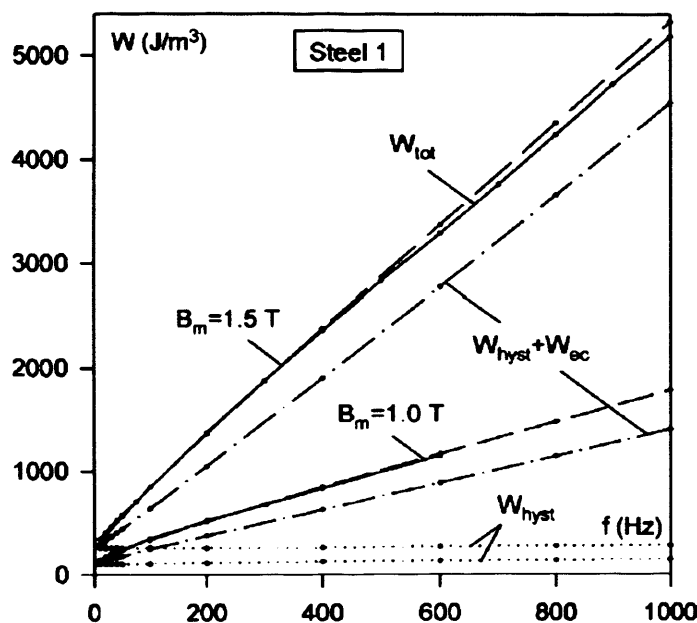


Figure 4. Measured (solid lines) and calculated (dotted lines) total and loss components variation with frequency in typical low silicon non-oriented steel [11]

The performance of any steel under PWM conditions compared to its sinusoidal flux characteristics depends on the relative proportions of the loss components in figure 4. In this case at 400 Hz for example, the hysteresis loss is around 30 % of the total so the more frequency dependent components dominate and the material will be quite susceptible to additional PWM losses.

Two other approaches, which require a data bank of either sinusoidal loss data or loss values under known distorted  $B$  conditions, are required to predict loss under arbitrary magnetisation conditions. Neural network based software has been developed for loss prediction of strip wound cores at medium frequency and predicts to within 7 % of measured values over the induction range 0.1 T to 1.8 T at up to 100 kHz in grain-oriented steels [12]. The method depends on the development of a well distributed extensive data base to account for variation of silicon content, thickness and geometrical factors. This has been extended to predict loss and permeability in

non-oriented steels under PWM conditions [13]. Here parameters were predicted in 0.5 mm thick non-oriented steel with silicon contents from 0.2 % to 4 % at a fixed fundamental component of flux density (50 Hz) and frequency ratio (12) and modulation index in the range 0.5 to 1.0. The predictions at arbitrary magnetisation conditions were generally within 5.5 % of measured values. Table 1 shows results for two non-oriented steels at peak flux density of 1.6 T with a range of different flux density and form factors.

Input data for recall				Predicted (W/kg)	Measured (W/kg)	Error (%)
$\hat{B}$ (T)	$D$ (kg/m <sup>3</sup> )	Si (%)	form factor			
1.6	7850	0.3	1.00	6.46	6.24	3.6
1.6	7850	0.3	1.11	6.98	6.65	5.0
1.6	7850	0.3	1.19	7.39	7.42	0.4
1.6	7850	0.3	1.31	8.02	8.06	0.5
1.6	7850	0.3	1.63	9.71	10.11	3.9
1.6	7650	3.0	1.00	2.78	2.70	2.9
1.6	7650	3.0	1.11	2.98	2.74	8.8
1.6	7650	3.0	1.19	3.14	3.17	0.8
1.6	7650	3.0	1.31	3.38	3.37	0.2
1.6	7650	3.0	1.63	4.05	4.16	2.7

Table 1. Input and recall values at different form factors of 0.3 % and 3 % Si non-oriented steels [13]

This technique has been successfully applied to wound toroidal cores of different sizes. Apart from the geometrical factors, the internal stresses induced during the manufacturing, interlaminar flux, distorted magnetisation, etc. can increase the power loss and/or reduce the permeability. These dependencies can be very complex and prove to be difficult to calculate with analytical methods. Theoretically, the ANN is capable of modelling any non-linear dependencies with any given accuracy. However, in practice this is limited by the accuracy of measured data, availability of the samples covering the whole dimension range of interest. The increased amount of training data requires greater number of processing nodes in the ANN, which in turn can significantly slow down the training procedure. Also, once the ANN is trained new data cannot be added easily – the whole training procedure has to be repeated, which can be time consuming. However, in industrial practice the ANN can be a very useful and accurate tool for prediction of magnetic properties under arbitrary magnetising conditions [14]. Figure 5 illustrates the accuracy of such an approach.

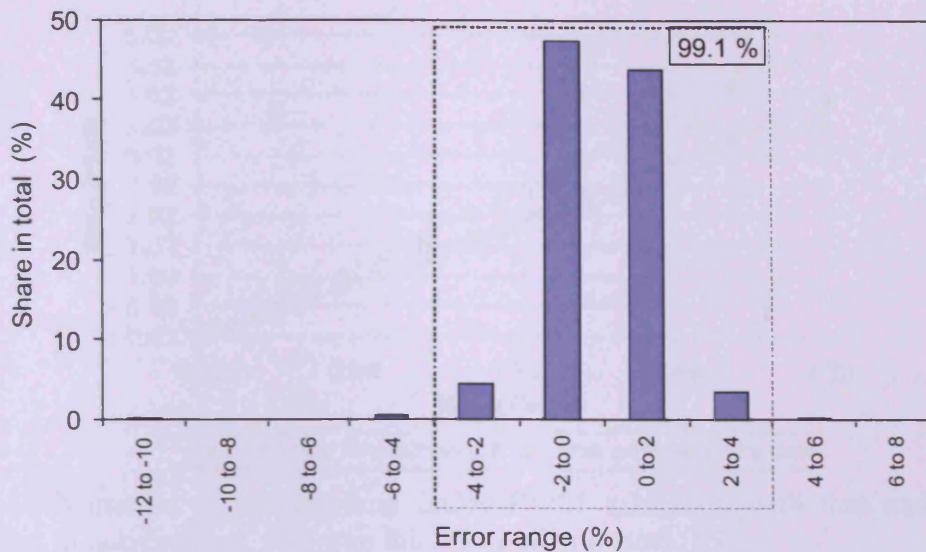


Figure 5. Error distribution of power loss under PWM magnetisation predicted by the ANN for a range of toroidal cores wound from conventional grain-oriented electrical steel (flux density 0.5-1.8 T, frequency 20-2000 Hz, outer diameter 60-144 mm, strip width up to 30 mm). [14]

The other approach makes use of a linear relationship found between the loss under PWM and loss under sinusoidal flux density for any given PWM wave shape [15]. This gives agreement to within 5 % between measured and predicted loss values over a wide range of material compositions. In some cases it appears to be potentially more accurate than the neural network approach. Figure 6 shows the measured variation of loss with silicon content of a wide range of non-oriented steels under PWM and sine wave excitation. It can be seen that the relative harmful effect of the PWM harmonics reduces with increasing silicon content due to the increased resistivity. In all these materials linear relationships were found of the type shown in Fig. 7 between loss under PWM and sine excitation.

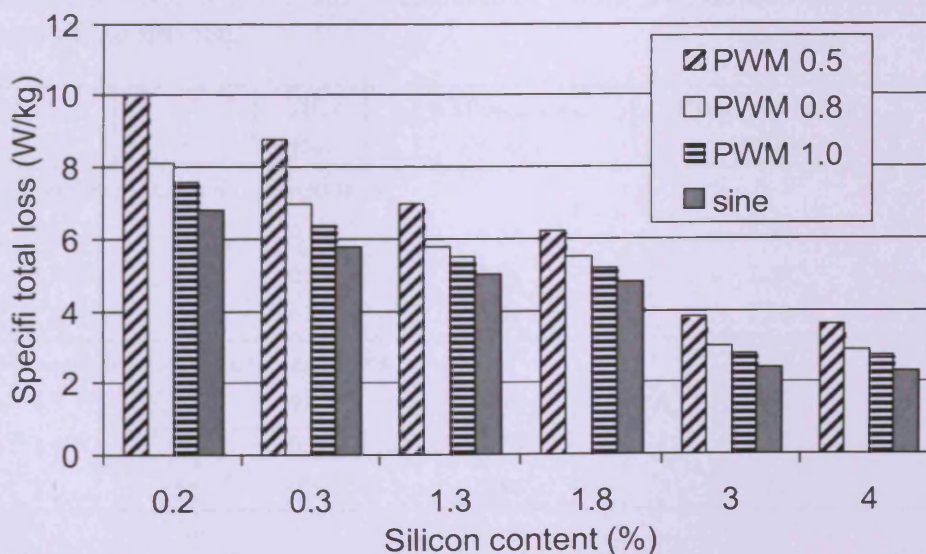


Figure 6. Variation of loss under PWM and sinusoidal flux excitation in non-oriented materials with different silicon contents at 1.5 T peak, 50 Hz fundamental [15]

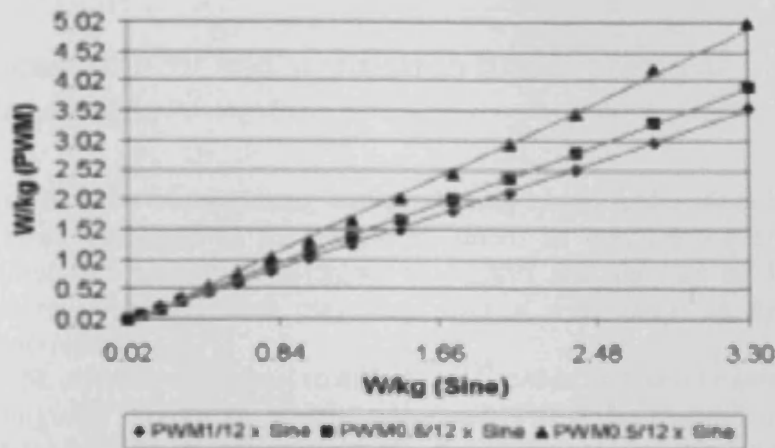


Figure 7. Variation of specific loss under PWM excitation with that under sine excitation in non-oriented, 0.65 mm thick 3 % silicon steel [15]

The slopes of the curves depend on the harmonics present in the PWM waveform and can be used to build up equations of the form below

$$P_{PWM} = C_A \cdot P_{sine} + C_B \quad (5)$$

Where

$$C_A = C_C f + C_D \quad (6)$$

And

$$C_B = C_E \cdot f^2 + C_F \cdot f + C_G \quad (7)$$

The coefficients  $C_C$  and  $C_D$  in equation (6) and  $C_E$ ,  $C_F$ , and  $C_G$  in equation (7) can be represented in terms of a second order polynomial variation with harmonic distortion from which  $P_{PWM}$  can be calculated. Table 2 illustrated the high predictive accuracy of the method.

$B$ (T)	$f$ (Hz)	THD (%)	PWM measured (W/kg)	PWM calculated (W/kg)	Error (%)
Non-oriented 0.2 % Si, 0.5 mm thick					
1.5	50	0.67	8.58	8.62	0.5
1.5	50	0.59	7.96	7.59	0.2
1.0	50	0.67	3.91	3.90	0.2
Non-oriented 1.8 % Si, 0.5 mm thick					
1.5	50	0.67	5.48	5.65	3.0
1.5	50	0.59	5.26	5.32	1.2
1.0	50	0.67	2.54	2.62	2.9

Table 2. Measured and predicted values of loss where magnetising conditions were not included in development of the equations [15].

#### 4. Loss measurement and simulation under practical inverter voltage conditions

The difficulties of measuring and predicting losses under ideal PWM voltage waveforms were discussed in the earlier sections. In practice the inverter output voltages are not as symmetrical as shown in figure 1 and also the modulation index and fundamental frequency both may vary over a wide range as the speed of a machine is controlled.

Classical PWM inverters and novel matrix AC-AC converters can be modelled by using a "C-language" algorithm, which implements PWM (traditional converters) and space-vector modulation (matrix converters). A signal generator that provides strips of non-oriented electrical steel with voltage excitation stores the waveforms obtained. Moreover, voltage wave shape from commercial inverters can also be stored with the purpose of measuring iron losses, allowing therefore closed experimental conditions to reality. Figure 8 shows real output voltage waveforms produced by a three-phase matrix converter and a back-to-back PWM converter.

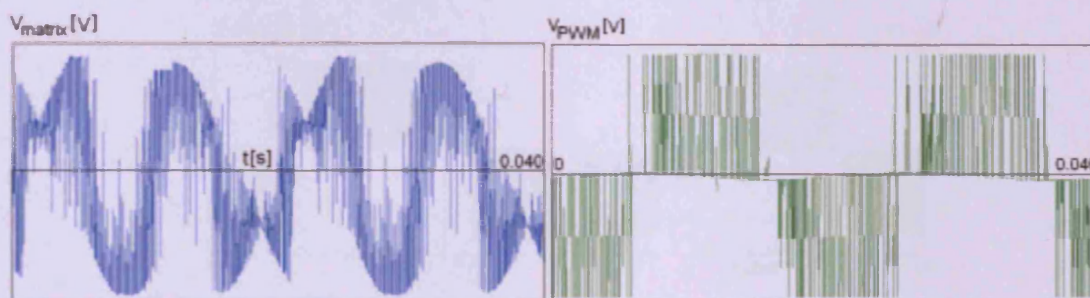


Fig 8. Output voltage in a three-phase matrix converter (line-neutral) and back-to-back PWM converter (line-line)

Since a real matrix converter is not yet commercially available, a computational method can be used to obtain typical voltage excitation waveforms of matrix/back-to-back PWM converters and perform their harmonic analysis. Fig 9 shows the principle of the computational technique mentioned.

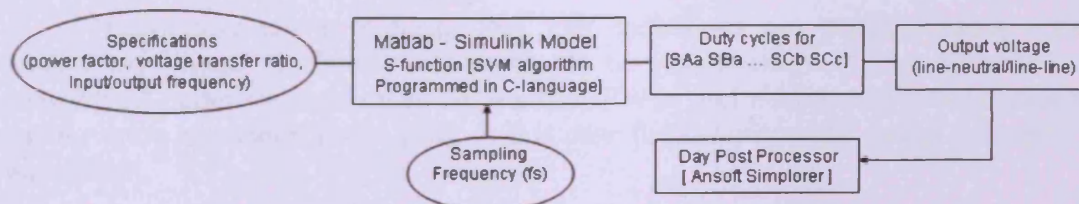


Figure 9. Computational technique for modelling matrix converters

Matrix converters are potential candidates for AC-AC converters because of their near sinusoidal output voltage [16]. Laboratory simulations and experiments show that the matrix converter supplies produce different clusters of higher harmonics than some PWM sources and hence have a beneficial effect on losses. Figure 9 shows simulated PWM and matrix converter voltages and harmonic components and the resulting lower total harmonic distortion in the case of the matrix converter [17].

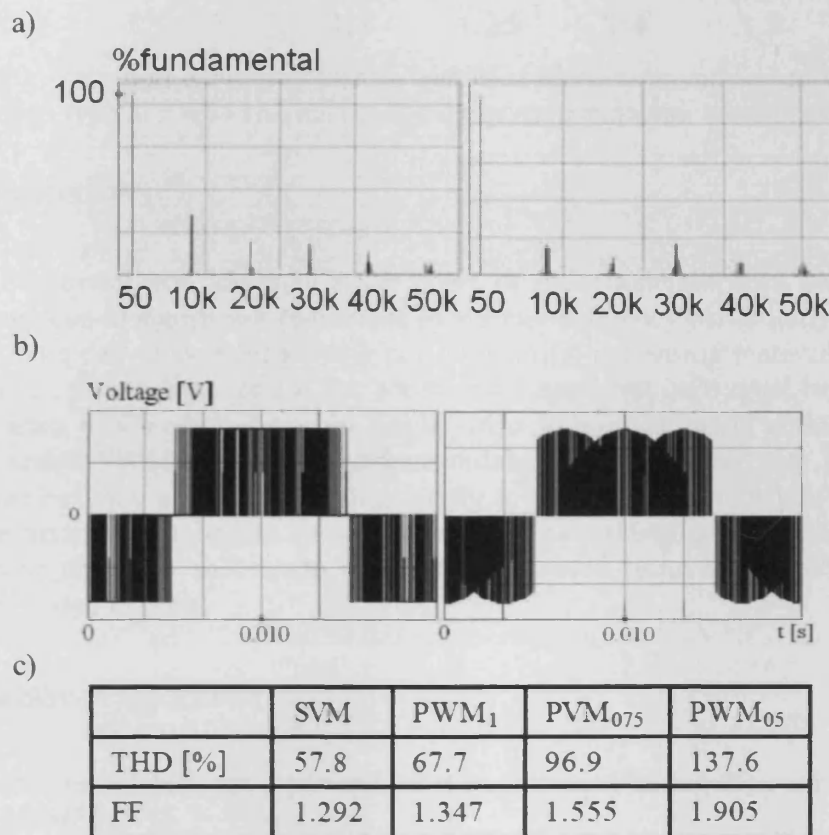


Figure 9. Results of PWM and matrix converter simulations (a) harmonic spectrum (left – PWM  $m_i = 1.0$ , right – matrix), (b) corresponding phase to phase voltage waveforms, (c) THD and form factors for matrix converter (SVM) and PWM waveforms with  $m_i = 1.0, 0.75, 0.5$ .

Laboratory results indicate that loss reductions are possible using matrix converters. Figure 10 shows measurements on single strips of non-oriented steel magnetised under voltages saved from actual PWM and matrix converters compared to sine wave excitation losses [18]. In this case the benefit of the matrix converter is significant.

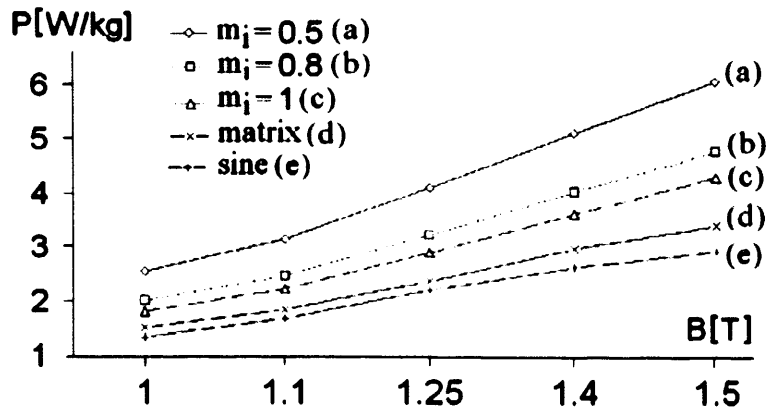


Figure 10. Variation of power losses with flux density in non-oriented steel strips subjected to typical PWM and matrix converter magnetisation conditions [18]

## 5. Conclusions

Additional iron losses in stator cores of induction machines used in inverter drives can lead to significant reductions in system efficiency particularly at low PWM modulation index or switching frequency. Generally, increasing material resistivity or reducing thickness does reduce the additional losses, but care must be exercised in extrapolation of the conclusions for single strips to laminations in actual stator cores. Losses under PWM or other non-sinusoidal flux conditions can be accurately calculated but they are still difficult to apply in practice particularly to the electrical machine environment. Matrix converters are being promoted as alternatives for PWM in some applications and it appears that they would bring the benefit of reduced magnetic losses in cores.

## 6. Acknowledgement

Some of the recent findings reported here were obtained during the course of EPSRC grant EP/C518616/1.

## 7. References

- [1] Designing for energy efficiency. Drives Supplement-Energy Special January 2006 13-14
- [2] Boglietti A., Ferraris P., Lazzari M. and Profumo F. – Effects of different modulation index on the iron losses of soft magnetic materials supplied by PWM inverter, IEEE Trans. Mag. (1993) 29 (6), pp. 3224-7
- [3] Moses A. J. and Anayi F. – Effect of PWM voltage excitations on iron loss of inverter fed motors, Proc. of the IASTED International Conference Power and Energy Systems (2003) Palm Springs USA, pp. 351-354
- [4] Moses A J. – Characterisation of the loss behaviour in electrical steels and other soft magnetic materials, Proc. of Workshop on Metallurgy and Magnetism, TUB Freiberg, June (2004)

- [5] Zurek S., Marketos P., Meydan T and Moses A J. – Use of novel adaptive digital feedback for magnetic measurements under controlled magnetising conditions. *IEEE Trans. Mag.* (2005) 41 (11), pp. 4242-9
- [6] Moses A. J. – Measurement and Prediction of iron loss in electrical steel under controlled magnetisation conditions, *Przeglad Elektrotechniczny* (2004) R80, 12, pp. 1181-7
- [7] Boglietti A., Ferraris P., Lazzari M and Pastorelli M – Change of the iron losses with switching supply frequency in soft magnetic materials supplied by PWM inverter, *IEEE Trans. Mag* (1995) 31 (6), pp. 4250-4252
- [8] Yao X. G., Sagarduy J., Moses A. J. and Anayi F. J. – Impact of the switching frequency on the eddy current losses in a three-phase transformer core subjected to PWM excitation (submitted to IECON 2006)
- [9] Bertotti G. – General properties of power losses in soft ferromagnetic materials, *IEEE Trans. Mag.* (1988) 24(1), pp. 621-630
- [10] Zirka S. E., Moroz Y., Marketos P. and Moses A. J. – Viscosity-based magnetodynamic model of soft magnetic materials for prediction of behaviour under non-standard conditions, *British Electromagnetic Measurements Conference Proceedings (BEMC)* (2005), Teddington, UK, pp. 115-121
- [11] Zirka S. E., Moroz Y. I., Marketos P. and Moses A. J. – Viscosity-based magnetodynamic model of soft magnetic materials, (submitted to *IEEE Trans. Mag.* 2006)
- [12] Miti G. K. and Moses A. J. – Neural network-based software tool for predicting magnetic performance of strip-wound magnetic cores at medium to high frequency. *IEE Proc-Sci Meas. Technol.* (2004) 151 (3), pp. 181-7
- [13] Moses A. J. and Leicht J – Iron loss prediction under sinusoidal and non-sinusoidal excitation using a neural network approach, *Stahleisen* (2004), pp. 329-334
- [14] Zurek S, Moses A. J., Packianather M – Implementing an Artificial Neural Network Using National Instruments LabVIEW, *Customer Solutions*, [www.ni.com, http://sine.ni.com/csol/cds/item/vw/p/id/681/nid/124200](http://sine.ni.com/csol/cds/item/vw/p/id/681/nid/124200), Feb 2006
- [15] Moses A. J. and Leicht J. – Iron loss prediction under pulse width modulation conditions, *Journal of Applied Physics* (2005) 97 10R507, pp. 1-3
- [16] Wheeler P. W., Rodriguez J, Clare J. C., Empringham L and Werstein A. – Matrix converters: a technology review, *IEEE Trans. Ind. Electron* 49 (2), pp. 276-288
- [17] Sagarduy J., Moses A. J., Anayi F. J., Clare J. and Wheeler P. W. – Computational technique for modelling of frequency converters and analysis of generated waveforms. *Proc 6th int. Conf. on Electromagnetics; (2006) CEM 2006*, pp. 171-172
- [18] Sagarduy J., Moses A. J., Anayi F. J., Clare J. and Wheeler P. W., *Matrix vs. Pulse-Width-Modulation Frequency Converters. Iron losses under Pulsating Forms of Voltage Excitation 37<sup>th</sup> IEEE Power Electronics Specialist Conference*, June 2006, Jeju (South Korea).

- A.1.10. X. G. Yao, A. J. Moses, J. Sagarduy, F. J. Anayi, "Influence of Switching Frequency on Eddy-Current Losses in a Three-Phase, Three-Limb Transformer Core Subjected to PWM Voltage Excitation", *Power Engineering Conference (POWERENG)*, Setubal (Portugal), pp 324-329, 12-14 April 2007.

# Influence of Switching Frequency on Eddy-Current Losses in a Three-Phase, Three-Limb Transformer Core Subjected to PWM Voltage Excitation

Xiao Guang Yao, Anthony J. Moses, Juan Sagarduy, Fatih J. Anayi

Wolfson Centre for Magnetics  
School of Engineering-Cardiff University  
Queen's Building-The Parade  
Cardiff-CF24 3AA  
Wales, United Kingdom  
E-Mail: [YaoXG@Cardiff.ac.uk](mailto:YaoXG@Cardiff.ac.uk)

**Abstract** - Transformers are key elements in power generation, transmission and distribution systems. Transformers under PWM supply are essential elements in industrial applications such as the power line conditioning, electrified railway power systems, and DC-DC power converters. Assessing the performance of transformers under PWM supplies is relevant to these applications. In this paper, the variation of iron losses with switching frequency in the range of 1 kHz – 3 kHz in a three-phase, three-limb transformer core under no-load conditions was measured. Classical eddy-current losses were calculated for various values of modulation index and magnetization conditions (frequency 50 Hz, 100 Hz; induction 1.3 T, 1.5 T). Results showed a reduction of the eddy-current component of loss by up to 40% at high frequency of magnetization and low modulation index with high switching frequency.

## I. INTRODUCTION

Extensive research on iron losses in ferromagnetic sheets, as used in motors, has been carried out under non-sinusoidal voltage excitation (in particular Pulse-Width-Modulated [PWM] inverter supply) [1]-[6]. Pulsating forms of voltage excitation produced by PWM inverters result in an increase in losses in soft magnetic materials compared to sinusoidal supply

Research has been carried out on iron losses in transformer cores of various materials (grain-oriented Si-Fe materials, amorphous materials) and different configurations [8]-[11]. However, only sinusoidal voltage supply has been considered in these studies. Limited research work had been reported on non-sinusoidal excitation [12]-[14].

Recently, industrial applications, such as active power line conditioners, AC-AC and DC-DC power converters and electrified railway power systems, are based upon classical capacitors to store electrostatic energy by means of a DC-link. An inverter in active mode is used to inject power to the grid network [15] [16]. The transformer between the inverter and the line is therefore subjected to PWM voltage excitation, due to the PWM control of the converter [17] [18]. Tight regulations on energy management in the context of distributed generation

and integration with renewable energy sources will strengthen the position in the market of active power line conditioners, of which transformers under PWM supply are essential elements [19]. Therefore, transformers subjected to PWM voltage excitation are becoming more common.

This paper covers an investigation of the variation of the iron loss, and its classical eddy-current component, in a transformer core of grain-oriented steel under PWM excitation with switching frequency  $f_s$  for assigned values of modulation index  $m$ , at no-load. The analysis highlights the form factor  $K_f$  of the induced voltage as a key parameter in controlling the performance of eddy-current losses in the transformer core.

## II. THEORETICAL BASIS

In the loss separation model, the total iron loss can be divided into three parts, namely, static hysteresis loss, eddy-current loss and anomalous loss and written as

$$P_i = K_h B_p^x f + K_e B_p^2 f^2 + K_a B_p^{1.5} f^{1.5} \quad (1)$$

where  $f$  is the magnetizing frequency,  $B_p$  is the peak value of flux density,  $x$  is the Steinmetz coefficient and  $K_h$ ,  $K_e$ ,  $K_a$  are coefficients defining static hysteresis, eddy-current and anomalous loss, respectively.

The flux density  $b(t)$  in a core is determined from

$$b(t) = \frac{1}{NA} \int e(t) dt \quad (2)$$

where  $e(t)$  is the induced voltage,  $N$  is the number of turns of the secondary windings and  $A$  is the cross sectional area of the transformer core. It is important to highlight that  $b(t)$  contains odd harmonics of amplitude  $B_n$  and

frequency  $f_n$ . In transformer core with laminations of thickness  $l$  [m], resistivity  $\rho$  [ $\Omega m$ ] and density  $\gamma$  [ $kg/m^3$ ], the classical eddy-current component loss  $P_e$  [W/kg] is given by [20]

$$P_e = \frac{4\delta^2 K_f^2}{3\gamma\rho} \sum B_n^2 f_n^2 \quad (3)$$

where  $K_f$  is the form factor of the induced voltage in the secondary windings of the transformer core.

### III. DEFINITIONS

Key parameters in PWM voltage waveform are modulation index  $m_i$  and frequency ratio  $m_f$  which are defined as

$$m_i = \frac{A_{ref}}{A_c} \quad m_f = \frac{f_c}{f} \quad (4)$$

where amplitude  $A_{ref}$  and amplitude  $A_c$  are sinusoidal reference and carrier signal respectively. Magnetizing and switching frequencies are  $f$  and  $f_s$  (frequency of the carrier voltage waveform  $f_c$ ) respectively. The form factor  $K_f$  of a periodic waveform  $v(t)$  of one period  $T$  is given by

$$K_f = \frac{v_{rms}}{v_{rectmean}} = \frac{\sqrt{(1/T) \int_0^T v^2(t) dt}}{(1/T) \int_0^T |v(t)| dt} \quad (5)$$

where  $v_{rms}$  and  $v_{rectmean}$  are root-mean-square and rectified mean values respectively.

The harmonic content of a periodic waveform  $v(t)$  is described by the Total Harmonic Distortion  $THD$  [%] given by

$$THD[\%] = \frac{\sqrt{\sum_{n=2}^{\infty} v_n^2}}{v_1} \times 100 \quad (6)$$

where  $v_n$  and  $v_1$  are the amplitude of the fundamental and harmonic component of order  $n$  respectively.

### IV. EXPERIMENTAL SETUP

#### Iron loss characterization using Epstein Frame standard test

The material used to assemble the transformer core was 0.27 mm thick, 3% silicon, grain-oriented electrical steel (UNISIL

M089-27N). The resistivity and density were  $46 \mu\Omega cm$  and  $7650 kg/m^3$ , respectively.

Epstein strips from a batch of material cut parallel to the rolling direction and annealed were magnetized by sinusoidal and PWM waveforms under normalized Epstein test conditions [21]. A synthesized arbitrary waveform generator (TGA 1230 30 MHz) supplied the ideal PWM and sinusoidal waveforms. Measured specific total loss  $P_t$  [W/kg] are shown in fig. 1 and fig. 2. As expected, maximum total losses were found at  $m_i = 0.5$ . At 1.3 T and 1.5 T peak flux densities, they were 71.3% and 68.4% greater than under sinusoidal condition respectively. At  $m_i = 1.2$ , losses were 13.4% and 12.5% larger than under sinusoidal excitation respectively.

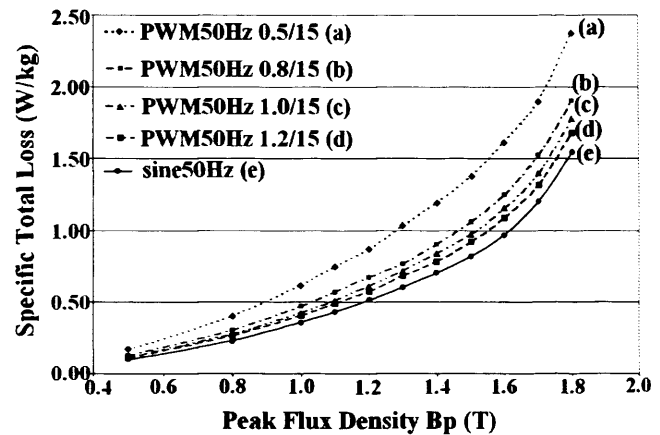


Fig. 1. Variation of  $P_t$  under sinusoidal and PWM excitation,  $m_i = 0.5$ , 0.8, 1.0, 1.2,  $f = 50$  Hz,  $m_f = 15$ .

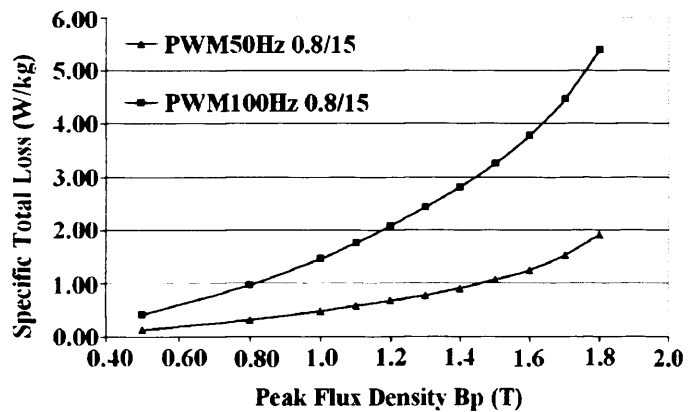


Fig. 2. Variation of  $P_t$  under PWM excitation,  $f = 50$  Hz and  $f = 100$  Hz,  $m_i = 0.8$ ,  $m_f = 15$ .

At 1.3 T and 1.5 T peak flux densities, total losses in laminations subjected to identical PWM excitation were increased by 215% and 206% when magnetizing frequency reached 100 Hz. This was caused by higher values of dynamic hysteresis and classical eddy-current losses in the steel.

### 1. Experimental setup for three-phase, three-limb transformer core

A three-phase, three-limb laminated transformer core with 10 layers comprising five laminations per layer was assembled. Associated equipment was used to magnetize the core and measure the total power loss. The core was clamped with three non-magnetic bars having bolts fixed at each end. The core mass  $m$  was 96.1kg. The layout of the core and its dimensions are given in fig. 3.

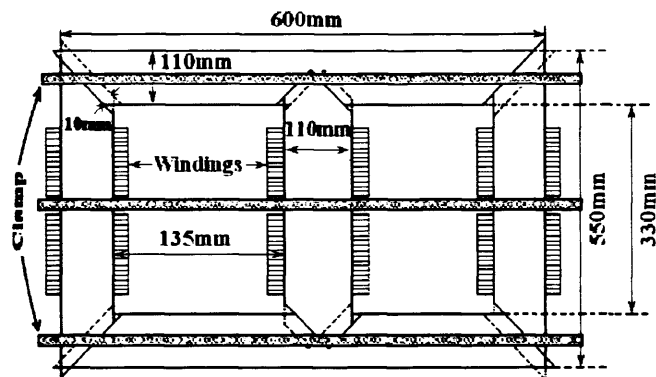


Fig. 3. Three-phase three-limb model transformer core.

A three-phase PWM inverter (TOSHIBA - Transistor Inverter TOSVERT VF-A3) was connected to the three independent variacs, which supplied the three primary windings of the core and enabled the core to be magnetized at peak flux density values up to 1.5 T (because of the output voltage limit of variac). No-load conditions were applied. The primary and secondary windings, all connected in delta configurations, had 50 turns of copper wire each. The primary phase voltages could be adjusted by means of three independent input variacs to produce equal flux densities in the three limbs.

A power analyzer (NORMA D600 Wideband Power Analyzer System) was used to measure the total power loss of the core following the two-wattmeter method. The current coils of the power analyzer were connected in series with the primary windings and the voltage coils were connected across the open-circuit secondary windings. The power analyzer gave direct reading of the total power loss in the core. This type of connection eliminates the need for calculation of copper loss in the primary windings.

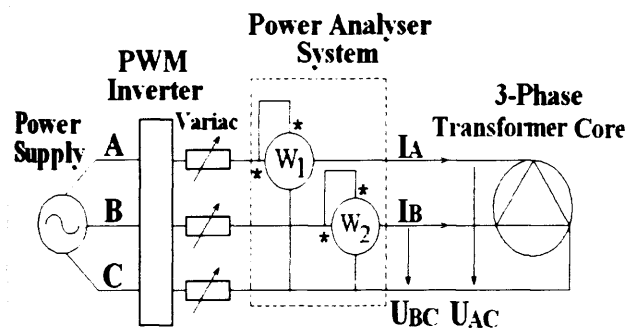


Fig. 4. Experimental setup.

The voltages applied to the primary windings and the induced voltages in the secondary windings were recorded by a digital oscilloscope (YOKOGAWA DL716 - 16CH Digital Scope). Experimental setup is shown in fig. 4.

The quantities  $P_1$  and  $P_2$  measured by the power analyzer were added to determine the total power loss  $P_o$  [W] in the core, as given by (8).

$$P_o = P_1 + P_2 = R_e[\overline{U}_{AC} \overline{I}_A^*] + R_e[\overline{U}_{BC} \overline{I}_B^*] \quad (8)$$

Output Voltage Regulation Function OV [%] is an important function in the PWM inverter, which controls the modulation index. Throughout the experiment, OV [%] was varied in the range of 40% to 70%, which corresponds approximately to a modulation index range of 0.5 to 0.8. Moreover, the switching frequency  $f_s$  was varied in the range of 1 kHz - 3 kHz while the fundamental frequency  $f$  of magnetization was set to 50 Hz and 100 Hz, respectively.

### V. DISCUSSION

Total power loss  $P_o$  [W] was measured when the transformer core was subjected to sinusoidal and PWM supplies for values of  $m_i$  approximately equal to 0.5, 0.7, 0.8 (OV% = 40%, 60%, 70%) and  $m_i$  approximately equal to 0.6, 0.7, 0.8 (OV% = 50%, 60%, 70%) at magnetizing frequency 50 Hz and 100 Hz, respectively at a peak flux density of 1.3 T. Total power loss was also measured in the same conditions but the peak induction was set to 1.5 T. At 100 Hz, measurement of losses at 1.5 T was only performed for  $m_i = 0.8$  (OV%=70%) because very high values of  $K_f$  at low values of modulation index caused high magnetizing voltages. Under these conditions, protective circuits in the inverter would be operated so that normal function was impeded. Also, there was no 100 Hz (3-phase sinusoidal) power supply available and that is the reason why no measurement of 100 Hz was taken. For assigned values of  $m_i$  and  $f$ , the switching frequency  $f_s$  was varied from 1 kHz to 3 kHz. Fig. 5 and fig. 6 show the variation of the specific total loss  $P_t$  [W/kg] with  $f_s$ , where  $P_t = P_o / m$ .

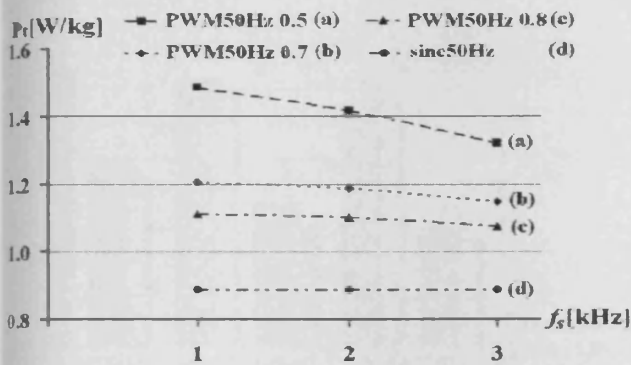


Fig. 5. Variation of  $P_t$  with  $f_s$  under sine and PWM excitation,  $m_i = 0.5$ , 17, 0.8,  $f = 50$  Hz,  $B_p = 1.3$  T.

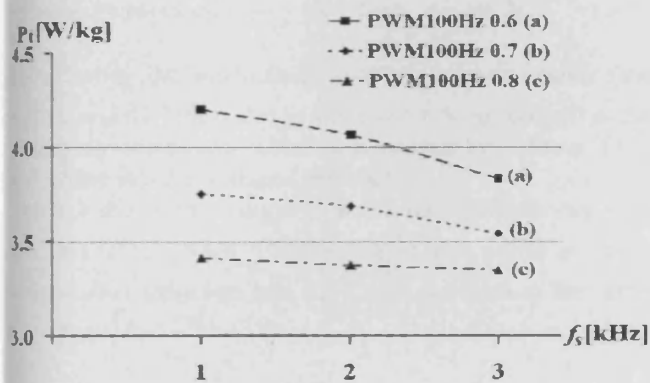


Fig. 6. Variation of  $P_t$  with  $f_s$  under sine and PWM excitation,  $m_i = 0.6$ , 17, 0.8,  $f = 100$  Hz,  $B_p = 1.3$  T.

The voltage  $u_1$  produced by the PWM inverter across the primary windings and the induced voltage  $e$  in the secondary windings were recorded by the digital oscilloscope. The THD [%] of  $u_1$  and the form factor  $K_f$  of  $e$  were calculated after Fast Fourier Transform (FFT) analysis. Results are shown in tables 1 and 2 for different values of switching frequency  $f_s$ .

From fig. 5 and fig. 6, the highest losses are seen to be at the lowest values of modulation index  $m_i$  equal to 0.5, 0.6 and lowest value of switching frequency (1 kHz) for  $f$  set to 50 Hz and 100 Hz respectively. This was caused by higher harmonic contents in the voltage waveform produced by the inverter (see table 1), which resulted in higher form factors of the induced voltage (see table 2).

It is also noticeable that an increase in the switching frequency  $f_s$  leads, under all conditions, to a reduction in core losses. The beneficial effect observed was enhanced at low values of  $m_i$  and 50 Hz. As can be seen in table 2, the form factor  $K_f$  was highest (10.2%) for  $m_i = 0.5$  and lowest (3.1%) for  $m_i = 0.8$ .

TABLE 1  
THD [%] of  $u_1$  UNDER SINUSOIDAL AND PWM EXCITATION WITH  $f_s$  FOR ASSIGNED  $m_i$ ,  $B_p = 1.3$  T

$f_s$	1 kHz	3 kHz	-	1 kHz	3 kHz
sine	-	-	2.4	-	-
0.5 (40%)	117	109	-	-	-
0.6 (50%)	-	-	-	121	114
0.7 (60%)	90.1	83.5	-	95.9	88.6
0.8 (70%)	71.8	62.5	-	76.4	74.0
$f$	50 Hz			100 Hz	

TABLE 2  
 $K_f$  OF  $e$  UNDER SINUSOIDAL AND PWM EXCITATION WITH  $f_s$  FOR ASSIGNED  $m_i$ ,  $B_p = 1.3$  T

$f$	$m_i$ (OV %)	1 kHz	2 kHz	3 kHz	
50 Hz	sine	-	-	-	1.15
	0.5 (40%)	1.57	1.42	1.41	-
	0.7 (60%)	1.38	1.34	1.28	-
	0.8 (70%)	1.28	1.28	1.24	-
100 Hz	0.6 (50%)	1.45	1.45	1.40	-
	0.7 (60%)	1.38	1.38	1.35	-
	0.8 (70%)	1.35	1.35	1.30	-

Analysis of the flux density using FFT, performed with Day Post Processor in the Ansoft Simplorer environment, was carried out to obtain the harmonic components of amplitude  $B_n$  and frequency  $f_n$ . These were used to calculate the eddy-current component of loss (3). Fig. 7 and fig. 8 show the variation of the specific total losses and its eddy-current component losses with switching frequency under selected PWM conditions at 50 Hz and 100 Hz respectively. The peak flux density was 1.3 T.

It was found that the classical eddy-current losses were

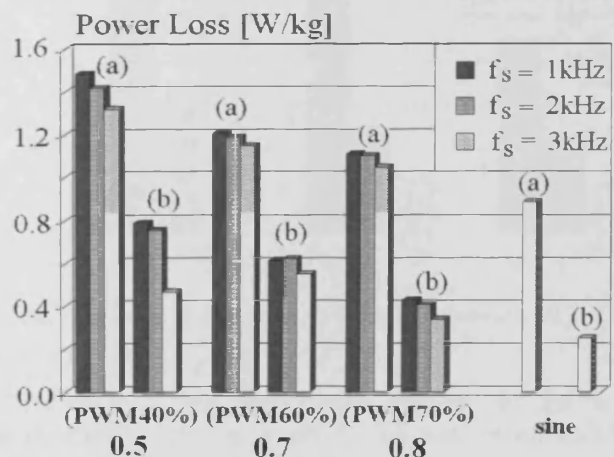


Fig. 7. Variation of specific total losses (a) and its eddy-current component (b) with  $f_s$  under sinusoidal and PWM excitation,  $m_i = 0.5, 0.7, 0.8$ ,  $f = 50$  Hz,  $B_p = 1.3$  T.

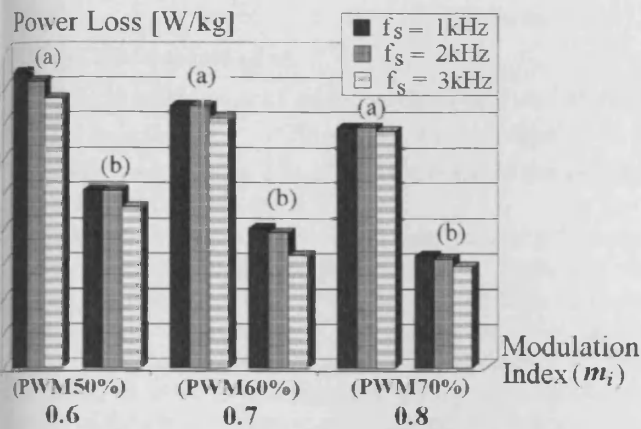


Fig. 8. Variation of specific total losses (a) and its eddy-current component (b) with switching frequency  $f_s$  under PWM excitation,  $m_i = 0.6, 0.7, 0.8$ ,  $f = 100$  Hz,  $B_p = 1.3$  T.

reduced when the modulation index  $m_i$  was increased (see figures 7 and 8). This is due to a higher harmonic content in the flux density waveform, which was caused by a lower form factor of the induced voltage (see table 2).

Table 3 shows the reduction of the eddy-current loss  $P_e$  at 50 Hz and 100 Hz when  $f_s$  was increased from 1 kHz to 3 kHz. The peak flux induction was 1.3 T and  $m_i$  varied in the range from 0.5 to 0.8.

TABLE 3

REDUCTION OF  $P_e$  UNDER DIFFERENT PWM EXCITATION WITH AN INCREASE OF  $f_s$  FROM 1 KHz TO 3 KHz,  $B_p = 1.3$  T

$f$	$m_i$ (OV %)	Reduction [%]
50 Hz	0.5 (40%)	40.8
	0.8 (70%)	20.8
100 Hz	0.6 (50%)	9.4
	0.8 (70%)	9.7

At 50 Hz, eddy-current losses were affected by variations in switching frequency, especially for low values of  $m_i$  (see table 3). However, at 100 Hz, although higher values of  $f_s$  proved beneficial, their effect on eddy-current losses was not apparent (see table 3).

Throughout the experimental work, the variac had a filtering effect on the voltage waveform produced by the inverter. It was believed that at low modulation indices, the narrowest pulses in the excitation were suppressed, which led to a reduction of RMS and rectified mean values of the voltage. Therefore, a higher amount of energy was required to magnetize the core and even higher power losses were expected at low modulation indices, due to this shortcoming of the set-up.

When the peak induction was set to 1.5 T, the increase in specific total loss  $P_t$  compared to sinusoidal was defined by the ratio  $I$  [%]

$$I[\%] = \frac{P_{1.5T} - P_{\text{sin e}}}{P_{\text{sin e}}} \times 100 \quad (9)$$

where losses under sinusoidal and PWM excitations are  $P_{\text{sin e}}$  and  $P_{1.5T}$  respectively.

Table 4 shows the variation of the specific total losses  $P_t$  and its eddy-current component losses  $P_e$  with switching frequency  $f_s$  under selected PWM voltage excitations at 50 Hz and 100 Hz respectively. The peak flux induction was set to 1.5 T.

TABLE 4

VALUES OF  $P_t$  AND  $P_e$  UNDER SINUSOIDAL AND PWM EXCITATION WITH  $f_s$  FOR ASSIGNED  $m_i$ ,  $B_p = 1.5$  T

$m_i$ (OV %)	1 kHz		2 kHz		3 kHz	
0.5 (50Hz-40%)	2.07	1.14	1.96	0.87	1.84	0.64
0.7 (50Hz-60%)	1.64	0.79	1.58	0.64	1.55	0.60
0.8 (50Hz-70%)	1.47	0.62	1.43	0.51	1.42	0.49
0.8 (100Hz-70%)	4.49	2.15	4.49	2.06	4.40	1.72
	$P_t$	$P_e$	$P_t$	$P_e$	$P_t$	$P_e$
sine 50Hz	1.27	0.35	-	-	-	-

Fig. 9 shows the variation of  $I$  [%] with switching frequency  $f_s$  under various PWM conditions at 50 Hz.

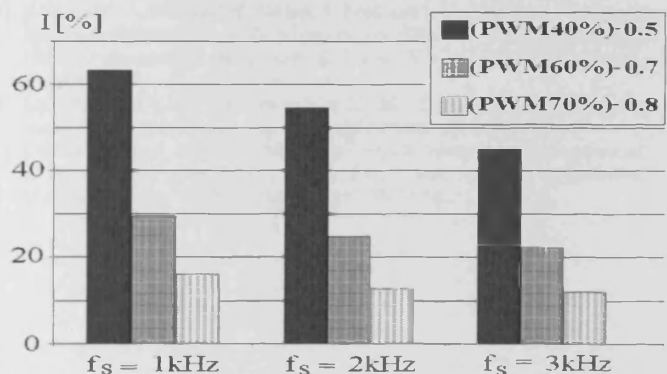


Fig. 9. Variation of  $I$  [%] with  $f_s$  under PWM excitation,  $m_i = 0.5, 0.7, 0.8$ ,  $f = 50$  Hz,  $B_p = 1.5$  T.

The ratio  $I$  [%] was highest (63.0%) for the lowest modulation index  $m_i$  equal to 0.5 and lowest switching frequency (1 kHz); and lowest (12.0%) for the highest modulation index  $m_i$  equal to 0.8 and highest switching frequency (3 kHz). These results enhanced the benefit on the

performance of the transformer core of high values of  $f_s$ , especially for low values of  $m_i$ .

At 1.5 T, the reduction of eddy-current losses was highest (3.9%) at  $m_i = 0.5$ ,  $f = 50$  Hz when  $f_s$  was increased from 1 kHz to 3 kHz (see table 4). These results confirmed the validity of the analysis carried out for 1.3 T.

In high power applications consisting of current-source inverters, high switching frequencies are not applicable to thyristors, the primary choice when dealing with high voltages and currents. An increase in PWM switching frequency in the low range leads to a substantial improvement of the performance of steel in transformers, owing to a significant reduction of the classical eddy-current component of loss.

## VI. CONCLUSION

Iron loss  $P_i$  in a three-phase, three-limb transformer core, subjected to PWM voltage excitation under no-load conditions, was measured and its classical eddy-current component  $P_e$  calculated. The effect of switching frequency on both terms was also investigated for different modulation indices and magnetizing frequencies.

Results show that iron losses subjected to PWM voltage excitation can be significantly higher than under sinusoidal voltage excitation. Loss increases with decreasing modulation index as found previously, but at a given modulation index the loss drops as the switching frequency  $f_s$  is increased from 1 kHz to 3 kHz. This improvement is due to significant reduction in classical eddy current losses at 50 Hz,  $m_i = 0.5$  and  $B_p = 1.5$  T. The beneficial impact on loss at high values of  $m_i$  is not apparent due to improved harmonic spectra in flux density waveforms.

In the future, the impact of higher switching frequencies on power semiconductor losses of inverter must also be studied thoroughly, due to their effect on the overall efficiency.

## REFERENCES

- [1] N. Tutkun, A. J. Moses, "Investigation of power loss in non-oriented electrical steels under pulse width modulated voltage excitation", *J. Magn. Magn. Mater.*, Vol. 277, pp. 359-362, 2004.
- [2] Aldo Boglietti, Andrea Cavagnino, Mario Lazzari, and Michele Pastorelli, "Predicting iron losses in soft magnetic materials with arbitrary voltage supply: an engineering approach", *IEEE Transactions on Magnetics*, Vol. 27, No. 2, pp. 981-988, March 2003.
- [3] Marcelo S. Lancarotte and Aderbal de A. Pentecado, "Estimation of core losses under sinusoidal or non-sinusoidal induction by analysis of magnetization rate", *IEEE Transactions on Energy Conversion*, Vol. 16, No. 2, pp. 174-179, June 2001.
- [4] A. Boglietti, P. Ferraris, M. Lazzari, F. Profumo, "Iron losses in magnetic materials with six-step and PWM inverter supply [induction motors]", *IEEE Transactions on Magnetics*, Vol. 27, Issue 6, Part 2, pp. 5334-5336, November 1991.
- [5] Z.C. Papazacharopoulos, A. G. Kladas and S. N. MManias, "Investigation of the switching frequency harmonic impact on PWM Induction Motor Drive Efficiency", *IEEE Power Electronics Specialist Conference*, Vol. 2, pp. 1203-1208, June 17-21, 2001.

- [6] A. J. Moses and N. Tutkun, "Localized losses in stator laminations of an induction motor under PWM excitation", *Journal of Materials Processing Technology*, Vol. 161, pp. 79-82, 2005.
- [7] T.C. Green, C.A. Hernandez-Aramburo, A.C. Smith, "Losses in grid and inverter supplied induction machines drives", *Electric Power Applications, IEE Proceedings*, Vol. 150, No. 6, pp. 712-724, November 2003.
- [8] A. J. Moses and A. Sakaïda, "Effect of distorted flux density on three phase transformer cores assembled from high quality electrical Steels", *IEEE Transactions on Magnetics*, Vol. 22, No. 5, pp. 532-534, September 1986.
- [9] A. Basak, A. J. Moses, "Effect of stacking and clamping on distribution transformers built with amorphous magnetic material", *IEEE Transactions on Magnetics*, Vol. 27, No. 6, pp. 5196-5198, November 1991.
- [10] Zvonimir Valkovic, "Influence of transformer core design on power losses", *IEEE Transactions on Magnetics*, Vol. 18, No. 2, pp. 801-804, March 1982.
- [11] A. J. Moses, "Effect of magnetic properties and geometry on flux harmonics and losses in 3-Phase, 5-Limb, split-limb, transformer Cores", *IEEE Transactions on Magnetics*, Vol. 23, No. 5, pp. 3780-3782, September 1987.
- [12] Günther F. Mechler and Ramsis S. Girgis, "Magnetic flux distributions in transformer core joints", *IEEE Transactions on Power Delivery*, Vol. 15, No. 1, pp. 198-203, January 2000.
- [13] Hüseyin Akcay and Dogan Gökhan Ece, "Modeling of hysteresis and power losses in transformer laminations", *IEEE Transactions on Power Delivery*, Vol. 18, No. 2, pp. 487-492, April 2003.
- [14] Edoardo Barbisio, Fausto Fiorillo and Carlo Ragusa, "Predicting loss in magnetic steels under arbitrary induction waveform and with minor hysteresis loops", *IEEE Transactions on Magnetics*, Vol. 40, No. 4, pp. 1810-1819, July 2004.
- [15] H. Akagi, "Trends in active power line conditioners", *IEEE Transactions on Power Electronics*, Vol. 9, No. 3, pp. 263-268, May 1994.
- [16] V. B. Bharavaju and P. N. Enjeti, "An active line conditioner to balance voltages in a three-phase system", *IEEE Transactions on Industry Applications*, Vol. 32, No. 2, pp. 287-292, March/April 1996.
- [17] T.W. Kim, J.H. Choi and B.H. Kwon, "High performance line conditioner with output voltage regulation and power factor correction", *IEE Proceedings Power Applications*, Vol. 151, No. 1, pp. 91-97, January 2004.
- [18] C.A. Petry, J.C. Fagundes and I. Barbi, "Study of an AC-AC indirect converter for application as line conditioner", *IEEE International Symposium on Industrial Electronics*, pp. 757-762, June 20-23, 2005.
- [19] F. Barrero, S. Martinez, F. Yeves, F. Mur and P.M. Martinez, "Universal and reconfigurable to UPS active power filter for line conditioning", *IEEE Transactions on Power Delivery*, Vol. 18, No. 1, pp. 283-290, January 2003.
- [20] Lu C.B., Zhu Y.H., "Calculations in Electrical Transformers", *Hei Long Jiang Institute of Technology - Scientific Press*, pp. 46, 1990.
- [21] British Standard, Magnetic Materials—Part 2: Methods of measurement of the magnetic properties of electrical steel sheet and strip by means of an Epstein frame, BS EN 60404-2:1998, IEC 404-2:1996.

***A2. Modelica code for space-vector PWM simulation (Dymola environment)***

```
model vect_sel
```



```
Real vect_0[3,1];
```

```
Real vect_a[3,1];
```

```
Real vect_b[3,1];
```

```
Real vect_7[3,1];
```

```
Real vect_sel[3,1];
```

```
Real index;
```

```
Real Ic;
```

```
Real I;
```

```
Real t1;
```

```
Real t2;
```

```
Real t3;
```

```
Real t4;
```

```
Real t5;
```

```
Real t6;
```

```
Real t7b;
```

```
Real t8;
```

```
Real sum;
```

```
Real sector;
```

equation

sum = t0+ta+tb+t7;

Ic = 1/fc;

T = 1/f;

if (tid\_I>=0) and

(tid\_I<T/6) then

sector = 1;

vect\_a = {{1},{0},{0}};

vect\_b = {{1},{1},{0}};

else

if (tid\_I>=T/6) and

(tid\_I<T/3) then

sector = 2;

vect\_a = {{0},{1},{0}};

vect\_b = {{1},{1},{0}};

else

if (tid\_I>=T/3) and (tid\_I<T/2) then

sector = 3;

vect\_a = {{0},{1},{0}};

vect\_b = {{0},{1},{1}};

else

if (tid\_I>=T/2) and (tid\_I<2\*T/3) then

sector = 4;

vect\_a = {{0},{0},{1}};

vect\_b = {{0},{1},{1}};

else

if (tid\_I>=2\*T/3) and (tid\_I<5\*T/6) then

sector = 5;

vect\_a = {{0},{0},{1}};

vect\_b = {{1},{0},{1}};

else

sector = 6;

vect\_a = {{1},{0},{0}};

vect\_b = {{1},{0},{1}};

end if;

end if;

end if;

end if;

end if;

```

t1 = t0;
t2 = t0+ta;
t3 = t0+ta+tb;
t4 = t0+ta+tb+t7;

t5 = (Ic/2)+t7;
t6 = (Ic/2)+t7+tb;
t7b = (Ic/2)+t7+tb+ta;
t8 = (Ic/2)+t7+tb+ta+t0;

if (tid>=0) and
    (tid<t1) then
    vect_sel = vect_0;
    index = 1;
else
    if (tid>=t1) and
        (tid<t2) then
        vect_sel = vect_a;
        index = 2;
    else
        if (tid>=t2) and (tid<t3) then
            vect_sel = vect_b;
            index = 3;
        else
            if (tid>=t3) and (tid<t5) then
                vect_sel = vect_7;
                index = 4;
            else
                if (tid>=t5) and (tid<t6) then
                    vect_sel = vect_b;
                    index = 3;
                else
                    if (tid>=t6) and (tid<t7b) then
                        vect_sel = vect_a;
                        index = 2;
                    else
                        vect_sel = vect_0;
                        index = 1;
                    end if;
                end if;
            end if;
        end if;
    end if;
end if;

Sa = vect_sel[1,1];
Sb = vect_sel[2,1];
Sc = vect_sel[3,1];

end vect_sel;

```

***A3. Eupec IGBT-modules for a matrix converter***


 vorläufige Daten  
 preliminary data

### Höchstzulässige Werte / maximum rated values

#### Elektrische Eigenschaften / electrical properties

Kollektor Emitter Sperrspannung collector emitter voltage		$V_{CES}$	1200	V
Kollektor Dauergleichstrom DC collector current	$T_c = 80^\circ\text{C}$	$I_{C, nom}$	35	A
	$T_c = 25^\circ\text{C}$	$I_C$	55	A
Periodischer Kollektor Spitzenstrom repetitive peak collector current	$t_p = 1\text{ms}, T_c = 80^\circ\text{C}$	$I_{CRM}$	70	A
Gesamt Verlustleistung total power dissipation	$T_c = 25^\circ\text{C}$	$P_{tot}$	200	W
Gate Emitter Spitzenspannung gate emitter peak voltage		$V_{GES}$	$\pm 20$	V
Dauergleichstrom DC forward current	$T_c = 80^\circ\text{C}$	$I_F$	35	A
Periodischer Spitzenstrom repetitive peak forward current	$t_p = 1\text{ms}$	$I_{FRM}$	70	A
Grenzlastintegral $I^2t$ value	$V_R = 0\text{V}, t_p = 10\text{ms}, T_{vj} = 125^\circ\text{C}$	$I^2t$	300	$\text{A}^2\text{s}$
Isolations Prüfspannung insulation test voltage	RMS, $f = 50\text{Hz}, t = 1\text{min}$	$V_{ISOL}$	2,5	kV

### Charakteristische Werte / characteristic values

#### Transistor Wechselrichter / transistor inverter

			min.	typ.	max.	
Kollektor Emitter Sättigungsspannung collector emitter saturation voltage	$V_{GE} = 15\text{V}, T_{vj} = 25^\circ\text{C}, I_C = I_{C, nom}$	$V_{CEsat}$	-	1,70	2,00	V
	$V_{GE} = 15\text{V}, T_{vj} = 125^\circ\text{C}, I_C = I_{C, nom}$		-	2,00	t.b.d.	V
Gate Schwellenspannung gate threshold voltage	$V_{CE} = V_{GE}, T_{vj} = 25^\circ\text{C}, I_C = 1,5\text{mA}$	$V_{GE(th)}$	5,0	5,8	6,5	V
Gateladung gate charge	$V_{GE} = -15\text{V} \dots +15\text{V}$	$Q_G$	-	0,33	-	$\mu\text{C}$
Eingangskapazität input capacitance	$f = 1\text{MHz}, T_{vj} = 25^\circ\text{C}, V_{CE} = 25\text{V}, V_{GE} = 0\text{V}$	$C_{ies}$	-	2,5	-	nF
Rückwirkungskapazität reverse transfer capacitance	$f = 1\text{MHz}, T_{vj} = 25^\circ\text{C}, V_{CE} = 25\text{V}, V_{GE} = 0\text{V}$	$C_{res}$	-	0,09	-	nF
Kollektor Emitter Reststrom collector emitter cut off current	$V_{CE} = 1200\text{V}, V_{GE} = 0\text{V}, T_{vj} = 25^\circ\text{C}$	$I_{CES}$	-	-	5	mA
Gate Emitter Reststrom gate emitter leakage current	$V_{CE} = 0\text{V}, V_{GE} = 20\text{V}, T_{vj} = 25^\circ\text{C}$	$I_{GES}$	-	-	400	nA

prepared by: M. Münzer

date of publication: 2001-02-26

approved: M. Hierholzer

revision: 1



vorläufige Daten  
preliminary data

### Charakteristische Werte / characteristic values

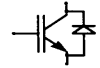
#### Transistor Wechselrichter / transistor inverter

			min.	typ.	max.	
Einschaltverzögerungszeit (induktive Last) turn on delay time (inductive load)	$I_C = I_{C, nom}, V_{CC} = 600V$ $V_{GE} = \pm 15V, R_G = 27\Omega, T_{vj} = 25^\circ C$	$t_{d,on}$	-	85	-	ns
	$V_{GE} = \pm 15V, R_G = 27\Omega, T_{vj} = 125^\circ C$		-	90	-	ns
Anstiegszeit (induktive Last) rise time (inductive load)	$I_C = I_{C, nom}, V_{CC} = 600V$ $V_{GE} = \pm 15V, R_G = 27\Omega, T_{vj} = 25^\circ C$	$t_r$	-	30	-	ns
	$V_{GE} = \pm 15V, R_G = 27\Omega, T_{vj} = 125^\circ C$		-	45	-	ns
Abschaltverzögerungszeit (induktive Last) turn off delay time (inductive load)	$I_C = I_{C, nom}, V_{CC} = 600V$ $V_{GE} = \pm 15V, R_G = 27\Omega, T_{vj} = 25^\circ C$	$t_{d,off}$	-	420	-	ns
	$V_{GE} = \pm 15V, R_G = 27\Omega, T_{vj} = 125^\circ C$		-	520	-	ns
Fallzeit (induktive Last) fall time (inductive load)	$I_C = I_{C, nom}, V_{CC} = 600V$ $V_{GE} = \pm 15V, R_G = 27\Omega, T_{vj} = 25^\circ C$	$t_f$	-	65	-	ns
	$V_{GE} = \pm 15V, R_G = 27\Omega, T_{vj} = 125^\circ C$		-	90	-	ns
Einschaltverlustenergie pro Puls turn on energy loss per pulse	$I_C = I_{C, nom}, V_{CC} = 600V, L_o = 70nH$ $V_{GE} = \pm 15V, R_G = 27\Omega, T_{vj} = 125^\circ C$	$E_{on}$	-	3,5	-	mJ
Ausschaltverlustenergie pro Puls turn off energy loss per pulse	$I_C = I_{C, nom}, V_{CC} = 600V, L_o = 70nH$ $V_{GE} = \pm 15V, R_G = 27\Omega, T_{vj} = 125^\circ C$	$E_{off}$	-	4,8	-	mJ
Kurzschlussverhalten SC data	$t_p \leq 10\mu sec, V_{GE} \leq 15V, T_{vj} \leq 125^\circ C$ $V_{CC} = 900V, V_{CEmax} = V_{CES} - L_{oCE} \cdot di/dt$	$I_{SC}$	-	140	-	A
Modulinduktivität stray inductance module		$L_{oCE}$	-	-	-	nH
Leitungswiderstand, Anschluss-Chip lead resistance, terminal-chip	$T_c = 25^\circ C$	$R_{CC/EE}$	-	8	-	mΩ

### Charakteristische Werte / characteristic values

#### Diode Wechselrichter / diode inverter

Durchlassspannung forward voltage	$I_F = I_{C, nom}, V_{GE} = 0V, T_{vj} = 25^\circ C$	$V_F$	-	1,65	2,10	V
	$I_F = I_{C, nom}, V_{GE} = 0V, T_{vj} = 125^\circ C$		-	1,65	t.b.d.	V
Rückstromspitze peak reverse recovery current	$I_F = I_{C, nom}, -di_F/dt = 1500A/\mu s$ $V_R = 600V, V_{GE} = -15V, T_{vj} = 25^\circ C$	$I_{RM}$	-	49	-	A
	$V_R = 600V, V_{GE} = -15V, T_{vj} = 125^\circ C$		-	51	-	A
Sperrverzögerungsladung recovered charge	$I_F = I_{C, nom}, -di_F/dt = 1500A/\mu s$ $V_R = 600V, V_{GE} = -15V, T_{vj} = 25^\circ C$	$Q_r$	-	3,7	-	$\mu Q$
	$V_R = 600V, V_{GE} = -15V, T_{vj} = 125^\circ C$		-	6,8	-	$\mu Q$
Ausschaltenergie pro Puls reverse recovery energy	$I_F = I_{C, nom}, -di_F/dt = 1500A/\mu s$ $V_R = 600V, V_{GE} = -15V, T_{vj} = 25^\circ C$	$E_{rec}$	-	1,4	-	mJ
	$V_R = 600V, V_{GE} = -15V, T_{vj} = 125^\circ C$		-	2,7	-	mJ



vorläufige Daten  
preliminary data

### Thermische Eigenschaften / thermal properties

Innerer Wärmewiderstand; DC thermal resistance, junction to case; DC	Transistor Wechselr. / transistor inverter	$R_{thJC}$	-	-	0,60	KW
	Diode Wechselrichter / diode inverter		-	-	0,95	KW
Übergangs Wärmewiderstand thermal resistance, case to heatsink	pro Modul / per module $\lambda_{paste} = 1W/m^2K$ / $\lambda_{grease} = 1W/m^2K$	$R_{thCK}$	-	0,01	-	KW
Höchstzulässige Sperrschichttemp. maximum junction temperature		$T_{vj}$	-	-	150	°C
Betriebstemperatur operation temperature		$T_{op}$	-40	-	125	°C
Lagertemperatur storage temperature		$T_{stg}$	-40	-	125	°C

### Mechanische Eigenschaften / mechanical properties

Gehäuse, siehe Anlage case, see appendix						
Innere Isolation internal insulation					Al <sub>2</sub> O <sub>3</sub>	
CTI comperative tracking index					225	
Anzugsdrehmoment, mech. Befestigung mounting torque	Schraube M 5 screw M 5	M	3	-	6	Nm
Anzugsdrehmoment, elektr. Anschlüsse terminal connection torque		M	-	-	-	Nm
Gewicht weight		G			300	g

Mit dieser technischen Information werden Halbleiterbauelemente spezifiziert, jedoch keine Eigenschaften zugesichert. Sie gilt in Verbindung mit den zugehörigen technischen Erläuterungen.

This technical information specifies semiconductor devices but promises no characteristics. It is valid with the belonging technical notes.

***A4. Specifications on the PM3000 power analyser***

# Ordering Information

## Products

PM3000ACE-001 Fitted with Torque and Speed Inputs  
PM3000ACE-002 Single Phase for Full-compliance IEC61000-3 Testing  
PM3000ACE-002 Three Phase for Full-compliance IEC61000-3 Testing  
IMP555 Impedance Network for Full-compliance IEC61000-3 Testing

## Accessories

PS1000 Switch for Inrush Testing  
Ballast CT for HF Electronic Lighting Applications  
CL100 100:1 Clamp-on Current Transformer  
CL1000 1000:1 Clamp-on Current Transformer  
CL3000 3000:1 Clamp-on Current Transformer  
CT1000 Precision Dual-ratio 1000/100:1 Current Transformer  
Rack Mounting Kit

## PC Software

VPAS General-purpose Software  
IEC61000-3 Software

Although every care has been taken in compiling the information in this publication, Voltech Instruments cannot accept legal liability for any inaccuracies. Voltech Instruments has an intensive program of design and development that may alter product specification. Voltech Instruments reserves the right to alter specification without notice and whenever necessary to ensure optimum performance from its product range.  
© Voltech Instruments 1998-2003. All rights reserved.

Voltech's customers include major household names and leading industrial companies in Asia, Europe, and the USA. Our world-wide network of trained distributors provides first-level applications support and product service. Our main offices and top-level customer support facilities are based in the USA and the UK.



Voltech Instruments, Inc.  
Fort Myers, Florida  
USA

Voltech Instruments, Ltd.  
Harwell, Oxfordshire  
UK



**Voltech Instruments Inc.**  
11637 Kelly Road, Suite 306  
Fort Myers, FL 33908  
USA  
Tel: +1 239 437 0494  
Fax: +1 239 437 3841  
E-mail: sales@voltech.com

**Voltech Instruments Ltd.**  
148 Sixth Street  
Harwell International Business Centre  
Didcot, Oxon OX11 0RA, UK  
Tel: +44 (0)1235 834555  
Fax: +44 (0)1235 835016  
E-mail: sales@voltech.co.uk

[www.voltech.com](http://www.voltech.com)

**Voltech**<sup>TM</sup>

**THE WORLD'S MOST POPULAR POWER ANALYZERS**

VPN 86-264/3

# Specification

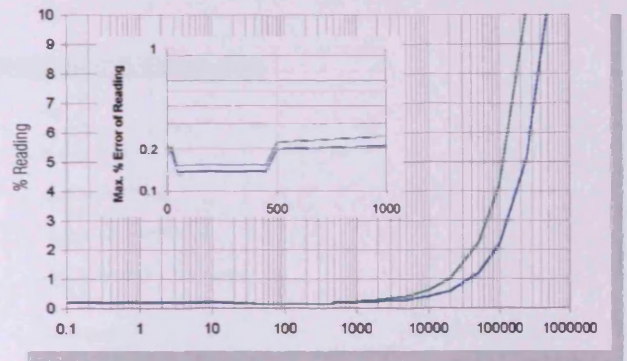
Specifications can often be confusing and time consuming to interpret for use in real-life applications. The effects due to frequency, power factor and instrument range must all be considered when calculating total errors.

The graphs below show the total maximum errors of the PM3000A at 115Vrms and 5Arms as a percentage of the reading.

NB: All specifications are valid for one year from calibration and at  $23^{\circ}\text{C} \pm 5^{\circ}\text{C}$ .

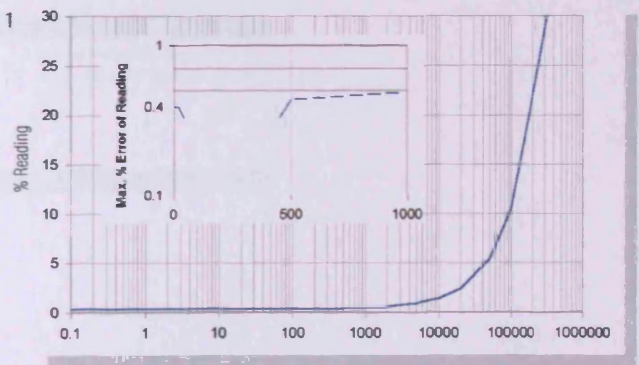
## Maximum Voltage and Current Error Vs Frequency

- 115V rms
- 5A rms
- Volts** 45 to 450Hz  
 $\pm 0.05\% \text{ rdg} \pm 0.05\% \text{ rng}$
- Amps** 45 to 450Hz  
 $\pm 0.05\% \text{ rdg} \pm 0.05\% \text{ rng}$   
 $\pm 100\mu\text{A}$



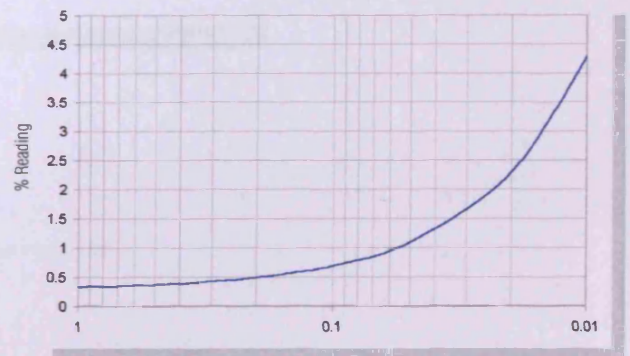
## Maximum Power Error Vs Frequency

- Watts** 45 to 450Hz, PF = 1
- $\pm A \text{ rdg} \times V \text{ error}$
- $\pm V \text{ rdg} \times A \text{ error}$
- $\pm 0.04\% \text{ rdg}$



## Maximum Power Error Vs Power Factor

- Watts** 45 to 450Hz
- $\pm A \text{ rdg} \times V \text{ error} \times \text{PF}$
- $\pm V \text{ rdg} \times A \text{ error} \times \text{PF}$
- $\pm (0.04/\text{PF})\% \text{ rdg}$



# Specification

## Voltage Channels

Input Impedance	0.5V to 2000Vpk (1400Vrms) 5000Vpk for 1 second 1MΩ and 10pF	12 ranges in 1-2-5 sequence
Common Mode Voltages:		
1000V rms at 60Hz	Less than 20mV	
100V rms at 100kHz	Less than 500mV	1V PM3000ACE-002

## Current Channels

Input Shunt Ranges	0.05A to 200Apk (30Arms)	12 ranges in 1-2-5 sequence
Input Shunt Ranges	6.25mVrms to 2.5Vpk	
Input Withstand	200A rms for 1 second	
Input Impedance	0.0125Ω	PM3000ACE-002: 0.0035Ω
Input Impedance	1MΩ in parallel 10pF	20kΩ in parallel 33pF PM3000ACE-002
Common Mode Voltages:		
1000V rms at 60Hz	Less than 2mA	
100V rms at 100kHz	Less than 20mA	(50mA PM3000ACE-002)

## Basic Accuracy

	V	A	W	VA <sub>r</sub>
	±0.05% rdg ±0.05% mg	±0.05% rdg ±0.05% mg	±A rdg x V error x PF ±V rdg x A error x PF	±A rdg x V error x (1-PF <sup>2</sup> ) <sup>0.5</sup> ±V rdg x A error x (1-PF <sup>2</sup> ) <sup>0.5</sup>
<b>Basic Maximum Errors, PM3000ACE and PM3000ACE-001</b>				
10Hz to 450kHz	±1mV*	±100μA	±(0.04/PF)% rdg	±(0.04 / (1-PF <sup>2</sup> ) <sup>0.5</sup> )% rdg
10Hz to 250kHz	±0.05% rdg ±0.02% rdg per kHz	±200μA*	±(kHz x 0.04%/PF) rdg	±(kHz x 0.04 / (1-PF <sup>2</sup> ) <sup>0.5</sup> )% rdg
10Hz to 500kHz	±0.05% rdg ±0.02% rdg per kHz	±0.05% rdg ±(kHz x 0.04)% rdg ±100μA	±(kHz + 750) x 0.01%/PF) rdg	±(kHz + 750) x (0.01 / (1-PF <sup>2</sup> ) <sup>0.5</sup> )% rdg
<b>Basic Maximum Errors, PM3000ACE-002</b>				
10Hz to 450kHz	±1mV*	±100μA	±(0.04/PF)% rdg	±(0.04 / (1-PF <sup>2</sup> ) <sup>0.5</sup> )% rdg
10Hz to 250kHz	±0.05% rdg ±0.02% rdg per kHz	±800μA*	±(kHz x 0.06%/PF) rdg	±(kHz x 0.06 / (1-PF <sup>2</sup> ) <sup>0.5</sup> )% rdg
10Hz to 500kHz	±0.05% rdg ±0.02% rdg per kHz	±0.05% rdg ±(kHz + 250) x ±0.02% rdg ±100μA	±(kHz + 1250) x 0.01%/PF) rdg	±(kHz + 1250) x (0.01 / (1-PF <sup>2</sup> ) <sup>0.5</sup> )% rdg
<b>VA</b>				
	±A rdg x V error x ±V rdg x A error			

## Harmonics

	Voltage	Current PM3000ACE and PM3000ACE-001	Current PM3000ACE-002
Fundamental or 1st Harmonic	±0.1% rdg ±0.1% mg (kHz x 0.02)% rdg	±0.1% rdg ±0.1% mg ±(kHz x 0.04)% rdg ±100μA	±0.1% rdg ±0.1% mg ±(kHz x 0.08)% rdg ±100μA
Harmonics 2 to 99	±((kHz x 0.05) + 0.1)% of fundamental	Harmonic series formula, dc excluded	
Bandwidth	±((kHz x 0.01) + 0.2)%		
Resolution	0.1Hz to 1MHz		

## Other Functions

Power Factor (PF)	0.000 to ±1.000 ±0.002 ±(kHz x 0.001/PF)
Power Factor	1.000 to 19.999
Voltage	±0.10% rdg ±0.05% mg ±0.02
Current	±0.10% rdg ±0.01% mg ±0.01
Max Current	0.1A to 200Apk (with scaling to 200MA) 2.0% mg
Impedance	0.0001Ω to 9.999MΩ
10Hz to 450kHz	±0.5% rdg
10Hz to 500kHz	±0.5% rdg ±(kHz x 0.05/PF)% rdg
Binary Inputs A and B (Type and Speed)	0 to 1V and 0 to 10V ranges, software selectable ±0.5% rdg ±0.5% mg
Manual Integrator Trigger	Close switch to trigger. Max. current < 5mA
Manual Frequency Input	4V to 20V p-p; 0.1Hz 1MHz
Relay Outputs	8 outputs. 0 to +5V dc; 5mA max.

## Environment

Temperature	5° to +40°C operating
Humidity	10% to 80% RH non-condensing
Electric Strength	
Case to Case or Power Supply	4kV AC 50/60Hz for 1 minute
Case to Input	2kV AC 50/60Hz for 1 minute
Power Supply to Case	2.9kV DC for 1 minute
Power Requirement	90 - 264Vac 48 to 440Hz
Power Consumption	30W, 60VA max.

\* = displayed reading

mg = analyzer range

kHz = measured frequency in kHz

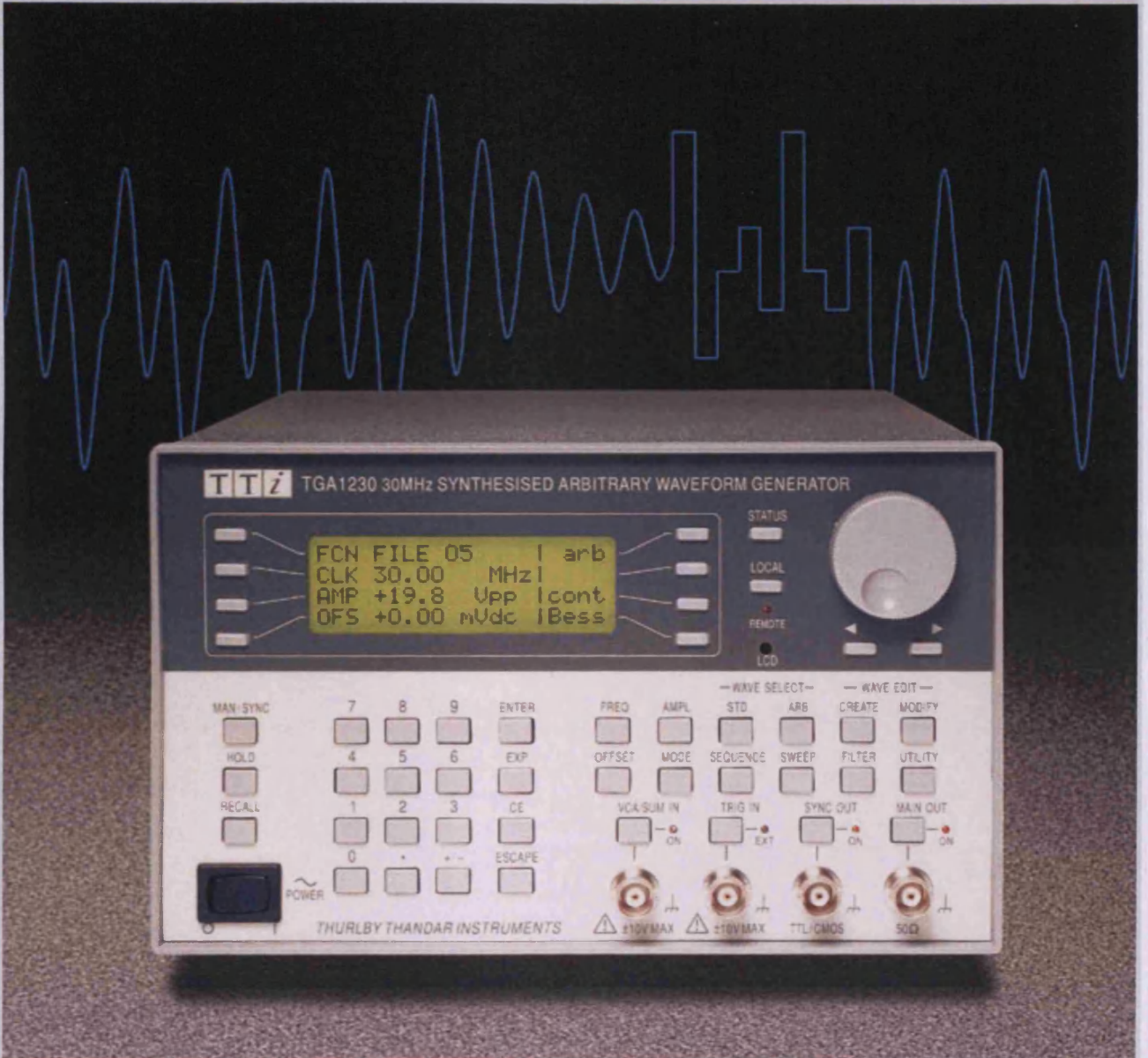
Accuracy specification after performing a manual zero.

***A5. Specifications on the TTI TGA 1230 signal generator***



# THURLBY THANDAR INSTRUMENTS

## TGA1230



*Universal signal source*

*30MS/s, 12-bit, 64K word arbitrary generator*

*full function generator and pulse generator features*

# Technical Specifications

## WAVEFORMS

### Standard Waveforms

Waveform types: square, triangle, DC, positive ramp, negative ramp, sin(x)/x, pulse train, cosine, haversine and haversine cosine.

### Cosine, Haversine, Haversine Cosine

Frequency Range: 0.1 mHz to 10 MHz.  
Resolution: 0.1mHz (7 digits)  
Accuracy: Better than 10 ppm for 1 year.  
Temperature Stability: Typically <1 ppm/°C  
Output Level: 5mV to 20V p-p from 50 Ω  
Total Harmonic Distortion: <0.1% THD to 100kHz;  
<-50dBc to 1MHz, <-35dBc to 10MHz.  
Spurious: <-50dBc to 7MHz.

### Square Wave

Frequency Range: 1 mHz to 15MHz.  
Resolution: 1mHz (4 digits)  
Accuracy: ±1 digit of setting.  
Output Level: 5mV to 20V p-p from 50 Ω  
Rise and Fall Times: <25ns

### Triangle

Frequency Range: 0.1 mHz to 100kHz.  
Resolution: 0.1mHz (7 digits)  
Accuracy: Better than 10 ppm for 1 year.  
Output Level: 5mV to 20V p-p from 50 Ω  
Frequency Error: <0.1% to 30 kHz

### Pulses and Sin(x)/x

Frequency Range: 0.1 mHz to 100kHz.  
Resolution: 0.1mHz (7 digits)  
Accuracy: Better than 10 ppm for 1 year.  
Output Level: 5mV to 20V p-p from 50 Ω  
Frequency Error: <0.1% to 30 kHz

### Rise and Pulse Train

Output Level: 5mV to 20V p-p from 50 Ω  
Rise and Fall Times: <25ns  
Duty Cycle: Range - 133.3ns to 100s. Resolution - 4-digits.  
Accuracy - ±1 digit of setting.  
Delay: Range - -99.9s to +99.99s.  
Resolution - 0.002% of period or 33.33ns.  
Jitter: Range - 33.3ns to 99.99s.  
Resolution - 0.002% of period or 33.33ns.

Transitions of up to 10 pulses may be specified, each having independently defined width, delay and level. The baseline voltage is separately defined and the sequence repetition rate is set by the pulse train period.

## ARBITRARY

Up to 50 user defined waveforms may be stored in RAM. Arbitrary waveforms can be defined by front panel editing controls or by downloading of waveform data via RS232 or GPIB.

Memory Size: 64K points. Maximum waveform size is 64K points, minimum waveform size is 4 points.  
Vertical Resolution: 12 bits  
Sample Clock Range: 100mHz to 30MHz  
Resolution: 4 digits  
Accuracy: ±1 digit of setting.  
Output Filter: Selectable between 10MHz Elliptic, 10MHz Bessel or none.

### Sequence

Up to 4 waveforms may be linked. Each waveform can have a loop count of up to 32768. A sequence of waveforms can be looped up to 48575 times or run continuously.

## MODULATION MODES

### Triggered Burst

Each active edge of the trigger signal will produce one burst of the waveform, starting and stopping at the waveform position specified by the sync marker setting.

Carrier Waveforms: All standard and arbitrary  
Number of Cycles: 1 to 1048575  
Trigger Rate: dc to 50 kHz internal, dc to 1MHz external.  
Source: Internal from keyboard or trigger generator.  
External from TRIG IN or remote interface.

### Gated

Waveform will run while the Gate signal is true and stop while false.

Carrier Waveforms: All standard and arbitrary.  
Trigger Rate: dc to 50 kHz internal, dc to 1 MHz external.  
Gate Signal Source: Internal from keyboard or trigger generator.  
External from TRIG IN or remote interface.

### Sweep

Capability provided for both standard and arbitrary waveforms. Arbitrary waveforms are expanded or condensed to exactly 4096 points and DDS techniques are used to perform the sweep.

Carrier Waveforms: All standard and arbitrary except pulse, pulse train and sequence.

Sweep Mode: Linear or logarithmic; up or down; single, continuous or triggered.

Sweep Range: 1mHz to 10 MHz in one range. Phase continuous. Independent setting of start/stop frequency.

Sweep Time: 30ms to 999s (3 digit resolution).

Marker: Variable during sweep.

Sweep Trig. Source: The sweep may be free run or triggered from the following sources: Manually from keyboard. Externally from TRIG IN input or remote interface.

Sweep Hold: Sweep can be held and restarted by HOLD key.

### Tone

Capability provided for both standard and arbitrary waveforms. Arbitrary waveforms are expanded or condensed to exactly 4096 points and DDS techniques used to allow instantaneous frequency switching.

Carrier Waveforms: All waveforms bar pulse, pulse train, sequence.

Frequency List: Up to 16 frequencies from 1mHz to 10MHz.

Switching Sources: External trigger input. True level will output the tone, false level stops the tone and switches to next frequency on list ready for the next true level.

Min. switch time: 20ms per tone.

Using 2 instruments with their outputs summed together it is possible to generate DTMF test signals.

### External Amplitude Modulation

Carrier frequency: Entire range for selected waveform.  
Carrier waveforms: All standard and arbitrary waveforms  
Modulation source: VCA/SUM IN socket.  
Frequency Range: DC - 100 kHz.  
Signal Range: Approx. 2.5V pk-pk for 100% level change at maximum output.

### External Signal Summing

Carrier frequency: Entire range for selected waveform.  
Carrier waveforms: All standard and arbitrary waveforms.  
Sum source: VCA/SUM IN socket.  
Frequency Range: DC to 10MHz.  
Signal Range: Approximately 5Vpk-pk input for 20Vpk-pk output.

### Trigger Generator

Internal source 0.005 Hz to 50kHz squarewave adjustable in 20us steps. 3 digit resolution.

Available for external use from the SYNC OUT socket.

## Technical Specifications continued

### ARBITRARY WAVEFORM EDITING

Basic arbitrary waveform creation and editing tools are built into the instrument. Arbitrary waveforms can be built-up using insertion of standard waveforms between points, point by point value setting, and straight line drawing between points.

### WAVECAD Software

The TGA1230 is supplied with a copy of WaveCad, an arbitrary waveform editing software for Windows 95 or Windows 3.1. It has a graphical environment and uses drawing tools, mathematical expressions and insertion from waveform libraries to rapidly create or modify waveforms which are then downloaded using RS-232 or GPIB interfaces.

### DATA IMPORT AND EXPORT

#### Direct Import from DSOs

PC based software Applet is available which enables data captured by Tektronix DSOs to be imported into the TGA1230.

#### LabVIEW® driver

LabVIEW driver for National Instruments LabVIEW is available. This enables data to be loaded from other instruments (such as DSOs) that have a LabVIEW driver.

### INTERFACES

All remote control and waveform download facilities are available through the RS232 (standard) or optional GPIB interfaces.

RS-232: Variable Baud rate, 9600 Baud maximum. 9-pin D-connector. Fully compatible with TTI ARC (Addressable RS232 Chain) system.

GPIB (Option): Conforming with IEEE488.1 and IEEE488.2

### INPUTS

#### Trig In

Frequency Range: DC - 1MHz.  
Signal Range: Threshold nominally TTL level; max. input  $\pm 10V$ .  
Pulse Width: 50ns for Trigger and Gate modes; 50 $\mu s$  for Sweep mode; 20ms for Tone mode.  
Output Impedance: 10k

#### MAN In

Frequency Range: DC - 100kHz.  
Signal Range: 2.5V for 100% level change at maximum output.  
Output Impedance: Typically 6k

#### Man In

Frequency Range: DC - 10MHz.  
Signal Range: Approximately 5Vpk-pk input for 20Vpk-pk output.  
Output Impedance: Typically 1k2

#### Hold

Holds an arbitrary waveform at its current position. A TTL low level or switch closure causes the waveform to stop at the current position. The front panel HOLD key or remote command may also be used to control the Hold function. While held a rising edge at TRIG IN will return the waveform to the start. The front panel MAN/SYNC key or remote command may also be used to return the waveform to the start.

Output Impedance: 10k

#### Reference Clock In/Out

Reference to Input: Input for an external 10MHz reference clock. TTL/CMOS threshold level.

Reference to Output: Buffered version of the internal 10MHz clock. Output levels nominally 1V and 4V from 50

Reference to Phase Lock: Used together with SYNC OUT on a master and the TRIG IN on a slave to synchronise (phase lock) multiple instruments.

### OUTPUTS

#### Main Output

Output Impedance: 50  
Amplitude: 5mV to 20V pk-pk open circuit (2.5mV to 10V pk-pk into 50). Amplitude can be specified open circuit (Hi Z) or into an assumed load of 50 or 600, in Vpk-pk, Vrms or dBm.

Amplitude Accuracy: Better than 2%  $\pm 1mV$  at 1kHz into 50  
Amplitude Flatness:  $\pm 0.2dB$  to 200 kHz;  $\pm 1dB$  to 5MHz;  $\pm 2dB$  to 10MHz.  
DC Offset Range:  $\pm 10V$ . DC offset plus signal peak limited to  $\pm 10V$  from 50

DC Offset Accuracy: Typically within  $\pm 3\% \pm 10mV$ , unattenuated.  
Resolution: 3 digits or 1mV for both Amplitude and DC Offset

#### Sync Out

Multifunction output user definable or automatically selected to be any of the following:

Waveform Sync: (all waveforms) A square wave with 50% duty cycle at the main waveform frequency, or a pulse coincident with the first few points of an arbitrary waveform.  
Position Markers: (Arbitrary only) Any point(s) on the waveform may have associated marker bit(s) set high or low.  
Burst Done: Produces a pulse coincident with the last cycle of a burst.

Sequence Sync: Produces a pulse coincident with the end of a waveform sequence.

Trigger: Selects the current trigger signal. Useful for synchronising burst or gated signals.

Sweep Sync: Outputs a pulse at the start of sweep to synchronise an oscilloscope or recorder.

Phase Lock Out: Used to phase lock two or more generators. Produces a positive edge at the 0° phase point.

Output Signal Level: TTL/CMOS logic levels from typically 50

#### Cursor/Marker Out

Adjustable output pulse for use as a marker in sweep mode or as a cursor in arbitrary waveform editing mode. Can be used to modulate the Z-axis of an oscilloscope or be displayed on a second scope channel.

Output Signal Level: Adjustable from nominally 2V to 14V, normal or inverted; adjustable width as a cursor.

Output Impedance: 600 typical

### GENERAL

Display: 20 character x 4 row alphanumeric LCD.  
Data Entry: Keyboard selection of mode, waveform etc.; value entry by numeric keys or by rotary control.  
Stored Settings: Up to 9 complete instrument set-ups may be stored and recalled from battery-backed memory. Up to 50 arbitrary waveforms can also be stored independent of the instrument settings.  
Size: 3U (130mm) height; half-rack (212mm) width; 330mm deep.  
Weight: 4.1kg. (9lb.)  
Power: 230V, 115V or 100V nominal 50/60Hz, adjustable internally; operating range  $\pm 14\%$  of nominal; 40VA max. Installation Category II.  
Operating Range: +5°C to 40°C, 20-80% RH.  
Storage Range: -20°C to +60°C.  
Environmental: Indoor use at altitudes to 2km, Pollution Degree 1.  
Options: IEEE-488 interface; 19 inch rack mounting kit.  
Safety: Complies with EN61010-1.  
EMC: Complies with EN50081-1 and EN50082-1.

Thurlby Thandar Instruments Ltd. operates a policy of continuous development and reserves the right to alter specifications without prior notice.

Designed and built in the U.K. by:



Thurlby Thandar Instruments Ltd.

Glebe Road, Huntingdon, Cambs. PE18 7DX England

Tel: 01480 412451 Fax: 01480 450409

Email: sales@ttinst.co.uk Web: www.ttinst.co.uk

**A6. Specifications on the BK electronics MXF900 power amplifier**



Pro Audio



Ref. No	Description	
<b>MXF900</b>	450W x 450W Mosfet Amplifier 19" 3U	

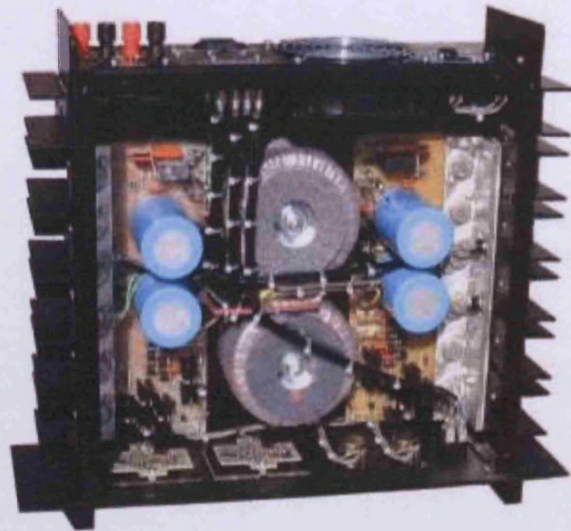
### FEATURES

- Independent power supplies (one per channel)
- Two toroidal mains transformers
- Power ratings R.M.S. with both channels driven
- Twin L.E.D. Vu Meters
- DC Loudspeaker Protection
- 3 Second Anti-Thump Delay
- Thermal Protection
- Fan Cooling
- Earth Lift Switch
- Jack and XLR Input connections
- XLR and Binding Post Output Connections
- Advanced Mosfets Design



The MXF 900 utilises the latest Mosfet output devices incorporated into a sophisticated design. The advanced circuitry achieves a superb specification which results in the exceptional clarity and realism now essential to complement today's high-technology sound equipment

Realising that reliability is another important factor, Independant power supplies are used with two toroidal mains transformers. These features, and more, combined with a rugged construction, are offered at a very realistic price/power/performance ratio which is a must for the discerning musician, bands, groups disco's, clubs theatres and the studio recording industry



### Specifications

R.M.S. Watts into 4 Ohms	455 Per Channel
R.M.S. Watts into 8 Ohms	305 Per Channel
3dB Power Bandwidth	1Hz - 50Khz
Damping Factor	>300
Slew Rate	75/uS
Full Power t.h.d.	0.005%
T.h.d. Typical	0.001%
T.i.d	Zero
Input Sensitivity	775mV
Input Impedance	7.5K Ohms
S/N Ratio	110dB
Vu Metering	Visual Display of 11 L.E.D.s zero dBs at rated power
DC loudspeaker Protection	+/- 3V DC
Anti - Thump Loudspeaker Connection Delay	3 Seconds
Thermal Protection	90 Deg Centigrade
Fan Cooling	60 Deg Centigrade
Power Requirements - Supply	240V AC 50 - 60Hz
Weight	15Kg
Size - Front Panel	19" (482.6mm) x (3U)
Size - Depth	374.5mm

***A7. S-function code for space-vector modulation of matrix converters (Matlab-Simulink environment)***

```

#define S_FUNCTION_NAME svm_matrix
#define S_FUNCTION_LEVEL 2

#define NUM_PARAM      1
#define NUM_INPUTS     4
#define NUM_OUTPUTS    9
#define NUM_SAMPLETIMES 2
#define NUM_RWORK      14

#define PI      3.1415926535897932384626433832795
#define TWOPI  6.283185307179586476925286766559
#define TWOPI_3 2.0943951023931954923084289221863
#define PI_2   1.5707963267948966192313216916398
#define PI_3   1.0471975511965977461542144610932
#define TWO_3  0.66666666666666666666666666666667
#define SQRT2  1.4142135623730950488016887242097
#define SQRT3  1.7320508075688772935274463415059
#define I_SQRT3 0.57735026918962576450914878050196

#define Tc (mxGetPr(ssGetSFcnParam(S,0))[0]) // parameter 0

```

```

#include <math.h>
#include "simstruc.h"

```

```

static void mdlInitializeSizes(SimStruct *S)
{
    ssSetNumSFcnParams(S, NUM_PARAM);
    if (ssGetNumSFcnParams(S) != ssGetSFcnParamsCount(S)) return; //
parameter mismatch will be reported by Simulink

    if (!ssSetNumInputPorts(S, 1)) return;
    ssSetInputPortWidth(S, 0, NUM_INPUTS);
    ssSetInputPortDirectFeedThrough(S, 0, 1);

    if (!ssSetNumOutputPorts(S,1)) return;
    ssSetOutputPortWidth(S, 0, NUM_OUTPUTS);

    ssSetNumSampleTimes(S, NUM_SAMPLETIMES);

    ssSetNumRWork(S, NUM_RWORK);

    ssSetOptions(S, SS_OPTION_EXCEPTION_FREE_CODE);
}

```

```

static void mdlInitializeSampleTimes(SimStruct *S)
{
    ssSetSampleTime(S, 0, CONTINUOUS_SAMPLE_TIME);
    ssSetOffsetTime(S, 0, 0);

    ssSetSampleTime(S, 1, Tc);
    ssSetOffsetTime(S, 1, 0);
}

```

```

#define MDL_INITIALIZE_CONDITIONS
static void mdlInitializeConditions(SimStruct *S)
{
    real_T *rwork = ssGetRWork(S);
    int_T i;

    for (i = 0; i < ssGetNumRWork(S); i++) rwork[i] = 0;
}

```

```

static void mdlOutputs(SimStruct *S, int_T tid)
{
    InputRealPtrsType u = ssGetInputPortRealSignalPtrs(S,0);
    real_T *y = ssGetOutputPortRealSignal(S,0);
    real_T *rwork = ssGetRWork(S);

    int Ki, Kv, vector;
    float tI, tII, tIII, tIV, t0, t0_3, twot0_3;
    float time;
    float q, qT_sqrt3, bm, br, am, ar;
    float cosbminus, cosbplus, cosaminus, cosapulus;
    float ualpha_in, ubeta_in, ualpha_out, ubeta_out;
    float Vop, wot, Vip, wit;
    float t1, t2, t3, t4, t5, t6, t7, t8, t9, t10, t11, t12;

    typedef int VectorSequence[13];

    VectorSequence *pVS;

    VectorSequence VS[6][6]=
    {
        { // Ki = 1, Kv = 1..6
        {21, 6, 17, 19, 14, 1, 20, 1, 14, 19, 17, 6, 21}, // {O3 -3 9 O1 -7 1 O2}
        {21, 12, 17, 19, 14, 7, 20, 7, 14, 19, 17, 12, 21}, // {O3 -6 9 O1 -7 4 O2}
        {21, 12, 5, 19, 2, 7, 20, 7, 2, 19, 5, 12, 21}, // {O3 -6 3 O1 -1 4 O2}
        {21, 18, 5, 19, 2, 13, 20, 13, 2, 19, 5, 18, 21}, // {O3 -9 3 O1 -1 7 O2}
        {21, 18, 11, 19, 8, 13, 20, 13, 8, 19, 11, 18, 21}, // {O3 -9 6 O1 -4 7 O2}
        {21, 6, 11, 19, 8, 1, 20, 1, 8, 19, 11, 6, 21} // {O3 -3 6 O1 -4 1 O2}
        },
}

```

{ // Ki = 2, Kv = 1..6

{20, 16, 3, 21, 6, 17, 19, 17, 6, 21, 3, 16, 20}, // {O2 -8 2 O3 -3 9 O1}  
{20, 16, 9, 21, 12, 17, 19, 17, 12, 21, 9, 16, 20}, // {O2 -8 5 O3 -6 9 O1}  
{20, 4, 9, 21, 12, 5, 19, 5, 12, 21, 9, 4, 20}, // {O2 -2 5 O3 -6 3 O1}  
{20, 4, 15, 21, 18, 5, 19, 5, 18, 21, 15, 4, 20}, // {O2 -2 8 O3 -9 3 O1}  
{20, 10, 15, 21, 18, 11, 19, 11, 18, 21, 15, 10, 20}, // {O2 -5 8 O3 -9 6 O1}  
{20, 10, 3, 21, 6, 11, 19, 11, 6, 21, 3, 10, 20} // {O2 -5 2 O3 -3 6 O1}  
},

{ // Ki = 3, Kv = 1..6

{19, 2, 13, 20, 16, 3, 21, 3, 16, 20, 13, 2, 19}, // {O1 -1 7 O2 -8 2 O3}  
{19, 8, 13, 20, 16, 9, 21, 9, 16, 20, 13, 8, 19}, // {O1 -4 7 O2 -8 5 O3}  
{19, 8, 1, 20, 4, 9, 21, 9, 4, 20, 1, 8, 19}, // {O1 -4 1 O2 -2 5 O3}  
{19, 14, 1, 20, 4, 15, 21, 15, 4, 20, 1, 14, 19}, // {O1 -7 1 O2 -2 8 O3}  
{19, 14, 7, 20, 10, 15, 21, 15, 10, 20, 7, 14, 19}, // {O1 -7 4 O2 -5 8 O3}  
{19, 2, 7, 20, 10, 3, 21, 3, 10, 20, 7, 2, 19} // {O1 -1 4 O2 -5 2 O3}  
},

{ // Ki = 4, Kv = 1..6

{21, 18, 5, 19, 2, 13, 20, 13, 2, 19, 5, 18, 21}, // {O3 -9 3 O1 -1 7 O2}  
{21, 18, 11, 19, 8, 13, 20, 13, 8, 19, 11, 18, 21}, // {O3 -9 6 O1 -4 7 O2}  
{21, 6, 11, 19, 8, 1, 20, 1, 8, 19, 11, 6, 21}, // {O3 -3 6 O1 -4 1 O2}  
{21, 6, 17, 19, 14, 1, 20, 1, 14, 19, 17, 6, 21}, // {O3 -3 9 O1 -7 1 O2}  
{21, 12, 17, 19, 14, 7, 20, 7, 14, 19, 17, 12, 21}, // {O3 -6 9 O1 -7 4 O2}  
{21, 12, 5, 19, 2, 7, 20, 7, 2, 19, 5, 12, 21} // {O3 -6 3 O1 -1 4 O2}  
},

{ // Ki = 5, Kv = 1..6

{20, 4, 15, 21, 18, 5, 19, 5, 18, 21, 15, 4, 20}, // {O2 -2 8 O3 -9 3 O1}  
{20, 10, 15, 21, 18, 11, 19, 11, 18, 21, 15, 10, 20}, // {O2 -5 8 O3 -9 6 O1}  
{20, 10, 3, 21, 6, 11, 19, 11, 6, 21, 3, 10, 20}, // {O2 -5 2 O3 -3 6 O1}  
{20, 16, 3, 21, 6, 17, 19, 17, 6, 21, 3, 16, 20}, // {O2 -8 2 O3 -3 9 O1}  
{20, 16, 9, 21, 12, 17, 19, 17, 12, 21, 9, 16, 20}, // {O2 -8 5 O3 -6 9 O1}  
{20, 4, 9, 21, 12, 5, 19, 5, 12, 21, 9, 4, 20} // {O2 -2 5 O3 -6 3 O1}  
},

{ // Ki = 6, Kv = 1..6

{19, 14, 1, 20, 4, 15, 21, 15, 4, 20, 1, 14, 19}, // {O1 -7 1 O2 -2 8 O3}  
{19, 14, 7, 20, 10, 15, 21, 15, 10, 20, 7, 14, 19}, // {O1 -7 4 O2 -5 8 O3}  
{19, 2, 7, 20, 10, 3, 21, 3, 10, 20, 7, 2, 19}, // {O1 -1 4 O2 -5 2 O3}  
{19, 2, 13, 20, 16, 3, 21, 3, 16, 20, 13, 2, 19}, // {O1 -1 7 O2 -8 2 O3}  
{19, 8, 13, 20, 16, 9, 21, 9, 16, 20, 13, 8, 19}, // {O1 -4 7 O2 -8 5 O3}  
{19, 8, 1, 20, 4, 9, 21, 9, 4, 20, 1, 8, 19} // {O1 -4 1 O2 -2 5 O3}  
}  
};

```

typedef int SwitchesStates[9];

SwitchesStates *pVCT;

SwitchesStates VCT[22] =
{
    // SAa, SBa, SCa, SAb, SBb, SCb, SAc, SBc, SCc
    {0, 0, 0, 0, 0, 0, 0, 0, 0}, // dummy for vectors to start from VCT[1]
    {1, 0, 0, 0, 1, 0, 0, 1, 0}, // +1
    {0, 1, 0, 1, 0, 0, 1, 0, 0}, // -1
    {0, 1, 0, 0, 0, 1, 0, 0, 1}, // +2
    {0, 0, 1, 0, 1, 0, 0, 1, 0}, // -2
    {0, 0, 1, 1, 0, 0, 1, 0, 0}, // +3
    {1, 0, 0, 0, 0, 1, 0, 0, 1}, // -3
    {0, 1, 0, 1, 0, 0, 0, 1, 0}, // +4
    {1, 0, 0, 0, 1, 0, 1, 0, 0}, // -4
    {0, 0, 1, 0, 1, 0, 0, 0, 1}, // +5
    {0, 1, 0, 0, 0, 1, 0, 1, 0}, // -5
    {1, 0, 0, 0, 0, 1, 1, 0, 0}, // +6
    {0, 0, 1, 1, 0, 0, 0, 0, 1}, // -6
    {0, 1, 0, 0, 1, 0, 1, 0, 0}, // +7
    {1, 0, 0, 1, 0, 0, 0, 1, 0}, // -7
    {0, 0, 1, 0, 0, 1, 0, 1, 0}, // +8
    {0, 1, 0, 0, 1, 0, 0, 0, 1}, // -8
    {1, 0, 0, 1, 0, 0, 0, 0, 1}, // +9
    {0, 0, 1, 0, 0, 1, 1, 0, 0}, // -9
    {1, 0, 0, 1, 0, 0, 1, 0, 0}, // O1
    {0, 1, 0, 0, 1, 0, 0, 1, 0}, // O2
    {0, 0, 1, 0, 0, 1, 0, 0, 1} // O3
};

```

```
time = ssGetT(S);
```

```
if (ssIsSampleHit(S, 1, tid))
```

```

{
    ualpha_in = *u[0];
    ubeta_in = *u[1];
    ualpha_out = *u[2];
    ubeta_out = *u[3];

    // start voltage input vector Vip - wit
    if (ubeta_in == 0) ubeta_in = 0.00000001;
    wit = atan2(ubeta_in, ualpha_in);
    if (wit < 0) wit += TWOPI;
    Vip = sqrt(ualpha_in*ualpha_in+ubeta_in*ubeta_in);
    // end voltage input vector Vip - wit

    // start voltage output vector Vop - wot
    if (ubeta_out == 0) ubeta_out = 0.00000001;
    wot = atan2(ubeta_out, ualpha_out);
}

```

```

if (wot < 0) wot += TWOPI;
Vop = sqrt(ualpha_out*ualpha_out+ubeta_out*ubeta_out);
// end voltage output vector Vop - wot

// start calculate modulation index
q = Vop/Vip;
if (q > sqrt(3)/2) q = sqrt(3)/2;
qT_sqrt3 = q*Tc/SQRT3;
// end calculate modulation index

// start determine Ki and angle bm
Ki = (wit+PI_2)/PI_3;
if (Ki == 7) Ki = 1;
br = ((float)Ki-1)*PI_3;
bm = wit-br;
if (bm > PI) bm -= TWOPI;

cosbminus = cos(bm-PI_3);
cosbplus = cos(bm+PI_3);
// end determine Ki and angle bm

// start determine Kv and angle am
Kv = (wot+PI_3)/PI_3;
ar = ((float)Kv-0.5)*PI_3;
am = wot-ar;

cosaminus = cos(am-PI_3);
cosaplus = cos(am+PI_3);
// end determine Kv and angle am

// start times calculation for unitary power factor (phi_in = 0)
tI = qT_sqrt3*cosaminus*cosbminus;
tII = qT_sqrt3*cosaminus*cosbplus;
tIII = qT_sqrt3*cosaplus*cosbminus;
tIV = qT_sqrt3*cosaplus*cosbplus;

t0 = Tc/2-(tI+tII+tIII+tIV);

t0_3 = t0/3;
twot0_3 = 2*t0_3;
// end times calculation for unitary power factor (phi_in = 0)

if ((Ki+Kv) & 1)
{
    t1 = time+t0_3;
    t2 = t1+tI;
    t3 = t2+tIII;
    t4 = t3+t0_3;
    t5 = t4+tIV;
    t6 = t5+tII;
}

```

```

    t7 = t6+twot0_3;
    t8 = t7+tII;
    t9 = t8+tIV;
    t10 = t9+t0_3;
    t11 = t10+tIII;
    t12 = t11+tI;
}
else
{
    t1 = time+t0_3;
    t2 = t1+tIII;
    t3 = t2+tI;
    t4 = t3+t0_3;
    t5 = t4+tII;
    t6 = t5+tIV;
    t7 = t6+twot0_3;
    t8 = t7+tIV;
    t9 = t8+tII;
    t10 = t9+t0_3;
    t11 = t10+tI;
    t12 = t11+tIII;
}

```

```

rwork[0] = Ki;
rwork[1] = Kv;
rwork[2] = t1;
rwork[3] = t2;
rwork[4] = t3;
rwork[5] = t4;
rwork[6] = t5;
rwork[7] = t6;
rwork[8] = t7;
rwork[9] = t8;
rwork[10] = t9;
rwork[11] = t10;
rwork[12] = t11;
rwork[13] = t12;
}

```

```

Ki = rwork[0];
Kv = rwork[1];
t1 = rwork[2];
t2 = rwork[3];
t3 = rwork[4];
t4 = rwork[5];
t5 = rwork[6];
t6 = rwork[7];
t7 = rwork[8];
t8 = rwork[9];
t9 = rwork[10];

```

```
t10 = rwork[11];
t11 = rwork[12];
t12 = rwork[13];
```

```
    pVS = &VS[Ki-1][Kv-1]; // determine switching sequence for current
Ki, Kv
```

```
if (time < t1) pVCT = &VCT[*pVS][0];
else if ((time >= t1) && (time < t2)) pVCT = &VCT[*pVS][1];
else if ((time >= t2) && (time < t3)) pVCT = &VCT[*pVS][2];
else if ((time >= t3) && (time < t4)) pVCT = &VCT[*pVS][3];
else if ((time >= t4) && (time < t5)) pVCT = &VCT[*pVS][4];
else if ((time >= t5) && (time < t6)) pVCT = &VCT[*pVS][5];
else if ((time >= t6) && (time < t7)) pVCT = &VCT[*pVS][6];
else if ((time >= t7) && (time < t8)) pVCT = &VCT[*pVS][7];
else if ((time >= t8) && (time < t9)) pVCT = &VCT[*pVS][8];
else if ((time >= t9) && (time < t10)) pVCT = &VCT[*pVS][9];
else if ((time >= t10) && (time < t11)) pVCT = &VCT[*pVS][10];
else if ((time >= t11) && (time < t12)) pVCT = &VCT[*pVS][11];
else if (time >= t12) pVCT = &VCT[*pVS][12];
```

```
y[0] = (*pVCT)[0];
y[1] = (*pVCT)[1];
y[2] = (*pVCT)[2];
y[3] = (*pVCT)[3];
y[4] = (*pVCT)[4];
y[5] = (*pVCT)[5];
y[6] = (*pVCT)[6];
y[7] = (*pVCT)[7];
y[8] = (*pVCT)[8];
```

```
}
```

```
static void mdlTerminate(SimStruct *S)
```

```
{
}
```

```
#ifndef MATLAB_MEX_FILE // Is this file being compiled as a MEX-file?
```

```
#include "simulink.c" // MEX-file interface mechanism
```

```
#else
```

```
#include "cg_sfun.h" // Code generation registration function
```

```
#endif
```

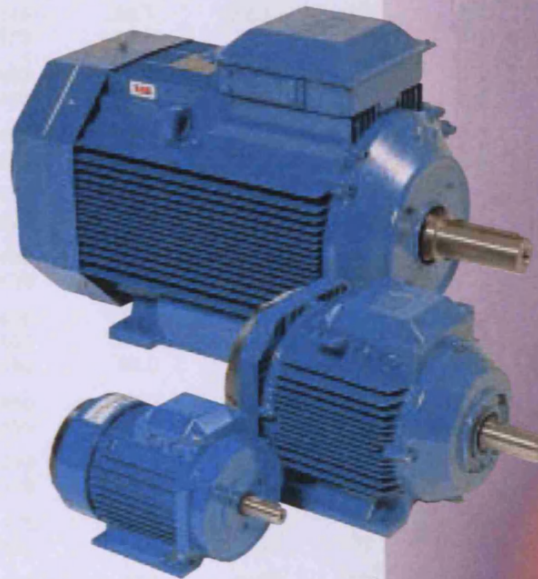
***A8. Technical data on 15kW and 3kW ABB induction motors***

*Basse tension*

## MOTEURS FERMÉS IP 55 ROTOR A CAGE GAMME ALUMINIUM



- Type 71 à 250
- 0,09 à 55 kW
- Mono et bivitesse



### Une gamme de moteurs performants

- Rendement élevé
- Isolation classe F échauffement classe B pour une durée de vie quadruplée
- Réserve thermique de 25 %
- Conçu pour être alimenté par un réseau triphasé européen 220/230, 380/415 V 50 Hz
- Palier-bridés en fonte
- Roulements à forte capacité de charge

### Une protection efficace

- IP 55
- Haute protection contre la corrosion en environnement industriel, chimique et extérieur

### Moteurs d'une exceptionnelle adaptabilité

- Système de brides modulaires à partir d'un seul type de moteur de base sans changement de rotor

### Une disponibilité immédiate

- Stock disponible chez votre concessionnaire
- Livraison d'usine en 72 heures

**Totally enclosed squirrel cage  
three phase motors, aluminium frame  
IP 55 IC 411**

**400 V 50 Hz**

Output kW	Motor type M2AA	Product code 3GAA	Speed r/min	Effi- ciency %	Power factor cos φ	Current		Torque		
						$I_N$ A	$\frac{I_s}{I_N}$	$T_N$ Nm	$\frac{T_s}{T_N}$	$\frac{T_{max}}{T_N}$
<b>1500 r/min = 4 poles</b>										
<b>Basic design</b>										
0.18	63 B	062 001-●	1370	58.7	0.63	0.72	3.0	1.25	2.2	2.6
0.18	63 B <sup>1)</sup>	062 002-●	1370	58.7	0.63	0.72	3.0	1.25	2.2	2.6
0.25	71 A	072 001-●	1400	66.8	0.67	0.83	3.5	1.7	2.2	2.7
0.37	71 B	072 002-●	1410	70.5	0.69	1.12	4.0	2.5	2.2	2.7
0.55	80 A	082 001-●	1420	74	0.73	1.45	4.0	3.7	2.2	2.7
0.75	80 B	082 002-●	1420	77	0.74	1.9	4.5	5.0	2.2	2.7
1.1	90 S	092 001-●	1410	77.5	0.81	2.59	5.0	7.5	2.2	2.7
1.5	90 L	092 002-●	1420	80.3	0.79	3.45	5.0	10.0	2.4	2.9
2.2	100 LA	102 001-●	1430	81.7	0.81	4.8	5.5	15.0	2.4	2.9
3	100 LB	102 002-●	1430	83.5	0.81	6.48	5.5	20.0	2.5	2.9
4	112 M	112 001-●	1435	84.5	0.80	8.6	7.0	26.6	2.9	3.1
5.5	132 S	132 001-●	1450	87.0	0.83	11.1	7.3	36.2	2.2	3.0
7.5	132 M	132 002-●	1450	88.0	0.83	14.8	7.9	49.4	2.5	3.2
11	160 M	162 001-●	1460	90.3	0.81	21.5	6.7	72	2.9	2.8
15	160 L	162 002-●	1455	91.1	0.84	28.5	6.8	98	3.0	2.8
18.5	180 M	182 001-●	1470	92.3	0.84	35	7.0	120	3.1	2.7
22	180 L	182 002-●	1470	92.4	0.83	41	7.0	143	2.9	2.8
30	200 MLA	202 001-●	1475	92.9	0.83	56	6.7	194	2.6	2.8
37	225 SMA	222 001-●	1480	93.6	0.84	68	6.6	239	2.4	2.5
45	225 SMB	222 002-●	1480	94.2	0.83	83	6.7	290	2.7	2.6
55	250 SMA	252 001-●	1480	94.6	0.86	98	7.5	355	2.3	2.8

**1500 r/min = 4 poles**      **High-output design <sup>2)</sup>**

0.55 <sup>3)</sup>	71 C	072 003-●	1380	72.5	0.73	1.5	4.0	3.7	2.2	2.4
1.1 <sup>3)</sup>	80 C	082 003-●	1380	76.1	0.80	2.65	4.5	7.5	2.0	2.2
1.85 <sup>3)4)</sup>	90 L	092 003-●	1390	79.5	0.80	4.4	4.5	13.0	2.2	2.4
2.2 <sup>3)</sup>	90 LB	092 004-●	1390	80.3	0.83	4.85	4.5	15.0	2.2	2.4
4 <sup>3)</sup>	100 LC	102 003-●	1420	82.7	0.82	8.73	5.5	27.0	2.5	2.8
5.5 <sup>3)</sup>	112 MB	112 002-●	1425	84.5	0.83	11.4	7.1	36.9	2.8	3.1
11 <sup>3)</sup>	132 MB	132 003-●	1450	88.0	0.86	21	8.3	72.4	3.0	2.7
18.5 <sup>3)</sup>	160 LB	162 003-●	1450	90.5	0.84	36	6.9	122	2.9	2.9
30 <sup>3)</sup>	180 LB	182 003-●	1465	92.5	0.84	56	6.9	195	3.2	2.8
37	200 MLB	202 002-●	1475	93.4	0.84	68	7.8	236	3.6	3.2
55	225 SMC	222 003-●	1480	94.6	0.84	100	7.3	355	3.1	2.8
75	250 SMB	252 002-●	1480	95.0	0.86	132	7.0	484	2.4	3.0

<sup>1)</sup> Shaft Ø14 mm, large flange F 130. <sup>2)</sup> **High-output design** The output of these motors is one step higher than the basic design with rated outputs in accordance with CENELEC. Motor sizes 112 to 132 are somewhat longer than the basic design. <sup>3)</sup> Temperature rise class F. <sup>4)</sup> Lower than CENELEC +1.

The bullet indicates a 3-letter product code supplement for choice of mounting arrangement (page 11, pos. 12), voltage and frequency (below) and generation code (page 11, pos. 14).

**Code letters for supplementing the product code**

Motor size	Code letter for voltage and frequency Direct start or, with Δ-connection, also Y/Δ-start									
	S		D		H	E	F	T	U	- X
	50 Hz	60 Hz	50 Hz	60 Hz	50 Hz	50 Hz	50 Hz	50 Hz	50 Hz	
63-100	220-240 VΔ 380-420 VY	440-480 VY	380-420 VΔ 660-690 VY	440-480 VΔ	-	500 VΔ	500 VY	660 VΔ <sup>1)</sup>	690 VΔ <sup>1)</sup>	Other rated voltage, connection or frequency, 690 V maximum
112-132	220-240 VΔ 380-420 VY	440-480 VY	380-420 VΔ 660-690 VY	440-480 VΔ	415 VΔ	500 VΔ		660 VΔ	690 VΔ	
160-250	220, 230 VΔ 380,400,415 VY	440 VY	380,400,415VΔ 660, 690 VY	440 VΔ	415VΔ	500 VΔ		660 VΔ	690VΔ	

<sup>1)</sup> On request.

## Insulation class F Temperature rise class B

**380 V 50 Hz**

**415 V 50 Hz**

Output kW	Speed r/min	Efficiency %	Power factor cos φ	Current I <sub>N</sub> A	Speed r/min	Efficiency %	Power factor cos φ	Current I <sub>N</sub> A	Moment of inertia J = 1/4 GD <sup>2</sup> kgm <sup>2</sup>	Weight Foot-mounted motor kg	Sound pressure level L <sub>p</sub> dB(A)
<b>1500 r/min = 4 poles      Basic design</b>											
0.18	1370	60.6	0.68	0.68	1370	56.9	0.60	0.75	0.00028	4.5	37
0.18	1370	60.6	0.68	0.68	1370	56.9	0.60	0.75	0.00028	4.5	37
0.25	1400	67.9	0.72	0.80	1410	65.4	0.63	0.89	0.00073	5.5	45
0.37	1400	70.8	0.74	1.11	1420	69.7	0.66	1.15	0.00098	6.5	45
0.55	1410	73.6	0.78	1.45	1420	73.5	0.70	1.48	0.0017	9	48
0.75	1410	76.4	0.78	1.90	1430	76.7	0.70	1.95	0.0021	10	48
1.1	1410	76.3	0.83	2.66	1430	77.7	0.76	2.60	0.0032	13	50
1.5	1420	79.9	0.82	3.5	1430	80.3	0.77	3.45	0.0043	16	50
2.2	1430	80.6	0.85	4.96	1430	81.8	0.78	4.85	0.0069	21	54
3	1430	82.6	0.85	6.61	1430	83.1	0.77	6.55	0.0082	24	54
4	1425	84.0	0.83	8.7	1440	85.0	0.75	8.80	0.015	27	56
5.5	1445	86.0	0.85	11.5	1455	87.5	0.81	10.9	0.031	40	59
7.5	1445	87.0	0.86	15.3	1455	88.0	0.82	14.5	0.038	48	59
11	1450	89.9	0.83	22.5	1465	90.5	0.79	21.5	0.067	75	62
15	1445	90.6	0.84	30.0	1460	91.4	0.83	28	0.091	94	62
18.5	1465	91.7	0.85	36.0	1470	92.2	0.83	34.0	0.161	124	62
22	1465	92.1	0.85	42.5	1475	92.6	0.82	40.0	0.191	141	63
30	1470	92.6	0.83	59	1475	93.0	0.83	54	0.29	180	63
37	1475	93.4	0.84	72	1480	93.7	0.81	68	0.37	215	66
45	1475	94.0	0.85	86	1480	94.2	0.81	82	0.42	230	66
55	1475	94.3	0.86	103	1480	94.7	0.84	96	0.72	275	67

### 1500 r/min = 4 poles      High-output design <sup>2)</sup>

0.55 <sup>3)</sup>	1370	71.9	0.78	1.51	1390	72.5	0.68	1.55	0.0012	7.5	45
1.1 <sup>3)</sup>	1370	73.7	0.84	2.76	1400	76.8	0.76	2.6	0.0024	11	48
1.85 <sup>3)4)</sup>	1380	78.8	0.83	4.4	1400	79.5	0.76	4.35	0.0043	16	50
2.2 <sup>3)</sup>	1380	78.4	0.85	5.1	1400	80.8	0.80	4.9	0.0048	17	50
4 <sup>3)</sup>	1410	81.5	0.85	8.89	1420	82.9	0.77	8.8	0.009	25	54
5.5 <sup>3)</sup>	1415	84.5	0.85	11.7	1430	85.5	0.79	11.4	0.018	34	56
11 <sup>3)</sup>	1445	87.5	0.87	22	1455	88.5	0.83	21	0.048	59	59
18.5 <sup>3)</sup>	1440	89.8	0.85	37	1450	90.8	0.83	34	0.102	103	63
30 <sup>3)</sup>	1465	92.2	0.85	58	1470	92.7	0.82	55	0.225	161	63
37	1475	93.3	0.85	71	1475	93.3	0.82	67	0.34	205	63
55	1475	94.5	0.84	105	1480	94.6	0.82	99	0.49	265	66
75	1475	94.5	0.87	139	1480	95.1	0.86	128	0.88	335	67

<sup>3)</sup> Temperature rise class F.

<sup>4)</sup> Lower than CENELEC + 1.

### Recalculation factors

Recalculation factors for current at rated voltages other than 400 V 50 Hz

Rated voltage at 50 Hz  
and motor wound for

Recalculation factor

220 V	1.82
230 V	1.74
415 V	0.96
500 V	0.80
660 V	0.61
690 V	0.58

